II.H Beyond Li-ion R&D: Metallic Lithium and Solid Electrolytes

II.H.1 Mechanical Properties at the Protected Lithium Interface (ORNL)

Nancy Dudney, Principal Investigator
Oak Ridge National Laboratory
P.O. Box 2008, MS6124
Oak Ridge, TN 37831
Phone: 865-576-4874
E-mail: dudneynj@ornl.gov

Erik Herbert, Principal Investigator
Michigan Technological University
604 M&M Building
1400 Townsend Drive
Houghton, MI 49931
Phone: 906-4872633
E-mail: eherbert@mtu.edu

Jeff Sakamoto, Principal Investigator
University of Michigan
2350 Hayward Avenue
Ann Arbor, MI 48109
Phone: 734-763-2219
E-mail: jeffsaka@umich.edu

Tien Duong, Technology Manager
U.S. Department of Energy
Phone: 202-586-7836
E-mail: Tien.Duong@ee.doe.gov

Project Introduction

A stable lithium anode is critical to achieve high energy density with excellent safety, lifetime and cycling efficiency. Instability and/or high resistance at the interface of lithium metal with various solid electrolytes limit the use of the metallic anode for batteries with high energy density batteries, such as Li-air and Li-S. The critical impact of this endeavor will be a much deeper analysis of the degradation, so that materials can be engineered to fulfill the target level of performance for EV batteries, namely 1000 cycles and 15 year lifetime, with adequate pulse power.

Objectives

This project will develop the understanding of the Li metal-solid electrolyte interface through state of the art nanoindentation and other mechanical methods coupled with solid electrolyte fabrication and electrochemical cycling. Our goal is to provide the critical information that will enable transformative insights into the complex coupling between the microstructure, its defects and the mechanical behavior of Li metal anodes.

Approach

Generally, the cycling of lithium is investigated electrochemically. Here we are testing the mechanical properties the solid electrolyte and the lithium independently, and then the interfaces formed of lithium with the solid electrolyte. This provides not only important materials characterization, but a real-time measure of how lithium moves in response to cycling through a solid electrolyte. The solid electrolytes investigated included a glassy lithium phosphorus oxynitride (Lipon) electrolyte and the polycrystalline garnet electrolyte of lithium lanthanum zirconium oxide (LLZO). In addition, Li metal was characterized on smooth glass surfaces. In all cases the samples were well protected from air and humidity during processing and tests.

Mechanical properties studies through state of the art nanoindentation techniques are used to probe the surface properties of the solid electrolyte and the changes to the lithium that result from prolonged electrodeposition and dissolution at the interface. High speed mapping of large indentation arrays provides statistically relevant distributions of the properties relative to microstructural features. The nanoindentation approach benefitted from a close collaboration with associates at Nanomechanics, Inc. of Oak Ridge TN for continuing refinements in both hardware, software and firmware for the NanoFlip and iNano systems used in this investigation. Further, Prof. Steve Hackney of Michigan Technological University has contributed to the detailed understanding and modeling to elucidate the creep mechanisms operative in the lithium metal.

Other mechanical tests of the Li/LLZO interface were performed using a precision Instron in an Ar-filled glove box. The interface was formed using protocols developed under program II.B.1.ii, led by Jeff Sakamoto.

Results

Li metal studies

Two studies were completed this year. In the first, we addressed the elastic and ductile creep behavior of lithium metal thin films using dynamic nanoindentation. In the second, the redistribution of the thin film of lithium as incorporated into a thin film battery was analyzed during prolonged cycling with different cathodes and duty cycles.

Elastic modulus measurements from 20 and 5 μm thick films (course and fine grained, respectively) indicate the films have different texture. For each film thickness, maps of 30 or more indentations were used to assess homogeneity. Numerous experimental challenges were addressed to extract the elastic modulus from the very ductile behavior of the lithium. In a relatively coarse-grained 20 μm thick film, the range in elastic modulus from 5 to 9 GPa correlates well to the expected value of 8.9 in 110 type directions. On the other hand, results of the elastic modulus from 35 measurements in a more fine-grained 5 μm thick film range from 9 to 18 GPa. This suggests the thinner film has less texture, as the data show a broad mixture of elastic moduli ranging from 110 and 111 type directions (111 is expected to be approximately 23 GPa). These observations are consistent with lithium's shear anisotropy factor of 9.3 and previously published measurements of lithium's elastic constants. Continuing efforts will be made to quantify the plastic anisotropy as well.

To address the ductile properties of the lithium, nanoindentation experiments performed on vapor deposited lithium films reveal a remarkable length scale dependence in the measured hardness. (Hardness is defined in this study such that it physically represents the mean pressure lithium will support; this is highly relevant to the mechanics of successfully confining the lithium anode.) Figure II-448 (a) shows a unique inflection point in the hardness that coincides with an abrupt change in the mechanism that controls the plastic flow of lithium. Hardness data to the right of the inflection point are consistent with the well-documented indentation size effect. Differences in the hardness between the 5 and 18 μm thick films are generally consistent with Hall-Petch strengthening due to the smaller grain size of the thinner film. Hardness data to the left of the inflection point, on the other hand, are entirely unique. While an increase in hardness with increasing indentation depth has been observed in BCC iron, unlike iron, this observation in lithium is not the result of dislocation interaction with a nearby grain boundary. Figure II-448 (b) shows 20 residual hardness impressions in the grain interior and 68 impressions in proximity to a boundary. As shown in Figure II-448 (c), there is no discernable difference in the measured hardness at these positions relative to the boundary and the grain

interior (red and green). The difference in hardness between the bulk arrays (yellow) and data obtained within the grain and near the boundary (Figure II-448 (c)) are potentially due to plastic anisotropy. In addition to the length scale dependence, Figure II-448 (d) shows the hardness near the free surface also depends on the strain rate. As the data show, the rate effect is most pronounced near the free surface, it diminishes with increasing indentation depth and it is completely exhausted by the inflection point. To rationalize these unique experimental observations, effort is underway to develop a diffusional creep-based model capable of describing the change in stress with strain rate and indentation depth.
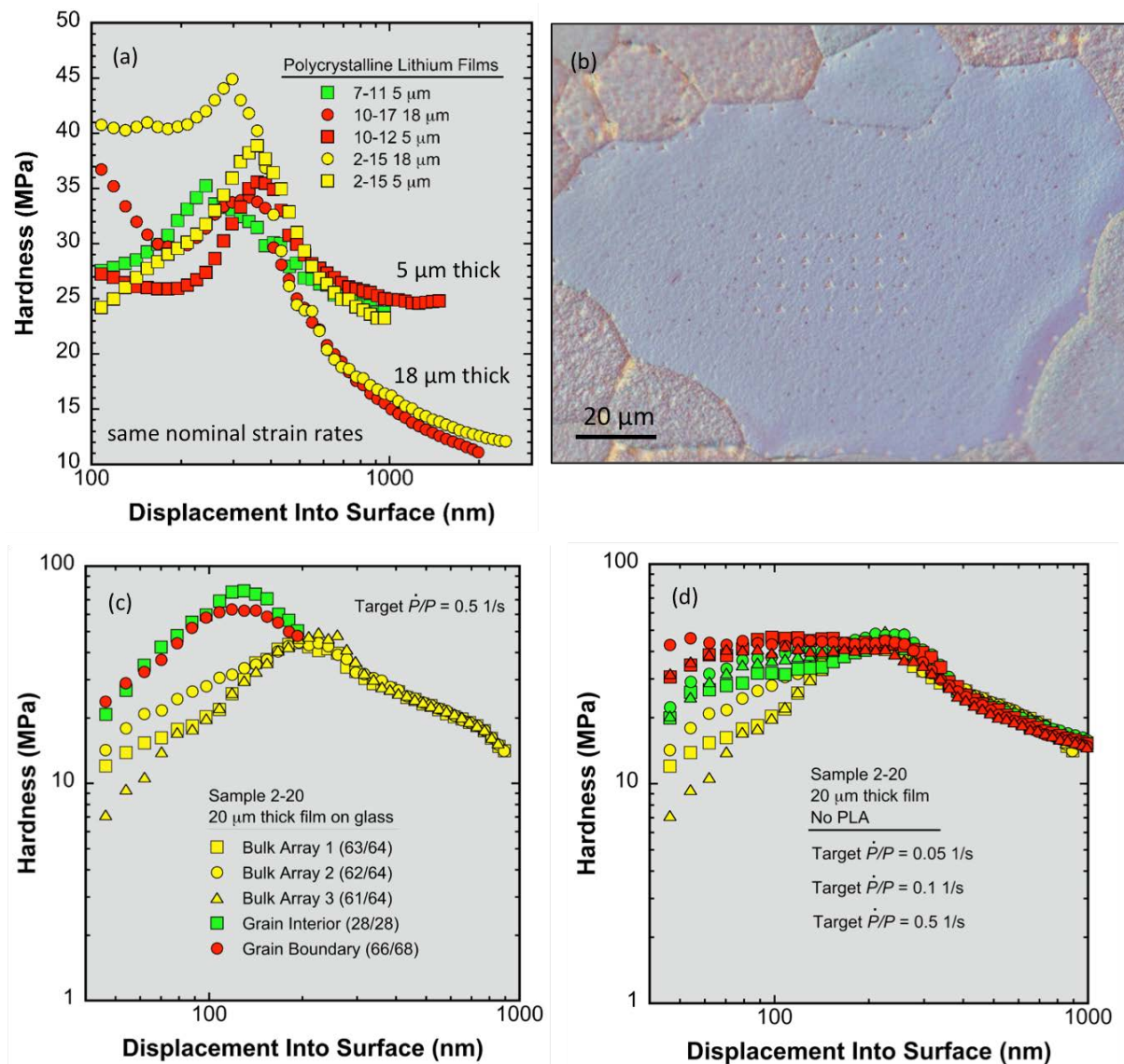

Figure II-448. (a), (c) – (d): Hardness as a function of indentation depth, deposition date, film thickness, location and strain rate. (b) Micrograph of residual hardness impressions in lithium.

Analysis and models have been developed to describe the mechanical properties of thin film lithium as revealed by numerous nanoindentation experiements. The complex dependence on the strain rate and displacement into the film indicates several processes contribute to plastic deformation. A manuscript is being prepared to describe and map these effects. To summarize, Figure II-448 (a) shows the hardness as a continuous function of indentation depth for Li films (5 and 18 μm thick) and 4 indentation strain rates. This is

the average of many indentation maps across the surface. The different creep mechanisms are shown in Figure II-448(b). At slower strain rates and smaller displacement, Nabarro-Herring creep is the primary mechanism. Here lattice defects (vacancies) diffuse between the tip and the free surface of the Li film. At higher strain rate, plastic flow must be accommodated by the diffusion of vacancies from nearby dislocations within the plastic zone. This Harper-Dorn mechanism correctly predicts that the pressure is inversely proportional to the square root of the length scale. At the inflection point in the hardness, an avalanche of dislocations occurs. The power law relationship in Figure II-448(c) strongly suggests, the avalanche occurs only after a threshold limit of energy per unit area has been exceeded. These stresses far exceed the yield or tensile strengths reported for bulk polycrystalline lithium. After the dislocation avalanche, the deformation mechanism capitalizes on the significant increase in the dislocation density and reverts from diffusional creep mechanisms to a balance between of the rate of defect anneal (recovery) and the rate of strain hardening.

Collectively, these observations demonstrate that the Li/SE interface cannot be accurately modeled based on the bulk plastic properties of polycrystalline Li. Moreover, in any small-scale defects at the Li/SE interface, the strength of Li will depend dramatically on the local defect structure, the temperature and strain rate, which presumably correlates directly with the current density. To fully enable the development of safe and efficient cycling of lithium over many cycles, more information is needed to better understand how defects formed in the Li during electrochemical cycling migrate, agglomerate, or anneal with further cycling, time and temperature. Ultimately, we need to understand how these changes affect Li's ability to alleviate stress. This knowledge will serve as a cornerstone in understanding the failure mechanism(s) of solid electrolytes.

LLZO and Li/LLZO interface studies

A coordinated effort with II.B.1.ii, this program provided nanoindentation analysis of the well prepared LLZO. High-speed nanoindentation experiments were performed in LLZO to assess changes in the hardness and elastic modulus as a function of grain size. Results from 300 measurements indicate there is no significant difference in the mechanical properties of LLZO that has been annealed for 1 hour versus 50 (50 hours produces grains on the order of 25 μm). However, when the indentation depth is decreased from 500 to 100 nm, the ratio of modulus to hardness shifts to a slightly lower value. This suggests the near surface region will accommodate strain somewhat more elastically than the bulk.

In other mechanics testing, we used a precision Instron housed in an inert glove box to assess the Li/LLZO interface. Results of the lap shear and tensile adhesive strength show that the adhesive strength of interfaces associated with low interfacial resistance exceed the yield strength of the Li metal itself.

There is a clear correlation between the area specific ionic resistance (ASR) and the tensile adhesive strength of the Li/LLZO interface, as shown in Figure II-449. The tensile strength was determined as Li/LLZO/Li cells were pulled in tension. Analysis of the fracture surfaces showed that at high ASRs, there is a clean separation of the Li from the LLZO surface, leaving behind negligible Li residue. In contrast, at the lowest ASRs reported, the adhesive strength of the Li/LLZO interface exceeds the tensile strength of the Li metal. To support these results, the tensile strength of Li foil was measured to be ~8MPa, which is the maximum interface strength observed in Li/LLZO/Li stacks (red-dashed line in Figure II-449). The fact that the strength of the interface is stronger than the Li metal itself at low ASRs suggests that there is good surface chemistry and wettability of Li on LLZO. From these studies, it can be concluded that both the adhesive strength and ASR of the interface are governed by the surface chemistry and wettability of the LLZO surface.

Finally, using our precision Instron, the interface resistances of Li-LLZO-Li cells were recorded while cycling the compressive stress (stack pressure) applied to the cell. We believe a critical stack pressure is needed to maintain a flux of Li to the interface to maintain contact and avoid formation of pits due to the Kirkendall effect. Li-LLZO-Li cells were fabricated using the best cell assembly protocol to achieve low and consistent interface resistance. While varying the stack pressure, we monitored the potential to maintain a constant current finding that there was a noticeable correlation between cell polarization and stack pressure.
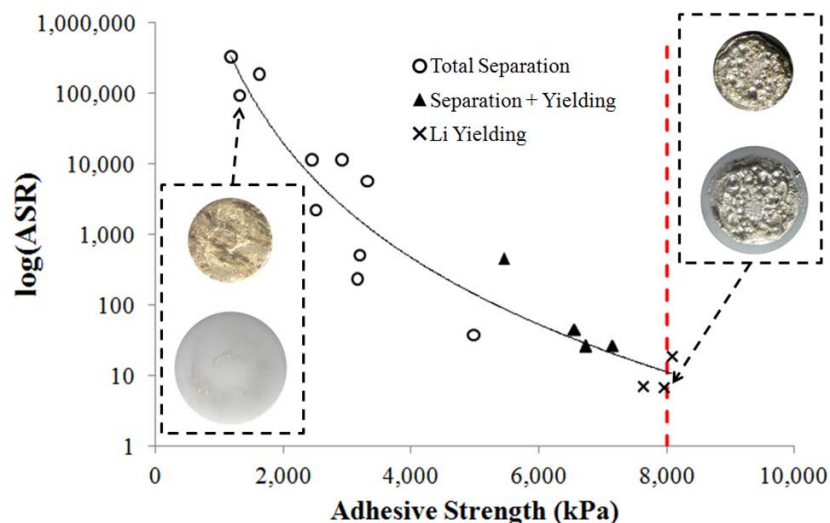
Figure II-449. Area specific resistance as a function of the adhesion strength of the Li-LLZO interface. Optical microscope images show the fracture surface of the Li and LLZO disks at low and high ASR. The red dashed line indicates the measured tensile strength of Li metal

Conclusions

1. The elastic properties of vapor deposited lithium metal thin films where characterized and found to be higher than expected, but well within the published values for the orientation dependent modulus.

2. The plastic properties were found to be dependent on the length scale and strain rate. At the smallest lengths scale, the mean pressure supported by the lithium is 40-350 time higher than the nominal yield strength of bulk polycrystalline lithium, shedding light on the mechanical behavior of lithium at defects near the lithium/solid electrolyte interface.

3. Extended cycling of lithium contacting the Lipon solid electrolyte in a thin film battery shows significant redistribution that depends on the duty cycle and surprisingly also the particular cathode.

4. The adhesive strength of Li with LLZO and the ASR of the interface are governed by the surface chemistry and wettability of the LLZO interface. For optimal interfaces, the adhesive strength exceeds the tensile strength of the lithium metal itself.

5. The electrochemical cell polarization for a Li/LLZO/Li cell correlates to the applied stack pressure when oscillated between 1.2 and 2.4 MPa.

Key Publications

1. "Stability and cycling of metallic Lithium with an inorganic solid electrolyte", Nancy J. Dudney, Miaofang Chi, Jeff Sakamoto, and Erik Herbert, ACS meeting, San Francisco March 2017, invited presentation

2. "Evolution of the Lithium Morphology from Cycling of Thin Film Solid-State Batteries," Nancy J. Dudney, Journal of Electroceramics **38** (2017) 222-229. Invited for Solid State Batteries Issue.

3. "Mechanical Properties at the Protected Lithium Interface," Nancy Dudney, Erik Herbert, Jeff Sakamoto.

4. DOE Vehicle Technologies Program, Annual Merit Review and Peer Evaluation Meeting, June 2107. Oral presentation.

5. "The Mechanical Behavior of Vapor Deposited Lithium Films," <u>Erik Herbert</u>, Nancy Dudney, Steve Hackney, 10th Meeting for Beyond Lithium Ion Batteries (BLI-10), IBM Almaden CA, June 27, 2017. Invited presentation.

6. "Nanoindentaion of High Purity Vapor Deposited Lithium Films: The Elastic Modulus," E. G. Herbert, P. S. Phani, N. J. Dudney, and S. A. Hackney In preparation.

7. "Nanoindentaion of High Purity Vapor Deposited Lithium Films: A Mechanistic Rationalization of Diffusion-Mediated Flow," E. G. Herbert, S. A. Hackney, N. J. Dudney, V. Thole and P. S. Phani, In preparation.

8. "Nanoindentaion of High Purity Vapor Deposited Lithium Films: A Mechanistic Rationalization of the Transition to Dislocation-Mediated Flow," E. G. Herbert, S. A. Hackney, N. J. Dudney, V. Thole and P. S. Phani, In preparation.

II.H.2   Solid electrolytes for solid-state and lithium-sulfur batteries (University of Michigan, ORNL, ARL, Oxford University)

Jeff Sakamoto, Principal Investigator
University of Michigan
Mechanical Engineering
2350 Hayward Avenue
Ann Arbor, MI 48109
Phone: 734-769-2213
E-mail: jeffsaka@umich.edu

Tien Duong, Technology Manager
U.S. Department of Energy
Phone: 202-586-7836
E-mail: Tien.Duong@ee.doe.gov

Start Date: January 1, 2015   End Date: December 31, 2017
Total Project Cost: $1,200,000   DOE share: $1,200,000   Non-DOE share: $0

Introduction

Batteries that surpass Li-ion systems require advanced anode, cathode, and electrolyte technology. In theory, the lithium-sulfur (Li-S) system offers over a six-fold increase in specific energy (2567 Wh/kg) compared to state-of-the-art (SOA) Li-ion (387 Wh/kg). However, the potential of the Li-S system has not been realized due to instabilities at the interface between the Li metal anode and the electrolyte. First, other than LIPON, no electrolyte has demonstrated stability against metallic Li. Second, dissolution of Li-polysulfides in SOA liquid electrolytes results in passivation of the Li anode. Thus, there is a compelling need to develop novel electrolyte technology to enable beyond Li-ion battery technologies employing Li metal anodes.

Objectives

Enable advanced Li-ion solid-state and lithium-sulfur EV batteries using LLZO solid-electrolyte membrane technology

Owing to its combination of fast ion conductivity, stability, and high elastic modulus, LLZO exhibits promise as an advanced solid-state electrolyte. To demonstrate relevance in EV battery technology, several objectives must be met. First, LLZO membranes must withstand current densities approaching ~1 mA/cm^2 (commensurate with EV battery charging and discharging rates). Second, low area specific resistance (ASR) between Li and LLZO must be demonstrated to achieve cell impedance comparable to conventional Li-ion technology (~10 Ohms/cm^2). Third, low ASR and stability between LLZO and sulfur cathodes must be demonstrated.

Approach

Our effort will focus on the promising new electrolyte known as LLZO ($Li_7La_3Zr_2O_{12}$). LLZO is the first bulk-scale ceramic electrolyte to simultaneously exhibit the favorable combination of high conductivity (~1 mS/cm at 298K), high shear modulus (61 GPa) to suppress Li dendrite penetration, and apparent electrochemical stability (0-6V vs Li/Li$^+$). While these attributes are encouraging, additional R&D is needed to demonstrate that LLZO can tolerate current densities in excess of 1mA/cm^2, thereby establishing its relevance for PHEV/EV applications. We hypothesize that defects and the polycrystalline nature of realistic LLZO membranes limit the critical current density. However, the relative importance of the many possible defect types (porosity, grain boundaries, interfaces, surface & bulk impurities), and the mechanisms by which they impact current density, have not been identified. Using our experience with the synthesis and processing of LLZO (Sakamoto and Wolfenstine), combined with sophisticated materials characterization (Nanda), we will precisely control atomic and microstructural defects and correlate their concentration with the critical current

density. These data will inform multi-scale computation models (Siegel and Monroe) which will isolate and quantify the role(s) that each defect plays in controlling the current density. By bridging the knowledge gap between composition, structure, and performance we will determine if LLZO can achieve the current densities required for vehicle applications.

Results

As has previously been shown[1], the surface chemistry of LLZO is sensitive to air exposure. A contamination layer readily forms and is predominantly composed of lithium carbonate (Li_2CO_3), lithium hydroxide (LiOH), and other adventitious carbon species; which collectively result in high interfacial resistance between LLZO and metallic Li. It has been reported that dry polishing in an inert atmosphere can lower the interfacial resistance by partially cleaning the surface; however, the efficacy of this approach is limited to reducing the interface resistance from ~1000 Ω.cm^2 to ~100 Ω.cm^2. Here, several surface conditioning protocols, including dry polishing (DP), wet polishing (WP), and heat treatments (HT) were employed in an attempt to reduce the interfacial resistance, and their impact on LLZO surface chemistry was evaluated. Heat treatment between 200 and 500°C in an inert atmosphere was conducted after dry and wet polishing.

The surface chemistry of LLZO was analyzed using X-ray photoelectron spectroscopy (XPS) after each conditioning protocol (Figure II-450). Measurements were performed on samples transferred without air exposure between an argon-filled glovebox and the ultra-high vacuum XPS chamber. Figure II-450a shows that in samples conditioned with DP or WP (no HT) a surface layer blocks nearly all the signal attributed to La and Zr. Thus, in these cases the surface layer is composed almost entirely of H, Li, C, and O (H content cannot be directly detected by XPS, but can be observed as hydroxyl bonds). The nature of the bonds in which these species participate can be examined through high-resolution core-scans. The O 1s peak reveals a significant difference between the surface layer after wet vs. dry polishing (Figure II-450b). The WP surface consists of predominantly hydroxide species, while a greater concentration of carbonate species exists on the DP sample. This suggests that the use of polishing fluid protects the LLZO surface from reformation of carbonate species.

Samples that underwent HT were first polished (DP or WP in ambient air) and then immediately transferred into an argon-filled glovebox where the samples were heated to different temperatures. Subsequent XPS analysis demonstrated significant variations in the surface chemistry of these samples. In Figure II-450a the plot of the ratio of the C content to the summed La and Zr contents is used as a metric to quantify the amount of surface contamination. The lower the ratio, the more closely the surface resembles bulk LLZO. Some adventitious carbon is always observed on the LLZO surface, even for samples kept continuously in an argon atmosphere after HT, Figure II-450c. The amount of contamination is observed to dramatically decrease after heating to 400 and 500°C. This is consistent with the O 1s core scans shown for these samples, which demonstrate that the predominantly hydroxide and carbonate surfaces before heating are converted to primarily oxide species (as expected in bulk LLZO) after heating (Figure II-450b). In contrast, heating a DP sample to 400°C did not change the surface as dramatically, with carbonate species still dominating (Figure II-450c). A plot of the fractional surface composition of the oxygen-containing species is shown in Figure II-450d for WP samples heated to different temperatures. As the HT temperature increases to 500°C, the oxide fraction steadily increases, the hydroxide fraction decreases, and the amount of carbonate remains roughly constant. In total, these observations suggest that: (1) compared to dry polishing, wet polishing is more effective at achieving a surface with low carbonate content, (2) heat treatment up to 500°C can remove LiOH, but is less effective at removing Li_2CO_3, and (3) of the strategies examined, the successive combination of WP and HT is the most effective at removing surface contamination layers.
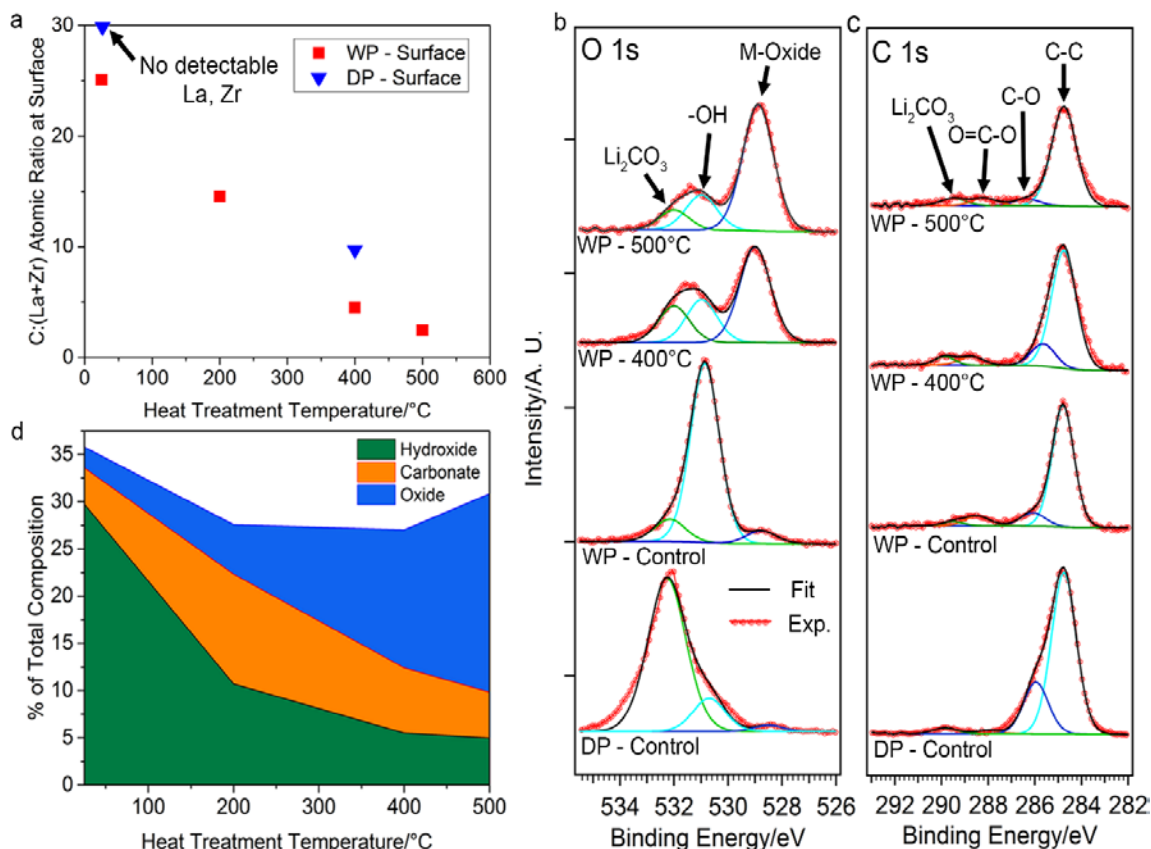
Figure II-450. XPS analysis of LLZO before and after heat treatment at 400 and 500 °C. a) C:(La+Zr) atomic ratio as a function of heat treatment temperature, b) O 1s and c) C 1s core levels, d) percentage of total composition of different oxygen species on the LLZO surface as a function of heat treatment temperature after wet polishing (WP).

The wettability of a SSE by metallic Li has been proposed to influence interfacial resistance in SSBs. However, quantitative analysis of the Li contact angle and direct correlation with surface chemistry has not been reported. To characterize wettability, sessile drop tests were performed to measure the contact angle of molten Li on Li_2CO_3 and on LLZO samples after various surface conditioning processes (Figure II-451). Molten Li was deposited onto heated Li_2CO_3 or LLZO from a heated stainless-steel syringe. Importantly, the native layers (composed of oxide, nitride, and carbonate species) present on the surface of the Li foil did not melt, and thus were easily removed from the molten Li source. This allowed for deposition of purified molten Li onto the LLZO surface. The present approach differs from a scenario involving the melting of solid Li foil directly on LLZO, as wettability in the latter approach will be influenced by the presence of native layers on the Li surface and at the Li-LLZO interface. All experiments were performed inside an argon-filled glovebox, and high-resolution cross-sectional images were captured and digitally analyzed to determine contact angles.
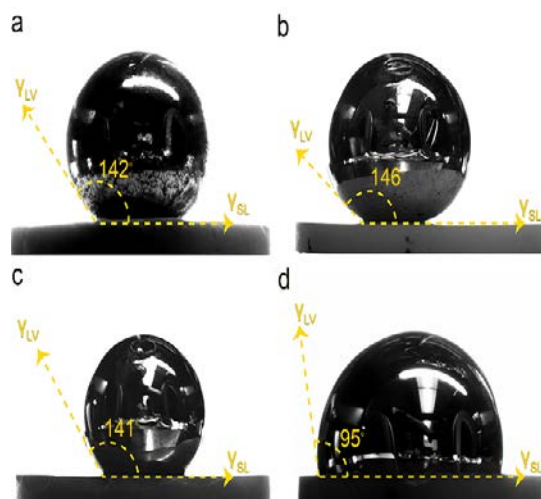
Figure II-451. Contact angle measurements of molten metallic Li on a) Li_2CO_3, b) DP-LLZO, c) WP-LLZO, d) WP-LLZO after heat treatment at 500ºC.

As shown in Figure II-451, the DP-LLZO sample exhibited the highest contact angle amongst all LLZO samples, $\theta = 146°$, which was nearly identical to the value measured for a pure Li_2CO_3 surface ($\theta = 142°$). Such a large contact angle is consistent with a non-wetting interaction typical of an interface exhibiting weak adhesion. The similar wetting behavior between the DP-LLZO sample and Li_2CO_3 is expected, given that the DP-LLZO surface is composed predominantly of Li_2CO_3. Similarly, the WP-LLZO contact angle was 141°, which is consistent with the presence of the hydroxide and carbonate contamination layer which was observed with XPS. In contrast, the WP-LLZO heat treated at 500°C exhibited a significantly lower contact angle ($\theta = 95°$). We hypothesize that this reduction in contact angle is caused by the removal of hydroxide and carbonate species, resulting in a surface more closely resembling bulk LLZO, which interacts more strongly with Li metal.

To validate the correlation between surface chemistry and wettability, the wetting angle of Li on LLZO, Li_2CO_3, and LiOH was evaluated using DFT calculations. Li-LLZO, Li-Li_2CO_3 and Li-LiOH interfaces were constructed from the low-energy surfaces of each respective material. Large simulation cells were used, to accommodate geometries that minimize interfacial strain. The interfacial distance and translation state within the interfacial plane were optimized to identify the most energetically-favorable interface structures.

Figure II-452 shows the atomic structure of the low-energy interfaces for Li-LLZO and Li-Li_2CO_3. The contact angle, θ, for these interfaces was calculated by combining the Young-Dupré equation, $W_{ad} = \sigma_{Li}(1 + \cos\theta)$, with DFT calculations of the interfacial work of adhesion, W_{ad}, and the surface energy of Li, $\sigma_{Li} = 0.45$ J.m^{-2}. Using the Li-LLZO interface as an example, W_{ad} was evaluated as: $W_{ad} = E_{int} - E_{Li\text{-slab}} - E_{LLZO\text{-slab}}$. Here E_{int} is the energy of the interface cell and $E_{X\text{-slab}}$ refers to the energy of an isolated Li (X = Li) or LLZO slab (X = LLZO). The calculated values for W_{ad} and θ are shown in Figure II-452 below their respective interfaces. The trend predicted by our calculations – that Li strongly wets LLZO, but not Li_2CO_3 – is consistent with the measurements shown in Figure II-451. More specifically, the wetting angle predicted for the Li-Li_2CO_3 interface, $\theta = 142°$, is in excellent agreement with the measured value (142°, Figure II-451a) indicating a weak interfacial interaction between Li and Li_2CO_3 ($W_{ad} = 0.10$ J.m^{-2}). In contrast, the calculated W_{ad} for the Li-LLZO interface is nearly seven times larger, $W_{ad} = 0.67$ J.m^{-2}, resulting in a relatively small wetting angle, $\theta = 62°$. This value is qualitatively consistent with the measured value of 95° reported in Figure II-451d. The smaller value predicted by our calculations is expected, given that approximately 15% of carbonate and/or hydroxide remains on the LLZO surface after heating to 500°C (Figure II-451d). Calculations on the Li-LiOH interface predict a relatively large contact angle of 125°, similar to the non-wetting behavior observed for the Li-Li_2CO_3 system.
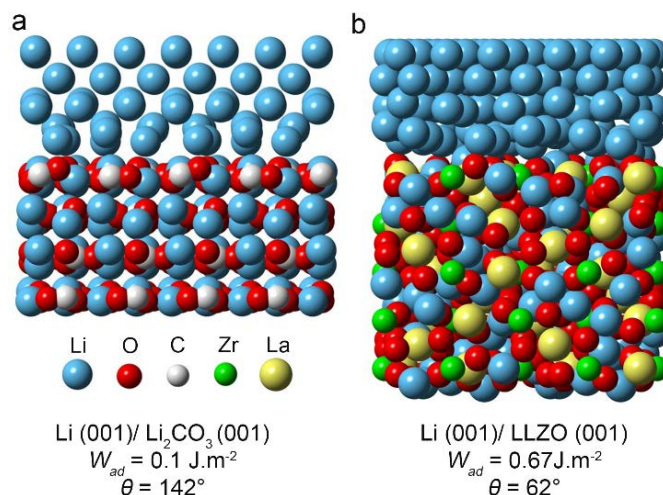
Figure II-452. Calculated work of adhesion (W$_{ad}$), contact angle (θ), and atomic structure for the a) Li-Li$_2$CO$_3$ and b) Li-LLZO interfaces.

Electrochemical impedance spectroscopy (EIS) was performed on Li-LLZO-Li symmetric cells (Figure II-453a) to measure the LLZO bulk (R$_{bulk}$), grain boundary (R$_{gb}$), and Li-LLZO interfacial (R$_{Li-LLZO}$) resistances for WP and HT samples between 200 and 500°C. EIS data were modelled using an equivalent circuit shown in Figure II-453b. This approach allows for the direct measurement of the individual contributions to cell resistance and involves the correlation between characteristic frequencies and transport phenomena. Representative EIS spectra for a cell consisting of a WP and HT at 500°C LLZO sample before and after preconditioning at 175°C are shown in Figure II-453c (Preconditioning was used to ensure good contact between metallic Li and LLZO by heating the Li-LLZO-Li cell to 175°C for 12 h).[6] From Figure II-453c, it is apparent the LLZO total resistance (R$_{bulk}$ + R$_{gb}$) has remained constant (500 Ω.cm^2) while R$_{Li-LLZO}$ dramatically decreased upon preconditioning at 175°C and cooling. Initially, R$_{Li-LLZO}$ was approximately 400 Ω.cm^2 which is significantly lower than previous values reported for LLZO after dry polishing in literature.[6] After preconditioning at 175°C, a further dramatic reduction in R$_{Li-LLZO}$ was observed. The combination of wet polishing, HT, and preconditioning results in an extremely small interfacial resistance of 2 Ω.cm^2.
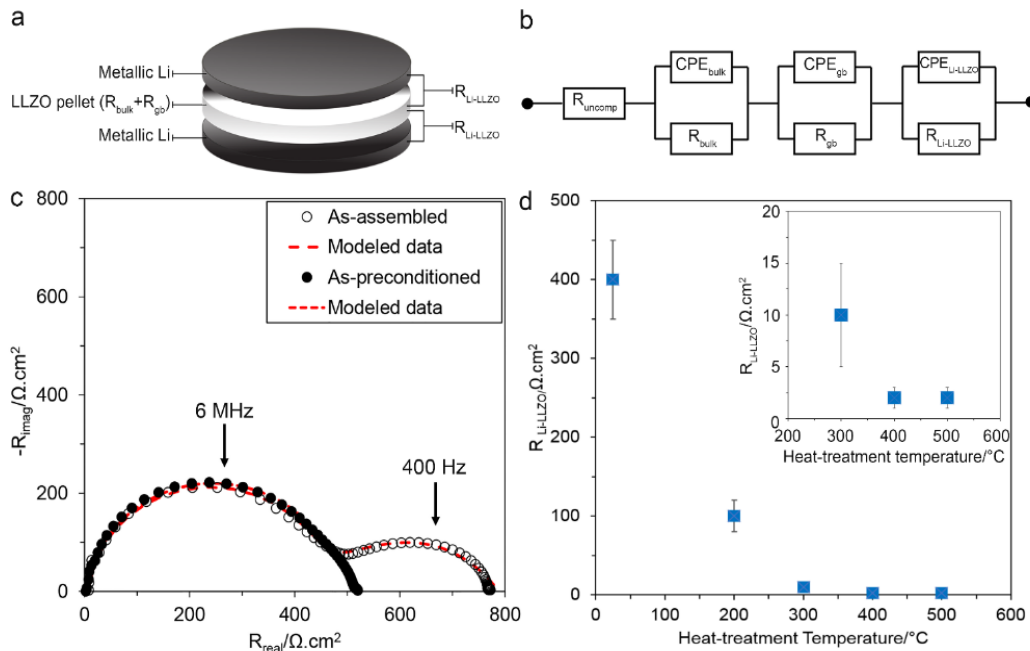
Figure II-453. a) Schematic of the all solid-state Li-LLZO-Li cell, b) the equivalent circuit used for modeling the EIS data c) representative Nyquist plot of the Li-LLZO-Li cell (for LLZO heat-treated at 500°C), as-assembled (○) and after preconditioning at 175°C (●). Markers indicate experimental data and dotted lines are simulated lines extrapolated from the equivalent circuit modeling using the circuit shown in b, d) the Li-LLZO interfacial resistance after preconditioning at 175°C versus the heat-treatment temperature. N=3 for each HT condition. Error bars represent standard deviations.

Figure II-453d shows $R_{Li-LLZO}$ after preconditioning for WP LLZO samples with no HT and HT at several temperatures between 200 and 500°C. With increasing HT temperature, $R_{Li-LLZO}$ decreases from 400 to 2 $\Omega.cm^2$. Importantly, the low interfacial resistance coincides with the removal of the surface contamination layer. Furthermore, the decrease in interfacial resistance closely follows the trend in surface chemistry with HT temperature observed in XPS measurements, and with the improved wettability of the LLZO surface after HT. Taken together, these observations provide quantitative evidence of the strong coupling between surface chemistry, wettability, and interfacial resistance.

The cycling behavior and critical current density (CCD) of a WP LLZO sample HT to 500°C (WP+HT) were characterized using a combination of DC cycling and EIS analysis (Figure II-454). The CCD is defined as the lowest current density at which cell shorting occurs due to Li metal penetration. After removal of the surface contamination, the CCD was determined to be 0.3 mA.cm^{-2} (Figure II-454a). The CCD from the WP+HT sample prepared here is compared in Figure II-454b to other Li-LLZO-Li symmetric cells reported in the literature. The CCD measured in this study is one the highest values reported in literature for an LLZO SSE. Our data indicates that the CCD and $R_{Li-LLZO}$ are inversely correlated, suggesting that higher power density can be achieved by controlling interfacial chemistry, and thus $R_{Li-LLZO}$.
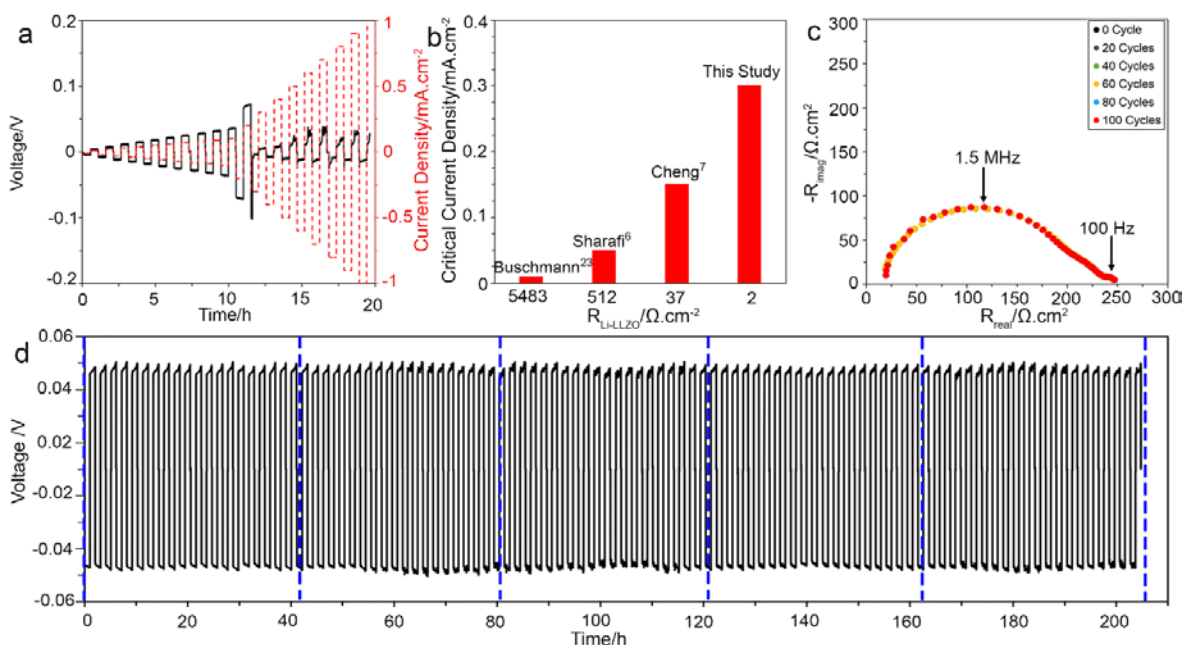
Figure II-454. a) DC cycling of Li-LLZO-Li cells (LLZO HT to 500°C after WP) at room temperature, stepping the current density from 0.01 to 1 mA.cm⁻², b) the critical current density versus Li-LLZO interfacial resistance comparing the result of this study with other studies available in the literature, c) Nyquist plots of Li-LLZO-Li cell after each 20 cycles for cell cycled 100 time, d) Galvanostatic cycling of Li-LLZO-Li at 0.2 mA.cm⁻² for 100 cycles at 0.4 mAh.cm⁻². The blue dotted line shows the times at which EIS was collected and is shown in c.

To evaluate the stability of the interface after WP+HT upon cycling, a Li-LLZO-Li cell was cycled for one hundred cycles at ± 0.2 mA.cm⁻² at room temperature (Figure II-454d). After every 20 cycles, EIS analysis was conducted to assess changes in R_{bulk}, R_{gb}, and $R_{Li\text{-}LLZO}$. Figure II-454c shows that negligible changes in the EIS spectra were observed, implying excellent stability of the interface and the absence of short-circuiting. Furthermore, the total cell resistance ($R_{bulk} + R_{gb} + R_{Li\text{-}LLZO}$) estimated using the DC cell polarization voltage (230 Ω.cm²) (Figure II-454a) agrees well with the total cell resistance measured using EIS (240 Ω.cm²). This confirms that the DC and EIS analyses are in good agreement, and further validates the interpretation of the EIS data to quantitatively decouple resistance values and correlate them to their respective transport phenomena.

The DC and EIS characterization illustrate the importance of achieving low and stable interfacial resistance. First, a low $R_{Li\text{-}LLZO}$ enables a path toward low resistance solid-state cell designs employing metallic Li anodes. Second, reducing $R_{Li\text{-}LLZO}$ increases the CCD. Although 0.3 mA.cm⁻² is one of the highest reported CCD values, it must be further increased to demonstrate relevance to vehicle electrification; the data in Figure II-454b suggest further tuning surface chemistry and reducing $R_{Li\text{-}LLZO}$ may be an approach to achieve higher CCD. Lastly, a clean and discrete Li-LLZO interface is preferred to minimize side reactions and mechanical degradation. In preliminary cycling tests, the interface kinetics appear to be stable when cycling at ± 0.2 mA.cm⁻² at room temperature.

Conclusions

This study has revealed the mechanism by which surface chemistry controls the resistance of the Li-LLZO interface. By exploiting this mechanism, very low interfacial resistances – 2 Ω.cm⁻², comparable to solid-liquid interfaces in Li-ion cells – can be achieved *without the need for coatings*. The removal of LLZO surface contamination was demonstrated to enhance Li wetting of LLZO, which was quantitatively evaluated using molten Li contact angle measurements through sessile drop tests. The interfacial chemistry and wettability measurements agree with atomic-scale DFT calculations of interfacial adhesion and wetting angle. The lower

interfacial resistance made possible by controlling surface chemistry resulted in a doubling of the critical current density. This study clarifies the relationships between interfacial chemistry, lithium wettability, interfacial resistance, and stable cycling. The knowledge gained enables the rational design of electrode/electrolyte interfaces, and has general implications for solid-state transport phenomena.

Key Publications

1. A. Sharafi, S. Yu, M. Naguib, M. Lee, C. Ma, H. Meyer, J. Nanda, M. Chi, D. J. Siegel, and J. Sakamoto, "Impact of Air Exposure and Surface Chemistry on the Li-Li$_7$La$_3$Zr$_2$O$_{12}$ Interfacial Resistance" *J. Mater. Chem. A., J. Mater. Chem. A* 2017.

2. Yu, S. and Siegel, D. Grain Boundary Contributions to Li-ion Transport in the Solid Electrolyte Li$_7$La$_3$Zr$_2$O$_{12}$ (LLZO), *ChemMater*, Accepted 2017.

3. A. Sharafi, E. Kazyak, A. L. Davis, S. Yu, T. Thompson, D. J. Siegel, N. P. Dasgupta, and J. Sakamoto, "Achieving low resistance all-solid-state Li-LLZO interfaces through surface chemistry control" *ChemMater*, Accepted 2017.

4. E. J. Cheng, A. Sharafi, and J. Sakamoto, "Intergranular Li metal propagation through polycrystalline Li$_{6.25}$Al$_{0.25}$La$_3$Zr$_2$O$_{12}$ceramic electrolyte" *Electrochim. Acta* 223, 85-91 (2017).

5. T. Thompson, S. Yu, L. Williams, R. D. Schmidt, R. Garcia-Mendez, J. Wolfenstine, J. A. Allen, E. Kioupakis, D. J. Siegel, and J. Sakamoto, "Electrochemical Window of the Li-Ion Solid Electrolyte Li$_7$La$_3$Zr$_2$O$_{12}$" *ACS Energy Letters*, 2(2), 462-468 (2017).

6. Jeff Wolfenstine, Jan L. Allen, Jeff Sakamoto, Donald J. Siegel, and Heeman Choe[3] "Mechanical Behavior of Li-Ion Conducting Crystalline Oxide-based Solid Electrolytes: A Brief Review," IONICS, Accepted, (2017).

7. Priyamvada Goyal and Charles W. Monroe, "New Foundations of Newman's Theory for Solid Electrolytes: Thermodynamics and Transient Balances," Journal of The Electrochemical Society, 164 (11) E3647-E3660 (2017).

8. Smith, S., Thompson, T., Sakamoto, J., Allen, J. L., Baker, D. R., & Wolfenstine, J. (2017). Electrical, mechanical and chemical behavior of Li$_{1.2}$Zr$_{1.9}$Sr$_{0.1}$(PO$_4$)$_3$. Solid State Ionics, 300, 38-45.

9. Kim, Y., Yoo, A., Schmidt, R., Sharafi, A., Lee, H., Wolfenstine, J., & Sakamoto, J. (2016). Electrochemical Stability of Li$_{6.5}$La$_3$Zr$_{1.5}$M$_{0.5}$O$_{12}$ (M= Nb or Ta) against Metallic Lithium. Frontiers in Energy Research, 4, 20.

10. C. Ma, Y. Cheng, K. Yin, J. Luo, A. Sharafi, J. Sakamoto, J. Li, K. L. More, L., N. J. Dudney, and M. Chi, "Interfacial Stability of Li Metal–Solid Electrolyte Elucidated via in Situ Electron Microscopy: *Nano Letters*, 16(11), 7030-7036 (2016).

11. S. Yu, R. D. Schmidt, R. Garcia-Mendez, E. Herbert, N. J. Dudney, J. B. Wolfenstine, J. Sakamoto, and D. J. Siegel, "Elastic Properties of the Solid Electrolyte Li$_7$La$_3$Zr$_2$O$_{12}$ (LLZO)" Chem. Mater., 2016, 28 (1), 197–206.

12. Y. Kim, H. Jo, J. L. Allen, H. Choe, J. Wolfenstine, and J. Sakamoto, "The Effect of Relative Density on the Mechanical Properties of Hot-Pressed Cubic Li$_7$La$_3$Zr$_2$O$_{12}$" *J. Am. Ceram. Soc.,* 99 [4] 1367–1374 (2016).

13. Sharafi, A., Meyer, H. M., Nanda, J., Wolfenstine, J., & Sakamoto, J. (2016). Characterizing the Li–Li$_7$La$_3$Zr$_2$O$_{12}$ interface stability and kinetics as a function of temperature and current density. *Journal of Power Sources*, *302*, 135-139.

II.H.3 Composite Electrolytes to Stabilize Metallic Lithium Anodes (ORNL)

Nancy Dudney, Principal Investigator
Oak Ridge National Laboratory
P.O. Box 2008, MS6124
Oak Ridge, TN 37831
Phone: 865-576-4874
E-mail: dudneynj@ornl.gov

Tien Duong, Technology Manager
U.S. Department of Energy
Phone: 202-586-7836
E-mail: Tien.Duong@ee.doe.gov

Start Date: October 1, 2015   End Date: September 30, 2018
Total Project Cost: $1,200,000   DOE share: $1,200,000   Non-DOE share: $0

Project Introduction

A stable lithium anode is critical to achieve high energy density with excellent safety, lifetime and cycling efficiency. This study will identify the key design strategies that should be used to prepare composite electrolytes to meet the challenging combination of physical and chemical and manufacturing requirements to protect and stabxilize the lithium metal anode for advanced batteries. By utilizing well characterized and controlled component phases, the design rules developed for the composite structures will be generally applicable toward the substitution of alternative and improved solid electrolyte component phases as they become available. Success in this program will enable these specific DOE technical targets: 500-700Wh/kg, 3000-5000 deep discharge cycles, robust operation.

Objectives

- Prepare composites of representative polymer and ceramic electrolyte materials to achieve thin membranes which have the unique combination of electrochemical and mechanical properties required to stabilize the metallic lithium anode while providing for good power performance and long cycle life.

- Understand the lithium ion transport at the interface between polymer and ceramic solid electrolytes which is critical to the effective conductivity of the composite membrane.

- Identify key features of the composite composition, architecture and fabrication that optimize performance and develop practical and scalable fabrication methods.

Approach

This program seeks to develop practical solid electrolytes that will provide stable and long-lived protection for the lithium metal anode. Current electrolytes all have serious challenges when used alone: oxide ceramics are brittle, sulfide ceramics are air sensitive, polymers are too resistive and soft, and many electrolytes react with lithium. Composites provide a clear route to address these issues. This program does not seek discovery of new electrolytes, rather the goal is to study combinations of current well-known electrolytes that can provide critical understanding towards the effects of the interfaces and architecture on the ion transport and stability with the Li anode. The program emphasizes the investigation of polymer-ceramic interfaces formed as bilayers and as simple composite mixtures where the effects of the interface properties can be readily isolated. In general, the ceramic phase is several orders of magnitude more conductive than the polymer electrolyte, and interfaces can contribute an additional source of resistance. Using finite element simulations as a guide, composites with promising compositions and architectures are fabricated and evaluated for lithium transport

properties using AC impedance and DC cycling with lithium in symmetric or half cells. General design rules will be determined that can be widely applied to other combinations of solid electrolytes.

In FY16, we fabricated thin composite membranes using aqueous spray coating technique. This is an environmental friendly, inexpensive and scalable processing route that can achieve high loadings of the ceramic component to ensure a high shear modulus. In the past year, an automatic spray coater (Prism 400, Ultrasonic Systems Inc.) was setup in our lab for battery prototyping. We fabricated a full battery using aqueous spray coating for both the cathode and composite electrolyte incorporating a protected Li metal anode. Battery performance is being evaluated. In the meantime, we established a spray-on polymer-ceramic-polymer (trilayer) method to quantify the interfacial resistance between the polymer and ceramic electrolyte. This method provides a platform for us to explore strategies to minimize interfacial resistance.

Results

Following FY16, we fabricated composite membranes consisting of Ohara powder, polyethylene oxide (PEO, MW=600,000), lithium triflate salt (LiTFS, $LiCF_3SO_3$) with a 16:1 atomic ratio of PEO ether oxygens per dissolved Li^+ ion ($[EO]:[Li^+] = 16:1$) by the aqueous spray coating + hot pressing procedure. The density of the polymer electrolyte and composite electrolyte membranes were measured using a gas pycnometer (Micromeritics AccuPyc II 1340). We also measured the density of the membranes containing a plasticizer, tetraethylene glycol dimethyl ether (TEGDME) with a concentration of $[TEGDME]:[Li^+] = 2:1$. From the density data we calculated the volume of each sample. The results are shown in Figure II-455. Two sets of predicted values were overlaid on the experimental data for comparison: the first set (squares) is a simple sum of the volume of each individual component in the membrane, assuming conservation of volume upon mixing; 2. The second set (crosses) is based on complete dissolution into free volume theory, assuming that all of salt and plasticizer molecules occupied the free volume of PEO. Comparing experimental data with the predicted values, we found that when adding LiTFS into PEO, the salt completely dissolved into the free volume of PEO. In the membrane containing PEO, LiTFS and TEGDME, a portion of TEGDME occupied the free volume of PEO. For the composite membrane, experimentally obtained composite volume matched the lowest predicted value. This means that there are no voids in this sample, and all the LiTFS and TEGDME went into the free volume of PEO. This proved that a good dense membrane was fabricated using our spray coating protocol. The conductivity of spray coated composite membranes is an order of magnitude higher than dry milled + melt pressed membranes with the same composition (Figure II-456).
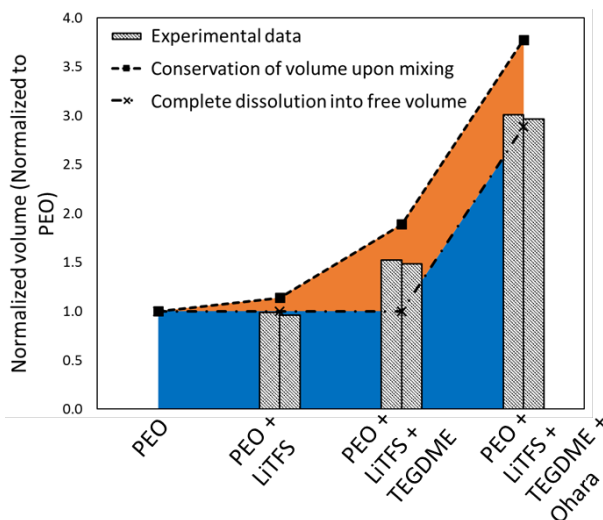

Figure II-455. Normalized volume (to that of PEO) of PEO, polymer electrolyte (with and without TEGDME) and composite electrolyte calculated from experimentally measured density values, compared to the predicted values.
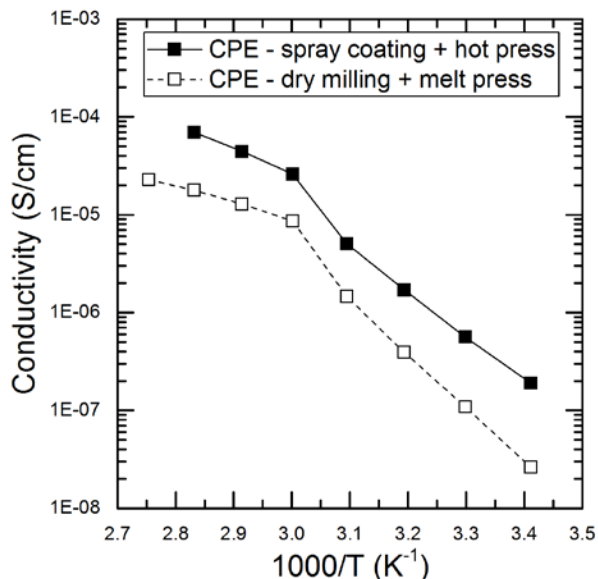
Figure II-456. Arrhenius plot of composite formed by spray coating and hot pressing, compared to that formed by dry milling and melt pressing.

Li/ electrolyte /Li symmetrical cell was constructed to obtain the Li transference number (t_{Li+}) of polymer electrolytes and composite electrolytes. Chrono-amperometric measurement was carried out at an applied potential (ΔV) of 10 mV. The current response was monitored over time until a steady state is reached (Figure II-457). The transference number for TEGDME plasticized polymer electrolyte is found to be 0.69, higher than that of polymer electrolyte without TEGDME, reported to be 0.47 – 0.57. Moreover, a transference number of 0.79 was obtained from TEGDME plasticized composite electrolyte with 50 vol% ceramic. Adding Ohara ceramic further increased the transference number of the electrolytes.
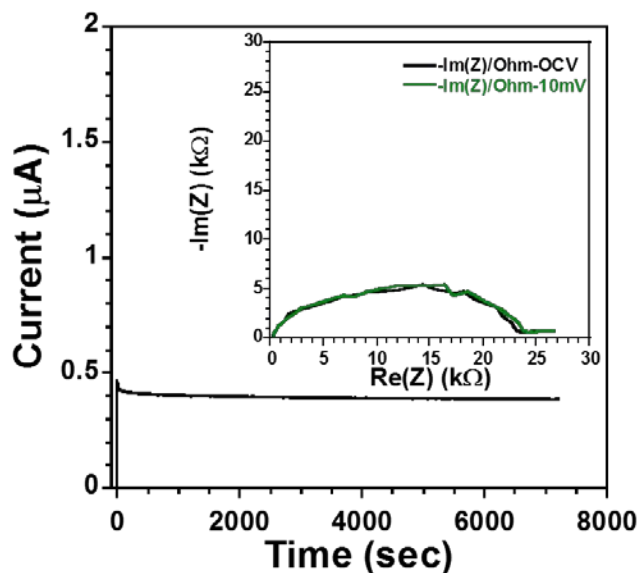

Figure II-457. DC response of a symmetrical cell of configuration Li/Composite Electrolyte/Li for obtaining Li transference number. Inset, EIS response of the symmetrical cell.

In order to optimize the conductivity of spray coated composite membranes, we varied the salt, plasticizer and ceramic content, see Figure II-458. Increasing the salt concentration from $[Li^+]:[EO] = 1/16$ to $1/8$ lead to one order of magnitude decrease in the composite conductivity. Varying TEGDME concentration between $[TEGDME]: [Li^+] = 2:1$ and $4:1$ did not result in significant change in conductivity. We also examined the effect of ceramic volume fraction on the conductivity of composites (containing TEGDME). Adding 30 vol% of Ohara ceramic led to 1.5 orders of magnitude decrease in conductivity compared to neat polymer electrolyte. Between 30 vol% and 50 vol%, composite conductivity is not a significant function of ceramic volume fraction. With 60 vol% ceramic, the composite conductivity further decreased by 1 order of magnitude. At this high loading, particle packing becomes less dense. The best performing sample contains 50 vol% Ohara ceramic, a salt concentration of $[EO]:[Li^+] = 16:1$ and a plasticizer concentration of $[TEGDME]:[Li^+] = 2:1$. The room temperature conductivity of this sample is 1×10^{-6} S/cm, lower than the conductivity of both plasticized polymer electrolyte (2×10^{-5} S/cm) and Ohara ceramic plate (1×10^{-4} S/cm). At this point, the resistive polymer-ceramic interface became the key challenge of our approach.
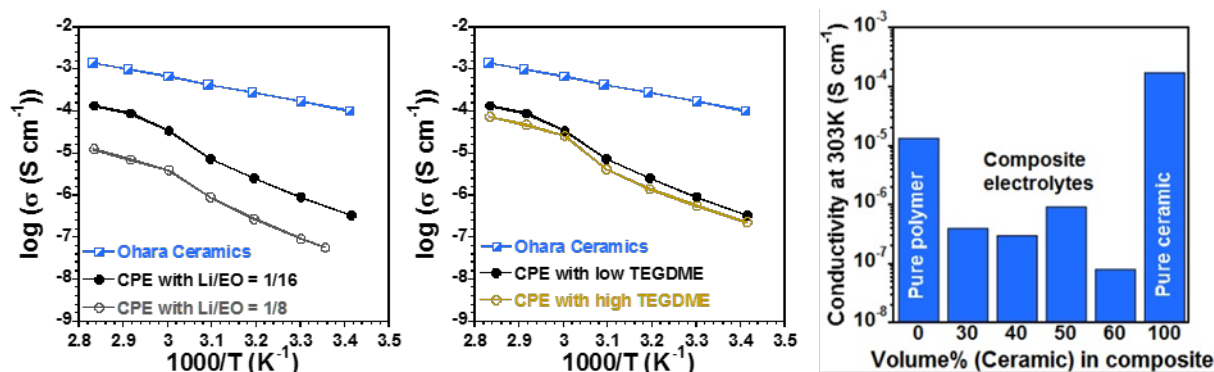

Figure II-458. Left, Arrhenius plot of TEGDME-plasticized composite electrolyte with different salt concentration; Middle, Arrhenius plot of TEGDME-plasticized composite electrolyte with different TEGDME content; Right, Room temperature conductivity of the TEGDME-plasticized composite as a function of the volume fraction of the Ohara ceramic.

Polymer-ceramic-polymer electrolyte (trilayer) cell was constructed to study the interfacial resistance between the polymer and ceramic electrolyte. Sintered ceramic plate from Ohara Corporation was sandwiched between two thin layers of polymer electrolyte of the same thickness, obtained by spray coating. The EIS results of single layer ceramic plate, single layer polymer electrolyte and trilayer are shown in Figure II-459a-c. The resistance of the trilayer is at least one order of magnitude larger than the two single layers combined. An SEM image of the cross-section of the trilayer is shown in the inset of Figure II-459c. Uniform coating and smooth interface are observed. We calculated the interfacial resistance from the data of the single layers and the trilayer cells, shown in Figure II-459d. At 30 °C, the interfacial resistance is 10000 Ohm. As an effort to decrease the interfacial resistance, we tried plasticized polymer electrolyte and the ceramic, using the same protocol. The plasticizer, TEGDME, which enhances the ionic conductivity of the polymer electrolyte does not facilitate ion transport across the polymer-ceramic interface (Figure II-459d).
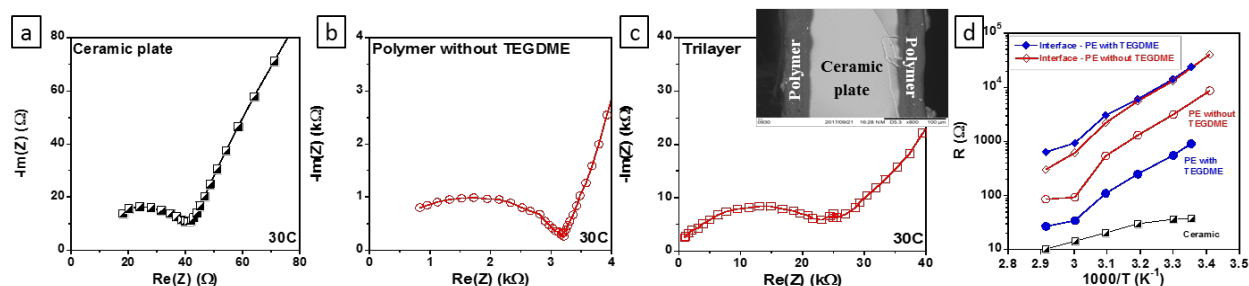
Figure II-459. Results for trilayer cell polymer /ceramic/polymer electrolyte. a-c, EIS responses of ceramic plate, polymer electrolytes and trilayer cells. All EIS response are measured at 30C. Inset of c, SEM of trilayer cell. d, Arrhenius plot of interfacial resistance calculated from the trilayer cell data.

We thus carried out investigations of other possible candidates for plasticizer attempting to improve the interface between the Ohara ceramic and polymer electrolyte. We tried diethyleneglycol dibutylether (DEGDBE) and hexamethylphosphoramide (HMPA), both are good candidates due to their low vapor pressure. Results for the conductivities of the composite coatings with 50 vol% Ohara powder and the new candidate plasticizer molecules are shown in Figure II-460. Composite containing DEGDBE did not show any improvement in conductivity compared to unplasticized composite. With the same molar concentration, HMPA and TEGDME showed similar effect ion composite conductivity. These results indicated that similar to TEGDME, DEGDBE and HMPA did not effectively decrease the interfacial resistance between Ohara ceramic and the polymer electrolyte.
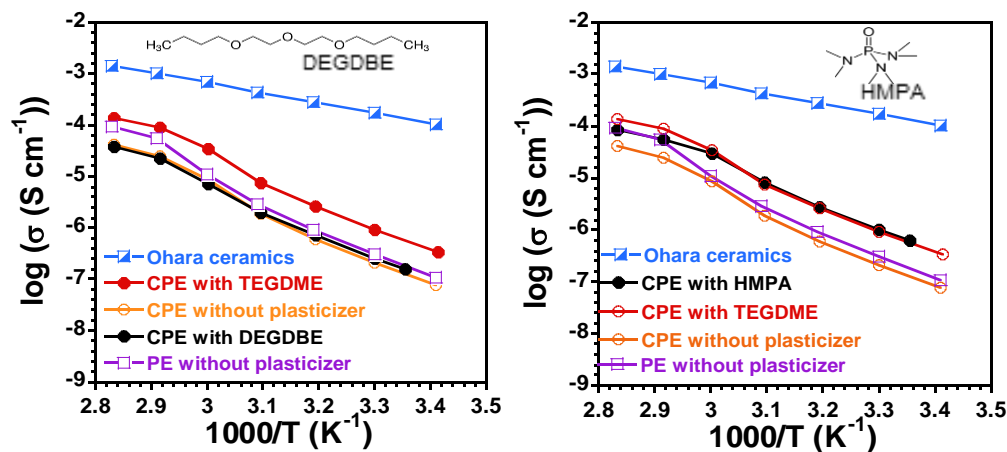

Figure II-460. Comparison of spray coated composite containing DEGDBE (left) and HMPA (right) as plasticizer with results obtained using TEGDME as plasticizer. Conductivity of composite and polymer that does not contain plasticizers is also presented.

To continue to address the interfacial resistance between Ohara powder and the polymer electrolyte, we studied the effects of acid and base treatment of the Ohara powders. Previous studies have shown moderate change in the ion conductivity of PEO-LiX-alumina composites by using alumina with acidic, neutral and basic surfaces. We treated Ohara powder with HNO_3 and NaOH aqueous solutions with 4 pH values, 1.4, 3.3, 10.6 and 12.7. XRD revealed change in the ceramic's crystalline structure after treatment in pH = 12.7 solution; IR spectra did not show significant differences in the treated and untreated Ohara powders. Results in Figure II-461 (left) show that treating Ohara with mild acid (pH = 3.3) and base (pH = 10.6) led to 2-3 fold reduction of conductivity, whereas the composite containing Ohara powder treated with strong base (pH = 12.7) showed conductivity similar to composite containing untreated Ohara powder. These composites were

formed by spray coating of an aqueous slurry and they did not contain a plasticizer. We repeated the experiments for composites formed by dry milling and melt pressing (Figure II-461, right). All of the dry milled samples presented lower conductivity than the spray coated samples, as discussed in Figure II-456. But the conclusion is consistent with spray coated samples – acid/base treatment did not facilitate the interfacial ion transport across the polymer-ceramic boundary.
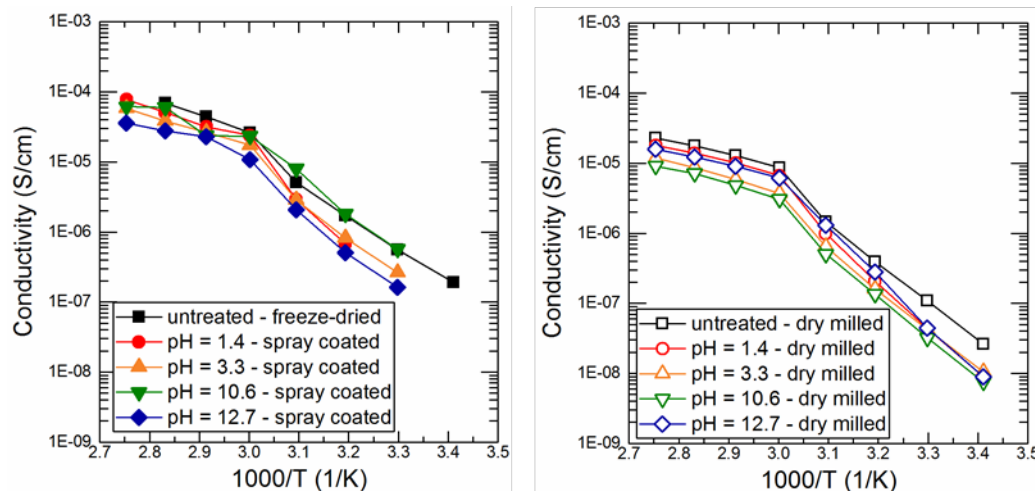

Figure II-461. Arrhenius plot of composite containing acid/based treated Ohara powders, compared to that of untreated composite. Left, spray coated samples; Right, dry milled samples.

Lastly, an automatic spray coater was set up for battery prototyping. We fabricated a full battery using aqueous spray coating for both the cathode and composite electrolyte incorporating a protected Li metal anode. Battery performance is under evaluation. In FY18, efforts will be focused on decreasing the interfacial resistance and optimizing cycling performance.

Conclusions

1. We confirmed that the densities of membranes formed by aqueous spray coating + hot pressing matched the highest predicted values. The conductivity of spray coated composite membranes is an order of magnitude higher than dry milled + melt pressed membranes with the same composition.

2. A transference number of 0.79 of TEGDME-plasticized composite electrolyte was determined, compared to that of polymer electrolyte, 0.47 – 0.57.

3. A series of salt, plasticizer and ceramic content were examined to optimize the conductivity of spray coated composite membranes. The best performing sample contains 50 vol% Ohara ceramic, a salt concentration of [EO]:[Li$^+$] = 16:1 and a plasticizer concentration of [TEGDME]:[Li$^+$] = 2:1. The room temperature conductivity of this sample is 1×10^{-6} S/cm, lower than the conductivity of both plasticized polymer electrolyte (2×10^{-5} S/cm) and Ohara ceramic plate (1×10^{-4} S/cm). The resistive polymer-ceramic interface became the key challenge of our approach.

4. Polymer-ceramic-polymer (trilayer) cell was constructed to study the interfacial resistance between the polymer and ceramic electrolyte. A very large interfacial resistance for ion transport (10000 Ohms at room temperature) was identified. In order to decrease the interfacial resistance, we tried two other plasticizers (DEGDBE and HMPA) and acid/base surface treatment of Ohara ceramic. The results showed limited success. Nevertheless, this method provides a platform for us to explore more strategies to minimize interfacial resistance.

5. In FY18, efforts will be focused on decreasing the interfacial resistance and optimizing cycling performance. We will reevaluate the effect of dimethyl carbonate (DMC) on the composite conductivity and interfacial resistance. Further, we will move beyond model materials like Ohara and PEO, to include single ion conducting polymers and polymer gels.

Key Publications

1. Amaresh Samuthira Pandian, Frank Delnick and Nancy Dudney, "Composite Polymer-Ceramic Electrolyte for High Energy Lithium Secondary Batteries", presented at PRiME meeting of Electrochemical Society, 2016 Hawaii.

2. Nancy Dudney, Amaresh Samuthira Pandian and Frank Delnick, "Composite Electrolyte to Stabilize Metallic Lithium Anodes", presented at DOE Vehicle Technologies Program, Annual Merit Review and Peer Evaluation Meeting, June 2017.

3. "Composite Polymer Ceramic Electrolyte for High Energy Lithium Secondary Batteries," In preparation.

II.H.4   Overcoming Interfacial Impedance in Solid-State Batteries (U of MD)

Eric Wachsman, Principal Investigator
University of Maryland
1206 Engineering Laboratory Building
University of Maryland
College Park, MD 20742
Phone: 301-405-8193
E-mail: ewach@umd.edu

Liangbing Hu, Co-Principal Investigator
University of Maryland
1208 Engineering Laboratory Building
University of Maryland
College Park, MD 20742
Phone: 301-405-9303
E-mail: binghu@umd.edu

Yifei Mo, Co-Principal Investigator
University of Maryland
1137 Engineering Laboratory Building
University of Maryland
College Park, MD 20742
Phone: 301-405-7613
E-mail: yfmo@umd.edu

Tien Duong, Technology Manager
U.S. Department of Energy
Phone: 202-586-7836
E-mail: Tien.Duong@ee.doe.gov

Project Introduction

Solid state garnet-electrolyte lithium ion batteries have tremendous potential due to their inherent safety, high voltage stability, and reasonably high conductivity. However, the interfacial impedance between solid state electrolytes and electrodes is currently too high. This work focuses on reducing the interfacial impedance, by making controlled structures on the garnet electrolyte surface, and introducing conductive and conformal interfacial layers between the garnet and the electrodes. These results, informed by computational modeling, address the primary issue and significantly advance solid-state Li-battery technology.

Objectives

Develop a multifaceted and integrated (experimental and computational) approach to solve the key issue in solid-state Li batteries (SSLiBs), interfacial impedance, with a focus on garnet-based solid-state electrolytes (SSEs), the knowledge of which can be applied to other SSE chemistries. The focus is to develop methods to decrease the impedance across interfaces with the solid electrolyte, and ultimately demonstrate a high power/energy density battery employing the best of these methods.

Approach

Innovative Approach: The objectives outlined above will be accomplished by optimizing the garnet surface structure and electrode material, and investigating high conductivity conformal interfacial layers.

1. Effect of interfacial structure on impedance

While we and others have made tremendous advances in understanding interfacial resistance in solid oxide fuel cells (SOFCs), to date no one has applied these techniques to SSLiBs. Therefore, we used SOFC techniques to develop a fundamental understanding of interfacial impedance in terms of intrinsic charge transfer rates, ionic and electronic transport, and effect of interfacial structure.

Electrochemical impedance spectroscopy (EIS) of solid electrolyte and electrode or interfacial layer pellets were performed to identify the mechanistic frequency dependence of EIS response for each material as well as blocking electrode and DC measurements to separate out ionic vs.electronic conductivity for each material. Then bilayer electrolyte and electrode/interfacial layer pellets with smooth and controlled interfaces were fabricated and tested with EIS.

This allowed for determination of the specific interfacial impedance, which could then be resolved as an additional EIS frequency response. This interfacial impedance was used to calculate the charge transfer reaction rate across the electrolyte/electrode and electrolyte/interfacial layer interfaces. Bilayered pellets with tailored nano/micro-rod interfaces have been fabricated (by templated deposition and additive manufacturing) with different rod length to diameter aspect ratios. The EIS data from these cells is deconvoluted and compared with known ionic and electronic transport rates, and charge transfer rates, to create fundamental models of interfacial impedance as a function of 3-dimensional interfacial structure.

2. Investigate interfacial modifications and cell performance

We are investigating four types of materials as interfacial layers in SSLiBs.

For **Type 1**, we used nonflammable organic electrolytes such as perfluoropolyethers (PFPE)-based electrolytes. It has been confirmed that such organic electrolytes cannot catch fire and are intrinsically safe. Although, PFPE-based electrolytes have very low ionic conductivity ($\sim 10^{-5}$ S/cm) and cannot meet the power density requirement in the FOA by itself, PFPE-based organic electrolyte can greatly improve the interfaces across electrolyte grain boundaries, or electrolyte/electrode interface for enhancing the battery performance.

For **Type 2**, we also used a polymer electrolyte or gel electrolyte, which is bis(trifluoromethane)sulfonimide lithium salt (LiTFSI) in poly(vinylidene fluoride-co-hexafluoropropylene) (PVDF-HFP). Although the polymer or gel electrolyte has a much lower ionic conductivity, its thickness is small as an interface layer and thus its contribution in overall impedance was expected to be negligible.

For **Type 3**, we are investigating thin inorganic layers formed by atomic layer deposition (ALD) and other thin film deposition techniques to form a nano-thin conducting phase between the garnet and the electrode.

For **Type 4**, we are using a soft conformable materials such as β-Li$_3$PS$_4$ (LPS) or liquids to bridge the gap between the garnet and electrode material.

For each approach, we fabricated half cells to investigate interfacial impedance and their changes during cycling. SSLiB interfaces are typically planar resulting in high impedance due to low specific surface area, and attempts to make 3D high surface area interfaces can also result in high impedance due to poor contact (e.g, pores) at the electrode-electrolyte interface that hinder ion transport or degrade due to expansion/contraction with voltage cycling. We have investigated the fundamentals of solid-solid interfacial impedances in FY 2015 and investigated interfacial modification (layers between SSE and electrode) to see if we can extend these structure-property relationships to higher performance in FY 2016. In FY 2017 we applied these interfacial modifications to develop solid-state batteries. The objective of FY 2017 was accomplished by developing full cells based on the interfacial impedance reducing techniques and the structurally optimized garnet SSEs. We

developed high energy density batteries based on multi-layer garnet, Li metal anode, and two different types of cathodes: $Li(Ni_xMn_yCo_{1-x-y})O_2$ (NMC) and sulfur. For each type of battery chemistry, the battery morphologies, electrochemical stabilities, and cycling performances were evaluated.

Throughout this work, we collaborated with with Dr. Kang Xu at the US Army Research Lab with preparation of liquid electrolytes. SSEs and electrode materials were synthesized in University of Maryland Energy Research Center, and characterized in the Nanocenter and FabLab at University of Maryland. Fabrication of the SSLiBs was accomplished using the comprehensive state-of-art multilayer ceramic fabrication facilities. The facilities include tape casting, screen printing, and furnaces for fabrication, as well as extensive electrochemical testing capabilities.

Results

1. Cathode interface resistance

1.1 Characterization of electrolyte/cathode interface impedance

We tested the impedance of LLCZN solid state electrolyte, and its interface impedance with LFMO electrodes. The LLCZN ($Li_{6.8}La_{2.95}Ca_{0.05}Zr_{1.75}Nb_{0.25}O_{12}$) garnet was synthesized by conventional solid state reactions. The starting materials, $Li(OH)$, $La(OH)_3$, $Ca(OH)_2$, ZrO_2, and Nb_2O_5 were mixed by planetary ball-milling, and then calcined at 700°C for 48 h. The calcined LLCZN powder was mixed with additives (both Al_2O_3 and Li_3BO_3, only Al_2O_3 or only Li_3BO_3) by planetary ball-milling. The mixture was die-pressed at 10 MPa into a pellet and sintered in air. EIS of LLCZN electrolyte and LFMO cathode was tested with Solartron 1260 impedance analyzer at room temperature using gold paste current collectors. EIS plots were collected at 50 mV voltage signal over a frequency range of 10 Hz -20 MHz.

Figure II-462a is the EIS curves of thick and thin LLCZN electrolyte samples. A semicircle and Warburg-type impedance appeared at high and low frequency regions, respectively. The high-frequency semicircle is the sum of bulk and grain boundary responses. The low-frequency tail corresponds to the capacitive behavior of gold blocking electrode. The total lithium-ion conductivity of LLCZN electrolyte is estimated from the intercepts from the semicircle at low frequency side. The thin pellet shows a slightly lower total conductivity than the thick pellet sample.

Figure II-462b is the EIS curves of thick and thin LFMO cathode samples at initial state (0%SOC). The Nyquist plot contains one depressed semicircle in the high frequency and another semicircle in the medium frequency ascribed to the resistance of Li^+ diffusion through the SEI layer and charge transfer reaction, respectively. The EIS plot indicates similar conductivity exhibited by both the thick and thin pellets of LFMO.

Knowing the frequency response of both LLCZN electrolyte and LFMO cathode we then analyzed the system consisting of electrolyte, cathode and their interface. Finely polished electrolyte and cathode with gold electrode on outer side were tightly pressed together. The electrolyte/cathode system was then characterized by EIS. Figure II-462c shows the Nyquist plots of LLCZN electrolyte/LFMO cathode system. Both thick and thin pellet samples were examined to identify the interfacial effect in the system. The impedance arc is the total resistance of LLCZN electrolyte, LFMO cathode and their interface. The arc in the medium-low frequency range is the dominant interfacial resistance between LLCZN electrolyte and LFMO cathode. The high frequency response in the magnified plot is the sum of LLCZN electrolyte resistance and LFMO cathode resistance. This process was repeated with other cathode materials beyond LFMO.

The garnet/cathode interface impedance was lowered by making structured garnet surfaces. Sintered dense garnet discs were sanded to 150 µm and polished. To make the column structures, polymer mesh was glued on disc surface as a template, after that a garnet slurry was drop coated to fill the open area. The coated sample was dried in oven and sintered at 800°C for 2h. Figure II-463a shows the structured garnet surface. The white shinning areas are the deposited column structures.

Symmetric cathode/electrolyte/cathode cells were made by screen printing thick cathode slurry on the garnet discs. LFMO cathode was sintered at 500°C for 1h. Silver paste was used as current collector. Thickness of the cathode was about 20μm. EIS plots were collected at 50 mV voltage signal in a frequency range of 10 Hz -10 MHz at room temperature. Figure II-463b is the EIS response of cathode coated as-polished and structured garnet discs which exhibits lower interfacial resistance, compared to that with smooth surface due to the larger interfacial cathode/electrolyte contact area provided by the surface column structure.
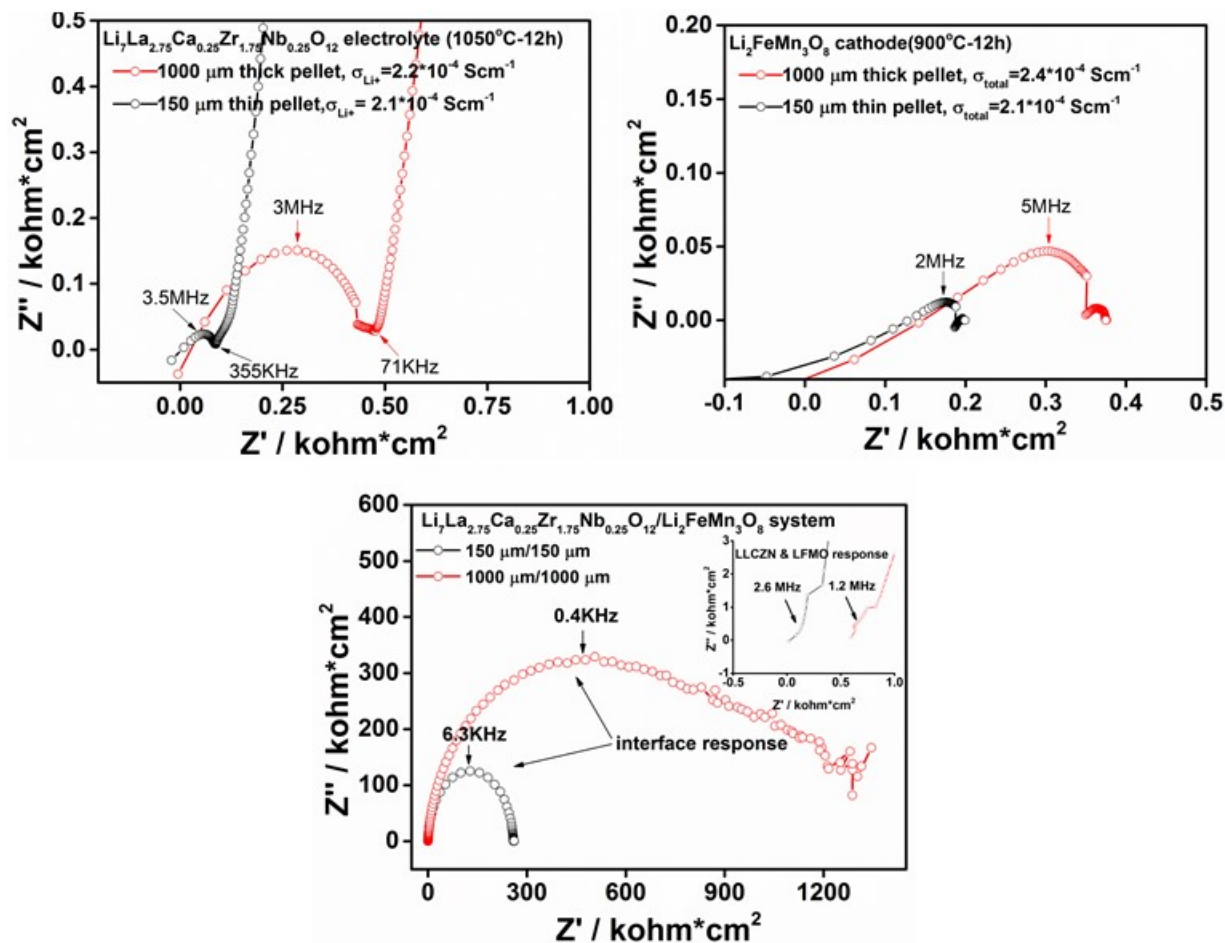

Figure II-462. (a) EIS of thick and thin LLCZN pellets, (b) thick and thin LFMO pellets, and (c) thick and thin LLCZN/LFMO pellets.

1.2. Synthesis and characterization of nonflammable PFPE-based interface (Type 1)

PFPE-DMC was prepared from Fluorolink D10 and triethylamine in 1,1,1,3,3-pentafluorobutane at 0°C under nitrogen atmosphere, followed by dropping a solution of methyl chloroformate in 1,1,1,3,3- pentafluorobutane. After the mixture was stirred at 25°C for 12 h, the PFPE-DMC product was obtained by filtering and washing with water and brine, followed by evaporation under reduced atmosphere. The PFPE-DMC electrolyte was then produced by dissolving Lithium bis(Trifluoromethanesulfonyl)Imide into PFPE-DMC. The synthesis method of PFPE-DMC is shown in Figure II-464a.
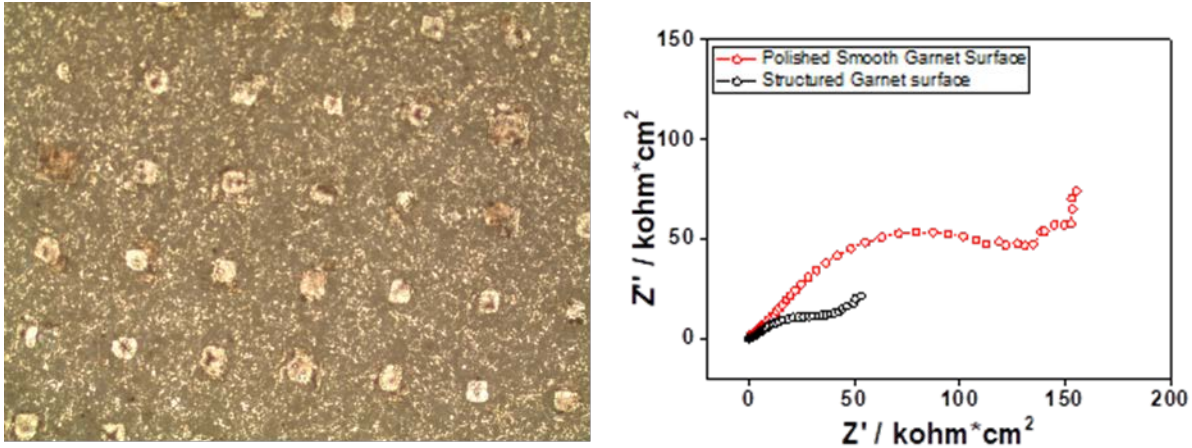
Figure II-463. (a) Photograph of structured garnet surface, bright white spots are garnet columns. (b) EIS of polished smooth garnet surface and structured garnet surface.

A Li/PFPE/Ti structure in a CR2025 coin cell was used to test cyclic voltammetry (CV) of the PFPE/LiTFSI electrolyte. The area of the cell is 1.98 cm^2 (radius=5/16 inch), and the area of Ti cathode is 0.712 cm^2 (radius=5/32 inch). The voltage range was -0.3~4.2 V, and the voltage scan speed was 1 mV/s.

The CV results are shown in Figure II-464b. The reaction current density is less than 0.002 mA/cm^2 in 0.3~4.2 V region, which is very small. And after the first few cycles, the CV curve becomes stable. The two facts show that the PFPE electrolyte is electrochemically stable between 0-4 V. Also, for the PFPE electrolyte, no obvious peaks appear in the voltage region of -0.3 ~ 4.2 V, which means that the Li stripping occurs at a higher voltage than 4.2 V, and the Li platting occurs at a lower voltage than -0.3 V. The electrochemical stability of PFPE/LiTFSI in the voltage range of 0~4.2 V ensures that this electrolyte is stable in the reactions of LLCZN garnet electrolyte lithium ion batteries, and can be used as the interfacial layer between garnet and cathode.
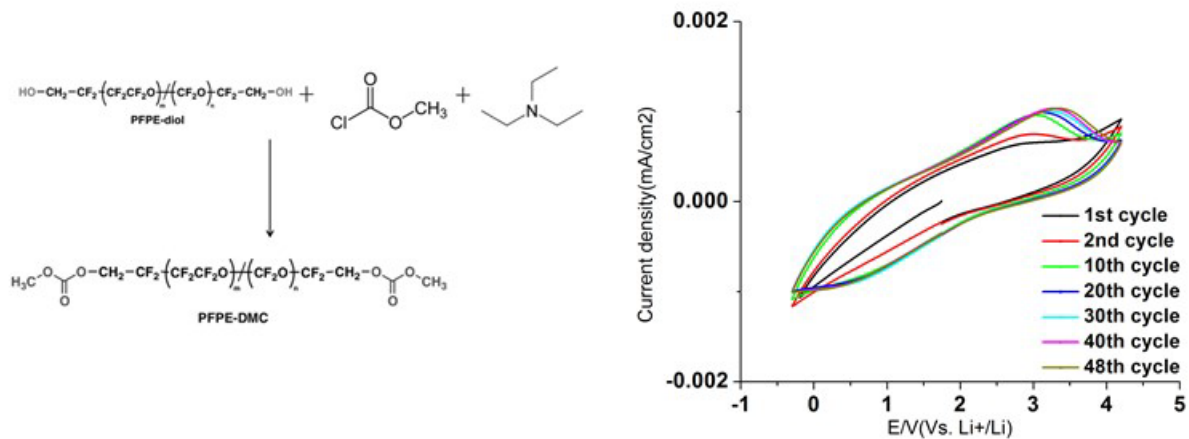

Figure II-464 (a) Synthesis procedure of PFPE-DMC. (b) Cyclic voltammetry study of LiTFSI-PFPE electrolyte.

1.3. Synthesis and characterization of gel-based interface (Type 2)

A PVDF-HFP-based gel polymer was prepared (Figure II-465) from 0.25 g PVDF-HFP dissolved into a mixture of 4.75 g acetone and 0.25 g DI water (95:5, m/m) under continuous stirring. The solution was cast onto an Al foil and the solvent evaporated at ambient temperature. After drying under vacuum at 100°C a homogeneous free standing membrane was obtained. The as-prepared porous membrane was immersed into 1 M LiTFSI in a mixture of 1:1 volume ratio of tetraethylene glycol dimethyl ether and n-methyl-(n-butyl)

pyrrolidinium bis(trifluoromethanesulfonyl)imide (Py14TFSI) at room temperature for 30 mins in an argon-filled glovebox.

CV testing cell was set up by sandwiching the gel electrolyte membrane between lithium and titanium disks and sealing the configuration in CR2032 coin cells. The CV (Figure II-465b) at a scan rate of 1 mV/s suggests a stable electrochemical window up to 4.2 V. The sharp peak at -0.2 V corresponds to the Li plating, while the peak around 0.1 V is due to the Li stripping.

Figure II-466a is the electrochemical impedance spectroscopy (EIS) plot of a cathode/garnet/cathode symmetric cell without any interfacial layer modification. The total resistance of cathode/garnet/cathode symmetric cell without gel interfacial layer is ~106 Ohm-cm^2 due to the poor contact between garnet and LiFePO$_4$ cathode material, the difficulty of charge transfer through the interface between two solid materials, the non-conductive binder, and the rough surface of the garnet pellet.

Figure II-466b is the EIS plot of cathode/garnet/cathode symmetric cell with gel interface. The impedance curve has three components. In the high frequency region (f >9 kHz) is an incomplete semi-circle, corresponding to the bulk and grain boundary impedance of the garnet electrolyte. In the middle frequency region (7 Hz <f< 9 kHz) is a combination of two semi-circles corresponding to interfacial charge transfer impedance between garnet and cathode, including impedance on the gel/garnet and cathode/gel interfaces, as the impedance of the gel layer itself is very small. In the low frequency region (f <7 Hz) is a straight line, corresponding to diffusion impedance of the cathode.
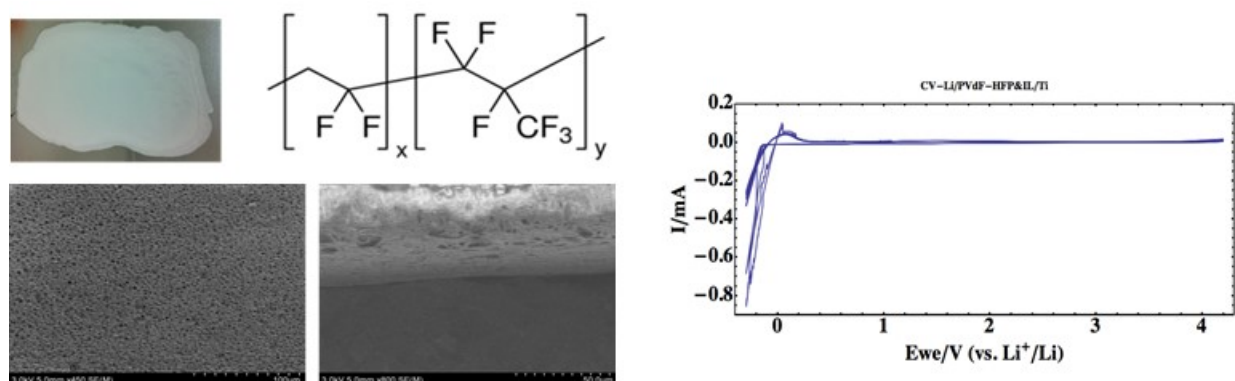

Figure II-465. (a) Photograph, (b) structure, (c) top and (d) side SEM images of PVDF-HFP gel membrane. (e) Cyclic voltammetry study of Li|PVDF-HPF+IL|Ti. (f) EIS of LLCZN/LFMO interface without (black) and with (red) PVDF-HFP gel electrolyte interface.

The interfacial resistance is obtained by subtracting the garnet resistance obtained separately by EIS of garnet samples from the total symmetric cell resistance, then dividing by two as there are two interfaces, e.g.,:

- Thickness of garnet pellet is 500 µm, and garnet conductivity is 2.1*10^{-4} S/cm (Figure II-466c). Therefore, area specific resistance (ASR) of garnet pellet is 239 Ohm-cm^2.

- The total symmetric cell resistance (Figure II-466b) is 600 Ohm-cm^2. Therefore, the ASR of one interface is (600-239)/2 =180 Ohm-cm^2, which is ~4 orders of magnitude less than the same symmetric cell without the interfacial layers.

To further reduce the garnet/cathode interfacial impedance the procedure was improved by making a gel/cathode composite, instead of using separate gel layers, thus reducing the gel thickness and improving the contact between gel and cathode. Figure II-466d shows the structure of symmetric cell using LiFePO$_4$/gel cathode on both sides of garnet, and Figure II-466e shows the impedance of this structure. The corresponding interfacial ASR is now reduced to only 67 Ohm-cm^2 for one interface (using same approach described above).
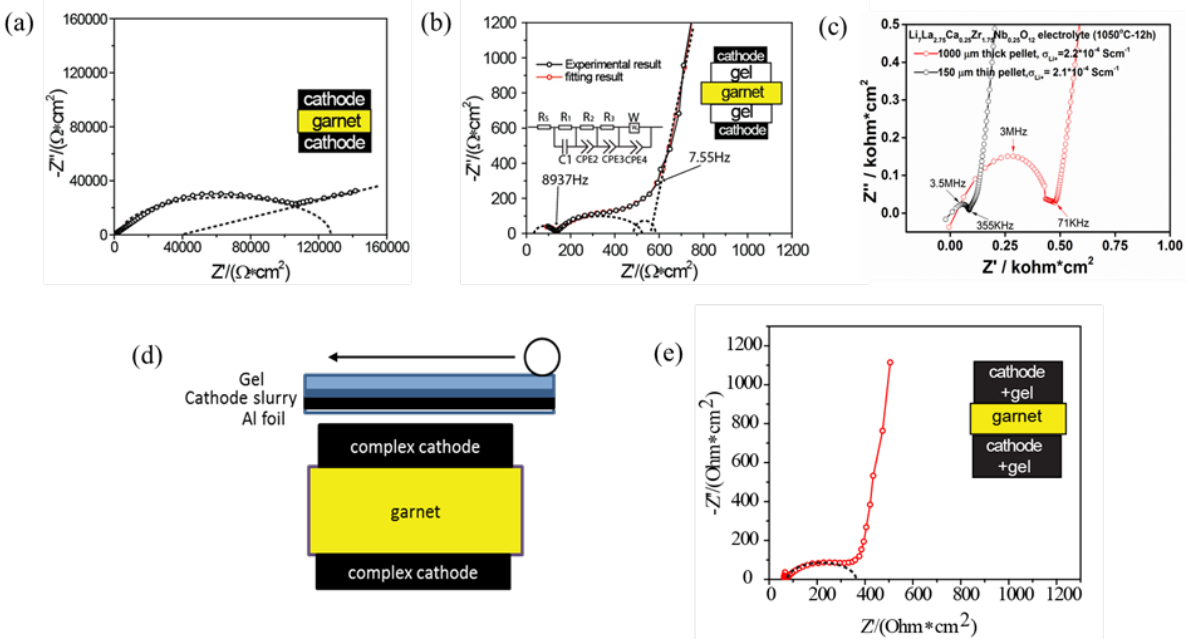
Figure II-466. (a) EIS plot of cathode/garnet/cathode symmetric cell without gel electrolyte. (b) EIS of cathode/gel/garnet/gel/cathode symmetric cell and the equivalent circuit. (c) EIS of garnet itself. (d) Schematic of making garnet cell with mixed cathode. (e) EIS of symmetric cell with mixed cathode and gel.

1.4 Synthesis and characterization of aqueous interface (Type 4)

To further reduce the cathode/garnet interfacial resistance we evaluated an aqueous solution interface (e.g., Type 4). We anticipated a lower cathode/garnet interfacial resistance with the aqueous interface compared with the gel interface as the aqueous solution has higher conductivity and fluidity than the organic electrolyte used for the gel interfaces. Figure II-467a shows a schematic of the symmetric cell with the aqueous cathode/garnet interface. The cathode material (LiFePO$_4$, Carbon black and PVDF) was coated on a carbon cloth. Then these electrodes were immersed into a saturated aqueous LiCl solution to wet them and then the two electrodes and a garnet pellet were pressed together.

As shown in Figure II-467b, the EIS semi-circle of the cell yields a resistance of 253 Ohm-cm^2, which after correcting for garnet ASR and dividing by 2 for the dual interfaces results in a single cathode/garnet interfacial resistance of only 7.5 Ohm-cm^2, 5 orders of magnitude lower than the non interfacial layer cell, and achieving the Q4FY16 and budget period 2 Go/NoGo milestones.
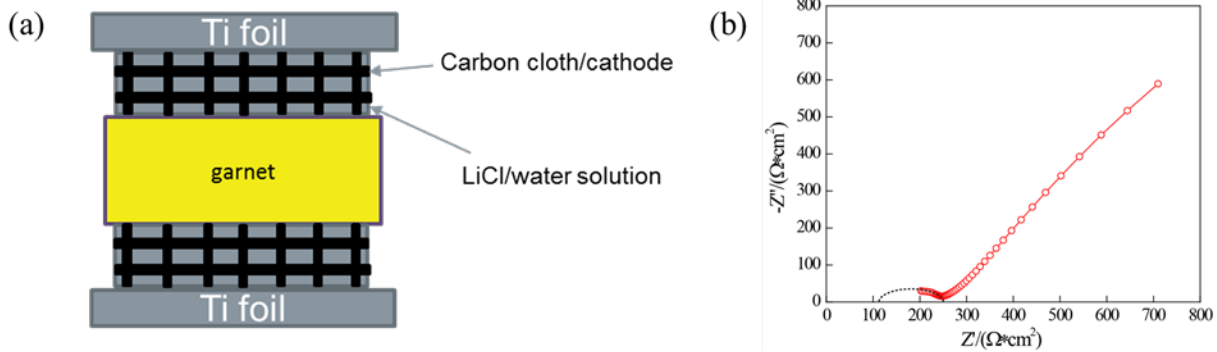

Figure II-467. (a) Schematic of a cathode/garnet/cathode symmetric cell with aqueous interface. (b) Impedance of this cell with aqueous interface.

1.5 Characterization of structured garnet interface

A 3D garnet surface structure can dramatically increase the effective surface area relative to the planar areal surface area. 3D structured garnet line patterns were printed on surface polished garnet pellets and sintered to form structured ionic conductive paths with varying line spacing (Figure II-468). Cathode slurries (LiFePO$_4$, CNT, and gel) were coated on both flat and structured garnet surfaces. EIS of the symmetrical cells was obtained at room temperature.

The depressed arcs, which can be assigned to Li$^+$ diffusion and charge transfer steps, became much smaller after effective extension of surface area. The 3D printed lines (40 μm height and 70 μm width) increased the effective sample surface areas from 36 mm^2 for polished pellet to 39.9, 42.3 and 48 mm^2 with increasing line density, resulting in 22%, 35% and 52% reduction of interfacial resistance (from the intercept of real axis high frequency arc (Figure II-468a)) proportional to the increase in effective surface area (Figure II-468b). Therefore, as expected the 3D printed structures reduced the cathode-electrolyte interfacial resistance linearly with increasing effective surface area.
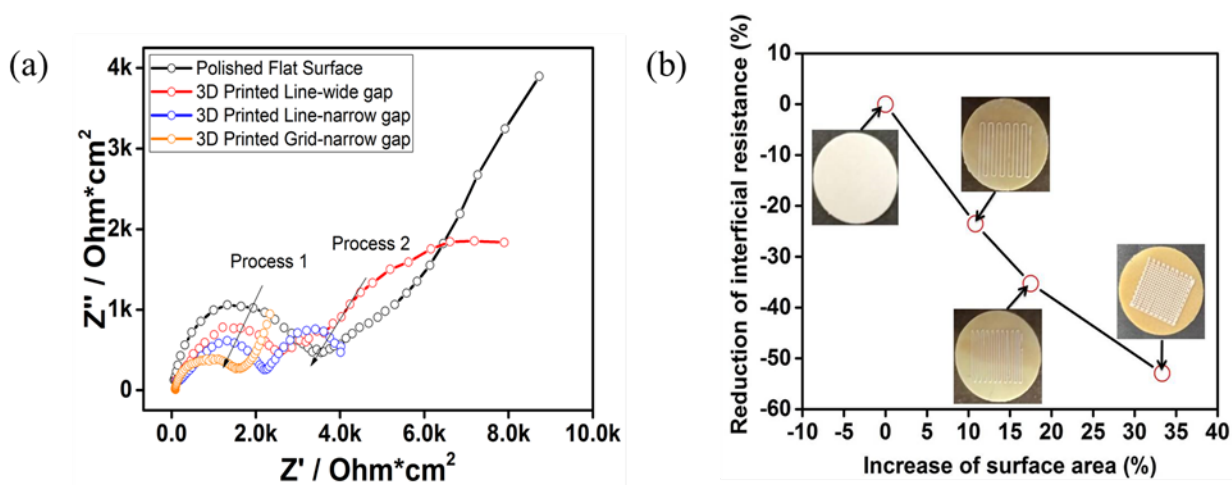

Figure II-468. Comparison of cathode/electrolyte interfacial impedance on flat and 3D-structured garnet pellets. (a) EIS plot of garnet without 3D printing and with different 3D printings. (b) Reduction of interfacial resistance with increase in surface area.

2. Anode interface impedance

2.1 Characterization of gel electrolyte interface

Figure II-469a shows that the total resistance of a Li/garnet/Li symmetric cell (formed by melting Li metal on the garnet surfaces) without an interfacial layer is about 3000 Ohm-cm^2. Figure II-469b shows the EIS plot of Li/gel/garnet/gel/Li plot has four components. In the high frequency region is an incomplete semi-circle, from the garnet impedance. In the middle frequency region are two semi-circles, due to interfacial charge transfer impedance between garnet and Li metal, which mainly comes from impedance on the gel/garnet and Li/gel interfaces, as the impedance of the gel layer itself is very small. In the low frequency region is a tail, corresponding to diffusion impedance of the interface of gel/stainless steel outside of the lithium metal. Correcting for garnet impedance, the ASR with the gel interlayer is reduced to 200 Ohm-cm^2 for one interface; however, this is done without melting the Li metal as was done for the other cell.
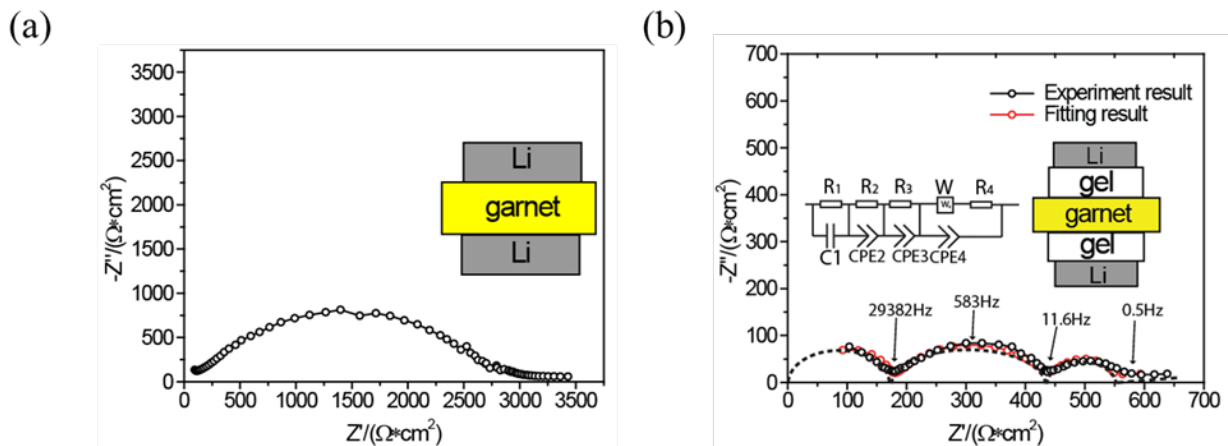

Figure II-469. (a) EIS plot of Li/garnet/Li symmetric cell. (b) EIS plot and equivalent circuit of Li/gel/garnet/gel/Li symmetric cell.

2.2 Characterization of Si interface

LLZ and Si-coated LLZ was sandwiched by two Li metal electrodes to assemble symmetric cells (Figure II-470a, and Figure II-470b). Prior to the electrochemical measurements, all the cells were heated at ~200 µC for twenty minutes in a glovebox since thermal treatment promotes superior contact between Li and LLZ. Due to the high reactivity of molten Li, lithiated Si will be formed in situ between the Li metal and the Si-coated LLZ. The Nyquist plots of symmetric cells in Figure II-470c exhibit two distinct semi-circles: one at high frequency and another at low frequency. The Li/LLZ/Li symmetric cell delivers a large resistance of 2064 Ohm-cm^2, where the interfacial resistance between Li and LLZ was calculated to be 925 Ohm-cm^2.

The first semi-circle at relatively high frequency was used to analyze the interfacial resistance between the Li metal electrode and the LLZ solid electrolyte with/without Si coating. As shown in Figure II-470d, the overall resistance of the LLZ (bulk and grain boundary) measured using Au electrodes is 215 Ohm-cm^2. As shown in Figure II-470e, the first semi-circle of the Li/LLZ/Li cell yields a resistance of 2064 Ohm-cm^2, which can be divided into two parts: one is the resistance of the LLZ (bulk and grain boundary) and the other is the Li metal-LLZ interfacial resistance. Thus, the overall Li metal-LLZ interfacial resistance is 1849 Ohm-cm^2. Since two Li metal-LLZ interfaces are present in the Li/LLZ/Li symmetric cells, the single Li metal-LLZ interfacial resistance is approximately 925 Ohm-cm^2. On the other hand, the Si-coated LLZ cell displays a much smaller resistance of 469 Ohm-cm^2 in the first semi-circle. By subtracting the resistance of the LLZ (215 Ohm-cm^2) and dividing by two, the Li metal/Si-coated LLZ interfacial resistance can be calculated: 127 Ohm-cm^2, which is about 7.3 times lower than bare LLZ.
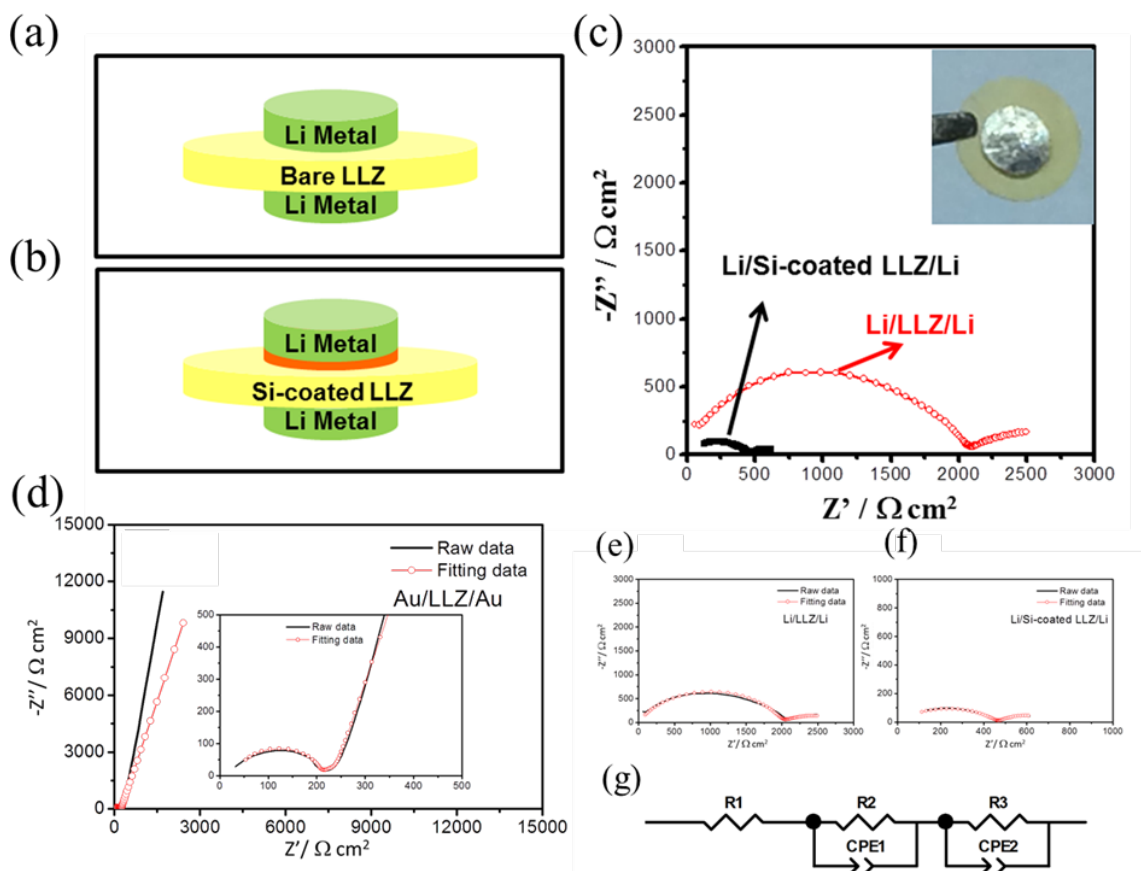
Figure II-470. Schematic illustration showing the structure of symmetric cells with (a) LLZ or (b) Si-coated LLZ SSEs. (c) Electrochemical impedance spectroscopy (EIS) measurements of symmetric cells where the interfacial resistance of the Si-coated garnet cell significantly decreased. Inset of (c) is a digital image of a Li/Si-coated LLZ/Li symmetric cell. (d) Nyquist plots of the Au/LLZ/Au symmetric blocking electrode system at room temperature. The solid black line denotes the experimental data while the red line with hollow spheres represents the fitting data using the equivalent circuit modeling. (e-g) Nyquist plots of (e) Li/LLZ/Li and (f) Li/Si-coated LLZ/Li symmetric cells. (g) The equivalent circuit model used in this study.

2.3 Characterization of Al interface

Two symmetric cells, Li | Garnet SSE | Li and Li | Al-Garnet SSE-Al | Li, were prepared and tested directly in an argon-filled glovebox. The two cells showed large differences in total resistance, which depend on both the garnet's total resistance and the interface charge transfer resistance, as shown in the Nyquist plots (Figure II-471a and Figure II-471b). The Li | Garnet SSE | Li cell had a total resistance of ~2000 Ohm-cm^2. However, the Li | Al-Garnet SSE-Al | Li cell exhibited a resistance of ~300 Ohm-cm^2, which is almost one order of magnitude smaller than the uncoated SSE. The small partial semicircle at high frequency can be assigned to the total resistance of the garnet material. The large semicircle at medium frequency and low frequency correspond to the charge transfer resistance, which is the combination of the solid-state electrolyte resistance as well as the Li interfaces within the symmetric cells. The decreased size of the semicircle indicates that the interfacial resistance was significantly reduced using the Al coating. The total garnet resistance was ~150 Ohm-cm^2 and remained unchanged during the Li melting process. By subtracting the garnet ASR, the Li | Garnet SSE | Li cell charge transfer resistance was ~1900 Ohm-cm^2 at 20°C. For the Li | Al-Garnet SSE-Al | Li cell, the charge transfer resistance was decreased to ~150 Ohm-cm^2. Note that the interfacial resistance corresponds to two symmetric interfaces. Therefore, the interfacial resistance is ~950 Ohm-cm^2 and ~75 Ohm-cm^2 for Li | Garnet SSE and Li | Al-Garnet SSE-Al, respectively.
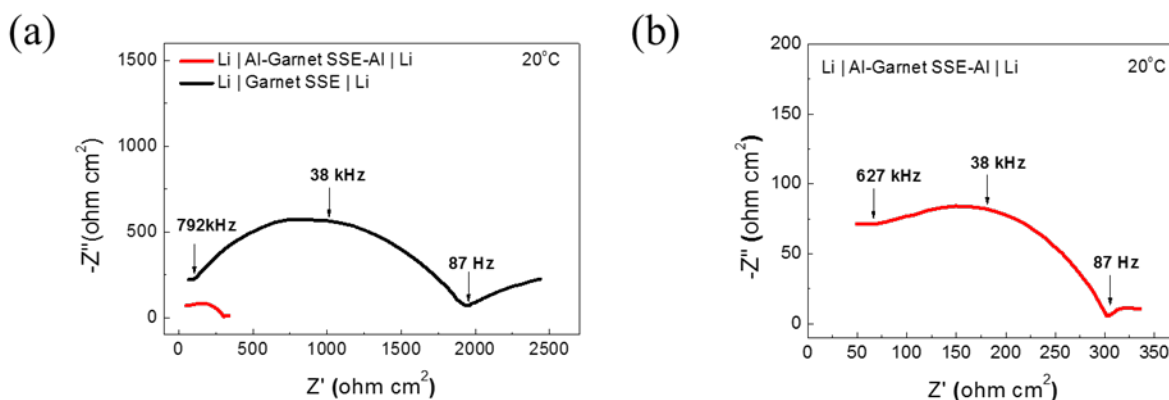
Figure II-471. Nyquist plots of Li | Garnet SSE | Li (a) and Li | Al-Garnet SSE-Al | Li (b) in the frequency of 1 MHz to 100 mHz at 20°C.

2.4 Characterization of ALD Al₂O₃ interface

To make Li/garnet/Li symmetric cell with ALD Al_2O_3 interface, a ~ 5-6 nm thick ALD-Al_2O_3 coating was applied to the garnet surface. Then a piece of Li metal foil was pressed on the garnet pellets and heated at 250°C for 1 hour under a small pressure. A control sample was made using bare LLCZN pellets in the same way.

Figure II-472a shows the schematic of the interface between garnet and Li metal. The SEM images in Figure II-472b clearly demonstrated that the enhancement of interfacial contact by applying ALD Al_2O_3 ultrathin layer on garnet interface. Inset are photo images to show the surface wetting of garnet and the ALD treated garnet.

To quantify the effect of ALD on the improvement of garnet/Li interface, symmetric Li/garnet/Li cells were prepared and evaluated by EIS (Table II-21 and Figure II-472). As shown in Figure II-472c, two distinct arcs were seen in each sample. The bulk garnet ASRs, obtained from the high frequency intercept, are 26 and 28 Ohm-cm² for cells with and without ALD coating, respectively. The first arc represents most likely the overlap of the grain boundary and interface impedances, which were 176 Ohm-cm² and 3500 Ohm-cm² for cells with and without ALD coating, respectively. Interfacial ASR was calculated by subtracting the garnet impedance measured with Au electrodes (~108 Ohm-cm²) and dividing this result by two before normalizing to the electrode surface area. It can be seen that the ALD treatment decreased the interfacial ASR by EIS from 1750 Ohm-cm² to 34 Ohm-cm². However, DC cycling (Figure II-472e) further reduced the interfacial impedance. The total ASR from DC cycling is calculated as 110 Ohm-cm², which after substracting 108 Ohm-cm² for the garnet contribution leaves 1 Ohm-cm² for each Li-garnet interface.

Table II-21: Electrochemical impedance with fitting data for Li/LLCZN/Li cells with and without ALD coating on both sides of the garnet SSEs.

| LLCZN SSE	Bulk ASR (Ω-cm²)	Grain Boundary ASR (Ω-cm²)	Grain Boundary Capacitance (F)	Interfacial ASR (Ω-cm²)	Interfacial Capacitance (F)
No ALD	28	4500	2.09×10^{-9}	490	9.9×10^{-4}
ALD	26	150	3.09×10^{-9}	16	2.8×10^{-5}
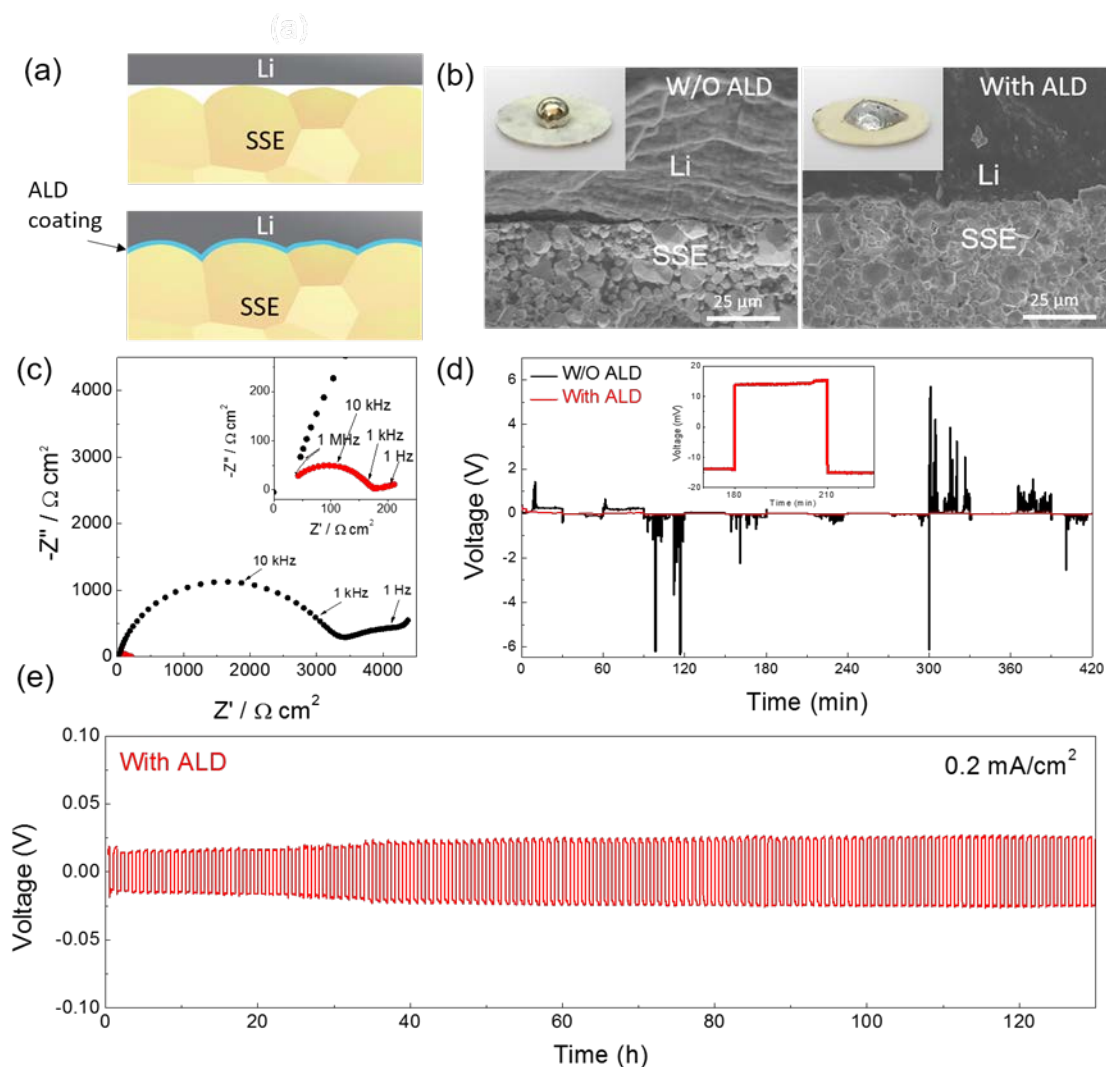
Figure II-472. Characterization of garnet solid state electrolyte/Li metal interface. (a) Schematic of the wetting behavior of garnet surface with molten Li. (b) SEM images of the garnet solid state electrolyte/Li metal interface. Without ALD Al$_2$O$_3$ coating, garnet has a poor interfacial contact with Li metal. Inset are photo images of contacts between melted Li-metal and garnet surface. (c) Comparison of EIS profiles of the symmetric Li non-blocking garnet cells. Inset shows the enlarged impedance curve of the ALD treated garnet cell. (d) Comparison of Li tripping/plating behavior of the symmetric garnet SSE/Li cells. Inset is the one cycle of stripping/plating for the ALD treated garnet cell, exhibiting a low overall impedance and stable interfacial property. (e) Voltage profile of the ALD treated garnet symmetric cell at a current density of 0.2 mA/cm^2.

3. Modeling of interfacial coating layers on garnet-electrode interfaces

First principles modeling of garnet solid electrolyte materials were performed on both tetragonal and cubic LLZ phases. The ordering of Li was determined using computational methods, and the ground state ordering of Li was determined. The Li grand canonical phase diagram of the Li-La-Zr-O system based on first principles computation methods and electrochemical stability of garnet against Li metal was determined (Figure II-473).

In addition, first principle models were constructed to evaluate the structure and energetics of the electrolyte-electrode interfaces between garnet and Li metal. We found that Li metal has a very weak interfacial binding with Li$_2$CO$_3$, which are found on the garnet surfaces, and Li metal binds strongly with oxide materials that may form on the garnet surfaces. The weak interface binding may lead to forming interfacial gaps and

intervals, thus a low contact area and a high interfacial resistance. Stronger interface binding would lead to enhanced interfacial contacts with larger contact area and good interfacial conductance.
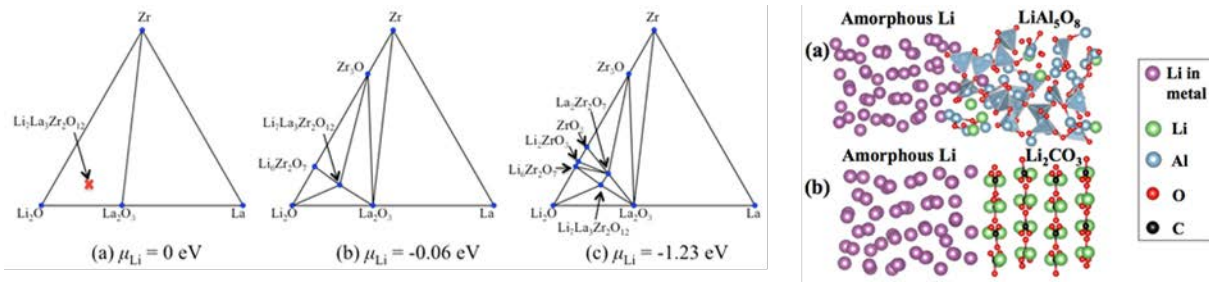

Figure II-473. (a) Li grand cannonical phase diagram of Li-La-Zr-O system. (b) Models for the interfaces between Li metal and garnet surface materials.

We developed a computational model for garnet-electrode interfaces (Figure II-474). The comprehensive interface model is based on a large variety of inputs provided by a range of first principles computation and actual experimental parameters to model the interface properties. The interface model has been developed and demonstrated for garnet materials with electrode materials, such as $LiCoO_2$ and LFMO. The interphase layers between the garnet and the electrode were determined using grand potential phase diagram at the applied voltage of the battery at the input for the model. The formation of the interphase was found to be thermodynamically favorable for the interfaces of garnet with anode and cathode. In addition, the properties of the materials comprising the interphase, such as defect and migration energy, were also evaluated in first pricniples calculations. The effects of the space-charge layer were incorporated as a part of interface model. Using all these predicted input parameters, the conductivity and interfacial resistance of the interfacial layer were determined. The model is now ready to be applied to any composition of garnet solid electrolyte in contact with any electrode materials. The inputs for the interface model are generated by the first principles computation and experimental parameters. The model was able to demonstrate that a poor interfacial layer causes high interfacial resistance in all-solid-state batteries.
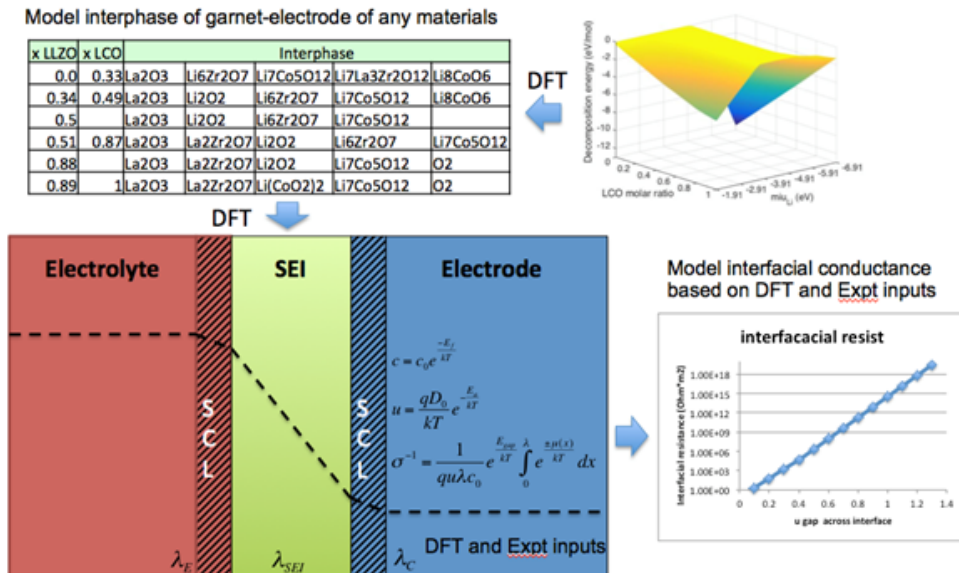

Figure II-474. Model for garnet-electrode interfaces, which take inputs from first principles calculations and experimental condition parameters.

We applied first principles calculations to investigate the interface stability between garnet and formed Li-Al alloys (Figure II-475a). We considered the interface as a pseudo-binary of Li-Al alloy and garnet, then constructed the related phase diagram to identify possible thermodynamically favorable reactions. The compositional phase diagrams were constructed, and the mutual reaction energy of the pseudo-binary calculated using same approach defined in our previous work (Figure II-475b). We found that three kinds of Li-Al alloy showed mutual reactions with garnet because of the slightly thermodynamic "welding" at their interface. Since the calculated reaction enthalpy is only around -60 ~ -40 meV/atom, the small reaction energy indicates that the interfacial reactions are likely to be limited and the formed interface could be relatively thermodynamic stable. Therefore, the interface between Li-Al alloy and garnet may exhibit good chemical stability, which might facilitate Li ion transport through.
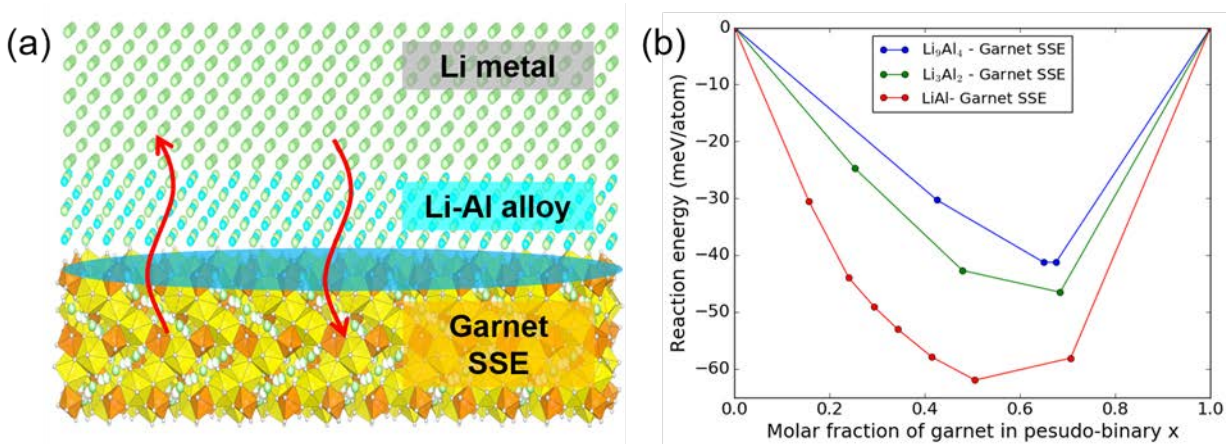

Figure II-475. Calculated mutual reaction energy, ΔE_D, of garnet and Li-Al alloy interfaces.

We apply the computational scheme to investigate interfacial chemical compatibility of these two interfaces with the coating layer with the SE and LCO, respectively. The previously demonstrated coating layer materials, such as $Li_4Ti_5O_{12}$, $LiTaO_3$, $LiNbO_3$, Li_2SiO_3, and Li_3PO_4, have excellent chemical stability with the LCO and $L_{0.5}CO$ with zero or negligible decomposition energy $\Delta E_{D,min,mutual}$ (Table II-22). In addition, all coating layer materials show relatively better stability with the sulfide SE comparing to the original sulfide SE-LCO interfaces, which have the interfacial reaction energy $\Delta E_{D,min,mutual}$ of ~ -500 meV/atom. As a result, the interface with the coating layer has significantly improved stability and suppresses the formation of thick interphase layer. In addition to stabilizing the interface, the coating layer of only a few nanometers is significantly thinner than the decomposition interphase layer of ~10 to 100 nm. The reduced thickness of the coating layer may significantly reduce the high interfacial resistance caused by the thick decomposition interphase layer.

In addition, we also computationally investigated other compounds (listed in Figure II-476 and Table II-22) based on the same cations, such as Ti, Nb, Si, Ta, and P, as potential coating layer materials. All these lithium metal oxide materials have a wide electrochemical window (Figure II-476a). The compounds with higher Li content generally show lower reduction potential, and the compounds with lower Li content or higher O content show higher oxidation potential. Most of these compounds have excellent chemical stability against LCO and $L_{0.5}CO$ cathode materials with zero or small $\Delta E_{D,min,mutual}$ (Table II-22). All these coating layer materials significantly improve the stability of sulfide SE-LCO interfaces. The chemical stability between LLZO-coating layer interface varies significantly with the compositions of the coating layer materials. The other Li-rich coating layers, such as Li_4TiO_4, Li_2TiO_3, Li_8SiO_6, Li_4SiO_4, Li_5TaO_5, and Li_3TaO_4 may work better with LLZO than those previously demonstrated for sulfide SEs, such as $Li_4Ti_5O_{12}$, $LiTaO_3$, and Li_2SiO_3.
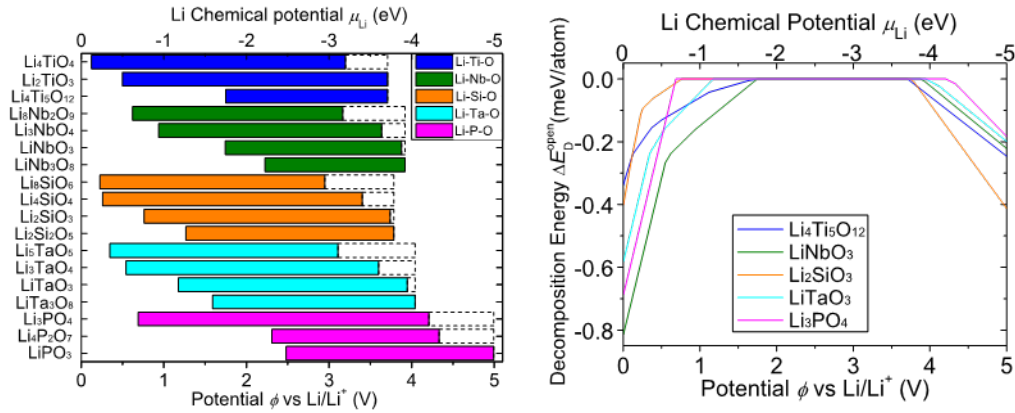
Figure II-476. Electrochemical window (left) and the decomposition energy ΔE_D^{open} (right) of the proposed and previously demonstrated coating layer materials applied between SE and cathode materials. The dashed line in (a) marks the equilibrium voltage to fully delithiate the materials.

Table II-22: The mutual reaction energy $\Delta E_{D,min,mutual}$ (in meV/atom) of the coating layer materials with the SE or LCO materials.

	Li$_3$PS$_4$	LLZO	LCO	L$_{0.5}$CO
Li$_4$TiO$_4$	-125	0	0	-30
Li$_2$TiO$_3$	-75	-5	0	0
Li$_4$Ti$_5$O$_{12}$	-80	-75	-1	0
Li$_8$Nb$_2$O$_9$	-147	0	0	-20
Li$_3$NbO$_4$	-132	-4	0	0
LiNbO$_3$	-155	-76	0	0
LiNb$_3$O$_8$	-173	-115	-16	0
Li$_8$SiO$_6$	-177	0	-3	-50
Li$_4$SiO$_4$	-81	-1	0	-12
Li$_2$SiO$_3$	-19	-29	0	0
Li$_2$Si$_2$O$_2$	-10	-69	-4	0
Li$_5$TaO$_5$	-117	0	0	-32
Li$_3$TaO$_4$	-64	-3	0	0
LiTaO$_3$	-49	-68	0	0
LiTa$_3$O$_8$	-64	-105	-22	0
Li$_3$PO$_4$	0	0	0	0
Li$_4$P$_2$O$_7$	-9	-101	-44	-3
LiPO$_3$	-32	-201	-76	-19

4. Computational modeling study for interface for Li-S and Li-NMC SSLiBs.

Thermodynamic computation predicted potential reaction and interphase formation between LLZO and Li polysulfides in all-solid-state Li-S batteries (Figure II-477a). Li_2SO_4 is identified as a dominant reaction product, which is confirmed in the XPS spectra (Figure II-477b). The formed interphase layer may serve as a protection layer between garnet solid electrolyte and S cathode. The Li-ion transport mechanism in these interphase layers would be crucial for assessing interfacial ion transport. First principles computation based on nudged-elastic-band methods were performed to identify the Li^+ transport pathway (Figure II-477c) and migration energy barrier (Figure II-477d) of ~0.6-0.8eV, showing reasonable Li^+ interfacial transport across the formed interphase layers in Li-S solid-state battery.

Thermodynamic computation also predicted potential reaction and interphase formation between LLZO and NMC cathode in solid-state Li-ion batteries, and such reaction is energetically more favorable at high applied voltages. As potential formed products, the interphase equilibria include Li_6ZrO_7, $La_2Zr_2O_7$ and various Li/La transition metal oxides. The Li^+ transport was studied in Li_6ZrO_7, a dominant interphase product, using first principles computation. The Li-ion transport pathway is shown in Figure II-477e. The migration energy barrier (Figure II-477f) of ~0.2-0.8eV suggests decent Li-ion transport across the interface from garnet electrolyte and NMC cathode in an all-solid-state Li-ion battery.

In summary, our developed computation models reveal the interphase layer formation between garnet solid electrolyte and S or NMC cathode materials in all-solid-state Li batteries. The formation of such layers serves an important protection role at the electrolyte-cathode interfaces. The Li-ion transport in these interphase layers are crucial for the battery performance. First principles calculations revealed Li-ion diffusion mechanisms and showed decent Li-ion transport in these materials and across the interfaces.
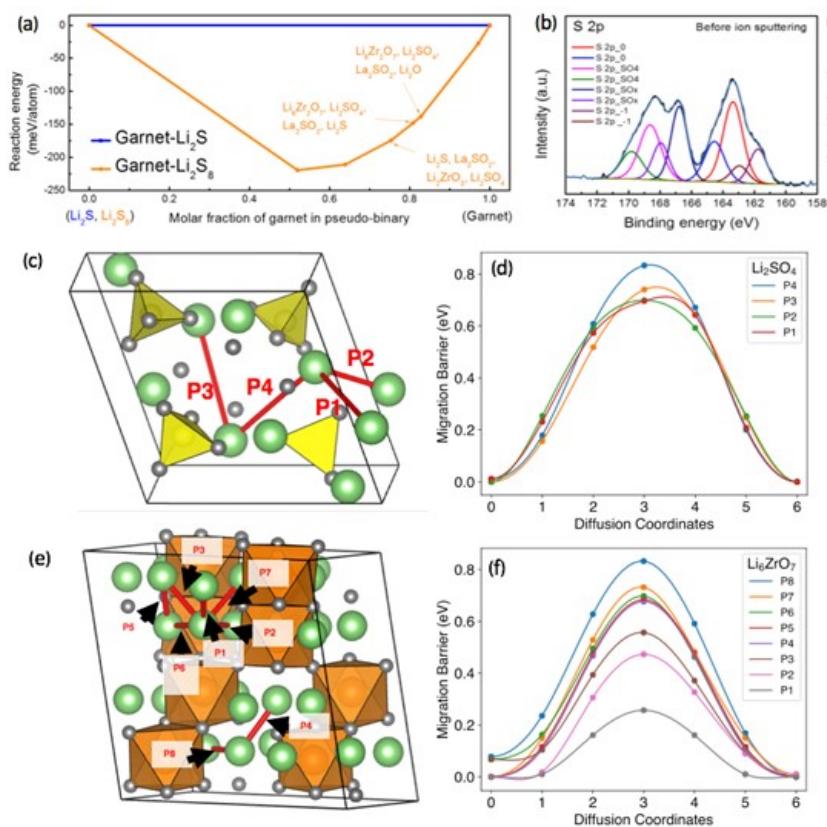

Figure II-477. (a) Calculated interphase equilibria and reaction energy between LLZO and Li polysulfides. (b) XPS spectra of garnet interface in Li-S battery. Calculated Li^+ transport pathway (c) and energy barriers (d) of Li_2SO_4. Calculated Li^+ transport pathway (e) and energy barriers (f) of Li_6ZrO_7.

5. Fabrication of full cell SSLiBs

5.1 SSLiBs with Li-NMC chemistry

Solid-state batteries consisting of Li metal anode, NMC cathode, and garnet-type $Li_7La_3Zr_2O_{12}$ (LLZO) solid electrolyte were fabricated and evaluated. The LLZO solid electrolyte has a bi-layer dense-porous structure with thicknesses of 20 µm and 50 µm, respectively (Figure II-478a). Li metal anode is hosted in the porous layer of garnet electrolyte (Figure II-478b). NMC cathode is laminated on the dense layer. Figure II-478c is the electrochemical impedance spectroscopy (EIS) of the battery. The interfacial resistance is around 250 Ohm-cm^2, which is at the same level as our results for the gel interface previously reported. It proves that the bi-layer garnet and Li anode have a good interfacial contact. The cyclic voltammetry (CV) test result (Figure II-478d) shows that there is an oxidation peak around 4.2 V, which is the charging voltage plateau, and there is a reduction peak around 3.4 V, for the discharging plateau. Outside this voltage range, there is no reaction current. The conclusion is that a battery with a NMC cathode and bi-layer garnet electrolyte can have stable cycling performance up to ~4.5 V.

Cycling performances of Li/NMC cells with NMC mass loadings of 13.5 and 32 mg/cm^2 are shown in Figure II-479. Figure II-479a is the voltage profile of a cell with 13.5 mg/cm^2 NMC loading cycled at 0.1 C rate (1 C = 170 mA/g). Figure II-479b shows the capacity and Coulombic efficiency of this cell. The capacity is stable at 175 mAh/g over 30 cycles. The energy density of the cell is calculated to be 232 Wh/kg. Capacities and Coulombic efficiencies of high rate cycling for this cell are in Figure II-479c. The Coulombic efficiency is over 99% during the 200 cycles, and the battery shows 80% capacity retention at 0.2 C after 200 cycles at varying rates up to 0.5 C. Figure II-479d shows the voltage profiles of a cell with a high-mass-loading (32 mg/cm^2) NMC cathode. The cell is cycled at 0.05 C rate in 2 ~ 4.6 V voltage window. The capacity is 175 mAh/g, and the battery energy density is 357 Wh/kg, calculated based on the masses of the cathode, Li anode and electrolyte.
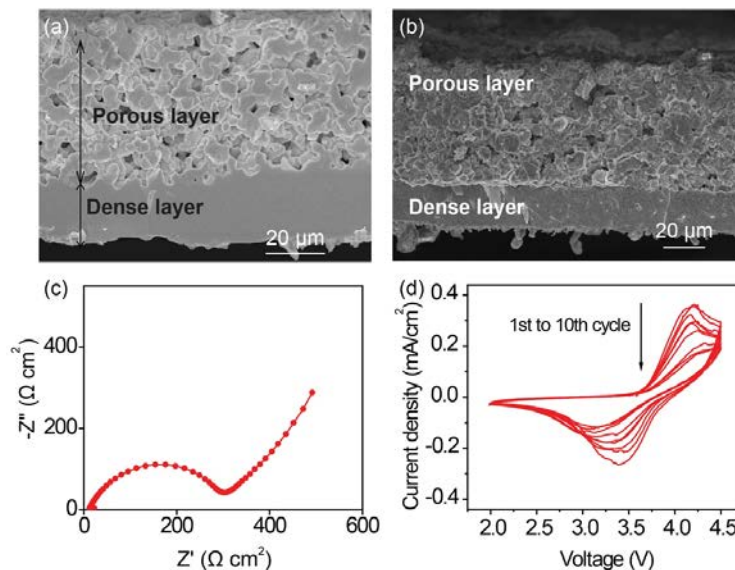

Figure II-478. Characterization of bi-layer garnet and performance of Li-NMC battery. (a) Cross sectional SEM image of bi-layer garnet SSE. (b) SEM of garnet SSE with Li metal inside. (c-d) EIS and CV of the Li-NMC battery with garnet SSE.
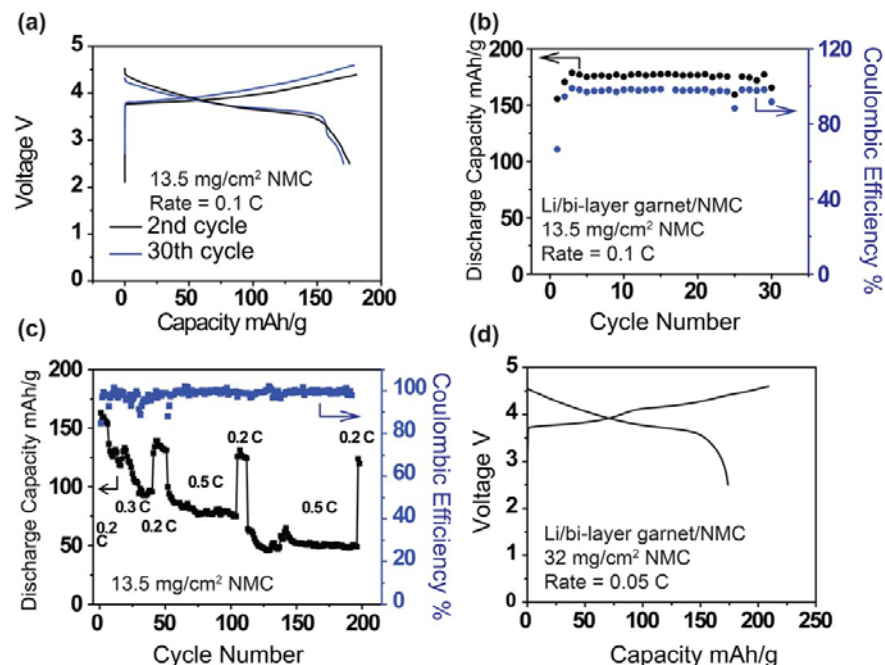
Figure II-479. Cycling performances of Li-NMC cells with garnet SSE. (a-b) Voltage profiles and cycling performance of Li-NMC cell with 13.5 mg/cm² cathode at 0.1 C rate. Stable capacity at 175 mAh/g was achieved. (c) Cycling performance of Li-NMC cell with 13.5 mg/cm² cathode at various rates. High Coulombic efficiency and capacity retention were achieved over 200 cycles. (d) Voltage profiles of a Li-NMC cell with high NMC loading of 32 mg/cm² at 0.05 C rate.

5.2 SSLiBs with Li-S chemistry

Solid state lithium batteries with a sulfur (S) cathode, bi-layer garnet SSE, and Li metal anode were fabricated (Figure II-480a). The structure of the bi-layer garnet and the S cathode is shown by the scanning electron microscope (SEM) image (Figure II-480b). The S fills the pores of garnet in the porous layer, as confirmed by the energy-dispersive X-ray spectroscopy (EDS) in Figure II-480c. Li metal anode was coated on the dense side of the bi-layer garnet, with a polymer interface for better contact. The cycling performance is shown in Figure II-480d. The Coulombic efficiency remains > 99%, confirming that no shuttling effect occurs in the cell. The bilayer Li-S cell with a S mass loading of 7.5 mg/cm² has an energy density of 280 Wh/kg on the basis of the cathode, Li anode and electrolytes.

We also demonstrated Li-S batteries based on tri-layer garnet SSE. The tri-layer SSE is composed of a porous-dense-porous structure. The thickness of each porous layer is 70 µm and the thickness of the dense layer is 30 µm. Li metal anode is stored in one porous layer, and sulfur cathode is stored in the other porous layer. Mass loadings of lithium and sulfur are 4.3 mg/cm² and 5.4 mg/cm², respectively. The battery performance is shown in Figure II-481. The voltage profiles in Figure II-481a show a typical Li-S two plateau behavior with a high capacity of ~1200 mAh/g. The cell shows high capacity retention and nearly 100% Coulombic efficiency during 50 cycles (Figure II-481b). The total energy density of the tested cell is 272 Wh/kg as calculated from the integrated cycling curve, measured masses of sulfur, carbon, garnet electrolyte, and lithium metal anode.
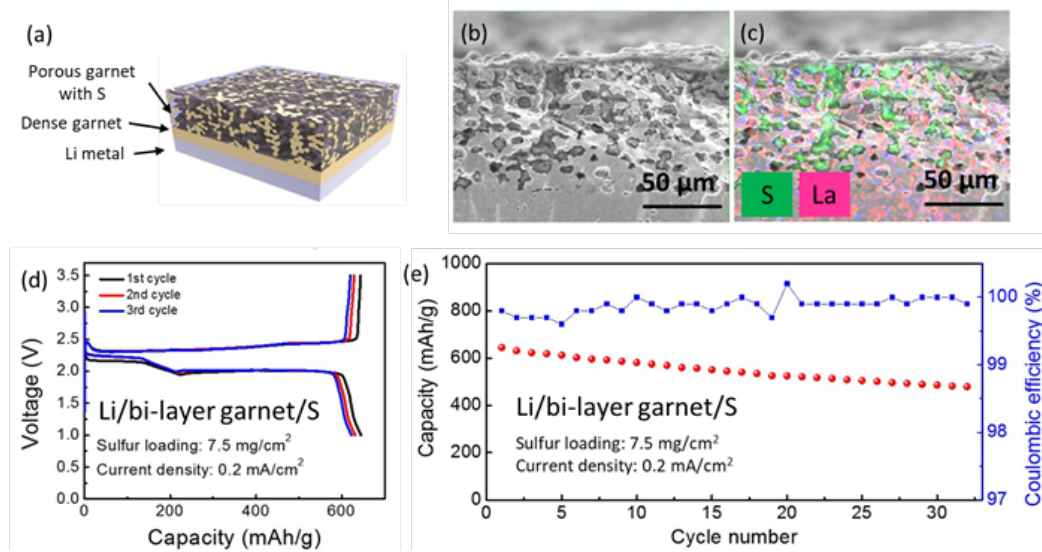
Figure II-480. Characterization of bi-layer garnet and performances of Li-S battery. (a) Schematic of Li-S battery based on bi-layer garnet. (b) Cross sectional SEM of bi-layer garnet filled with S. (c) EDS of S (green) and La (red) distribution in bi-layer garnet. (d-e) Voltage profile and cycling performance of the solid state Li-S cell with a loading of 7.5 mg/cm² at 0.2 mA/cm².
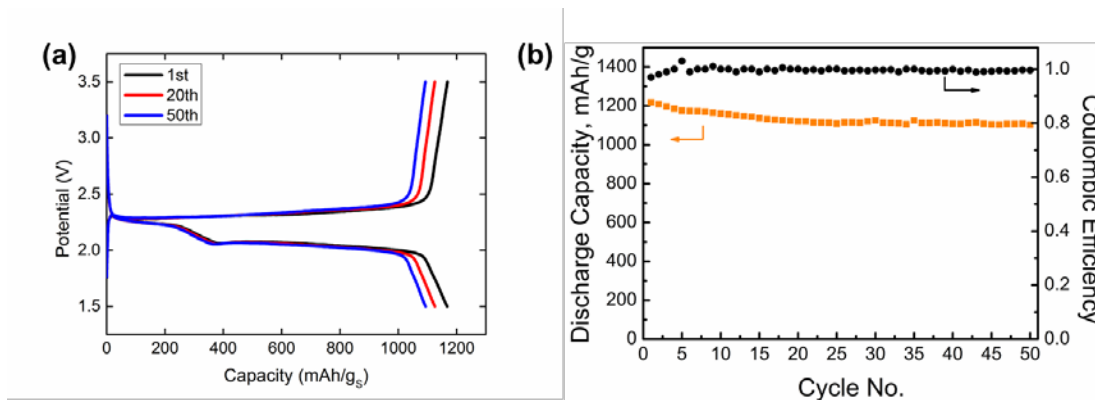
Figure II-481. Cycling performances of Li-sulfur cell with garnet electrolytes. (a) Voltage profiles of the 1st, 20th and 50th cycle of the solid-state Li-S cell. 1200 mAh/g capacity and low capacity loss were achieved. (b) Cycling results of the solid state Li-S cell. High capacity retention was achieved with near 100% coulombic efficiency.

Conclusions

Computational understanding of SSE-electrode interface:

- Achieved fundamental understanding of interfacial impedance as demonstrated by consistency between computational and experimental results.

- Developed computational models to investigate stability and interfacial ion transport with varying types of interlayers

- Predicted formation of protective interfaces between garnet and S and NMC cathodes

For garnet-cathode interface:
- We demonstrated that gel electrolyte can reduce the interfacial resistance by over 4 orders of magnitude achieving an interfacial ASR of ~67 Ohm-cm^2 for planar cathode/garnet interface.

- We demonstrated that increasing surface area can effectively decrease the interface resistance, achieving a 52% decrease in interfacial ASR.

- Aqueous interface lead to 7.5 Ohm-cm^2 cathode/garnet interfacial resistance planar cathode/garnet interface. Therefore, we met the ~10 Ohm-cm2 garnet/cathode goal.

For Li-garnet interface:
- We demonstrated gel electrolyte, Si, and Al can reduce interfacial resistance to 200 Ohm-cm^2, 127 Ohm-cm^2, and 75 Ohm-cm^2, respectively for planar Li metal-garnet interface.

- We further demonstrated that ALD-Al$_2$O$_3$ can reduce interfacial resistance to ~1 Ohm-cm^2 for planar Li metal-garnet interface. Therefore, we met the ~10 Ohm-cm^2 garnet/anode goal.

Full cell demonstration:
- Fabricated and tested SSLiBs with Li-NMC Chemistry.

- Fabricated and tested SSLiBs with Li-S Chemistry.

- Achieved full cell (Li-NMC) performance of 352Wh/kg.

- Achieved full cell (Li-NMC) performance of 200 cycles.

- Achieved full cell (Li-S) performance of 272 Wh/kg and 50 cycles.

Key Publications

1. W. Luo, Y. Gong, Y. Zhu, Y. Li, Y. Yao, Y. Zhang, K. K. Fu, G. Pastel, C. F. Lin, Y. Mo, E. D. Wachsman, L. Hu, Reducing Interfacial Resistance between Garnet-Structured Solid-State Electrolyte and Li-Metal Anode by a Germanium Layer. *Adv. Mater. 29* (22), 1–7, (2017).

2. B. Liu, K. Fu, Y. Gong, C. Yang, Y. Yao, Y. Wang, C. Wang, Y. Kuang, G. Pastel, H. Xie, E. D. Wachsman, L. Hu, Rapid Thermal Annealing of Cathode-Garnet Interface toward High-Temperature Solid State Batteries. *Nano Lett.* 9. 4917-4923 (2017).

3. K. Fu, Y. Gong, B. Liu, Y. Zhu, S. Xu, Y. Yao, W. Luo, C. Wang, S. D. Lacey, J. Dai, Y. Chen, Y. Mo, E. Wachsman, L. Hu, Toward Garnet Electrolyte–based Li Metal Batteries: An Ultrathin, Highly Effective, Artificial Solid-State Electrolyte/metallic Li Interface. *Sci. Adv.* 3, e1601659 (2017).

4. K. Fu, Y. Gong, S. Xu, Y. Zhu, Y. Li, J. Dai, C. Wang, B. Liu, G. Pastel, H. Xie, Y. Yao, Y. Mo, E. Wachsman, L. Hu, Stabilizing the Garnet Solid-Electrolyte/polysulfide Interface in Li-S Batteries. *Chem. Mater.* 29, 8037–8041 (2017).

5. K. Fu, Y. Gong, S. Xu, Y. Zhu, Y. Li, J. Dai, C. Wang, B. Liu, G. Pastel, H. Xie, Y. Yao, Y. Mo, E. Wachsman, L. Hu, Transient Behavior of the Metal Interface in Li Metal-Garnet Batteries. *Angew. Chemie Int. Ed.* 1–7 (2017).

6. C. Wang, H. Xie, L. Zhang, Y. Gong, G. Pastel, J. Dai, B. Liu, E. D. Wachsman, L. Hu, Universal Soldering of Lithium and Sodium Alloys on Various Substrates for Batteries. *Adv. Energy Mater.* 1701963 (2017).

7. C. Yang, K. Fu, Y. Zhang, E. Hitz, L. Hu, Protected Lithium-Metal Anodes in Batteries: From Liquid to Solid. *Adv. Mater.* 29, 1–28 (2017).

8. B. Liu, Y. Gong, K. Fu, X. Han, Y. Yao, G. Pastel, C. Yang, H. Xie, E. D. Wachsman, L. Hu, Garnet Solid Electrolyte Protected Li-Metal Batteries. *ACS Appl. Mater. Interfaces* 9, 18809–18815 (2017).

9. Y. Zhu, X. He, Y. Mo, First Principles Study on Electrochemical and Chemical Stability of the Solid Electrolyte-Electrode Interfaces in All-Solid-State Li-ion Batteries, *J. Mater. Chem. A*, 4, 3253-3266 (2016).

10. Y. Zhu, X. He, Y. Mo, Origin of Outstanding Stability in the Lithium Solid Electrolyte Materials: Insights from Thermodynamic Analyses Based on First-Principles Calculations, *ACS Appl. Mater. Interfaces*, 7, 23685-23693 (2015).

11. F. Han, Y. Zhu, X. He, Y. Mo, C. Wang, Electrochemical Stability of Li10GeP2S12 and Li7La3Zr2O12 Solid Electrolytes", *Adv. Energy Mater.*, 6, 1501590 (2016).

12. W. Luo, Y. Gong, Y. Zhu, K. Fu, J. Dai, S. D. Lacey, C. Wang, B. Liu, X. Han, Y. Mo, E. D. Wachsman, L. Hu, Transition from Super-lithiophobicity to Super-lithiophilicity of Garnet Solid Electrolyte, *J. Am. Chem. Soc.*, 138, 12258-12262 (2016).

13. X. Han, Y. Gong, X. He, G. T. Hitz, J. Dai, Y. Mo, V. Thangadurai, E. D. Wachsman, L. Hu, Negating Interfacial Impedance in Garnet-Based Solid-State Li-Metal Batteries, *Nat. Mater.*, 16, 572-580, (2017). DOI: 10.1038/NMAT4821

14. K. Fu, Y. Gong, G. T. Hitz, D. W. McOwen, Y. Li, S. Xu, Y. Wen, L. Zhang, C. Wang, G. Pastel, J. Dai, B. Liu, H. Xie, Y. Yao, E. D. Wachsman, L. Hu, Three-Dimensional Bilayer Garnet Solid Electrolyte High Energy Density Lithium Metal-Sulfur Batteries, *Energy Environ. Sci.*, 10, 1568-1575, (2017). DOI: 10.1039/c7ee01004d

II.H.5   High Conductivity and Flexible Hybrid Solid State Electrolyte (U of MD)

Eric Wachsman, Principal Investigator

University of Maryland
1206 Engineering Laboratory Building
College Park, MD 20742
Phone: 301-405-8193
E-mail: ewach@umd.edu

Tien Duong, Technology Manager

U.S. Department of Energy
Phone: 202-586-7836
E-mail: Tien.Duong@ee.doe.gov

Start Date: October 1, 2016   End Date: September 30, 2019
Total Project Cost: $1,250,000   DOE share: $1,250,000   Non-DOE share: $0

Project Introduction

Metallic lithium is considered the "Holy Grail" for high-energy density batteries. However, using lithium metal in organic liquid electrolyte systems faces many challenges in terms of both battery performance and safety. A fundamental strategy is to develop a solid-state electrolyte (SSE) to mechanically suppress lithium dendrites and intrinsically eliminate SEI formation. Among the different types of SSEs, solid-polymer electrolytes have been the most extensively studied. In polymer-based composite SSEs, nanoparticles are incorporated to influence the recrystallization kinetics of the PEO polymer chains to promote local amorphous regions, thereby increasing the ionic conductivity of the Li salt/polymer system. The fillers can be either non-Li^+ conductive nanoparticles, such as Al_2O_3, SiO_2, TiO_2, ZrO_2, and organic polymer spheres, or Li^+ conductive nanoparticles, such as $Li_{0.33}La_{0.557}TiO_3$, and $Li_{1.3}Al_{0.3}Ti_{1.7}(PO_4)_3$. Developing nanostructured fillers is an essential approach to increase the ionic conductivity of composite electrolytes due to the increased surface area of the amorphous region and improved interface between fillers and polymers. Meanwhile, numerous solid-state inorganic Li^+ electrolytes are being investigated to replace liquid organic electrolytes. Due to their high ion conductivity and excellent stability, Li-stuffed garnets exhibit the most promising physical and chemical properties for SSEs. However, major challenges still exist in garnet-based electrolytes, including: (1) Being either too thick with corresponding high ASR or too mechanically fragile when thin (~20 μm); (2) High temperature processing that is incompatible with most anode/cathode materials; and (3) High interfacial impedance. Moreover, flexible SSEs with high ionic conductivity and excellent processability are completely lacking.

Instability and/or high resistance at the interface of lithium metal with various solid electrolytes limit the use of the metallic anode for batteries with high energy density, such as Li-air and Li-S batteries. The critical impact of this endeavor will be focused on developing a new type of solid-state electrolyte (SSE) that is highly conductive, highly flexible and electrochemically stable. In particular, the new SSE will enable Li metal anodes with excellent interfacial impedance and blocking formation of Li dendrites.

Objectives

The objective of this project is to develop a flexible hybrid electrolyte with garnet nanofibers to achieve the following: (1) Flexibility with greater mechanical strength (~ 10 MPa) and thermal stability than polymer electrolytes; (2) High room temperature ionic conductivity, ~ 0.5 mS/cm; (3) Stable interface with Li metal and effectively block Li dendrites at current densities up to 3 mA/cm^2; and (4) Battery performance with Li-S chemistry with an energy density of $\geq$ 450 Wh/kg and ($\geq$1000 Wh/L), and maintain $\geq$80% of capacity up to 500 cycles.

Approach

We will synthesize garnet nanofibers, fill the porous region with polymer electrolyte, and characterize and tune the flexible hybrid membrane properties. The flexible hybrid SSE microstructure will be analyzed by leveraging the UMD AIMLab Focused Ion Beam Scanning Electron Microscopy (FIB-SEM) tools and integrated with electrochemical methods at the UMERC Battery Fabrication Lab to investigate the properties and stability with Li metal anode. We will develop a fundamental understanding of the mechanism of Li ionic diffusion in garnet nanofibers and their mechanical properties, as well as these properties for hybrid garnet-fiber/polymer hybrids. Work will progress toward the study of the electrode assembly during electrochemical cycling of the anode.

Results

1. Fabrication of 4 cm x 4 cm garnet fiber membrane

Two templating methods were developed to fabricate garnet nanofiber membranes. The first method utilized electrospun polyacrylonitrile (PAN) fibers while the second used cellulose textiles. Al-doped LLZO with the chemical composition of $Li_{6.28}Al_{0.24}La_3Zr_2O_{11.98}$ was prepared by dissolving stoichiometric amounts of $LiNO_3$ (15 wt% excess), $Al(NO_3)_3 \cdot 9H_2O$, $La(NO_3)_3 \cdot 6H_2O$, and zirconium propoxide solution in ethanol with 15 vol % acetic acid. Cellulose textile templates were pretreated by annealing in air at 270ºC for 10 h, then rinsed with ethanol and dried at 100ºC for 12 h. After pretreatment, the templates were soaked in a 2.5 mol/L LLZO precursor solution for 24 h. The multi-scale porosity existing in the porous templates enabled homogenous impregnation by the LLZO precursor. Calcination of the precursor impregnated templates was conducted in oxygen at different temperatures to obtain garnet fibrous membrane. Figure II-482 shows a photograph of garnet fibrous membranes sintered at 800ºC made from electrospun fibers or cellulose textiles. The cellulose template better retained the characteristic physical features and is more easily tailored for particular shapes in large dimensions (4 cm × 4 cm).
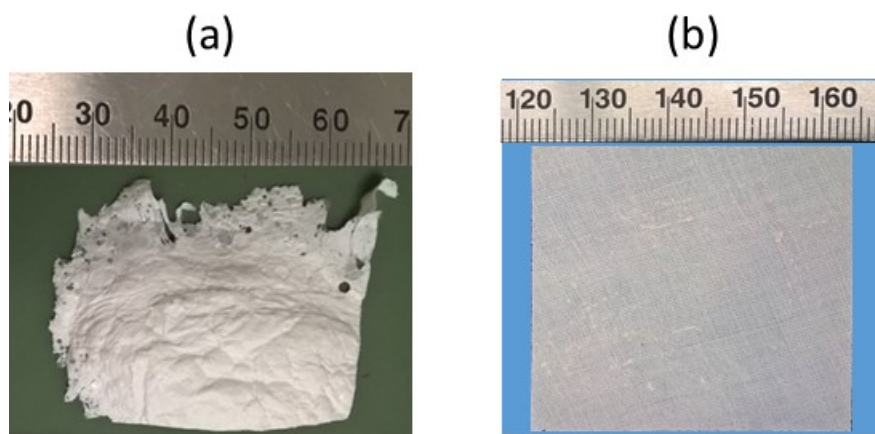

Figure II-482. Photograph of flexible garnet fibrous membranes made from (a) electrospun PAN (3.5 x 3.0 cm) and (b) cellulose textile (4.0 x 4.0 cm) templates.

The crystallographic phase of the LLZO was analyzed by powder X-ray diffraction on a D8 Advance with LynxEye and SolX (XRD, Bruker AXS) using a Cu Kα radiation source operated at 40 kV and 40 mA. The microstructure and element distribution were examined by analytical SEM (Hitachi SU-70) equipped with an Energy Dispersive Spectrometer (EDS, Oxford Instruments). Figure II-483 shows the XRD pattern and SEM image of the garnet fibrous membrane. Through simple composition design by doping with supervalent cations and optimizing lithium concentration in the precursor solution, stabilization of the cubic phase can be achieved at sintering temperatures as low as 800ºC. The garnet fibers retained the characteristic physical features of the original cellulose template, which consisted of continuous individual microfibers of approximately 10 µm in diameter that were arranged mostly parallel and twisted around each other. The fibers were wrapped into

bundles about 200 μm in diameter interlacing with each other to form the periodically ordered woven pattern. Inter-fiber pores ranged from 10 to 20 μm in diameter and larger pores between yarns were formed after thermal treatment.
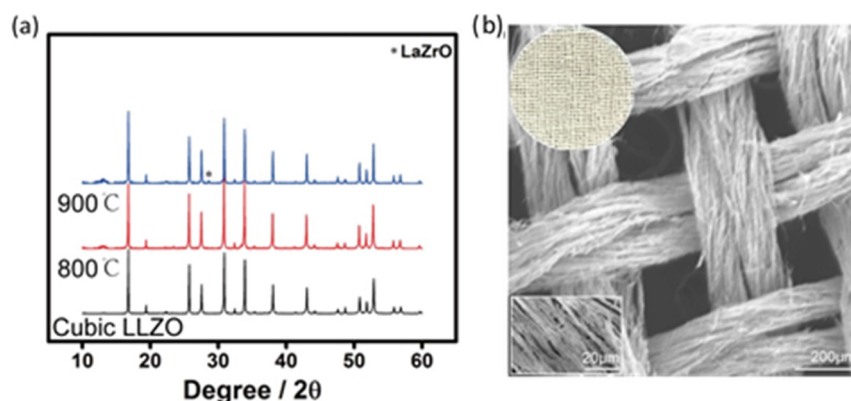

Figure II-483. Characterization of garnet fibrous membrane: (a) Powder XRD patterns of the crushed garnet textile sintered at different temperatures; (b) SEM image of the garnet textile converted from the precursor solution impregnated template.

2. Hybrid Garnet-Polymer Electrolyte

The polymer matrix was prepared by dissolving LiTFSI and PEO (MW 600,000) in acetonitrile. Plasticizer was added to reduce the crystallinity and improve Li-ion conductivity. The polymer electrolyte was casted on a Teflon block and dried in an argon glove box, followed by drying in a vacuum oven to remove residual solvent before electrochemical performance characterization. Electrochemical impedance of the polymer electrolyte was measured in a stainless steel/polymer/stainless steel configuration using a Solartron 1260 Impedance Analyzer. A Teflon spacer was included to fix the polymer thickness. Impedance tests were conducted with AC amplitude of 20 mV in the frequency range of 1 Hz and 1 MHz from 25ºC to 100ºC. Figure II-484 presents the typical impedance plot for the polymer electrolyte measured at room temperature. Lithium-ion transfer processes were divided into ion conduction within the CPE (high frequency arc) and ion blocking at the CPE/stainless steel interface (low frequency inclined tail). The resistance of the CPE was obtained by reading the real impedance values at the high frequency intercept of the arc. The measured lithium-ion conductivity of the polymer electrolyte was 0.9×10^{-4} S/cm at 25ºC.
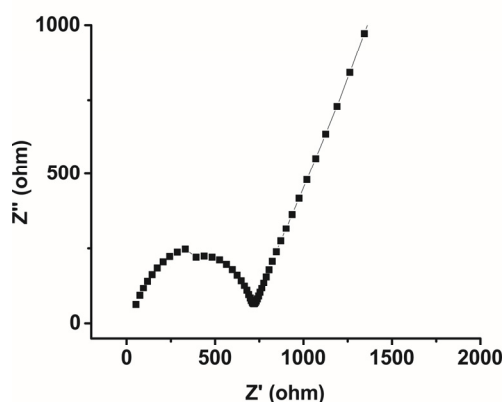

Figure II-484. Impedance spectra of the polymer electrolyte at room temperatures. The Li-ion conductivity is 0.9×10^{-4} S/cm.

Nanoindentation is a technique widely used for determining mechanical properties of the near-surface region of materials. By combining the application of low loads, measuring the resulting displacement, and determining the contact area between the tip of the indenter and the sample, the hardness (H) and elastic modulus (E) are able to be measured. Nanoindentation was performed on a Hysitron Inc. TriboIndenter. The evaluated garnet fiber was soaked in melted crystal bond. The dried composite sample was then mounted in slow-curing epoxy glue and polished. The optical microscope in the nanoindenter was used to select positions for indentation on the center of the fibers. The position of the center of the fiber was evaluated with individual scans of the AFM image and the location of the fiber was manually adjusted. (See Figure II-485.) Hardness and Young's modulus of garnet fiber was measured to be 0.28 ±0.04 GPa and 6.3±0.5 GPa, respectively.
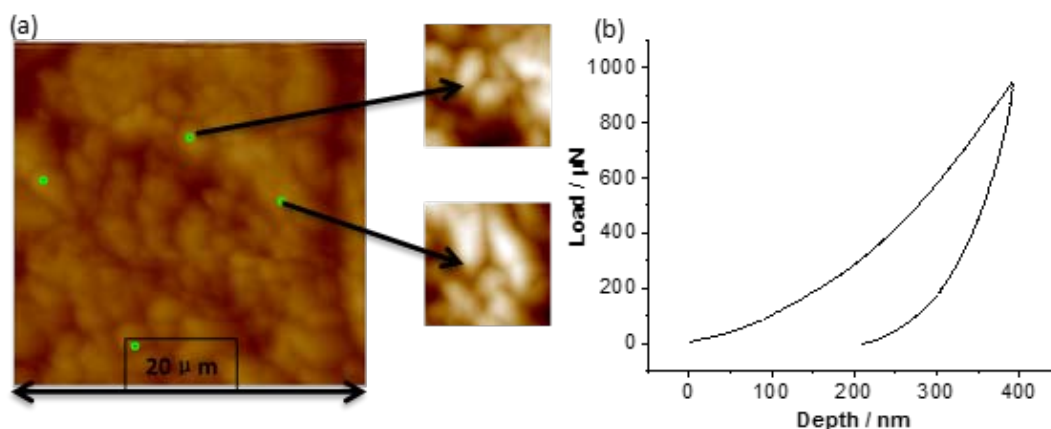
Figure II-485. Mechanical characterization of garnet fiber: (a) AFM scanning of the nano-indent points on garnet fiber; (b) Load-depth profile of garnet fiber.

Hybrid composite polymer electrolyte was prepared by mixing the garnet fibers with polymer electrolyte in N-methyl-2-pyrrolidinone (NMP) at 70 ℃ using a magnetic stirrer. After 6 hours of stirring, the mixture was tape cast onto a Teflon block and left to dry at 80ºC over-night. Figure II-486 shows the photograph of the flexible hybrid composite polymer electrolyte. Figure II-487 shows the AC impedance and CV of the composite electrolyte. The Li-ion conductivity is 6.07×10^{-4} S/cm measured at room temperature, representing a significant enhancement over the conductivity of the polymer electrolyte. The composite is also stable up 4.5 V.

Figure II-486. Photograph of the flexible hybrid composite polymer electrolyte.
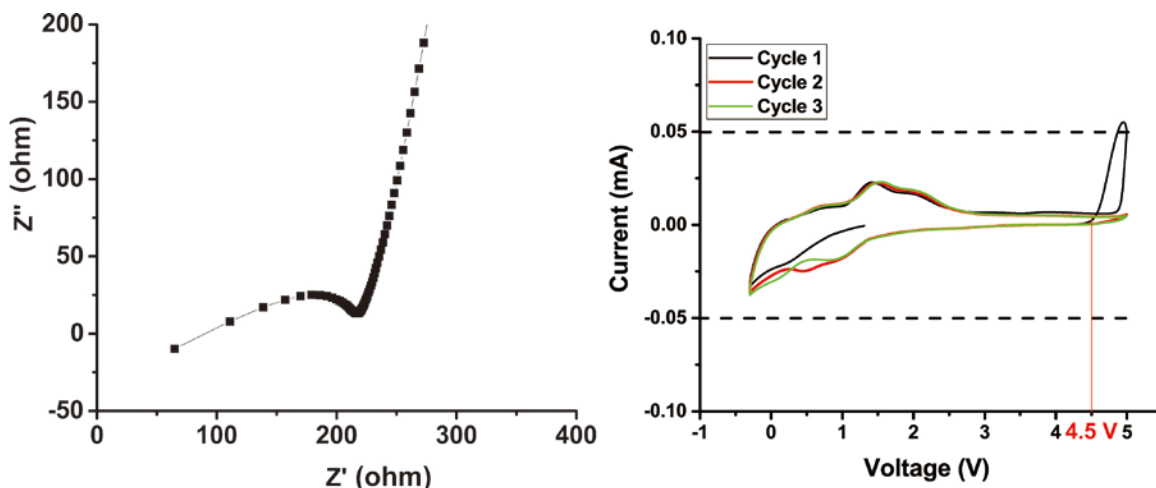
Figure II-487. Electrochemical characterization of hybrid composite polymer electrolyte: (a) Ac impedance, Li-ion conductivity is 6.07×10^{-4} S/cm; (b) CV, stable up to 4.5 V

3. Understand Li ionic diffusion in garnet nanofibers and its response to mechanical deformation.

In order to perform molecular dynamics (MD) simulations for garnet nanofibers, we implemented and tested force fields for lithium garnet $Li_7La_3Zr_2O_{12}$ (LLZO). Using the newly tested force field, the lattice parameters in tetragonal and cubic phases of LLZO were calculated using MD simulations as a function of temperature, in good agreement with experimental values. Li^+ diffusion in LLZO was also modeled using MD simulations. The calculated Li^+ conductivity and activation energy of LLZO are in good agreement with *ab initio* calculations and experimental measured values.

An atomistic model of garnet nanofibers was constructed and equilibrated in MD simulations (Figure II-488). The Li^+ transport in a single garnet nanofiber was modeled using MD simulations at different temperatures. The Li^+ conductivities at different temperatures and the activation energies for Li^+ diffusion were calculated in single garnet nanofibers. Comparison of the Li^+ diffusion properties from MD simulations to the bulk phase of LLZO shows faster Li^+ diffusion in single garnet nanofibers. In addition, the Li^+ migration mechanism was analyzed for Li^+ transport along and perpendicular to the nanofiber direction, and at surface and core regions of the nanofiber. Insight into Li^+ diffusion in garnet nanofiber was obtained.
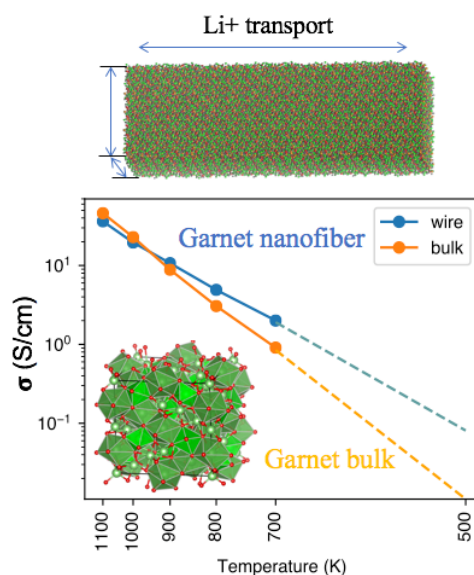

Figure II-488. Computer modeling of Li+ transport in garnet nanofibers.

Mechanical deformation on bulk and nanofiber garnet was performed under MD simulations. The elastic moduli from our calculations are in good agreements with experiments and previous studies. The Li^+ diffusion under mechanical deformation was studied using MD simulations (Figure II-489). We simulated the garnet at both tensile and compressive stress with different strain (1% and 3%). We found the mechanical deformation significantly impacts the Li^+ diffusion. Li conductivity decreases and activation energy increases in both stressed states. This change is in good agreement with experiments. The MD simulations in both bulk and nanofiber show similar results. Mechanical deformation decreases Li^+ conductivity in garnet. Both tensile and compressive deformation drives garnet towards slow-conducting tetragonal phase. In summary, MD simulations were performed to understand Li^+ diffusion in garnet nanofibers and the effect of mechanical deformation.
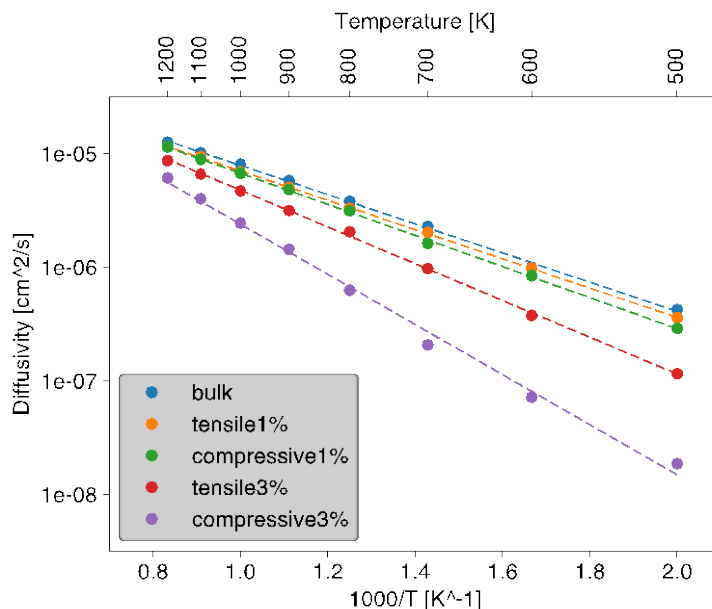
Figure II-489. Li diffusion of garnet under strain.

Conclusions

We synthesized garnet fibrous membrane, which essentially retained the characteristic physical features of the original cellulose template and can be tailored for particular shapes in large dimensions (4 cm x 4 cm). We synthesized ion insulating polymer PEO, ion conductive polymer PEO-LiTFSI, and in-situ polymer electrolyte coated garnet nanofibers. Our flexible electrolyte combining conductive cubic LLZO garnet and lithium-PEO could therefore reach a reasonably high ionic conductivity of 6.07×10^{-4} S/cm at room temperature and voltage stability up to 4.5 V. Molecular dynamics simulations were performed to understand Li^+ diffusion in garnet nanofibers and the effect of mechanical deformation. The MD simulations in both bulk and nanofiber show mechanical deformation decreases Li^+ conductivity in garnet.

Key Publications

1. Eric Wachsman, "All-Solid-State Li-ion Batteries for Transformational Energy Storage," 21st International Conference on Solid State Ionics, June 23-29, 2017, Padua, Italy - Invited

2. Yifei Mo, "Enabling All-Solid-State Li-ion Batteries Through Computation-Guided Design of Materials and Interfaces", Beyond Lithium Ion Symposium-10 (BLI-X), CA (06/2017) – Invited

3. Yifei Mo, "Computation-Guided Understanding and Design of Interfaces in All-Solid-State Li-ion Batteries", 17th Annual Advanced Automotive Battery Conference, San Francisco, CA (06/2017)-Invited

4. Eric Wachsman, "All-Solid-State Li-ion Batteries for Transformational Energy Storage," U.C. Berkeley, April 6, 2017, Berkeley, CA – Invited

5. Y. Gong, K. Fu, S. Xu, J. Dai, T. R. Hamann, L. Zhang, G. T. Hitz, X. Han, L. Hu, E. D. Wachsman, Lithium-Ion Conductive Ceramic Textile: A New Architecture for Flexible Solid-State Lithium Metal Batteries, *Materials Today*, Minor Revision

II.H.6   Nanoscale Interfacial Engineering for Stable Lithium Metal Anodes (Stanford University)

Yi Cui, Principal Investigator
Stanford University
476 Lomita Mall, Room 343
Stanford, CA 94305
Phone: 650-723-4613
E-mail: yicui@stanford.edu

Tien Duong, Technology Manager
U.S. Department of Energy
Phone: 202-586-7836
E-mail: Tien.Duong@ee.doe.gov

Start Date: October 1, 2015   End Date: September 30, 2018
Total Project Cost: $600,000   DOE share: $600,000   Non-DOE share: $0

Project Introduction

Li-ion battery has gain great success as the power source for portable electronics, electric vehicles and grid scale energy storage. However, its energy density has achieved a bottleneck which calls for the further innovation of battery technologies especially those beyond Li-ion. Li metal anode has long been regarded as the "holy grail" for Li battery research, which is not only due to its highest theoretical capacity of 3860 mAh/g and lowest electrochemical potential, but also its key role in Li-S and Li-air battery systems, both of which are the most prominent battery chemistries for the next-generation energy storage technology. However, many challenges have been encountered on its way to commercialization. Among all problems of Li metal, there are two root causes, namely high reactivity of Li and its infinite relative volume change during cycling. On one hand, the high reactivity of Li results in the excess side reactions once is exposed to liquid electrolyte, which further lead to complex interfacial chemistry, blocked ion transport and the consumption of materials. On the other hand, the infinite relative volume change makes the solid electrolyte interphase (SEI) prone to fracture, which not only creates hot spots for uneven Li-ion flux distribution and thus dendritic deposition, but also exposes fresh Li for further side reactions, leading to low Coulombic efficiency. Under the circumstance, it is necessary to develop surface protection techniques as well as to improve the electrode volume stability in order to solve all the abovementioned problems. We plan to develop a set of nano-synthesis techniques to realize the proposed concepts.

Objectives

This study aims to render lithium (Li) metal anode with high capacity and reliability by developing chemically and mechanically stable interfacial layers between Li metal and electrolytes, which is essential to couple with sulfur cathode for high-energy Li-sulfur batteries. With the nanoscale interfacial engineering approach, various kinds of advanced thin films will be introduced to overcome the issues related to dendritic growth, reactive surface and virtually "infinite" volume expansion of Li metal anode.

Approach

- Achieve minimal volume change of the electrode by designing stable hosts for Li metal

- Realize stabilized SEI and much more stable cycling by interfacial engineering

- Improved the rate capability in full cells

- Develop and employ further surface protection to 3D Li surface

Results

In recognition of the problems associated with the "hostless" nature of Li metal, we have successfully introduced stable hosts for metallic Li. The approach resulted in three-dimensional porous Li, which reduced the effective current density and the degree of interface fluctuation during cycling, leading to more uniform Li deposition with greatly improved cycling stability. Engineering the solid electrolyte interphase (SEI) on porous Li electrodes shall be the next step needed to further improve the cycling efficiency. Herein, we propose the rational design of an artificial SEI layer, composed of Cu_3N nanoparticles in styrene butadiene rubber matrix (Cu_3N + SBR). This composite artificial SEI can simultaneously possess high mechanical strength due to the densely packed inorganic nanoparticles, good flexibility due to the polymeric binder matrix, and importantly, high Li-ion conductivity thanks to the conversion of Cu_3N to ion-conducting Li_3N in the presence of Li.

The Coulombic efficiency (CE) of our artificial SEI protected anode was first measured on Cu foil. At a current density of 1 mA cm^{-2} in carbonate electrolyte (1 M lithium hexafluorophosphate in 1:1 ethylene carbonate/diethyl carbonate with 10 wt% fluoroethylene carbonate additive), the CE of bare Cu started at around 95% and quickly decayed to merely 70% within 50 stripping/plating cycles due to the growth of Li dendrites and the continuous breakdown/repair of SEI that consumed both Li and the electrolyte (Figure II-490a).
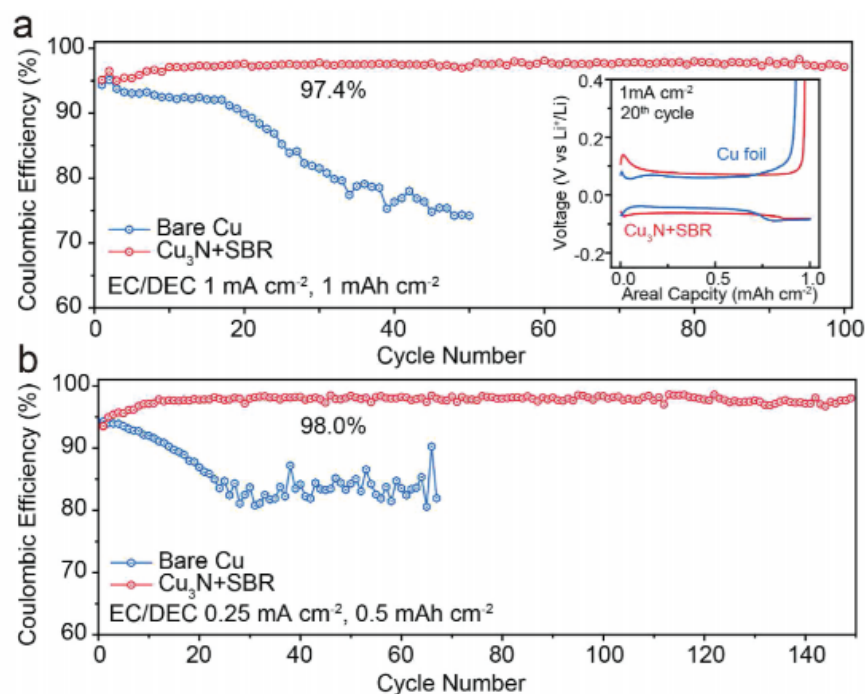
Figure II-490. Coulombic efficiency of artificial SEI protected Cu foil and bare Cu foil at a current density of a) 1 mA cm^{-2} (cycling capacity 1 mAh cm^{-2}; inset, the corresponding voltage profiles at the 20th cycle) and b) 0.25 mA cm^{-2} (cycling capacity 0.5 mAh cm^{-2}).

Surprisingly, the artificial SEI protected Cu demonstrated a much improved Coulombic efficiency of ≈97.4% averaged between the 20th and 70th cycles and such high efficiency performance can sustain for more than 100 cycles. In addition, the overpotential increase due to the existence of the artificial SEI was minimal (Figure II-490a Inset), thanks to its relatively high ionic conductivity. Since the effective current density can be significantly reduced on porous Li metal anodes, CE at a lower current density of 0.25 mA cm^{-2} was also studied to better resemble the real working condition of the artificial SEI protected porous Li. With reduced current density, the CE increased to as high as ≈98%, which was stable for at least 150 cycles (Figure II-490b).

The morphology of Li deposition after cycling was also studied (Figure II-491). After five galvanostatic plating/stripping cycles at a current density of 0.5 mA cm^{-2} and a capacity of 0.5 mAh cm^{-2}, no observable dendrites on Cu foil protected by the mechanically robust and highly Li-ion conducting artificial SEI, while excessive wire-shaped Li with diameter around 1–2 µm has already formed on the bare Cu counterpart. The color of the Li deposit on the protected Cu foil remained silver and shiny, similar to that of pristine Li metal. However, dark gray Li was observed for deposition directly on bare Cu, stemming from a less compact Li deposition morphology. The dendrite suppression mechanism can be attributed by the more uniform Li-ion flux across the ion-conducting artificial SEI and its good mechanical property. Accordingly, the elastic modulus of the artificial SEI was measured via nanoindentation with proper mathematical corrections based on the contact model. The elastic modulus was measured on the order of 1 GPa, which can be considered sufficient in suppressing Li dendrite formation.
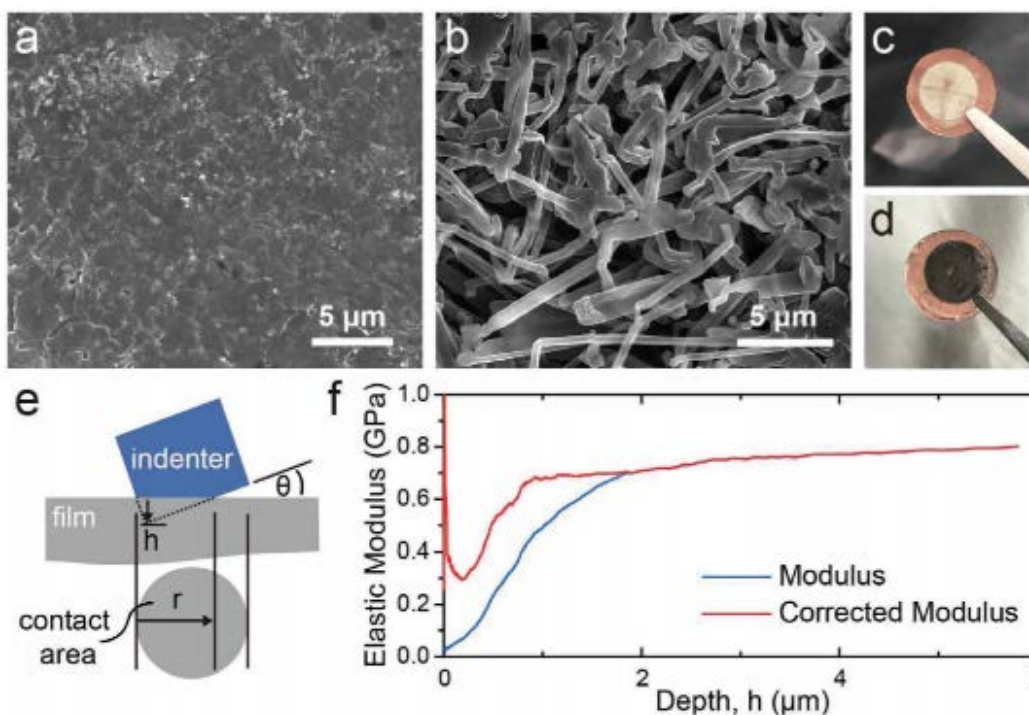

Figure II-491. Top-view SEM images and the corresponding digital photographs of Li deposition after five cycles on a,c) artificial SEI protected Cu and b,d) bare Cu foil. e) Schematic showing the configuration of nanoindentation measurements. f) Elastic modulus versus depth of a representative indentation test.

Previously, we have employed the nanoscale interfacial engineering approach using inter-connected hollow carbon spheres, two-dimensional boron nitride and graphene on Cu current collectors as stable artificial SEI for Li metal. The strategies effectively suppressed Li dendrite growth and greatly enhanced the Coulombic efficiency during cycling. Recently, we continue to explore the different coating materials in search for better surface protections on Li metal anode. Here, we took the advantages of the "solid-liquid" hybrid behavior of Silly Putty (SP), a popular children's toy, as the interfacial layer for Li metal anodes. SP can reversibly switch between its "liquid" and "solid" properties in response to the rate of Li growth to provide uniform surface coverage and dendrite suppression, respectively, therefore enabling the stable operation of Li metal electrodes.

The idea is illustrated schematically in Figure II-492. Silly Putty (SP), primarily comprised of polydimethylsiloxane (PDMS) crosslinked by transient boron-mediated bonds, is technically termed as a "shear thickening material". Namely, the rigidity of SP increases significantly as the deformation rate increases. It can even temporarily become an elastic solid if the deformation rate is too fast for the dynamic crosslinks to temporally break and reconnect. Therefore, when coated on the surface of Li metal, SP flows on

the time scale of each charging and discharging circle and can uniformly covers the electrode surface to serve as a stable interface between the Li metal and the electrolyte. However, if occasionally there are some "hot-spots" where the deposition and expansion of Li is faster than at other places on the electrode, the stiffness of the local SP coating consequently increases. As such, SP acts as a clamping layer to help eliminate fast local overgrowth or expansion of Li metal and the SEI breakage, effectively suppressing Li dendrite growth.
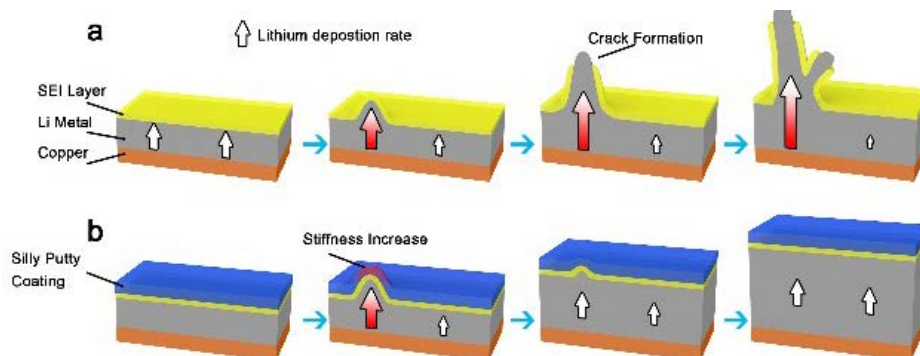
Figure II-492. Schematic showing the design of silly putty (SP) modified Li anode. Top shows the conventional Li dendrite evolution process, while the bottom shows the Li deposition behavior on a SP modified surface.

The viscoelastic behavior of the SP was first studied by rheometer. As shown in Figure II-493, when the stain rate is low ($<10^{-2}$ s^{-1}), the loss modulus (G'', which represents the viscous property), is significantly larger than the storage modulus (G', which represents the elastic property), indicating that the viscous property dominates the behavior and the SP behaves more like a flowable liquid. As the strain rate increases, G' increases significantly, indicating that the SP becomes stiffer. G' even exceeds G'' by almost an order of magnitude at high strain rates ($>10^{-2}$ s^{-1}), at which SP exhibits more elastic solid-like behaviors. Therefore, similar to our expectation, SP indeed possess the interesting viscoelastic behavior, which makes it a favorable candidate as artificial SEI for Li metal anode.
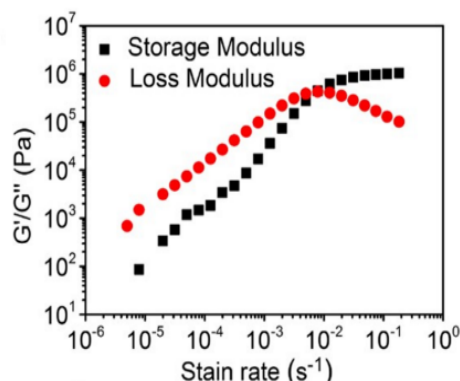
Figure II-493. The rheological study of SP.

The Li stripping/plating Coulombic efficiency (CE) of SP-coated Cu electrode was tested (Figure II-494). The SP-coated electrode showed good cycling performance, maintaining an average CE of 97.6% for over 120 cycles at 0.5 mA cm^{-2}. In comparison, control electrodes without SP coatings exhibited poor performance, with CE dropping below 90% after only 75 cycles. At a higher current density of 1 mA cm^{-2}, the SP-modified electrode achieved an average CE of 97.0% over 120 cycles, while the control electrodes maintained a CE of over 90% for only 65 cycles.
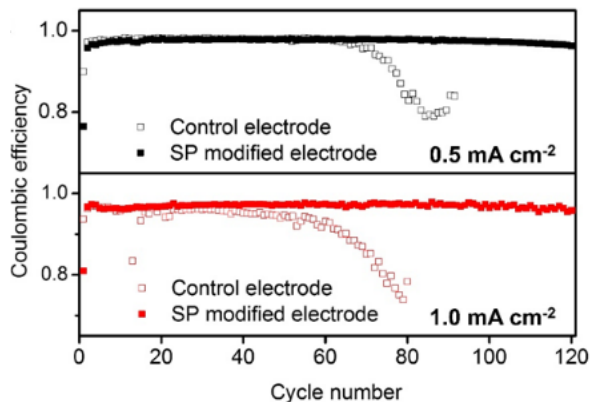
Figure II-494. CE of Li deposition/stripping (1 mAh cm⁻²) on SP-modified electrodes and control Cu electrodes at different current densities.

Previously, we have developed three-dimensional (3D) Li anode composites, which realized minimum volumetric change at the electrode level during cycling, more uniform Li deposition behavior and better electrochemical performance. To further improve the 3D Li metal anode design towards practical applications, effective protective surface coatings are essential. Among the surface protection materials, Li fluoride (LiF) has gained special attention due to its wide electrochemical stability window with negligible solubility in most of the electrolytes as well as its capability of regulating surface tension. In the early stage, it was found that the addition of HF or fluorinated compounds into electrolyte would help form LiF in SEI and enable more uniform Li deposition. However, these methods are unlikely to produce high-quality continuous and conformal LiF coating on Li metal. Instead, dispersive LiF domains would form with many weakly linked grain boundaries, which would easily fracture during Li metal plating and stripping. Moreover, HF and other fluorinated compounds are highly hazardous reagents, which might impose extra challenges in either industrial processing or battery packaging. Herein, we explored the possibility of gas phase reaction (using Freon R134a, 1,1,1,2-tetrafluoroethane, as the reagent) in attempt to produce high-quality LiF passivation layers conformally on 3D Li metal anode. The idea is illustrated schematically in Figure II-495. By exposing Li metal to Freon R134a gas, assisted with controlled gas pressure, and reaction temperature, we were able to coat a dense and uniform LiF layer with tunable thickness directly onto metallic Li.
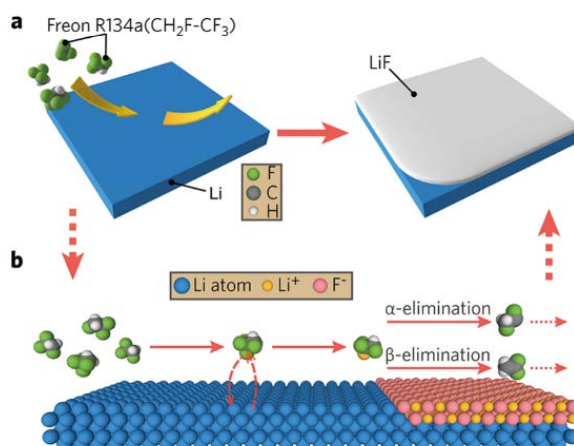

Figure II-495. (a) Schematic showing the surface treatment of Li metal with Freon R134a.(b) Proposed major chemical reactions at the early stage of surface treatment.

It was found that at a fixed temperature, increasing gas pressure would accelerate the reaction and afford rougher surface; and when gas pressure was fixed, the reactivity increased with temperature. At temperature below 150 °C, the surface was smooth without visible domains, while once the temperature was increased to approaching the melting point of Li metal, the reaction occurred in a much more vigorous fashion and formed micron-sized and porous LiF domains. Thus, to obtain high-quality LiF coating and sufficient reaction rate, 150°C and 0.5 atm is a good condition for conducting the surface coating. Figure II-496 shows the SEM images of a LiF-coated Li foil, where the top view shows smooth LiF surface, and the cross-section indicates a uniform thickness of ~40 nm.
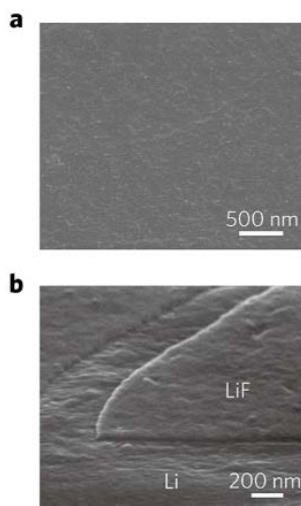
Figure II-496. High-resolution SEM images showing the (a) surface morphology and (b) cross-section of a LiF-coated Li foil.

To study the efficacy of the LiF coating for improving electrochemical stability of 3D Li metal anode (Li metal infused into layered graphene oxide matrix, Li-rGO), time-dependent electrochemical impedance spectroscopy studies were carried out, as shown in Figure II-497. LiF-coated Li-rGO do not show obvious increase in impedance within the tested period of time, indicating robust surface passivation that suppressed continuous side reactions and reduced the initial SEI formation. In addition, more stable symmetric cell cycling with suppressed increase in polarization was also observed.
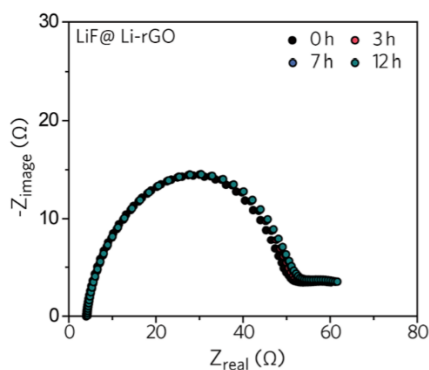
Figure II-497. Time-dependent electrochemical impedance measurement on 3D Li metal symmetric cells with LiF coating.

To address the challenges and make Li metal anode a viable technology, an attractive strategy is to replace the volatile liquid electrolytes with nonflammable solid counterparts that are electrochemically stable against Li and mechanically robust to suppress dendrite growth. Although a wide variety of solid electrolytes for Li

batteries have been developed throughout the years, the same critical challenge, which is the interfacial detachment between solid electrolytes and electrodes, awaits to be solved for all the systems.

Unlike liquid electrolytes, solid electrolytes barely have any fluidity to form a continuous contact with active materials inside the electrodes. Therefore, the electrochemical process can be severely limited by the contact area, leading to great interfacial resistance and low utilization of electrode capacity. The issue is even more pronounced for the Li metal anode, whose interfacial fluctuation in practical applications can be as large as tens of micrometers, making it difficult to cycle the solid-state Li batteries at high capacity and current density. Here, we present a paradigm shift on the structural design of solid-state Li batteries: Unlike all the previous studies where solid-state cells were constructed using planar Li foil, we adopted three-dimensional (3D) Li anode with high electroactive surface area for the first time, and the challenge of creating a conformal and continuous ionic contact between the 3D Li anode and the bulk solid electrolyte was successfully addressed via a flowable ion-conducting interphase (Figure II-498). This structural design has several major advantages: first, the adoption of a 3D Li anode significantly increases the electrode-electrolyte contact area, dissipating the current density to facilitate charge transfer and offering the opportunities to high-power operation. Second, by dividing bulk Li into small domains, the interfacial fluctuation during cycling can be reduced to the submicrometer scale, enabling the cells to be cycled at a much higher capacity. More importantly, the incorporation of a flowable interfacial layer can accommodate the varying morphology at the 3D Li anode surface during cycling, which is desirable for maintaining a continuous electrode-electrolyte contact. Finally, the 3D Li anode design can be adopted as a general approach in solid-state Li batteries, which is compatible with both solid polymer and inorganic ceramic electrolytes.
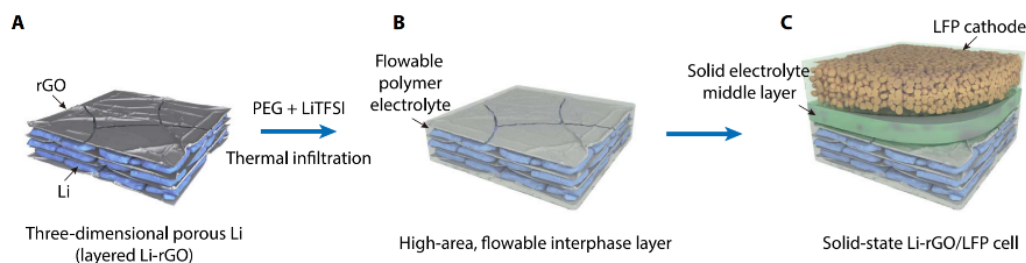
Figure II-498. Schematics illustrating the fabrication process of the 3D Li anode with flowable interphase for solid-state Li battery. (A) 3D Li-rGO composite anode was first fabricated. (B) A flowable interphase for the 3D Li-rGO anode was created via thermal infiltration of liquid-like PEG-LiTFSI at a temperature of 150°C. (C) A CPE layer consisting of PEO, LiTFSI, and fumed silica or an LLZTO ceramic membrane was used as the middle layer, and high–mass loading LFP cathode with the CPE as the binder was overlaid to construct the solid-state Li-LFP full cell.

The electrochemical performance was tested pairing with LiFePO$_4$ (LFP) cathode. Notably, different from many previous studies on solid Li batteries where the cathode mass loading was kept low to minimize the interfacial delamination, a relatively high capacity cathode (~1 mAh cm^{-2}) was used here to highlight the effectiveness of our design strategy toward improving the interfacial contact. As can be seen from Figure II-499, significantly improved rate performance and cycling stability can be achieved.
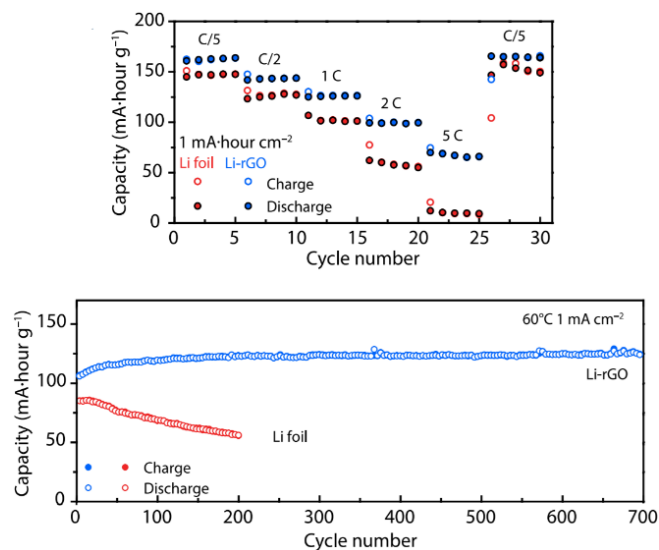
Figure II-499. Electrochemical performance of solid-state Li-LFP batteries.

Conclusions

In all, in the past one year, we have made significant progress in further developing stable host and passivation techniques for Li metal to afford minimal volume change and more stable cycling. By designing a Cu_3N nanoparticle/polymer composite as the passivation coating, we are able to *in-situ* convert the Cu_3N into Li_3N with high Li-ion conductivity. The coated anode exhibited highly improved cycling stability with high Coulombic efficiency. Due to the improved mechanical properties and homogenized Li-ion flux, the Li deposits exhibited more uniform and dense morphology. Later, we developed a new class of polymer coating with shear thickening effect, inspired by the silly putty. The polymer shows high stiffness under fast deformation, which can locally inhibit the fast dendrite growth, and facilitate the Li deposition in other areas. The new polymer coating enables smoother Li surface after deposition and thus more stable cycling.

The conventional spin coating method is good to protect Li metal with planar surface, but it is hard to be applied to a three-dimensional (3D) surface with our "stable host" design. As a consequence, we further developed Freon as gaseous reagent to conformally coat LiF onto 3D surface of Li. With the conformal LiF coating onto a Li-rGO composite anode we developed previously, we are able to demonstrate further improved cycling stability.

The 3D form of Li and the resulting minimal volume change offers the opportunity to design all-solid-state batteries with much better interfacial contact. In this consideration, we combined a flowable interface with 3D Li-rGO composite anode to build all-solid-state batteries. By pairing with $LiFePO_4$ cathode, we demonstrated highly improved rate capability and cycling stability in the all-solid-state full batteries.

In the past year, we have fulfilled the milestones of the projects, including 1) Rational design of composite artificial solid electrolyte interphase for the stabilization of three-dimensional nanoporous Li metal anode; 2) Explore novel materials and their properties as artificial SEI layer on Li metal; 3) Explore surface coating techniques for Li metal stabilization; 4) Stabilizing three-dimensional Li metal anode with solid electrolytes. Great progress has been achieved and the project is on track as planned.

Key Publications

1. W. Liu, W. Li, D. Zhuo, G. Zheng, Z. Lu, K. Liu, and Y. Cui, "Core-Shell Nanoparticle Coating as an Interfacial Layer for Dendrite-Free Lithium Metal Anodes", *ACS Central Science* 3, 135-140 (2017)

2. Y. Liu, Y. Cui, et al., "An Artificial Solid Electrolyte Interphase with High Li-Ion Conductivity, Mechanical Strength, and Flexibility for Stable Lithium Metal Anodes", *Adv. Mater.* **29**, 1605531 (2017)

3. D. Lin, Y. Liu, and Y. Cui, "Reviving the lithium metal anode for high-energy batteries", *Nature Nanotech.* **12,** 194-206 (2017)

4. K. Liu, A. Pei, Z. Bao, Y. Cui, et al., "Lithium Metal Anodes with an Adaptive "Solid-Liquid" Interfacial Protective Layer", J. Am. Che. Soc. **139 (13)**, 4815–4820 (2017)

5. A. Pei, G. Zheng, F. Shi, Y. Li, and Y. Cui, "Nanoscale Nucleation and Growth of Electrodeposited Lithium Metal", *Nano Lett.* **17 (2)**, 1132–1139 (2017)

6. D. Lin, Y. Cui, et al., "Conformal Lithium Fluoride Protection Layer on Three-Dimensional Lithium by Nonhazardous Gaseous Reagent Freon", *Nano Lett.* **17 (6)**, 3731-3737 (2017)

7. D. Lin, Y. Liu, A. Pei, and Y. Cui, "Nanoscale perspective: Materials designs and understandings in lithium metal anodes", *Nano Res.* (2017) DOI: 10.1007/s12274-017-1596-1

8. D. Lin, Y. Cui, et al., "Three-dimensional stable lithium metal anode with nanoscale lithium islands embedded in ionically conductive solid matrix", *PNAS*, **114**, 18 4613-4618 (2017)

9. Y. Li, Y. Cui, et al., "Revealing Nanoscale Passivation and Corrosion Mechanisms of Reactive Battery Materials in Gas Environments", *Nano Lett.* **17 (8)**, 5171–5178 (2017)

10. H. Wang, Y. Cui, et al., "Ultrahigh–current density anodes with interconnected Li metal reservoir through overlithiation of mesoporous AlF_3 framework", *Sci. Adv.* **3(9),** e1701301 (2017)

11. Y. Li, Y. Li, Y. Cui, et al., "Atomic structure of sensitive battery materials and interfaces revealed by cryo-electron microscopy", *Science* **358(6362)**, 506-510 (2017)

II.H.7   Lithium Dendrite Prevention for Lithium Batteries (PNNL)

Wu Xu, Principal Investigator
Pacific Northwest National Laboratory
902 Battelle Boulevard
Richland, WA 99354
Phone: 509-375-6934
E-mail: wu.xu@pnnl.gov

Ji-Guang Zhang, Co-Principal Investigator
Pacific Northwest National Laboratory
902 Battelle Boulevard
Richland, WA 99354
Phone: 509-372-6515
E-mail: jiguang.zhang@pnnl.gov

Tien Duong, Technology Manager
U.S. Department of Energy
Phone: 202-586-7836
E-mail: Tien.Duong@ee.doe.gov

Start Date: October 1, 2015   End Date: September 30, 2018
Total Project Cost: $1,200,000   DOE share: $1,200,000   Non-DOE share: $0

Project Introduction

Lithium (Li)-metal batteries are regarded as the "Holy Grail" of high density energy storage systems because Li-metal anode has an ultrahigh theoretical specific capacity (3860 mAh g^{-1}), the lowest negative electrochemical potential (-3.040 V vs. standard hydrogen electrode), and very low density (0.534 g cm^{-3}). However, their commercial applications have been hindered by the safety concerns due to Li dendrite growth and the short cycle life associated with low Coulombic efficiency (CE) of Li deposition/stripping. The dendritic Li generated at the anode surface can be self-amplified and lead to internal short circuiting of the battery and even more serious safety problems such as thermal runaway, fire, and explosion. The thermodynamically unstable Li in organic electrolytes often leads to low CE, more reactions between Li and electrolyte components to generate thick surface layer with high impedance, thus causing significant change in the morphology of Li metal and depletion of electrolyte. In our previous works, we discovered that an appropriate cycling protocol of slow charging and fast discharging can greatly improve the stability of Li metal anode and the long-term cycling stability of the Li metal cells. We also found that the LiTFSI-LiBOB dual-salt electrolytes with and without additives can significantly enhance the fast charging capability of the Li metal batteries. However, the fundamental mechanism behind these experimental observations have not been well understood. In FY17, our works have been focused on understanding the fundamental mechanism related to the stabilization of Li metal/liquid interface in various conditions. This will guide further development of the electrolytes to protect Li metal anode and to enhance the fast charging capability and the long cycle life of Li metal batteries.

Objectives

- Enable Li metal to be used as an effective anode in rechargeable Li-metal batteries for long cycle life at a reasonably high current density.

- Investigate the effects of various lithium salts, additives and carbonate-based electrolyte formulations on Li anode morphology, Li Coulombic efficiency (CE) and battery performances in terms of long-term

cycling stability at room temperature and elevated temperatures and at various current density conditions, rate capability, and low temperature discharge behavior.

- Characterize the surface layers on Li anode and cathode.

- Use computational calculations to get the theoretical data of solvates of cation-solvent molecules to explain the obtained battery performances.

Approach

The following approaches have been used to reach the objectives outlined above. First, the mechanism of $LiPF_6$ additive in LiTFSI-LiBOB dual-salt electrolyte on the protection of Li metal was investigated. Second, the charge process was verified experimentally by *in-situ* time-of-flight secondary ion mass spectrometry (ToF-SIMS) to detect the possible formation of a transient high-concentration Li^+ electrolyte layer on Li metal surface during fast discharge process. Third, the effects of $LiAsF_6$ and cyclic carbonate additives on Li deposition and Li CE were investigated. Fourth, four lithium imide-lithium orthoborate dual-salt electrolytes were further investigated to find out the effects of different dual-salt chemistries on the protection of Li metal anode and the cycle life of related Li metal batteries. Fifth, the effects of Li capacity utilization and charge current density on the stability of Li metal anode and the cyclability of related Li metal batteries were investigated using high cathode areal loading of 3.5 mAh/cm^2. Finally, new dual-salt electrolytes with an electrochemical stability window of 0 to 4.5 V were developed through screening solvents, lithium salts and additives. Various characterization technologies, including high-resolution scanning electron microscopy (SEM), transmission electron microscopy (TEM), X-ray photoelectron spectroscopy (XPS) and ToF-SIMS were used to analyze the morphology and composition of the interfacial films on Li-metal surfaces. The results obtained in these investigations will be combined with density functional theory (DFT) calculations to reveal the mechanisms that led to the enhanced performance in Li-metal batteries.

Results

1. Mechanism of LiPF₆ additive in LiTFSI-LiBOB dual-salt electrolyte on Li metal protection

The LUMO energies of the lithium salts and solvents studied in this work reveal that the reduction voltages of these salts and solvents decrease in the following order: LiBOB >> LiTFSI > ~$LiPF_6$ >> EC > EMC (Figure II-500a). LiBOB could be easily reduced to form an SEI layer on the Li metal surface and dictates the morphology of Li during the deposition process. Cyclic voltammetry analysis is consistent with the LUMO energies, demonstrating that LiBOB in the pure and the LiTFSI-LiBOB dual-salt electrolytes shows a reduction peak with an onset potential of ca. 1.1 V vs. Li/Li$^+$, while the onset reduction potentials for pure LiTFSI and $LiPF_6$ electrolytes are hard to find. The addition of $LiPF_6$ additive in the dual-salt electrolyte greatly suppresses the reduction peak at 1.1 V for LiBOB, probably due to the superior SEI layer formed. The XPS and EDS results are also in good agreement with the calculated LUMO energies.
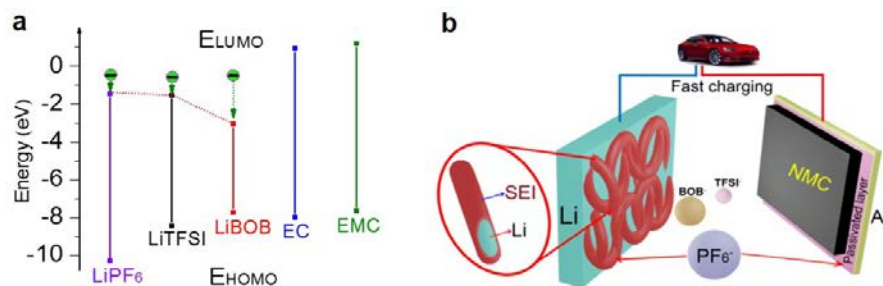

Figure II-500. (a) HOMO and LUMO energies of lithium salts ($LiPF_6$, LiTFSI, LiBOB) and solvents (EC, EMC). The vertical lines indicate the electrochemical stability window of related lithium salts and solvents. (b) Schematic illustration demonstrating that $LiPF_6$ additive in LiTFSI-LiBOB dual-salt electrolyte improves the stability of the Al current collector and the Li metal anode.

Based on the electrochemical performance and post-mortem analysis, a functioning mechanism of $LiPF_6$ additive in LiTFSI-LiBOB dual-salt electrolyte has been proposed (Figure II-500b). On one hand, the $LiPF_6$ additive plays an important role in stabilising the aluminium (Al) current collector and maintaining good electrical contact between the active material and Al. On the other hand, a small amount of $LiPF_6$ in the LiTFSI-LiBOB dual-salt electrolyte significantly alters the nature of the SEI layer formed on the Li metal anode. The decomposition products of $LiPF_6$, i.e., PF_5 and POF_3, act as catalysts and induce the formation of polycarbonates and polyethers from the ring-opening polymerisation of EC molecules. The SEI layer formed on Li metal in the $LiPF_6$-added dual-salt electrolyte is highly conductive and can minimize electrode polarisation. It can also prevent the accumulation of isolated or "dead" Li during each deposition/stripping cycle. In addition, the polycarbonates and polyethers formed in the SEI layer are flexible, can efficiently cover the Li metal surface, reduce the side reactions, hold the isolated/"dead" Li particles tightly and adhere to the bulk Li anode thus preventing the separation of the SEI layer from the bulk Li metal. Therefore, the utilization of Li metal initiates at the surface and slowly propagates inward. More importantly, there is no internal short circuit occurring at a charge current density even up to 5.25 mA cm^{-2}. The high charging capability and the excellent cycle life validate the $LiPF_6$-added LiTFSI-LiBOB dual-salt electrolyte as an appealing functional electrolyte for high performance Li metal batteries.

2. Verify the formation of a transient high Li$^+$-concentration electrolyte layer during fast discharging

The composition of the surface passivation layer of Li anode during fast and slow discharge rates of the Li‖LiCoO$_2$ cells were characterized by *in-situ* ToF-SIMS. The electrolyte was 1.0 M $LiPF_6$ in EC-EMC. The schematic configuration and a photo of the cell are shown in Figure II-501. The Cu‖LiCoO$_2$ cell was charged first to deposit Li on Cu substrate at a slow rate, and then the cell was discharged at fast (1C) and slow (C/5) rates. The compositions of the surface layers formed on Li anode were analyzed *in operando* by ToF-SIMS. The test results indicate that the difference in Li$^+$-content in SEI formed on Li anode during fast and slow discharge rates (1C vs. C/5) is not significant enough to show whether a concentrated Li$^+$ electrolyte is formed during fast discharge (Li stripping). This is probably because of the technical limitations of the current electrochemical cell and/or *in-situ* ToF-SIMS.
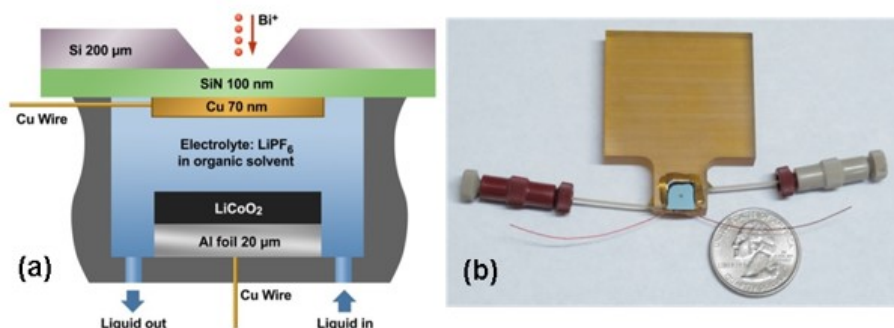
Figure II-501. (a) A schematic drawing of the liquid cell device with both anode and cathode integrated into the liquid cell. (b) A photo of the real device.

3. Guided Li deposition and improved Li CE through synergistic effects of LiAsF$_6$ and VC additives

The effects of additives in the $LiPF_6$/PC electrolyte on the morphologies of deposited Li metal and the cycling performance of Li‖NMC cells were investigated, and the results are shown in Figure II-502 and Figure II-503, respectively. It is seen from Figure II-502 that the baseline electrolyte leads to disordered and dendritic Li growth. Adding VC or FEC can eliminate Li dendrite formation but the surface of deposited Li is rough. Adding additive $LiAsF_6$ gives ordered Li nanorods growth but the Li surface is still rough. When using the additive mixtures of VC+$LiAsF_6$ and FEC+$LiAsF_6$, the Li surface is more smooth and uniform and the Li nanorods are more compact and well aligned. Figure II-503a indicates that the addition of $LiAsF_6$ does not increase the Li CE much, but VC or FEC improves the Li CE significantly. The combination of VC+$LiAsF_6$ or FEC+$LiAsF_6$ can increase Li CE from 73.2% for the baseline electrolyte to about 96.5%. The improved Li CE

brings to longer cycle life of LI‖NMC111 cells and the VC+LiAsF$_6$ additive mixture shows the best cycling stability in the Li‖NMC111 cells (Figure II-503b). The deposited Li morphologies, Li CE and cycling performance all indicate the synergistic effects of LiAsF$_6$ and VC or FEC additives. Such synergistic effects of additives LiAsF$_6$+VC in the electrolyte of 1 M LiPF$_6$/PC were investigated through linear sweep scan (LSV), XPS, and SEM. It is revealed for the first time that LiAsF$_6$ can be reduced to Li$_x$As alloy phase and LiF, which can act as nano-sized seeds for Li growth and form a robust SEI layer. The addition of VC or FEC not only enables the uniform distribution of Li$_x$As seeds because of the initial surface passivation of the Cu substrate, but also improves the SEI layer flexibility due to the formation of polymeric components in the SEI.
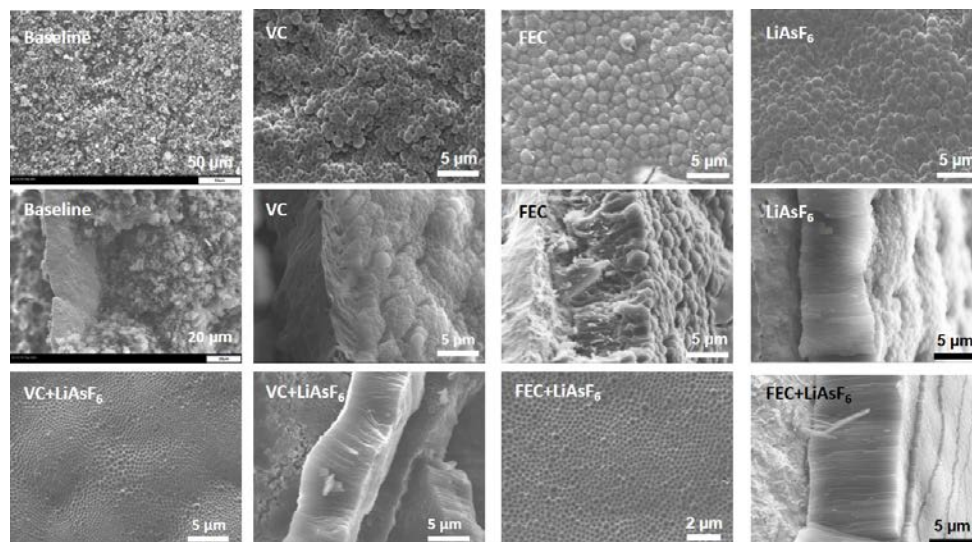
Figure II-502. SEM images (surface and cross-section views) of the deposited Li metal on Cu foils in electrolytes of 1 M LiPF$_6$/PC with different additives (VC, FEC and X) and additive mixtures (VC+X and FEC+X) at 0.1 mA cm^{-2} for 15 hours.
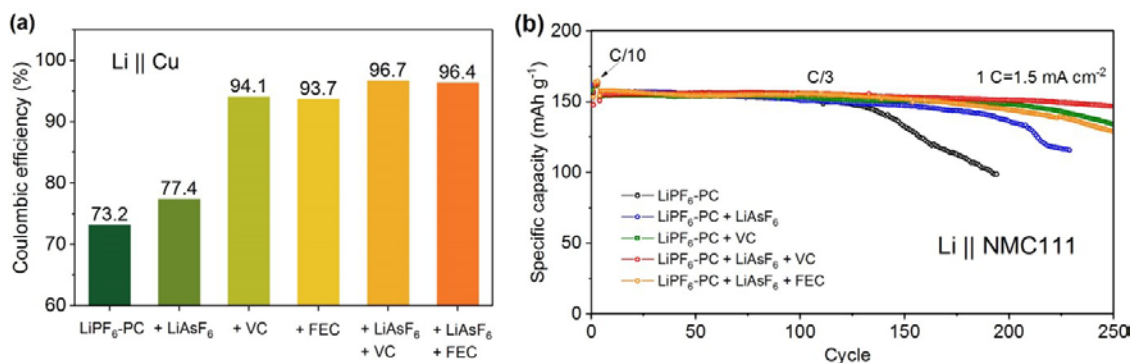
Figure II-503. (a) Average Li CE in electrolytes of 1 M LiPF$_6$/PC with different additives (VC, FEC and LiAsF$_6$) and additive mixtures (VC+LiAsF$_6$ and FEC+LiAsF$_6$) tested in Li‖Cu cells. (b) Cycling stability of these electrolytes in Li‖NMC111 cells at C/3 rate after two formation cycles at C/10 rate, in the voltage range of 2.7 and 4.3 V.

4. Effects of lithium imide-lithium orthoborate dual-salt electrolytes on stability of Li metal batteries

The effects of lithium imide and lithium orthoborate dual-salt electrolytes of different salt chemistries in carbonate solvents on the cycling stability of Li metal batteries were systematically and comparatively investigated. Two imide salts (LiTFSI and LiFSI) and two orthoborate salts (LiBOB and LiDFOB) were chosen for this study and compared with the conventional LiPF$_6$ salt. Density functional theory calculations indicate that the chemical and electrochemical stabilities follow the order of LiTFSI-LiBOB > LiTFSI-LiDFOB > LiFSI-LiBOB > LiFSI-LiDFOB. The experimental cycling stability of the Li metal cells with the

electrolytes follows the order from good to poor as LiTFSI-LiBOB > LiTFSI-LiDFOB > LiPF$_6$ > LiFSI-LiBOB, indicating that LiTFSI behaves better than LiFSI and LiBOB over LiDFOB in these dual-salt mixtures. The LiTFSI-LiBOB can effectively protect the Al substrate and form a more robust surface film on Li metal anode, while the LiFSI-LiBOB results in serious corrosion to the stainless steel cell case and a thicker and looser surface film on Li anode.
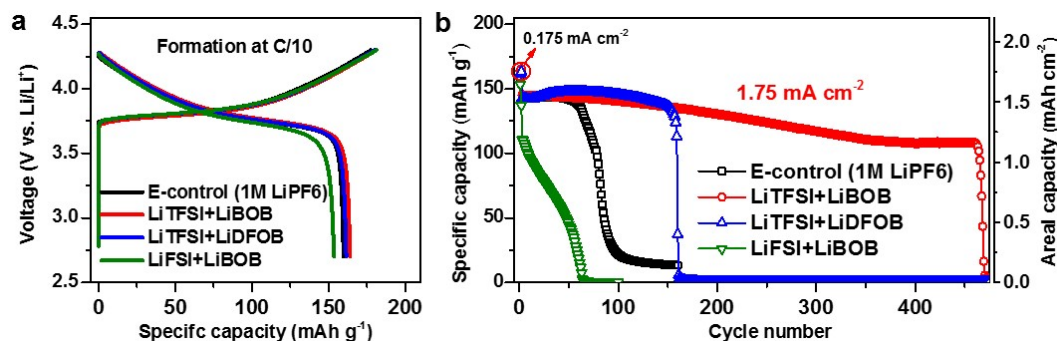
Figure II-504. (a) Initial charge/discharge voltage profiles at 0.175 mA cm^{-2} and (b) cycling performances of the baseline LiPF$_6$ electrolyte and the three different dual-salt electrolytes at a current density of 1.75 mA cm^{-2} after 3 formation cycles at 0.175 mA cm^{-2}.

5. Effects of Li capacity utilization and charge current density on stability of Li metal batteries

The effects of Li anode areal capacity utilization during each deposition/stripping cycle and the charge current density on the stability of Li metal anode and the cycling performance of the Li metal battery have been systematically investigated uasing the dual-salt electrolyte of LiTFSI-LiBOB in EC-EMC with 0.05 M LiPF$_6$ additive between 2.7 and 4.3 V. NMC111 cathodes with different areal capacities (from ~1.0 to ~4.0 mAh cm^{-2} with an interval of ~0.5 mAh cm^{-2}) were used to represent the Li areal capacity utilization. Under the same charge current density at 1.0 mA cm^{-2}, very decent long-term cycling performance can be achieved for the NMC cathode with all areal capacity loadings or the Li areal capacity usages in the case of excess Li metal and electrolyte amount, meaning that the utilization of Li amount in each cycle does not affect the cycling stability of the Li metal cells when excess Li and electrolyte are used. Increase of Li capacity usage in each cycle causes variations in components of the SEI layer on Li anode and generates more ionic conductive species from this electrolyte. Further studies reveal for the first time that Li anode degradation and SEI thickness show linear relationship with the areal capacity usage. The amount of the consumed Li and the ratio of SEI thickness to NMC areal loading are kept almost the same values with increasing cathode loading, respectively. It implies that Li metal batteries with the same Li metal anode loading but higher cathode loading will degrade faster than those with lower cathode loading, thus lead to shorter cycle life. On the other hand, a higher charge current density results in a quicker capacity fade, meaning a shorter cycle life. The effect of charge current density is more significant than that of Li capacity utilization on the stability of Li metal anode and the cycle life of Li metal batteries.

6. Development of new electrolytes for stabilizing Li metal anode

The CE of Li cycling was also studied by optimizing the solvent compositions and adding combinational additives in dual-salt electrolytes of LiTFSI-LiBOB in EC-EMC. The increase of EC content in the solvent mixture will slightly improve the average Li CE from 87.4% for EC-EMC (4:6 wt) to about 91.6% for EC-EMC (7:3, 8:2 and 9:1 wt). Further addition of additives (LiPF$_6$, VC and FEC, in single or combination) will largely increase the average Li CE. For the additive combination of 0.05 M LiPF$_6$ + 2% VC + 2% FEC in the dual-salt electrolyte with EC-EMC (7:3 wt), the average Li CE can be further increased to 98.1%. This electrolyte also shows excellent stability with Li metal anode by the stable and low polarization voltage in Li‖Li symmetric cells for at least 800 h at a current density of 0.5 mA cm^{-2}, and exhibits about 99.7% CE of Li

cycling in Li‖NMC111 cells between 2.7 and 4.3 V at 2.0 mA cm^{-2}. More performance testing and characterization are under way.

Conclusions

1. In the LiTFSI-LiBOB dual-salt electrolyte, the additive level LiPF$_6$ induces the generation of a robust and conductive SEI layer enriched with polycarbonate species that can effectively bond the isolated or "dead" Li as well as other organic and inorganic components together with the bulk Li metal anode, mitigates the reduction of lithium salts especially LiBOB, and stabilizes Al current collector of the NMC cathode. Therefore, the Li metal anode can be well protected and the fast charging capability and the long-term cycle life of Li metal batteries can be significantly enhanced.

2. The SEI components on Li metal anodes during fast and slow discharge processes were analyzed by in-situ ToF-SIMS, but a concentrated electrolyte layer was not observed probably because the difference in Li$^+$-content in SEI from fast and slow discharge rates is small.

3. Additive mixtures of LiAsF$_6$ and cyclic carbonate additives (VC or FEC) show synergistic effects on guiding the formation of smooth, uniform and dense nanorod Li metal deposition and largely increasing the Li CE from 73% to about 97%. The best additive combination of LiAsF$_6$+VC can enable the Li‖NMC111 cells to be cycled stably for more than 250 cycles.

4. Among the four imide-orthoborate dual-salt mixtures, LiTFSI-LiBOB shows the best cycling stability because of its effective protection on Al substrate and formation of a more robust surface film on Li metal anode. Optimization of solvent composition and addition of VC+FEC additive mixture can further stabilize Li metal anode and increase Li CE to over 98%, thus extending the cycling stability of Li metal batteries.

5. Li capacity utilization and charge current density have significant effects on Li anode stability. A higher Li capacity utilization and a higher charge current density lead to more serious corrosion of Li metal, thus a less cycle life of related Li metal batteries.

Key Publications and Presentations

1. J. Zheng, M. H. Engelhard, D. Mei, S. Jiao, B. J. Polzin, J.-G. Zhang,* and W. Xu,* "Electrolyte Additive Enabled Fast Charging and Stable Cycling Lithium Metal Batteries", *Nature Energy*, 2017, **2**, 17012.

2. S. Jiao, J. Zheng, Q. Li, X. Li, M. H. Engelhard, R. Cao, J.-G. Zhang*, and W. Xu*, "Behavior of Lithium Metal Anode under Various Capacity Utilization and High Current Density in Lithium Metal Batteries", *Joule*, 2017, DOI: 10.1016/j.joule.2017.10.007.

3. X. Ren, Y. Zhang, M. H. Engelhard, Q. Li, J.-G. Zhang*, and W. Xu*, "Guided Lithium Metal Deposition and Improved Lithium Coulombic Efficiency through Synergistic Effects of LiAsF$_6$ and Cyclic Carbonate Additives", *ACS Energy Letters*, 2017, DOI: 10.1021/acsenergylett.7b00982.

4. X. Li, J. Zheng, M. H. Engelhard, D. Mei, Q. Li, S. Jiao, N. Liu, W. Zhao, J.-G. Zhang*, and W. Xu*, "Effects of Imide-Orthoborate Dual-Salt Mixtures in Organic Carbonate Electrolytes on the Stability of Lithium Metal Batteries", submitted.

5. W. Xu, H. Xiang, J. Zheng, Q. Li, J.-G. Zhang, D. Mei, P. Yan, R. Cao, P. Bhattacharya, S. D. Burton, M. H. Engelhard, M. E. Bowden, Z. Zhu, C. Wang, S. Jiao, S. S. Cartmell, A. V. Cresce, K. Xu, B. Polzin, "CsPF$_6$ and Propylene Carbonate in Conventional LiPF$_6$/Carbonate Electrolytes for Enhanced Lithium-Ion Battery Performances in Wide Temperature Range", Invited talk at *PRiME 2016*, October 3, 2016, Honolulu, HI.

6. S. Jiao, J. Zheng, H. Xiang, P. Shi, D. Mei, Q. Li, S. S. Cartmell, J.-G. Zhang, W. Xu, "Optimization of Dual-Salt Electrolytes for Rechargeable Lithium Metal Batteries", Oral presentation at *PRiME 2016*, October 4, 2016, Honolulu, HI.

7. W. Xu and J.-G. Zhang, "Lithium Dendrite Prevention for Lithium Batteries", Invited talk at *DOE BES/BMR/ABR/Battery500 Battery Research Information Exchange Meeting*, January 18, 2017, Berkeley, CA.

8. W. Xu, F. Ding, Y. Zhang, J. Qian, B. D. Adams, H. Xiang, J. Zheng, and J.-G. Zhang, "Lithium Metal Anodes and Rechargeable Lithium Metal Batteries", Invited talk at *2017 MRS Spring Meeting & Exhibit*, April 19, 2017, Phoenix, AZ.

9. W. Xu, J. Zheng, H. Xiang, X. Chen, S. Jiao, F. Ding, Y. Zhang, J. Qian, M. H. Engelhard, D. Mei, and J.-G. Zhang, "Development of Dual-Salt/Carbonate-Solvents Electrolytes for Fast Charging and Stable Cycling Lithium Metal Batteries", Invited talk at *231st ECS Meeting*, May 30, 2017, New Orleans, LA.

10. W. Xu and J.-G. Zhang, "Lithium Dendrite Prevention for Lithium Batteries", Invited talk at *DOE's 2017 Annual Merit Review and Peer Evaluation Meeting*, June 8, 2017, Washington DC, DC.

11. J. Zheng, H. Xiang, M. H. Engelhard, D. Mei, S. Jiao, J.-G. Zhang, and W. Xu, "LiTFSI-LiBOB Electrolytes and $LiPF_6$ Additive to Enhance Charging Capability and Cycling Stability of Rechargeable Lithium Metal Batteries", Poster presentation at *The 10th Beyond Li-Ion symposium (BLI-X)*, June 28, 2017, San Jose, CA.

II.H.8   Understanding Strategies for Controlled Interfacial Phenomena in Li-Ion Batteries and Beyond (TAMU)

Perla B. Balbuena, Principal Investigator
Texas A&M University
3122 TAMU
College Station, TX 77843
Phone: 979-845-3375
E-mail: balbuena@tamu.edu

Jorge M. Seminario, Co-Principal Investigator
Texas A&M University
3122 TAMU
College Station, TX 77843
Phone: 979-845-3301
E-mail: seminario@tamu.edu

Partha P. Mukherjee, Co-Principal Investigator
Texas A&M University
3123 TAMU
College Station, TX 77843
Phone: 979-862-6498
E-mail: pmukherjee@tamu.edu

Tien Duong, Technology Manager
U.S. Department of Energy
Phone: 202-586-7836
E-mail: Tien.Duong@ee.doe.gov

Start Date: October 1, 2016   End Date: September 30, 2019
Total Project Cost: $1,333,335   DOE share: $1,200,000   Non-DOE share: $133,335

Project Introduction

This project will develop and apply novel first-principles-based theoretical-computational methods and mesoscale schemes to elucidate fundamental issues associated with ionic and electronic transport through solid-electrolyte interphase (SEI) components and their interfaces. These include growth and dissolution of SEI layer components as functions of evolving Si anode morphologies during cycling; role of the electrolyte on tuning of surface healing and SEI reforming; role of the electrolyte on surface wetting during Li plating; connection between microscopic electrode morphology and electrolyte structure, dynamics, and reactivity and macroscopic battery performance. We plan to use the knowledge gained with this fundamental understanding to elaborate strategies based on electrolyte formulation and electrode morphology design to solve practical issues associated with the instability of SEI at Si anodes during cycling and dendrite formation in Li metal anodes.

Objectives

The objective of this project is to evaluate and characterize interfacial phenomena in lithiated Si and Li metal anodes and to develop guidelines for potential solutions leading to controlled reactivity at electrode/electrolyte interfaces of rechargeable batteries using advanced modeling techniques based on first-principles.

Approach

The plan to overcome shortcomings, limitations, and challenges is based on obtaining a deeper understanding leading to sound strategies for solutions to the targeted issues. The approach combines density functional theory, ab initio molecular dynamics, and other ab initio techniques to characterize the chemical and electrochemical reactions in well-defined models and to explore the behavior of new electrolyte mixtures in specific electrode configurations and various states of charge. Details of the interfacial chemistry gained with ab initio techniques are used into classical molecular dynamics involving millions of atoms to investigate structural and dynamic behaviors of the electrode/electrolyte interface under applied fields. In the next step, Kinetic Monte Carlo and other mesoscopic models developed in our own groups are used to characterize long-time behavior in larger and more complex systems (for example dendrite growth or nanostructure assembly) and their impact on macroscopic properties and performance. Thus, computational analyses will be the basis to provide a comprehensive understanding for physics-based designs and completely new ideas for overcoming the described issues.

Results

SEI growth and cracking of lithiated Si nanoparticles

We studied several aspects of the SEI formation on pre-lithiated Si nanoparticles: a) effects of the electrolyte composition on the rate of SEI growth during lithiation; b) effects of specific coatings (graphene or graphene oxide, and self-healing polymers) on the interfacial stability of the pre-lithiated Si nanoparticle during lithiation. Regarding the first point, our main findings can be summarized in Figure II-505. The graph represents the change in the electronic charge of the Si atoms (average) due to electron transfer to the electrolyte. Therefore, this change in charge is proportional to the rate of growth of the SEI layer. Figure II-506 shows that when the nanoparticle is lithiated in presence of different electrolyte compositions the rate of SEI growth changes dramatically. In all cases there is a sharp increase in the initial stage of electrolyte reduction (the colored region) followed by a stabilization period (the plateau region). In absence of salt, the kinetics of initial reduction is slower (blue region) and the number of electrons transferred (i.e., the number of solvent molecules reduced) is larger than in the presence of salt (pink region). This simple test, obtained from ab initio molecular dynamics (AIMD) simulations gives significant information regarding the quality of the SEI. When the anion is present, the anion reduces first and the SEI nucleation starts (usually as LiF and other organic or inorganic radical anion fragments that bind to Li$^+$), and the number of solvent molecules reduced decreases. When EC is substituted by FEC the initial rate of growth is much faster and the green region is narrower, indicating the faster stabilization. The rapid reduction of the fluorinated salt or fluorinated solvent/additive leads to formation of LiF, as already found in our previous work, which prevents the further reduction of EC molecules. More work is needed to elucidate the details of such prevention mechanism. Our initial results indicate that it is due to changes in the electronic structure and ionic transport at the solid/liquid interface. New DFT/AIMD studies were conducted to determine the role of coatings in controlling interfacial phenomena. We have tested two types of surfaces: graphene and graphene oxide, and also self-healing polymers. We have found that both coatings have advantages and disadvantages that are clearly found from the atomistic studies. The advantage of these structures is that they are able to control reactivity. However, the self-healing mechanism may be compromised by additional reactions. A work in collaboration with Dr. Chunmei Ban (NREL) is also being finalized respect to identification of reaction products when alucone is used as an artificial SEI layer on Si anodes. We were able to follow changes in the coordination structure and oxidation state of Al atoms and on the interfacial reactivity. We also published a letter regarding the initial stages of SEI layer formation on a alucone-coated lithiated Si surface. This work revealed the active role of Al in the SEI layer formed modifying the alucone coating.
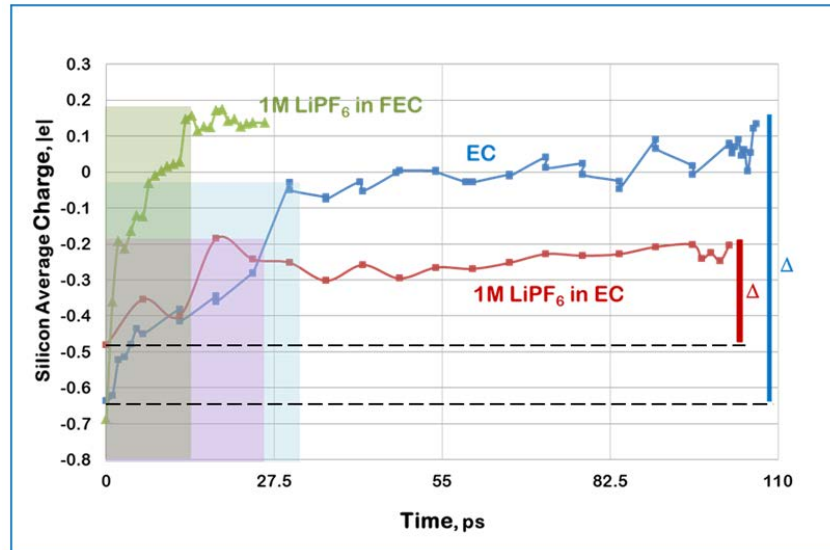
Figure II-505. Time evolution of the average Si charge obtained from AIMD simulations. The change of the Si electronic charge is due to electron transfer to the electrolyte, and therefore is proportional to the SEI layer rate of growth. These results were presented at the AMR meeting and published in the Journal of the Electrochemical Society.

In addition, the team was actively engaged in the characterization of cracking phenomena after the SEI layer is grown over the lithiated Si surface. Classical molecular dynamics simulations were employed to investigate nanoparticles of the order of 4 nm, and a mesoscopic model was employed for particles of ~500 nm.
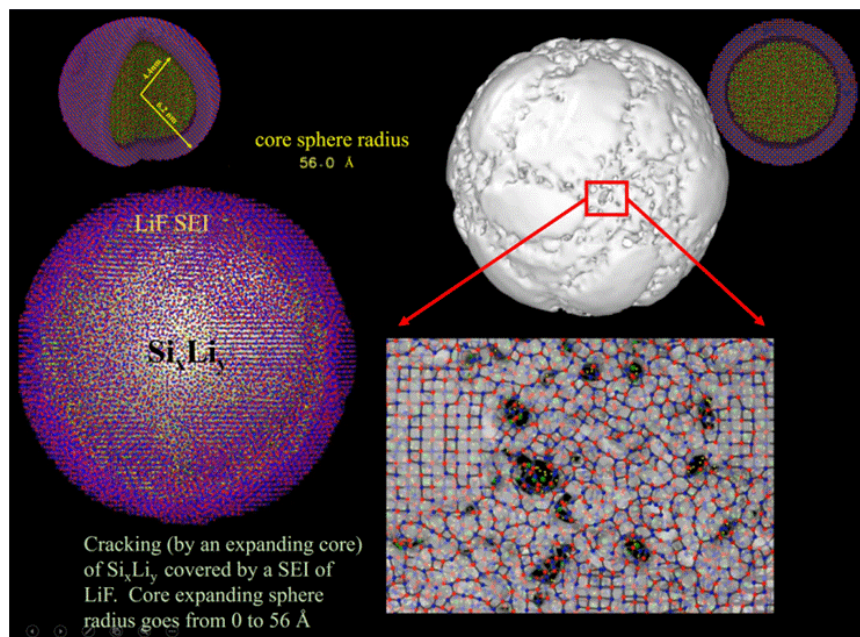
Figure II-506. Molecular dynamics simulations of surface cracking of a lithiated Si nanoparticle of ~4 nm covered by a LiF model SEI of ~1.5 nm. The expansion of the core leads to cracking which is manifested by bond damaging of the SEI coating initially, then resulting in macroscopically visible fractures.

The study characterized the swelling, alloying, and amorphization of a silicon nanocrystal anode in a full nanobattery model during the first charge. A dissolved salt of $LiPF_6$ in EC was chosen as the electrolyte solution and $LiCoO_2$ as cathode. External electric fields were applied to emulate the charging, causing the migration of the Li-ions from the cathode to the anode, by drifting through the electrolyte solution, thus converting pristine Si gradually into $Li_{14}Si_5$ when fully lithiated. The volume of the anode increases with the amorphization of Si. This model allowed the evaluation of stress changes in the electrode during the first charge. Current efforts are oriented to adding the solid-electrolyte interphase and determining the changes in volume and structure occurring during lithiation and delithiation. In parallel, a mesoscopic random lattice spring model was utilized to evaluate similar behavior in much larger nanoparticles. The model was coupled with solid state diffusion of Li in active particles and SEI formation to characterize fracture in the active material along with SEI film growth. It solves the Li-induced mechanics interaction (i.e., stress generation) in active particles and captures microcrack formation and propagation. The Li diffusion induced stress deforms the spring elements. Fracture occurs when the strain energy in a spring exceeds the fracture energy threshold and consequently these springs are removed from the network. The effect of fracture on diffusion inside the active material is incorporated by diffusion coefficients modified using a damage parameter. The cracks provide additional sites for Li intercalation electrochemical reaction as well as SEI reaction. It was found that peripheral (surface) cracks form easily during delithiation and central cracks (close to active material center) during lithiation (Figure II-507). The surface cracks provide extra area for intercalation and SEI reaction while isolated central cracks only hinder diffusion of Li ions inside the active material.
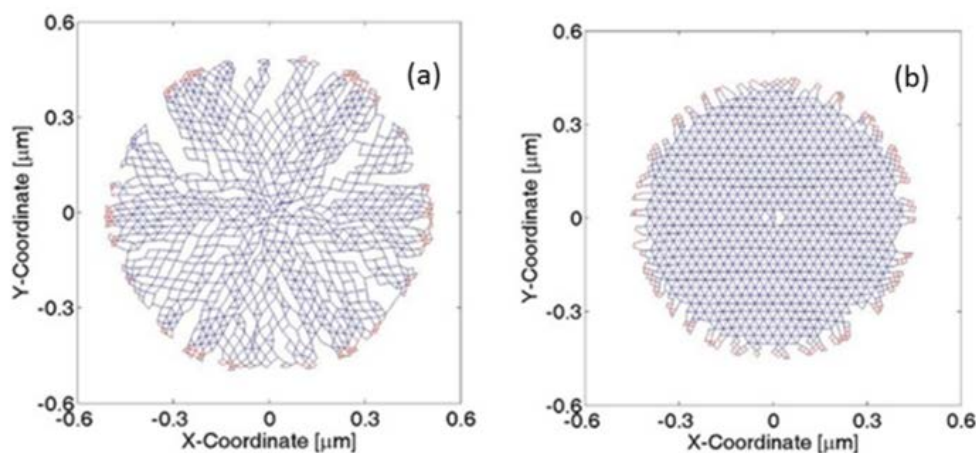
Figure II-507. Effect of core structure on cracking of ~500 nm nanoparticles. (a) crystalline core; (b) amorphous core. An SEI film covers the particle. There is a larger damage observed in the crystalline than in the amorphous particle.

The impact of high volumetric expansion during lithiation in Si on the damage stochastics inside a larger 500 nm diameter particle and in the SEI film is also studied with a mesoscopic model. Figure II-507 shows the lithium transport induced damage characteristics in crystalline (Figure II-507a) and amorphous (Figure II-507b) Si particle covered by a SEI film. It is evident that fracture in the crystalline Si particle exhibits significantly higher fracture due to two-phase diffusion as compared to a single-phase diffusion in amorphous Si, which generates large mismatch in volumetric strain between the core and surface. The SEI film shows complete rupture for both scenarios due to large stress from the expanding Si particle. Si particle diameter below 200-300 nm is preferable, which can reduce the microcrack-induced damage inside the particle as well as in the SEI film. This suggests that an appropriate combination of the mechanical properties of the SEI film and Si active particle may enable better strain accommodation.

Multiscale Model of SEI film Growth

Li-ion transport through the SEI layer influences the anode reactions, including Li reduction and intercalation into active material, as well as the SEI formation. In reality, there is a multiphase SEI growing on the electrode surface. Diffusion kinetics in the SEI layer along with multiphase SEI growth is modeled to understand the underlying physics. As shown in Figure II-508, two components: A (purple) and B (white) are considered. Here, Li-ion transport in component B is assumed much slower compared to that in A. The activation energies of Li-ion diffusion in the SEI are 46.1 KJ/mol for A and 65.3 KJ/mol for B, which means that the diffusion rate in A is over 2200 times that in B, and the activation energy for solvent diffusion within the SEI is fixed at 67.2 KJ/mol. The values of these activation energies fall within DFT ranges calculated by us for Li^+ in Li_2CO_3. The model assumes that the solvent diffuses through the porous SEI and is reduced at the surface of the electrode. The effects of the volume fraction of B are depicted in Figure II-508(c). As the volume fraction increases, the total charging time increases, leading to a thicker SEI film for the first charging cycle. It is worth pointing out that the total charging time and SEI growth have non-linear relationships with the volume fraction of B. Figure II-508(a) and (b) illustrate the SEI film configurations, with volume fractions of 5% and 33%. Increasing the V volume fraction could induce nucleation of B hindering the fast transport pathways in component A. Figure II-508(d) shows that the content of active Li inside the SEI varies up-and-down along the SEI's depth, and the fluctuation becomes larger increasing the B volume fraction. In contrast, for the one-component SEI, it exhibits a predominantly linear Li-ion content trend near the electrode-SEI interface.
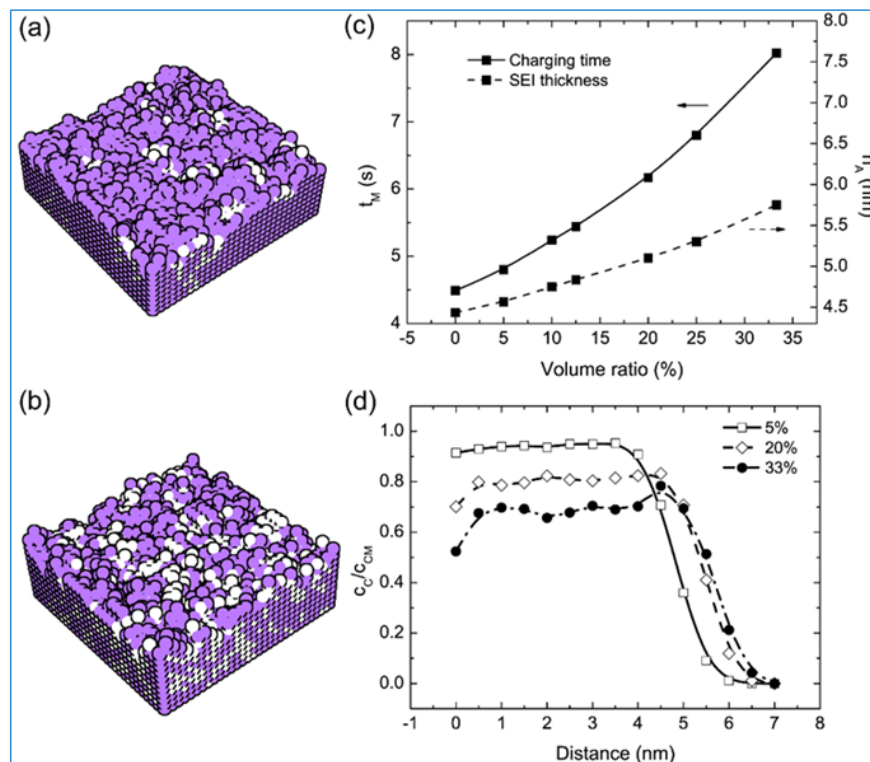
Figure II-508. SEI of two components with different activation barriers for Li diffusion: purple (A, Ea = 46.1 KJ/mol) and white (B, Ea = 65.3 KJ/mol). SEI morphologies at B volume fractions of 5% in (a) and 33% in (b). (c) Total charging time and SEI thickness for the first charge with varying B volume fraction. (d) Concentration of active Li traveling through the SEI interstitials (c_c) respect to the theoretical maximum (c_M) as a function of SEI thickness for various B volume fractions.

The non-uniform distribution of component B largely accounts for the fluctuation in Li-ion content. Compared to the fast Li-ion diffusion in component A, Li-ions seem to be trapped after they enter the component B. Therefore, this "trapping effect", along with the non-uniform distribution of B, induces the results in

Figure II-508(d). Moreover, Li-ion diffusion in SEI could become the rate-determining step to govern the overall electrode reactions when the volume fraction of B is large enough.

Conclusions

New insights were obtained regarding the SEI layer formation and cracking in lithiated Si anodes. It was found that the rate of SEI growth is extremely dependent on the nature of the electrolyte, and formation of specific SEI components such as LiF may stabilize the reactions. When a coating such as alucone is molecularly deposited to precover the anode surface, reactions can occur where the coating components (such as Al) participate in the reaction. As a consequence a new coating is generated that includes SEI components. Once the SEI is formed on lithiated Si surfaces of nanoparticles, volume expansion generated during battery charge may induce stress that ends up into bond damaging and finally the formation of cracks. Crystalline materials are more easily damaged than amorphous, that can release the stress easily. The microscopic details of crack formation were elucidated and quantified as a function of stress. Various coatings were computationally tested including graphene and graphene oxide, and a H-bonding forming polymer. The graphene and graphene-oxide materials were found helpful to control SEI formation, whereas the H-bonding polymer was found to be easy to deteriorate during lithiation and delithiation. A multiscale model of SEI growth was developed and tested for a 2-components SEI, and ionic transport through the layers was quantified as a function of the relative barriers for Li diffusion in each material. The model is able to quantify several important macroscopic properties as a function of microscopic parameters.

Key Publications

1. Kie Hankins, Fernando A. Soto, and Perla B. Balbuena, "Insights into the Li Intercalation and SEI Formation on LiSi Nanoclusters," *J. Electrochem. Soc.*, 164, (11), E3457-E3464, (2017).

2. L. Benitez; J. M. Seminario, "Ion Diffusivity through the Solid Electrolyte Interphase in Lithium-Ion Batteries," *J. Electrochem. Soc.* 164, (11), E3159-E3170. (2017).

3. V. Ponce; D. E. Galvez-Aranda; J. M. Seminario, "Analysis of a Li-Ion Nanobattery with Graphite Anode Using Molecular Dynamics Simulations," *J. Phys. Chem. C*, 121, 12959-12971, (2017).

4. Jose L. Gomez Ballesteros and Perla B. Balbuena, "Reduction of Electrolyte Components on a Coated Si Anode of Lithium-Ion Batteries," *J. Phys. Chem. Lett.*, 8, 3404-3408, (2017).

5. Feng Hao, Zhixiao Liu, Perla B. Balbuena, and Partha P. Mukherjee, "Mesoscale Elucidation of Solid Electrolyte Interphase Layer Formation in Li-ion Battery Anode," *J. Phys. Chem. C*, in press.

6. Luis E. Camacho Forero and Perla B. Balbuena, "Elucidating Electrolyte Decomposition under Electron-Rich Environments at the Lithium-Metal Anode," *Phys. Chem. Chem. Phys.*, in press.

II.H.9　Engineering Approaches to Dendrite Free Lithium Anodes (U of Pittsburgh)

Dr. Prashant N. Kumta, Principal Investigator
University of Pittsburgh
815C Benedum Hall
3700 O'Hara Street
Pittsburgh, PA 15261
Phone: 412-648-0223
E-mail: pkumta@pitt.edu

Dr. Moni K. Datta, Co-Principal Investigator
University of Pittsburgh
815C Benedum Hall
3700 O'Hara Street
Pittsburgh, PA 15261
Phone: 412-648-0223 Fax: 412-624-3699
E-mail: mkd16@pitt.edu

Dr. Oleg I. Velikokhatnyi, Co-Principal Investigator
University of Pittsburgh
815C Benedum Hall
3700 O'Hara Street
Pittsburgh, PA 15261
Phone: 412-648-0223
E-mail: olv3@pitt.edu

Tien Duong, Technology Manager
U.S. Department of Energy
Phone: 202-586-7836
E-mail: Tien.Duong@ee.doe.gov

Start Date: October 1, 2016　　　　End Date: September 30, 2019
Total Project Cost: $1,562,500　　　DOE share: $1,250,000　　　Non-DOE share: $312,500

Project Introduction

Dendrite formation in electrochemical systems occurs due to inhomogeneous current densities coupled with local diffusion gradients, surface roughness, and kinetic roughening. However, Li dendrite formation and growth are not well-understood. Adding to the complexity is the formation of the solid-electrolyte interphase (SEI). Control and elimination of Li metal dendrite formation is a veritable challenge and, if overcome, would render the universal adoption of lithium anode batteries (LAB) for stationary and mobile applications. The current project is a scientific study of novel approaches to address dendrite formation in LABs, electrolyte decomposition, and associated cell-failure. Development of dendrite free high-performance Li anodes will enable the use of Li-free cathodes opening up a myriad of possibilities pushing the envelope in terms of cathode capacity and battery energy density.

Objectives

This project will yield lithium metal anodes with specific capacity $\geq$2000 mAh/g ($\geq$10 mAh/cm^2), ~1000 cycles, coulombic efficiency loss $\leq$ 0.01%, coulombic efficiency: $\geq$99.99% with superior rate capability. The goal is to systematically characterize the different approaches for generation of dendrite-free Li-metal anodes while also providing an understanding of the scientific underpinnings, and evaluate the microstructure and electrochemical performance of the dendrite free Li metal anodes. Generation of high performance dendrite

free Li metal anodes will successfully demonstrate generation of novel sulfur cathodes affording the fabrication of Li-S batteries meeting the targeted gravimetric energy densities ≥ 350 Wh/kg and ≥ 750Wh/l with a cost target \$125/kWh and cycle life of atleast 1000 cycles for meeting the *EV everywhere* blueprint.

Approach

This is a multi-year project comprised of three major phases to be successfully completed in three years.

- Phase – 1 (Year 1): Synthesis, characterization and scale up of suitable porous metal foams (PMFs) for use as current collectors for lithium anodes and Li-ion conductor (LIC) materials to prepare multilayer porous foams (MPFs).

- Phase – 2 (Year 2): Development of Li-rich structurally isomorphous alloy (SIA) anodes and Generation of composite multilayer anodes (CMAs).

- Phase-3 (Year 3): Advanced high energy density, high rate, extremely cycleable cell development.

The project will involve collaboration with Dr. Moni Kanchan Datta (UPitt) and Dr. Oleg I. Velikokhatnyi (UPitt) as Co-PIs. In addition, collaborations will be undertaken and continued with Dr. D. Krishnan Achary (UPitt) for solid-state nuclear magnetic resonance (MAS-NMR) characterization.

Results

Phase – 1 of the current project was aimed at the development of porous foam materials and multilayer porous foam materials with the aim of reducing orthogonal lithium nucleation and growth. Work in Q1 and Q2 of this project involved the use of electrochemically prepared foams. Figure II-509 shows attempts at the use of this innovative architecture to inhibit the formation of Li-dendrite during cycling (i.e., porous metal foams (PMFs) as novel dendrite resistant electrodes). Electrochemically made porous metal foams were prepared with varying amounts of hierarchical porosity/wall roughness. Figure II-510 shows the effect of using structurally isomorphous alloys (SIA) as electrodes for lithium metal plating/de-plating. It can be seen in Figure II-510a that upon cycling lithium metal on a copper current collector (cyclic voltammetry), most of the lithium is consumed via dendrite formation and solid electrolyte interphase (SEI) occurrence. On the other hand, it can be seen in Figure II-510b and Figure II-510c that the SIA electrodes exhibit excellent charge retention as well as coulombic efficiency over extended cycling at very high current densities on the order of ~80-100 mA/cm^2.
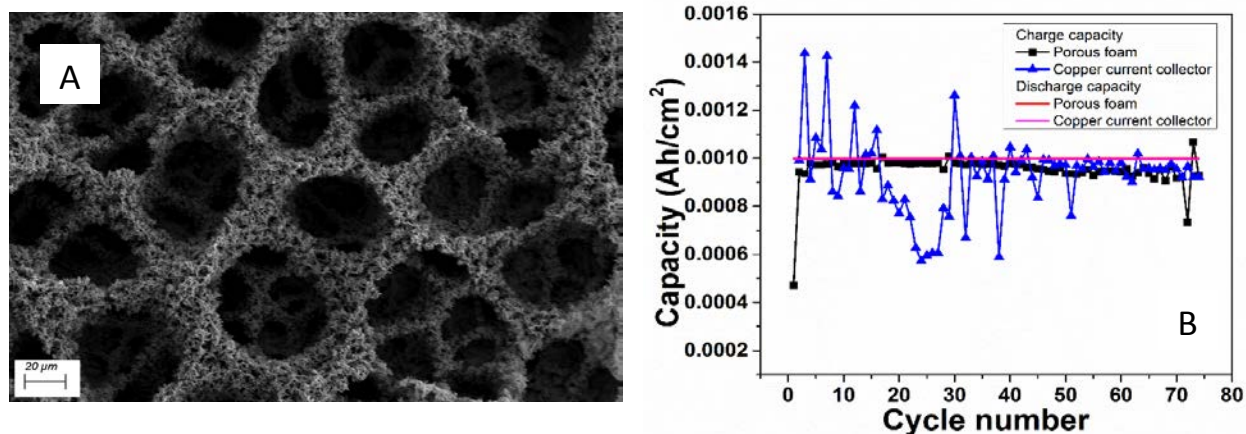
Figure II-509. (a) Electrochemically prepared porous metal foam (PMF). (b) Improvement in coulombic efficiency afforded by use of porous metal foam architecture.
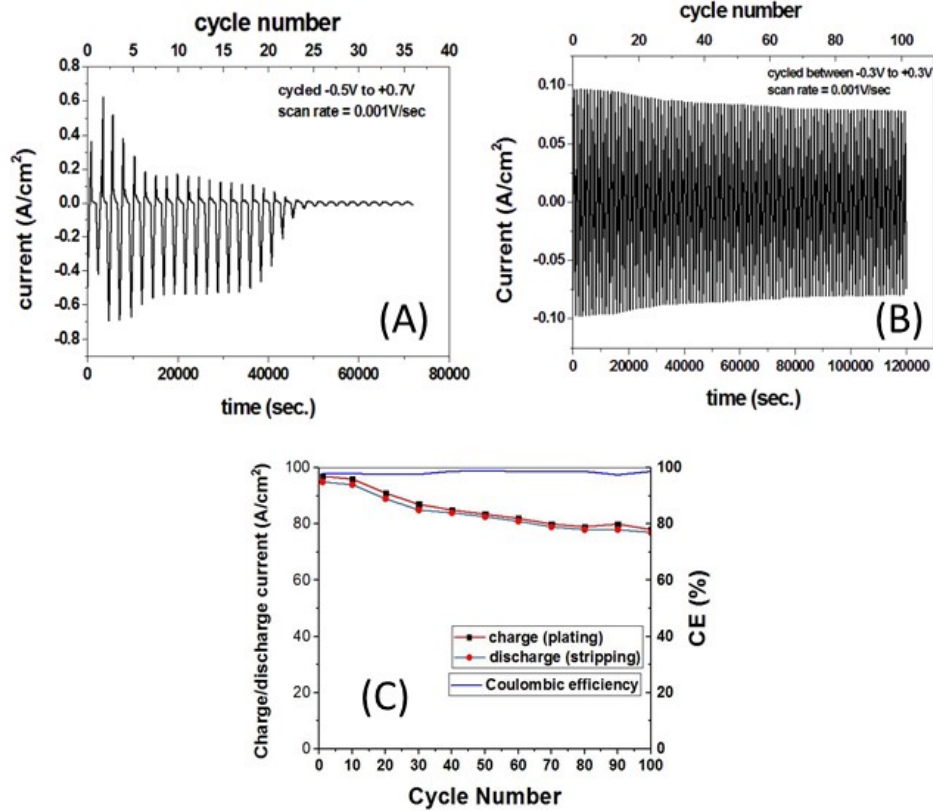
Figure II-510. Current-time profiles of cyclic voltammetry of (a) lithium-copper current collector cell (b) lithium-Li-SIA cell; (c) Coulombic efficiency of Li-SIA cell showing stability thereof.

It was, however, observed during post-cycling that the lithium dendrites tend to deposit at the edge of the porous foam materials since the separator contacts the stainless-steel spacer behind the foam structure (Figure II-511a). This issue was partially resolved by applying non-conductive polymeric coatings to the spacer (Figure II-511b).
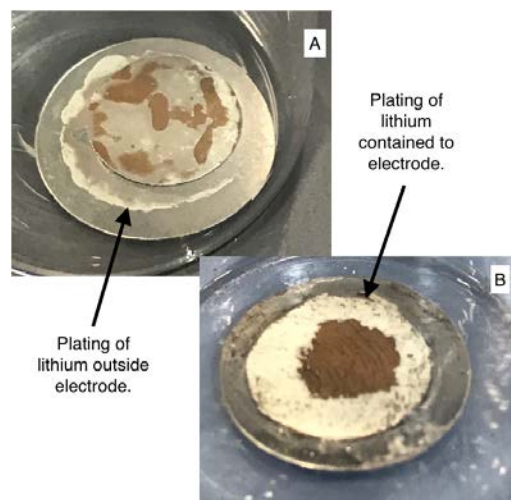
Figure II-511. (a) Formation of lithium on stainless steel spacer in coin cell tests (b) Diffusion pathways causing plating of lithium on polymeric coated stainless-steel spacers.

Figure II-512 demonstrates long-term cycling of 34 mAh/cm^2 at 1.6 mA/cm^2 using the SIA electrodes. Overpotential of $\pm$~30-100 mV is maintained for ~30 cycles with visible instabilities observed in the 30-60 cycles after which the overpotential is stabilized in the range of ~$\pm$ 12-15 mV for over 120 cycles. The intermediate instability region is possibly due to phase segregation and compositional inhomogeneity as observed in Figure II-512.
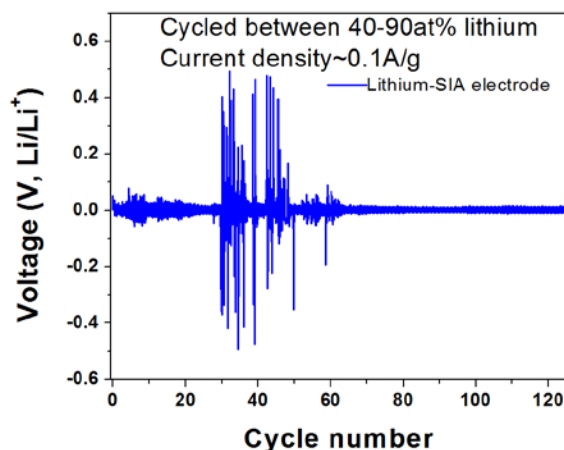
Figure II-512. SIA electrodes demonstrate long-term stability though there is a rise in overpotential due to possible phase segregation.

1. Powders are mixed together for desired porosity.

2. Powders are pellet pressed at 1.3 metric tons.

3. Pellet is sintered in tube furnace under argon (750°C for 3 hrs).

4. Sintered pellets are washed to remove template (often discoloration of the surface occurs while drying).

5. Pellets are heat treated in 6.5% H$_2$/Balance Argon to remove the oxide layer.

Dendritic Cu Powder (<45µm)

Precipitated Template (~10-20µm)

Figure II-513. Preparation method for Gen-2 porous metal foams.

Following Q1 and Q2, research migrated to Gen-2 PMFs with easily controlled porosities of up to 90% generated using the sacrificial template approach outlined in Figure II-513. Figure II-514a shows the SEM image of the Gen-2 PMFs after sintering and removal of the sacrificial template. A continuous network of pores (porosity ~85%) is observed. Figure II-514b shows the cycling efficiency of Li plating and deplating on Gen-2 Cu foams at a current density of 1 mA/cm^2 for 1 h with a deplating cutoff voltage of 1V in 1.8 M LiTFSI, 0.1 M LiNO$_3$ in DOL:DME (50:50 vol.) electrolyte. The Cu foams demonstrate stable cycling to 60 cycles with a columbic efficiency of ~90% after which they transition into a region of constant fade similar to Li plating/deplating seen on the Cu foil. This transition from stable cycling to constant fade is attributed to

transition of the globular Li plating morphology within the porous architecture to a columnar morphology forming on the foam surface. Figure II-515a shows the cross section of the cycled foam electrodes. Figure II-515b and Figure II-515c show different deposition morphologies in each region attributed to competitive SEI layer formation.
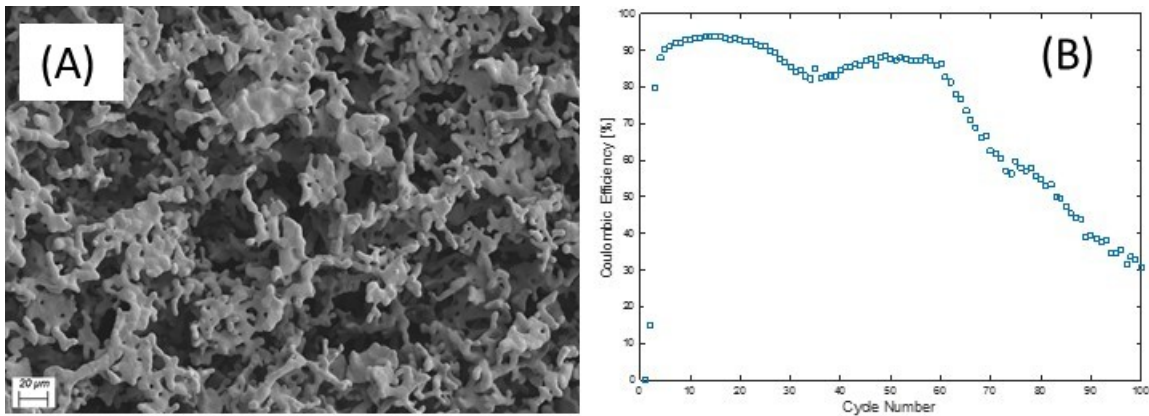
Figure II-514. (a) SEM image of the high porosity (~85%) Cu foams after sintering and removal of the sacrificial template. (b) Gen-2 Cu Foam electrodes demonstrate stable cycling region of 60 cycles at ~90% coulombic efficiency.
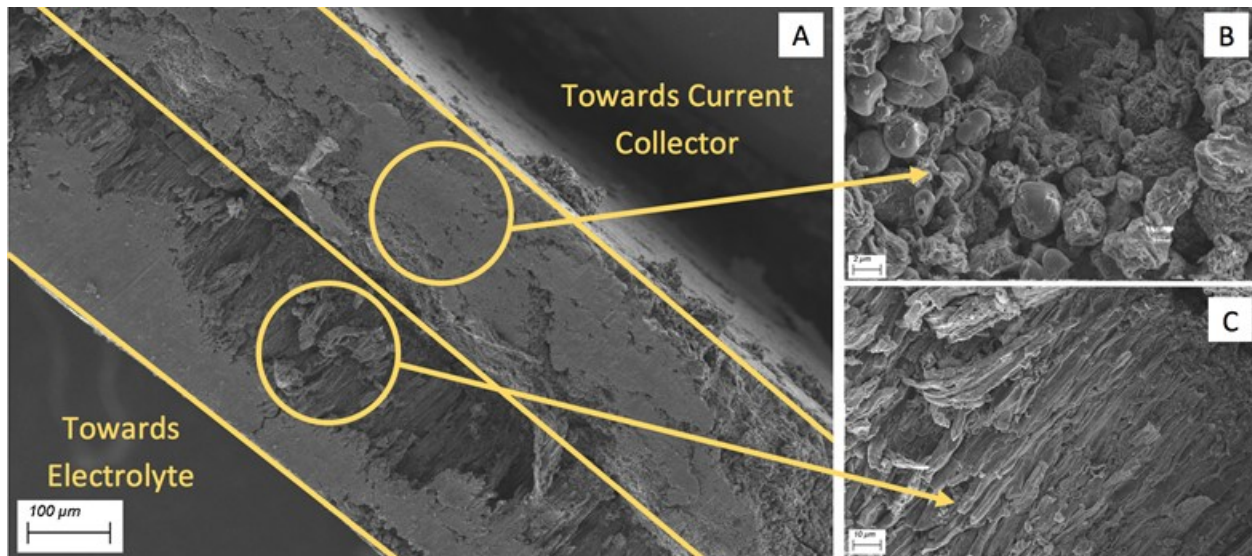
Figure II-515. SEM images of the porous Cu foam electrodes after cycling (~200 cycles). (A) Cross-section view, (B) Close up of lithium deposited within the foam structure, and (C) Close up of lithium deposited on top of the foam surface following pore closure by competitive SEI formation in the foam structure.

The most recent work of this project has involved attempts at controlling the formation of the SEI layer and limiting growth during extended cycling. Unfortunately, increasing the thickness of the PMFs offered only minimal increase in the number of achievable stable cycles, with almost no difference being shown when increasing from 80mg of active material to 120mg of active material. Work is currently being performed on surface modification of the porous metal foams through the use of additives to address this same problem. Initial unoptimized studies have already yielded promising results, increasing the coulombic efficiency from 95% to 99% and the number of stable cycles from ~60 cycles to ~100 cycles.

Conclusions

Phase – 1 of the current project was successful in developing porous metal foam architectures capable of eliminating dendrite formation during cycling of lithium metal. Additionally, important modifications were made to the coin cells in order to ensure accurate testing of the studied anodes. Future work is needed to further examine the role of SEI formation on cycling stability and capacity loss. Early work has already demonstrated the ability of surface additives to control initial SEI formation and slow additional growth, resulting in extended stability. Phase – 2 of the current project will continue to examine ways of addressing this problem in the porous metal foam electrodes, in addition to possible modifications to the Li-rich structurally isomorphous alloy electrodes.

Key Publications

1. Jampani, P.H.; Shanthi, P.M.; Day, B.A.; Gattu, B.; Velikokhatnyi, O.I.; Datta, M.K.; Kumta, P.N. Lithium Metal Anode based Rechargeable Batteries: Recent Advances and Challenges for the Future, Progress in Materials Science (2017) (under review)

2. Shanthi, P.M.; Jampani, P.H.; Gattu, B.; Velikokhatnyi, O.I.; Kumta, P.N. Doped Lithium Orthosilicates - Promising High Rate Lithium-Ion Conductors for Li-S Batteries, The Electrochemical Society (Fall 2016), Honolulu, HI

3. Jampani, P.H.; Gattu, B.; Datta, M.K.; Shanthi, P.M.; Kumta, P.N. Engineering Approaches to Dendrite Prevention in Lithium Anode Based Batteries, The Electrochemical Society (Fall 2016), Honolulu, HI

4. Day, B.A.; Gattu, B.; Jampani, P. H.; Shanthi, P.M.; Datta, M.K.; Kumta, P.N., Engineered Porous Foam Electrodes - New Approaches to Dendrite-Free Anodes for Li-Metal Batteries, The Electrochemical Society (Fall 2017), National Harbor, MD

II.H.10 Solid-State Inorganic Nanofiber Network-Polymer Composite Electrolytes for Lithium Batteries (WVU)

Nianqiang Wu, Principal Investigator
Department of Mechanical & Aerospace Engineering
West Virginia University
P.O. Box 6106
Morgantown, WV 26506
Phone: 304-293-3326
E-mail: nick.wu@mail.wvu.edu

Tien Duong, Technology Manager
U.S. Department of Energy
Phone: 202-586-7836
E-mail: Tien.Duong@ee.doe.gov

Start Date: October 1, 2016　　　　End Date: September 30, 2019
Total Project Cost: $1,400,193　　　DOE share: $1,244,012　　　Non-DOE share: $156,181

Project Introduction

Safety concerns regarding commercial lithium batteries are ever growing due to the use of highly volatile and flammable organic solvent-based electrolytes. In addition, the energy density and the long-term durability need to be further improved. Batteries comprising solid-state electrolytes have drawn significant attention because of their enhanced safety features. Some of ceramic electrolytes have been found to have Li-ion conductivity comparable to liquid electrolytes. However, ceramic electrolytes require high temperature for sintering, and exhibit high interfacial charge transfer resistance due to poor electrolyte-electrode contact. In particular, brittle and rigid bulk ceramic electrolytes make it difficult to have intimate contact with electrodes in all-solid-state batteries. In contrast, solid-state polymer electrolytes are highly flexible to fit in any battery shape besides the improved safety and stability features. However, the ionic conductivities of the polymer electrolytes are generally significantly lower than those of liquid electrolytes. To increase the ionic conductivity of solid polymer electrolytes, several methods have been reported such as increasing the content of lithium salt in the electrolyte structure and introducing low-molecular-weight liquid plasticizers into the polymer matrix. Although these methods can enhance the ionic conductivity, they reduce the mechanical strength and stability of polymer electrolytes. On the other hand, researchers have reported that the integration of nanoscale inorganic fillers into polymer electrolytes not only enhances the ionic conductivity but also improves the mechanical strength and stability of the solid-state polymer electrolytes.

Objectives

The objective of this project is to develop the solid-state electrolytes based on the highly-conductive inorganic nanofibrous network in the polymer matrix for lithium batteries. Specifically, the project will develop the inorganic nanofiber-polymer composite electrolytes with $>8\times10^{-4}$ S/cm of ionic conductivity, which also have good mechanical, thermal and electrochemical stability (with decomposition voltage higher than 4.5 V versus elemental Li). The lithium metal batteries with the developed composite electrolytes will achieve ≥ 350 Wh/kg (≥ 750 Wh/L) of specific energy, ≥ 800 W/kg of specific discharge pulse power, and $\geq 1,000$ cycles of life-time. The proposed lithium-sulfur batteries with the composite electrolytes will achieve ≥ 500 Wh/kg of specific energy, ≥ 850 W/kg of specific discharge pulse power, and $\geq 1,000$ cycles of life-time.

Approach

Integration of the highly Li$^+$-conductive inorganic nanofiber network into the polymer matrix not only provides the continuous Li$^+$ transport channels but also kinetically inhibits the crystallization from the

amorphous state of polymer electrolyte. The inorganic nanofibers will be fabricated with electrospinning technique. The ionic conductivity of inorganic nanofibers will be improved by chemical substitution or doping. Highly ionic-conductive polymers will be developed by cross-linking and/or creation of a block-copolymer structure. The composition and microstructure of the composite electrolyte will be designed to suppress the lithium dendrite formation.

This project funds work at West Virginia University (WVU) and North Carolina State University (NCSU). Dr. Nianqiang (Nick) Wu at WVU serves as PI; and Dr. Xiangwu Zhang at NCSU acts as Co-PI. Sujan Kasani (Ph.D. student at WVU), Hui Yang (Postdoctoral Fellow at WVU), Botong Liu (Ph.D. student at WVU), Chaoyi Yan (Ph.D. student at NCSU) and Mahmut Dirican (Postdoctoral Fellow at NCSU) contributed to the project.

Results

Task 1.1.2 - Synthesis of inorganic nanofibers

Perovskite-type lithium lanthanum titanate $Li_{0.33}La_{0.56}TiO_3$ (LLTO) and Garnet-type lithium lanthanum aluminum zirconium oxide $Li_{6.4}La_3Al_{0.2}Zr_2O_{12}$ (LLAZO) nanofibers were successfully fabricated by electrospinning. The ionic conductivity of inorganic LLTO nanofibers was improved from 7.7×10^{-4} S/cm to 1.08×10^{-3} S/cm through 0.5% aluminum doping. The theoretical calculation has demonstrated that the aluminum doping reduces the transporting barrier of Li atom the LLTO lattice, transporting barrier for pure, single-Al and double-Al decorated structure are 0.365 eV, 0.165 eV and 0.225 eV, respectively.

(1) Lithium lanthanum zirconium oxide (LLZO) nanofibers

Highly ionic-conductive $Li_{6.4}La_3A_{0.2}Zr_2O_{12}$ (LLAZO) nanofibers with average fiber diameter of around 300 nm were successfully obtained after calcination of electrospun LLAZO precursor nanofibers. X-ray diffraction patterns of LLAZO nanofibers indicated that pure cubic LLAZO phase was achieved.

(2) Lithium lanthanum titanate (LLTO) nanofibers

Perovskite-type lithium lanthanum titanate $Li_{0.33}La_{0.56}TiO_3$ (LLTO) nanofibers were successfully synthesized by the electrospinning technique. The LLTO pellet exhibited an ionic conductivity of 7.7×10^{-4} S/cm. A narrow concentration range of Ti^{4+} substitution by Al^{3+} was carried out to enhance the ionic conductivity of the LLTO nanofibers, which would change the bond strength between the B-site cation and the oxygen, thus influence the conductivity. We have doped the LLTO nanofibers with different percentage (0.5%~10%) of aluminum. The experimental results show that 0.5% aluminum doped $Li_{0.33}La_{0.56}Al_{0.005}Ti_{0.995}O_3$ (LLATO) nanofibers (Figure II-516) exhibited the highest ionic conductivity of 1.08×10^{-3} S/cm.

To study the transporting behavior of Li atoms in pure and Al-decorated $Li_{0.33}La_{0.56}TiO_3$ structures, we constructed La-full and La-deficient layers along stuck direction in Figure II-517. Figure II-517d gives the ideal transporting direction to simplify the research. The calculation results show transporting barrier for pure, single-Al and double-Al decorated structure were 0.365 eV, 0.165 eV and 0.225 eV, respectively. This tendency was consistent with experiments. To explain this behavior, we analyzed the Bader charge of those structures. Before Li atom transporting across the door, we found that the charge value on O atoms in the door had the sequence as "double-Al > single-Al > pure structure", which indicated that Coulomb potential between Li with O atoms became stronger as more Ti atoms were doped by Al. However, when two Ti atoms were doped by Al atoms, the Coulomb potential was too strong so that the most stable site for Li changed to the door not in the cubic center (in Figure II-517e). To obtain higher mobility for Li atoms in $Li_{0.33}La_{0.56}TiO_3$ structure, the Coulomb potential between Li atom O atoms must be controlled reasonably.
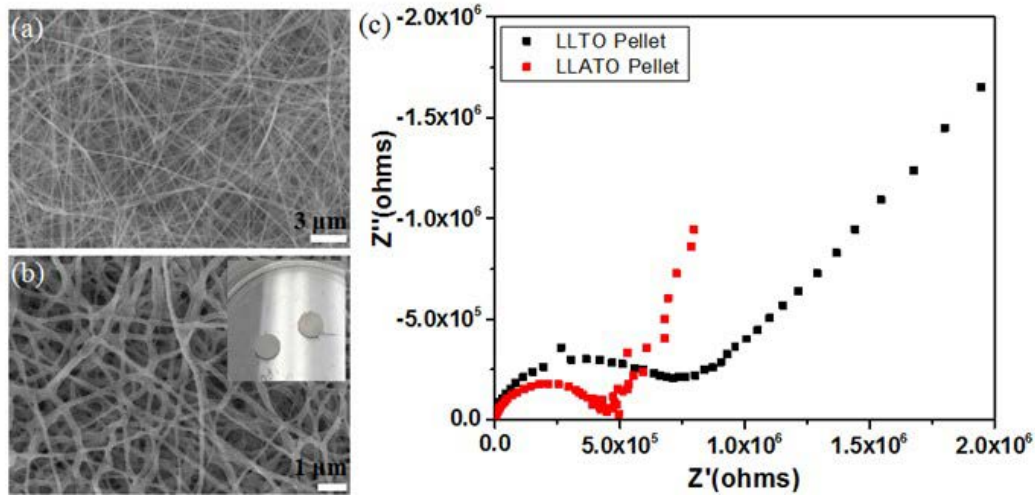
Figure II-516. (a) SEM image of the as-electrospun LLATO nanofiber network. (b) SEM image of the perovskite LLATO nanofibers (the insert is the photograph of the LLATO pellet). (c) Electrochemical impedance spectroscopy (EIS) plot of the LLTO and LLATO pellet.
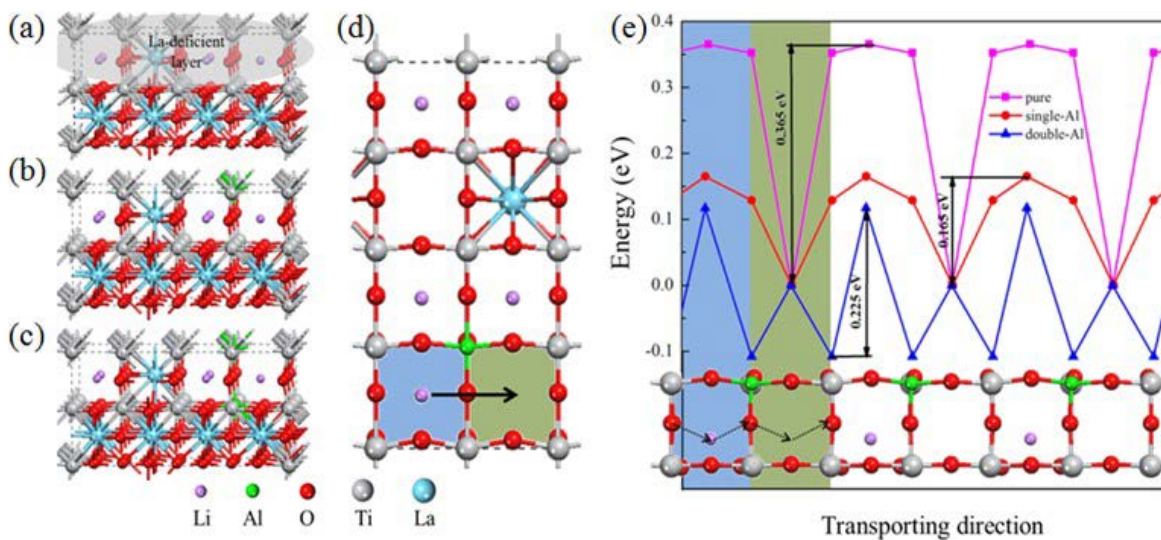
Figure II-517. Pure and Al-decorated $Li_{0.33}La_{0.56}TiO_3$ structures. (a), (b) and (c) are side views of pure, most stable single-Al and double-Al decorated $Li_{0.33}La_{0.56}TiO_3$, respectively. (d) the top view of La-deficient layer of (b). Blue and green color blocks in (d) are used to represent two different regions in Li atom transporting direction. (e) Transporting barriers for Li atoms along transporting direction in pure, single-Al and double-Al decorated $Li_{0.33}La_{0.56}TiO_3$ structure. The transporting trajectory is marked by dash line in the inset.

Task 1.2.2 - Synthesis of polymer matrix

Three kinds of poly(ethylene oxide) (PEO)-based polymers, including cross-linked, block co-polymer, combination of block co-polymer formation and cross-linking, were fabricated. Cross-linking can effectively reduce the crystallinity of the PEO, leading to an increase in the content of amorphous phase in the PEO, which can improve the ionic conductivity. The cross-linked PE/PEO polymer plasticized with poly(ethylene glycol) PEG reached the ionic conductivity of 1.65×10^{-4} S cm^{-1} at room temperature. Single-ion conductor triblock copolymer was synthesized.

(1) Cross-linked PE/PEO polymer with lithium salt

Cross-linked polyethylene/poly (ethylene oxide) (PE/PEO) polymers were synthesized by free radical polymerization as shown in Figure II-518. The cross-linked polymer with concentration of lithium salt [EO]/[Li$^+$] = 24 showed the highest ionic conductivity of 1.15×10^{-4} S cm^{-1} at room temperature. Introducing poly (ethylene glycol) PEG into the cross-linked polymer reduced the glass transition temperature of the cross-linked polymer, and also increased the ionic conductivity; higher ionic conductivity was resulted with higher PEG content. Ionic conductivity of 40 wt% (monomer amount) PEG plasticized polymer reached 1.65×10^{-4} S cm^{-1} at room temperature.
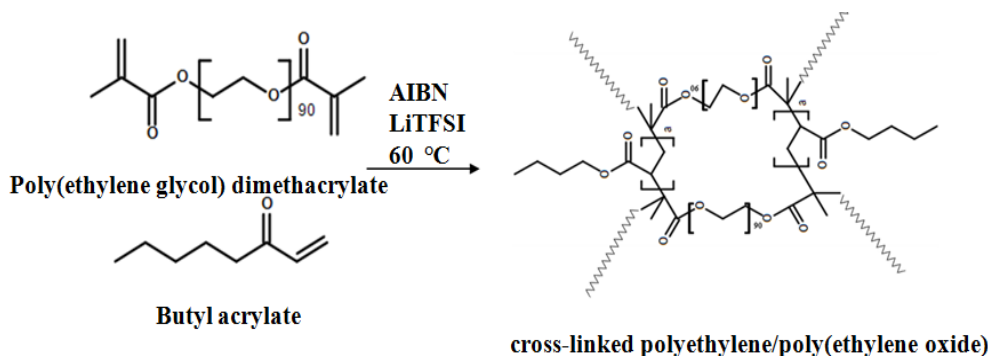

Figure II-518. Synthesis procedure of PE/PEO cross-linked polymer.

(2) Li[PSTFSI-b-MPEGA-b-PSTFSI] triblock copolymer

Triblock copolymer Li[PSTFSI-b-MPEGA-b-PSTFSI] block copolymer with different feed EO/Li$^+$ ratio of 32, 24 and 16 were synthesized using (4-styrenesulfonyl) (trifluoromethanesulfonyl)imide (STFSI) and methoxy-polyethylene glycol acrylate (MPEGA) monomers through free radical polymerization and nitroxide-mediated polymerization (NMP), exhibiting the ionic conductivity of 1.16×10^{-5} S/cm, 3.30×10^{-5} S/cm, 8.90×10^{-6} S/cm, respectively.

(3) Lithium block cross-linked PE/PEO polymer

Monomer (4-styrenesulfonyl) (trifluoromethanesulfonyl)imide (STFSI) was introduced to the cross-linked polyethylene/poly(ethylene oxide) (PE/PEO) polymers, which were synthesized using butyl acrylate (BA) as the PE monomer and poly(ethylene glycol) dimethacrylate (PEGDMA) as the cross-linker. The ionic conductivity of lithium block cross-linked polymer was in order of 10^{-6} S/cm. Increasing the lithium monomer ratio reduced the ionic conductivity. The ionic conductivity was estimated to be 7.68×10^{-6} S/cm, 3.94×10^{-6} S/cm, 1.88×10^{-6} S/cm with different feed EO/Li$^+$ ratio of 32, 16 and 8, respectively.

Task 2.1 - Development of inorganic nanofibers-polymer composites

The composite electrolytes based on cross-linked polymer and polyvinylidiene fluoride-hexafluoropropylene (PVDF-HFP) were fabricated and tested. The mobility and the concentration of free Li$^+$ played important roles in the ionic conductivity of solid electrolytes, which were affected by the interaction between lithium ions and the polymer. Coating a thin layer of lithium phosphate on the surface of the LLATO nanofibers enhanced the lithium ion concentration of the surface of the nanofibers. Also, better wettablity of the nanofiber with the PVDF-HFP/LiTFSI composite would facilitate the transport of the lithium ions.

(1) Inorganic nanofibers/cross-linked polymers with 40 wt% (monomer content) PEG plasticizer

Incorporating the LLTO nanofibers into the cross-linked polymer (CLP) with 40 wt% (monomer content) PEG plasticizer resulted in the ionic conductivity of 4.72×10^{-4} S/cm. The ionic conductivity of 15 wt% LLAZO nanofiber dispersed cross-linked polymer (CLP) with 40 wt% (monomer content) PEG plasticizer composite electrolytes can reach up to 3.46×10^{-4} S/cm of ionic conductivity at room temperature.

(2) Inorganic nanofibers/ polyvinylidiene fluoride-hexafluoropropylene (PVDF-HFP) / Li salt

We have fabricated the composite electrolyte with the Al-doped perovskite-type $(Li_{0.33}La_{0.557})_{1.005}Ti_{0.995}Al_{0.005}O_3$ (LLATO) nanofibers in the PVDF-HFP/LiTFSI the matrix. The surface of LLATO nanofibers were further modified with lithium phosphate, which not only helped form a fully continuous lithium-ion–conducting network but also improved the lithium ion mobility at the LLATO nanofiber grain boundaries by compensating the serious Li_2O evaporation. The ionic conductivity of PVDF-HFP/LiTFSI/LLATO/Li_3PO_4 reached 5.1×10^{-4} S/cm, leading to improvement in the ionic conductivity by 26.9% as compared to the unmodified PVDF-HFP/LiTFSI/LLATO. (See Figure II-519.)
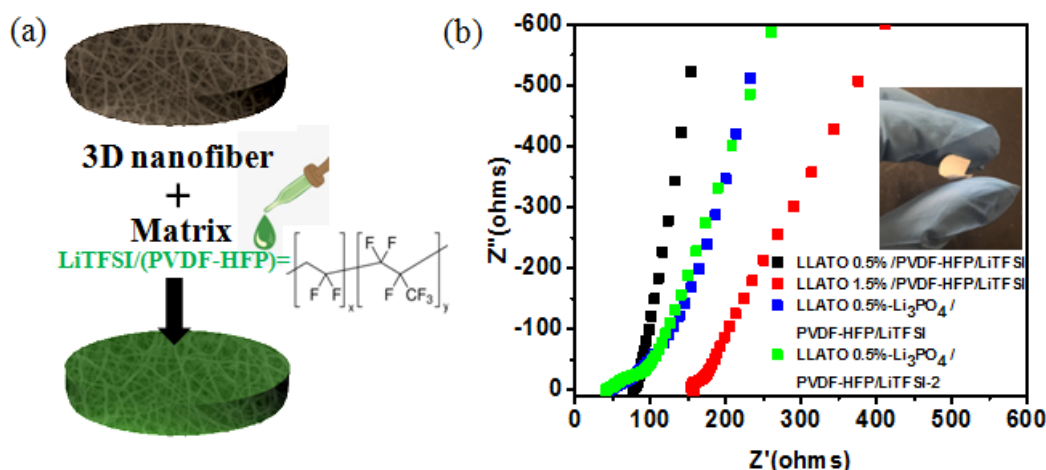

Figure II-519. (a) Schematic illustration of the fabrication procedure for the lithium-ion–conducting membrane. (b) EIS profiles of the PVDF-HFP/LiTFSI/LLATO and the PVDF-HFP/LiTFSI/LLATO/Li_3PO_4 electrolyte membranes.

Conclusions

We have synthesized and tested the proposed inorganic nanofibers and polymer matrix in Year 1, including the perovskite-type lithium lanthanum titanate $Li_{0.33}La_{0.56}TiO_3$ (LLTO) and Garnet-type lithium lanthanum aluminum zirconium oxide $Li_{6.4}La_3Al_{0.2}Zr_2O_{12}$ (LLAZO) nanofibers and three types of polymers. The ionic conductivity of the inorganic LLTO nanofibers improved from 7.7×10^{-4} S/cm to 1.08×10^{-3} S/cm by 0.5% aluminum doping. For the polymer matrix, the random copolymer Li[PSTFSI-co-MPEGA] and the [PSTFSI-b-MPEGA-b-PSTFSI] triblock copolymer, the cross-linked PE/PEO polymer and the lithium block cross-linked PE/PEO polymer were synthesized. The ionic conductivity of PE/PEO cross-linked polymer reached 1.65×10^{-4} S/cm at room temperature. A bare polymer electrolyte polyvinylidiene fluoride-hexafluoropropylene (PVDF-HFP)/LiTFSI was fabricated, achieving the ionic conductivity of 2.36×10^{-4} S/cm at room temperature.

We have fabricated and investigated the ionic conductivity of composite electrolyte based on the cross-linked polymer and the PVDF-HFP. The ionic conductivity of the LLTO nanofiber-cross linked polymer (CLP) with 40 wt% PEG plasticizer reached 4.72×10^{-4} S/cm. The ionic conductivity of PVDF-HFP/LiTFSI/LLATO/Li_3PO_4 reached 5.1×10^{-4} S/cm after surface modification of LLATO nanofibers with Li_3PO_4.

Key Publications

1. P. Zhu, C. Yan, M. Dirican, J. Zhu, J. Zang, R. K. Selvan, C-C. Chung, H. Jia, Y. Li, Y. Kiyak, N. Wu, X. Zhang, $Li_{0.33}La_{0.557}TiO_3$ ceramic nanofiber fillers enhanced PEO-based composite polymer electrolyte for all-solid-state lithium batteries, Submitted Manuscript, Journal of Materials Chemistry A (under revision).

2. H. Yang, B. T. Liu, X. W. Zhang, N. Q. Wu, Three-Dimensional Cross-Linked Inorganic/organic Composite Solid Electrolyte for Lithium Batteries, to be submitted to Energy Environ Sci.

II.H.11 Electrochemically Responsive Self-Formed Li-ion Conductors for High Performance Li Metal Anodes (Penn State U)

Donghai Wang, Principal Investigator
The Pennsylvania State University
134 Energy and the Environment Lab Building
University Park, PA 16802
Phone: 814-863-1287
E-mail: dwang@psu.edu

Tien Duong, Technology Manager
U.S. Department of Energy
Phone: 202-586-7836
E-mail: Tien.Duong@ee.doe.gov

Project Introduction

The project will develop and optimize organo-Li_xS_y, organo-$Li_xP_yS_z$, and organo-Li_xS_y/organo-$Li_xP_yS_z$ composite materials as protective layers for Li metal anodes in Li-S batteries. The core focus will be on synthesis methods and precursors for new organic/inorganic hybrid Li-ion conductors, protective layer composition, and protective layer fabrication methods. This will be accompanied by property measurement and characterization (conductivity, mechanical properties, etc.) for the protective layer on Li metal, as well as detailed diagnostics and cell testing. At the conclusion of the project, twelve ~300 mAh pouch cells will be delivered which use the optimal protection layer.

Objectives

The objective of this project is to develop and deliver an electrochemically responsive self-formed hybrid Li-ion conductor as a protective layer for Li metal anodes, enabling Li metal anodes to cycle with a high efficiency of ~99.7% at high electrode capacity (>6 mAh/cm^2) and high current density (>2 mA/cm^2) for over 500 cycles. The project will also demonstrate prototype ~300 mAh Li-S battery cells with energy densities of ~200 Wh/kg and ~ 80% capacity retention for ~300 cycles at ~80% depth of discharge (DOD) using Li metal anodes with this protective layer.

Approach

The novel multiphase organo-Li_xS_y or organo-$Li_xP_yS_z$ hybrid ion conductors with tunable multifunctional organic components and controlled Li_xS_y and $Li_xP_yS_z$ inorganic components will be designed and prepared, and thus enable safe use of lithium metal with high Coulombic efficiency. In the first year, the team will develop the organo-Li_xS_y lithium protection layers with tuned functionality: 1) finding appropriate composition and 2) developing proper synthesis and fabrication methods.

Results

For the sulfur cathodes, dimethyl disulfide as a functional co-solvent has been demonstrated to show an alternate electrochemical reaction pathway for sulfur cathodes by the formation of dimethyl polysulfides and lithium organosulfides as intermediates and reduction products. Our studies show that this new path not only provides high capacity but also enables excellent capacity retention through a built-in automatic discharge shutoff mechanism by tuning carbon/sulfur ratio in sulfur cathodes to reduce unfavorable Li_2S formation. Furthermore, this new electrolyte system enables high capacity of high-sulfur-loading cathodes at low electrolyte/sulfur (E/S) ratios. Specifically, a stable specific capacity of around 1000 mAh g^{-1} using a low electrolyte amount (i.e., E/S ratio of 5 mL g^{-1}) and high sulfur-loading (4 mg cm^{-2}) cathodes (Figure II-520).
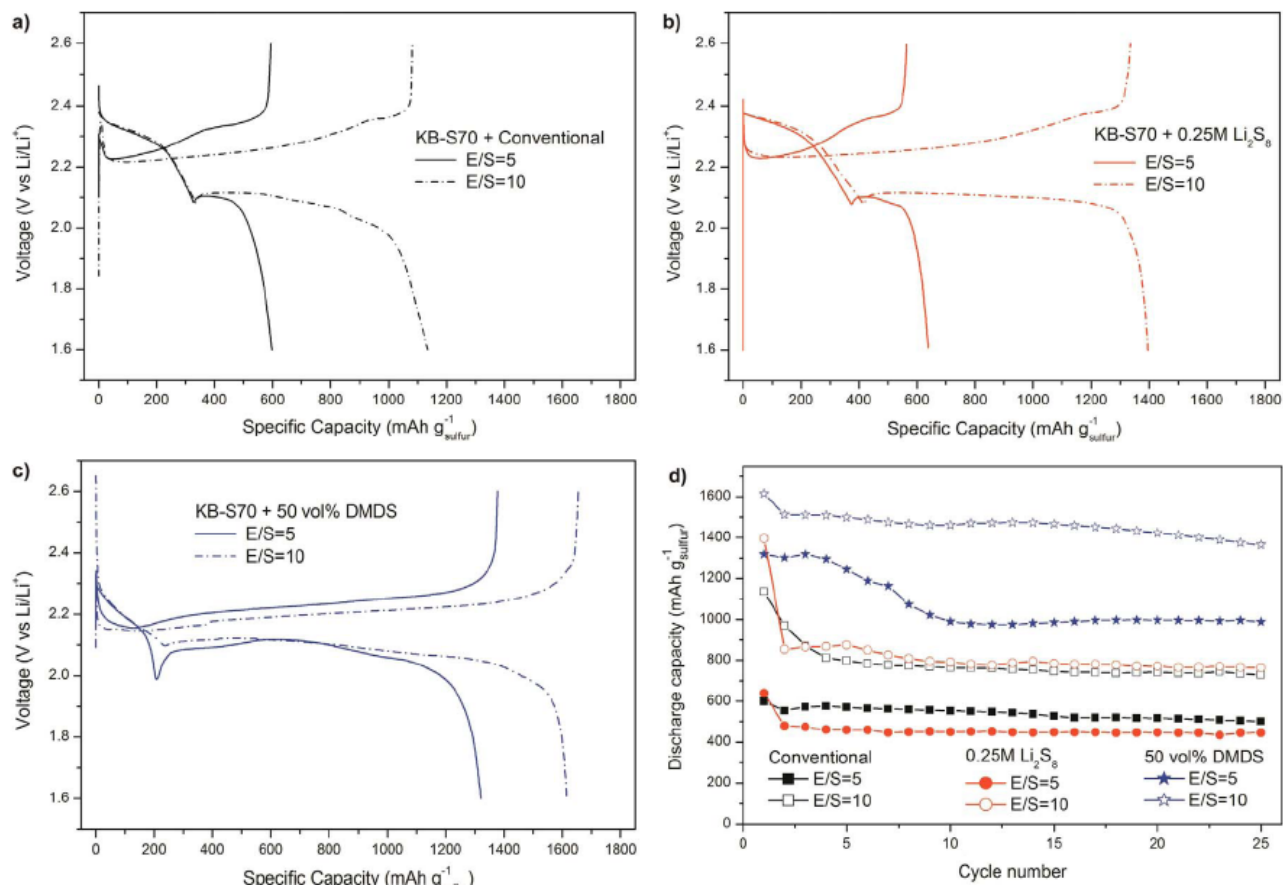
Figure II-520. Initial discharge-charge profiles of KB-S70 cathodes in (a) conventional, (b) 0.25 M polysulfide-containing, and (c) 50 vol% DMDS-containing electrolytes with E/S=5 and 10 mL g^{-1} at a current density of 0.2 mA cm^{-2}, and (d) their corresponding cycling performance. (*Nano Energy*, **2017**, 31, 418.)

Constructing a rechargeable prelithiated graphite/sulfur battery is a feasible strategy to address the issues of polysulfide shuttling and unstable lithium/electrolyte interface. A fluorinated ether of bis(2,2,2-trifluoroethyl) ether (BTFE) was blended with 1,3-dioxolane (DOL) for making a multifunctional electrolyte of 1.0 M LiTFSI DOL/BTFE (1:1, v/v) to enable high performance prelithiated graphite/S batteries. First, the electrolyte significantly reduces polysulfide solubility to suppress the deleterious polysulfide shuttling and thus improves capacity retention of sulfur cathodes. Second, thanks to the low viscosity and good wettability, the fluorinated electrolyte dramatically enhances the reaction kinetics and sulfur utilization of high-areal-loading sulfur cathodes. More importantly, this electrolyte forms a stable solid−electrolyte interphase (SEI) layer on graphite surface and thus enables remarkable cyclability of graphite anodes. By coupling prelithiated graphite anodes with sulfur cathodes with a high areal capacity of ~3 mAh cm^{-2}, we demonstrate prelithiated graphite/sulfur batteries that show high sulfur-specific capacity of ~1000 mAh g^{-1} and an excellent capacity retention of >65% after 450 cycles at C/10 (Figure II-521).
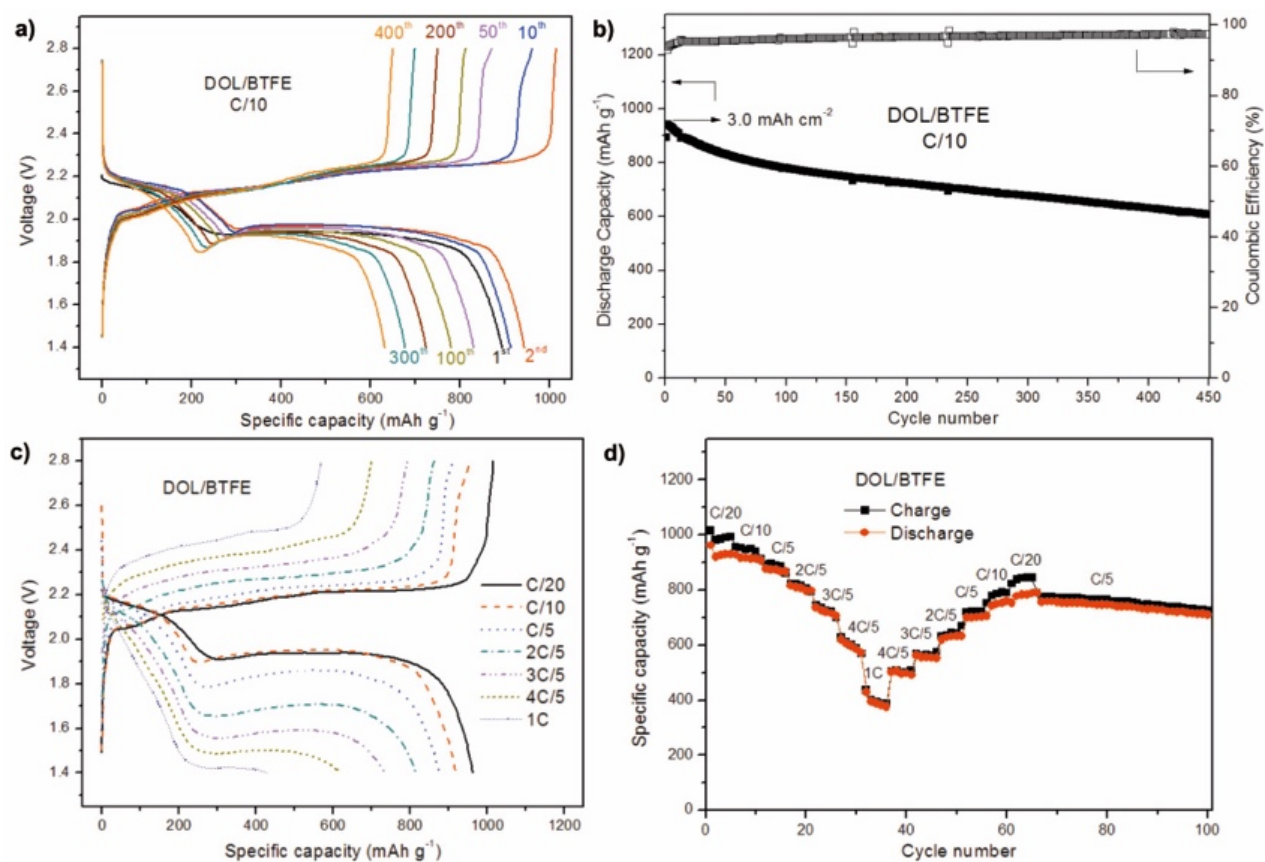
Figure II-521. (a, c) Discharge−charge profiles and (b, d) cycling performance of prelithiated graphite/sulfur full cells at (a, b) C/10 and (c, d) different C rates in the DOL/BTFE electrolyte. (*ACS Appl. Mater. Interfaces*, **2017**, 9, 6959.)

For the protection of the Li metal anode, appropriate compositions for organo-Li_xS_y lithium protection layers have been found. The sulfur-containing polymers (SCPs), which contain the sulfur chains and organic units, are the suitable candidate for the fabrication of organo-Li_xS_y lithium protection layers. The effect of sulfur contents in the SCPs on the cycling performance of Li metal anode was investigated. 2 wt% SCPs were added to the electrolyte, the electrolyte used here was 1 M LiTFSI (lithium bis(trifluoromethanesulfonyl)imide) and 1 wt% $LiNO_3$ in the dioxolane/dimethoxyethane (DOL/DME = 1:1, V/V). As shown in Figure II-522, The SCPs with 90 wt% sulfur exhibited the best cycling performance, and the cycling stability dropped with the decrease of sulfur content in the SCPs.
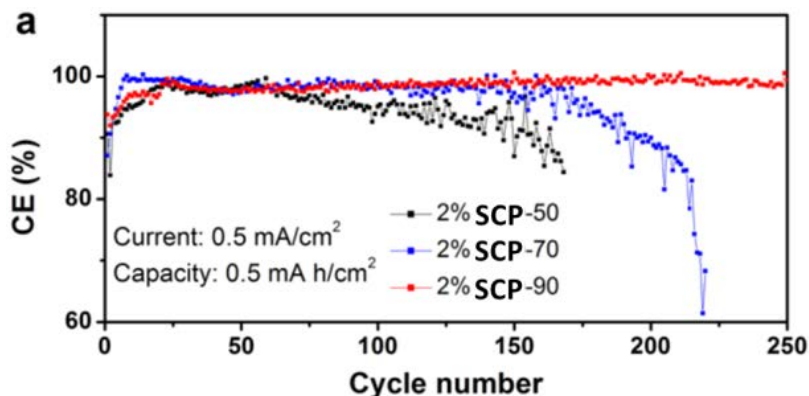
Figure II-522. Cycling performance of 2 wt% SCPs containing different sulfur contents as additives. (a) PSD containing different sulfur contents. (b) PST containing different sulfur contents. (*Nat. Commun.*, **2017**, 8, 850.)

The morphologies of the deposited lithium metal using SCP as additives (Figure II-523) show that dense and dendrite-free lithium film was deposited on the substrate, and the pancake-like lithium film was continuous and uniform. The cross-section view consolidated that the deposited lithium grew very compact and no obvious dendritic lithium was observed in the surface and interior of the lithium film.
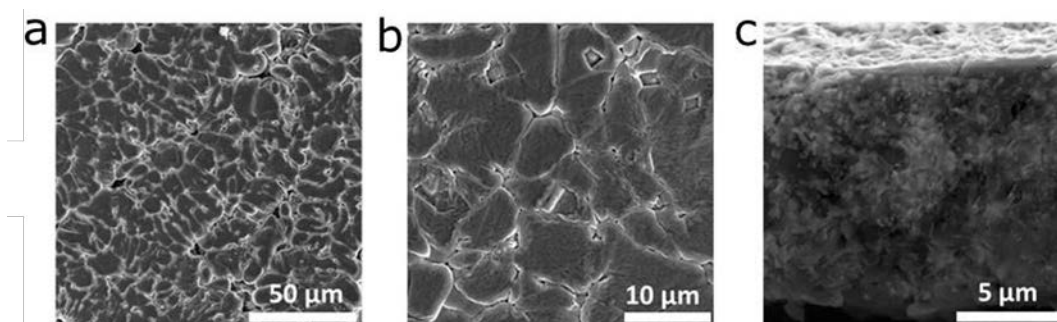
Figure II-523. Morphologies of lithium metal deposited onto stainless steel substrate. SEM images of lithium metal deposited onto bare stainless steel substrate in the electrolyte with the addition of 8 wt% the SCP-90. (*Nat. Commun.*, **2017**, 8, 850.)

The content of SCP-90 as additives in the electrolyte affects the Li plating/stripping cycling performance. Comparing the Li plating/stripping performance of using electrolyte containing 2 wt%, 5 wt%, 8 wt% and 10 wt% of SCP-90, we found that the cycling life is improved with increasing content of SCP-90 additive till reaching 8 wt% (Figure II-524). When the content of SCP-90 in the electrolyte increased to 10 wt%, the cycling life deteriorates. Using SCP-90 as additives, the growth of Li dendrite is effectively suppressed, and uniform and compact deposited Li film was obtained. After 100 cycles at a current density of 2 mA cm^{-2} and a deposition capacity of 2 mAh cm^{-2}, the deposited Li exhibits very smooth and uniform surface and morphological compactness without any growth of Li dendrites (Figure II-525).
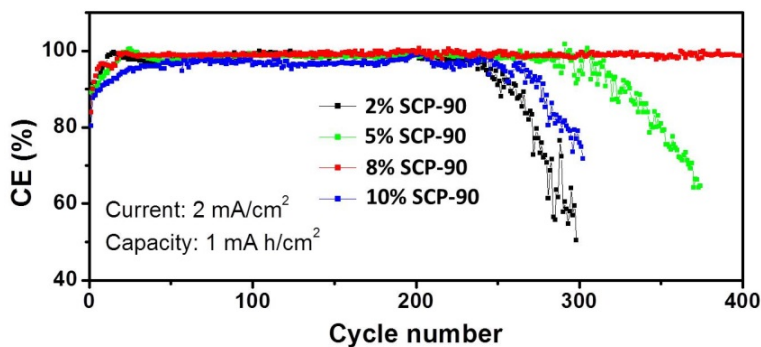
Figure II-524. Cycling performance of cells using electrolytes containing different contents of SCPs. (*Nat. Commun.*, **2017**, 8, 850.)
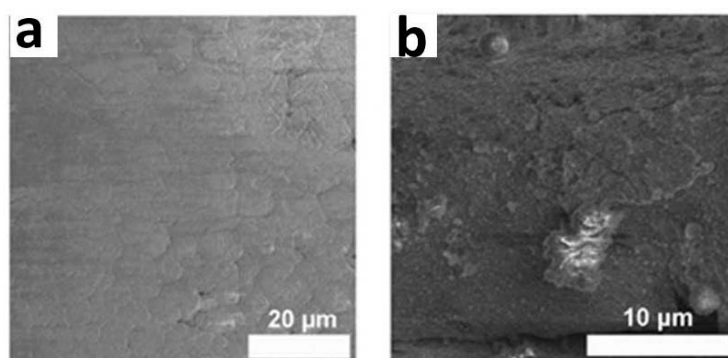
Figure II-525. SEM images of the deposited Li after 100 cycles at a current density of 2 mA cm^{-2} and a deposition capacity of 2 mA h cm^{-2}. (*Nat. Commun.*, **2017**, 8, 850.)

SEI layers formed from electrolyte containing sulfur-containing polymer with 90 wt% sulfur (SCP-90) were characterized. The SEI layers formed from the control electrolyte, the S-Electrolyte and SCP-90-Electrolyte are named C-SEI, S-SEI, SCP-90-SEI, respectively. Morphologically, as shown in the SEM images (Figure II-526), the C-SEI layer shows a porous and loose structure, indicating its continual break during the Li plating/stripping process (Figure II-526a). The S-SEI layer becomes smooth, but cracks are observed (Figure II-526b), which should be ascribed to non-continuous Li_2S/Li_2S_2 phase in the S-SEI layer. In contrast, the as-formed SCP-90-SEI layers show a mostly planar, smooth and uniform layer with no cracks (Figure II-526c).
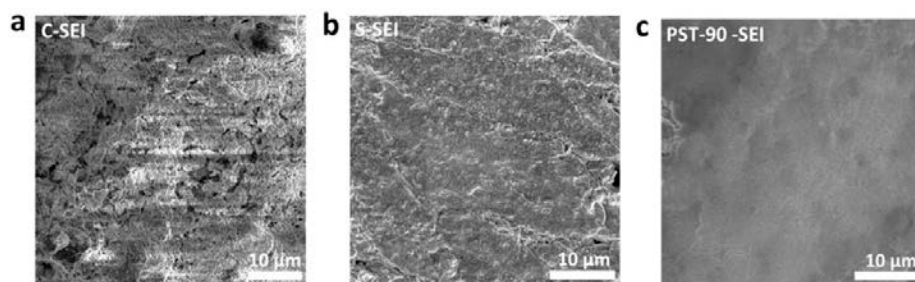
Figure II-526. SEM images of C-SEI layer (a), S-SEI layer (b) and SCP-90-SEI layer (c). (*Nat. Commun.*, **2017**, 8, 850.)

The morphology of SEI layers was further investigated using Atomic Force Microscopy (AFM). Figure II-527 displays topographic images of different SEI layers. The C-SEI layer shows large granular features (Figure II-527a), while small particulates are observed everywhere on the surface of S-SEI layer and cracks are

also observed (Figure II-527b). In contrast, the SCP-90-SEI layers are very smooth and uniform covering, as shown in Figure II-527c. The 3D topographic features observed from AFM results are consistent with the SEM investigation (Figure II-526). Such SEI layers can suppress the growth of Li dendrites and thus prevent further contact of Li with the electrolyte, which could lead to an enhanced CE correspondingly.
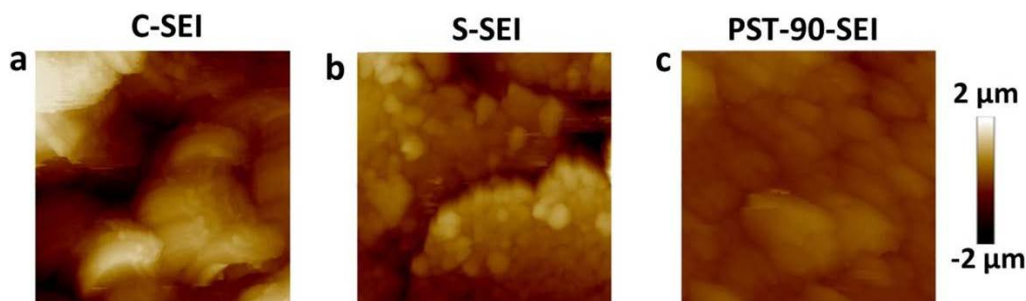
Figure II-527. AFM images (10 × 10 μm² scan size) of the C-SEI layer (a), S-SEI layer (b), and SCP-90-SEI layer (c). (*Nat. Commun.*, **2017**, 8, 850.)

The composition of SEI layer formed from an electrolyte containing sulfur-containing polymer with 90 wt% sulfur (PST-90) was characterized. The SEI layers formed from the control electrolyte, the S-Electrolyte and SCP-90-Electrolyte are named C-SEI, S-SEI, PST-90-SEI, respectively. The S 2p XPS spectra exhibit major difference among these three SEI layers (Figure II-528a). For the S-SEI, the peaks at 160.5 and 161.7 eV reflect the composition of Li2S and Li2S2 in the SEI layer, and the small peak at 163.0 eV is also observed, corresponding to the small amount of Li polysulfides (Li2Sx, such as Li2S3) in the SEI layer. This result demonstrates that the S-SEI layer is mainly composed of inorganic species. For PST-90-SEI layer, besides the peaks at 160.5, 161.7 and 163.0 eV observed in XPS spectra, the additional peak at 162.2 eV corresponding to the S 2p3/2 from organosulfides is observed, confirming the existence of organosulfides (RS_6Li_6) in the SEI layers. The relatively stronger peak at 163.0 eV corresponds to the Li polysulfides (Li_2S_x) and organopolysulfides (RS_xLi_6) which have similar position with Li polysulfides. In the C 1s XPS spectra (Figure II-528b), the peak at ~292.1 eV can be found in the C-SEI and corresponds to the C 1s from the functional group –CF_3, which may originate from the decomposition of LiTFSI in the control electrolyte. Whereas, this peak disappears when using the PST-90 as the additive in the electrolyte. Moreover, the F 1s XPS spectra show two peaks at 684.4 and 688.4 eV assigned to the F 1s from the LiF and –CF_3 respectively (Figure II-528c), and LiF is also the decomposition product of LiTFSI. The intensity of the peak assigned to LiF becomes stronger than that of –CF_3 when using PST-90 as the additive. Both the C 1s and F 1s spectra illustrate the –CF_3 component is suppressed, and comparatively the content of LiF increases when using PST-90 as an additive.
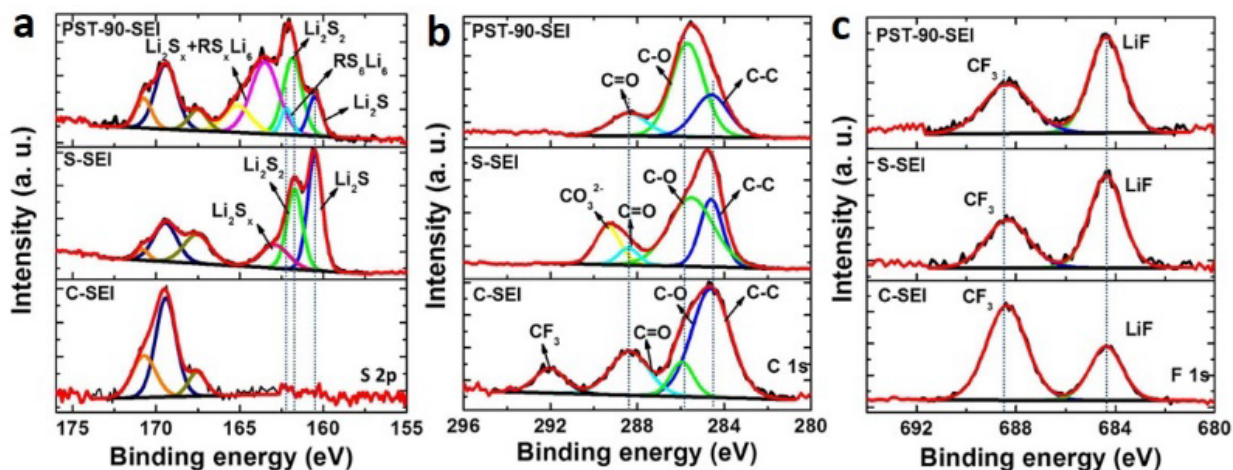
Figure II-528. XPS spectra of C-SEI layer, S-SEI layer and SCP-90-SEI layer. (a) S 2p XPS spectra, (b) C 1s XPS spectra, (c) F 1s XPS spectra. (*Nat. Commun.*, **2017**, 8, 850.)

FT-IR spectra of PST-90-SEI (Figure II-529) shows a peak at ~1170 cm-1, which can be found in the pure PST-90 polymer, and is attributed to the vibration of C-N bond. In addition, peaks at 1476 and 838 cm^{-1} are also observed in both PST-90-SEI and PST-90 polymer, indicating the organosulfide/organopolysulfide in the SEI layers originate from PST-90 polymer.
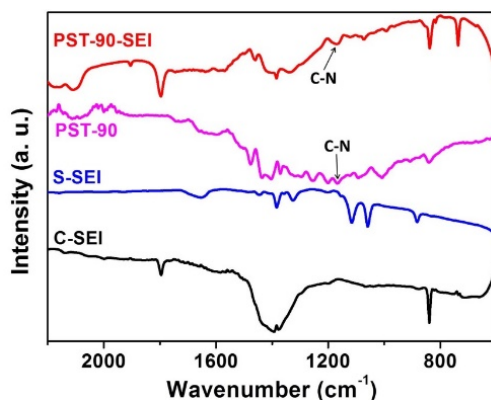
Figure II-529. FT-IR of C-SEI, S-SEI and PST-90 SEI layer. (*Nat. Commun.*, **2017**, 8, 850.)

Peak force tapping mode of AFM was used to investigate the mechanical properties of different SEI layers. For C-SEI (Figure II-530a) and S-SEI (Figure II-530b) layers, the slopes of the loading and unloading curves are quite high and overlap each other. This implies that the SEI layers are relatively stiff and viscoelasticity is negligible because these SEI layers are composed of inorganic Li salts, making them more rigid and brittle. In contrast, the surface of PST-90-SEI (Figure II-530c) layer deforms more and shows a significant hysteresis between the loading and unloading curves, along with a long pull-off or meniscus before the tip completely returned to the free-standing position. The reduced modulus of the different SEI layers could be estimated by fitting the unloading curves with the Johnson-Kendall-Roberts (JKR) models. The C-SEI and S-SEI layers show the modulus of 903 and 740 MPa from the JKR model fit, respectively. In contrast, PST-90-SEI layer displays a low modulus estimated to be 367 MPa. These results suggest that the organosulfides/organopolysulfides-containing SEI layer (PST-90-SEI) becomes soft and viscoelastic to render it flexible, which is beneficial to withstand the large mechanical deformation originating from the Li plating/stripping and to both suppress the growth of Li dendrite and improve cycling CE.
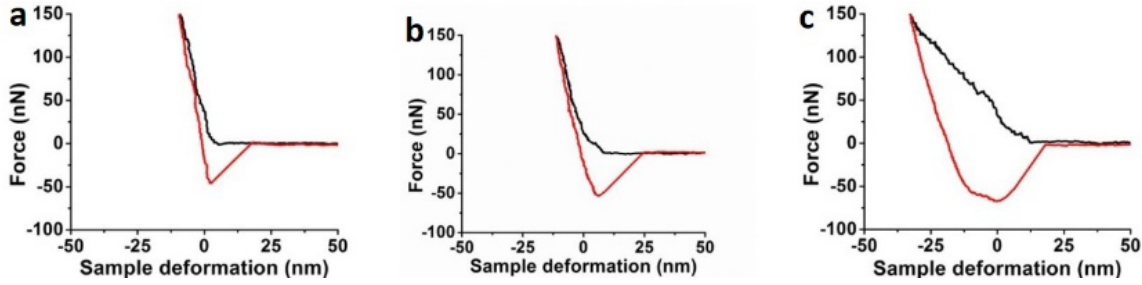
Figure II-530. Indentation curves of the C-SEI layer (a), S-SEI layer (b), and PST-90-SEI layer (c). (*Nat. Commun.*, **2017**, 8, 850.)

Figure II-531 shows the cycling performance of cells using the PST-90-Electrolyte at a current density of 2 mA cm-2 and a deposition capacity of 1 mA h cm-2, the cells deliver an enhanced average CE of 99% over 400 cycles.
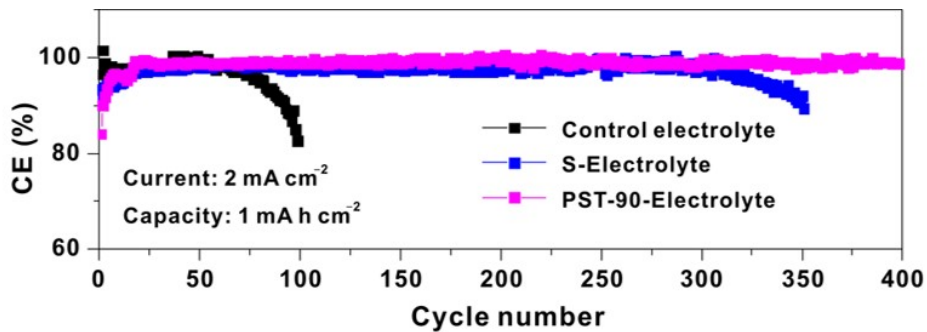
Figure II-531. Cycling performances of the cells using different Electrolytes at a current density of 2 mA cm-2 with a deposition capacity of 1 mA h cm-2. (*Nat. Commun.*, **2017**, 8, 850.)

Li-S baseline pouch cells were assembled and tested. The cathode with an areal sulfur loading of around 4.2 mg cm-2 was made of sulfur, commercial carbon additives, and polyvinylpyrrolidone binder. The weight ratio of sulfur in the cathode is around 50%. 1 M LiTFSI and 0.4M LiNO$_3$ in DOL/DME were used as electrolyte here. The electrolyte/sulfur (E/S) ratio is around 10 mL g^{-1}. Being cycled at C/30, the pouch cell shows an areal capacity of ~5 mA h cm-2 and the average Coulombic efficiency is around 99% (Figure II-532).
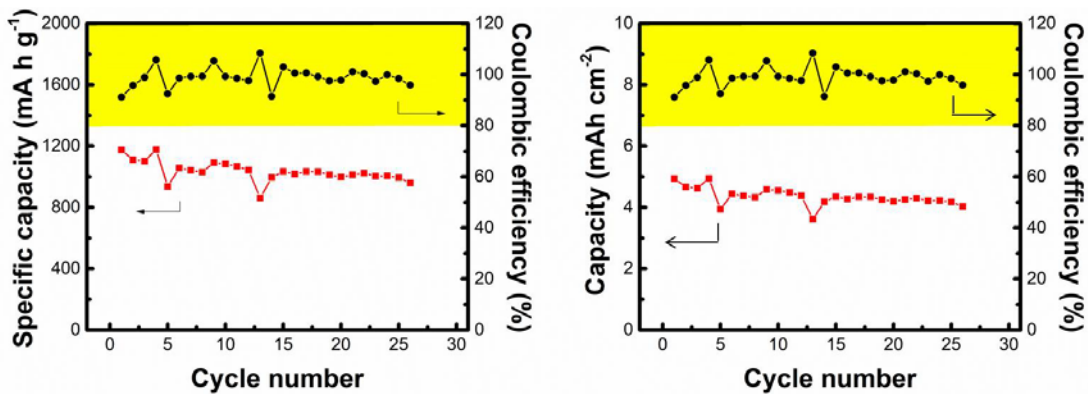
Figure II-532. Cycling performance of Li-S pouch cells.

Conclusions

We successfully developed an organo-Li_xS_y lithium protection layers with the tuned functionality. Sulfur-containing polymers, which contain the sulfur chains and organic units, were used to fabricate organo-LixSy lithium protection layers. SCPs retain electrochemical properties similar to those of elemental sulfur and can electrochemically generate both inorganic Li salts (Li_2S/Li_2S_2) and organic units (i.e., organosulfides/organopolysufides) simultaneously to form a stable hybrid organo-Li_xS_y layer on Li metal. Using this protection layer, lithium anodes were protected effectively without any dendritic and mossy lithium, high Coulombic efficiency (CE) of lithium plating/stripping was achieved.

Key Publications

1. Li, G. X., Gao, Y., He, X., Huang, Q. Q., Chen, S. R., Kim, S. H., Wang, D. H., Organosulfide-plasticized solid-electrolyte interphase layer enables stable lithium metal anodes for long-cycle lithium-sulfur batteries, *Nat. Commun.*, **2017**, 8, 850.

2. Chen, S. R., Yu, Z. X., Gordin, M., Ran, Y., Song, J. X., Wang, D. H., A Fluorinated Ether Electrolyte Enabled High Performance Pre-lithiated Graphite/Sulfur Batteries, *ACS Appl. Mater. Interfaces*, **2017**, 9, 6959.

3. Chen, S. R., Gao, Y., Yu, Z. X., Gordin, M. L., Song, J. X., Wang, D. H., High capacity of lithium-sulfur batteries at low electrolyte/sulfur ratio enabled by an organosulfide containing electrolyte. *Nano Energy*, **2017**, 31, 418.

II.I   Beyond Li-ion R&D: Lithium Sulfur Batteries

II.I.1   New Lamination and Doping Concepts for Enhanced Li–S Battery Performance (U Pittsburgh)

Dr. Prashant N. Kumta, Principal Investigator
University of Pittsburgh
815C Benedum Hall
3700 O'Hara Street
Pittsburgh, PA 15261
Phone: 412-648-0223
E-mail: pkumta@pitt.edu

Dr. Moni K. Datta, Co-Principal Investigator
University of Pittsburgh
815C Benedum Hall
3700 O'Hara Street
Pittsburgh, PA 15261
Phone: 412-648-0223
E-mail: mkd16@pitt.edu

Dr. Oleg I. Velikokhatnyi, Co-Principal Investigator
University of Pittsburgh
815C Benedum Hall
3700 O'Hara Street
Pittsburgh, PA 15261
Phone: 412-648-0223
E-mail: olv3@pitt.edu

Tien Duong, Technology Manager
U.S. Department of Energy
Phone: 202-586-7836
E-mail: Tien.Duong@ee.doe.gov

Start Date: October 1, 2014   End Date: September 30, 2017
Total Project Cost: $1,250,061   DOE share: $1,250,061   Non-DOE share: $0

Project Introduction

Lithium ion batteries (LIBs) clearly dominated the area of high energy storage systems for the past decade with significant research and development activity focused on the development of cathode and anode materials to maximize the specific energy storage, stability, and cycle life of the batteries. However, with the increasing demand in the EV industry for low cost, low weight, and high energy storage batteries to meet the *EV everywhere grand challenge*, the current focus of research has shifted towards the development of lithium sulfur batteries (LSB) owing to the high theoretical specific capacity exhibited by sulfur compared to other cathode materials currently available. Li–S battery shows a theoretical capacity of 1675 mAh/g corresponding to the formation of Li_2S which makes sulfur a promising electrode to replace the layered transition metal oxides (~150 mAh/g) and $LiFePO_4$ (~170 mAh/g) hitherto deployed in present LIB systems. Moreover, the abundance of sulfur in the earth's crust makes it a more economical and highly attractive proposition compared to currently existing cathodes. Despite advantages of sulfur, the existing Li-S battery technology display poor cyclability, low coulombic efficiency (CE) and very low cycle life due to the following issues: 1. Polysulfide

(PS) dissolution; 2. Sluggish kinetics of PS to Li_2S conversion; 3. High PS diffusivity in the electrolyte; 4. Insulating nature or poor conductivity of sulfur/Li_2S; 5. Volumetric expansion/contraction of sulfur; 6. Shuttling of PS along with Li^+. These issues result in loss of sulfur causing mechanical disintegration, surface passivation of both anode and cathode, thereby decreasing the specific capacity and columbic efficiency (CE). Present generation sulfur cathodes also show low specific storage capacity, very poor charging rates and low loading densities. Research is needed to overcome the issues impeding Li-S battery technology development.

Objectives

The objective of this project is to develop Lithium sulfur batteries capable of achieving the performance requirements shown in Table II-23:

Table II-23: Performance Requirements for Project Li-S Battery

Energy Storage Performance Requirements		Electric Vehicle
Characteristics	Unit	
Specific Discharge Pulse Power	W/kg	700
Discharge Pulse Power Density	W/l	1,500
Specific Regen Pulse Power	W/kg	300
Recharge Rate	kW	1.4
Specific Energy	Wh/kg	350
Energy Density	Wh/l	750
Calendar Life	Year	15
Cycle Life	Cycles	1000
Operating Temperature Range	ºC	-30 to +52

Approach

The objectives outlined above will be accomplished by engineering sulfur cathode materials primarily by laminating the electrodes with lithium ion conductor (LIC) coatings to prevent polysulfide dissolution and doping of sulfur to improve the electronic and ionic conductivity. Major technological innovations will be undertaken to accomplish the following objectives in this effort:

Phase – 1 (Year 1)

Synthesis, Characterization and Scale up of suitable LIC matrix materials and multilayer composite sulfur cathodes. This phase is completed.

Identify novel LIC coating materials and morphology for composite multilayer sulfur cathode architectures exhibiting: Specific capacity ≥1000 mAh/g (≥8 mAh/cm2), cyclability (~1000 cycles), loss per cycle ≤0.05% per cycle, Coulombic Efficiency (CE): ≥80%.

Phase – 2 (Year 2)

Development of LIC coated sulfur nanoparticles, scale up of high capacity engineered LIC coated multilayer composite electrodes and doping strategies for improving the electronic conductivity of sulfur.

Optimize and scale up of the interface engineered (I.E.) multilayer composite LIC coated sulfur cathode architectures exhibiting: Specific capacity ≥1200 mAh/g (≥4 mAh/cm2), cyclability (~1000 cycles), loss per cycle: ≤0.01% per cycle, CE: ≥80%.

Synthesize and scale up of doped sulfur nanoparticles on gram scale and demonstrate improvement in performance, reflected as an increase in sulfur weight percentage and improvement in rate capability of cycling of the electrodes.

Phase – 3 (Year 3)

Advanced high energy density, high rate, highly cyclable cell development.

Tie together the three different trees of development i.e., coating development/sulfur particle development/CNT based exploration by identifying suitable configuration integrated electrode (I.E.) with maximum sulfur weight percentage demonstrating high capacity ≥1400 mAh/g, cyclability (~1000 cycles), loss per cycle: ≤0.01% per cycle, CE: ≥80%.

Assemble 4 mAh high energy density Li-S pouch cells and performance testing.

Results

Phase-1 of the project involved replacement of commercial separator with a Lithium-ion conductor (LIC) and successful demonstration of prevention of polysulfide dissolution. In Phase – 2, the ionic conductivity of LIC was improved by doping, altering the electronic structure of sulfur by doping with like-sized dopants and designing effective methods for coating LIC onto sulfur cathodes. Generation of integrated doped nanoparticulate sulfur-carbon nanofiber electrode, business value analysis and fabrication of the desired 4 mAh full cell are the principle aims of Phase-3.

Phase-3 involved comprehensive study of the physical and chemical properties of the Composite Polymer Electrolytes (CPEs) developed in Phase-2 with three nano fillers. The CPEs when tested against commercial sulfur cathodes demonstrated very stable capacity of ~812 mAh/g after 100 cycles with minimal fade rate of 0.012%/cycle. The mechanical property analysis showed that the CPEs showed 2-3 times improvement in tensile strength as compared to their counterparts synthesized using conventional technique (Figure II-533).
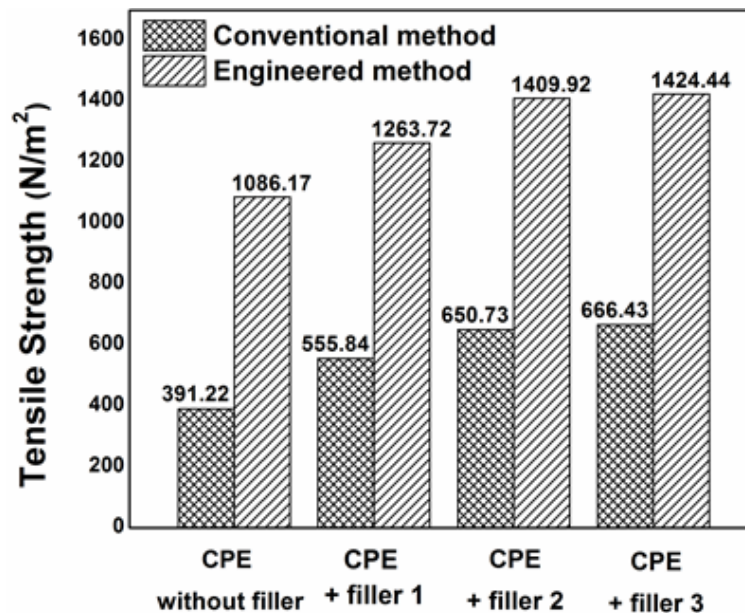
Figure II-533. Cycling performance of Sulfur – infiltrated framework material (SFM)
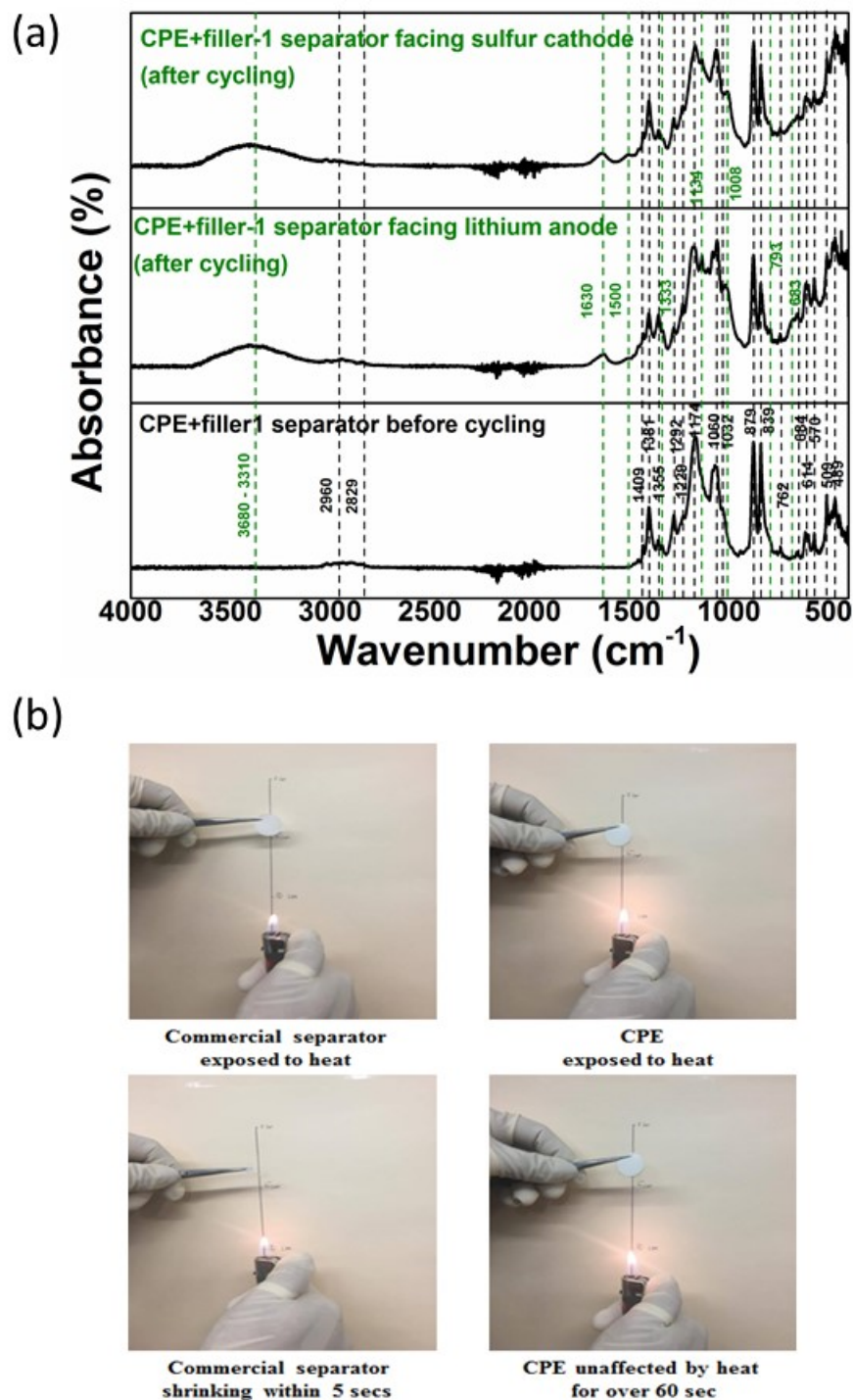
Figure II-534. (a) FT-IR spectra of CPE after cycling and (b) flammability test result of the CPE.

The CPEs also showed excellent chemical stability with minimal modification to the polymer backbone after cycling confirmed by FT-IR spectroscopy (FT-IR) (Figure II-534a) and good flammability properties as compared to commercial battery separator (Figure II-534b).

In addition, Phase-3 also involved development of Directly Doped Sulfur Architecture (DDSA) electrode with very high sulfur loadings of ~18 mg/cm^2 and generation of Polysulfide Trapping Agent (PTA) coated DDSA electrodes with excellent polysulfide trapping property depicted in Figure II-535.
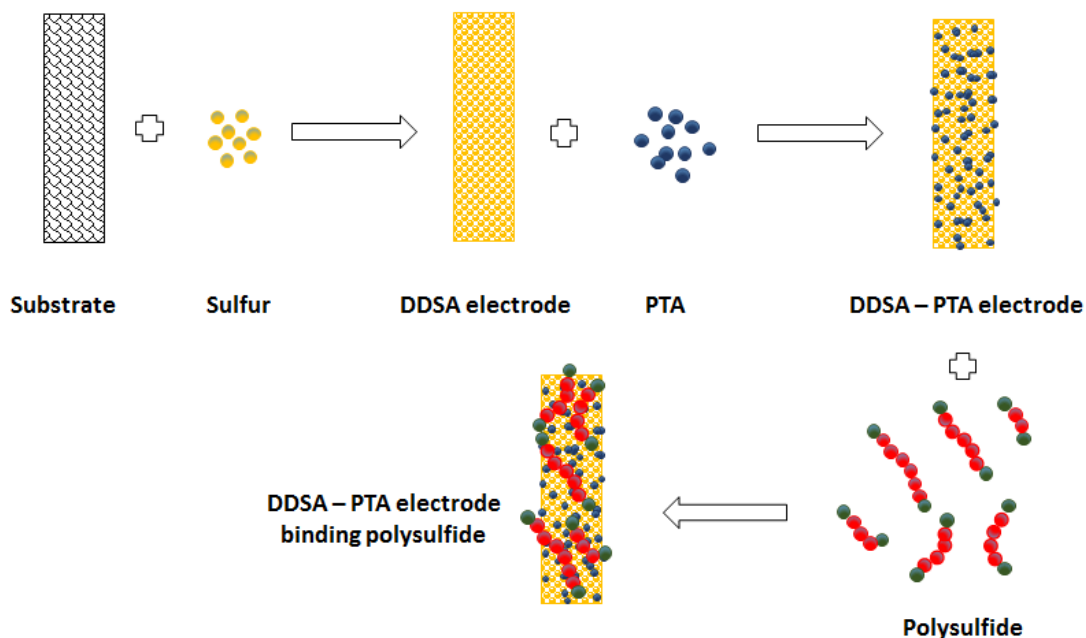
Figure II-535. Scheme of interaction of PTA with polysulfide.

The PTA coated DDSA electrode shows excellent electrochemical cycling performance with an initial capacity of 1305 mAh/g that stabilized at 1112 mAh/g to 200 cycles with less than 0.0014% when cycled at 0.2C rate (Figure II-536). The initial fade of ~0.2% likely due to parasitic reactions will be overcome by further optimization.
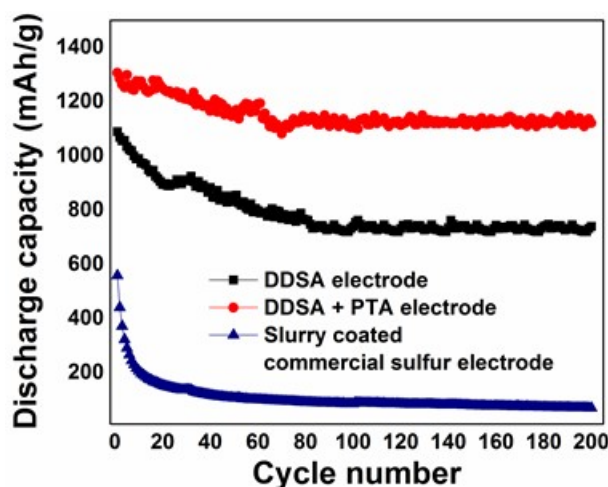
Figure II-536. Cycling performance of PTA coated DDSA electrode

The UV-VIS spectrum of PTA-DDSA (Figure II-537a) showed considerable decrease in the intensities of peaks corresponding to the higher and lower order polysulfides as opposed to the slurry coated electrode suggesting effective adsorption of the polysulfide by the PTA via physical/chemical binding. XPS study of the

electrodes after 200 electrochemical charge – discharge cycles (Figure II-537b) clearly shows the absence of polysulfide peaks showing the efficacy of the polysulfide trapping agents in completing eliminating polysulfide dissolution.
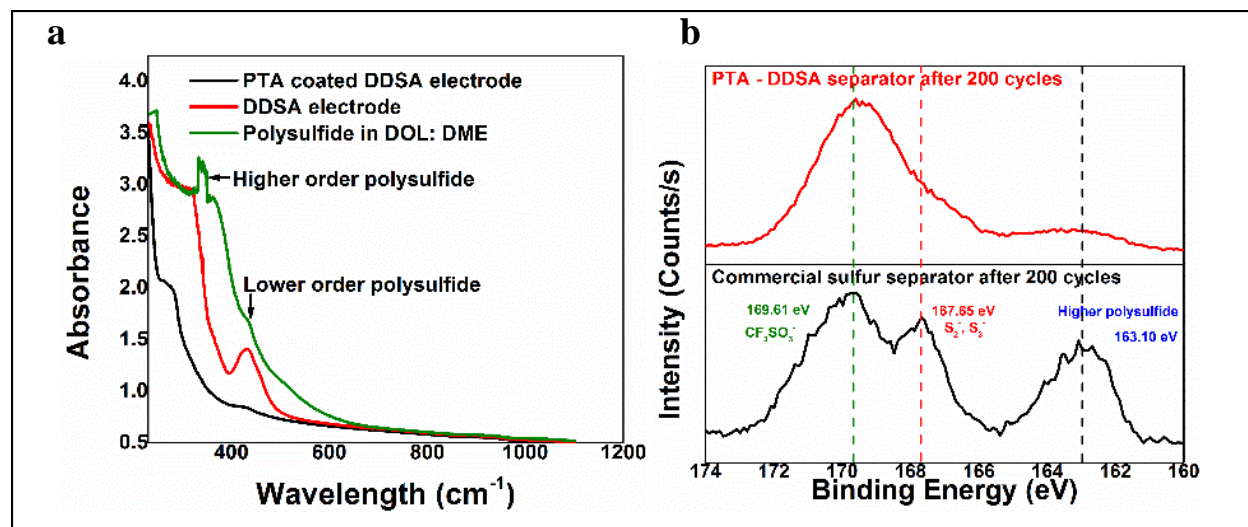
Figure II-537. (a) UV – VIS spectroscopy of PTA coated DDSA electrodes showing absence of polysulfide absorbance and (b) Comparison of XPS patterns of commercial sulfur and PTA - DDSA separators after 200 cycles.

A new sulfonic Complex Framework Material (CFM) was also designed, synthesized and characterized for electrochemical response. Figure II-538a shows the XRD pattern of the CFM compared with the pattern simulated using the crystallographic information file (CIF). The CFMs demonstrated a high sulfur loading of ~ 3-4 mg/cm^2 and maintained a capacity of 1051 mAh/g for over 100 cyces with 0.0011% fade at 0.2C rate (Figure II-538b).
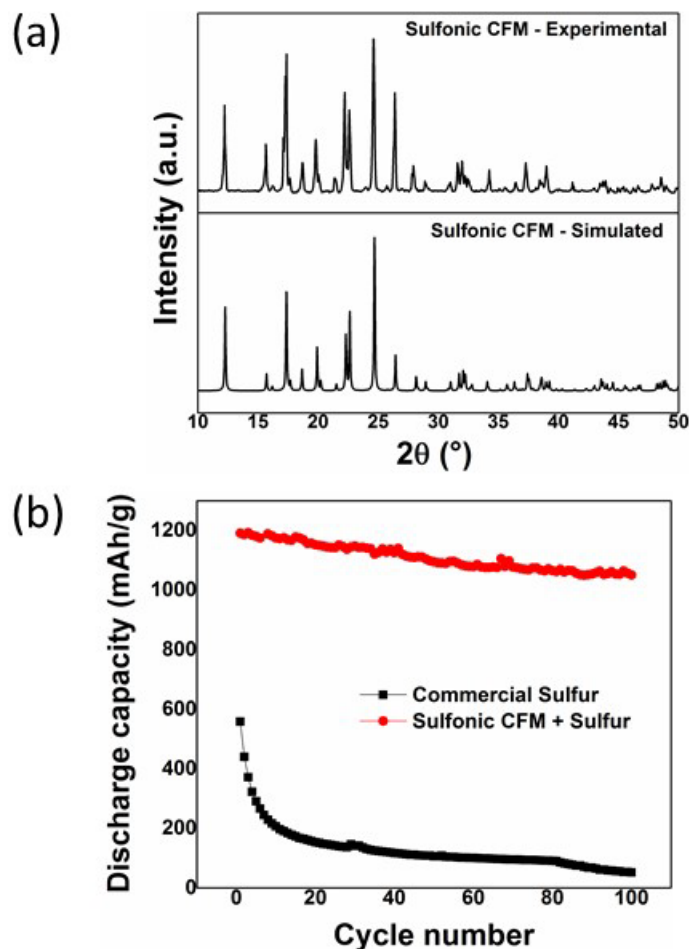
Figure II-538. (a) Comparison of experimental and simulated XRD patterns of sulfonic CMS (b) Electrochemical cycling performance of the sulfonic CFM compared with commercial sulfur.

Manufacturing cost analysis of the various electrode materials (sulfur hosted composite framework materials (CFM), PTA coated DDSA and the LIC coated sulfur nanoparticles), separators (nanofiller incorporated CPE, CFM added gel polymer electrolyte (GPE) and all solid LIC) and electrolytes developed during Phase 1-3 of the project was accordingly conducted to assess the scalabilty of all the laboratory derived materials. Prismatic pouch cells (4 mAh full cell) are currently being assembled and tested using the Phase-3 optimized systems. Accordingly, the PTA-DDSA materials as discussed above demonstrate the best electrochemical performance exhibiting stable capacity ~1112 mAh/g after 200 cycles with less than 0.0014% when cycled at 0.2C rate. This system will therefore, be selected for testing in pouch cells.

Conclusions

The aim of Phase-3 was to establish methods to improve sulfur cycling characteristics by replacing the commercial separator and electrolyte using a novel composite polymer electrolyte containing nanoscale fillers serving to provide improved mechanical strength, Li-ion conductivity and flame resistances. In addition, the work was directed at developing doped sulfur architectures with improved electronic conductivity, and complex framework materials as effective polysulfide trapping agents. By implementing such simple and scalable approaches, various materials have been generated with initial capacities close to 1400 mAh/g with retention of capacity >1100 mAh/g after 200 cycles. It can also be clearly observed that fade rates have been significantly reduced by using these novel approaches and exceptionally low fade rates of ~0.0014% loss per cycle have been obtained. Furthermore, in the case of PTA coated DDSA systems, a complete absence of

polysulfides at the separator has been shown after 200 cycles demonstrating the promise of this system for use in full cell fabrication against an engineered dendrite free lithium metal anode. Such a combined system will likely exhibit performance characteristics of ~400 Wh/kg meeting the Batt 500 goals.

Key Publications

1. Jampani, P.H.; Gattu, B.; Shanthi, P.M.; Damle, S.S.; Basson, Z.; Bandi, R.; Datta, M.K.; Park, S.K.; Kumta, P.N. Flexible sulfur wires (Flex-SWs) – A Versatile platform for lithium-sulfur batteries, Electrochimica Acta Vol. 212, pp. 286 - 293 (2016)

2. Shanthi, P.M; Jampani, P.H; Gattu, B; Sweeney, M; Datta, M.K; Kumta, P.N. Nanoporous Non-Carbonized Metal Organic Frameworks (MOFs): Understanding the Origin of Irreversible Capacity loss in Non-Carbonized Carbonate − based Metal Organic Framework (MOF) Sulfur hosts for Lithium − Sulfur battery, Electrochimica Acta, Vol, 229, pp 208–218 (2017)

3. Jampani, P.H.; Gattu, B.; Shanthi, P.M.; Kumta, P.N. Novel electro-spun sulfur wires for fabricating mattes of lithium-sulfur batteries, International Patent Number: WO 2016/145429 A1, U.S. Provisional Patent, Application Number: PCT/US2016/022283 (Filing date: 03/14/2016)

4. Shanthi, P. M, Jampani, P.H., Gattu, B.; Datta, M K, Velikokhatnyi, O. I., Kumta, P.N., "Electrospinning of PVdF-HFP: Novel Composite Polymer Electrolytes (CPEs) with enhanced ionic conductivities for Lithium-Sulfur batteries." U.S. Provisional Appln. Serial No. 62/529,638 (2017).

5. Jampani, P.H., Shanthi, P. M., Gattu, B., Datta, M K, Velikokhatnyi, O.I., Kumta, P.N., "High capacity, air-stable, Structurally Isomorphous lithium Alloy (SIA), Multilayer Porous Foams (MPFs) and Composite Multilayer Anodes (CMAs) for dendrite-free lithium metal anodes for Li-ion batteries", U.S. Provisional Patent Appln. No. 62/529,588 (2017).

6. Shanthi, P.M., Jampani, P.H., Gattu, B., Albuquerque T., Datta, M.K., Kumta, P.N., "Novel electrospun PVdF – HFP Composite Polymer Electrolytes (CPEs) with enhanced Ionic Conductivities for Lithium – Sulfur batteries", ACS Applied Energy, (2017) under review.

7. Shanthi, P.M., Jampani, P.H., Gattu, B., Datta, M.K., Velikokhatnyi, O.I., Kumta, P.N., "The effect of Mg, Ca and F doping on the ionic conductivity of Li4SiO4: Experimental and First Principles Investigation", Solid State Ionics (2017) under review.

II.I.2   Simulations and X-ray Spectroscopy of Li-S Chemistry (LBNL)

Nitash Balsara, Principal Investigator
University of California
201 C Gilman Hall
Berkeley, CA 94720
Phone: 510-642-8973; Fax: 510-643-5037
E-mail: nbalsara@berkeley.edu

Tien Duong, Technology Manager
U.S. Department of Energy
Phone: 202-586-7836
E-mail: Tien.Duong@ee.doe.gov

Start Date: October 1, 2013   End Date: October 31, 2017
Total Project Cost: $2,000,000   DOE share: $2,000,000   Non-DOE share: $0

Project Introduction

Li-S batteries infamously suffer from dissolution of reaction intermediates – lithium polysulfides – formed during charge and discharge. These species can dissolve out of the cathode into the electrolyte reducing the cell capacity, by placing active material out of electrical contact with the cathode, and causing competitive reactions at the anode surface that ultimately result in cell failure. The reaction mechanisms that underlie the formation of polysulfides are still unclear. Uncertainty regarding these reactions has historically stemmed from ambiguity in the interpretation of in situ spectro-electrochemical data, especially since pure solutions of individual lithium polysulfide molecules cannot be isolated.

Studies of Li-S reaction mechanisms have been challenged by the difficulty of differentiating lithium polysulfide reaction intermediates experimentally. In this work, we aim to overcome these issues by leveraging theoretical calculations of polysulfide X-ray absorption spectra, and to elucidate the mechanisms by which redox reactions in the sulfur cathode proceed.

Objectives

- Develop method of characterizing Li-S battery reaction mechanisms consisting of *in situ* X-ray absorption spectroscopy and molecular simulations.

- Examine Li-S charge/discharge reaction mechanisms from the front and the back of the cathode.

- Elucidate physical and chemical nature of Li-S battery reaction intermediates in different electrolytes.

Approach

Innovative Approach: Molecular dynamic simulations of lithium polysulfide dianions and radical anions in various solvents are used to obtain simulated X-ray absorption spectra (XAS) for isolated polysulfide species. This is done using a first-principles method, dubbed the excited electron and Core Hole (XCH) approach, based on density functional theory, in conjunction with ab initio or classical molecular dynamic simulations of dissolved polysulfide species. Experimental XAS is used to (1) examine Li-S battery reaction mechanism as they take place in the Li-S cathode, and (2) to probe, *ex situ*, chemically prepared/synthesized mixtures of lithium polysulfide species.

1. Obtain experimental XAS for lithium polysulfide species dissolved in SEO, the polymer electrolyte which will be used for *in situ* battery experiments

2. Perform first-principles calculations to obtain X-ray spectra that can be used to interpret and analyze experimentally obtained data

3. Perform *in situ* studies of Li-S reaction mechanisms by probing cells as they are charging/discharging and cells that have been discharged to various depths of discharge.

4. Analyze resulting experimental spectroscopy using theoretically obtained X-ray spectra for individual polysulfide species.

Results

In spite of considerable efforts, the reaction mechanism underlying the charging and discharging of Li-S batteries does not exist. We have used a combination of molecular modeling and experiments to provide a definitive understanding of reaction mechanisms in Li-S cells with different cathode thicknesses using in situ X-ray absorption spectroscopy.

Characterization of polysulfide speciation deep inside thick cathodes

In an earlier study this year, in situ X-ray absorption spectroscopy at the sulfur K-edge was used to probe the back of a thick Li-S cathode (115 µm) during discharge. The total fluorescence intensity reaching the detector during each scan was examined. This intensity is directly proportional to the concentration of sulfur atoms in the back of the cathode that is probed by XAS. For each scan, the fluorescence intensity was averaged over the energy range of 2490-2565 eV, where there are no absorption features. The averaged fluorescence intensity was then normalized by the incoming X-ray intensity measured during each scan. The normalized fluorescence intensity for the zeroth scan (prior to the start of discharge) is called I_0, and the normalized intensity for the 'nth' scan is referred to as I_n. Plotting the ratio of I_n to I_0 as a function of capacity reveals the changes in sulfur content at the back of the cathode through the discharge process (Figure II-539b).
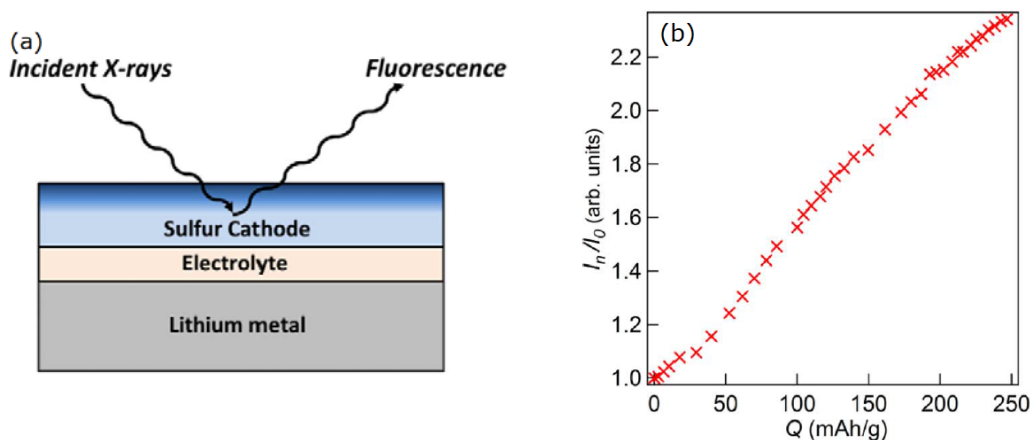
Figure II-539. (a) Simplified X-ray absorption spectroscopy experiment schematic of Li-S cell using a thick cathode where darkened (upper) region of the cathode represents the thickness that was probed by X-rays. (b) Ratio of fluorescence intensity to initial fluorescence intensity measured before discharge indicating the increase in the total amount of sulfur signal detected during discharge.

Because only the top 25 µm thickness of the cathode was probed by XAS, the increase in fluorescence intensity measured during each scan showed that the overall sulfur species in the back of the cathode increased during discharge, which indicated that polysulfide dianion species produced by electrochemical reactions at the front of the cathode diffused towards the back of the cathode during discharge. We explain this finding as follows: the limited diffusion of lithium ions to the back of a thick Li-S cathode will lead to higher reaction rates in the front of the cathode relative to the back of the cathode. This difference in reaction rate leads to a

higher concentration of polysulfide dianions in the front of the cathode, which in turn creates a concentration gradient that leads to the diffusion of polysulfide dianions to the back of the cathode.

Characterization of polysulfide speciation inside thin cathodes

In principle, polysulfides inside the cathode can be produced by either electrochemical reduction of sulfur or disproportionation reactions. Probing part of the cathode only allows us to detect part of both reactions depending on the depth of probe by X-ray. Our more recent study focused on capturing polysulfides produced through the entire depth within the area of probing in order to quantify the species being produced overall within the cathode. To do so, we have made cathode 5-10 µm thin, and probe the cell from the anode side (Li metal). X-rays near the sulfur K-edge transmit highly through Li metal ($> 90\%$) and our electrolyte ($40 - 50\%$). Figure II-540b plots I_n/I_0 during the 1st discharge, charge, and 2nd discharge of this cell. It is evident that I_n/I_0 is more-or-less constant (within 20%), in stark contrast to the data presented in Figure II-539b. Since the concentration gradient impacts polysulfide diffusion and thus will change the total amount of sulfur within a certain depth inside the cathode, the lack of variation in I_n/I_0 indicates that the entire depth of the cathode was probed and that we were capturing polysulfides produced both through electrochemical and disproportionation reactions.
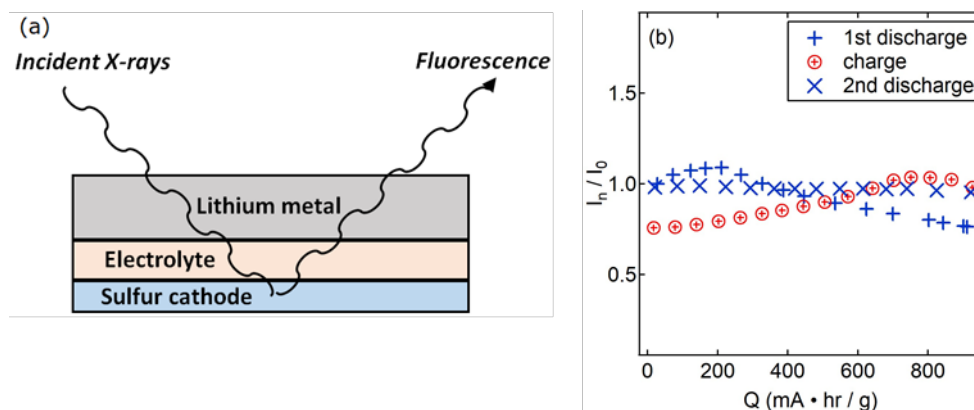

Figure II-540. (a) Simplified X-ray absorption spectroscopy experiment schematic of Li-S cell using a thin cathode. (b) Ratio of fluorescence intensity to initial fluorescence intensity measured before discharge indicating the total amount of sulfur signal detected during discharge and charge stayed constant (within 20% of error).

Theoretical spectra calculated for polysulfide dianions

Members of the program led by Prendergast have simulated X-ray spectra of lithium polysulfides based on first principles calculations shown in Figure II-541a. The calculations indicate that the pre-edge peak is the signature of X-ray excitations of the charged terminal sulfur ions, while the main-edge peak is related to the uncharged internal sulfur atoms of the polysulfide chain. Therefore, the main-edge to pre-edge peak area ratio reflects the relative population of these sulfur atom types in a given sample, and as such could be regarded as a proxy for the average polysulfide chain length, realizing that a given sample may comprise polysulfide molecules with a distribution of lengths. The relationship between spectral features and average chain length is quantified in Figure II-541b. The polysulfide chain length 'x' of a given polysulfide Li_2S_x is approximately a linear function of the area ratio, and the equation corresponding to the least squares fit of the data is given in Figure II-541b. We can think of this equation as a calibration for converting the XAS signal into a polysulfide chain length.
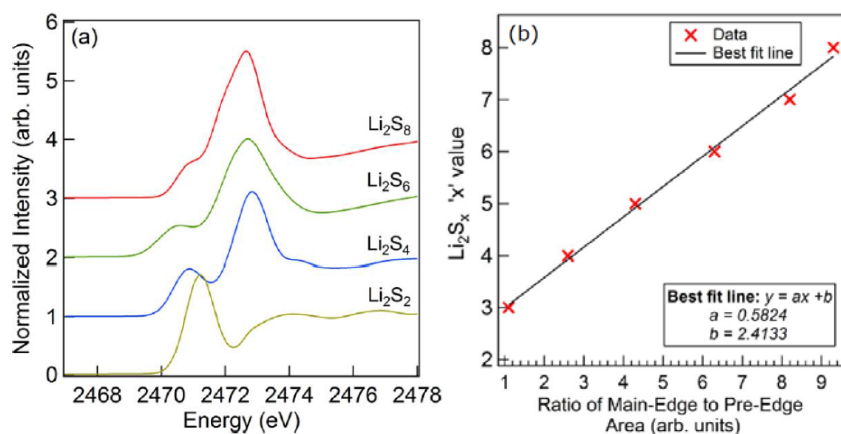
Figure II-541. (a) Selected lithium polysulfide dianion spectra simulated using first principles calculations. (b) Ratio of main-edge peak area to pre-edge peak area versus corresponding Li$_2$S$_x$ 'x' values, derived from theoretical spectra

Comparing Li-S discharge mechanisms with thick and thin cathode

Figure II-542a and Figure II-542b show the in situ XAS spectra obtained with a thick cathode with the back part of the cathode being probed during discharge, and the corresponding voltage to capacity curve, respectively. The poor performance of this cell is due to the amplified concentration polarization effects caused by the thick cathode and plating of solid products (Li$_2$S, and possibly Li$_2$S$_2$) at the front of the electrode which leads to pore blockage.
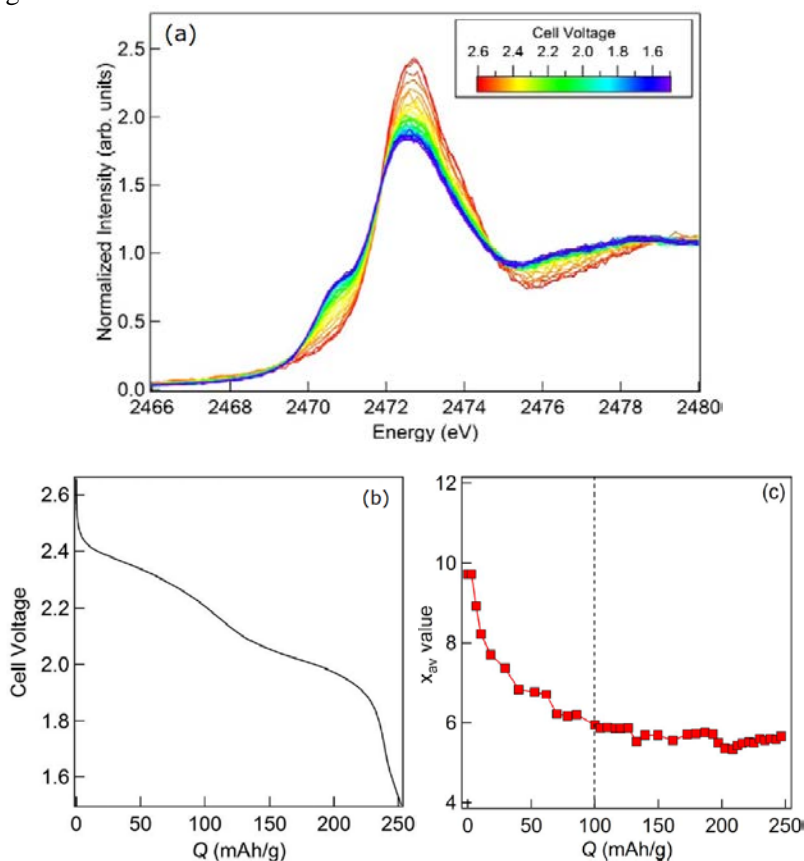
Figure II-542. Discharge of a Li-S cell with a thick cathode and its (a) Sulfur K-edge X-ray absorption spectra probed from the back of cathode, (b) voltage versus capacity (Q), and (c) Average polysulfide chain length for representing the distribution of polysulfide dianions species present in the cathode as a function of capacity.

The pre-edge and main-edge peaks in the spectra shown in Figure II-542a were fit using Gaussian peaks and an arctangent function to represent the absorption edge's increase in intensity. The resulting ratio of main-edge to pre-edge peak area was calculated, and was used to determine the approximate average polysulfide chain length, x_{av}, at a certain discharge capacity plotted in Figure II-542c. A decrease in x_{av} is detected in the range $0 \leq Q \leq 100$ mAh/g. In the range $100 \leq Q \leq 252$ mAh/g, x_{av} plateaued at around 6, suggesting the absence of electrochemical reactions in this regime. It is also noticed that no signal of Li_2S was detected (which would correspond to a peak at 2474.0 eV), which suggests that the reduction of sulfur at the back of the cathode was far from complete, consistent with the low capacity shown in Figure II-542b.

On the contrary, the cell with a thin cathode showed much better performance (Figure II-543b), and the spectra in Figure II-543a for the 1st discharge showed a more significant change of spectra compared to Figure II-542a. The red-cross points in Figure II-543b indicate where spectra were taken during the discharge step. The corresponding x_{av} versus capacity plot shows that the polysulfide chain length decreased all the way down to 3.5 before reaching a plateau, suggesting a more complete reduction compared to the previous cell with a thick cathode. An obvious peak begins to emerge at 2474.0 eV at the start of the lower plateau in the discharge curve, indicating the formation of the solid Li_2S.

Notice that the peak ratio analysis is only reliable for longer chain polysulfides ($x > 3$), for shorter chain polysulfides, the ratio cannot represent the shorter chain polysulfides due to the significant shift in the pre-edge peak (Figure II-541a).
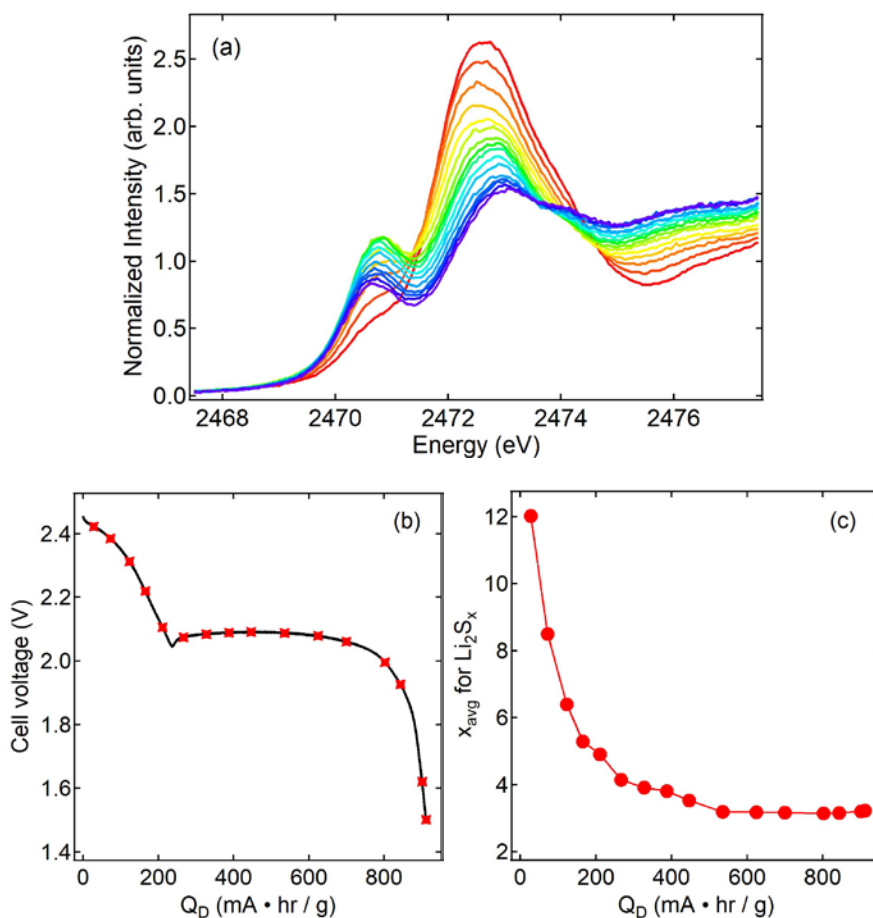
Figure II-543. Discharge of a Li-S cell with a thin cathode and its (a) Sulfur K-edge X-ray absorption spectra probed from the anode, (b) voltage versus capacity (Q), and (c) Average polysulfide chain length for representing the distribution of polysulfide dianions species present in the cathode as a function of capacity.

Furthermore, during the discharge of the cell with a thin cathode, the decrease of x_{av} with Q (Figure II-543c) started to slow down when the discharge voltage versus Q curve (Figure II-543b) reached the beginning of the lower plateau, consistent with the detection of the early formation of Li_2S where reactions become slow due to the transition to a solid phase. On the contrary, the slowing down of x_{av} with Q in the thick cathode, however, started before the lower voltage plateau, which is probably due to the saturation of polysulfides within the electrolyte inside the back of the cathode.

Mechanism during the 1st discharge for Li-S batteries with thin cathodes

The simplest proposed reaction mechanism postulated to occur in the sulfur electrode may be written as:

(a) $S_{8(s)} + 2\ Li^+ + 2\ e^- \rightarrow Li_2S_8$

(b) $Li_2S_8 + 2/3\ Li^+ + 2/3\ e^- \rightarrow 4/3\ Li_2S_6$

(c) $4/3\ Li_2S_6 + 4/3\ Li^+ + 4/3\ e^- \rightarrow 2\ Li_2S_4$

(d) $2\ Li_2S_4 + 4\ Li^+ + 4\ e^- \rightarrow 4\ Li_2S_2$

(e) $4\ Li_2S_2 + 8\ Li^+ + 8\ e^- \rightarrow 8\ Li_2S_{(s)}$

The curve in Figure II-544 shows the theoretical dependence of x_{av} versus moles of electron passed per mole of S_8-based on this scheme. The experimental data obtained from the thin cathode are also shown in Figure II-544. The agreement in Figure II-544 indicates that the data are consistent with the proposed mechanism. Further work is needed to determine the distribution of species formed in the cell and the reasons for the observed departures when the moles of electrons consumed per mole of S_8 exceeds 5.
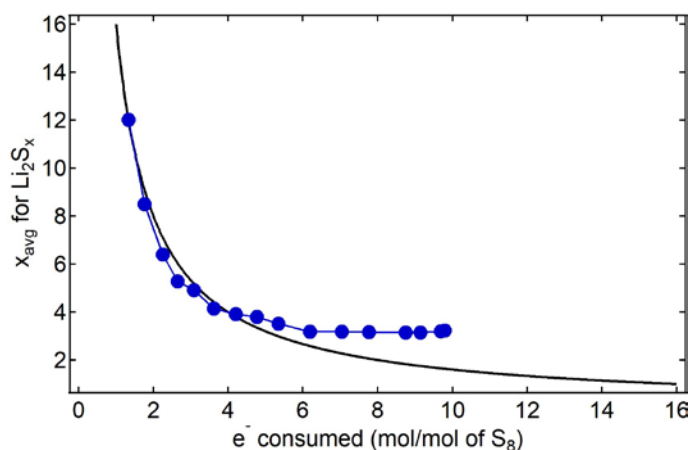
Figure II-544. Voltage versus capacity for Li-S cell with a thin cathode during charge, and average polysulfide chain length as a function of capacity during charge.

Charging Li-S batteries thin cathodes

During charging, the polysulfides within the cathodes are oxidized. Figure II-545a and Figure II-545b show the voltage versus capacity curve and the calculated x_{av} from XAS, respectively, during charging. As expected, the behavior of x_{av} versus capacity is the reverse of discharge; x_{av} is a weak function of Q at $0 \leq Q \leq 780$ mAh/g, and it starts to increase rapidly for $Q > 780$ mAh/g. The transition between these regimes occurs at the same capacity wherein the voltage increases abruptly. The high voltage capacity thus arises from conversion of Li_2S and Li_2S_2 to longer chain polysulfides. We notice that x_{av} only reached 4.3 at the end of charging, most likely due to loss of electronic contact with soluble polysulfides.
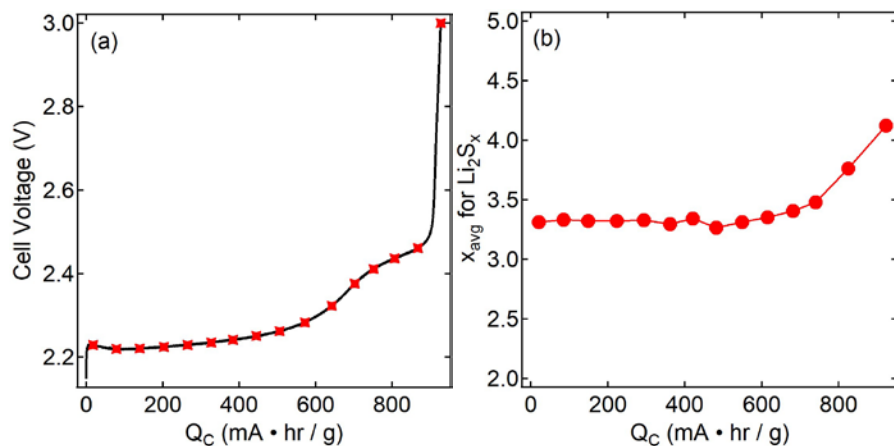
Figure II-545. (a) voltage versus capacity for Li-S cell with a thin cathode during charge, and (b) Average polysulfide chain length as a function of capacity during charge.

Conclusions

This program has led to a fundamental understanding of charge-discharge mechanisms in Li-S cells. We have established a way to study Li-S sulfur reaction mechanism with *in situ* X-ray absorption spectroscopy. The distinguishing feature of our work is the tight coupling between molecular modeling and *in situ* experiments. Practical Li-S cells will comprise cathodes with thicknesses in the 100 μm range. However, in such cells, XAS only probes a small portion of the cathode located at the back of the cell. We established that lithium polysulfide diffusion from the front to the back of the cathode was dominant. In addition, the electrochemical reactions occurring in other parts of the cathode could not be studied. It is thus logical to compare the redox reactions within thick cathodes and a cell with thin cathode that is probed in its entirety, included the electrolyte. The difference in the cell performance and the analyzed species indicates the inhomogeneity of the polysulfide species at different depths inside the cathode, and this phenomenon was reported for the first time in literature. We also provide a comparison of the average polysulfide chain length to electrons consumed theoretically and experimentally, and find good agreement between the two. We have also studied the species during charging and showed the agreement in the reverse in the average chain length with the charging step. However, the dissolution of polysulfides into the electrolyte limited our analysis of the average species being recovered during charging.

Key Publications

1. Kevin H. Wujcik, Dunyang Rita Wang, Tod A. Pascal, David Prendergast, Nitash P. Balsara, "In situ X-ray absorption spectroscopy studies of discharge reactions in a thick cathode of a lithium sulfur battery", *Journal of the Electrochemical Society*. 2017, 164, A18-A27. DOI: 10.1149/2.1441614jes.

2. Tod A. Pascal, Irune Villaluenga, Kevin H. Wujcik, Didier Devaux, Xi Jiang, Dunyang Rita Wang, Nitash Balsara and David Prendergast, "Liquid Sulfur Impregnation of Microporous Carbon Accelerated by Nanoscale Interfacial Effects" *Nano Letters*. 2017, 17 (4), 2517-2523. DOI: 10.1021/acs.nanolett.7b00249.

3. Tod A. Pascal, Kevin H. Wujcik, Dunyang Rita Wang, Nitash P. Balsara and David Prendergast, "Thermodynamic Origins of the Solvent-Dependent Stability of Lithium Polysulfides from First Principles" *Physical Chemistry Chemical Physics*. 2017, 19, 1441-1448. DOI: 10.1039/C6CP06889H.

4. Kevin H. Wujcik, Dunyang Rita Wang, Alexander A. Teran, Eduard Nasybulin, Tod A. Pascal, David Prendergast, Nitash P. Balsara. "Determination of Redox Reaction Mechanisms in Lithium Sulfur Batteries", book chapter with *Wiley-VCH*, under review.

II.I.3 Novel Chemistry: Lithium-Selenium and Selenium-Sulfur Couple (ANL)

Khalil Amine, Principal Investigator

Argonne National Laboratory
9700 South Cass Avenue
Lemont, IL 60439-4837
Phone: 630-252-3838
E-mail: amine@anl.gov

Tien Duong, Technology Manager

U.S. Department of Energy
Phone: 202-586-7836
E-mail: Tien.Duong@ee.doe.gov

Project Introduction

Rechargeable Li/sulfur battery has attracted extensive attention for energy storage application due to its much higher energy density and lower cost than that of state-of-the-art lithium-ion batteries. However, the insulating nature of sulfur and the dissolution of intermediary polysulfides into the electrolyte significantly hinder its practical application. Recently, selenium and selenium-sulfur systems have received considerable attention as cathode materials for rechargeable batteries because of the high electronic conductivity (20 orders of magnitude higher than sulfur) and high volumetric capacity (3254 mAh cm^{-3}) of selenium. Selenium-Sulfur mixtures are miscible in a wide concentration range, and many Se-S composites including Se_5S, Se_5S_2, Se_5S_4, SeS, Se_3S_5, SeS_2, and SeS_7 can be prepared, including materials with a small amount of Se such as SeS_{20}. These Se-S materials can offer higher theoretical specific capacities than Se alone, and improved conductivity compared to pure S. However, as a new chemistry, the electrochemistry of Se-S cathodes in different electrolytes was not well understood. The lack of such acknowledge significantly hinders the rational design of Li/electrolyte/Se-S chemistries with outstanding electrochemical performance.

Objectives

The objective of this project is to develop a novel SeS_x cathode material for rechargeable lithium batteries with high energy density (500 Wh kg^{-1}), long life (>500 cycles) along with low cost and high safety.

Approach

To prevent the dissolution of polysulfides and increase the active material utilization, S or Li_2S are generally impregnated in a conducting carbon matrix. However, this approach makes it difficult to increase the loading density of practical electrodes. It is proposed here to solve the above barriers using following approaches: (1) partially replacing S with Se, (2) confinement of the S_xSe_y in a porous conductive matrix with high pore volume and (3) exploration of low polysulfides/polyselenides dissolution electrolytes.

COLLABORATIONS:

Cathode development (Prof. Chunsheng Wang at University of Maryland)
Porous carbon with high pore volume (Dr. Luis Estevez at PNNL)
Synchrotron X-ray characterization (Dr. Yang Ren and Dr. Chengjun Sun at APS of ANL)
Computational modeling (Dr. Larry Curtiss at MSD of ANL)

Results

1. Solvent-induced reaction mechanism change for Li/Se-S batteries

Figure II-546a, Figure II-546b, and Figure II-546c show the voltage-capacity curve for the first discharge of the S_5Se_2/KB cathode in the carbonate-, DME-, and HFE-based electrolyte at C/20 (1C=1389 mA g^{-1}), respectively. Figure II-546a clearly shows a single discharge plateau in the carbonate-based electrolyte, corresponding to the direct electrochemical transformation of S_5Se_2 to Li_2S/Li_2Se without the formation of polysulfides/polyselenides, which has been proved to be a solid-state lithiation/de-lithiation reaction by advanced spectroscopy analyses (*Chem. Commun.*, 2014, **50**, 5576-5579). For the DME-based electrolyte (Figure II-546b), there are four main discharge voltage plateaus, which can be assigned to the well-known two-step solid-liquid-solid reactions of Li with S and Se, respectively. The upper voltage plateau was generally attributed to the dissolution region, while the lower voltage plateau was related to the formation of solid Li_2S and Li_2Se (*J. Am. Chem. Soc.*, 2013, **135**, 8047-8056). In addition, a small plateau was observed at ca. 1.6 V, which was related to the reduction of $LiNO_3$ additive. For the HFE-based electrolyte (Figure II-546c), the single long discharge plateau indicate a solid-state lithiation-delithiation process, while the very short sloping region corresponds to very little formation of polysulfides/polyselenides in the initial discharge stage. Figure II-546d shows the cycle performance of the S_5Se_2/KB cathode in three different electrolytes at C/20. The S_5Se_2/KB cathode can only deliver a capacity of around 300 mAh g^{-1} in the carbonate-based electrolyte, although the discharge reaction bypassed the formation of soluble Li_2S_n and Li_2Se_n (n≥4), which can be ascribed to the widely reported nucleophilic reaction between polysulfides/polyselenides and carbonate-based electrolyte (*Adv. Energy Mater.*, 2014, **4**, 1301473). In the DME-based electrolyte, the cathode showed continuous capacity degradation over 50 cycles, together with a severe shuttle effect. This result is similar to that for previously reported Se-based cathodes and was attributed to the aggravation formation of highly soluble long-chain polyselenides during cycling (*Nano Lett*, 2016, **16**, 2663-2673). As a comparison, after an activation process in the initial three cycles, the S_5Se_2/KB cathode in the HFE-based electrolyte attained a much higher reversible capacity of over 700 mAh g^{-1} and displayed minimal shuttle effect within 50 cycles. This may result from its solid-state lithiation-delithiation mechanism, which can greatly suppress the formation of soluble polysulfides/polyselenides during electrochemical cycling. The result also indicates that compared to carbonate-based electrolyte; HFE is much more stable against polysulfides/polyselenides.
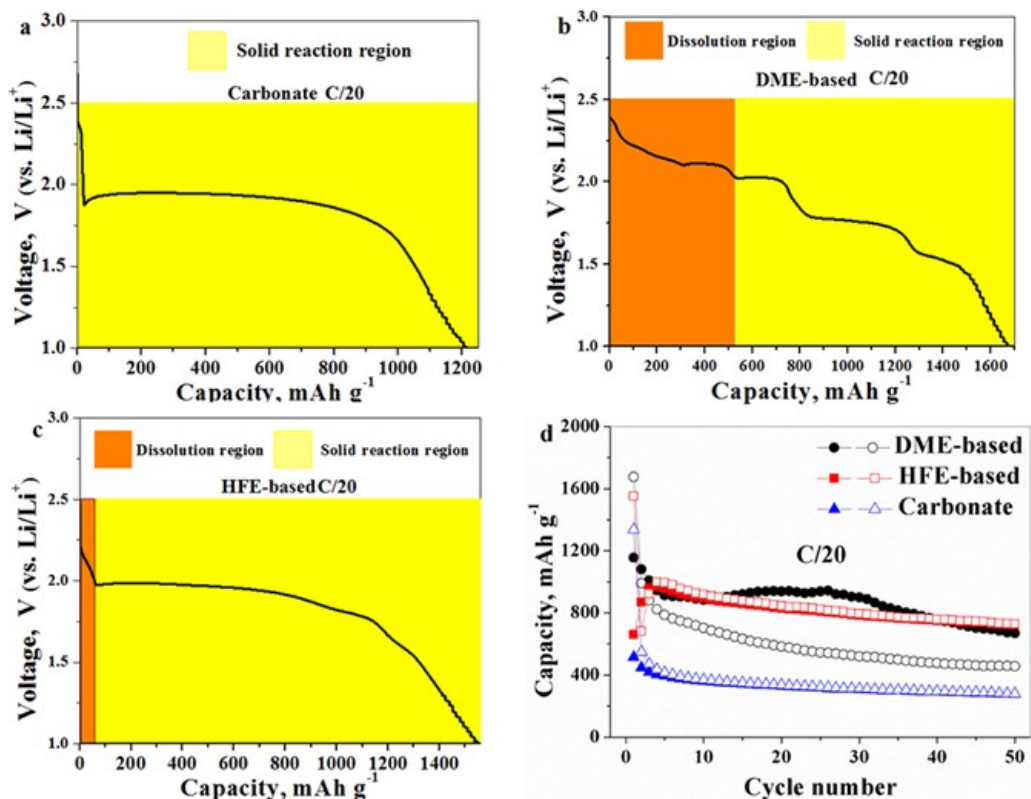
Figure II-546. The first discharge curve of S₅Se₂/KB cathode in (a) carbonate-based, (b) DME-based and (c) HFE-based electrolyte at C/20. (d) Cycling performance of S₅Se₂/KB cathode in the three electrolytes. Open symbols indicate discharge; solid symbols mean charge in panel d.
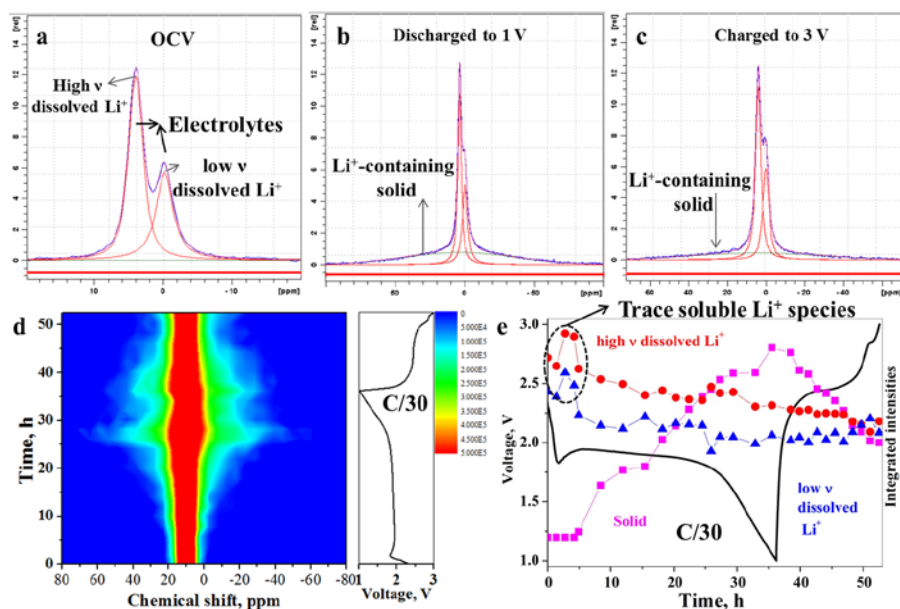
Figure II-547. In-operando 7Li NMR studies of the S₅Se₂/KB cathode in the HFE-based electrolyte: fit curves to the NMR line shape at (a) open circuit voltage, (b) discharged to 1.0 V, and (c) charged back to 3.0 V. (d) 2D contour plot of NMR signal versus charge/discharge curve at C/30; (e) integrated areas of Li⁺ species as a function of charge/discharge process.

To unravel its (de)lithiation mechanism in HFE-based electrolyte, we carried out in-situ ^{7}Li NMR spectroscopy, as it is very sensitive to the solid and soluble Li^+ species inside the test cells. The solid components generally result in broader signals while the solution components usually present narrow line widths due to the presence of anisotropic interactions. Figure II-547a shows the typical ^{7}Li NMR spectra of the pristine S_5Se_2/KB cathode before charge/discharge, which shows two sharp signals including one at higher frequency and one at lower frequency. The NMR spectra can be well fitted by two resolvable peaks with a high overlap of 91.3% by using the software suite included in Topspin 3.1, which are assigned to the soluble Li^+ species in the cell. It is hard to distinguish the contributions of either electrolyte or other battery components, such as $LiNO_3$ additive, to the peaks. Nonetheless, the noticeable changes in intensity for these two sharp signals during charge/discharge are generally ascribed to the formation/decomposition of soluble polysulfides or polyselenides. When the cell was discharged to 1.0 V, as shown in Figure II-547b, in addition to two sharp signals from the soluble Li^+ species, a broad resonance signal is apparent, which is related to the formation of a Li^+-containing solid such as Li_2S and Li_2Se. When the cell was charged back to 3.0 V (Figure II-547c), the intensity of these two sharp peaks changed very little while the broad signal dramatically decreased.

Figure II-547d shows the 2D contour plot of the NMR spectra of the S_5Se_2/KB cathode in the HFE-based electrolyte along with the first discharge/charge curve at C/30. The color represents the intensity of the NMR signals, with red being high intensity and blue being low intensity. As shown, as the discharge proceeded, the intensities of two sharp signals (represented by the red color) changed little while the signal of the broad resonance gradually increased, indicating more and more Li^+-containing solid formation. During charge, the signals for the Li^+-containing solid gradually decreased. To quantify the change of the soluble and solid Li^+ species, in-situ NMR data were fit by fixing the widths of the sharp resonances but allowing the line width of the broad resonance to float. The integrated areas of the high frequency, low frequency, and broad resonance along with the charge/discharge process are compared in Figure II-547e. As shown, the integrated areas of the soluble Li^+ species at both high and low frequency slightly increase at the very beginning of the discharge and then keep relatively stable for the remaining charge/discharge process, which means that a small amount of polysulfides/polyselenides formation occurred during the early discharge stage in the HFE-based electrolyte, a finding that is consistent with the prediction from the voltage profiles. Moreover, the integrated area of the Li^+-containing solid changed little at the very beginning of the discharge. However, its intensity was significantly increased after the consumption of the trace polysulfides/polyselenides and reached a maximum at the end of discharge. During charge, the integrated area of solid Li^+ species gradually decreased, while the soluble Li^+ species remained relatively stable. Hence, in-situ ^{7}Li NMR study revealed very little soluble polysulfides/polyselenides formation in the HFE-based electrolyte during the whole charge/discharge process, and most of the S_5Se_2 was converted directly to Li_2S and Li_2Se, indicating a solid-state lithiation-delithiation process.
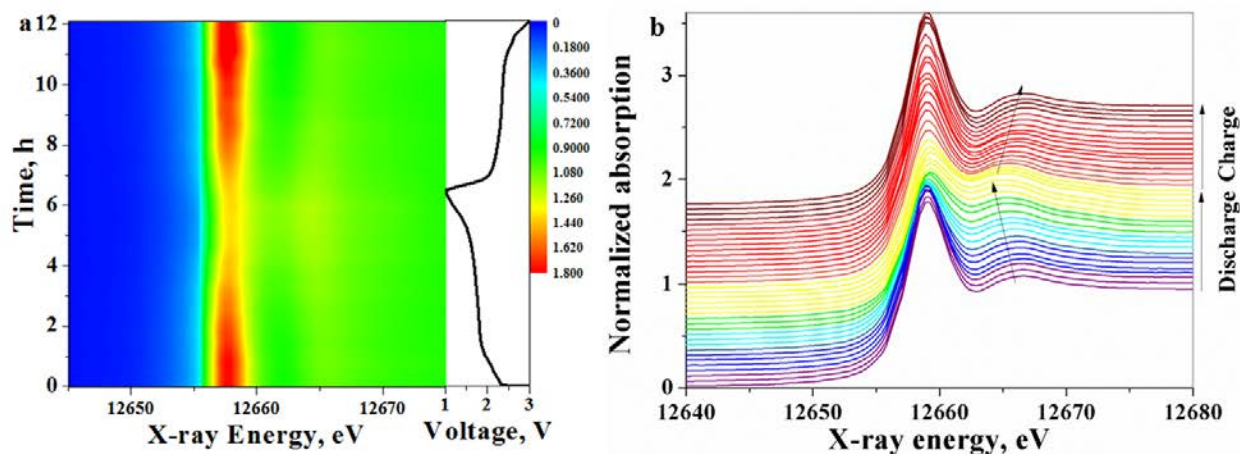
Figure II-548. (a) contour plot of In-operando Se K-edge XANES and (b) representative Se K-edge XANES spectra on the 4th cycle of S_5Se_2/KB cathode at C/10 in HFE-based electrolyte.

To further confirm this conclusion, we further carried out in-operando Se K-edge X-ray absorption near edge spectroscopy (XANES) on the 4th cycle of the S_5Se_2/KB cathode in the HFE-based electrolyte to bypass the activation process in the initial three cycles. Figure II-548a shows a 2D contour plot for the in-operando Se K-edge XANES data at C/10. As shown, the absorption intensity of Se (12658 eV) gradually decreased during the discharge and was completely recovered at the end of charge. Representative Se XANES spectra during the discharge/charge process are shown in Figure II-548b, in which no energy shift for Se from 12658 eV to 12665 eV is evident. This is consistent with our previous result for carbonate-based electrolyte and different from that for DME-based electrolyte. Therefore, we concluded that space-confined Se-S/KB cathodes undergo a solid-state lithiation/de-lithiation process in the HFE-based electrolyte.

2. Exploration of advanced Se-S/micro-mesoporous carbon composite with high capacity, long cycle life and low self-discharge
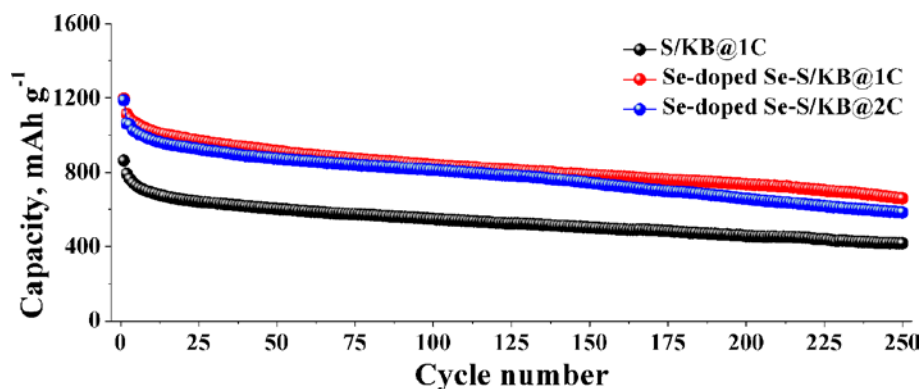
Figure II-549. Cycling performance at high rates of Se-doped Se-S/KB cathode (50 wt.%) and S/KB cathode with in HFE-based electrolyte.

The above results suggest that the dissolution of polysulfides/polyselenides can be suppressed by tailoring the interfacial chemistry of space-confined Se-S cathodes. Since Se has a higher electronic conductivity but lower gravimetric capacity (675 mAh g^{-1}) than S, by rational design for the atomic ratio between S and Se, one can develop an optimal Se-S material with similar theoretical gravimetric capacity and improved electronic conductivity compared to S. In this report, an amorphous S-rich $S_{22.2}$Se/KB (50 wt.%) cathode was further developed by adjusting the raw weight ratio between S and Se. Figure II-549 compares the cycling performance of Se-doped Se-S/KB and S/KB cathode at high rates. Both cathodes were cycled at C/20 for 3 cycles, and then the $S_{22.2}$Se/KB cathode was cycled at 1C and 2C, and the S/KB cathode at 1C. The results clearly show that the $S_{22.2}$Se/KB demonstrates much higher reversible capacity than Se-free S/KB during high rate cycling. This difference is likely due to the higher electronic conductivity of Se than S, which can improve the poor electronic conductivity and the sluggish kinetics, especially during solid-state (de)lithiation of Se-S cathodes. After 250 cycles of charge/discharge at 1C and 2C, the $S_{22.2}$Se/KB cathode still delivered a reversible capacity of 660 mAh g^{-1} and 583 mAh g^{-1}, respectively, demonstrating excellent long-term cycle stability. By comparison, the S/KB cathode only maintained 417 mAh g^{-1} after 250 cycles at 1C. Despite the cycle stability difference, they both show coulombic efficiency close to 100% after the second cycle, indicating a diminished shuttle effect in the HFE-based electrolyte. Therefore, by manipulating the interfacial chemistry of Se-S cathodes, the dissolution of polysulfides/polyselenides and the sluggish electrochemical reaction kinetics of S cathodes can be significantly improved.

3. Extending the optimal S_xSe_y confinement pore size from micro/mesopores to large mesopores and macropores with high pore volume for high loading Li/S_xSe_y systems
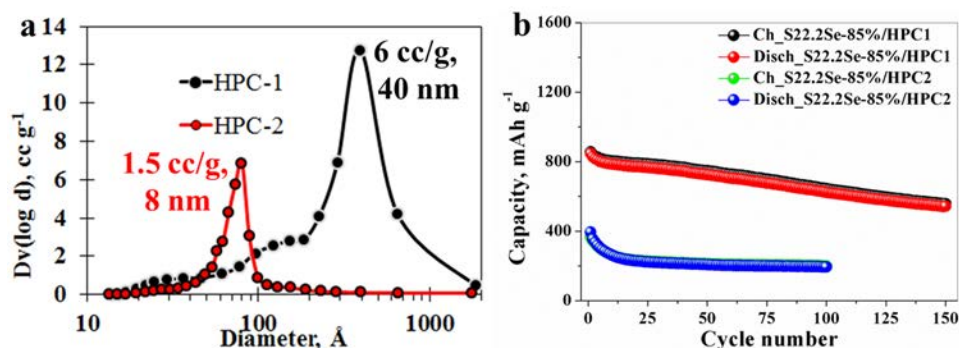
Figure II-550. (a) Pore size distribution of highly porous carbon with pore size of ca. 40 nm (HPC1) and 8 nm (HPC2), (b) cycle performance of $S_{22.2}Se/HPC1$ (85 wt.%) and $S_{22.2}Se/HPC2$ (85 wt.%) at C/2 in HFE-based electrolyte.

To attain higher energy densities, higher Se-S loading is needed in the composites and also in the electrodes. The loading in the electrodes could be further optimized through a laminate fabrication process and smart electrode structure design, while immobilizing polysulfides/polyselenides within the host materials should be at the core of high S loading system. However, the dissociation of polysulfides/polyselenides from the host material will become very challenging when go to high loading level. This is because of the required pore volume to trap S_xSe_y in the pores will be increased with increasing S_xSe_y loading. For example, for 70 wt.% S_xSe_y loading, a pore volume of at least 2.1 cc g^{-1} is required to constrain all the S_xSe_y in the pores and simultaneously accommodate the volume change during charge/discharge. However, this value is dramatically increased to as high as 5.77 cc g^{-1} for 85 wt.% S_xSe_y loading. Such a high pore volume is rarely reported in microporous carbon (<2 nm) and small mesoporous carbon (2-10 nm). To date, most of microporous carbons have a pore volume of <1.0 cc g^{-1}, and their S_xSe_y loading is generally below 50%. The pore volumes of small mesoporous carbons (2-10 nm) are in the range of 0-3.5 cc g^{-1}, and the reported S_xSe_y loadings are between 50% and 80%. The large mesoporous carbons (10-50 nm) generally have higher pore volume and higher affordable S loading than microporous carbon or small mesoporous carbon. However, large mesoporous carbon has long been considered as inferior host materials due to relatively weak S_xSe_y confinement.

Based on the above finding about solvent-induced reaction mechanism change, we further explored the interfacial chemistry of high S_xSe_y loading systems using HFE-based electrolyte. Figure II-550a shows the pore size distribution of two kinds of highly porous carbon (HPC). HPC1 has a main pore size of ca. 40 nm, and an extremely high pore volume of 6.053 cc g^{-1}, which can theoretically load ca. 86 wt.% Se-S. HPC2 has a smaller pore size of ca. 8 nm but also a lower pore volume of 1.464 cc g^{-1}, which can only encapsulate 64 wt.% Se-S in theory. We therefore prepared two Se-S/HPC composites with 85 wt.% $S_{22.2}Se$ loading using HPC1 and HPC2, respectively. Figure II-550b compares the cycle performance of $S_{22.2}Se/HPC1$ (85 wt.%) and $S_{22.2}Se/HPC2$ (85 wt.%) composites at C/2 in HFE-based electrolyte. As clearly shown, the $S_{22.2}Se/HPC1$-85 wt.% cathode can still deliver a reversible capacity of 542.7 mAh g^{-1} after 150 cycles with a very small polysulfide/polyselenide shuttle at C/2. By contrast, the reversible capacity of the $S_{22.2}Se/HPC2$-85 wt.% cathode is only ca. 400 mAh g^{-1} and quickly faded to ca. 200 mAh g^{-1} after 10 cycles, indicating very low utilization of active material. Hence, it can be clearly seen that by using HFE-based electrolyte to modify the electrode/electrolyte interface of Li-S batteries, large porous carbon that has long been regarded as inferior S host materials became effective. This finding is critical for the development of high loading Li-S batteries as large porous carbon generally possess much higher pore volume than microporous and small-mesoporous carbon.

Conclusions

In summary, by manipulating the interfacial chemistry of Li-S batteries through Se doping and electrolyte modification, the sluggish electron transport and the polysulfide dissolution can be remarkably improved. This effect can be attributed to the high electronic conductivity of Se and the diminished polysulfides/polyselenides dissolution in the HFE-based electrolyte. As a result, space-confined Se-S cathodes switched from a conventional two-step solid-liquid-solid reaction to solid-state (de)lithiation, as evidenced by in-situ ^{7}Li NMR and in-operando synchrotron X-ray probes. This switch bypassed the formation of highly soluble polysulfides/polyselenides during cycling and thus led to significantly improved electrochemical performance. Hence, S-rich Se-doped S/Ketjenblack cathode can deliver a reversible capacity of above 1000 mAh g^{-1} at C/20 within 50 cycles, 660 mAh g^{-1} at 1C after 250 cycles, and 583 mAh g^{-1} at 2 C after 250 cycles, as well as an excellent rate capability of 700 mAh g^{-1} at 5C together with good coulombic efficiency close to 100%. Moreover, the minimal polysulfide/polyselenide dissolution also extends the optimal confinement pore size from micropores and small mesopores to large mesopores and even macropores, which can benefit the development of high-loading Li-S batteries due to their much higher pore volume. Our results indicate that manipulating the interfacial chemistry could pave a new way for the development of high-performance and high-loading Li-S batteries. Combinational efforts on rational structure design and exploration of functional electrolytes can lead to advanced Li-S batteries with higher energy density and long calendar life in the near future.

Key Publications

1. Gui-Liang Xu, Jianzhao Liu, Zonghai Chen and Khalil Amine, POLY(ETHYLENEOXIDE)SILOXANE ELECTROLYTES FOR RECHARGEABLE BATTERIES, US. Patent, No. 15/760,295, filed, 2017.

2. Gui-Liang Xu, Jianzhao Liu, Rachid Amine, Zonghai Chen and Khalil Amine, Selenium and Selenium-Sulfur Chemistry for Rechargeable Lithium Batteries: Interplay of Cathode Structures, Electrolytes, and Interfaces, ACS Energy Letter, 2017, 2, 605-614.

3. Gui-Liang Xu, Hui Sun, Luis Estevez, Chao Luo, Tianyuan Ma, Jianzhao Liu, Rachid Amine, Xiaoyi Zhang, Cheng-Jun Sun, Yuzi Liu, Yang Ren, Steve M. Heald, Chun-Sheng Wang, Zonghai Chen and Khalil Amine. Enabling high performance Lithium-Sulfur Batteries by manipulating Interfacial Chemistry, under review.

II.I.4   Multi-Functional Cathode Additives (BNL)

Hong Gan, Principal Investigator
Brookhaven National Laboratory
P.O. Box 5000
Upton, NY 11973-5000
Phone: 631-344-4012
E-mail: hgan@bnl.gov

Esther Takeuchi, Co-Principal Investigator
Department of Chemistry
Stony Brook University
100 Nicolls Road, 104 Chemistry
Stony Brook, NY 11790-3400
Phone: 631-216-7414
E-mail: esther.takeuchi@stonybrook.edu

Tien Duong, Technology Manager
U.S. Department of Energy
Phone: 202-586-7836
E-mail: Tien.Duong@ee.doe.gov

Start Date: October 1, 2014   End Date: September 30, 2017
Total Project Cost: $1,500,000   DOE share: $1,500,000   Non-DOE share: $0

Project Introduction

In order for EVs to achieve mass adoption and make a significant dent in U.S and global CO_2 production, the key problems of driving range per charge and cost per kWh must be addressed. Barriers addressed for this project including: 1) low battery energy density (Wh/kg & Wh/L) and low power (W/kg & W/L); 2) battery low cycle life; and 3) high cost ($/kWh).

Objectives

Develop a low cost battery technology for PEV application utilizing Li-S electrochemical system by incorporating conductive Titanium Disulfide (TiS_2) as Multi-Functional Cathode Additives (MFCA) to improve the power performance, consistent with DOE's long-term goals of electric vehicle. In this period, our objective is to further optimize the Li-S cell at the cell component level and cell system level for improved cell performance and demonstrate the 4 mAh coin cells with good cycle life.

Approach

As MFCA for Li-S battery, transition metal sulfides are electronic conductive, electrochemically active with ability in adsorbing polysulfide intermediate to promote cell power, capacity and long cycle life. In the past two years, we have identified TiS_2 as the leading candidates for the sulfur cathode optimization studies. More attention has been directed towards electrode optimization and cell system optimization. New electrode binder was identified for improved sulfur cathode mechanical integrity. New type of carbon material was introduced to achieve electrode with high sulfur loading up to 10 mg/cm^2. During this year, we continued our effort on the system optimization by accomplishing the sulfur cathode formulation and preparation process optimization. We completed the studies of sulfur loading-density interaction and sulfur loading-electrolyte interaction. By incorporating all the improvement, 2032 coin cell with > 4 mAh delivered capacity has been demonstrated with excellent cycle life.

Results

During the present year, we continued the mechanism study of MFCA-sulfur interaction. In parallel, we completed the system optimization at the component and the cell levels and achieved the final 2032 coin cell design with > 4 mAh delivered and with good cycle life. The achievements are highlighted below.

Cathode formulation optimization

In our Phase I study, TiS_2 additive proved to be the true multifunctional, which is beneficial for Li-S cell discharge power capability and cycle life. This year, the cathode formulation optimization was executed using the previously identified binders and carbons, in combination with TiS_2 additive. In the experimental design, either part of the carbon in the formulation is replaced by TiS_2 (Table II-24 - Groups 1 and 2), or part of the S:C composite is replaced by TiS_2 (Table II-24 - Groups 1, 3 and 4).

Table II-24: S-TiS$_2$ hybrid electrode formulation optimization

Group	Sulfur%	Carbon%	TiS$_2$%	Binder%
1	62.0	30.0	0.0	8.0
2	62.0	25.4	4.6	8.0
3	56.0	27.0	9.0	8.0
4	50.0	24.2	17.8	8.0
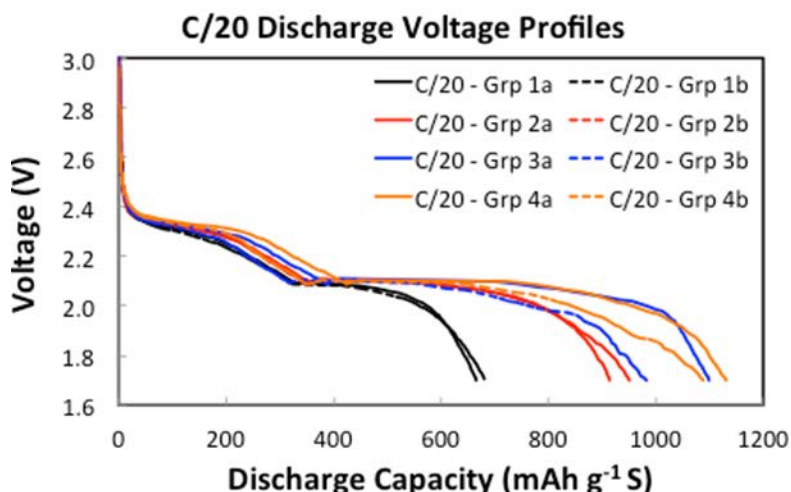
Figure II-551. Cathode formulation effect on sulfur utilization

Figure II-551 shows the effect of cathode formulation on cells sulfur utilization under C/20 discharge rate. The presence of TiS_2 (Group 2) improves the sulfur electrode discharge efficiency comparing with Group 1 cells. Replacing the S:C composite with TiS_2 leads to more improvement in sulfur utilization, from ~41% (Group 1) to ~65% (Groups 3 and 4). Considering the variation in sulfur content in each cathode formulation, the cell discharge capacities at C/5-rate are normalized against the total electrode weight (excluding Al foil). At practical level, Group 3 formulation is the best cathode formulation that results in highest energy density at the total cathode level. Therefore, Group 3 formulation is selected for additional process optimization.

Slurry preparation process evaluation

The TiS$_2$ BET surface area and its uniform distribution within the cathode have been previously identified as factors that correlate to the cell sulfur utilization and cycle life. The cathode slurry process is critical to achieve uniform TiS$_2$ particle distribution. Using Group 3 formulation (Table II-24), three slurry-mixing processes were evaluated. Mixing Process 1 resulted in uniform TiS$_2$ distribution within the coated electrode (Figure II-552), but difficult to obtain high sulfur loading. Mixing Process 2 afforded high sulfur loading, but difficult to achieve uniform TiS$_2$ distribution (Figure II-552). Mixing Process 3 yielded uniform TiS$_2$ distribution (Figure II-552) and ability in achieving high sulfur loading electrode with good mechanical integrity. Based on the consideration of achieving uniform TiS$_2$ distribution and the ability in coating electrode with high sulfur loading (> 6 mg/cm^2), Mixing Process 3 is chosen for further optimization.
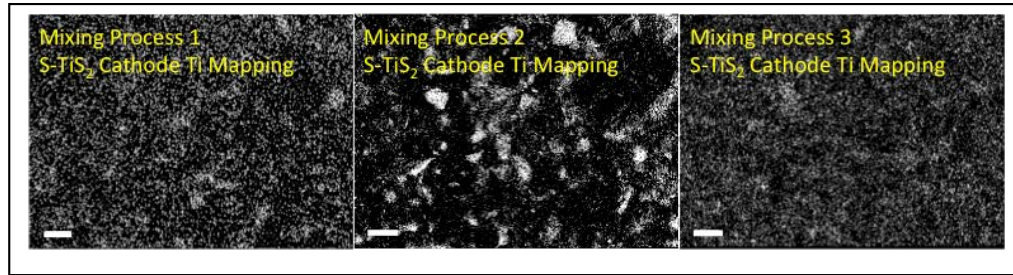
Figure II-552. Slurry mixing process methods vs. TiS2 distribution (EDS) within coated cathode

Sulfur loading and electrode density interaction study

Sulfur loading and electrode density interaction was evaluation. With cathode formulation 3 (Table II-24), the electrodes with sulfur loading of ~2.7, ~4.9, and ~6.7 mg/cm^2 were prepared. Good mechanical integrity was observed for all coated electrodes. The as coated pristine electrodes have density at ~ 0.8 g/cc for all three sulfur loadings. Higher electrode densities were achieved by hydraulic compressing the electrodes between the two flat surface metal blocks under various pressures. The electrode density increases with increasing pressure and starts to level off at ~1.20 to 1.35 g/cc.
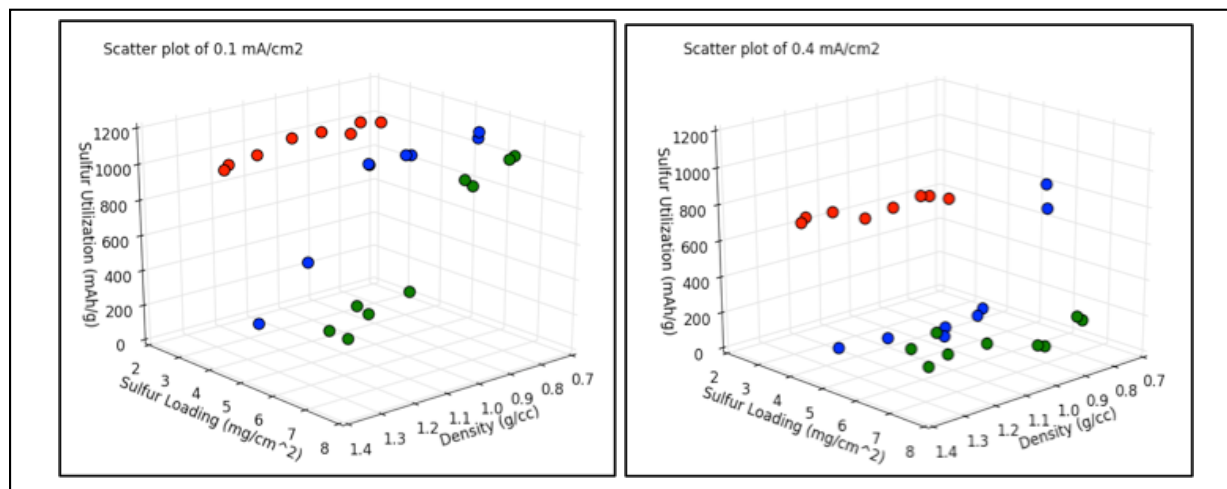
Figure II-553. Sulfur utilization vs. cathode density, sulfur loading and discharge rate

The electrode density has profound effect on coin cell discharge performance and the impact is more significant on the higher sulfur loading electrodes and at higher discharge rate (Figure II-553). Low sulfur loading and low electrode density favor the high sulfur utilization during cell discharge at all current densities

ranging from 0.1 mA/cm^2 to 4.0 mA/cm^2. The best electrochemical performance is derived from cells with pristine electrodes. Based on our estimation, the cathode porosity at density of 0.8g/cc is ~65%, which is about 1.4x the porosity of the 1.2 g/cc density electrode (47% porosity). The results suggest that maintaining the good ionic conductivity with increased electrolyte amount in the cathode pores and cell stack might be a critical factor for enhanced sulfur utilization.

Electrolyte-cathode interaction study

The cathode density-performance relationship uncovered above indicates the potential important role of electrolyte. Figure II-554 shows the relationship between electrolyte to sulfur weight ratio (E/S ratio) and the sulfur utilization under discharge current densities ranging from 0.1 mA/cm^2 to 4.0 mA/cm^2 for cathodes with sulfur loading from 2.5 mg/cm^2 to 11.0 mg/cm^2. With our 2032 coin cell design, the stable sulfur utilization can be achieved at all discharge rates when E/S ratio is $\geq$ 11.6. Although consistent with some literature report, the E/S ratio value is most likely cell design dependent.
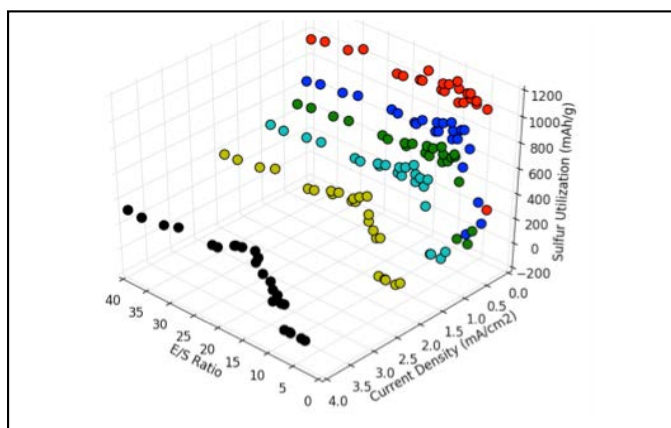
Figure II-554. Sulfur utilization vs. sulfur loading, discharge rate and E/S ratio

We also noticed that the cell cycle life and Coulombic Efficiency (CE) are strongly impacted by the sulfur loading and LiNO$_3$ concentration – suggesting the involvement of anode SEI. This phenomenon is closely associated with the high sulfur loading. Most literature report on Li-S battery study is based on sulfur loading electrode of < 2 mg sulfur per cm^2. However, high sulfur loading cells delivers high areal capacity, which results in deeper lithium anode cycling (high mAh/cm^2). As a consequence, low LiNO$_3$ concentration (0.15M) will no longer sufficient to passivate the lithium anode surface for long cycle life. Higher LiNO$_3$ concentration is preferred to alleviate the cycling efficiency issue for high sulfur loading Li-S cells.

Technology demonstration

By incoporating all the improvement including the material, the components and the process optimization, as well as the cell system level optimization, the > 4 mAh 2032 coin cells with good cycle life is designed and assembled. Various testing are performend to demonstrate the technology.

Coin cell cycle life study

Excellent cell cycle life up to 150 cycles is achieved with > 3.1 mAh/cm^2 areal capacity delivered at 1 mA/cm^2 charging/discharging rate as shown in Figure II-555. Cell capacities were stabilized at ~5 mAh. The goal of achieving 4 mAh delivered capacity is clearly demonstrated. More importantly, the stable cycle life up to 150 cycles is achieved with the high sulfur loading cathode cells.

Temperature effect on discharge efficiency

Discharge temperature has significant impact on cell voltage profiles and delivered capacity. The cell voltage is severely polarized at below 0°C. Higher test temperature leads to lower cell voltage polarization and more

efficient sulfur utilization (Figure II-556). Up to 7.35 mAh (~4.6 mAh/cm^2) is deliverable at 60°C at 1 mA/cm^2 discharge rate.
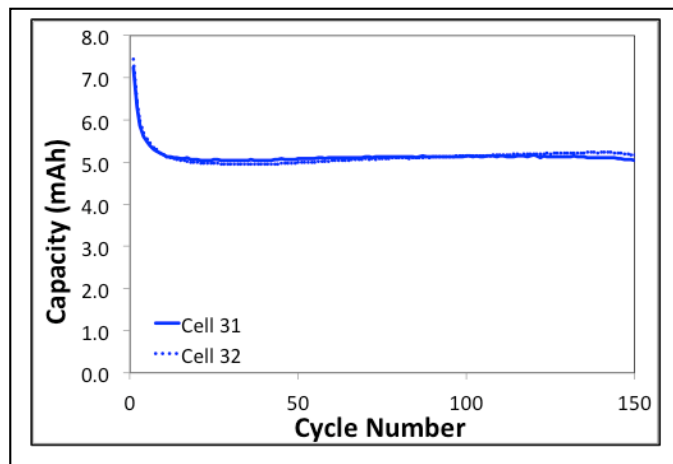
Figure II-555. 2032 coin cells cycle life
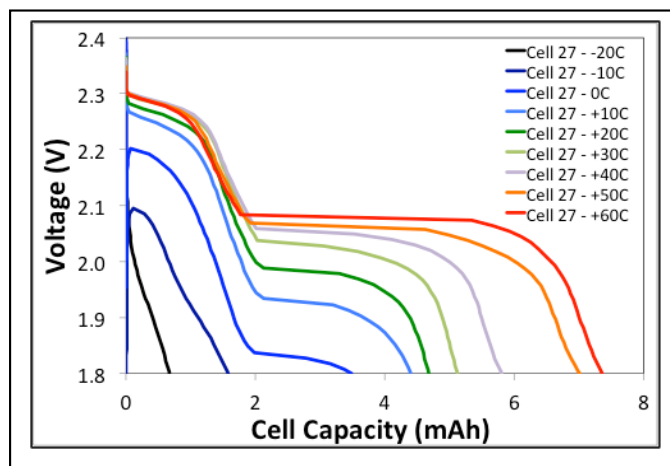
Figure II-556. 2032 coin cells discharge temperature effect

Coin cell shelf life

The shelf life study is executed by storing the coin cells for 30 days at 0°C, 20°C and 50°C respectively either at the freshly build state or at the fully discharged state before cycling testing at room temperature. Lower storage temperature is found to be beneficial for the cell cycle life and capacity retention. 50°C storage causes permanent damage to the fully discharged cells with poor cycle life (Figure II-557). RT or low temperature storage showed no damage to the cell cycling performance.

Coin cell self-discharge

The coin cell self-discharge is determined for cells stored at fully charged state for 1, 7, 14, 21 and 28 days respectively (Figure II-558) after the stabilization cycles. The cell self-discharge primarily happens at the soluble polysulfide discharge region. With the consumption of polysulfides, the self-discharge leveling off. Almost all capacity from the 2nd voltage plateau is still delivered after 4 weeks storage.
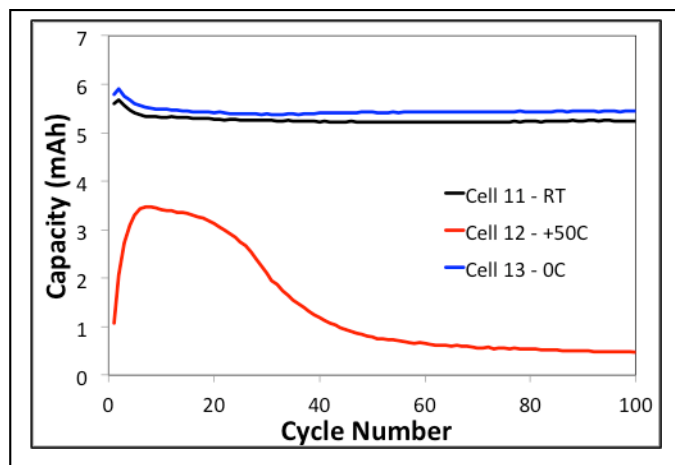
Figure II-557. 2032 coin cells cycling after storage at fully discharge state
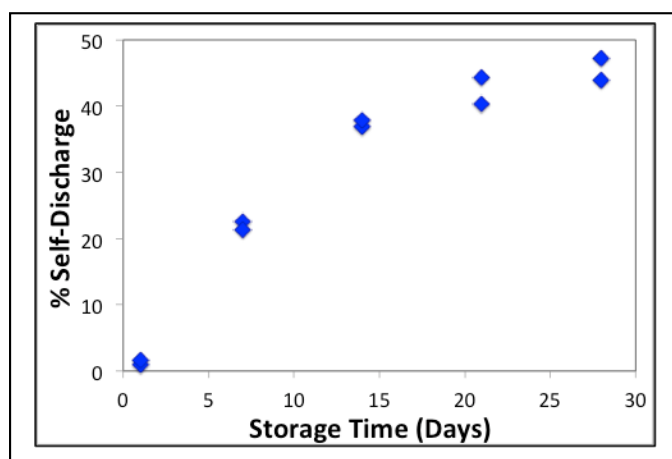
Figure II-558. 2032 coin cells self- discharge

Conclusions

We have successfully achieved all milestones for this 3 years program with the proof of concept MFCA demonstration and identification of TiS_2 as the leading candidate. TiS_2 has been demonstrated experimentally as the true multi-functional additive. In addition, we have achieved high sulfur loading (up to 10 mg/cm^2) by optimizing cathode components/formulation and cathode preparation processes. The optimization studies at the cell component and system level have been completed this year. With the integration of multiple cell design parameters, the 2032 coin cells with ≥ 4 mAh are demonstrated with excellent cycle life. With this performance as the new benchmark, additional research at material, electrode and cell system levels will continue to further improve the performance of Li-S battery technology.

Key Publications

1. Ke Sun, Hellen Liu, Hong Gan, "Cathode loading effect on sulfur utilization in lithium-sulfur battery", *J. Electrochem. En. Conv. Stor.* 13(2), 021002 (2016).

2. Hong Gan, Ke Sun, "Electrochemically Active Interlayers for Lithium Ion Batteries", Provisional patent application, S.N. 62/413,583, filed 10/27/2016.

3. Qing Zhang, David C. Bock, Kenneth J. Takeuchi, Amy C. Marschilok, and Esther S. Takeuchi, "Probing Titanium Disulfide-Sulfur Composite Materials for Li-S Batteries via In Situ X-ray Diffraction (XRD)", *J. of Electrochem. Society*, 164 (4) A897-A901 (2017).

4. Ke Sun, Christina A. Cama, Jian Huang, Qing Zhang, Sooyeon Hwang, Dong Su, Amy C. Marschilok, Kenneth J. Takeuchi, Esther S. Takeuchi and Hong Gan, "Effect of Carbon and Binder on High Sulfur Loading Electrode for Li-S Battery Technology", *Electrochimica Acta* 235 (2017) 399-408. http://dx.doi.org/10.1016/j.electacta.2017.03.023

5. Ke Sun, Qing Zhang, David C. Bock, Xiao Tong, Dong Su, Amy C. Marschilok, Kenneth J. Takeuchi, Esther S. Takeuchi and Hong Gan, "Interaction of TiS_2 and Sulfur in Li-S Battery System*", J. Electrochem. Soc.* **164** (6) A1-A7 (2017).

6. Ke Sun, Chonghang Zhao, Cheng-Hung Lin, Eli Stavitski, Garth Williams, Jianming Bai, Eric Dooryhee, Klaus Attenkofer, Juergen Thieme, Yu-chen Karen Chen-Wiegart, Hong Gan, *"Operando* Multi-modal Synchrotron Investigation for Structural and Chemical Evolution of Cupric Sulfide (CuS) Additive in Li-S battery", *Scientific Reports| 7: 12976 | DOI:10.1038/s41598-017-12738-0.

II.I.5 Development of High Energy Lithium-Sulfur Batteries (PNNL)

Jun Liu, Principal Investigator
Pacific Northwest National Laboratory
902 Battelle Boulevard
Richland, WA 99354
Phone: 509-375-4443; Fax: 509-371-6242
E-mail: jun.liu@pnnl.gov

Dongping Lu, Co-Principal Investigator
Pacific Northwest National Laboratory
902 Battelle Boulevard
Richland, WA 99354
Phone: 509-372-4483; Fax: 509-375-2186
E-mail: dongping.lu@pnnl.gov

Tien Duong, Technology Manager
U.S. Department of Energy
Phone: 202-586-7836
E-mail: Tien.Duong@ee.doe.gov

Start Date: October 1, 2015   End Date: September 30, 2018
Total Project Cost: $1,160,000   DOE share: $1,160,000   Non-DOE share: $0

Project Introduction

The lithium-sulfur (Li-S) battery is a promising alternative to the state-of-the-art Li-ion batteries, owing to its high theoretical specific energy (~2300 Wh kg^{-1}) and the low cost and abundance of sulfur. However, the practical deployment of Li-S batteries is hindered by a low accessible energy density and poor long-term cycle life. Recent attempts to improve performance of Li-S batteries focused on the development of nanostructured sulfur host materials and demonstrated encouraging progress in terms of either high sulfur utilization rate or stable battery cycling. However, most of those studies are based on thin-film electrodes with low sulfur loadings (<2 mg cm^{-2}). For practical applications, instead, high sulfur loading cathodes with the lowest possible parasitic content are needed. Unfortunately, it is quite challenging to improve sulfur mass loading while maintaining the high sulfur utilization rate and cycling stability demonstrated in thin-film electrodes. A widely adopted strategy to prepare high loading electrodes is to employ thick, porous current collectors or free-standing carbon paper substrates as sulfur hosts. However, the high content of porous carbon materials not only increases electrode volume but also requires excess electrolyte for full electrode wetting, which significantly lowers volumetric and gravimetric energy density of the battery. So, a way to achieve both high energy density and stable cycling on high loading and dense sulfur electrodes is of key importance for technology maturation of Li-S batteries. A facile integration approach was developed at PNNL for sulfur cathode material synthesis (U.S. Patent No. 9,577,250), and sulfur electrodes with adjustable loadings of 2-11 mg cm^{-2} can be successfully prepared at large scale using an industrial slurry casting method. The electrode wetting issues associated with high-loading sulfur electrodes were successfully addressed by using novel electrode additives (U.S. Patent Application No. 30459-E). To improve energy density (Wh L^{-1}) and specific energy (Wh kg^{-1}) of Li-S batteries, control of sulfur cathode porosity is essential but may negatively affect sulfur utilization rate and/or cell cycling. A clear understanding of such correlation is critical but rarely mentioned in the literature. In FY 2017, the benefits and drawbacks of controlling electrode porosity to improve cell performance were investigated based on high-loading sulfur cathodes. Issues associated with using high loading and dense electrodes were identified. Insight into the fundamental mechanism of those issues was gained using advanced characterization tools, and effective approaches were demonstrated to address the issues.

Objectives

- Improve volumetric energy density of sulfur cathodes through electrode porosity control and study its effects on cell performance.

- Study the fundamental reaction mechanism of electrolyte/additive with lithium sulfides/polysulfides using advanced characterization tools.

- Develop new approaches to retain high capacity in high-loading sulfur electrodes and enable stable operation of high energy Li-S batteries.

Approach

To develop high energy sulfur cathodes for practical Li-S battery and understand the underlying mechanisms, the following approaches were adopted:

- Study effects of cathode porosity on cell energy density, Li anode morphology, and cell cycling stability using sulfur electrodes with loading >4 mg cm^{-2}.

- Investigate the degradation mechanism of LiNO$_3$ in sulfur cathodes and its effects on cell coulombic efficiency and cycling stability.

- Develop cross-linked-polymer-coated separator to minimize quick capacity and efficiency decay in the early-stage cycling of thick sulfur electrodes.

- Employ pouch cells to advance the understanding of the Li-S battery at a practical scale.

Results

1. Effects of electrode porosity on cell performance with high-loading sulfur cathode.

Using nonporous Li metal as anode, the thickness and porosity of a sulfur cathode determine not only the energy density of the Li-S battery but also the minimum electrolyte amount for electrode wetting, which also has a significant effect on specific energy of batteries. This, however, is rarely discussed in the literature. In FY17, we studied effects of sulfur cathode porosity based on thick electrodes with sulfur loading >4 mg cm^{-2}. Sulfur electrode porosity shows strong dependence on calendering pressure, which can be explained by high porosity and low tap densities of the carbon and sulfur/carbon composites. Electrode porosity decreases quickly from the original ca. 64% (~120 μm) to ca. 29% (~60 μm) with calendering pressure increase from 0.2 to 1.5 ton (T) (electrode area, 1.6 cm^2) (Figure II-559a). A direct benefit of reducing electrode porosity is significant improvement of the electrode energy density, which is desirable for electric vehicle batteries. For a pristine, uncompressed electrode (4 mg cm^{-1}, 120 μm thick), the tested electrode energy density is only 650 Wh L^{-1}, which was easily doubled to 1300 Wh L^{-1} when the electrode was compressed to 60 μm (Figure II-559b). These results strongly suggest that appropriate control of electrode porosity/thickness is essential in developing high energy Li-S batteries. Another important benefit of decreasing electrode porosity is remarkable reduction of required electrolyte amount, which in fact has significant effect on cell specific energy. For thick, porous sulfur electrodes, more electrolyte is required to enable fast sulfur conversion kinetics and high utilization rate, but greatly decreases system specific energy. Figure II-559c shows the relationship of electrode porosity and required electrolyte amount, assuming that all the pores of both electrode and separator are filled with electrolyte. More than 11 μL electrolyte is required for a pristine 120 μm electrode, which converts to an electrolyte/sulfur (E/S) ratio of 2.75 μL electrolyte/mg S, while only 4. 7 μL electrolyte is needed for the 60 μm dense electrode with corresponding E/S ratio of 1.17 μL mg^{-1}. This provides an important guideline for sulfur cathode design when pursuing a very low E/S ratio for improved system specific energy. Reducing electrode porosity has negative effects on both sulfur utilization and cell cycling stability, due to reduced uptake of electrolyte amount and confined mass transport. Figure II-559d compares cycling stability of cells with electrodes of different porosities. Stable cycling with 83% capacity retention for 200 cycles was realized with a pristine electrode without calendering. For the calendered electrodes (80 and 60 μm thick), capacity retention decreased slightly to 76% after 200 cycles. These results

suggest that a tradeoff between cell energy density and cycle life should be considered when designing sulfur cathodes for different applications.
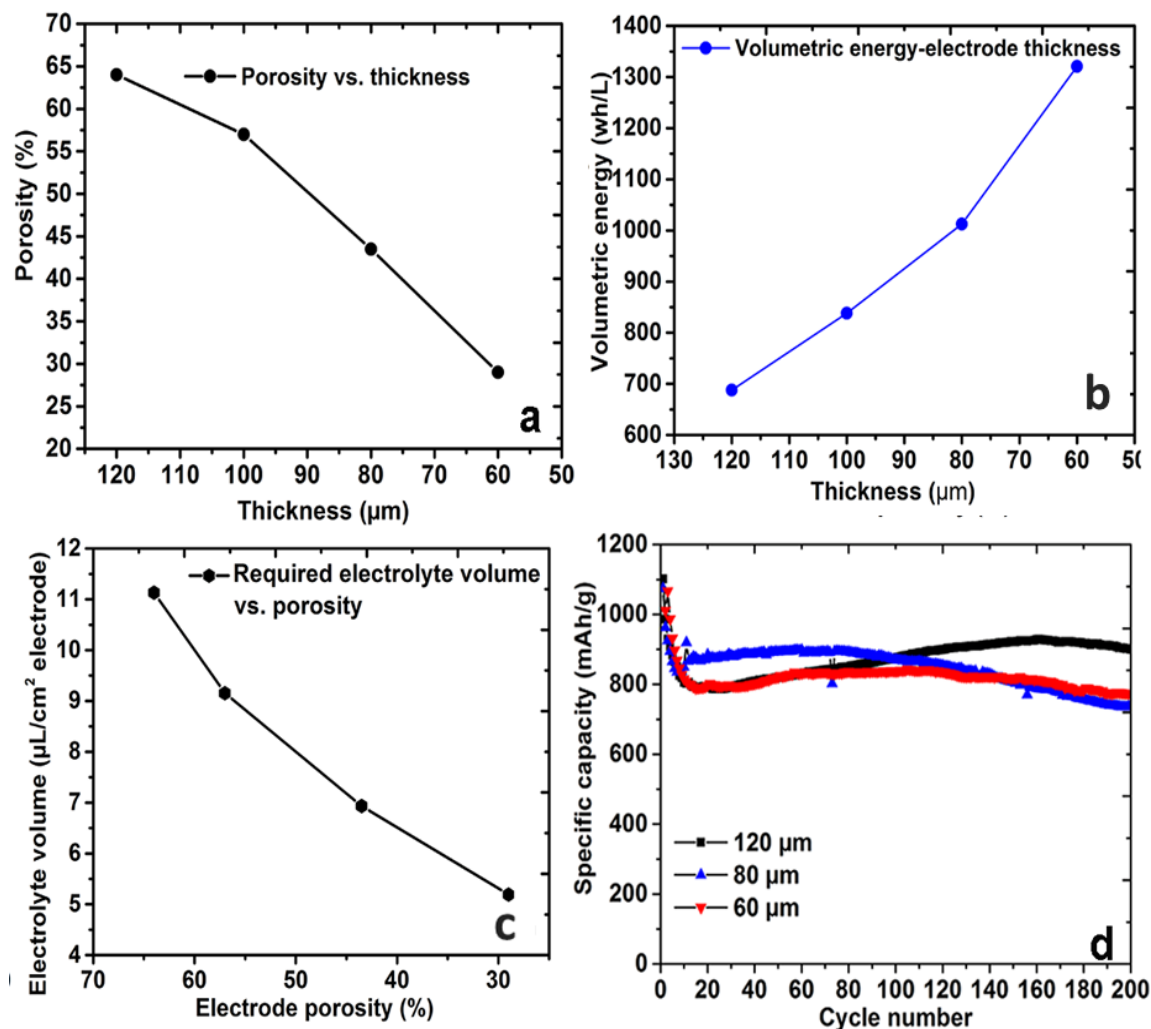
Figure II-559. (a) Correlation of electrode porosity and thickness, (b) dependence of volumetric energy density on electrode thickness, (c) minimum electrolyte amounts for electrodes with different porosities, and (d) cycling stability of electrodes compressed to different thicknesses/porosities (Sulfur loading of electrodes: 4 mg cm^{-2}; electrolyte 1 M LiTFSI/DOL/DME with 0.2 M LiNO$_3$ and 0.15 M Li$_2$S$_6$ as additives).

Large volume expansion of sulfur and quick growth of Li interphase upon repeated cycling are among the most significant challenges for practical Li-S batteries. It is interesting to find that a dense sulfur electrode with reduced porosity can not only help preserve cathode architecture but also suppress Li interphase growth. Scanning electron microscope (SEM) characterization indicates the dense sulfur cathodes expand slightly from ca. 60 to ca.75 µm after 200 cycles (Figure II-560b), a 25% volume expansion. In addition, significant sulfur redistribution and electrode reorganization both on the electrode surface and through the thickness are absent (Figure II-560a and Figure II-560b). This is because the low porosity and high tortuosity of the dense electrode can effectively minimize free migration of soluble polysulfides inside the electrode. The Li anode coupled with a dense sulfur cathode also exhibits much improved morphology after long-term cycling, i.e., smooth surface and dense interface layer (Figure II-560c and Figure II-560d), copying the morphology of the dense sulfur cathode. The interphase layer formed over the Li metal is compact and 127 µm thick after 200 cycles, which is only half that of the Li interphase when coupled with uncalendered sulfur electrodes. One explanation is that

the dense sulfur cathode can provide and maintain uniform internal pressure on the Li anode during cell cycling, which can suppress mossy Li growth and interphase formation to some extent. In contrast, with a porous and soft cathode, both polysulfide migration and Li plating/stripping are out of control without the uniform internal pressure; this usually results in nonuniform sulfur redistribution and random growth of thick and porous Li interphase.
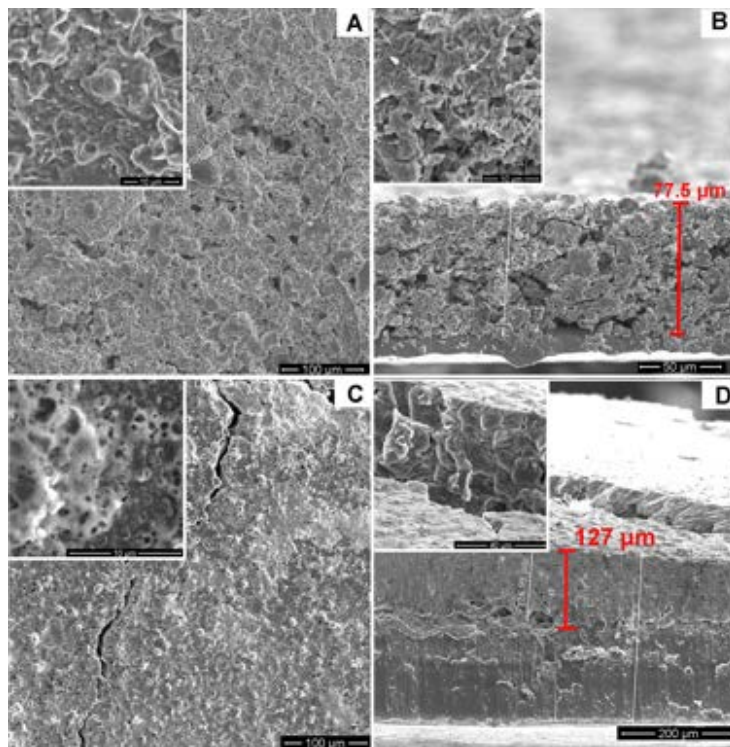
Figure II-560. SEM images of sulfur cathode (pressed to 60 µm) (A: surface; B: cross section) and corresponding Li metal anode (C: surface; D: cross section) after 200 cycles. (Sulfur loading 4 mg cm^{-2} and 250 µm Li).

2. Reaction mechanism of lithium sulfides/polysulfides with electrolyte/additive

While stable cycling has been demonstrated with high-loading sulfur cathodes (Figure II-559d), a common issue observed in those cells is the quick capacity and efficiency decay in the first 5 to 10 cycles. It becomes more serious when sulfur loading is further increased, for example, to around 6.5 mg cm^{-2}. After a certain number of cycles, the cell even failed with endless charging (Figure II-561b), indicating quick depletion of LiNO$_3$. A systematic study was performed to understand the reasons for this phenomenon. Results of in situ electron paramagnetic resonance (EPR) and high-performance liquid chromatography (HPLC) analysis indicate that LiNO$_3$ can directly react with Li$_2$S/Li$_2$S$_2$ in the cathode, which weakens its function and durability for Li protection. This is exacerbated in high-loading sulfur cathodes where excess of Li$_2$S/Li$_2$S$_2$ are generated. Electrochemical study proves that LiNO$_3$ can also react with some soluble polysulfide species, such as Li$_2$S$_6$. As shown in Figure II-561c, a solution containing both LiNO$_3$ and Li$_2$S$_6$ shows greatly reduced peak intensity at 1.6–1.7 V but increased peak intensity at ~2.0 V compared to the baseline electrolytes with the same concentrations of LiNO$_3$ or Li$_2$S$_6$ individually. This is due to chemical reduction of LiNO$_3$ by Li$_2$S$_6$ or other derived polysulfide species. X-ray photoelectron spectroscopy (XPS) analysis identified formation of high-valence sulfur species SO$_3^{2-}$/SO$_4^{2-}$ from the LiNO$_3$ and Li$_2$S$_6$ mixture solution, which further proved the direct chemical reactions between LiNO$_3$ and polysulfides, a new degradation pathway of LiNO$_3$ in Li-S batteries. From these new findings of LiNO$_3$ degradation pathways, more effective approaches or electrolyte additives for Li anode protection are required for highly efficient and long-term cycling of Li-S batteries.
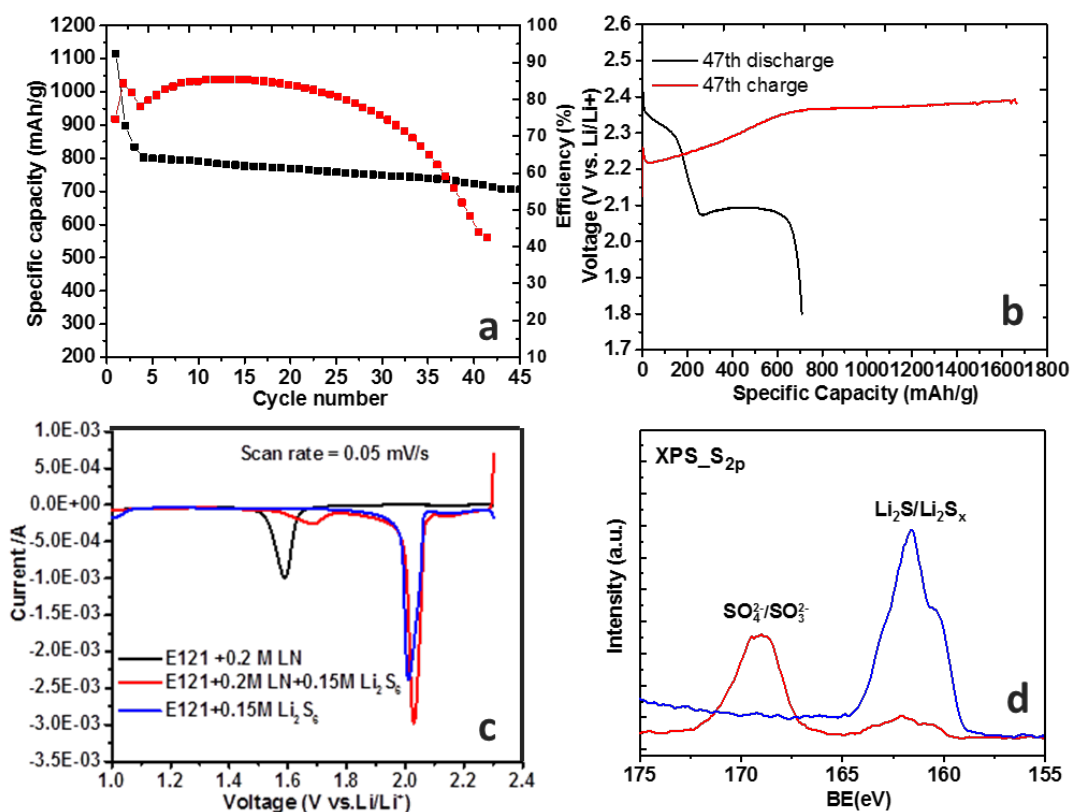
Figure II-561. (a) Cycling stability and coulombic efficiency of thick electrode with sulfur loading 6.5 mg cm^{-2} and (b) typical failed charge/discharge profiles (47th cycle), (c) cyclic voltammetry of carbon paper electrodes with electrolytes 1 M LiTFSI/DOL/DME+0.2 M LiNO₃ (black), 1 M LiTFSI/DOL/DME + 0.15 M Li₂S₆ (blue), and stored 1 M LiTFSI/DOL/DME + 0.2 M LiNO₃ + 0.15 M Li₂S₆ (red), and (d) XPS analysis of dried electrolytes 1 M LiTFSI/DOL/DME + 0.15 M Li₂S₆ (blue) and 1 M LiTFSI/DOL/DME + 0.2 M LiNO₃ + 0.15 M Li₂S₆ (red).

3. Cross-linked polymer coating to minimize early-stage quick capacity drop and efficiency fluctuation in thick sulfur electrodes

Direct chemical reactions of LiNO₃ with sulfide and polysulfides accelerate depletion of LiNO₃, resulting in fast efficiency decay of high-loading sulfur electrodes. To address this problem, we developed a cross-linked polyacrylic acid (C-PAA)-coated separator to partially trap LiNO₃ and suppress polysulfide diffusion. The blocking effect of C-PAA for polysulfide crossover was investigated with an H-type cell (Figure II-562), in which a highly concentrated polysulfide solution (0.15 M Li₂S₆ in 1 M bis(trifluoromethanesulfonyl)imide (LiTFSI)/1,3-dioxolane (DOL)/1,2-dimethoxyethane (DME)) and benchmark electrolyte (1 M LiTFSI/DOL/DME) were separated by a Celgard 2400 separator with or without C-PAA coating. Polysulfide could easily cross the pristine separator and migrate to the opposite chamber driven by concentration difference (Figure II-562a); however, this was suppressed significantly when a C-PAA coated separator was used (Figure II-562b). In addition, carbon nanofibers (CNFs) were introduced during the cross-linking of PAA, which provides reaction sites to reuse the blocked polysulfide on the separator. SEM images indicate the cross-linked PAA and CNFs form a relatively dense and uniform coating on the separator (Figure II-562c). Effectiveness of the C-PAA coated separator on cell performance was tested with high-loading sulfur cathodes (>4 mg cm^{-2}). Using an uncoated separator, the discharge capacity drops quickly from 1100 mAh g^{-1} to 810 mAh g^{-1} after 5 cycles, accompanied by an efficiency drop from 92% to 89% (Figure II-562d). For the cell with C-PAA coated separator, the first cycle discharge capacity and efficiency are 915 mAh g^{-1} and 97%, respectively, and are maintained as high as 950 mAh g^{-1} and 96.4%, respectively, after 5 cycles, suggesting effectively suppressed polysulfide crossover. Besides blocking the effects of polysulfides, the C-PAA coated

separator can also trap more $LiNO_3$ and thus extend the durability of $LiNO_3$ for Li protection compared to the pristine separator.
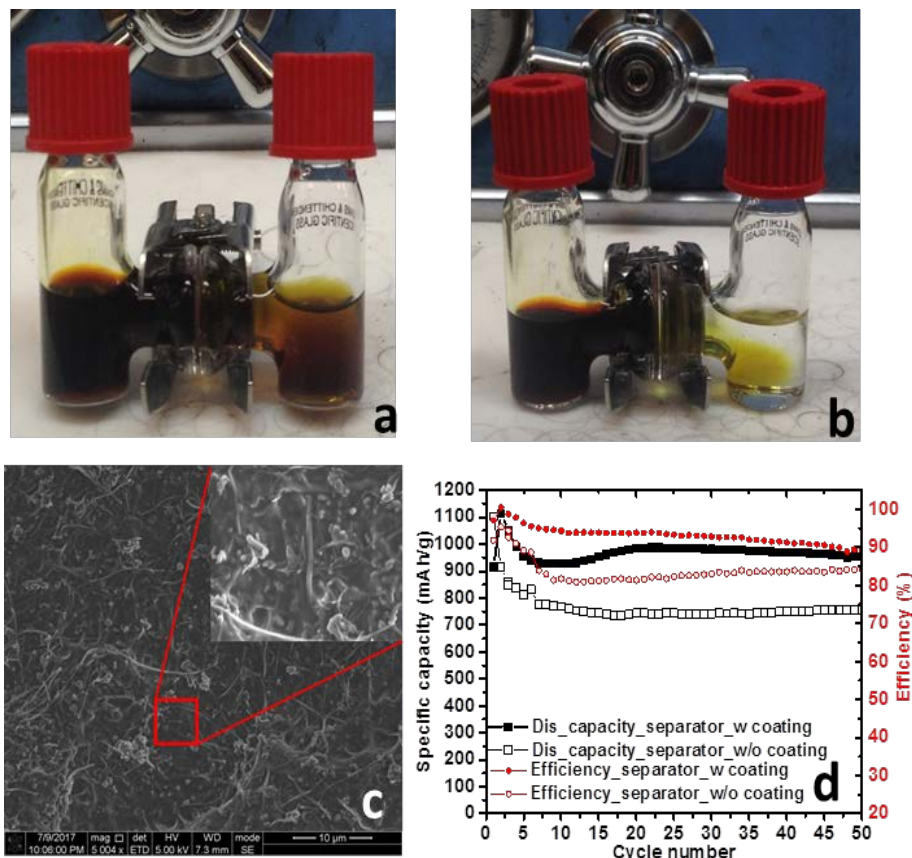
Figure II-562. Visual comparison of polysulfide diffusion in H-cell using Celgard 2400 separator with (a) and without (b) C-PAA coating after 1 h rest, (c) SEM image of C-PAA/CNF coated separator, and (d) capacity and coulombic efficiency of Li-S cells using separators with (solid symbols) and without (hollow symbols) C-PAA coating.

4. Study of electrolyte/sulfur ratio on cell performance with practical pouch cells

1.6 Ah Li-S pouch cells with specific energy of 247 Wh kg^{-1} has been demonstrated in this work. To achieve higher energy, not only should the areal capacity of sulfur cathodes be improved significantly but also the parasitic weight of the cell components must be minimized; for this, electrolyte amount is a key parameter (43.6 wt%, Figure II-563a). To reach 300 Wh kg^{-1}, the areal capacity of a sulfur cathode should be at least 5.0 mAh cm^{-2}, while the E/S ratio should be less than 3 μL mg^{-1}. Therefore, pouch cells in this study are based on cathodes with sulfur loading ~5.7 mg cm^{-2} and porosity < 55%, a 50 μm thick lithium anode (~10 mAh cm^{-2}, anode/cathode ratio < 2) and controlled E/S ratio from 2.7 to 7.2. Figure II-563c shows the dependence of electrode areal capacity and sulfur utilization rate on the E/S ratio. When E/S > 7, the deliverable areal capacity is 5.5 mAh cm^{-2} with a high sulfur utilization, above 950 mAh g^{-1}. Reducing the E/S ratio to 4.9, areal capacity and sulfur utilization rate decline slightly to 5.0 mAh cm^{-2} and 880 mAh g^{-1}, respectively. But for E/S < 2.8, a significant decrease of both areal capacity and sulfur utilization rate is observed. However, with the C-PAA coated separator (coating < 1 mg cm^{-2}), remarkable improvement is observed. 5.05 mAh cm^{-2} and 870 mAh g^{-1} are achieved at E/S = 2.7, which are comparable to those at E/S = 4.9 with a pristine separator. An even lower E/S ratio is predictable in practical multiple-layer pouch cells. These results verified that our approaches of dense cathode, electrode additives, and modified separator are applicable to fabrication of practical pouch cells

Figure II-563. (a) Component weight distribution of Li-S battery with energy density of 300 Wh kg^{-1}, (b) photo of single-layer pouch cell used in present study (Electrode working area 19.4 cm^2 and sulfur mass loading 5.7 mg cm^{-2}), and (c) dependence of first-discharge areal capacity and specific capacity on electrolyte/sulfur ratio (black symbol - pouch cell using pristine separator; red symbol - pouch cell using modified separator).

Conclusions

The effects of electrode porosity on cell performance as well as system energy density were investigated using high-loading sulfur electrodes. Electrode porosity reduction at a given sulfur loading significantly reduces both electrode volume and the amount of electrolyte required to wet the electrode, which leads to large increases in both energy density (Wh L^{-1}) and specific energy (Wh kg^{-1}) of Li-S batteries. To understand the quick capacity and coulombic efficiency degradation observed in the early-stage cycling of high-loading sulfur electrodes, systematic study was performed to probe the interactions between $LiNO_3$ and sulfur species. In situ EPR and HPLC study identified direct redox reactions of $LiNO_3$ with Li_2S/Li_2S_2, while electrochemical characterization combined with XPS analysis proved the interactions between $LiNO_3$ and polysulfides. This study uncovered a new degradation pathway of $LiNO_3$ in Li-S battery. Accordingly, a cross-linked polyacrylic acid (C-PAA)-coated separator was developed to partially trap $LiNO_3$ and concurrently suppress polysulfide crossover. Practical pouch cells were employed to extend our proposed approaches and study the effects of electrolyte/sulfur ratio on cell performance. Using a C-PAA-coated separator, a pouch cell with a dense sulfur cathode ($\sim$5.7 mg cm^{-2}, porosity < 55%), thin anode (50 μm Li anode), and lean electrolyte (E/S = 2.7) can deliver an areal capacity of 5.05 mAh cm^{-2} and a sulfur utilization of 870 mAh g^{-1}.

Key Publications

1. J. Xiao, D. Lu, J. Liu, J. Zhang, and G. Graff. Thick Electrodes Including Nanoparticles Having Electroactive Materials and Methods of Making Same. **U.S. Patent No. 9,577,250**, granted date: February 21, 2017.

2. J. Xiao, D. Lu, Y. Shao, W. Bennett, G. Graff, J. Liu, and J. Zhang. Electrolyte for Batteries with Regenerative Solid Electrolyte Interface, **U.S. Patent No. 9,722,277**, granted date: August 1, 2017.

3. D. Lu, Q. Li, J. Liu, J. Xiao, J. Zhang, J. Liu, and G. Graff. Additives to Enhance Electrode Wetting and Performance and Methods of Making Electrodes Comprising the Same, **Patent application: No. 30459-E**

4. D. Lu, Q. Li, J. Liu, J. Zheng, Y. Wang, S. Ferrara, S. Chen, J. Xiao, J. Zhang, and J. Liu. Enabling High Capacity and High Energy Density Cathode for Lithium-Sulfur Batteries, Submitted.

5. D. Lu, J. Tao, P. Yan, W. Henderson, Q. Li, Y. Shao, M. Helm, O. Borodin, G. Graff, B. Polzin, C. Wang, J. Zhang, J. Yoreo, J. Liu, and J. Xiao, Formation of Reversible Solid Electrolyte Interface on Graphite Surface from Concentrated Electrolytes, Nano Letters 2017 17 (3), 1602-1609.

6. D. Lu, Q. Li, J. Liu, S. Wilson, J. Zhang, and J. Liu, Enhanced Performance of High Energy Sulfur Cathode for Lithium-Sulfur Batteries, 253rd ACS National Meeting & Exposition, San Francisco, CA, April 2-6, 2017

7. D. Lu, J. Xie, Q. Li, Y. Wang, S. Wilson, J.-G. Zhang, and J. Liu, Development of High Energy Sulfur Cathode for Lithium-Sulfur Batteries, Beyond Lithium Ion X, Almaden, CA June 27-30, 2017.

II.I.6 Nanostructured Design of Sulfur Cathodes for High Energy Lithium-Sulfur Batteries (Stanford University)

Yi Cui, Principal Investigator
Department of Materials Science and Engineering
Stanford University
Stanford, CA 94305
Phone: 650-723-4613; Fax: 650-736-1984
E-mail: yicui@stanford.edu

Tien Duong, Technology Manager
U.S. Department of Energy
Phone: 202-586-7836
E-mail: Tien.Duong@ee.doe.gov

Start Date: October 1, 2016   End Date: September 30, 2017
Total Project Cost: $300,000   DOE share: $300,000   Non-DOE share: $0

Project Introduction

Lithium-sulfur batteries can bring about significant improvements to the current state-of-the-art battery technologies due to its high specific energy density and cost saving. The capacity decay of lithium-sulfur battery during cycling is a multifaceted problem. There exist multiple materials challenges that prevent it from reaching the cycling performance suitable for portable electronics and electrical vehicles. The rapid capacity decay of sulfur cathode can be attributed to several reasons: 1) significant volumetric expansion (~80% change) when sulfur is reduced to lithium sulfide (Li_2S); 2) dissolution of intermediate lithium polysulfides (Li_2S_x, $4 \leq x \leq 8$) in the electrolyte; 3) low ionic and electronic conductivity of both sulfur and Li_2S.

Introducing anchoring materials, which can induce strong binding interaction with Li_2Sx species, has been demonstrated as an effective way to overcome this problem and achieve long-term cycling stability and high-rate performance. The interaction between Li_2S_x species and anchoring materials should be studied at the atomic level in order to understand the mechanism behind the anchoring effect and to identify ideal anchoring materials to further improve the performance of Li-S batteries. The importance of balancing sulfide species adsorption and diffusion on anchoring materials with better surface diffusion will lead to higher Li_2S deposition efficiency. In the reverse reaction process, catalysis of the decomposition of Li_2S and oxidization of Li_2S to Li_2S_x and finally to sulfur near the surface of the substrate are crucial steps to realizing high capacity and Columbic efficiency, yet have been relatively neglected in the Li-S chemistry. In this respect, a systematic consideration of the substrates that are capable of catalyzing Li_2S decomposition is also critical to the development of advanced Li-S batteries.

Objectives

The charge capacity limitations of conventional transition metal oxide cathodes are overcame by designing optimized nano-architectured sulfur cathodes. This study aims to enable sulfur cathodes with high capacity and long cycle life by developing sulfur cathodes from the perspective of nanostructured materials design, which will be used to combine with lithium metal anodes to generate high-energy lithium-sulfur batteries. The selection criterion of anchoring materials is proposed to guide the rational design of cathode materials for advanced Li-S batteries. Novel sulfur nanostructures will be designed and adsorption/diffusion/catalytic mechanism will be proposed to overcome the issues related to sulfur volume expansion, polysulfide dissolution and insulating nature of sulfur/Li_2S. A standard procedure to quantitatively compare the polysulfide adsorption capability of candidate materials was also established.

Approach

Using first-principles approach with van der Waals interaction included, we systematically investigate the adsorption of Li_2S_x species on various oxides, sulfides and nitrides, and study the detailed interaction and electronic structure, including binding strength, diffusion energy barrier and catalytic effect. We gain insight into how van der Waals interaction and chemical binding contribute to the adsorption of Li_2S_x species for anchoring materials with strong, medium, and weak interactions. Combining theoretical calculations and experimental design, we select a series of metal oxides/sulfides/nitrides as model systems to identify the key parameters in determining the energy barrier for Li_2S oxidation and polysulfide adsorption. We also establish a standard procedure to quantitatively compare the polysulfide adsorption capability of various candidate materials.

Results

To understand the role of metal sulfides in catalytic decomposition of Li_2S, we systematically investigated the effect of six kinds of metal sulfides including VS_2, CoS_2, TiS_2, FeS, SnS_2 and Ni_2S_3 on tuning the decomposition energy barrier. According to our simulation of electronic band structures, Ni_3S_2, FeS and CoS_2 are metallic materials while VS_2 and TiS_2 are semi-metallic, which means that they are all materials with good electrical conductivities while SnS_2 is a semiconductor with a band gap of 2.2 eV. Carbon material (a graphene/carbon nanotube hybrid (G/CNT)) was chosen for comparison. The cathode consists of a commercial Li_2S cathode material mixed uniformly with various metal sulfides, carbon black and polyvinylidene fluoride (PVDF) binder. Coin cells were assembled with lithium metal as anode and reference electrode. The initial charge voltage profiles was used to clearly show the activation barrier (Figure II-564A). The G/CNT-Li_2S cathode without the addition of metal sulfide exhibits a high potential barrier at about 3.41 V in the initial charging process, indicating a sluggish activation process with high charge-transfer resistance. The SnS_2-Li_2S cathode shows a clear voltage jump with a potential barrier of 3.53 V during the activation process due to the semiconducting nature of SnS_2. The charge voltage plateaus after the short voltage jump represent the phase conversion reaction from Li_2S to low-order LiPSs, high-order LiPSs and sulfur. A similar charging phenomenon is observed for Ni_3S_2-Li_2S and FeS-Li_2S electrodes with high potential barriers of 3.47 and 3.25 V even though both are metallic. However, the addition of CoS_2, VS_2, and TiS_2 significantly reduces the height of the potential barrier to 3.01, 2.91 and 2.88 V, respectively. The lower potential barrier and longer voltage plateau of the CoS_2, VS_2 and $TiS_{2-based}$ electrodes compared to other metal sulfides indicate improved conductivity and reduced charge-transfer resistance.

To attain an in-depth understanding of the function of these metal sulfides, we use the climbing-image nudged elastic band (CI-NEB) method to calculate the barrier for Li_2S decomposition in order to evaluate the delithiation reaction kinetics on the surface of different metal sulfides. Here, we consider the decomposition process from an intact Li_2S molecule into a LiS cluster and a single Li ion ($Li_2S \rightarrow LiS + Li^+ + e^-$). The main evolution is composed of the Li ion moving far away from the S atom in the Li_2S molecule, which is accompanied by breaking of the Li-S bond. The energy profiles for the decomposition processes on different sulfides are shown in Figure II-564B. The Ni_3S_2 decomposition barrier is as high as 1.03 eV, much larger than the other five cases, and is consistent with the large initial voltage barrier for Ni_3S_2 added Li_2S cathode. The barriers for FeS, CoS_2, VS_2 and TiS_2 are 0.63, 0.56, 0.31 and 0.30 eV, respectively, and qualitatively agree with the voltage magnitudes measured experimentally. For SnS_2, the calculated barrier for decomposition is as low as 0.32 eV, but experimentally exhibits a very large initial charge potential. This can be probably attributed to the insulating nature of SnS_2 and the electron-ion recombination process, which is the rate-determining step for the delithiation process, but not the Li decomposition process. Figure II-564C-H illustrate the decomposition pathway for one Li ion departing from the LiS cluster on the surface of six kinds of sulfides. It can be clearly seen that the decomposition process is associated with the binding between the isolated Li ion and the sulfur in sulfides. This is the dominant reason that the sulfide anchor can induce a lower decomposition barrier compared with carbon materials. For graphene, the chemical interaction between the Li ion and carbon is much weaker, and therefore, the decomposition process should have a very large activation energy barrier (Figure II-564I, 1.81 eV according to our simulation).
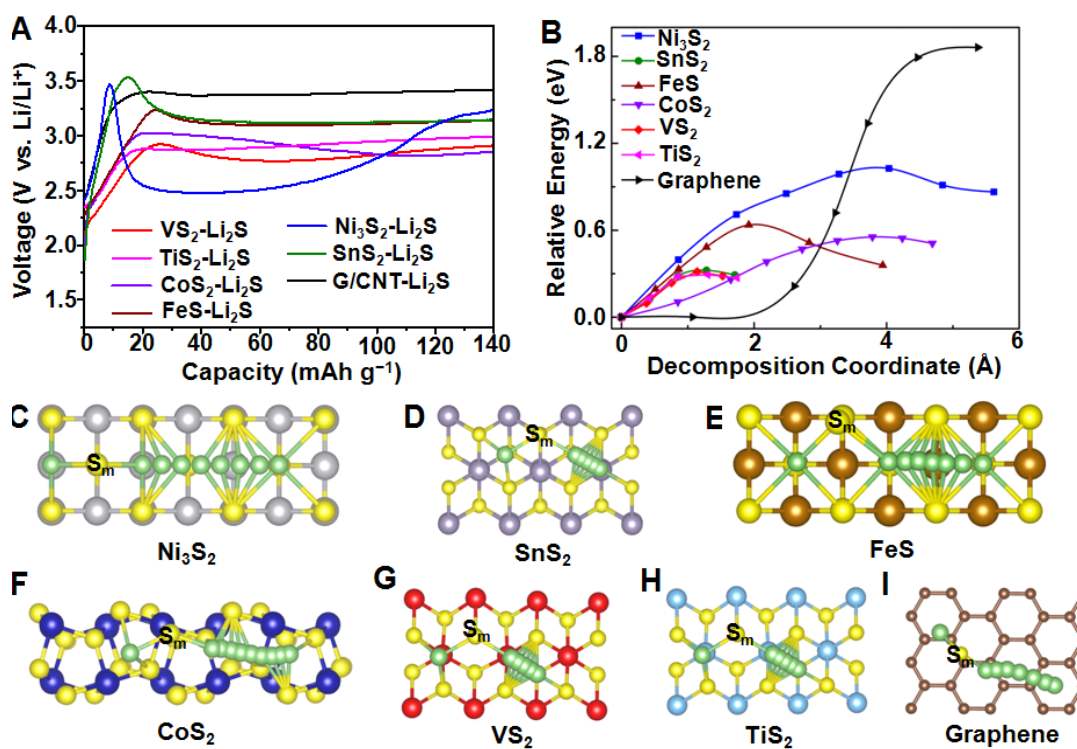
Figure II-564. (A) First cycle charge voltage profiles of Ni_3S_2-Li_2S, SnS_2-Li_2S, FeS-Li_2S, CoS_2-Li_2S, VS_2-Li_2S, TiS_2-Li_2S and G/CNT-Li_2S electrodes. (B) Energy profiles for the decomposition of Li_2S cluster on Ni_3S_2, SnS_2, FeS, CoS_2, VS_2, TiS_2 and graphene. Top view schematic representations of the corresponding decomposition pathways for (C) Ni_3S_2, (D) SnS_2, (E) FeS, (F) CoS_2, (G) VS_2, (H) TiS_2 and (I) graphene. Here, green, yellow, grey, purple, brown, blue, red, cyan and beige balls symbolize lithium, sulphur, nickel, tin, iron, cobalt, vanadium, titanium and carbon atoms, respectively. S_m represents the sulfur atom in the Li_2S cluster.

Figure II-565A shows the galvanostatic discharge/charge voltage profiles of S-VS_2@G/CNT electrode at various current rates from 0.2C to 4C in the potential range of 1.5-2.8 V. It exhibits excellent rate performance consisting of two discharge plateaus even at a very high current rate of 4C which can be ascribed to the reduction of S_8 to high-order lithium polysulphides at 2.3-2.4 V and the transformation to low-order Li_2S_2/Li_2S at 1.9-2.1 V. In the reverse reaction, two plateaus in the charge curve represent the backward reaction from lithium sulfides to polysulfides and finally to sulfur. Based on the discharge curves at 0.2C, the sulfur electrodes containing G/CNT, SnS_2, Ni_3S_2, FeS, TiS_2, CoS_2, and VS_2 exhibit average discharge capacities of 685, 836, 845, 900, 1008, 1033, and 1093 mA h g^{-1}, respectively (Figure II-565B). The higher discharge capacities of TiS_2, CoS_2, and VS_2 containing cathodes indicate the high utilization of sulfur due to the strong interaction between LiPSs and these sulfides. There are distinct differences in the voltage hysteresis and length of the voltage plateaus, which are related to the redox reaction kinetics and the reversibility of the system. The TiS_2, CoS_2, and VS_2 containing cathodes display flat and stable plateaus with relatively small polarizations of 177, 177 and 172 mV at 0.2C, much lower than G/CNT, SnS_2, Ni_3S_2, FeS containing cathodes with values of 272, 244, 259 and 217 mV. This suggests a kinetically efficient reaction process with a smaller energy barrier promoted by the M_xS_y (TiS_2, CoS_2, and VS_2) catalyzing process discussed previously. The charge/discharge plateaus obviously shift or even disappear for G/CNT, SnS_2, and Ni_3S_2 containing electrodes at high current rates, indicating high polarization and slow redox reaction kinetics with inferior reversibility.

Long-term cycling stability with high capacity retention is crucial for the practical application of Li-S batteries. Figure II-565C shows the cycling performance of the S@G/CNT and S-M_xS_y@G/CNT electrodes at 0.5C for 300 cycles after the rate capability test. The S-VS_2@G/CNT electrode delivers a high initial reversible capacity of 830 mA h g^{-1} and the capacity remains at 701 mA h g^{-1} after 300 cycles with stabilized Coulombic

efficiency above 99.5%, corresponding to a capacity retention of 84.5% and slow capacity decay rate of 0.052% per cycle. The high LiPSs adsorbing capability and good catalytic conversion of sulfur species alleviate the shuttle effect and improve the Coulombic efficiency. The S-CoS$_2$@G/CNT and S-TiS$_2$@G/CNT electrodes also retain reversible capacities of 581 and 546 mA h g^{-1}, respectively, accounting for 85.3% and 78.2% of their initial capacities with low capacity fading rates of 0.049% and 0.073% per cycle. The remarkable improvements in cycling stability and Coulombic efficiency can be ascribed to the immobilization of soluble polysulfide species through a strong chemical binding and facile redox reaction propelled by these metal sulfides. As for the S@G/CNT electrode, it only delivers an initial reversible capacity of 386 mA h g^{-1} at 0.5C rate and the capacity rapidly decreases to 218 mA h g^{-1} after 300 cycles with a capacity retention of 56.5% and fast capacity decay rate of 0.145% per cycle. This suggests a weak affinity with LiPSs that cannot retard their diffusion into the electrolyte and prevent active material loss. Compared with TiS$_2$, CoS$_2$ and VS$_2$ containing electrodes, the sulfur cathodes containing FeS (334 mA h g^{-1}, 47.4% capacity retention), SnS$_2$ (191 mA h g^{-1}, 31.3% capacity retention), and Ni$_3$S$_2$ (153 mA h g^{-1}, 29.1% capacity retention) demonstrate inferior cycling stability at 0.5C with quick capacity degradation and unstable Coulombic efficiency around 96%. The capacity fading rates reach 0.175%, 0.229% and 0.236% per cycle for FeS, SnS$_2$, and Ni$_3$S$_2$ containing electrodes, respectively, much higher than the other three metal sulfides. These results imply that the selection of suitable polar hosts in the cathode that can 1) strongly interact with LiPSs, 2) rationally control Li$_2$S deposition, 3) enable fast lithium ion diffusion, 4) effectively transform sulphur to LiPSs/Li$_2$S, and 5) catalytically reverse the reaction process, is crucial and could significantly decrease polarization, improve sulfur utilization, and enhance rate performance and long-term cycling stability.
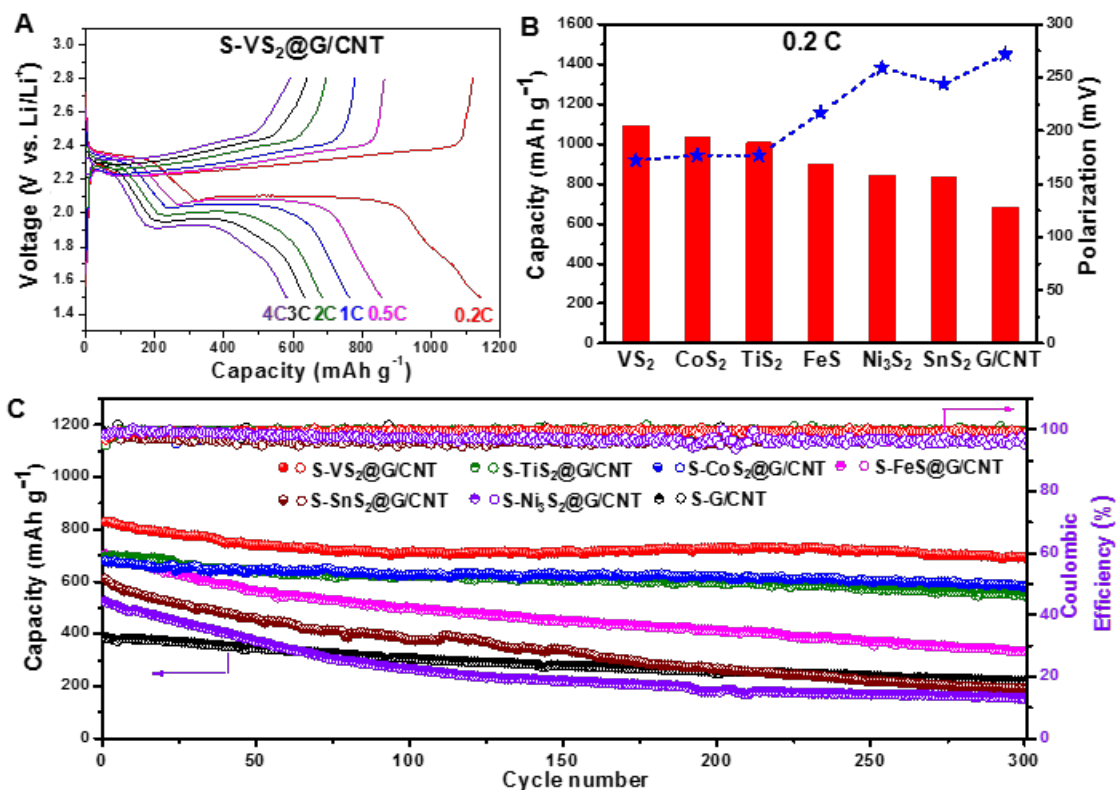
Figure II-565. (A) Galvanostatic charge/discharge voltage profiles of the S-VS$_2$@G/CNT composite electrodes at different current densities within a potential window of 1.5~2.8 V vs. Li$^+$/Li^0. (B) Comparison of the specific capacity and polarization voltage between the charge and discharge plateaus at 0.2C for different composite electrodes. (C) Cycling performance and Coulombic efficiency of the different composite electrodes at 0.5C for 300 cycles after the rate capability test.

We further establish a standard procedure to quantitatively compare the polysulfide adsorption capability of various candidate materials. Figure II-566 presents data for the setup where 0.5 m^2 surface area of candidate materials are added to 3mM of Li_2S_6 in 4mL of 1,3-dioxolane/1,2-dimethoxyethane solution (DOL/DME, 1:1 by volume) for 3 hours. Li_2S_6 is a representative soluble long-chain polysulfide species and is prepared by chemically reacting sulfur with Li_2S in DOL/DME solution which is a common electrolyte system for Li-S batteries. As Figure II-566A illustrates, varying degrees of color change can be observed which are attributed to the interactions between candidate materials and the polysulfide species. No observable color fading is associated with carbon black, suggesting weak physical adsorption. Other materials such as MoS_2 and TiO_2 demonstrate higher adsorption capability compared to carbon black, while CoS and TiN exhibit relatively low adsorption capability as indicated by the lack of significant color fading. In contrast, the polysulfide solutions become much lighter in color after the addition of V_2O_5, MnO_2, V_2O_3, TiS_2 and FeS, suggesting strong interactions between Li_2S_6 and these materials. However, the judgment of color shades is subjective to the human eyes and is also hindered by the powder color of the candidate materials. Therefore, upon completion of the adsorption tests, 2mL of the supernatant solutions are extracted from each sample to minimize the impact of powders and ultraviolet-visible spectroscopy (UV-Vis) is performed on these supernatant solutions for detailed examination.

Figure II-566B illustrates the UV-Vis performance in the visible spectrum of varying concentrations of Li_2S_6 without the addition of any candidate materials. There is strong absorbance towards the blue end of the visible spectrum, as blue is the complementary color of yellow. Unsurprisingly, higher concentrations of Li_2S_6 corresponds to darker shades of yellow and stronger absorbance around the blue spectrum. Figure II-566C shows the performance of carbon black and the metal oxides adsorption test supernatant solutions. The results are in good agreement with previous visual inspections. Carbon black demonstrates much higher blue spectrum absorbance corresponding to a higher concentration of Li_2S_6 remaining and thus weak polysulfide adsorption capability. In comparison to Figure II-564B, it can be seen that very little Li_2S_6 is adsorbed by carbon black with 3mM being the original concentration in each adsorption test sample. In contrast, V_2O_5, MnO_2 and V_2O_3 all illustrate much higher adsorption capability showing very low concentrations of Li_2S_6 remaining in the supernatant solutions. Ti_4O_7, TiO_2, SiO_2 and Al_2O_3 exhibit moderate polysulfide adsorption capabilities. Similarly, Figure II-566D shows the performance of the metal nitride and metal sulfides. TiS_2, FeS and MoS_2 exhibit great polysulfide adsorption capabilities, CoS displays poor capability, while Cu_2S, CuS, TiN and ZnS exhibit moderate capabilities. In Figure II-566C and Figure II-566D, CoS and carbon black display background absorbance throughout the entire spectrum, this is likely due to the scattering effect of the sample powders, which do not settle well and are present in the supernatant solutions.
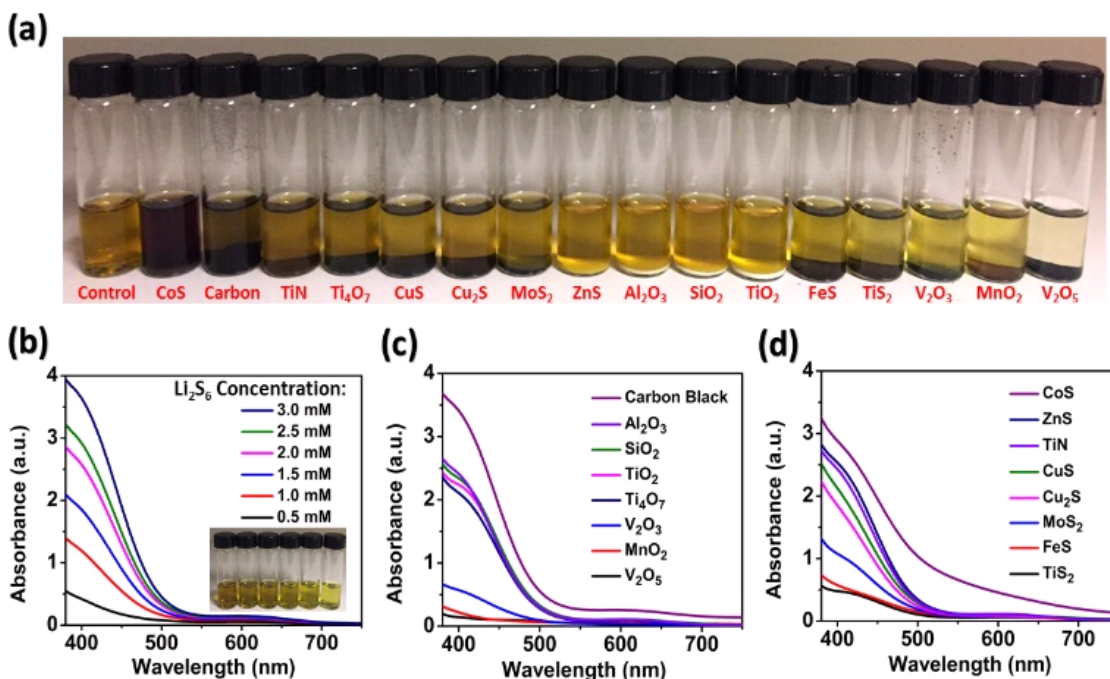
Figure II-566. Li$_2$S$_6$ polysulfide adsorption test: (a) photograph of setup. (b) UV-Vis data of varying concentrations of Li$_2$S$_6$ in DOL/DME solution without candidate materials, (c-d) with candidate materials added in 3mM Li$_2$S$_6$.

ICP-AES can detect the total concentration of lithium and sulfur atoms regardless of their chemical state, and therefore is much less susceptible to complications brought about by the instability of Li$_2$S$_6$ species. There is a linear relationship between ICP-AES lithium intensity and Li$_2$S$_6$ concentration. A similar relationship is shown for sulfur. The only source of lithium introduced to the samples are from the 3mM Li$_2$S$_6$ species, therefore based on the concentration of lithium atoms remaining in supernatant solution, it is possible to determine the amount of lithium adsorbed on the candidate materials. The calculated Li$_2$S$_6$ adsorption capability data for candidate materials based on ICP-AES analysis match reasonably well with UV-Vis approximations and similarly demonstrate one order of magnitude of difference between weak and strong candidate materials, with carbon black and CoS at 1.6 µmol/m^2 and 3.5 µmol/m^2 respectively, compared to MnO$_2$ and V$_2$O$_5$ at 22.9 µmol/m^2 and 22.3 µmol/m^2 respectively.

Conclusions

In all, in the past one year, we have made great progress in understanding the mechanism of surface adsorption, diffusion, and catalytic oxidation of Li$_2$S$_x$ species on anchoring materials. We present a standard procedure to systematically investigate the polysulfide adsorption capability of 16 candidate materials. Our results indicate MnO$_2$ and V$_2$O$_5$ to be particularly strong materials and carbon black to be a particularly weak material for polysulfide adsorption. We made quantitative comparisons with normalized surface areas and observed an order of magnitude of difference across the candidate materials. We elucidate different adsorption mechanisms may be present and probe possible adsorption species. We discover a novel catalytic effect that electrode materials previously designed for polysulfide binding and trapping can play a critical role in catalyzing the oxidation of Li$_2$S back to sulfur during battery charging. Combining theoretical calculations and experimental design, we select a series of metal sulfides as a model system to identify the key parameters in determining the energy barrier for Li$_2$S oxidation and polysulfide adsorption. We demonstrate that the Li$_2$S decomposition energy barrier is associated with the binding between isolated Li ions and the sulfur in sulfides; this is the dominating reason that sulfide materials can induce lower overpotential compared to commonly used carbon materials. It is also demonstrated that the inherent metallic conductivity, strong interaction with LiPSs, facilitated Li ion transport, controlled Li$_2$S precipitation, and accelerated surface-mediated redox reaction of

these metal sulfides are critical in reducing the energy barrier and contributing to the remarkably improved battery performance. Attaining such fundamental understanding of the reaction process is a crucial step towards rational design and screening of materials to achieve high reversible capacity and long cycle life in Li-S batteries.

Key Publications

1. G.M. Zhou, H. Tian, Y. Jin, X. Tao, B. Liu, R. Zhang, Z. W. Seh, D. Zhuo, Y. Liu, J. Sun, J. Zhao, C. Zu, D. Wu, Q. Zhang, Y. Cui, "Catalytic oxidation of Li2S on the surface of metal sulphides for Li-S batteries", PNAS, 2017, 114, 840-845.

2. David. S. Wu, F.F. Shi, G.M. Zhou, C. Zu, C. Liu, K. Liu, Y. Liu, J. Wang, Y. Peng, Y. Cui, "Quantitative Investigation of Polysulfide Adsorption Capability of Candidate Materials for Li-S Batteries", Energy Storage Materials, 2017, under revision.

II.I.7 Addressing Internal "Shuttle" Effect: Electrolyte Design and Cathode Morphology Evolution in Li-S Batteries (TAMU)

Perla B. Balbuena, Principal Investigator
Texas A&M University
3122 TAMU
College Station, TX 77843
Phone: 979-845-3375
E-mail: balbuena@tamu.edu

Partha Mukherjee, Co-Principal Investigator
Texas A&M University
3123 TAMU
College Station, TX 77843
Phone: 979-845-3211
E-mail: pmukherjee@tamu.edu

Vilas Pol, Co-Principal Investigator
Purdue University
610 Purdue Mall
West Lafayette, IN 47907
Phone: 979-845-3211
E-mail: vpol@purdue.edu

Tien Duong, Technology Manager
U.S. Department of Energy
Phone: 202-586-7836
E-mail: Tien.Duong@ee.doe.gov

Start Date: October 1, 2014   End Date: September 30, 2017
Total Project Cost: $990,000   DOE share: $990,000   Non-DOE share: $0

Project Introduction

This project focuses on developing new understanding of the main challenges of the Li/S cell obtained from first-principles atomistic and mesoscopic modeling and state of the art synthesis and characterization. Specifically, this work aims to elucidating: 1) the effects of the electrolyte chemistry on the formation of a solid-electrolyte interphasial film at the surface of the Li anode covered and modified by insoluble polysulfide species, as well as on reactions occurring at the C/S cathode surface as functions of state of charge, internal shuttle-induced changes to the chemistry, and intrinsic nature of the electrolyte, 2) the relative contributions to the cathode performance of the solid discharge products, and associated morphology and volume changes of the C/S cathode microstructure, compared to that of the electrolyte effect; 3) effects of the electrolyte chemistry and cathode microstructure on the coulombic and cyclic efficiency of composite C/S electrodes.

Objectives

The objective of this project is to elucidate the lithium-metal anode deterioration issues especially under the polysulfide shuttle environment, and the effects of the carbon/sulfur cathode morphology on the cathode performance, and to develop and test strategies based on Li-metal protection advanced cathode structure design to mitigate these issues.

Approach

A mesoscale model including different realizations of electrode mesoporous structures based on a stochastic reconstruction method allows virtual screening of the cathode microstructural features and the corresponding effects on electronic/ionic conductivity and morphological evolution. Interfacial reactions at the anode due to the presence of polysulfide species are characterized with ab initio methods. For the cathode interfacial reactions, data and detailed structural and energetic information obtained from atomistic-level studies are incorporated in a mesoscopic-level analysis. A novel sonochemical fabrication method is expected to generate controlled cathode mesoporous structures that will be tested along with new electrolyte formulations based on the knowledge gained from the mesoscale and atomistic modeling efforts.

Results

Effects and structure of PS species migration through the electrolyte to the Li metal anode

Our ab initio molecular dynamics (AIMD) study of the reactions at the surface of Li metal demonstrated the effects of concentrated electrolyte solutions on the first coordination shell of the Li ion, where a mixed shell composed of salt anion, PS anion, and solvent are present (Figure II-567). The importance of these differences in comparison to the low salt concentration is that as the Li ion travels near to the surface, electron transfer reduces first the PS anion and the salt anion and then the solvent. Thus, the work of desolvation needed for Li plating depends strongly on the composition of the first shell and also on the degree of reduction. Thus, for concentrated solutions the work for desolvation will be different from that in diluted solutions because the salt anion decomposes first, leading to SEI fragments that bind strongly to Li ions. Thus, Li reduction will take place later in presence of these SEI nucleating elements. Moreover, the possible scenario of simultaneous reduction of the Li ion and decomposition of the salt and PS anions modify the type of precursors for dendrite formation.
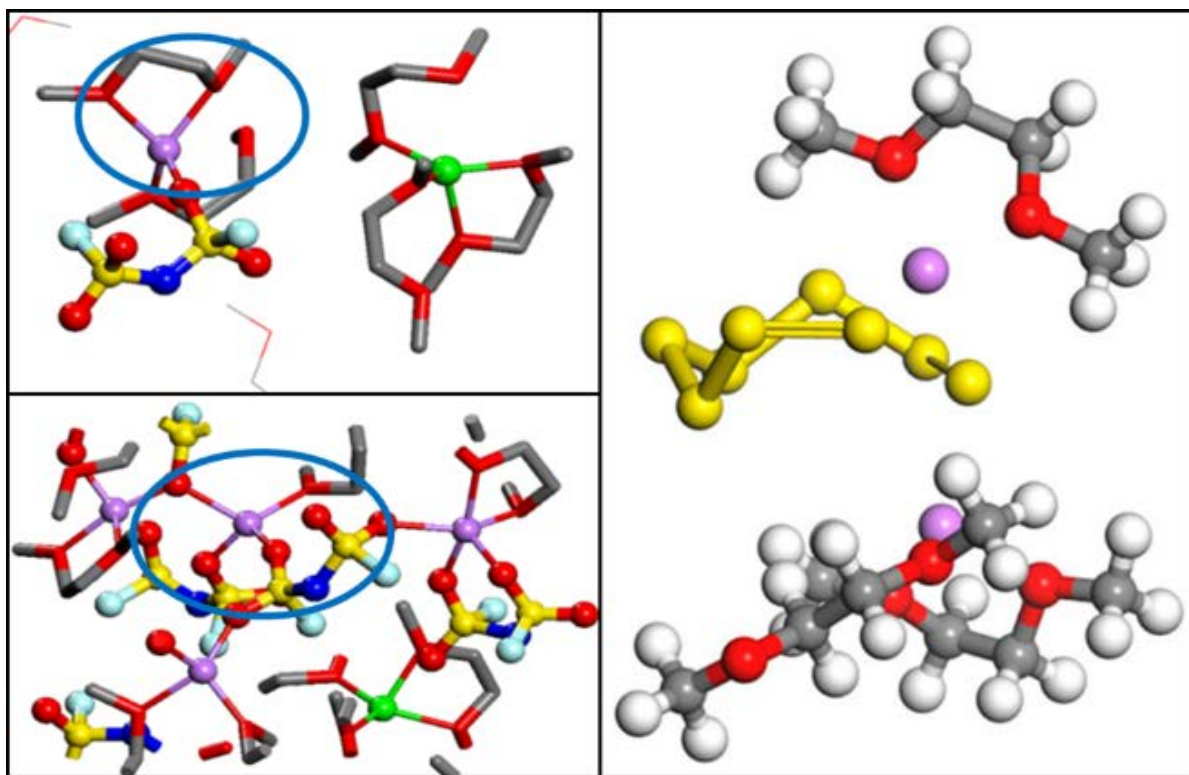

Figure II-567. First coordination shell of a Li ion (purple) surrounded by DME molecules (top left) at 1M LiFSI concentration, and solvated by salt anions and DME molecules at 4M LiFSI concentration (bottom left). O (red), c (grey), S (yellow), N (blue). Solvation structure of LiS8- in DME solution.

DFT and AIMD studies of Li$^+$ and long-chain PS solvation led us to conclude that these molecules have a peculiar mode of traveling the liquid electrolyte: PS anion species are not favored in most conditions; therefore PS exists as a *neutral species paired Li ions*. The Li-O rdf shows a clear first peak indicating the strong coordination of Li ions of the lithiated PS species with the solvent, whereas the Li-S rdf shows that the same Li ions are also well coordinated to the end-S atoms, and much less to those in the middle of the chain. However, under an electrical field, the PS ion pair will become at least partially dissociated (Figure II-567) and our current estimate is that the *monolithiated anion is the species that should migrate to the anode side*.

In presence of PS species, the reactions become much more complex. In collaboration with M. Vijayakumar at PNNL, DFT and AIMD simulations were used to explain XPS results and identify SEI products at the Li anode surface due to PS shuttle effects. The main findings include a) confirmation of our earlier prediction of Li$_2$S deposition at the Li metal surface, b) identification of an intermediate LiS$_5$ species as a reduction product at the anode surface. Such product explains the ratio of S neutral to S monoanion and the increase of Li$_2$S concentration observed in the *in-situ* XPS results. In addition a variety of products of the decomposition of the TFSI anion predicted by AIMD simulations were found in the observed XPS peaks (Figure II-568). The complexity of the SEI layer in this model experiment was further elucidated (Figure II-568). Moreover, it was demonstrated that this type of combined experimental-theoretical study could be extremely useful for elucidating the behavior of complex battery materials.
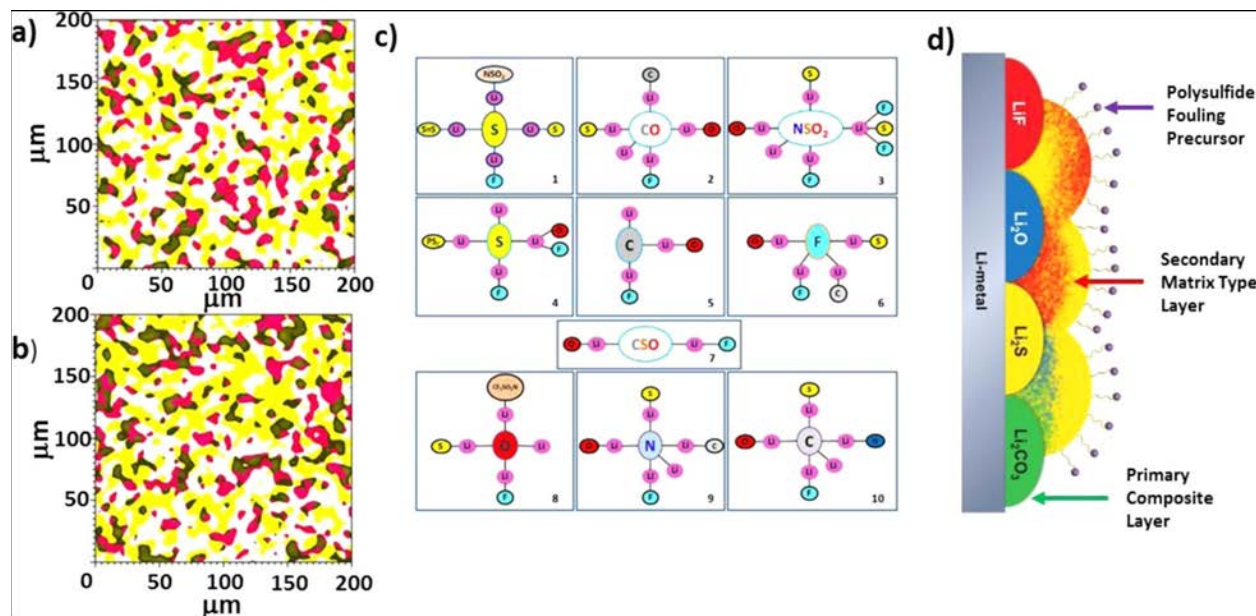
Figure II-568. XPS chemical imaging of the Li-electrolyte interfacial region after (a) first charging cycle and (b) first discharging cycle. The Li−F species from F 1s spectra and S0 polysulfide species from S 2p spectra are represented as yellow and red regions, respectively. The black region represents the overlapping regions of Li−F and S0polysulfide species. (c) Schematic representation of various fluorine-based Li−F species predicted from AIMD calculations. (d) Cartoon representation of SEI layer growth mechanism based on the combined XPS and computational results. From Chem. Mater. 29, 4718, (2017).

A summary of these findings include: a) salts do not totally dissociate (not even at 1M solutions); b) in 1M solutions the solvent dominates the first coordination shell of the Li ion; c) in 4M solutions very complex networks form, having mixed coordination shells (solvent and salt components); d) the kinetics of solvent decomposition (for DME and DOL) is much slower than those of typical anions (TFSI or FSI) and the extent of the reduction depends on the chemical nature of the salt; e) the PS migrates as a lithiated mono-anion and decomposes combining with fragments of the anion decomposition forming a complex multilayer SEI. All these conclusions have led us to a hypothesis with respect to plating of Li+ ions inside the SEI layer. We are

testing the effects of different functional groups on the process of Li+ plating. We expect to determine whether certain ion coordination shells are more favorable to induce Li plating inside the SEI layer and how this plating compares with Li deposition on the current collector.

Microstructure and reactions at the C/S cathode

Pressurized "autogenic" synthesis routes, studied by Co-PI Vilas Pol at Purdue University, have produced homogeneous carbon-sulfur composites with high sulfur content up to 74 %-wt.; the real S content is controlled by optimization of the precursor ratio. Material characterization of these composites suggests pristine orthorhombic S_8 is transformed into amorphous sulfur species during the autogenic process. It is hypothesized that high sulfur content is enabled by homogeneous penetration of sulfur vapor into the porous carbon substrate, followed by homogeneous deposition as amorphous sulfur species. The synthesis scheme of the autogenically-derived C/S composite (with 40 %-wt. sulfur loading) and the electrochemical rate cycling results are shown in Figure II-569. The performance of a conventional sample derived via ball milling is shown for comparison.
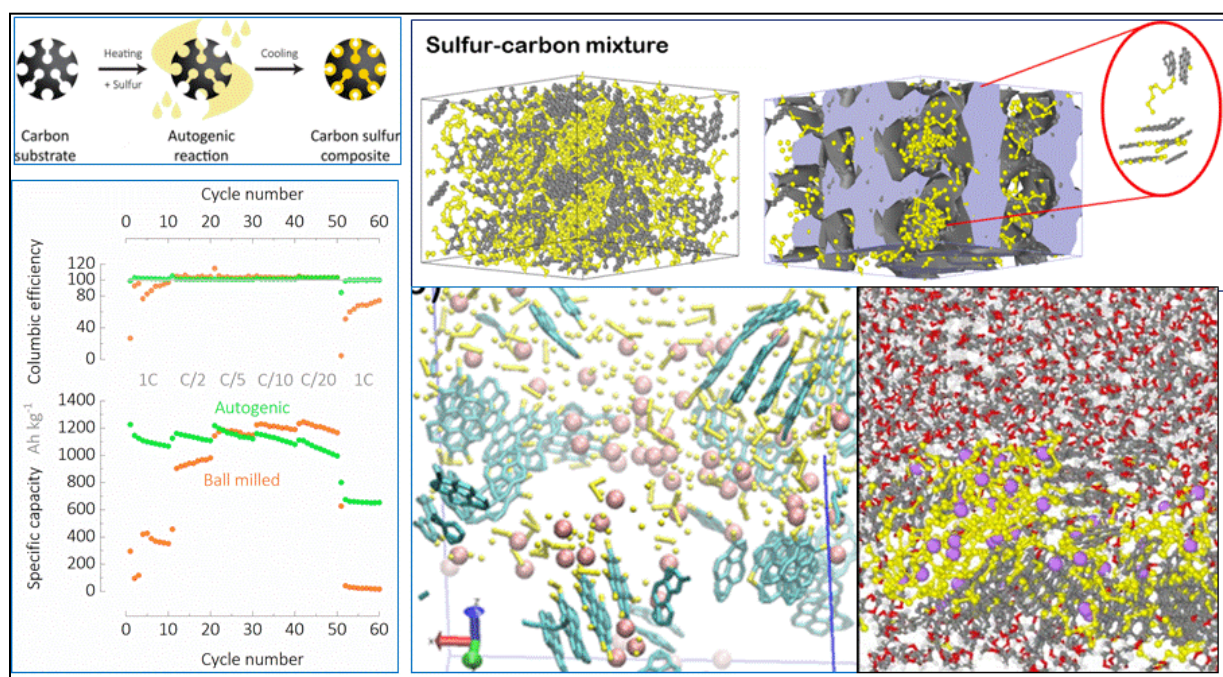
Figure II-569. A new synthesis method was implemented to facilitate a more intimate mixture of S and C via a pressurized autogenic reaction. Schematic figure top left and electrochemical tests bottom left. Top right: Model of the composite material obtained from molecular dynamics simulations (see text). Bottom, right: simulation of discharge reactions in the C/S phase in contact with the electrolyte: Li (purple), S(yellow), C (grey), O (red), H (white).

When cycled at various cycling rates, the autogenically-derived carbon-sulfur composite shows consistent capacity around 1100 Ah kg^{-1} between rates C/20 to 1C. After cycling at a slow rate of C/20, however, the capacity drops to ca. 700 Ah kg^{-1}. To further understand the underlying principles of autogenic synthesis, the quality of sulfur and its distribution were explored via electron microscopy and elemental mapping. It was found that C/S composites have a secondary particle diameter of 7 ± 3 μm. From elemental mapping, S is observed to be distributed uniformly across the C particles within a large sample area. After autogenic synthesis, the C/S composite particle generally retains the features of the original C morphology. The individual primary particle morphology of the carbon-sulfur composite is generally spheroidal and branched like the original carbon precursor. However, the pores in the composite are slightly less easily observable. The overall morphology of the composite is also branched, exhibiting bright signal due to the insulating property of elemental S. Line scans of the C/S composite show that S content occurs coincidently with carbon content.

Correspondingly, appreciable S content is not observed beyond the boundaries of C signal. Altogether, these observations suggest that sulfur content is generally confined within the substrate carbon phase. In parallel, Balbuena's group molecular simulations advanced the characterization of the microscopic morphology of these composites and their evolution during lithiation. This model of the C/S composite allows intimate mixing between S and C by randomly dispersing graphene sheets and 8-membered S rings at 47%-wt S and an approximate density of 1.67 g/cm^3. Molecular dynamics (MD) simulations using a reactive force field carried out at 300 K and 1 atm revealed opening of most of the S rings along with the formation of S-C bonds between S chains of various lengths and the C atoms at the edges of the graphene sheets, confirming our earlier AIMD analysis. Thus, the presence of discontinuous graphene sheets instead of continuous graphene layers allows a more realistic approach, as the low-coordinated C atoms at the edges of these graphene sheets favor C-S bond formation. We also observed that graphene sheets tend to agglomerate into graphitic clusters due to van der Waals interactions between sheets, with most of the short-chain PS species agglomerating around the edges (Figure II-569). On the other hand, the various morphology and loading effects in the cells were studied with a mesoscopic model in Mukherjee's group. Based on microstructure-scale simulations, effective property relations (e.g., tortuosity) were developed and used to identify cathode resistances (Figure II-570). If precipitation takes place in the form of film deposits, the electrode-electrolyte interface gets covered earlier and the cell shuts down due to predominant surface passivation. Alternatively, if precipitation occurs in a finger-like fashion, pore blockage is much severe and causes cathode starvation. For intermediate morphologies, cathode resistance evolution has joint contributions from both. As cathode pristine porosity changes, it leads to different pore blockages. As precipitate morphology becomes more finger-like, cell performance improves in response to decreased surface passivation. On the other hand, at higher initial sulfur loading, increasing cathode porosity improves discharge capacity.
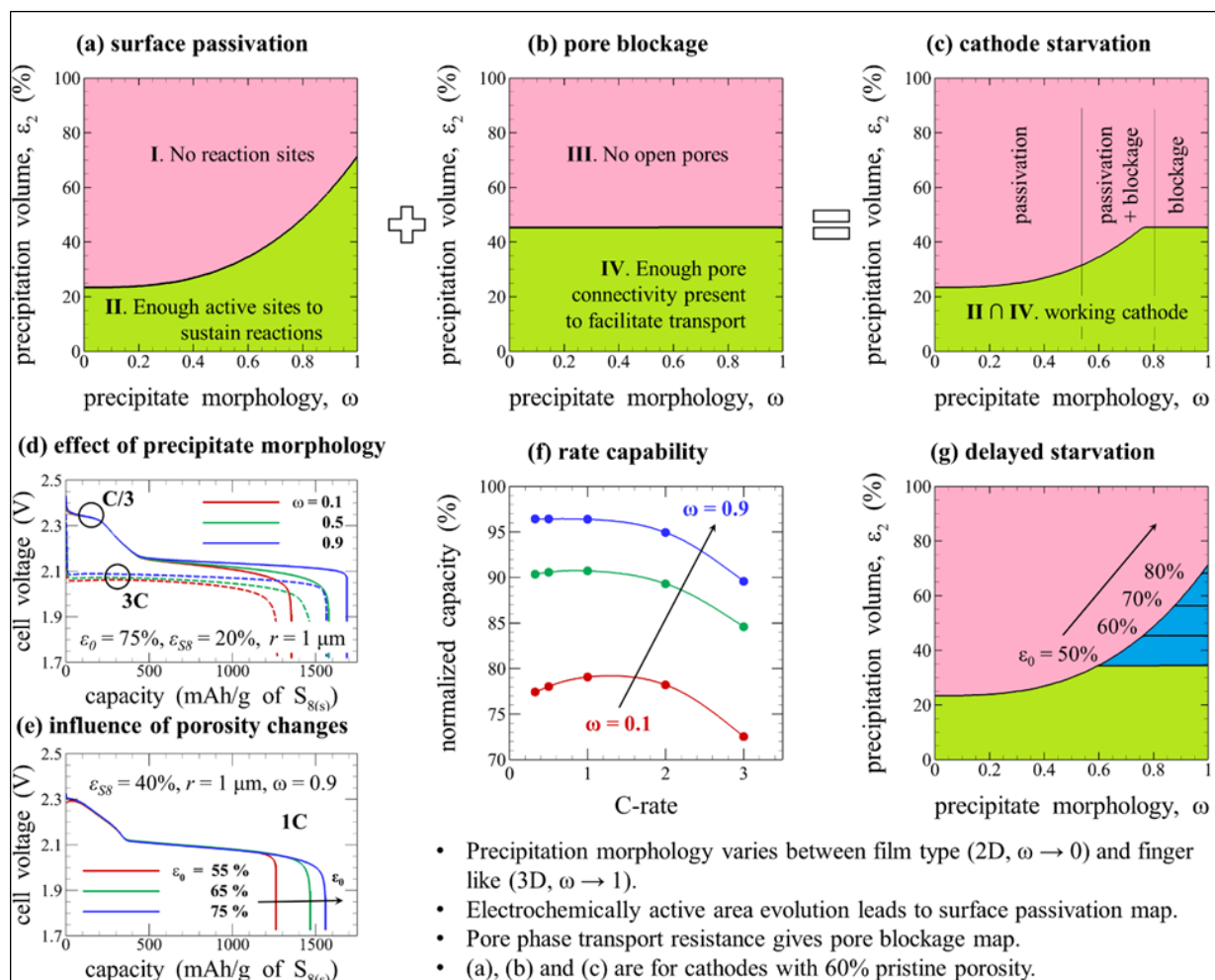
Figure II-570. Identification of different cathode microstructural resistances (a) surface passivation (b) pore blockage and (c) their joint contribution, based on effective property relations for mesoporous carbon structure. Pore blockage resistance is relatively more sensitive to porosity changes and leads to delayed cathode starvation (g). Tuning precipitate morphology (d, f) and pristine porosity (e) lead to different cell performance as expected from microstructural implications (c, g).

Li_2S_2 and Li_2S are the main discharge products of the Li-S battery. However, their electronic conductivity is too low to ensure a good kinetic charge rate. We studied the electronic structure of these solids and their main charge carriers. For Li_2S_2, it was found that similarly to the O_2 molecule, 12 electrons in a S_2 molecule occupy σ_s, σ_s^*, σ_p, π_p, and π_p^* orbitals. In an isolated S_2 molecule, the antibonding orbital π_p^* is half occupied. In Li_2S_2 bulk, Li 2s electrons are transferred to π_p^* orbital of S_2, leading to S_2^{2-}. The antibonding σ_p^* orbital is still empty in S_2^{2-}, and this orbital can accept an extra electron to form an electron polaron p^-. On the other hand, the π^* orbital can donate an electron to form a hole polaron p^+ which was found to be the main charge carrier. Similar studies done for Li_2S indicated that p^+ can also be the main barrier with relatively low diffusion barriers along various crystal directions. New evaluations are in progress to evaluate further enhancements of electronic conductivity via doping.

Conclusions

During this year, our project focused on various aspects derived from the complexity of the S chemistry in Li/S batteries. One is the effect of PS migration on the Li metal anode reactivity and formation of a solid-electrolyte interphase with different characteristics due to the PS decomposition. Among several strategies proposed to mitigate the extreme Li reactivity, one is the use of concentrated salt solutions. We investigated how Li ions

are conducted through these solutions and analyzed potential consequences of these solvation structures on the SEI, and the transport mechanisms for the long chain soluble PS traveling from cathode to anode. The second aspect centers on the cathode microstructure and reactivity. We studied the effects of cathode microstructure on the discharge reactions, and developed a very detailed atomistic level model of the C/S composite, which we are using to characterize the cathode reactivity, together with mesoscale descriptions that relate macroscopic properties such as impedance to cathode microstructural evolution. In parallel, our team developed and electrochemically tested new synthesis methods for the C/S systems. A final very crucial aspect relates to the short chain insoluble PS species deposited at the cathode surfaces. Their precipitation mode was analyzed and correlated with cathode microstructure, and hole polarons were identified as the main charge carriers in both crystals. Further directions were suggested for enhancement of the electronic conductivities of the discharge products.

Key Publications

1. Luis E. Camacho-Forero, Taylor W. Smith, and Perla B. Balbuena, "Effects of High and Low Salt Concentration in Electrolytes at Lithium-Metal Anode Surfaces," *J. Phys. Chem. C*, 121, (1), 182-194, (2017).

2. Zhixiao Liu, Perla B. Balbuena, and Partha P. Mukherjee, "Revealing Charge Transport Mechanisms in Li_2S_2 for Li-Sulfur Batteries," *J. Phys. Chem. Lett.,* 8, 1324-1330, (2017).

3. Zhixiao Liu and Partha P. Mukherjee, "Mesoscale Elucidation of Surface Passivation in the Li-Sulfur Battery Cathode." *ACS Applied Materials & Interfaces*, 9, 5263 (2017).

4. M. J. Nandasiri, L. E. Camacho-Forero, A. M. Schwarz, V. Sutthanandan, S. Thevuthasan, P. B. Balbuena, K. T. Mueller, M. Vijayakumar, "In-situ chemical imaging of SEI layer evolution in Li-S batteries using X-ray photoelectron spectroscopy,". *Chem. Mater.*, 29 (11), 4728–4737, (2017).

5. Z. Liu, P. Balbuena, and P. P. Mukherjee, "Mesoscale Evaluation of Titanium Silicide Monolayer as a Cathode Host Material in Lithium-Sulfur Batteries," *J. Min., Met.Mater. Soc.*, in press, DOI: 10.1007/s11837-017-2414-7.

6. C.-F. Chen, A. Mistry and P. P. Mukherjee, "Probing Impedance and Microstructure Evolution in Lithium-sulfur Battery Electrodes," *J. Phys. Chem. C*, 121, 21206, (2017).

7. Ethan P. Kamphaus and Perla B. Balbuena, "First Principles Investigation of Lithium Polysulfide Structure and Behavior in Solution," *J. Phys. Chem. C*, 121, 21105-21117, (2017).

8. Zhixiao Liu, Perla B. Balbuena, Partha P. Mukherjee, "Hole Polaron Diffusion in the Final Discharge Product of Lithium-Sulfur Batteries", *J. Phys. Chem. C*, 121, 17169-17175, (2017).

9. Juan Carlos Burgos, Perla B. Balbuena, and Javier Montoya, "Structural Dependence of the Sulfur Reduction Mechanism in Carbon-Based Cathodes for Lithium Sulfur Batteries," *J. Phys. Chem. C,* 121, 18369-18377, (2017).

10. Aashutosh Mistry and Partha P. Mukherjee, "Precipitation – microstructure interaction in Li-S battery cathode", *J. Phys. Chem. C,* in press.

11. Zhixiao Liu, Aashutosh Mistry, Partha P. Mukherjee, "Mesoscale Physicochemical Interactions in Lithium-Sulfur Batteries: Progress and Perspective", *J. Electrochem. Energy Conv. Storage*, 15, 010802, (2017).

12. Zhixiao Liu, Perla B. Balbuena, and Partha P. Mukherjee, "Mesoscale Evaluation of Titanium Silicide Monolayer as a Cathode Host Material in Lithium-Sulfur Batteries," *J. Minerals, Metals, and Materials Society*, 69, 1532-1536, (2017).

II.I.8   Mechanistic Investigation for the Rechargeable Li-Sulfur Batteries (U Of Wisconsin)

Deyang Qu Principal Investigator
University of Wisconsin Milwaukee
3200 N Cramer Street
Milwaukee, WI, 53211
Phone: 414-229-3716; Fax: 414-229-5191
E-mail: qud@uwm.edu

Xiao-Qing Yang, Co-Principal Investigator
Chemistry Department
Brookhaven National Laboratory
Bldg. 555
Upton, NY 11973
Phone: 631-344-3663; Fax: 631-344-5815
E-mail: xyang@bnl.gov

Tien Duong, Technology Manager
U.S. Department of Energy
Phone: 202-586-7836
E-mail: Tien.Duong@ee.doe.gov

Start Date: September 1, 2016   End Date: August 30, 2017
Total Project Cost: $300,000   DOE share: $300,000   Non-DOE share: $0

Project Introduction

Rechargeable Li-S battery is a potential candidate to meet the demand of high energy density for the vehicle applications. However the capacity loss for a rechargeable Li-S battery is still one of the major obstacles. The "polysulfide shuttle" which" is the equilibrium reactions between dissolved polysulfides and elemental sulfur, remains the major reason for the continuous decay of the capacity during cycling and high self-discharge during storage. There are other barriers which need to be overcome for the sulfur cathode, for example: low operation voltage, low conductivity for S_8 and Li_2S, radical species formed during the operation of Li-S batteries.

Li anode also remains as a major challenge even after decades of research. Besides all the traditional problems e.g., dendrite growth, safety etc., it is hard to find an electrolyte which can form a stable SEI layer on Li anode to prevent the reaction between Li and dissolved polysulfide ions.

During 2016, we have successfully established the HPLC-MS essays. So for the first time, the ALL dissolved polysulfide ions can be qualitatively and quantitatively determined during the operation of a Li-S cell. An electrochemical measurement procedure with either *in-situ* or *ex-situ* determination of the polysulfide ions were also established.

Based on the achievements in 2016, the collaborative project aims to further investigate the mechanism of Li-S batteries and to explore the innovative designs of rechargeable Li-S cells. The project includes extensive scientific investigation by mean of *in-situ* electrochemical spectroscopic techniques to explore the reaction mechanism at cell level. So the proper electrolytes and additives suitable to Li-S chemistry can be developed. With the understanding of the reaction mechanism, we will engage in the engineering design of the electrode materials, electrolytes including the additives and electrochemical cells. So the potential of high energy density

Li-S batteries can be unlocked. Potentially, Li-S batteries could enable competitive market entry of electric vehicles by reducing the cost and extending the driving distance per charge.

Objectives

Taking the advantages of the unique analytical essay developed in 2016, the primary objectives are to further conduct focused fundamental research on the mechanism for Li-S batteries, investigate the kinetics for the sulfur redox reaction, develop electrolytes and additives suitable for Li-S chemistry, optimize the sulfur electrode and cell designs. In this objective, special attentions will be paid to the investigation of the redox reaction of sulfur cathode, the management for the solubility of polysulfide ions, the formation of SEI layer and dead Li on the surface of Li anode, the rechargeability of Li anode in the solution containing polysulfide and the exploration of electrode and cell designs. Through such investigations, the Li-S chemistry will be studied systematically, the scientific understanding of the reaction mechanism can be well utilized to guide the system engineering design.

Approach

1. A combination of *High Performance Liquid Chromatography (HPLC)/Mass Spectroscopy(MS)* together with *in situ* electrochemical measurement in a specially designed cell. The electrochemically formed dissolved polysulfide ions can be separated (by HPLC) and determined (by MS).

2. *Ex-situ* X-ray diffraction (XRD) and X-ray photoelectron spectroscopy (XPS) to investigate the surface of sulfur cathode and Li anode to elucidate the surface changes during the Li-S battery operation'

3. *In-situ* Keyence 3D microscope and electrochemical measurement in a specially designed cell to investigate the surface modification of Li with e.g., various additives and at different stage of charge/discharge.

4. Extended collaboration with other US and international academic institutions and US industrial partners.

Results

Key Accomplishments:

1. *In-situ* electrochemical-HPLC/MS/UV system was developed to identify polysulfide ions real time during the cell operation of a Li-S cell.

2. *In-situ* electrochemical-laser confocal microscopic cell was made to investigate the surface of Li anode during the cycle of Li-S cell. The Li surface morphology change can be observed in real time.

3. By means of the in-situ methods, the distribution of dissolved polysulfide ions can be monitored real time during the discharge and recharge of a Li-S battery.

4. The chemical equilibriums of the dissolved polysulfide ions were determined, so did the sulfur redox reaction mechanism.

1. Proposal of the sulfur redox mechanism through the real-time Monitoring of the Changes of Sulfur and Polysulfide Species during the Discharge and Charge of sulfur cathode

The HPLC-MS-Electrochemical method we developed is the only reliable method for the analysis of the dissolved polysulfide species and sulfur during the discharge and recharge of a Li-S battery. It is a vital technique for the investigation of sulfur redox mechanism.

In Figure II-571A, the change of polysulfide ions in the electrolyte from elemental sulfur, long chain polysulfides to short chain polysulfides can be clearly demonstrated as the discharge proceeded. The vertical dash lines indicate the stoichiometric polysulfide calculated from the discharge capacity. The 2-electron electrochemical reduction of S_8 to S_8^{2-} mechanism of elemental sulfur was proven not actuate since S_8^{2-} was not generated electrochemically but through subsequent chemical reactions. The first flat discharge plateau

could be a result from the equilibrium among S_8^{2-}, S_7^{2-} and S_6^{2-}, since the ratio of the species remained almost constant. Another interesting observation from Figure II-571A is that even when the discharge reached the stoichiometric S_2^{2-} stage, the most abundant polysulfides in the electrolyte were S_4^{2-}, S_5^{2-} and S_3^{2-}. To the very end of the discharge, even though the concentration decrease, the relative distribution of the three polysulfides remained.
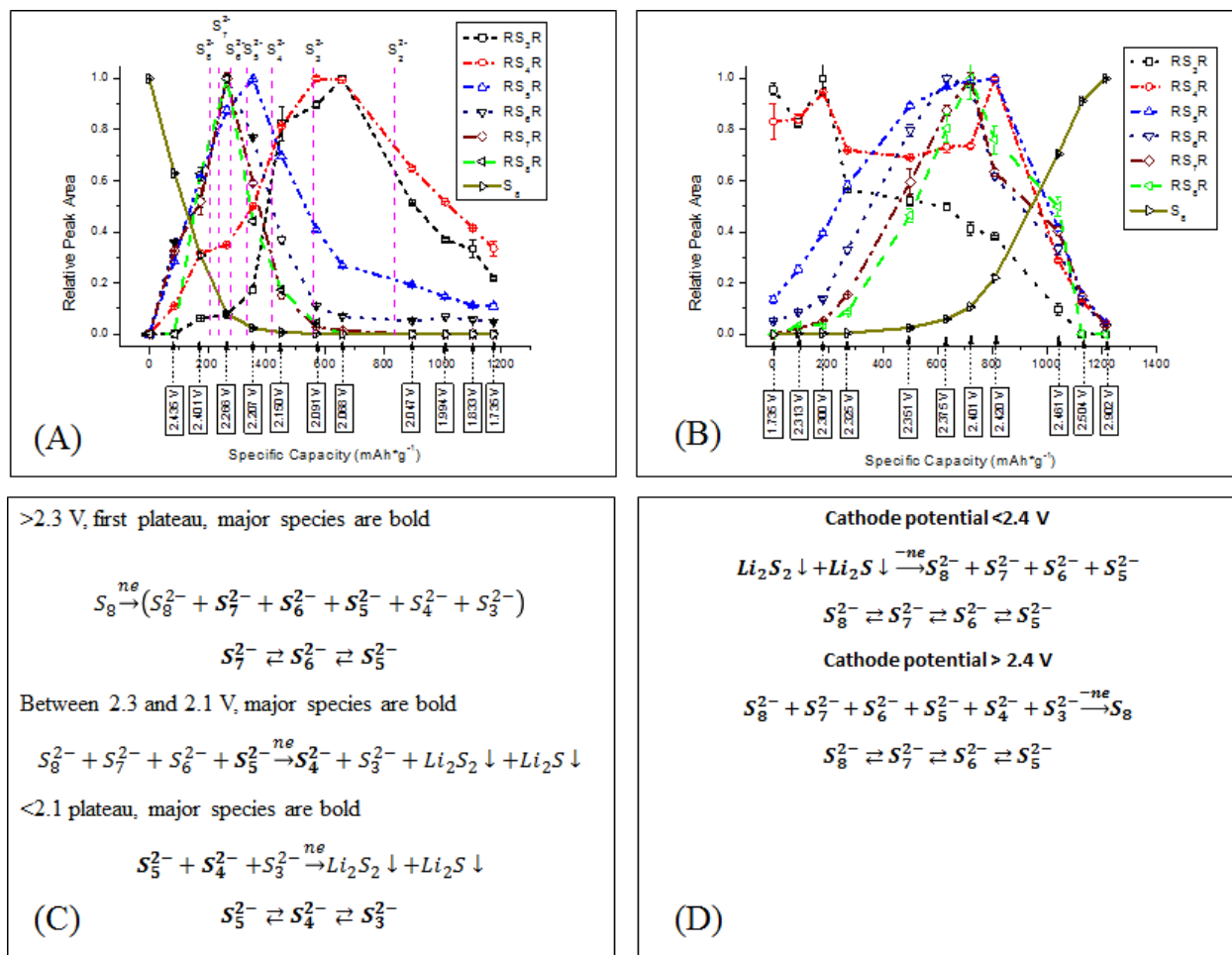
Figure II-571. The normalized chromatographic peak for each derivatized polysulfide species (R=CH$_3$) from real-time HPLC results during discharge (A) and charge (B) of Li-S cell. The proposed discharge mechanism (C) and charge mechanism (D) of Li-S cell. (D. Zheng, D. Liu, J. Harris, T. Ding, J. Si, S. Andrew, D. Qu, X.Q. Yang, D. Qu, ACS Appli. Mater. Interfaces 2017,9,4326-4332.)

Figure II-571B shows the change of polysulfide ions and elemental sulfur during the recharge. It was evident that the concentration of S_3^{2-} and S_4^{2-} remained constant while the concentration of S_5^{2-} and S_6^{2-} kept increasing during the potential dip. It appears that the initial oxidation of Li$_2$S and Li$_2$S$_2$ yielded soluble S_5^{2-} and S_6^{2-} polysulfide ions either through S_3^{2-} and S_4^{2-} as intermediates or directly. After the potential dip, the concentrations of S_3^{2-} and S_4^{2-} took sharp drops, the concentration of S_3^{2-} started to continuously decrease while the concentration of S_4^{2-} remained constant until elemental sulfur started to form at 2.4 V. In the meantime, S_5^{2-}, S_6^{2-}, S_7^{2-} and S_8^{2-} were formed and the ratio among the four polysulfide ions remained constant. It appears that the chemical equilibrium among these polysulfides remained. The increasing concentrations of S_5^{2-}, S_6^{2-}, S_7^{2-} and S_8^{2-} reversed coinciding with the increase of elemental sulfur concentration at about 2.4 V, while the concentration of S_4^{2-} took a nose dive. It is interesting that the concentration of S_3^{2-} and S_4^{2-} were never above their concentrations at the end of reduction (or beginning of oxidation), which could

mean that either S_3^{2-} and S_4^{2-} were not the products for the electrochemical oxidation of Li_2S and Li_2S_2, or they were the intermediates for the formation of longer chain polysulfide. Therefore, we suspected that the sharp decrease of S_3^{2-} and S_4^{2-} concentration resulted from the chemical reaction with newly formed elemental sulfur rather than electrochemical oxidation on the electrode. On the other hand, of course, the decrease of S_5^{2-}, S_6^{2-}, S_7^{2-} and S_8^{2-} concentration correlated very well with the production of elemental sulfur until the almost disappearance of polysulfide ions, so it must be an electrochemical oxidation process. It is also interesting to notice that during the decline, S_5^{2-}, S_6^{2-}, S_7^{2-} and S_8^{2-} still remained in a chemical equilibrium. Therefore, unlike the stepwise reduction process, the oxidation of polysulfide ions was conducted through the electrochemical formation of polysulfide ions S_n^{2-} ($5 \leq n \leq 7$) and sulfur while the chemical equilibrium among S_5^{2-}, S_6^{2-}, S_7^{2-} and S_8^{2-} remained throughout the whole oxidation process.

And based on the above results in Figure II-571A and Figure II-571B, a three-step reduction mechanism including two chemical equilibrium reactions was proposed as shown Figure II-571C, and a two-step oxidation mechanism for the Li_2S and Li_2S_2 with a single chemical equilibrium among soluble polysulfide ions was proposed as shown in Figure II-571D.

2. Reaction between Lithium Anode and Polysulfide Ions in a Lithium–Sulfur Battery

Polysulfide species (Li_2S_n, $n \geq 2$) are the important products in a Li-S battery during charge and discharge. The polysulfide species (with $n \geq 3$) are highly soluble and reactive in organic electrolytes, especially in the ether-based electrolytes. The soluble polysulfide species can migrate to the Li anode and subsequently react with Li anode chemically, which can cause polysulfide shuttle effect in Li-S batteries. To alleviate the problems associated with the dissolution of polysulfide ions, additives which can form a stable solid electrolyte interface (SEI) layer were investigated to prevent the reaction between dissolved polysulfide ions with Li anode. Among those additives $LiNO_3$ was reported to greatly improve the charge and discharge efficiency (columbic efficiency) for a rechargeable Li-S battery.

For polysulfide mixture without $LiNO_3$, the chromatograms of polysulfide mixture before and after contacted with Li metal were shown in Figure II-572-i-A to Figure II-572-i-E. By comparing Figure II-572-i-A with Figure II-572-i-B, the distribution of the polysulfide anions substantially changed after being in contact with Li metal, it became evident that polysulfide anions in electrolyte indeed react with lithium metal. It can be found that the S_n^{2-} species with $n \geq 6$ are more reactive (or less stable) to lithium metal than that of the S_n^{2-} species with $n \leq 5$. As the polysulfide mixture was contacted with lithium metal for 1 hour, the peak intensities of $(CH_3)_2S_6$ and $(CH_3)_2S_7$ decrease greatly in Figure II-572-i-B compared to the corresponding peak intensities in Figure II-572-i-A, while the peak intensity of $(CH_3)_2S_5$ just slightly decreases and the peak intensity of $(CH_3)_2S_4$ greatly increases in Figure II-572-i-B compared to the corresponding peak intensities in Figure II-572-i-A. The unexpected increase of the intensity of $(CH_3)_2S_4$ in Figure II-572-i-B to Figure II-572-i-E clearly indicates that the S_4^{2-} species is stable against lithium metal. Interestingly, the peak intensity for $(CH_3)_2S_3$ in all chromatograms of Figure II-572 is pretty low, it may indicate that the solubility of S_3^{2-} in ether-based electrolyte probably is lower than the polysulfide species with a longer S chain.

For polysulfide mixture with $LiNO_3$ additive, the chromatograms of polysulfide mixture before and after contacted with Li metal were summarized in Figure II-572-ii-A to 2-ii-E. Clearly, there are little changes in the polysulfide distribution in contact with Li metal over four hours with the existence of $LiNO_3$. Obviously, the reaction between Li metal and polysulfide species was inhibited greatly. The observation proved the hypothesis that the $LiNO_3$ in mixture can form a SEI layer on the Li metal surface, which prevented the reaction between Li and polysulfide anions. Unfortunately, the $LiNO_3$ became consumed during the storage. Evidentially, after being in contact with Li for 24 hours, the distribution of polysulfide starts to change. As shown in Figure II-572-ii-D, a slight increase of peak intensity for $(CH_3)_2S_4$ can be observed. After being in contact for 96 hours (Figure II-572-ii-E), momentous changes of the polysulfide distribution can be seen with the increase of peak intensity for $(CH_3)_2S_4$ and the decrease of the $(CH_3)_2S_6$ and $(CH_3)_2S_7$ peak intensities. It is worth pointing out that interaction between Li and polysulfide ions with the existence of $LiNO_3$ was trivial in comparison to those without $LiNO_3$.
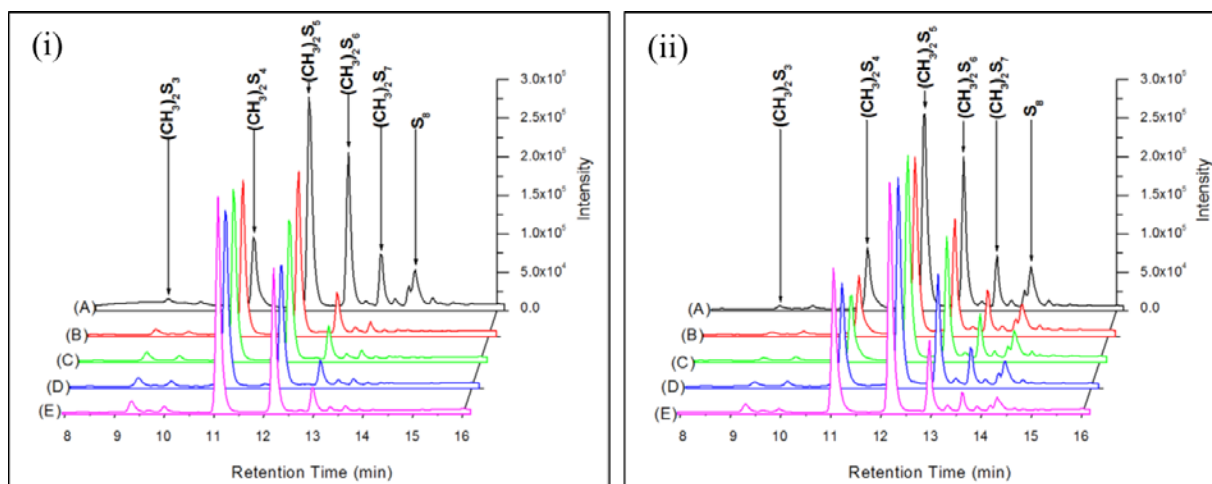
Figure II-572. Chromatograms of derivatized polysulfide mixtures without LiNO₃ (i) and with LiNO₃ (ii). For polysulfide mixture without LiNO₃ and Li metal (i-A), polysulfide mixture (without LiNO₃) with Li metal for 1hour (i-B), polysulfide mixture (without LiNO₃) with Li metal for 4hours (i-C), polysulfide mixture (without LiNO₃) with Li metal for 24hours (i-D), polysulfide mixture (without LiNO₃) with Li metal for 96hours (i-E); For polysulfide mixture with LiNO3 and without Li metal (ii-A), polysulfide mixture (withLiNO₃) with Li metal for 1hour (ii-B), polysulfide mixture (with LiNO₃) with Li metal for 4hours (ii-C), polysulfide mixture (with LiNO₃) with Li metal for 24hours (ii-D), polysulfide mixture (with LiNO₃) with Li metal for 96hours (ii-E) (D.Zheng, X.Q. Yang, D.Y. Qu, ChemSusChem,2016,9, 2348-2350.)

3. Direct evidence for superior electrocatalytic performance of sulfur redox reaction on defect sites

Since sulfur and its discharge products in Li-S batteries are non-conductive, this results in poor electrochemical accessibility and low utilization of the active material. In addition, the polysulfuides produced by multi-step electrochemical reductions or chemical disproportionation can easily dissolve into the electrolyte and cause rapid loss of the active material and an unfavorable shuttle effect. The other issue to be overcome is the remarkable volume change of sulfur and its final discharge product lithium sulfide (Li_2S) which can cause serious pulverization of the cathode and further accelerate the capacity fading. To address these aforementioned issues, confining sulfur within various hosts, mostly conducting carbon-based materials, is regarded as one of the most efficient approaches to improve the overall performance of Li-S batteries. Generally, the nonpolar carbons are considered as incapable of immobilizing sulfur and its as-reduced products, owing to a weak C-S interaction. Introducing defects or heteroatoms can effectively promote the chemical interaction with sulfur, suppress the shuttle effect and synchronously accelerate the reaction kinetics. However, these assumptions were mainly concluded from overall performance of batteries containing different cathodic materials, which could hardly exclude many of the other possible influencing factors (i.e., electrode microstructure). Thus fundamental research of sulfur redox reactions on flat model electrodes by varying the defect density could contribute to the design of high-performance lithium-sulfur batteries.

To evaluate the performance of sulfur's reduction and oxidation on different planes of HOPG (basal, step and edge), cyclic voltammetry (CV) tests were carried out by using a standard three-electrode system in a glovebox. Figure II-573a shows the comparison of iR-free CV curves for HOPG-1T (basal plane), HOPG-1L (edge plane), HOPG-2T (edge plane) and HOPG-2L (step plane). The solution resistance (R_s) was obtained from electrochemical impedance spectra (EIS). The CVs for the two edge planes (HOPG-1L and HOPG-2T) are similar, and both considerably differ from the basal plane (HOPG-1T) and step plane (HOPG-2L). Since the CVs of different surfaces (top surface and lateral surface) on a same electrode are quite different, obviously, this phenomenon should not result from the difference of the conductivity along and perpendicular to the graphite basal plane as described in the literature. We adopted the reduction & oxidation peak potentials as an indicator of electrochemical reversibility. A clear correlation between the reduction & oxidation peak

potentials and I_D/I_G values extracted from Raman analysis was observed (Figure II-573b). The reduction peak potential gradually increased and the oxidation potential simultaneously decreased with increasing the defect density. The sulfur redox reaction on the edge plane, which contains the highest defect density, exhibits a superior electrochemical reversibility compared to reactions on the step plane and the basal plane. Hence, the defect sites exhibit better electrocatalytic activity towards sulfur reduction and oxidation.
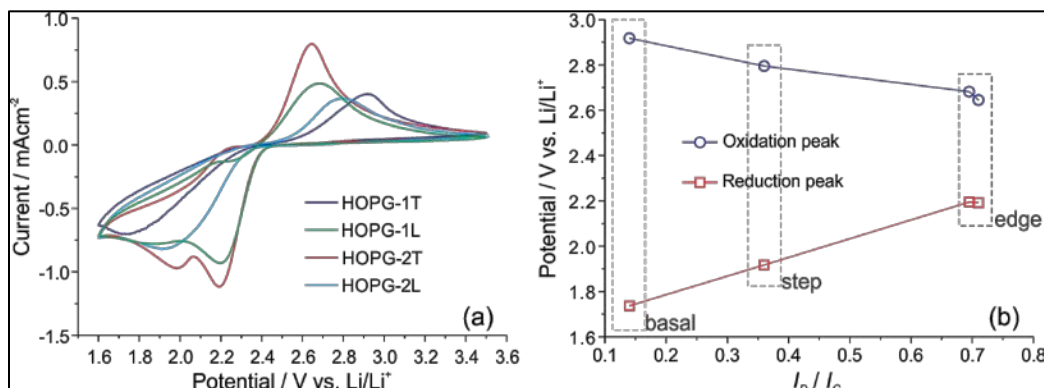
Figure II-573. (a) CVs of sulfur electrochemical reduction and oxidation on HOPG-1T (basal plane), HOPG-1L (edge plane), HOPG-2T (edge plane) and HOPG-2L (step plane) at a scan rate of 20 mV/s. (b) The relation between peak potential obtained from (a) and I_D/I_G obtained from Raman analysis. (G.W. Wang, D. Zheng, D. Liu, X.Q. Yang, D.Y. Qu, Carbon, 2017, 119, 460-463.)

Conclusions

1. Again the reliable and quantitative HPLC method we developed for the analysis of the dissolved polysulfide species and sulfur was demonstrated as a vital technique for the investigation of Li-S batteries. A three-step reduction mechanism was proposed for the sulfur cathode during the discharge, while a continuous oxidation of lithium sulfide and polysulfide ions to elemental sulfur was revealed. The two flat discharge plateau and a single flat recharge curve can be explained by the fast reaching chemical equilibrium of dissolve polysulfide ions, S_7^{2-}, S_6^{2-} and S_5^{2-} for the discharge plateau >2.3 V; S_5^{2-}, S_4^{2-} and S_4^{2-} for the discharge <2.1 V and S_5^{2-}, S_6^{2-}, S_7^{2-} and S_8^{2-} during recharge.

2. Both dissolved S and polysulfide ions can chemically react with Li metal in a Li-S cell during storage. LiNO3 additive can form a SEI layer on the Li electrode to prevent such reaction. However, the SEI layer was not stable enough for long term storage and needed to be maintained with the continuous consumption of LiNO3. Longer chain polysulfide ions (Sn2- with n≥6) were more reactive with Li than those with shorter chain (Sn2- with n≤5).

3. The defect sites on carbon could lower the polarization and exhibit superior electrocatalytic activity towards sulfur redox reactions. This observation has important implications not only for the design of advance cathodic materials for Li-S batteries, but also for research on sulfur related reaction catalysis.

Key Publications

1. Gongwei Wang, Dong Zheng, Xiao-Qing Yang, Deyang Qu, Sulfur Redox Reactions on Highly Oriented Pyrolytic Graphite (HOPG) Electrodes: Direct Evidence for Superior Electrocatalytic Performance on Defect Sites. *Carbon* 119(2017)460-463.

2. Dong Zheng, Dan Liu, Joshua Harris, Tianyao Ding, Jingyu Si, Sergi Andrew, Deyu Qu, Xiao-Qing Yang, Deyang Qu, Investigation of Li-S Battery Mechanism by Real-Time Monitoring the Changes of Sulfur and Polysulfide Species During the Discharge and Charge" *ACS Appl. Mater. & Interface*, 9(2017)4326-4332.

3. Dong Zheng, Xiao-Qing Yang, Deyang Qu, "Reaction between Lithium Anode and Polysulfide Ions in a Lithium-Sulphur Battery", *ChemSusChem*. 9(2016) 2348-2350.

4. Dong Zheng, Xiaoqing Yang, and Deyang Qu, "Stability of the solid electrolyte interface on the Li electrode in Li-S batteries", *ACS Appl. Mater. & Interface, 8(2016)10360-10366.*

5. Dong Zheng, Xuran Zhang, Jiankun Wang, Deyu Qu, Xiaoqing Yang, **Deyang Qu**, Reduction Mechanism of Sulfur in Lithium-Sulfur Battery: from elemental sulfur to polysulfide, *J. of Power Sources* 301(2016)312-316.

II.I.9   Statically and Dynamically Stable Lithium-sulfur Batteries (UTA)

Arumugam Manthiram, Principal Investigator

204 E. Dean Keeton Street, C2200
University of Texas at Austin
Austin, TX 78712
Phone: 512-471-1791
E-mail: manth@austin.utexas.edu

Tien Duong, Technology Manager
Phone: 202-586-7836
E-mail: Tien.Duong@ee.doe.gov

Start Date: October 1, 2015   End Date: September 30, 2018
Total Project Cost: $990,000   DOE share: $891,000   Non-DOE share: $99,000

Project Introduction

The commercialization of lithium-sulfur (Li-S) batteries is hampered by several scientific and technological challenges: low electronic and ionic conductivity of the active material, severe polysulfide (PS) migration from the cathode to the anode, and instability of the Li-metal anode. The poor conductivity limits the electrochemical utilization of the active material and often necessitates a high content of electrochemically inactive, conductive carbon or functional polymers in the cathode region, which lowers the practical energy density. The PS migration causes static and dynamic instabilities with high self-discharge, poisoning of Li-metal surface, and poor cycling efficiency, hindering the practical viability of Li-S batteries. Recently, a growing number of research articles caution that the proliferation of activities in Li-S technology might result from a presentation of overestimated battery chemistry and electrochemical characteristics obtained from testing cells with a low sulfur loading of less than 2.0 mg cm^{-2}, insufficient sulfur content of less than 65 wt.%, and high electrolyte/sulfur ratio of greater than 15. As a result, it is becoming obvious that the scientific and technological challenges are very sensitive toward and even strongly impacted by the sulfur loading in the cathode and the electrolyte/sulfur ratio in the tested cells.

To overcome the above challenges, our group has demonstrated that innovations in polysulfide (PS)-filter-coated separators and advanced electrode substrates can greatly enhance the electrochemical utilization and efficiency with reasonably high sulfur loadings and low electrolyte/sulfur ratios in the cells. This is because Li-S batteries involve conversion reactions unlike the insertion-reaction electrodes in commercial Li-ion batteries, so cell components/designs directly borrowed from Li-ion batteries may need new architectures or chemical/physical characteristics to be adapted to sulfur cathodes. Our cell-component design provides the fabricated Li-S cells with enhanced electrochemical performance: high utilization of the active material, extended cycle life, and good storage properties. More importantly, these custom cell configurations allow the cells to employ the easily prepared pure sulfur cathodes with high sulfur loading (> 2.0 mg cm^{-2}) and high sulfur content (> 65 wt.%) in the cells with low electrolyte/sulfur ratios of less than 11. Our progress illustrates that the approaches presented and developed in this project are inexpensive and offer a practically viable solution for the Li-S technology development.

Objectives

The objective of this project is to develop statically and dynamically stable Li-S batteries by integrating polysulfide (PS)-filter-coated separators with an advanced cathode design and/or a protected lithium-metal anode. The project includes a demonstration of electrochemically stable cells with sulfur capacities of > 1,000 mA h g^{-1} and cycle life in excess of 500 cycles (dynamic stability) along with improved storage properties (static stability) at > 70 wt.% sulfur content and ~ 5 mg cm^{-2} loading.

Approach

The electrochemical stability of the Li-S cells is improved by three approaches that are complementary to each other:

- The first approach focuses on the establishment of an electrochemically stable cathode environment by employing PS-filter-coated separators. The PS-filter coatings aim to suppress the severe polysulfide diffusion and improve the redox capability of the Li-S cells with high-sulfur loadings. The study includes an understanding of the materials characteristics, fabrication parameters, electrochemical properties, and battery performance of the PS-filter-coated separators.

- The second approach focuses on electrode engineering from two aspects. First, the investigation of a Li-metal anode with coating- and additive-supporting approaches aim at improving the safety of Li-S cells. Second, the research on activated-Li_2S cathode with little or no charge-barrier aims at promoting the performance and safety of the C-Li_2S cells.

- The integration of the above two approaches aims at creating statically and dynamically stable Li-S batteries for electric vehicles.

Results

In Year 2 of the project, we have realized three major key accomplishments with Li-S batteries by employing PS-filter-coated separators and advanced cathode architectures in the cells: (i) long-term dynamic electrochemical stability during cell cycling (Technical Milestone I, Quarter 1 (Q1)); (ii) long-term static electrochemical stability with low self-discharge during cell resting (Technical Milestone II, Q2); and (iii) remarkably improved electrochemical characteristics with high-loading sulfur cathodes (Technical Milestone II, Q3). As a result, we surpass the target values of 5.0 mg cm^{-2} and 70 wt.% sulfur that were set up to make the Li-S technology practically viable. We have realized sulfur loadings of as high as 30 – 60 mg cm^{-2} and sulfur content of up to 80 wt.% with good dynamic and static electrochemical performance of the Li-S cells (Go/No-Go Milestone, Q4).

Key accomplishment 1: long-term dynamic electrochemical performance

Our previous investigation in Year 1 initially selected four carbon materials with unique morphologies as the coating materials: spherical carbons, carbon nanofibers (CNFs), carbon nanotubes (CNTs), and graphene. These carbon materials were coated onto a polypropylene membrane (Celgard 2500) to form the PS-filter-coated separators. However, the carbon materials having abundant nanopores needed a high electrolyte/sulfur ratio for obtaining good cell performances. The needed electrolyte/sulfur ratios have been usually higher than 11 or even above 15, which leads to overestimated cell characteristics and would lower the practical energy density. In consideration of these facts, we focused on PS-filter-coated separators fabricated with nonporous CNFs and CNTs with a layer-by-layer (LBL) coating method, which allows the resulting Li-S cells to exhibit excellent cyclability with a low electrolyte/sulfur ratio fixed at 10 (Figure II-574).
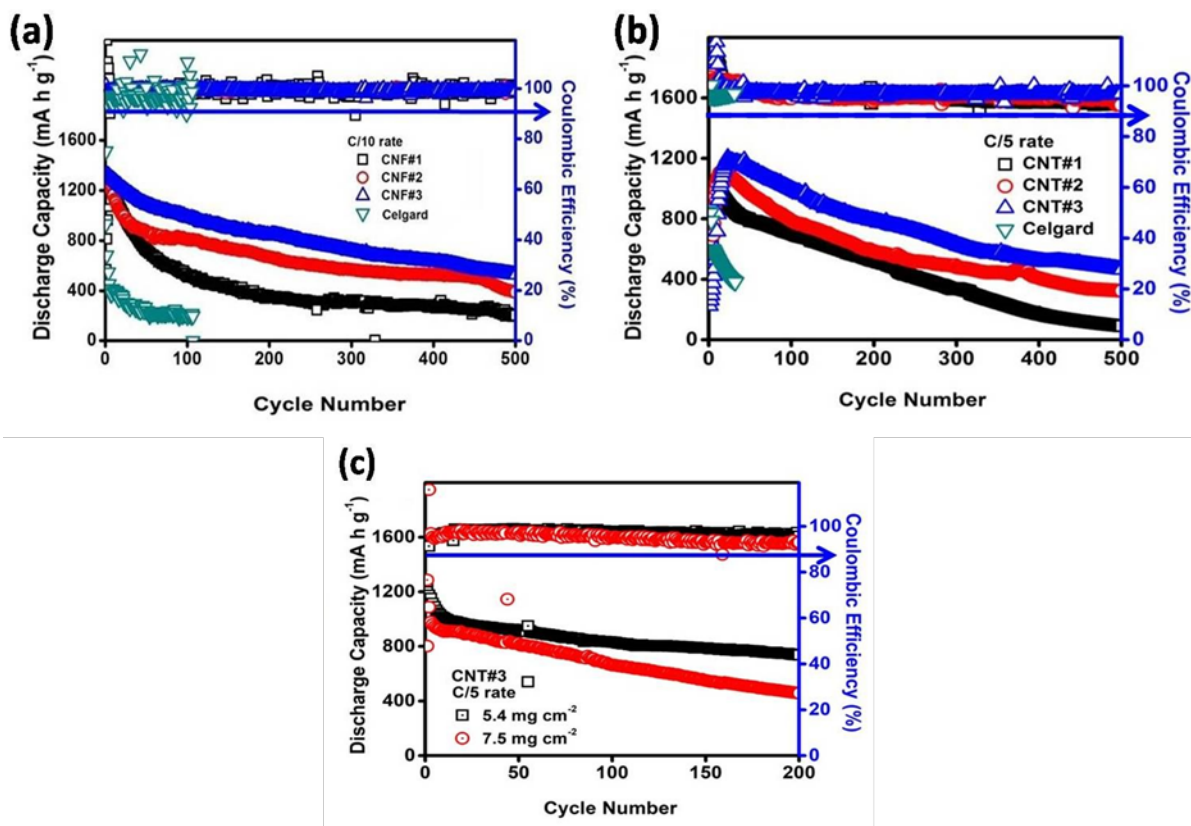
Figure II-574. Dynamic cycling performance of the cells fabricated with (a) LBL CNF-coated separators, (b) LBL CNT-coated separators, and (c) LBL CNT-coated separators with increasing sulfur loadings of 5.4 mg cm^{-2} (black line) and 7.5 mg cm^{-2} (red line).

Figure II-574a presents three LBL nonporous CNF-coated separators, which are termed as CNF#1 (0.1 mg cm^{-2} CNF coating), CNF#2 (0.2 mg cm^{-2} CNF coating), and CNF#3 (0.4 mg cm^{-2} CNF coating). The nonporous CNFs had a low surface area of 26 m^2 g^{-1} and no micropore absorption behavior. The Celgard membrane that is used as the substrate in our case and as the conventional separator in the Li-S literature weights 1.0 mg cm^{-2} and has a thickness of 25 μm. The cells fabricated with the thin-film CNF#3-coated separators displayed a high peak capacity of 1,329 mA h g^{-1} (areal capacity: 4.3 mA h cm^{-2}) at C/10 rate and a high reversible capacity of 529 mA h g^{-1} after 500 cycles. The enhanced electrochemical utilization and stability were based on the use of pure sulfur directly as the active material. The pure sulfur cathodes used in the tested cells were fixed with a high sulfur loading of 3.4 mg cm^{-2} and a high sulfur content of 70 wt.%.

In Figure II-574b, our follow-up study with a light-weight LBL CNT coating further reduced the coating mass to only 0.05 mg cm^{-2} with a thickness of 8 μm. The three presented LBL coated separators are named as CNT#1 (0.05 mg cm^{-2} CNT coating), CNT#2 (0.10 mg cm^{-2} CNT coating), and CNT#3 (0.15 mg cm^{-2} CNT coating). The selected nonporous CNTs had a low surface area of 40 m^2 g^{-1}. With the highly conductive CNT as the coating material, the cells were able to cycle well at a higher sulfur loading of 4.0 mg cm^{-2} and sulfur content of 80 wt.% at a higher cycling rate of C/5 for 500 cycles. With even higher sulfur loadings of 5.8 and 7.5 mg cm^{-2} (Figure II-574c), the cells fabricated with the LBL CNT#3 separator further exhibited a peak discharge capacity of 1,087 mA h g^{-1} with stable cyclability for 200 cycles, which translates to a high areal capacity and energy density of, respectively, 8 mA h cm^{-2} and 17 mW h cm^{-2}.

Key accomplishment 2: long-term static electrochemical performance with low self-discharge

Self-discharge is a serious problem in the development of Li-S batteries. Unfortunately, the lack of literature on the realities of self-discharge makes it a daunting challenge to develop a practically viable Li-S technology. Accordingly, we focused in this year on improving the long-term static electrochemical performance (shelf-life) of Li-S batteries by employing the above-mentioned LBL-coated separators. Herein, we present the cells fabricated with the LBL CNF-coated separators as a key example because of the lowest self-discharge and the longest shelf-life obtained (Figure II-575).
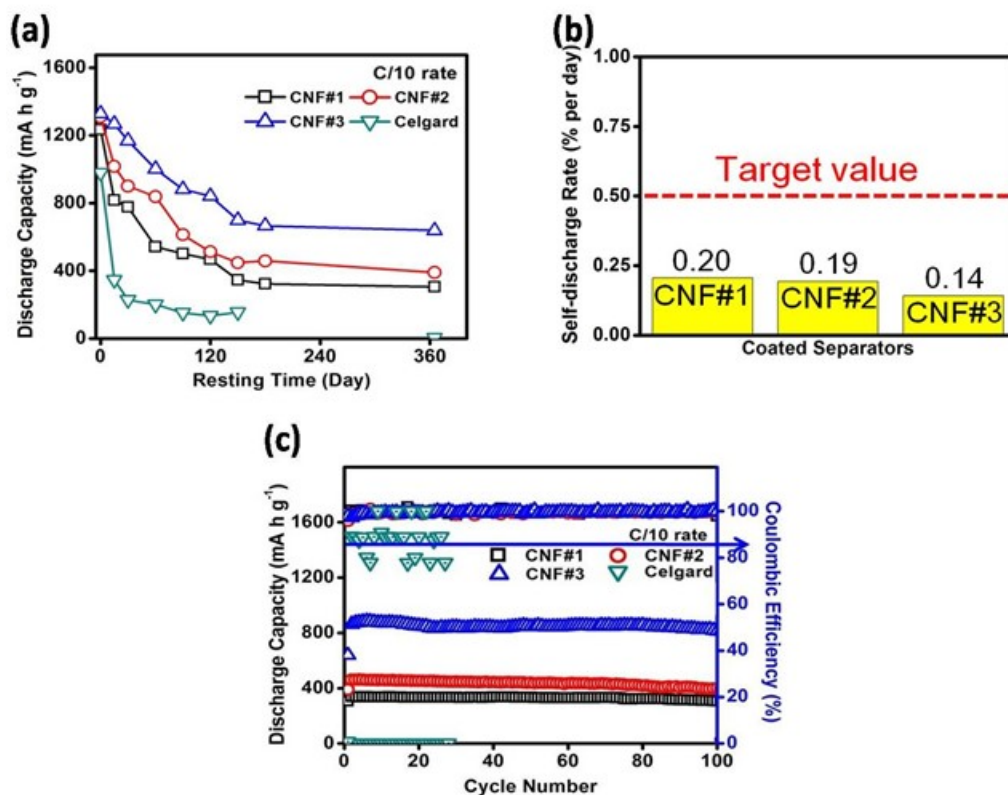
Figure II-575. Static electrochemical analysis of the Li-S cells fabricated with the LBL CNF-coated separators after resting for 365 days (black, red, and blue lines) and with the polypropylene membrane after resting for 150 days (green line): (a) static electrochemical stability, (b) self-discharge rate, and (c) cyclability.

The LBL CNF-coated separators provided the Li-S cells with an extended cell shelf-life of one year, which is the longest cell-storage period reported for Li-S cells in the literature (Figure II-575a). In this extended low self-discharge demonstration, the cells fabricated with the LBL CNF-coated separators retained 50% of the initial capacity after storing for 1 year and exhibited a low self-discharge rate of only 0.14% per day, much lower than the target value of less than 0.50% per day (Figure II-575b). In addition, the stored cells still displayed good cyclability. Figure II-575c shows that the cell rested for 365 days kept a high capacity with a low capacity-fade rate of 0.10% per cycle for 100 cycles. Thus, in developing Li-S batteries with a low self-discharge, we have made in this year three significant progresses: (1) the longest shelf-life, (2) the lowest self-discharge rate, and (3) good cyclability after resting (storing) for 1 year.
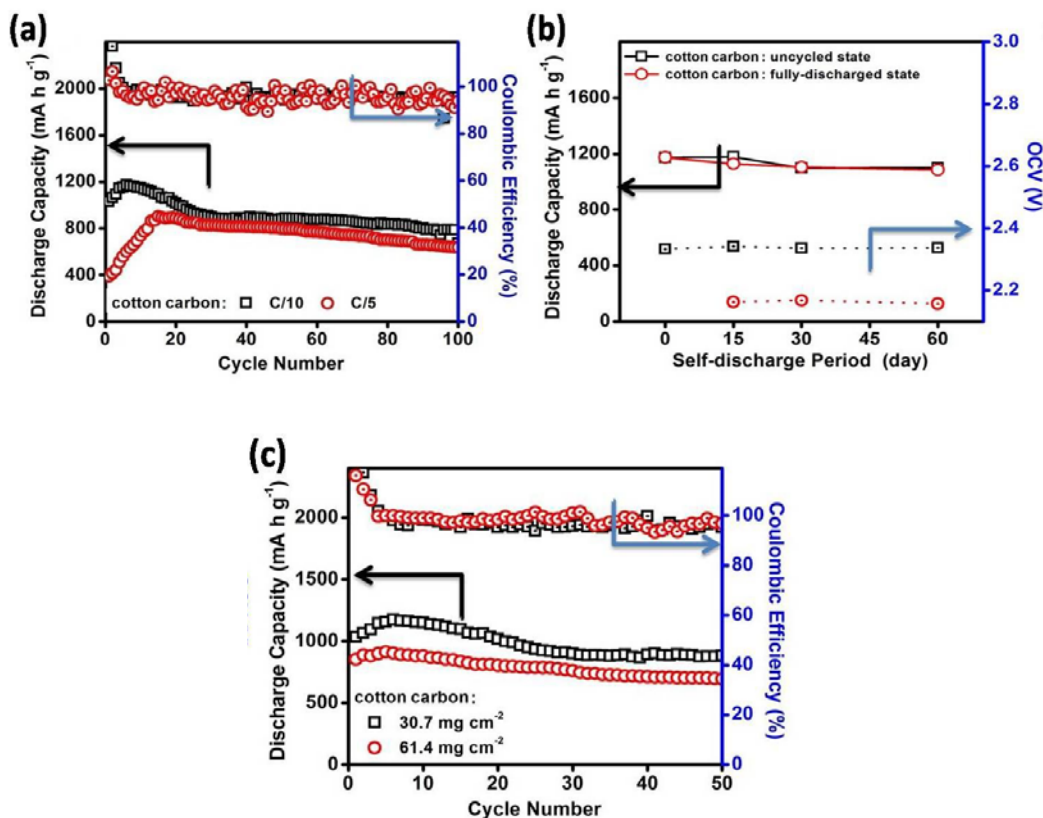
Figure II-576. Electrochemical analysis of the Li-S batteries fabricated with the cotton-carbon cathodes with a sulfur loading of 30 mg cm^{-2}, a sulfur content of 80 wt.%, and an electrolyte/sulfur ratio of 6.8: (a) cycling performance at C/10 and C/5 rates and (b) self-discharge analysis after resting for two months with freshly-made cells and fully-discharged cells. (c) Cycling performance of the cotton-carbon cathode with a higher sulfur loading of 60 mg cm^{-2} at C/10 rate.

Key accomplishment 3: impact from applying practically necessary parameters in the cells

It is becoming increasingly clear that the Li-S battery chemistry and the electrochemical performances are distinctly different between low-loading sulfur cathodes (< 2.0 mg cm^{-2}) and practically-relevant high-loading cathodes (> 4.0 mg cm^{-2}). Moreover, the electrolyte/sulfur ratio, another key issue that has been lacking in the literature investigation for years, has recently been pointed out to have a strong influence toward the electrochemical utilization and stability of Li-S cells, and even the basic cyclability of the cells. An even low electrolyte/sulfur ratio of less than 7.0 should be applied in the in the investigation of Li-S battery chemistry. Accordingly, we focused on improving the electrochemical characteristics of high-loading sulfur cathodes under a low electrolyte/sulfur ratio by integrating our findings above in accomplishments 1 and 2 (Q1 and Q2) with advanced cathode architectures. We have realized Li-S cells featuring a sulfur loading of as high as 30 – 60 mg cm^{-2}, a sulfur content of up to 80 wt.%, and a low electrolyte/sulfur ratio of only 6.8.

Figure II-576 shows an advanced cathode design that was fabricated with a cotton-carbon electrode, in which polysulfide was used as the catholyte. Our cotton-carbon cathodes with a high sulfur loading (30 mg cm^{-2}) and content (80 wt.%) represent the highest sulfur loading/content among the literature reports and are able to smoothly cycle and stably rest at a very low electrolyte/sulfur ratio of only 6.8, which is much lower than the values used in the literature. The cells show good cyclability with a capacity retention of 70% after 100 cycles, and improved cell-storage stability with a low self-discharge rate of just 0.12% per day after storing for 60 days (Figure II-576a and Figure II-576b). Such a well-designed cathode configuration further allowed an ultrahigh sulfur loading of 60 mg cm^{-2}, while the cells retained high electrochemical reversibility and efficiency with a high areal capacity and energy density of, respectively, 56 mA h cm^{-2} and 118 mW h cm^{-2}

(Figure II-576c). The cell performance metrics are higher than the values obtained with the current commercial Li-ion batteries (4 mA h cm^{-2} and ~ 10 mW h cm^{-2}) based on LiCoO$_2$ cathode.

Conclusions

In Year 2, we have completed the investigation on improving the dynamic and static electrochemical performances of Li-S batteries by assessing the cells fabricated with polysulfide-filter (PS-filter)-coated separators. The LBL coated separators with various nonporous CNF and CNT coatings allows the corresponding Li-S cells to cycle smoothly for over 500 cycles with a low self-discharge after storing for a long period of over one year. These enhanced electrochemical characteristics are all based on cells assembled with pure sulfur cathodes with a reasonably high sulfur loading and sulfur content as well as a low electrolyte/sulfur ratio in the cells. After understanding that the amount and ratios of the active material and electrolyte have a strong influence toward the basic Li-S battery performance, we developed advanced cathodes with a high sulfur loading of up to 60.0 mg cm^{-2} (target value: 5.0 mg cm^{-2}), a high sulfur content of 80 wt.% (target value: 70 wt.%), and a low electrolyte/sulfur ratios of 6.8 (the suggested ratio for conducting reasonable Li-S research is less than 11). We demonstrated that Li-S cells featuring these practically necessary parameters could still display good cyclability and low self-discharge with a long shelf life. More importantly, the areal capacity and energy density obtained with the cells attain, respectively, 56 mA h cm^{-2} and 118 mW h cm^{-2}. These performance values imply that the Li-S technology does have a chance to perform better than the current Li-ion battery cathodes based on LiCoO$_2$ with an areal capacity of 4 mA h cm^{-2} and an areal energy density of 10.1 mW h cm^{-2}.

Key Publications

Reports
1. DOE EE7218 Quarterly Report-01-17 (Jan. 15, 2017)

2. DOE EE7218 Quarterly Report-04-17 (Apr. 15, 2017)

3. DOE EE7218 Quarterly Report-07-17 (Jul. 17, 2017)

4. DOE EE7218 Quarterly Report-10-17 (Oct. 17, 2017)

Journal Articles
1. C.-H. Chang, S.-H. Chung, and A. Manthiram, "Dendrite-Free Lithium Anode via a Homogenous Li-Ion Distribution Enabled by a Kimwipe Paper," *Advanced Sustainable Systems*, **1**, 1600034 (2017).

2. S.-H. Chung, P. Han, C.-H. Chang, and A. Manthiram, "A Shell-Shaped Carbon Architecture with High-Loading Capability for Lithium Sulfide Cathodes," *Advanced Energy Materials*, **7**, 1700537 (2017).

3. S.-H. Chung and A. Manthiram, "Lithium–Sulfur Batteries with the Lowest Self-Discharge and the Longest Shelf life," *ACS Energy Letters*, **2**, 1056 (2017).

4. S.-H. Chung, P. Han, and A. Manthiram, "Quantitative Analysis of Electrochemical and Electrode Stability with Low Self-Discharge Lithium-Sulfur Batteries," *ACS Applied Material & Interfaces*, **9**, 20318 (2017).

5. C.-H. Chang, S.-H. Chung, S. Nanda, and A. Manthiram, "A Rationally Designed Polysulfide-Trapping Interface on the Polymeric Separator for High-Energy Li–S Batteries," *Materials Today Energy*, **6**, 72 (2017).

6. L. Luo, S.-H. Chung, C.-H. Chang, and A. Manthiram, "A Nickel-Foam@Carbon-Shell with a Pie-Like Architecture as an Efficient Polysulfide Trap for High-Energy Li–S Batteries," *Journal of Materials Chemistry A*, **5**, 15002 (2017).

7. L. Luo and A. Manthiram, "Rational Design of High-Loading Sulfur Cathodes with a Poached-Egg-Shaped Architecture for Long-Cycle Lithium–Sulfur Batteries," *ACS Energy Letters*, **2**, 2205 (2017).

8. C.-H. Chang, S.-H. Chung, P. Han, and A. Manthiram, "Oligoanilines as a Suppressor of Polysulfide Shuttling in Lithium-Sulfur Batteries," *Materials Horizons* **4**, 908 (2017).

Presentations

1. A. Manthiram, "Next-generation Battery Materials and Technologies for Electrical Energy Storage," *Lee Hsun Lecture Award on Materials Science, Institute of Metal Research*, Shenyang, China, October 19, 2016 (invited).

2. A. Manthiram, "Tailored Carbon Materials for Overcoming Critical Issues in Rechargeable Batteries," *International Union of Materials Research Society – 17th International Conference in Asia (IUMRS-ICA 2016)*, Qingdao, China, October 20 – 24, 2016 (invited).

3. A. Manthiram, "Role of Materials Chemistry in Electrical Energy Storage," *National Synchrotron Radiation Center*, Hsinchu, Taiwan, October 31, 2016 (invited).

4. A. Manthiram, "Next-generation Battery Chemistries: Materials Challenges and Prospects," *Applied Science Center*, Academia Sinica, Taipei, Taiwan, November 3, 2016 (invited).

5. A. Manthiram, "Electrical Energy Storage: Next-generation Battery Chemistries," *Distinguished Lecture at Colorado School of Mines and National Renewable Energy Laboratory*, Golden, CO, November 14, 2016 (invited).

6. A. Manthiram, "Next-generation Battery Chemistries: Challenges and Prospects," *International Symposium on Advances in Electrochemical Science and Technology (ISAEST)*, Chennai, India, December 8 – 10, 2016 (invited).

7. A. Manthiram, "Dynamically and Statically Stable Metal-sulfur Batteries with High Sulfur Loading," *2017 Spring Meeting of the Materials Research Society*, Phoenix, AZ, April 17 – 21, 2017 (invited).

8. S.-H. Chung, C.-H. Chang, and A. Manthiram, "Lithium-sulfur Batteries with an Ultrahigh-sulfur-loading Carbon-cotton Cathode," *231st ECS Meeting,* New Orleans, LA, May 28 – June 1, 2017.

9. A. Manthiram, "Dynamically and Statically Stable Lithium-sulfur Batteries," *Annual Merit Review Meeting, U.S. Department of Energy,* Washington, D.C., June 5 – 9, 2017 (invited).

10. A. Manthiram, "High Energy Density Lithium-sulfur Batteries with High Sulfur Loading," *International Conference on Materials for Advanced Technologies (ICMAT),* Singapore, June 18 – 23, 2017 (invited keynote talk).

11. A. Manthiram, "Next Generation Battery Technologies: Challenges and Opportunities," *NASA Workshop on Battery Technologies for Future Aerospace Applications*," Cleveland, OH, August 16 – 17, 2017 (invited).

12. A. Manthiram, "Electrical Energy Storage: Next Generation Battery Technologies," *China University of Hong Kong*, Hong Kong, September 29, 2017 (invited).

II.I.10 Dual Function Solid State Battery with Self-forming Self-healing Electrolyte and Separator (Stony Brook University)

Esther Takeuchi, Principal Investigator
Distinguished Professor
Stony Brook University
1000 Innovation Road
Stony Brook, NY 11794-6044
Phone: 631-216-7414
E-mail: esther.takeuchi@stonybrook.edu

Kenneth J. Takeuchi, Co-Principal Investigator
Stony Brook University
1000 Innovation Road
Stony Brook, NY 11794-6044
Phone: 631-632-8579
E-mail: kenneth.takeuchi.1@stonybrook.edu

Amy C. Marschilok, Co-Principal Investigator
Stony Brook University
1000 Innovation Road
Stony Brook, NY 11794-6044
Phone: 631-216-7419
E-mail: amy.marschilok@stonybrook.edu

Tien Duong, Technology Manager
U.S. Department of Energy
Phone: 202-586-7836
E-mail: Tien.Duong@ee.doe.gov

Start Date: October 1, 2016   End Date: September 1, 2019
Total Project Cost: $1,200,000   DOE share: $1,065,975   Non-DOE share: $134,025

Project Introduction

The goal of this project is to demonstrate a solid state rechargeable battery based on a lithium metal anode and iodine cathode with a self-forming, self-healing electrolyte and separator. The presence or formation of dendrites or pin holes can result in compromised cell performance or even failure for solid state cells which would be avoided by the proposed new technology. The theoretical energy density of the Li/I_2 couple is 560 Wh/kg, which provides the opportunity to meet or exceed the DOE target of 250 Wh/kg at the battery level.

The proposed concept is a solid state battery utilizing lithium iodide (LiI) combined with silver iodide (AgI) as the electrolyte with lithium (silver) metal as the anode and iodine as the cathode with a self-forming self-healing separator/electrolyte. The battery will be assembled in the discharged state where the anode and cathode will be created during the first formation (charge) step. Silver ion, Ag^+, will diffuse toward the negative electrode and be reduced to silver metal, Ag^0 and lithium ion, Li^+, will form a lithium metal-layer at the anode. Iodine ion, I^-, will be oxidized to elemental iodine, I_2, at the cathode side. As formation of the battery continues, Lithium iodide will remain and serve as both the separator and electrolyte, as shown schematically in Figure II-577.
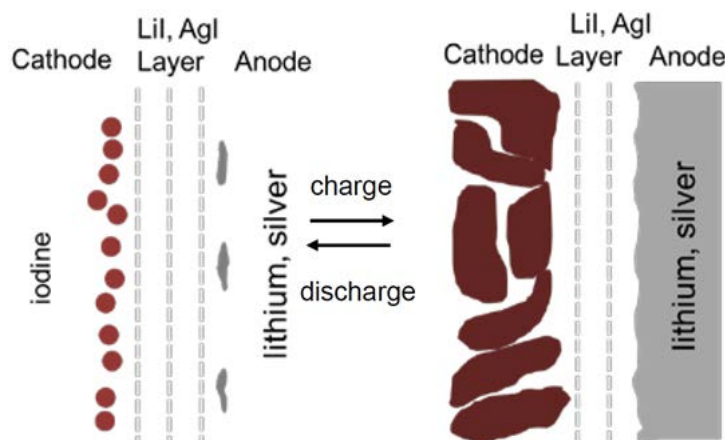
Figure II-577. Silver-lithium/iodine solid state dual function battery.

Objectives

The project goal will be addressed by focusing on the three major objectives outlined below:

Objective 1

Develop a LiI/AgI-based electrolyte with conductivity of $>10^{-3}$ S/cm at 30°C.

Objective 2

Form Li/I_2 batteries through the charging of the composite solid state electrolytes, determine relationship of coulombic efficiency to electrolyte type.

Objective 3

Determine the role of Ag ion in the anode:electrolyte interface as a function of electrolyte composition and cell test parameters through in-situ and ex-situ analyses.

Approach

The proposed solid state battery utilizes lithium iodide (LiI) combined with silver iodide (AgI) as the electrolyte with lithium (silver) metal as the anode and iodine as the cathode with a self-forming self-healing separator/electrolyte. The mechanism of the $Ag-Li/I_2$ solid state battery can be described as follows:

Charge: $Li^+ + e^- \rightarrow Li$ (anode)   Discharge: $1/2I_2 + Li \rightarrow LiI$

$\qquad Ag^+ + e^- \rightarrow Ag$ (anode) $1/2I_2 + Ag \rightarrow AgI$

$\qquad I^- \rightarrow 1/2I_2 + e^-$ (cathode)

This is a multiyear program where the effort is divided into three major tasks.

Year 1 involves preparation and characterization of solid state electrolytes and conductivity measurements. (See Table II-25.)

Year 2 will focus on cell construction and testing including both *in-situ* and *ex-situ* analysis.

Year 3 will focus on cell characterization. Under the program, cycle life, efficiency, energy density, and the functional capacity of cells will be determined.

The proposed work will be executed in the Advanced Power Sources (APS) Laboratories in the Chemistry Building at Stony Brook University (SBU), the Advanced Energy Research and Technology Center (AERTC) at SBU, and at Brookhaven National Laboratory (BNL). BNL offers core capabilities for the proposed program, including National Synchrotron Light Source-II (NSLS-II) and Center for Functional Nanomaterials (CFN).

Procurement of reagents (Q1)

All reagents have been procured commercially and characterized. X-ray diffraction patterns were recorded and analysis of the diffraction patterns showed that the AgI sample was a majority β-AgI phase with a small contribution from γ-AgI. Lithium iodide diffraction patterns showed LiI (95%) with (5%) hydrate (LiI·1H2O).

Table II-25: Quarterly milestones and verification for Year 1.

	Q1	Q2	Q3	Q4
Milestone	All reagents procured, water content verified	Develop methodology for AC impedance measurement as a function of temperature	Identify 4 most conductive Ag containing LiI solid electrolytes for further study	At least one electrolyte with conductivity ≥10^{-3} S/cm
Verification	Karl Fischer titration, XRD	Results consistent with prior literature for LiI electrolyte	Electrochemical impedance spectroscopy (EIS) at 30ºC	EIS at 30ºC

Results

Development of method for resistance measurements (Q2)

The development of methodology to accurately and reproducibly measure the resistance of the solids was developed using electrochemical impedance spectroscopy (EIS) as a function of temperature. Every set of measurements was conducted in triplicate. The results of a typical experiment showing the Nyquist plots as a function of the temperature for AgI are shown in Figure II-578A. Note that three samples at each temperature are shown with good reproducibility. The EIS data were analyzed where the data were fitted to an equivalent circuit, Figure II-578, inset. The values of the circuit elements were determined from the equivalent circuit fits which allowed quantitative analysis of the data. The results for AgI and LiI conductivity as a function of temperature including error bars are shown in Figure II-578B. The conductivity results obtained from the series of measurements are in agreement with prior literature. This method was used for all composite solid electrolyte testing.

$$R = \frac{\rho l}{S}$$
$$\sigma = \frac{l}{RS}$$
$$\sigma = \sigma_0 e^{-E_a/k_B T}$$
$$ln\sigma = ln\sigma_0 - E_a/k_B T$$
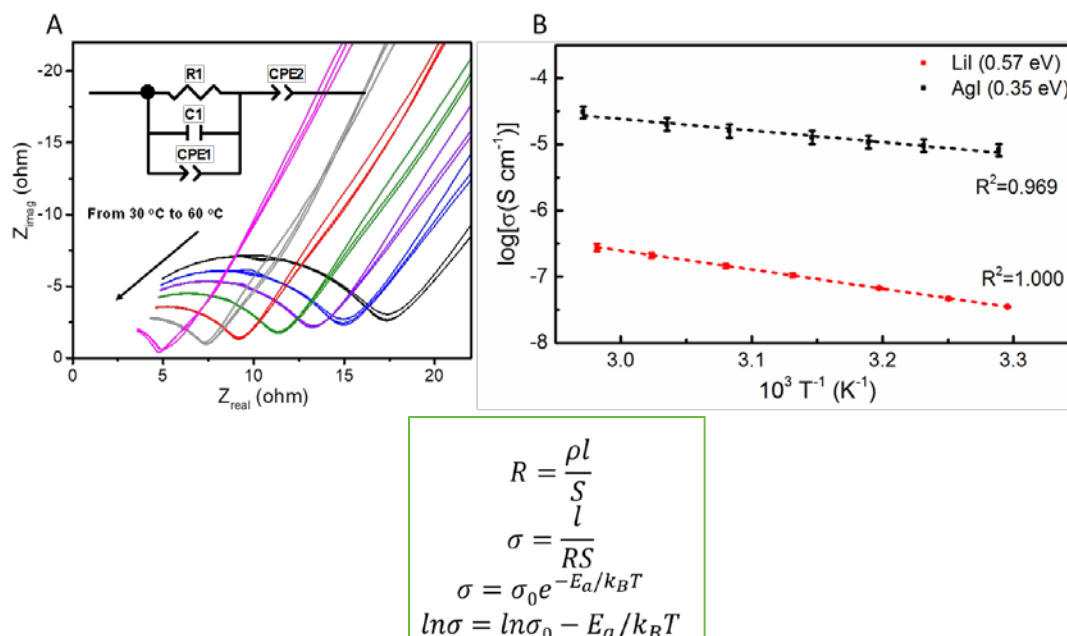
Figure II-578. EIS for AgI as a function of temperature (A), equivalent circuit model used for quantitative data analysis (Inset)/Source: B.J. Neudecker, W. Weppner, *J. Electrochem. Soc.,* **1996,** *143(7)*, 2198-2203. Poulsen, W. Finn, *S. S. Ionics,* **1981**, *2(1)*, 53-57, (B) Conductivity plotted as a function of temperature, (Right) Equation used to determine conductivity values from measurement of resistance.

Measurement of LiI Composite Solid Electrolytes (Q3)

A range of solid electrolyte compositions was tested. This included synthesized Ag ion conductors, $RbAg_4I_5$ and KAg_4I_5, (Figure II-579A-C), and composites prepared from $Ag/Al_2O_3/LiI$. (Figure II-579D) We used electrochemical impedance spectroscopy (EIS) methodology where the measurement method was validated by repeating measurements of the same material over a range of temperatures with at least triplicate measurements of each material. Over 75 samples of lithium iodide-based composite electrolytes, containing Ag ion conductor and polymer additives in a variety of combinations and ratios were tested. Sample data of initial EIS data of Ag^+/Li^+ ion conductors is shown in Figure II-580(A-F) where increased percentage of Al_2O_3 resulted in increased conductivity (Figure II-580G-H).
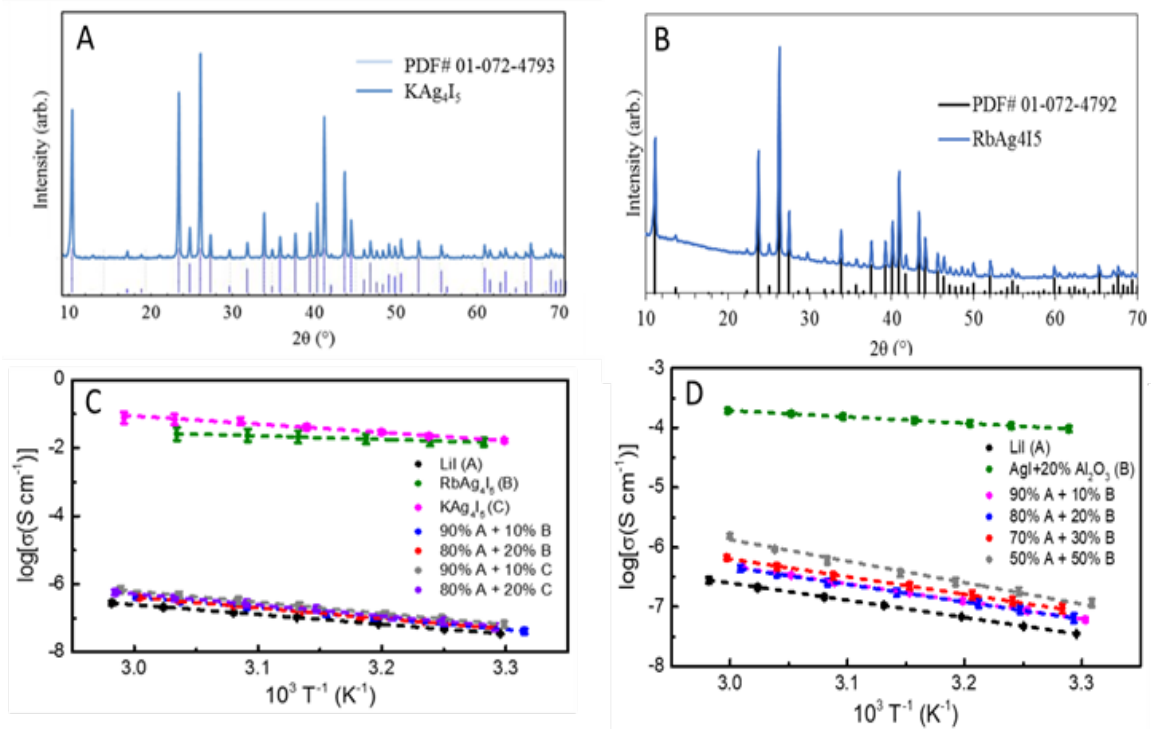
Figure II-579. XRD of synthesized Ag ion conductors, KAg_4I_5 (A) and $RbAg_4I_5$ (B). Conductivity as a function of temperature for LiI +x % MAg_4I_5 (M = K, Rb) (C), and for Li_x% (AgI+20% Al_2O_3).
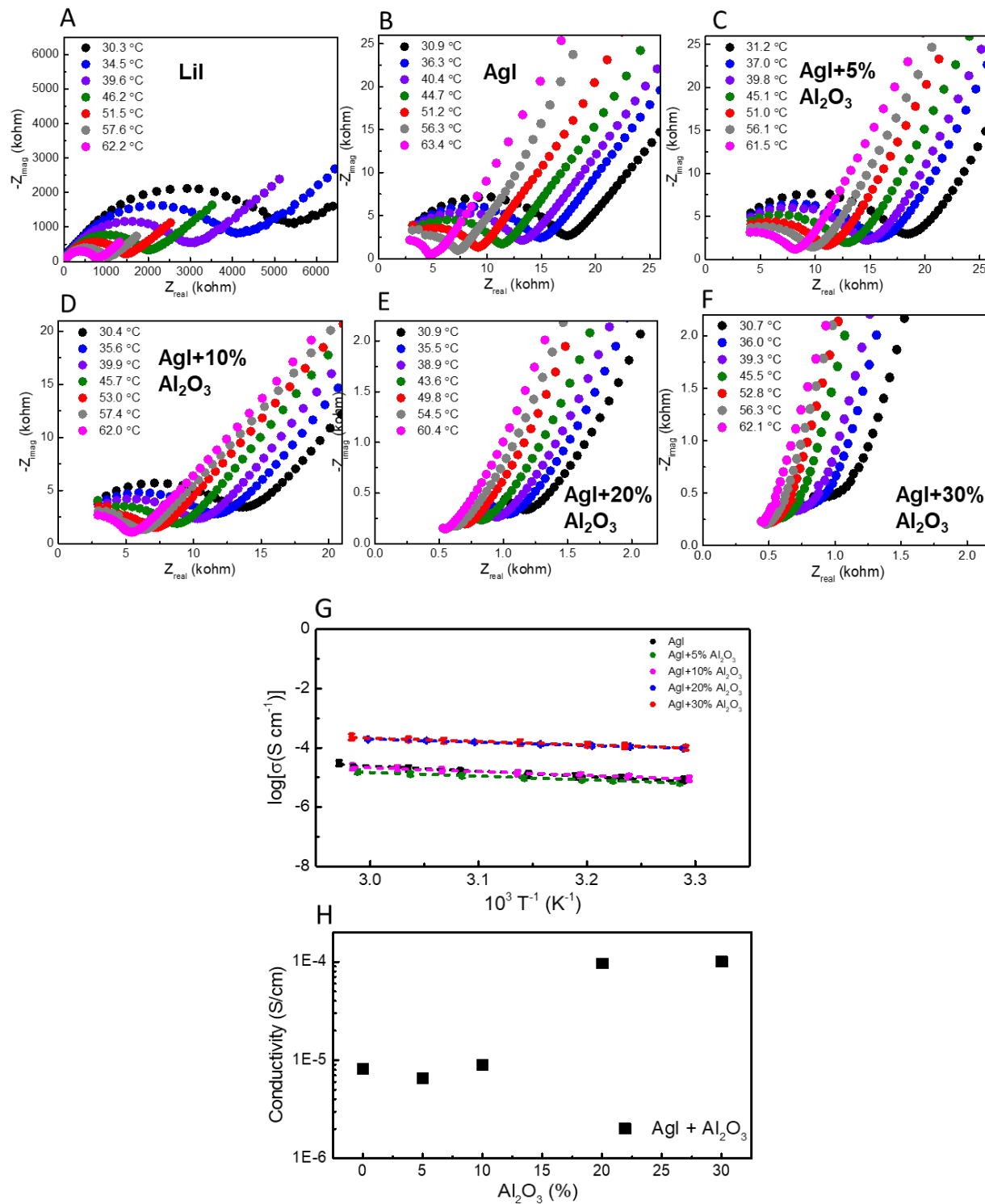
Figure II-580. (A-F) AC impedance of Ag+/Li+ conductors with varying amount of Al₂O₃ additive, G) Conductivities of AgI with 0, 5, 10, 20, 30% Al₂O₃ additive in temperature range from 30° to 60°C, H) AgI + *x* Al₂O₃ conductivities at 30°C.

Figure II-581 shows increases in conductivity observed with the addition of polymer to LiI composite electrolytes.
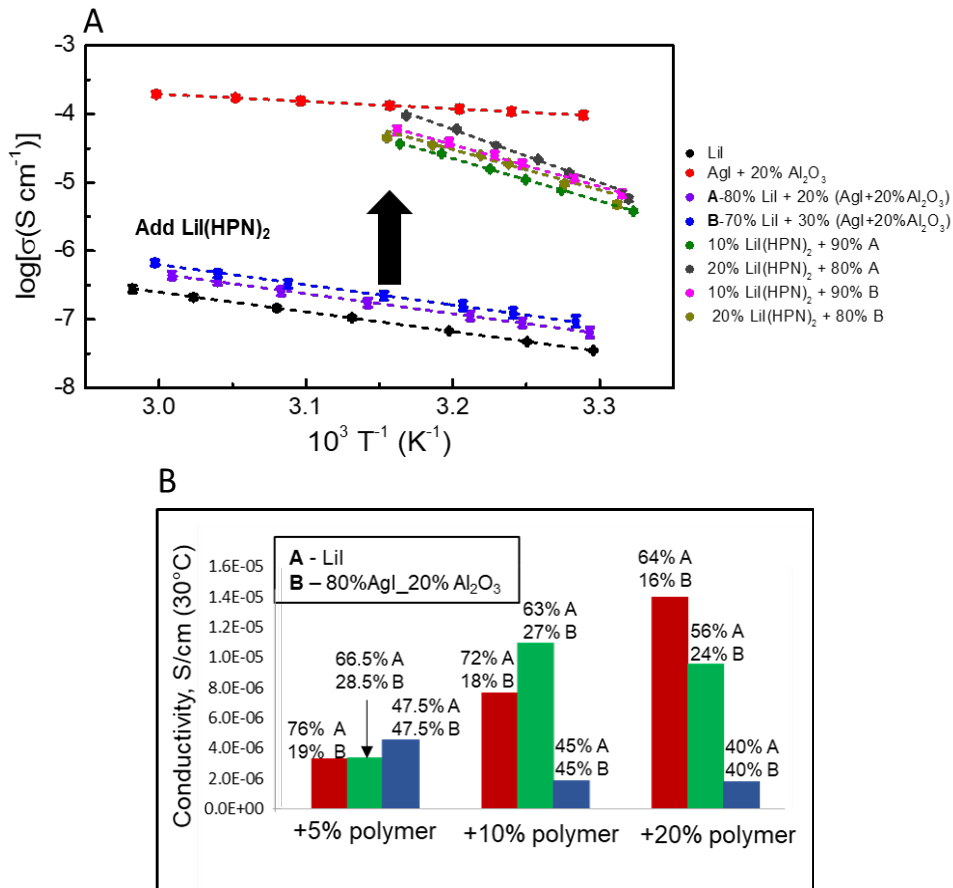
Figure II-581. A) Use of LiI(HPN)₂ in silver containing LiI electrolyte increases ionic conductivity, B) Various ratios of solid electrolyte and polymer were tested, and conductivity values compared at 30ºC.

Identification of electrolyte with conductivity ≥10^{-3} S/cm (Q4)

Two solid electrolytes were identified electrolyte with conductivity ≥10^{-3} S/cm, meeting the fourth quarter (Go/No Go) Milestone. LiI-based solid electrolytes with varying compositions including polymeric additives poly-2-vinylpyridine and 3-hydroxyproprionitrile were measured using our developed EIS methodology.

After exploration of lithium iodide-based composite electrolytes, we successfully achieved the Go/No Go goal by identifying two electrolyte compositions with conductivities ≥10^{-3} S/cm at 30°C as shown in Table II-26.

Table II-26: Conductivity of LiI composite electrolytes at 30ºC.

Sample	σ, 30° C (S/cm)
A. LiI composite electrolyte I	1.0 x 10^{-3}
B. LiI composite electrolyte II	1.1 x 10^{-3}

Feasibility demonstration

Initial charging data using coin cell type construction containing solid electrolytes, demonstrated proof of concept for the feasibility of *in situ* generation of anode, cathode and solid electrolyte/separator. A notable decrease in charge transfer resistance as determined by EIS after charging was observed (Figure II-582, A-C). Notably, the open circuit voltages of the cells were stable after the charging step. Disassembly of the cells followed by characterization demonstrated *in situ* generation of Li or Ag and I$_2$. (Figure II-583). A more highly conductive composite electrolyte (Composition II) containing LiI and AgI additives was also successfully charged. (Figure II-582C)
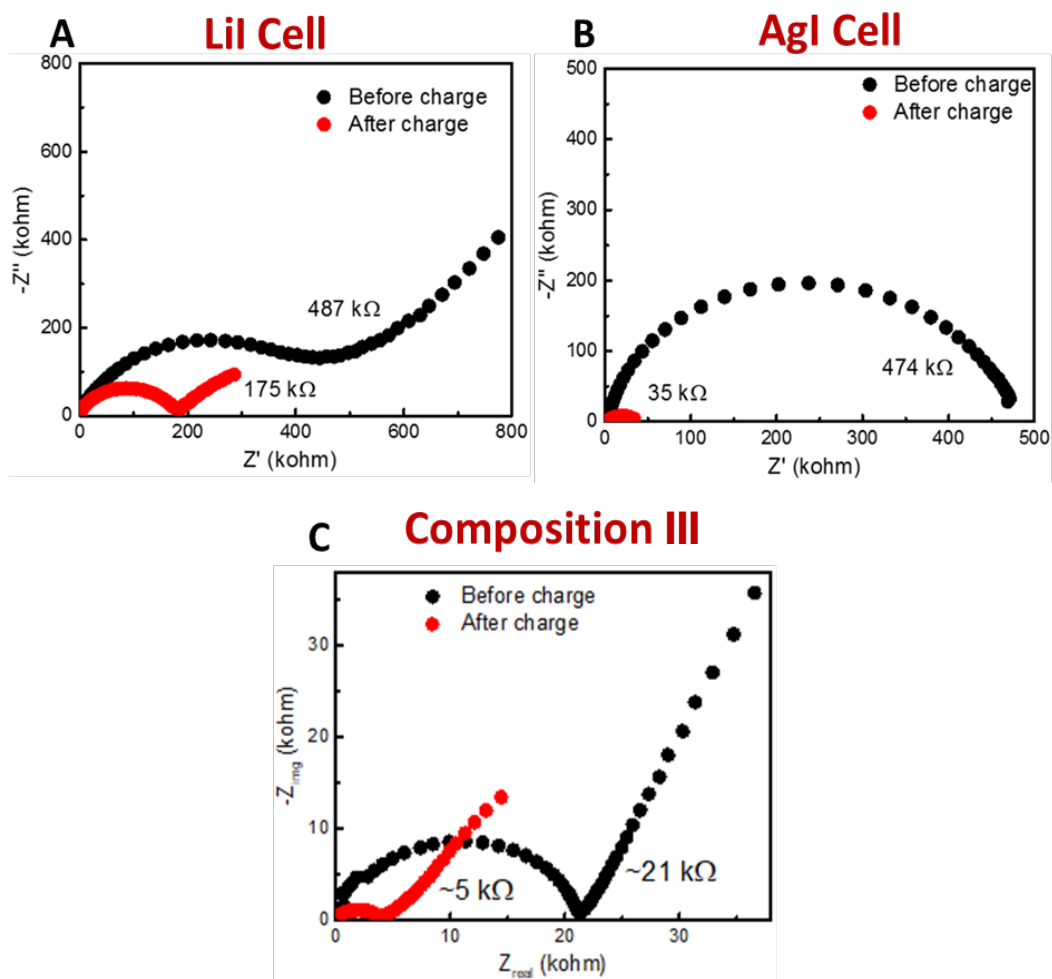
Figure II-582. EIS data: Pristine A) LiI, B) AgI solid electrolyte before and after charging, C) Composition I, a LiI-based electrolyte with AgI and polymer additive before and after charging.
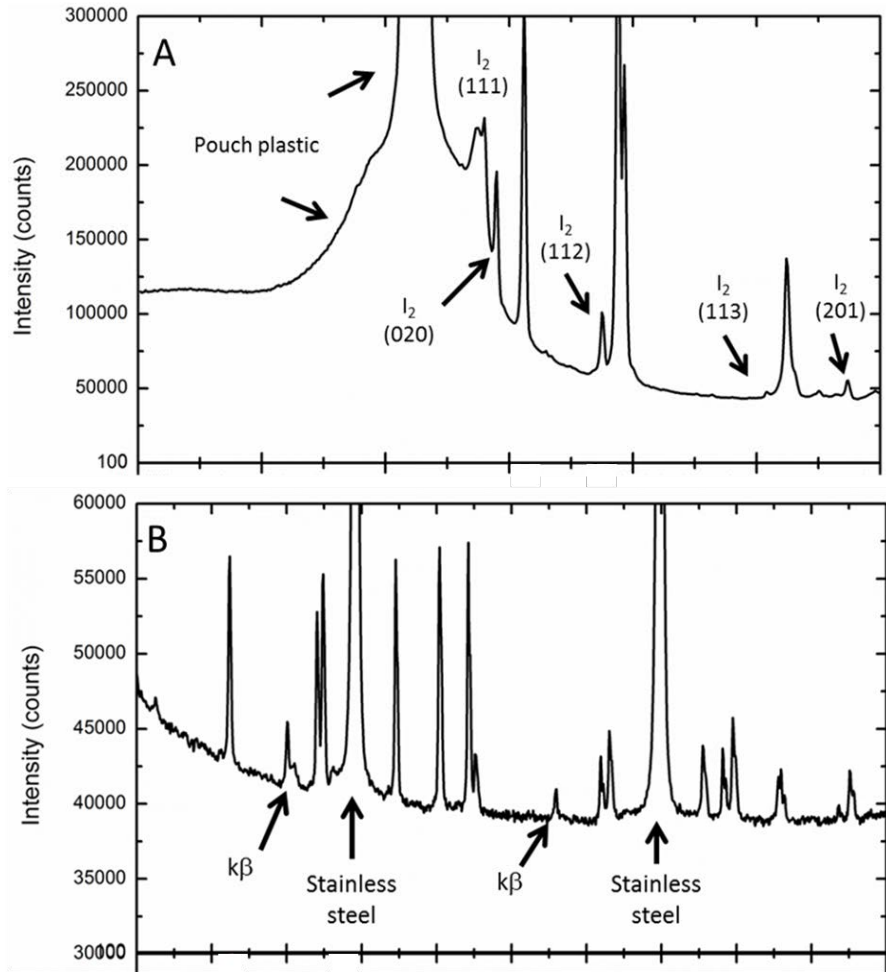
Figure II-583. A) I$_2$ clearly identified by XRD on positive side, B) Peaks consistent with Li observed on negative side.

A LiI-based composite electrolyte (Composition IV) was explored using four different interfaces demonstrating the role of the interface. Figure II-584A shows the resistance before and after charge (inset). Figure II-584B illustrates step-wise charging of the cells with increasing currents made possible by impedance decrease on charge. Figure II-584C shows OCV stability at 2.8 V for charged cells consistent with the Li/I$_2$ couple. Preliminary data using Energy Dispersive X-ray Diffraction (EDXRD) has been collected for an intact assembled cell (Figure II-585), and demonstrates feasibility for identification of localized phases within a stainless steel casing. Future work will focus on development of cell construction and both *ex-* and *in-situ* analysis.
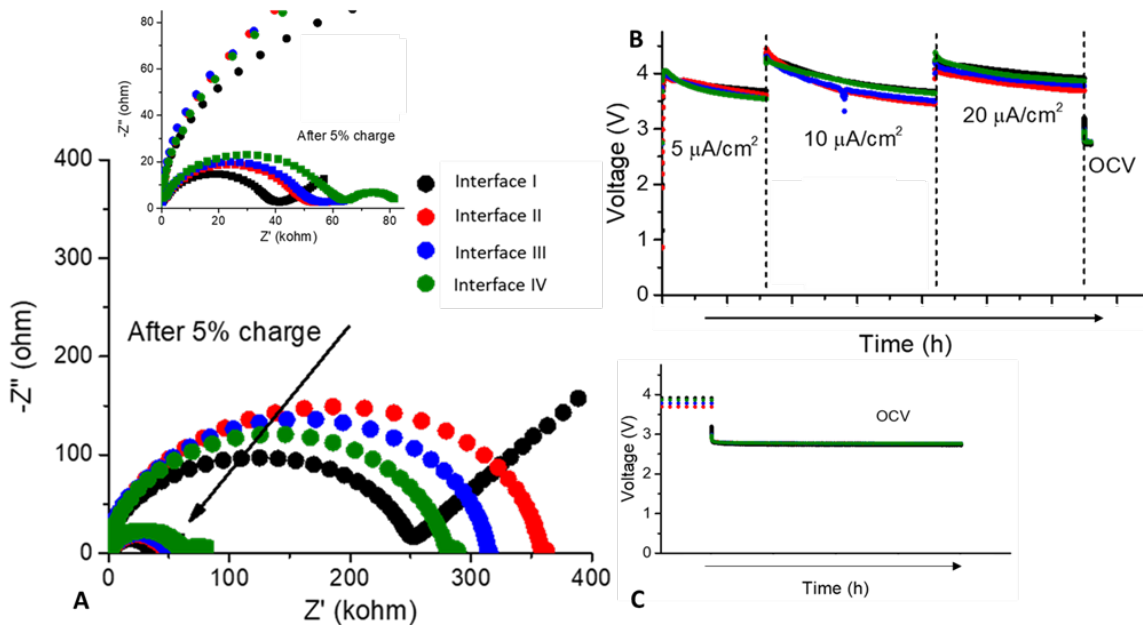
Figure II-584. A) EIS data of electrolyte Composition IV before and after (inset) charging with four different interfaces, B) Step-wise charging, C) After charging, all cells maintained stable OCV,
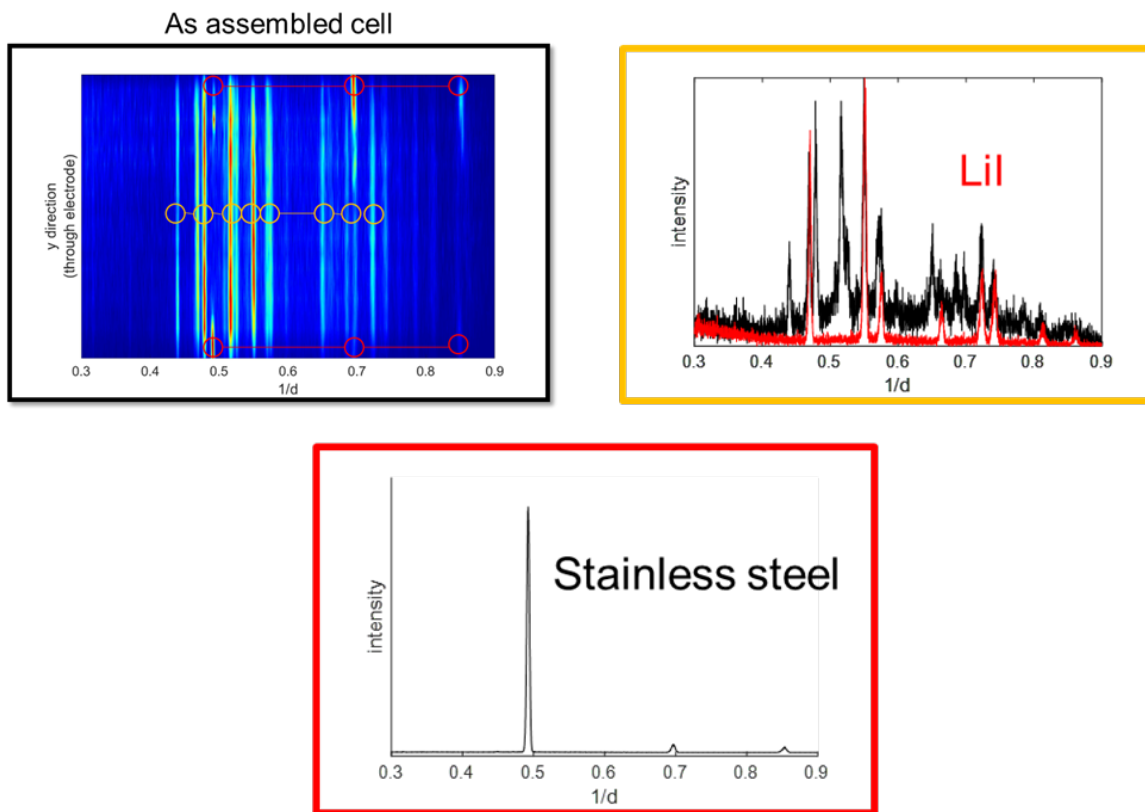
Figure II-585. Feasibility demonstration of Energy Dispersive X-ray Diffraction of a solid LiI cell in a stainless steel can.

Conclusions

- A method for measuring conductivity was developed and results are in agreement with prior literature for pristine AgI and LiI solid electrolytes.

- LiI-based solid electrolytes with conductivities $\geq 10^{-3}$ S/cm have been identified.

- Modifications of the electrolyte/substrate interface to reduce the total measured resistance were explored and will be considered in cell designs for the remainder of the project.

- We have demonstrated a step-wise charging procedure with increasing current levels that decreases total charge time.

- OCV stability followed by ex-situ analysis after charge shows successful *in situ* formation of a Li/I_2 cell.

Key Publications/Patents/Presentations

1. Patent disclosure on Dual Function Solid State Cell concept filed with Stony Brook University Technology Transfer Office.

2. Presentation: E. Takeuchi, A. Marschilok, K. Takeuchi, "Dual Function Solid State Battery with Self-forming Self-healing Electrolyte and Separator", BMR/ABR/Battery 500 Research Information Exchange, January 17-19, 2017.

3. Presentation: E. Takeuchi, A. Marschilok, K. Takeuchi, "Dual Function Solid State Battery with Self-forming Self-healing Electrolyte and Separator", Program Officer Site Visit, May 3, 2017, Stony Brook University, Stony Brook, NY 11794.

4. (Poster) Presentation: E. Takeuchi, A. Marschilok, K. Takeuchi, "Dual Function Solid State Battery with Self-forming Self-healing Electrolyte and Separator", DOE 2017 Annual Merit Review and Peer Evaluation Meeting (AMR) for the Hydrogen and Fuel Cells Program and Vehicle Technologies Office, June 5-9, 2017, Washington, DC.

II.I.11   Advancing Solid-Solid Interfaces in Li-ion Batteries (ANL)

Nenad Markovic, Principal Investigator
Argonne National Laboratory
9700 S Cass Avenue
Lemont, IL 60439
Phone: 630-252-5181
E-mail: nmmarkovic@anl.gov

Larry Curtiss, Co-Principal Investigator
Argonne National Laboratory
9700 S Cass Avenue
Lemont, IL 60439
Phone: 630-252-7380
E-mail: curtiss@anl.gov

Tien Duong, Technology Manager
U.S. Department of Energy
Phone: 202-586-7836
E-mail: Tien.Duong@ee.doe.gov

Project Introduction

One of the most important technological advances in sustainable energy harvesting and storage is the development of Li-ion battery technology. However, many challenges must be resolved in order to fully implement this technology, including: (i) development of high energy density cathode and anode materials (activity/cyclability); (ii) enhancement in stability of electrode materials and the corresponding electrolytes; (iii) improvement in selectivity of electrochemical interfaces, e.g., minimizing undesired side reactions at electrode surfaces; and (iv) improvement of many safety issues related to high flammability of organic solvents and Li dendrite formation on the anode electrode. As a result, the focus of much research in the field of Li energy storage is centered on development of methods that can enable Li metal anodes (required for high energy density Li-ion batteries) without dendrite formation and parasitic electrode-electrolyte interactions, as well as replacement of flammable organic solvents with solid electrolytes.

Today, two methods have been introduced to reduce the safety/performance issues. The first method relies on the hope that by modifying the Li metal anode with various types of "thin membranes" (either polymers or ceramics) Li dendrite formation will be significantly reduced relative to the "naked" metal Li anode along with reducing side reactions. The second method relies on the desire to develop an all solid-state battery, composed of Li ion conductive solid electrolytes that connect the metal Li anode with high energy cathode materials. Although for "hard" solid-state electrolytes various types of ceramics have been developed with suitable ionic bulk conductivity, these materials still need to have improved stability to prevent dendrite formation and interfacial Li diffusion. On the other hand, while dendrite formation is more controllable by introducing "soft" polymer materials, none of these polymeric materials have achieved ionic conductivity comparable to liquid electrolytes (0.1 S cm^{-1}). Overall, then, all of these issues must be overcome in order for Li-ion battery technology to move forward. Further advances will require the application of knowledge, concepts, and tools from a variety of fields including materials science, physics, engineering, theory and, in particular, interfacial electrochemistry.

Objectives

The project objectives are multifaceted, including: (i) the development of a new mechanically and chemically stable Li-selective solid "membrane" capable of protecting the Li metal anode during the discharge process in commercially available liquid electrolytes; and (ii) the development of a mechanically/chemically stable and Li ion conductive (≥ 2 x 10^{-4} S cm^{-1} at 298 K) solid electrolyte that can operate at potentials > 5 V for a solid-state battery encompassing a metal Li anode and a high voltage oxide cathode.

Project Impact

Protective organic and inorganic compounds can lead to enhanced stability of the interface, improve Li ion interfacial transport, minimize dendrite formation and increase safety in Li ion batteries. Developing and utilizing physical and chemical synthesis methods will enable the design of solid-solid interfaces with unique chemical/mechanical/conductivity properties of Li protective coatings and solid state electrolyte systems. The proposed work will develop and exploit a variety of *ex situ* and *in situ* optical and surface-sensitive techniques and electrochemical methods to explore and explain bulk and interfacial properties of the selected materials. The results will serve to unravel many of the puzzling bulk and interfacial properties of solid-solid interfaces and solid electrolyte materials.

Approach

We propose to use and develop interdisciplinary, atomic-/molecular-level insights obtained from integrating both experimental and computational methodologies to define the landscape of parameters that control interfacial properties for a new generation of solid-state Li-ion battery systems. Our strategy will involve transferring the knowledge gained from well-characterized thin film materials to real-world materials. This strategy forms a closed loop wherein the knowledge gained from model systems is used to design the more complex, real-world materials, and vice-versa, enable investigation of new phenomena observed in real materials via the development of new model systems. The work will focus on utilizing existing, in-house synthesis and characterization methods to enable a rapid transition from fundamental science to realistic cells.

Collaborators: This project funds work at Argonne National Laboratory and the University of Chicago-Illinois (Prof. Amin Salehi). We have also established collaboration with Prof. Jeff Sakamoto at the University of Michigan.

Results

Ionic transport across interfaces between dissimilar materials and the intrinsic stability of such interfaces is a fundamental challenge that cuts across many disciplines, including Li-ion-based solid-solid battery systems. However, understanding the interfacial stability of solid-state Li battery systems is a highly challenging task. To overcome many of these issues, we establish a surface science-based approach for assessing the intrinsic stability of oxide materials in contact with Li metal in order to understand the impact of crystallographic orientation and surface morphology on the extent of the chemical reactions that take place. Through the use of magnetron sputtering to deposit thin films of Li metal on single-crystalline, niobium-doped strontium titanate (Nb:STO) substrates at room temperature, a representative interface is created for investigating the intrinsic stability of the Li-STO system. Although not a solid electrolyte material itself, STO serves as an ideal model system as its surface chemistry has been extensively studied and single crystal substrates can be readily prepared with known surface termination.

Methods developed to study interfacial stability

In order to understand the intrinsic chemistry of Li metal in contact with a model oxide surface, Li was sputter deposited directly onto STO(hkl) surfaces and then transferred directly between the sputter and analysis chambers under ultrahigh vacuum (UHV) conditions ($\leq 5 \times 10^{-9}$ mbar throughout transfer). Central to these investigations was the preparation of well-defined, single crystal surfaces in order to identify differences in stability and reactivity based on crystallographic orientation.
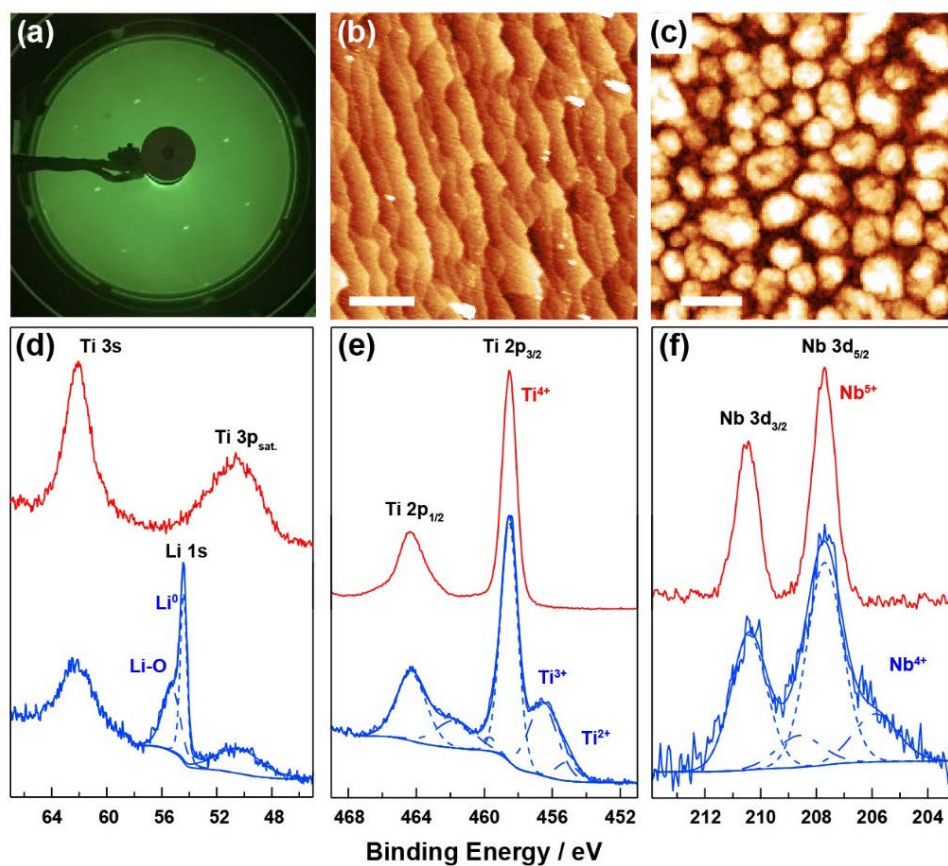
Figure II-586. (a) LEED and (b) AFM images of an etched and annealed STO(001) surface. (c) AFM image of the same STO(001) surface after Li deposition. (d-f) XPS core level spectra before (red) and after (blue) Li deposition.

Figure II-586 illustrates structural and chemical characterization of a representative STO(001) surface both before and after Li deposition. From low energy electron diffraction (LEED, Figure II-586a), a 1x1 surface reconstruction is clearly resolved on the as-prepared STO(001) surface, and from atomic force microscopy (AFM, Figure II-586b), the well-defined crystal terraces of HF-etched and annealed STO(001) surfaces can be easily seen. X-ray photoelectron spectroscopy (XPS) analysis of the Ti 2p, Nb 3d and Sr 3p core levels indicates that the pristine STO surface is fully oxidized, with only Ti^{4+}, Sr^{2+} and Nb^{5+} oxidation states. AFM imaging of the sample after Li deposition reveals an island morphology with an average island diameter of ~500 nm (Figure II-586c). Figure II-586e-f demonstrate that after Li deposition, ~38% of the total Ti signal corresponds to a mixture of 3+ and 2+ oxidation states, and 33% of the total Nb signal corresponds to the 4+ oxidation state. The oxidation state of Sr was unaffected by Li deposition. The persistence of Ti^{4+} and Nb^{5+} species after Li deposition indicates incomplete reduction of the STO, suggesting that only the first few monolayers of STO react), and/or the spaces between Li islands on the surface are essentially Li-free, resulting in regions of unreacted STO.

X-ray absorption spectroscopy (XAS) suggests that the reaction is at least partially surface-limited, as measurements of the Ti K-edge in total electron yield (TEY) and total fluorescence yield (TFY) modes before and after Li deposition reveal differing amounts of reduction (Figure II-587). The TEY spectra, which are sensitive only to the first ~5 nm of the surface, clearly indicate a mixture of Ti oxidation states, consistent with the XPS measurements. The TFY spectra, which measures the first ~50 nm of the sample, indicate that the "bulk" of the STO is largely unaffected by Li deposition. Taken together, the above results clearly demonstrate the power of our surface science-based approach to directly probe the intrinsic stability of solid-state Li/oxide interfaces. Below we investigate the structure-dependent stability of STO interfaces in contact with Li metal.
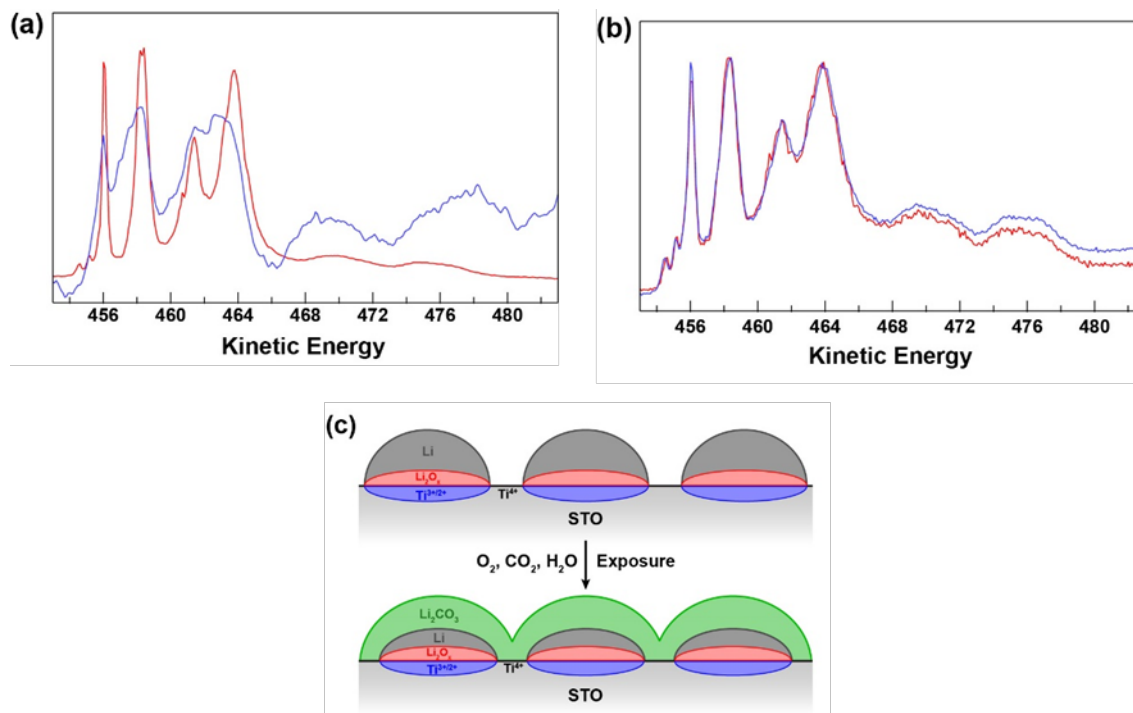
Figure II-587. XAS measurements of STO substrates in (a) TEY and (b) TFY modes before (red) and after (blue) Li deposition. (c) Schematic of surface structure after Li deposition (top) and air exposure (bottom).

Structure dependent stability of STO(hkl) interfaces

Deposition of an identical amount of Li on STO(110) and (111) surfaces reveals a similar reduction of the surface, with virtually identical ratios of Ti^{4+}, Ti^{3+} and Ti^{2+} as observed on STO(001). Given the above evidence for a surface-limited reaction of STO(001) with Li metal, it is likely that the STO surface structure should remain largely unperturbed by the deposition of Li as explored by AFM imaging of surfaces before and after Li deposition and removal. XPS measurements of STO(hkl) samples after sonication in water reveal that all residual Li is indeed removed, and the surface is fully reoxidized to pure Ti^{4+} and Nb^{5+}. Surprisingly, AFM imaging revealed that whereas STO(001) and (111) surfaces exhibit no changes in surface morphology after Li removal (Figure II-588a/d and Figure II-588b/e, respectively), STO(110) surfaces appear to be substantially etched (Figure II-588c/f). as demonstrated further below, DFT simulations were performed to understand the underlying thermodynamic factors that result in the lower stability of the STO(110) surface.
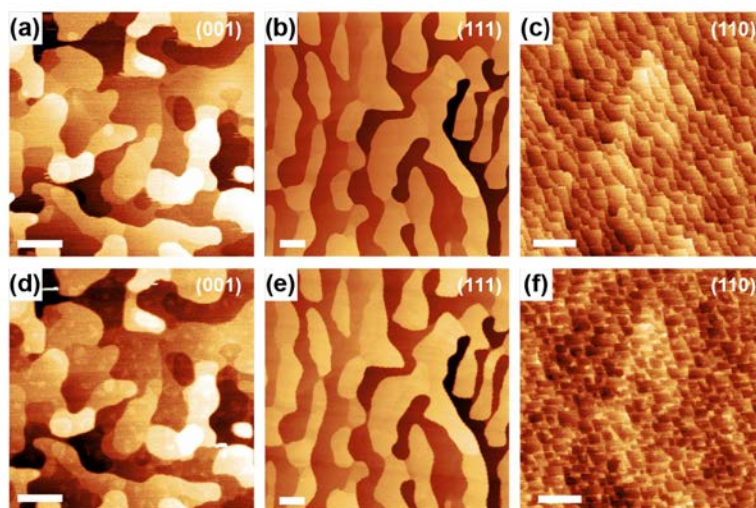
Figure II-588. AFM images of STO(001), (111) and (110) surfaces (a-c) before Li deposition and (d-e) after Li deposition. All images were taken in identical locations. Scale bars on (001) and (110) images are 500 nm, and scale bars on (111) images are 1 μm.

Understanding Morphological Stability via Computation

DFT calculations were performed on a variety of unreconstructed and reconstructed STO(hkl) surfaces, summarized in Figure II-589a, to rationalize and ultimately understand the structural origins of orientation-dependent morphological instabilities induced by Li interactions with STO single crystals. The binding energies of Li atoms on these different undoped STO surfaces indicate that the binding of Li becomes less energetically favorable with decreasing surface oxygen content (Figure II-589b), with $O_2(110)$ (-3.82eV) < $TiO_2(001)$ (-3.21 eV) << $SrTiO(110)$ (+0.27 eV). Li interactions with the Ti-terminated (111) surface lead to unstable configurations, and are therefore not included.
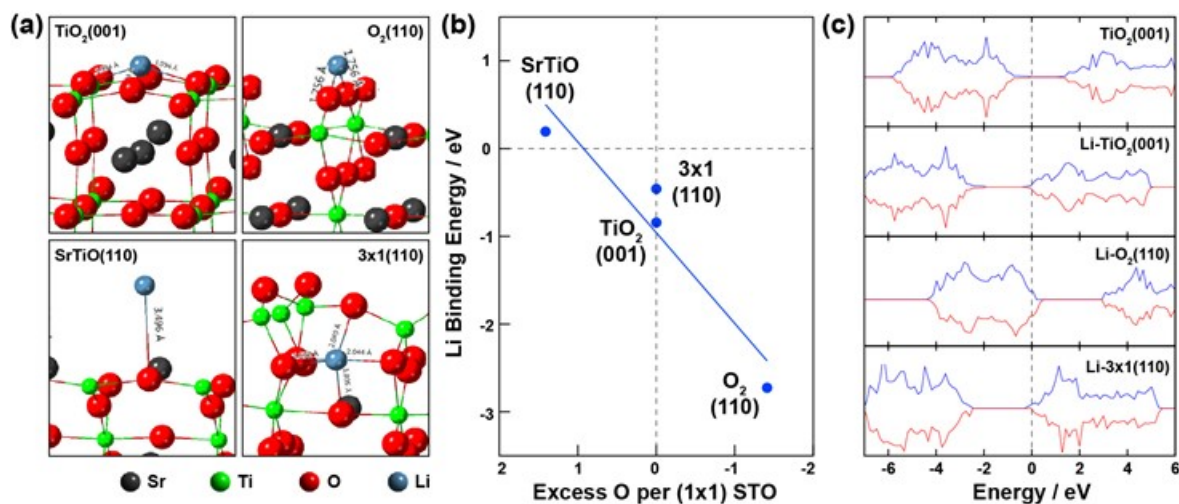
Figure II-589. DFT-calculated (a) structures (b) energy changes and (c) electronic densities of states for Li atoms on (100) and (110) surfaces of $SrTiO_3$ with different terminations.

Calculations of the electronic density of states (DOS) indicate charge transfer to Ti 3d states, consistent with the observed reduction of Ti and Nb in XPS. Consistent with the observation of self-limiting surface reduction, surfaces that are initially favorable for Li binding become more reduced with increasing Li coverage, e.g., for the TiO_2(001) surface decreasing from 3.21 eV (1/4 ML) to 2.38 eV (1/2ML) and further to 1.75 eV at 1 ML coverage. Interestingly, DFT results on the (3x1)-(110) reconstructed surface indicate that it is most favorable for Li ions to insert under the top TiO_x layer of the resulting reconstructed geometry (Figure II-589a). Incorporation of Li below the top TiO_x layer results in a lower stability of this layer, since its removal after Li insertion results in a much more stable termination than that in the absence of inserted Li. This likely explains the observed morphological instability of the STO(110) surface, with washing in H_2O resulting in removal of the TiO_x along with the underlying LiO_x. This would result in an overall thickness loss of ~5Å, close to the observed thickness loss in our AFM measurements. The combination of DFT with the experimental results on well-defined, model surfaces detailed above illustrates the power of our surface-science-based approach, as it enabled us to clearly distinguish and understand the interplay between interfacial reactivity and morphological transformations of oxide surfaces in contact with reactive metals at atomic and molecular levels.

From model to real systems – Nb-doped LLZO

Having demonstrated the power of our approach on model STO surfaces above, we expanded our analysis to a more technologically-relevant materials system: the so-called "stuffed garnet" phase, niobium-doped lithium lanthanum zirconate (Nb:LLZO, $Li_{6.5}La_3Zr_2Nb_{0.5}O_{12}$) in order to understand the reactions that may take place at the interface between this material and Li metal. Previous investigations of the stability of Al-doped LLZO yielded mixed results, with some studies concluding that surface-limited reduction and Li intercalation takes place upon contact with Li metal at room temperature while others indicate that no reduction takes place even after extended contact with molten Li metal at elevated temperatures. Here we make use of Nb-doped LLZO material, which, based on the above measurements of Nb-doped STO, will enable us to clearly distinguish any instability to contact with Li metal. As shown in Figure II-590, deposition of Li on Nb:LLZO indeed shows clear evidence of Nb reduction, a slight shift to lower binding energy (~0.3 eV) of the La $4p_{3/2}$ peak, and no evidence of Zr reduction. We emphasize it would not have been be possible to unambiguously confirm the presence of a surface reaction without first having established the feasibility of this approach on a model system in which chemical interactions clearly take place. Further work is ongoing to understand the origin of the slight reductive shift in the La peak, as well as how differences in surface cleanliness and defect structure can yield differences in the observed surface chemistry.
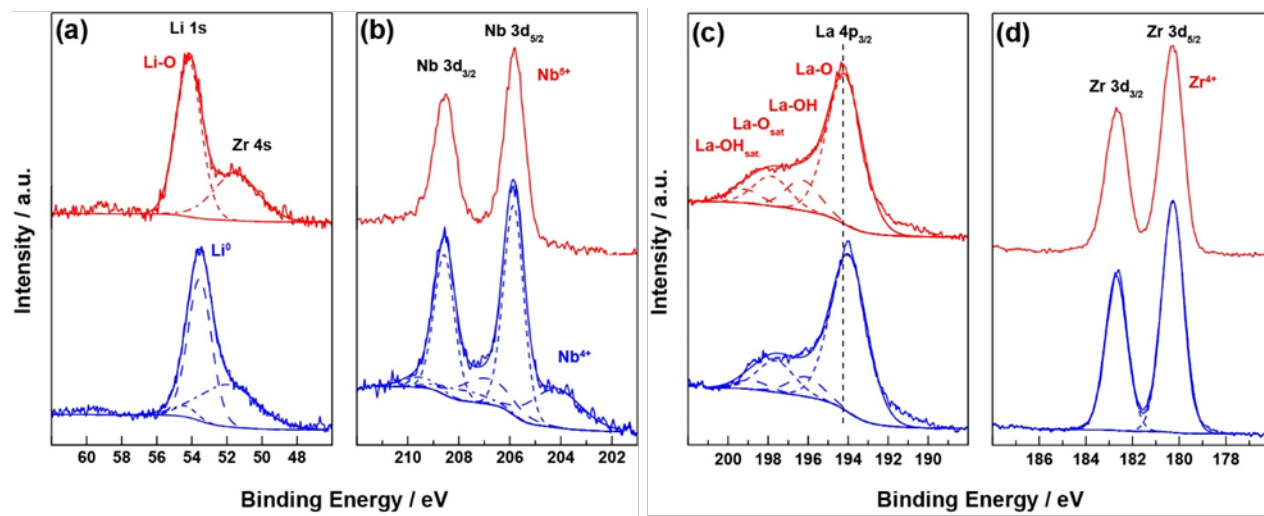

Figure II-590. XPS core level spectra from Nb:LLZO before (red) and after (blue) Li deposition.

Of paramount importance to these efforts will be the development of well-defined, single crystalline LLZO interfaces (as in the case of STO) in order to fully understand the interfacial and bulk properties of the Li/LLZO system. In doing so, it will be possible to rigorously assess the underlying factors that govern the intrinsic materials stability of not only the LLZO system, but other relevant crystalline oxides and glassy materials. Work is currently underway to develop thin film deposition of several solid oxide materials via pulsed laser deposition (PLD), and we have already developed in-house capabilities to synthesize oxide targets for PLD deposition. Furthermore, we have developed impedance spectroscopy to measure interfacial and bulk resistivity, along with Li-ion conductivity of both bulk and thin film oxide materials to characterize their performance in real cell environments.

Conclusions

We have introduced a surface science-based approach for rationalizing, and ultimately understanding, the intrinsic and orientation-dependent stability of oxide materials in contact with Li metal. Through the use of well-defined, single crystalline $SrTiO_3$(hkl) surfaces as model systems, we were able to clearly observe the reduction of Ti and Nb upon contact with Li metal. Furthermore, the observation of significant morphological instability of STO(110) surfaces relative to (001) and (111) after Li removal was explained through the use of DFT calculations, which revealed the insertion of Li below the surface TiO_x that results in destabilization of this layer. Extension of our surface science-based approach to the technologically-relevant Nb:LLZO system revealed clear reduction of Nb in this material, demonstrating the power of our approach to clearly identify surface (in)stability in real-world, polycrystalline materials in contact with Li metal. The presence of significant, orientation-specific changes in the surface stability highlights the importance of developing model systems for understanding the structure-sensitive reactivity of oxide materials for solid-state batteries. Only by understanding both the intrinsic chemistry *and* morphological stability of oxide interfaces in contact with reactive metals and disparate oxide surfaces will it be possible to rationally engineer a new generation of highly stable and reversible solid-state battery systems.

Key Publications

1. Justin G. Connell, Yisi Zhu, Peter Zapol, Sanja Tepavcevic, Jeff Sakamoto, Larry A. Curtiss, Dillon D. Fong, John W. Freeland, Nenad M. Markovic. "Crystal Orientation-Dependent Reactivity of Oxide Surfaces in Contact with Lithium Metal." *Submitted for Publication.*

2. Yisi Zhu, Justin G. Connell, Peter Zapol, Sanja Tepavcevic, Jeff Sakamoto, Larry A. Curtiss, Dillon D. Fong, John W. Freeland, Nenad M. Markovic. "Surface Chemistry and Intrinsic Stability of Doped Lithium Lanthanum Zirconium Oxides." *In Preparation.*

II.I.12 Multifunctional, Self-Healing Polyelectrolyte Gels for Long-Cycle-Life, High-Capacity Sulfur Cathodes in Li-S Batteries (University of Washington)

Alex K.-Y. Jen, Principal Investigator
University of Washington
Department of Chemistry and Materials Science and Engineering
Roberts Hall 302
Seattle, WA 98195
Phone: 206-543-2626
E-mail: ajen@u.washington.edu

Jihui Yang, Principal Investigator
University of Washington
Roberts Hall 315
Seattle, WA 98195
Phone: 206-543-7090
E-mail: jihuiy@u.washington.edu

Tien Duong, Technology Manager
U.S. Department of Energy
Phone: 202-586-7836
E-mail: Tien.Duong@ee.doe.gov

Start Date: October 1, 2016   End Date: September 30, 2019
Total Project Cost: $1,388,888   DOE share: $1,250,000   Non-DOE share: $138,888

Project Introduction

The current electric vehicle (EV) battery market is dominated by lithium-ion batteries (LIBs). However, conventional LIBs-based on this basic materials system have already begun to reach their performance limits due to progressive materials and device optimization over the past two decades. In order to meet EV Everywhere goals of 75% cost reduction and 50% weight reduction in electric vehicle batteries by 2022, radically new strategies must be employed.

One tantalizing solution is to look beyond traditional lithium-ion intercalation chemistry towards "beyond-lithium" systems such as the lithium-sulfur (Li-S) battery. A sulfur cathode has a theoretical gravimetric specific capacity of 1673 mAh/g at ~ 2 V vs Li/Li$^+$, rendering a theoretical energy density improvement of 500% as compared to the lithium metal oxide cathodes found in LIBs. This increase can be matched on the anode side by using lithium metal, which possesses an intrinsic theoretical gravimetric specific capacity of 3860 mAh/g – an order of magnitude higher than that of graphite. Additionally, sulfur is cheap and earth-abundant, making this redox couple highly attractive for EV battery use.

However, a commercially-viable Li-S battery has remained elusive due to technical challenges. Many of them stem from the formation of polysulfides (Li_2S_x, $3 \leq x \leq 8$) which are highly soluble in organic electrolytes, leading to self-discharge, passivation of the lithium anode, low Coulombic efficiency due to the escape of sulfur into the electrolyte, and voltage hysteresis from differences in forward and backward reaction mechanisms. In addition, both the starting material (sulfur) and end products (Li_2S, Li_2S_2) are highly insulating, necessitating the use of a large amount of conductive carbon in the electrode. Furthermore, because the overall reaction is accompanied by a large volume change, this composite matrix is prone to cracking, promoting battery failure. Finally, on the anode side, lithium metal tends to form dendrites upon repeated stripping and plating, which puncture the cell separator and cause internal shorting.

Researchers have addressed these issues, to a certain degree of success, using a variety of creative strategies, including ionic liquid electrolytes, SEI-improving additives, mesoporous carbon hosts, advanced binders, and many others. Still, despite these myriad strategies, a safe Li-S battery with long cycle life based on scalable fabrication techniques remains elusive, as no single strategy or even combination of several has proven to be totally effective at both preventing dendrite growth and stopping efficiency/capacity loss via polysulfide.

Objectives

The objective of this project is to develop self-healing and polysulfide-trapping polyelectrolyte gels containing ionic liquid (IL) for the Li-S battery system. The Li-S battery design will be capable of achieving gravimetric and volumetric energy densities of ≥ 800 Wh/kg and ≥ 1000 Wh/L, respectively.

The project will achieve the following performance targets (all cycles at C/10 rate unless otherwise specified):

- A cathode gravimetric specific capacity of ≥ 675 mAh/g after 10 charge/discharge cycles between 2.8 and 1.7 V vs Li/Li$^+$

- An average coulombic efficiency $\geq 99\%$ for the 10th cycle through the 100th

- $\geq 90\%$ capacity retention after 100 cycles as compared to the capacity of the 10th cycle.

- $\geq 30\%$ capacity retention when cycled at a C/2 rate, as compared to the capacity at C/10

- Ability to operate at temperatures between -20°C and 50°C.

Approach

During Budget Period 1 (quarters 1-6), we will synthesize a variety of starting materials for gel electrolytes and self-healing polymers, fabricate them into films both individually and together, and then test their electrochemical/mechanical properties relevant to use in a Li-S battery. Additionally, we will synthesize a variety of sulfur/carbon (S/C) composites, utilizing mesoporous carbons with varying properties and various functionalities placed onto their surfaces.

Organic synthesis will include NDI- (naphthalene diimide) and Py- (pyrene) containing materials, as well as monomers for the polyelectrolyte phase. Materials will be produced through established synthetic routes and characterized by nuclear magnetic resonance (NMR), gel permeation chromatography, and/or solution-phase cyclic voltammetry. Synthesis of S/C composites will be done by mixing of sulfur and carbon at above the melting point of sulfur, and will be characterized by Brunauer–Emmett–Teller (BET) surface area and pore size analysis to confirm successful integration of sulfur into the pore structure. Surface functionality will be studied by thermal gravimetric analysis (TGA) and x-ray photoelectron spectroscopy (XPS).

Fabrication and testing of ionomer gels with varying ratios of IL and molecular starting materials will be done. Basic electrochemical and mechanical properties of each gel composition will be tested and used to determine structure-property relationships, then gel compositions with favorable properties will undergo more detailed testing on long-term interfacial stability with Li foil, Li dendrite suppression, and polysulfide diffusion. Conductivity and thermal properties will be assessed by A/C impedance, TGA, and differential scanning calorimetry. Tensile testing will be carried out to determine mechanical properties. For advanced tests, Li/gel/Li symmetric cells will be constructed, and analyzed for development of interfacial resistance and dendrite suppression using cyclic stripping/plating. Polysulfide trapping ability will be quantified by measuring absorption from a fixed-concentration solution.

Fabrication and testing of self-healing films, made from various structures and ratios of NDI- and Py-containing moieties, will be performed. Mechanical and self-healing properties will be tested, as well as ionic conductivity. Static and dynamic mechanical testing will be carried out to determine tensile modulus, toughness modulus, and storage and loss modulus. Self-healing will be measured by slicing films in two, contacting the pieces, and annealing at fixed temperature, followed by re-testing tensile properties.

This will be followed by fabrication and testing of gel electrolytes containing both physically-crosslinked (self-healing) and chemically-crosslinked (ionomer) materials. All of the tests detailed in the two paragraphs above will be performed in order to determine how the performance of individual components of the gel translates to an interpenetrated structure containing all components.

Parallel to materials development efforts, we will undertake fabrication and testing of small-capacity coin cells utilizing a variety of cell design concepts, including organic electrolytes, IL electrolytes, non-self-healing polyelectrolyte gels, and interpenetrating gels in order to benchmark performance and demonstrate an interpenetrating materials system that is capable of significantly improving performance. Cells will be cycled for short periods ($\leq$100 cycles) at rates ranging from C/100 or C/50 to C/2. A/C impedance spectra will be collected at various points in order to observe the evolution of internal impedances during cell cycling. Voltages traces during charge and discharge will be observed and correlated to internal processes such as polysulfide speciation and insulating buildup of Li_2S/Li_2S_2 deposits. The origins of undesirable cell performance will be investigated using a combination of experimental techniques, including targeted cycling tests, cyclic voltammetry, A/C impedance tests, scanning electron microcopy, and x-ray diffraction (XRD).

During Budget Period 2 (quarters 7-12), we will continue synthesis of molecular components of gels and S/C composites from raw starting materials. Synthesis will proceed according to literature, as well as any modifications we may make in order to produce materials more efficiently. We will continue testing of gel electrolytes containing both physically-crosslinked self-healing and chemically-crosslinked ionomer materials, as well as continue development of self-healing polymer films. Basic electrochemical and mechanical (including self-healing) behavior will be characterized, and gel compositions with favorable properties will undergo more detailed testing on long-term interfacial stability with Li foil, Li dendrite suppression, and polysulfide diffusion. Minor structural and compositional adjustments will be made to the gel electrolyte formulation based on cell performance details.

We will continue to fabricate coin cells with sulfur-based cathodes and lithium metal anodes which utilize electrolyte materials in the cell structure, and study their performance as a function of gel design. Initially, low-mass-loading demonstration cells will be constructed, followed by practical-loading cells. This task will culminate directly in the production of deliverable 10 mAh Li-S cells for DOE testing. All of the experiments previously mentioned for cell testing will be performed as cell design is optimized. We plan to utilize instrumentation at the new Washington Clean Energy Testbeds on the University of Washington campus, the University of Washington Molecular Analysis Facility, and NMR/microscopy instrumentation available at the Environmental Molecular Sciences Laboratory at Pacific Northwest National Lab.

Results

Self-Healing Materials

We have undertaken detailed study of the π-π interaction between NDI and Py, with the intent of designing a tunable self-healing materials system. We began this investigation by studying model compounds N,N'-dibutylnapthalene diimide (dbNDI) and Py in dichloromethane. UV-Vis analysis shows that upon addition of small amounts of dbNDI to a Py solution, a clear, broad absorption peak appears at 500nm. A second peak at 514nm becomes apparent upon increasing the ratio of dbNDI to Py, peaking at a ratio of 1:0.5 (Figure II-591). This suggests that more than one type of complex can be formed. NMR data also suggests complex formation of stoichiometry 1:1 (dbNDI:Py) and 2:1 (dbNDI:Py).
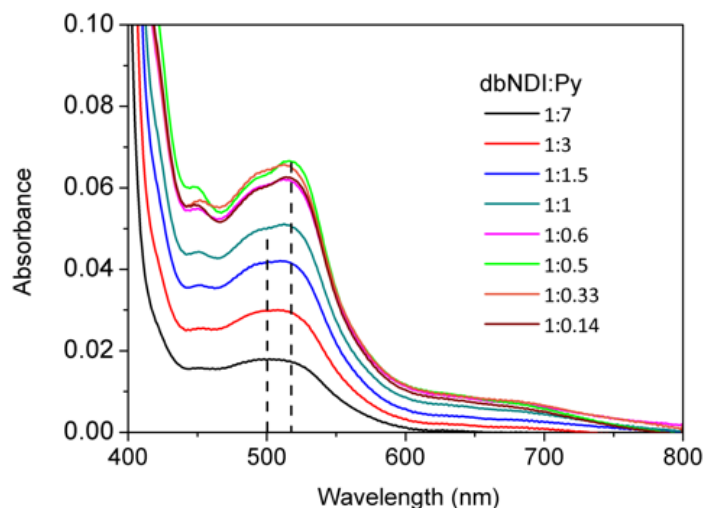
Figure II-591. UV-Visible spectra of dbNDI/Py solutions of varying ratios (constant total concentration) in dichloromethane, showing development of peaks in the visible region corresponding to complex formation.

Collecting UV-Vis spectra of these optimum stoichiometries while varying overall concentrations and applying Beer-Lambert Beer's law to the 500/514nm peaks, we calculated complexation free energies of the complexes as -8.19 kJ/mol for the 1:1 dbNDI:Py complex and -16.49 kJ/mol for the 2:1 dbNDI:Py complex.

Generalizing this interaction to polymeric systems, we expected that varying the ratio between an NDI-containing polymer and a Py-containing crosslinker would result in changes in self-healing behavior, in accordance with the changing strength of the dominant π-π interaction mode. We tested this using novel polymeric materials designed for self-healing: PENDI-C6, a methacrylate polymer bearing NDI pendants with a six-carbon tail (as well as triethylene glycol methyl ether pendants for processability and ionic conductivity) and triPy, a three-armed polyethylene glycol (PEG) derivative terminated on each branch by pyrene units. UV-Vis spectra of 1:1 (NDI:Py) mixtures of these materials produced the same 500nm peak as the small molecules, confirming that the same non-covalent interaction occurs between polymers. We produced free-standing films of mixtures of these polymers corresponding to a 1:1 molar ratio of NDI to Py units (termed as PP-1), and tested their mechanical and self-healing properties. In order to adjust the dominant interaction mode in these materials without changing the relative amounts of polymer, we selectively doped either dbNDI (PP-NDI) or Py (PP-Py) into the films during fabrication, forcing either the 1:1 or 2:1 complexes to form according to Le Chatelier's principle. The self-healing behavior that we observed is summarized in Figure II-592 below – changing the ratio of NDI to Py groups in the polymer composite does indeed produce large changes in behavior, allowing us to tune self-healing temperature from 30°C-70°C. Additionally, we observed that tensile modulus varied from 69MPa (PP-Py) to 219MPa (PP-NDI). These values are significantly higher than what has been reported for the vast majority of self-healing materials in literature.
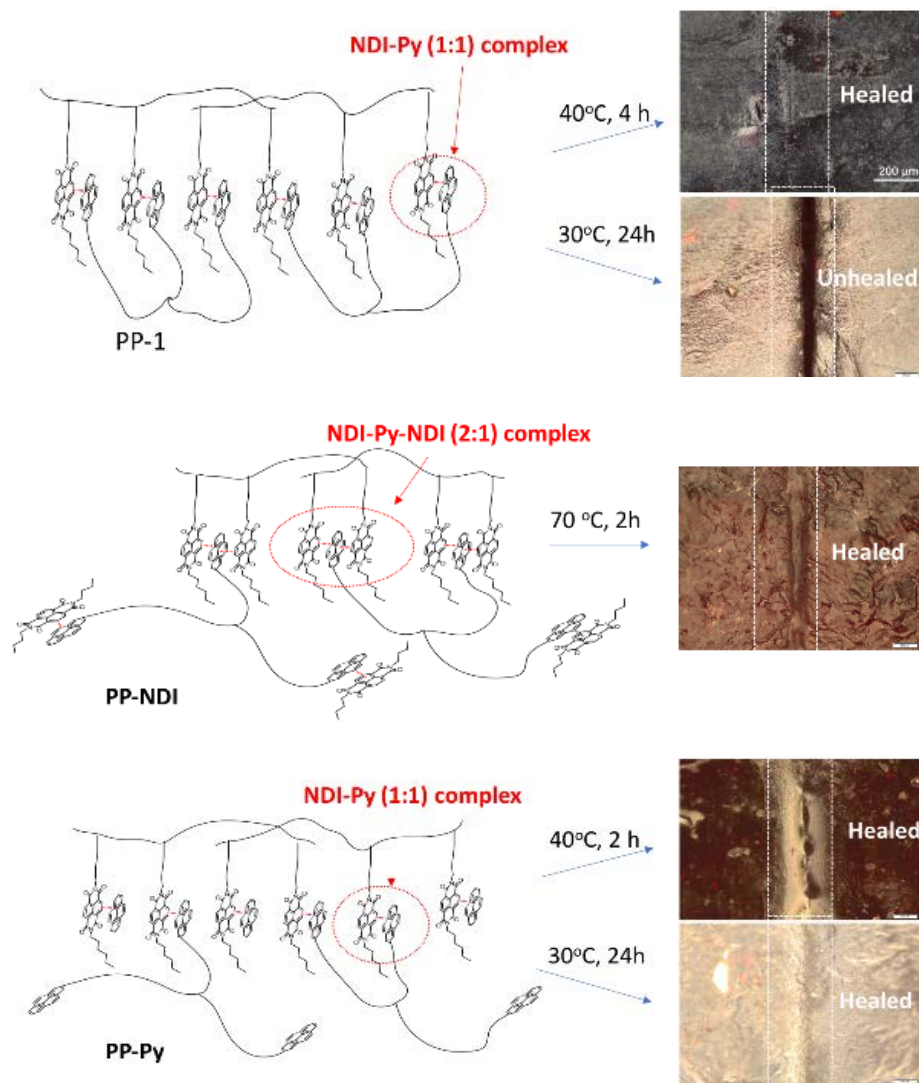
Figure II-592. Our novel polymeric materials form free-standing, self-healing films when mixed together in a 1:1 molar ratio of NDI to Py units. The self-healing temperature of these films can be adjusted over a wide range by doping small molecule NDI or Py compounds into the film, forcing formation of either 1:1 or 2:1 NDI:Py complexes, which have vastly different binding energies. These small molecules can also be used to "passivate" binding sites, adjusting the crosslinking density.

Finally, we tested the ability of the PP-1 polymer composite to transport Li$^+$ ions by doping films with LiTFSI in a 20:1 [ethyleneoxy]:[Li$^+$] ratio during fabrication. Ionic conductivities of the films were measured between 10-55°C by A/C impedance testing between stainless steel plates followed by fitting the data to a simple Debye impedance model with non-ideal interfacial capacitance. We found that the LiTFSI-doped composite had a conductivity in excess of 10^{-6} S/cm at 50°C, which is in a similar range to other solid polymer electrolytes based on PEG derivatives.

Ionomer Gels

We designed and optimized a synthetic procedure for producing crosslinked gel electrolytes containing ionic liquid, which can be thermally cured using a radical initiator. In addition to using commercially available PEG dimethacrylate (PEGDMA), with an average molecular weight of 750Da, as a starting material, we also chemically synthesized PEGDMA with a higher molecular weight of ~3500Da, as well as an ionic-liquid-like monomer containing a pyrrolidinium cation and TFSI$^-$ counterion. We have become interested in "solvate"

ionic liquids in particular as a liquid base for our gels, given their high Li$^+$ transference numbers (~0.5) relative to ternary pyrrolidinium$^+$:Li$^+$:TFSI$^-$ ionic liquids, as well as their facile synthesis and ability to be diluted with organic solvents for higher conductivity. Using our procedure, we have successfully produced solvate ionogels of varying composition and measured their ionic conductivities using the same A/C impedance method as detail above. Table II-27 below summarizes a few of our initial formulations, and the conductivities calculated for each. All of these ionogels display ionic conductivities in excess of 10^{-4} S/cm at 23°C, and we expect to demonstrate formulations with conductivities >10^{-3} S/cm very soon.

Table II-27: Initial Solvate Ionogel Formulations and Their Conductivities at 23ºC

	Composition (vol%)				Conductivity (x 10^{-4} S/cm)
	PEGDMA (750Da)	IL-like Monomer	Solvate IL	Ether Solvent Diluent	
Formula 1	20%	0%	80%	+0%	2.79
Formula 2	20%	0%	80%	+50%	9.23
Formula 3	10%	20%	70%	+40%	3.70

Chemical Modification of Mesoporous Carbons for S/C Composite Cathodes

We have successfully synthesized S/C composites of varying sulfur loading from mesoporous carbons of varying average pore size. Infiltration was confirmed *via* disappearance of crystalline sulfur peaks in XRD data on the composite surface, as well as a decrease in pore volume and average pore size as determined by BET analysis.

We have explored chemical surface modification of these carbon starting materials as an additional route to cathode performance improvement. Our procedure is based on well-studied diazonium chemistry, which attaches phenyl rings bearing customizable functional groups to unsaturated carbon surfaces. Functionalization was confirmed by pore shrinkage (determined by BET, as well as the appearance of nitrogen- or sulfur-associated peaks in XPS analysis and weight loss during TGA). The extent of functionalization, measured by %weight loss during TGA as compared to control samples, was easily varied by adjusting reaction conditions. We used this procedure to attach a variety of chemical moieties to carbon surfaces, including primary amines, tertiary amines, and sulfides. In particular, we are interested in sulfide-based surface modifiers, as reversible covalent bonding between sulfide groups is well-known and has potential for containment of lithium polysulfides within the cathode pore structure. We have done detailed study on S/C cathodes modified with phenylthiol functional groups using by analyzing cell cycling data. Figure II-593 below presents key data from this investigation.
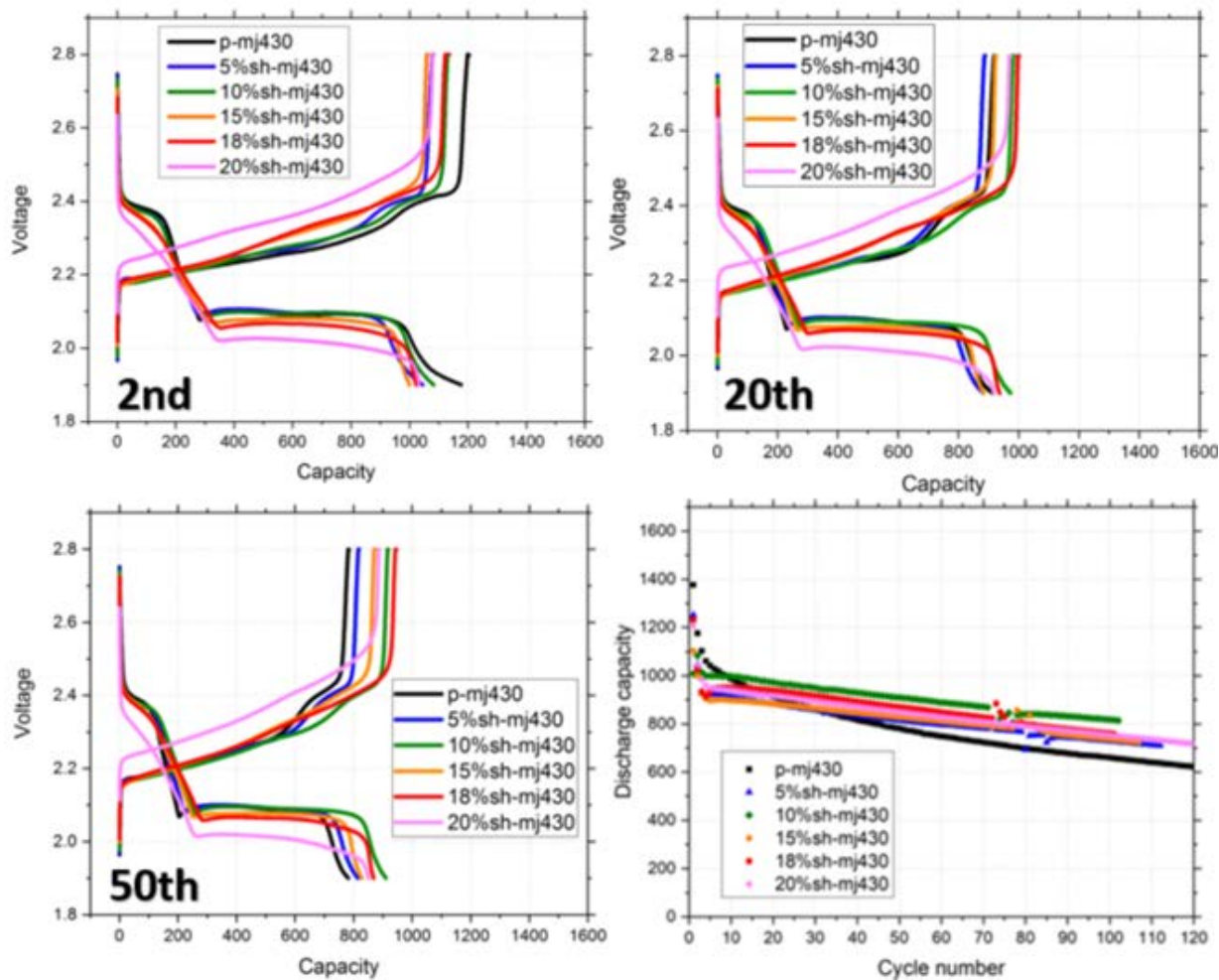
Figure II-593. Voltage curves of the 2nd, 20th, and 50th cycle (C/10 rate) of S/C cathodes, in which the mesoporous carbons contain 0-20%wt phenylthiol surface modifier, as well as capacity data over 100 cycles for each cathode. Notably, 10%wt modifier significantly improves capacity and retention while introducing minimal additional overpotential.

We note several important trends. Firstly, the introduction of phenylthiol modifiers progressively changes the voltage curves in predictable ways from the unmodified control (p-mj430). The initial discharge plateaus at ~2.4 V become increasingly sloped, a possible indicator of reaction mechanism shifting from a two-phase (solid-liquid) reaction to a single-phase (solid-solid) reaction. Lower discharge plateaus are shorter during initial cycling, but quickly become longer than the control, which decays rapidly. Similarly, initial charge capacities are slightly lower but, by later cycles, have surpassed that of the control. The control charge curve contains a large, gradual initial slope followed by a small plateau at around ~2.4 V; however, in modified samples this plateau gradually vanishes, with modifications above 10% barely having any discernable plateaus. In general, modification levels >10%wt result in very noticeable increases in overpotential during both charge and discharge, while overpotential increases in <10%wt samples are small. All modified samples display better capacity retention over 100 cycles than the control, but 10%wt possesses the best overall capacity.

There a few potential conclusions to draw from this data. First, the gradual disappearance of two-phase voltage behavior in highly-modified samples may point to successful covalent tethering of polysulfide species to modified surfaces, forcing reaction to occur largely through an all-solid-state mechanism. This shift in reaction mechanism, however, may also be responsible for the increased overpotential, as both Li$^+$ diffusion and polysulfide rearrangement resulting from charge transfer may be more difficult when not mediated by a liquid

solvent. Ideally, we would prefer to sequester a certain amount of polysulfide in surface-bound states to prevent its escape from the cathode, but leave enough polysulfide free in the interior liquid phase to afford rapid reaction kinetics and Li⁺ diffusion, a compromise that 10%wt modifier appears to achieve. However, these hypotheses are impossible to confirm using only cell data. We are currently doing detailed XPS and NMR studies on modified cathodes in order to obtain direct evidence of reaction between modified carbon surfaces and lithium polysulfides. We are also investigating improved modifier structures which may afford even greater performance enhancements.

Conclusions

Self-Healing Materials

- dbNDI and Py form non-covalent π-π complexes in either 1:1 or 2:1 molar ratios, respectively, depending on the concentration of dbNDI available relative to Py. The 2:1 complex is roughly twice as energetically favorable (-16.49 kJ/mol vs. -8.19 kJ/mol).

- We have designed polymers containing both NDI (PENDI-C6) and Py (triPy) moieties, which interact *via* the aforementioned π-π complexation to form non-covalently crosslinked films.

- These films are capable of self-healing following breakage, and the self-healing temperature can be tuned between 30-70°C by introducing small molecule dbNDI or Py groups to adjust both the type of complex formed and the density of crosslinks. This "doping" with small molecules can also adjust tensile modulus of the films between 69-219MPa, which is significantly higher than most previously-reported self-healing materials.

Ionomer Gels

- We have successfully developed a gel fabrication procedure and used it produce a variety of solvate ionomer gels of different composition.

- All of the gel formulations tested thus far have displayed ionic conductivities >10^{-4} S/cm at 23°C, and we expect to demonstrate conductivities >10^{-3} S/cm in the near future.

Chemical Modification of Mesoporous Carbons for S/C Composite Cathodes

- We have developed a procedure based on diazonium chemistry to covalently attach customizable functional groups to the surface of mesoporous carbons, and created S/C composites from both modified and unmodified samples.

- S/C cathodes based on phenylthiol-modified carbons display improved capacity and retention compared to unmodified samples. Voltage profiles exhibit significant changes upon modification, which may indicate covalent tethering of polysulfides to the carbon surface.

Key Publications

1. Qin, J., Hubble, D., Lin, F., Yang, J., Jen, A. K.-Y., "Tunable self-healing ability in a rigid, ion-conductive supramolecular polymer." (in preparation)

II.I.13 Self-Forming Thin Interphases and Electrodes Enabling 3-D Structures High Energy Density Batteries (Rutgers U)

Glenn G. Amatucci, Principal Investigator

Rutgers, The State University of New Jersey

671 US Highway 1

North Brunswick, NJ 08902

Phone: 848-932-0921

E-mail: gamatucc@rutgers.edu

Tien Duong, Technology Manager

U.S. Department of Energy

Phone: 202-586-7836

E-mail: Tien.Duong@ee.doe.gov

Start Date: October 1, 2016   End Date: September 30, 2019

Total Project Cost: $1,271,165   DOE share: $1,077,074   Non-DOE share: $194,091

Project Introduction

The ultimate goals of this project are to establish a step change in energy density, cost, safety, and high voltage scalability of battery technology compared to the current state of the art secondary battery technologies. This will be accomplished using a secondary battery technology enabled by a novel *in-situ* formed solid-electrolyte battery leading to high energy metal fluoride vs. lithium metal chemistry in a planar battery electrode format. This technology provides many advantages including: 1) enabling the use of lithium metal electrodes via solid-state electrolytes, 2) eliminating Li metal in fabrication and handling of cells, 3) providing the highest practical energy density electrochemical system, and 4) enabling a unique pathway to high voltage systems.

Objectives

The project objective is to develop and implement a novel *in-situ* formed lithium-metal-based metal fluoride battery that will enable packaged 10mAh batteries of energy density > 1000 Wh/L and specific energy > 400 Wh/kg at 12 V.

Approach

The *in-situ* self-formed battery is based on the formation by simple polarization of a Li metal negative electrode and a positive metal fluoride positive electrode from a LiF-based bi-ion conducting glass between a positive and a negative reactive current collector. As depicted in Figure II-594, under polarization the LiF-based glass decomposes with the release of the F^- and Li^+ ions to react with the positive and the negative reactive current collectors respectively, thereby forming the active electrodes in-situ.
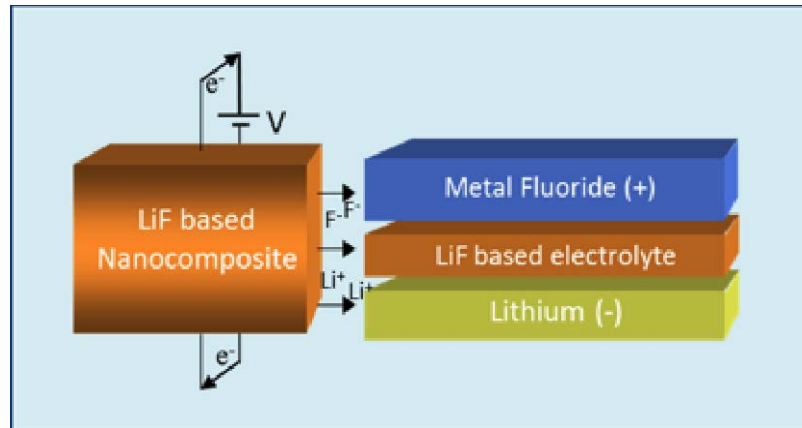
Figure II-594. Diagram illustrates the *in-situ* formation of a metal fluoride positive electrode and a lithium metal negative electrode from the electrolytic decomposition of a Li-based bi-ion glass under polarization

As such, the project is divided into two main tasks that focus on the advance of the self-forming chemistry concurrent to the cell design and fabrication as depicted in Figure II-595. The self-forming chemistry task is comprised of three subtasks encompassing the negative and positive reactive current collectors and the bi-ion glass conductor. Whereas the cell design and fabrication targets the development and integration of the bipolar configuration to achieve the 12 V single cell goal.
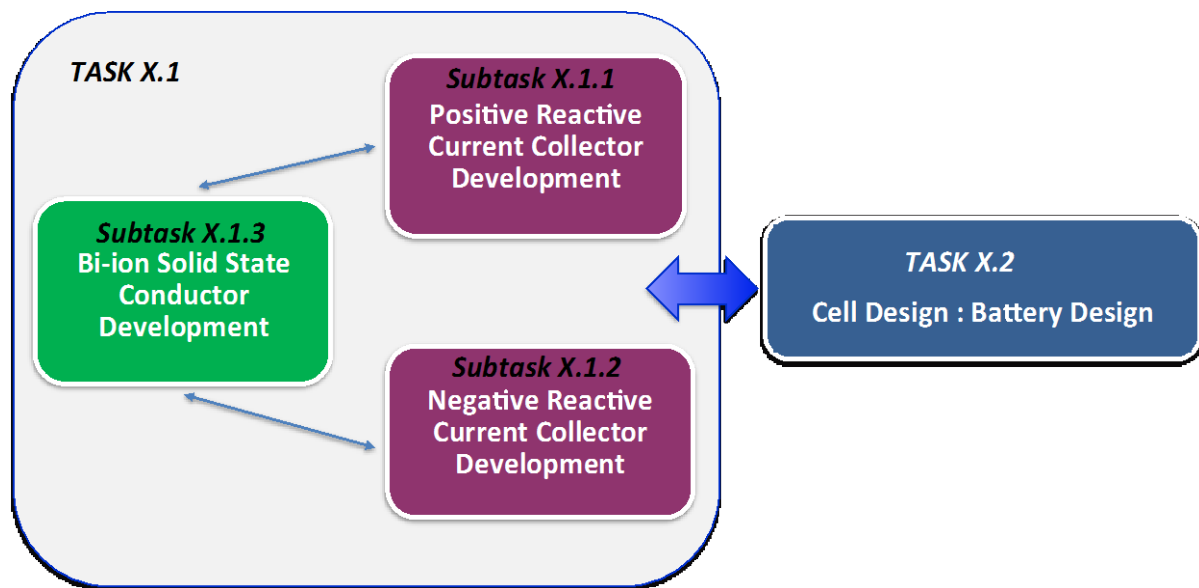
Figure II-595. Program approach breakdown

Results

Bi-ion conductor development

The bi-ion conductor is the heart of the electrochemical system as it enables the first formation cycle and the in-situ formation of the metal fluoride at the positive and lithium metal at the negative. Once the cell is formed, the majority of the subsequent charge/discharge reactions follow a mechanism similar to a lithium battery based on a MF_3 metal fluoride conversion into $3 LiF + M$ with lithium plating at the negative electrode. The bi-ion conductor will be essentially acting as a solid-state electrolyte development of bi-ion conductor. Therefore, this essential component must have the ability to electrolytically decompose at the positive electrode and release F^- anions to diffuse within the reactive positive current collector. This cannot be restricted to the simple surface decomposition of the bi-ion conductor at the interface as this is not nearly a sufficient amount of F^- to induce the fluorination reaction. Bulk diffusion of F^- and replenishment at the interface is required. The bi-ion conductor also needs to have the capability to conduct Li^+ throughout its bulk to enable continuous Li deposition at the negative electrode. As such, the main goal for FY17 was to establish bi-ion solid-state conducting glass compositions with ionic conductivity $>1x10^{-4}$ S/cm prior to in-situ formation. In order to accomplish this goal, a systematic experimental process was set in place for the fabrication and characterization of bi-ion glass conductors of different composition in order to rapidly determine if they would be good candidates for the *in-situ* self-formed solid-state batteries. After deposition, the compositions were characterized by 1) electrochemical impedance spectroscopy (EIS) to extract the ionic conductivity, 2) a combination of stepped and linear sweep voltammetry to investigate the electrochemical stability, and 3) x-ray diffraction (XRD) to investigate nano-crystallinity. More than 20 compositions and 80 cells were deposited and tested with some of the resulting EIS and direct current conductivity measurements presented in Figure II-596. Best results were obtained with dopants which were identified to increase conductivity from $1x10^{-8}$ S/cm to $1x10^{-5}$ S/cm pre-formation and $> 1x10^{-4}$ S/cm at operation voltage were obtained. In addition, all except one composition exhibited electrochemical stability to breakdown in excess of 6 V with no increase of interfacial impedance.
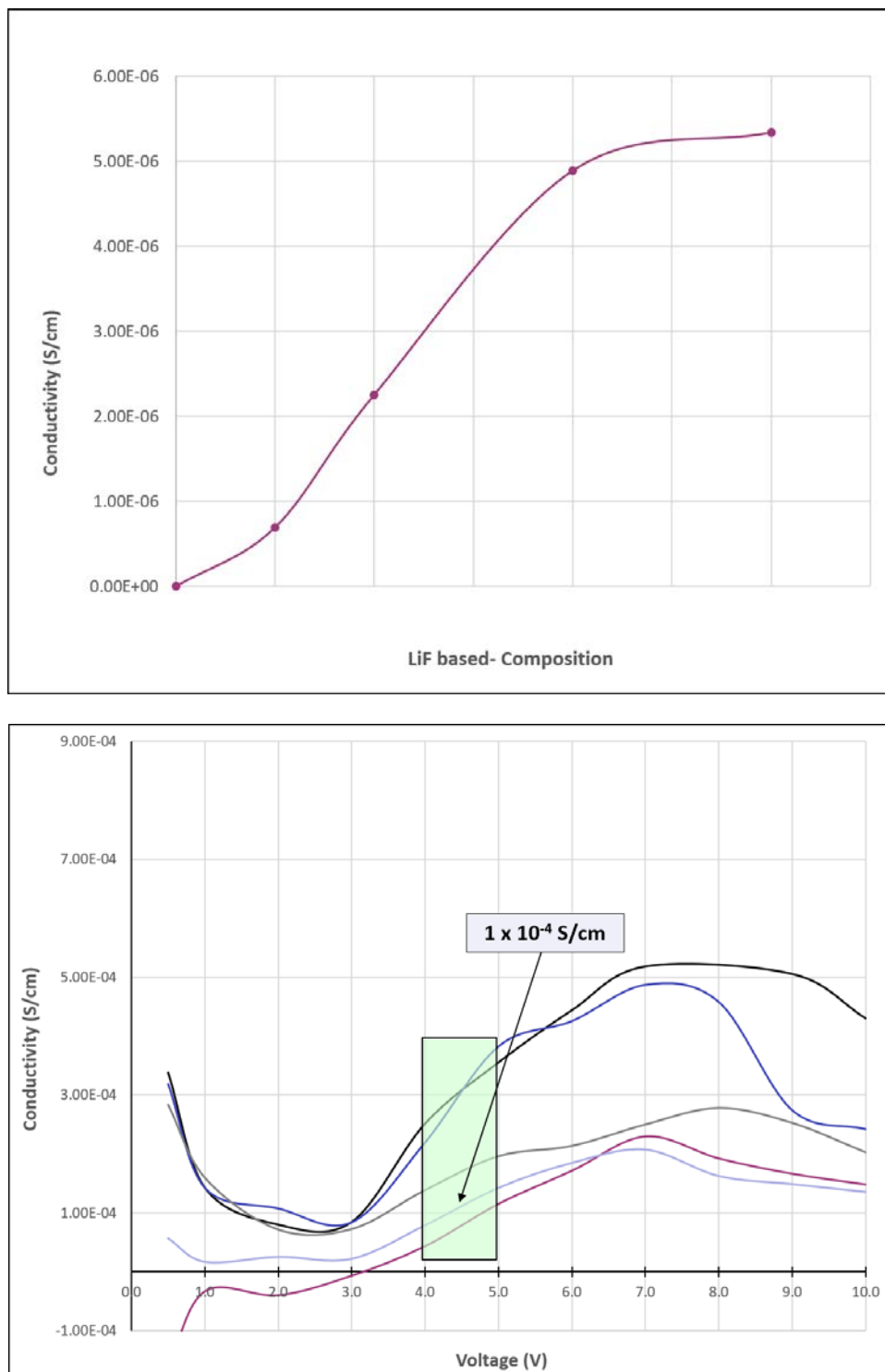
Figure II-596. Electrochemical impedance spectroscopy as a function of composition (left) and in-situ direct current conductivity as a function of voltage for several compositions (right)

Positive and negative reactive current collector development & design and fabrication: electrodes and cells.
Full solid-state cells were first fabricated in the second quarter using the newly developed bi-ion conductors with conductivities $> 1 \times 10^{-4}$ S/cm at operation voltage, baseline current collector compositions identified in the

first quarter, and baseline cell-stack designs established based on calculations and prior work. The viability of the *in-situ* formation of the entire electrochemical cell was demonstrated with limited cycling at output voltages of approximately 2 V as shown in Figure II-597, and low energy density represented by Generation 1 in the bar graph of Figure II-598. Transport is a critical aspect of this program and as such all components' chemistries, designs and structures have to be developed in order to maximize it. Our approach consisted of using planar configurations. The electrodes configurations impact diffusion distance, energy density, current density, and effective electron transport through the current collectors. Therefore, the focus of the third quarter was to improve the electrode architecture and combine these upgraded configurations with the improved bi-ion conduction composition described above. All cells were all fabricated with a newly implemented mask-less scalable patterning process described in the next section. Figure II-598 depicts the consistent progression in energy density that we have been able to achieve with time following this approach. The Generation 2 architecture brought forth an improvement of a factor 4 with respect to the initial Generation 1 design. Greater advance in energy density was obtained with the upgrade of the bi-ion conductor composition using the initial cell configuration leading to a factor 10 improvement compared to Generation 1 with the baseline bi-ion conductor. Finally, combining both approaches further increased the stack energy further by doubling the energy density obtained with the new bi-ion conductor alone (Generation 2 Bi-ion Conductor). Upon formation at 3.5 V, 76% of the 500 Wh/L go-no go goal was achieved, while a 4.0 V formation brought us closer with 96% of the 500 Wh/L goal. Additional architectural upgrades (Generation 3 and 4) demonstrated an effective path to effectively achieve and even surpass our go-no go goal with up to 570 Wh/L. The corresponding utilization of the reactive positive current collector also consistently increased from 16-20% for Generation 2 Bi-ion conductor to 24% for the Generation 2 Bi-ion conductor + Generation 2 architecture combination. The actual utilization is higher since the calculation assumed dense films, while experimental cells contain porosity.
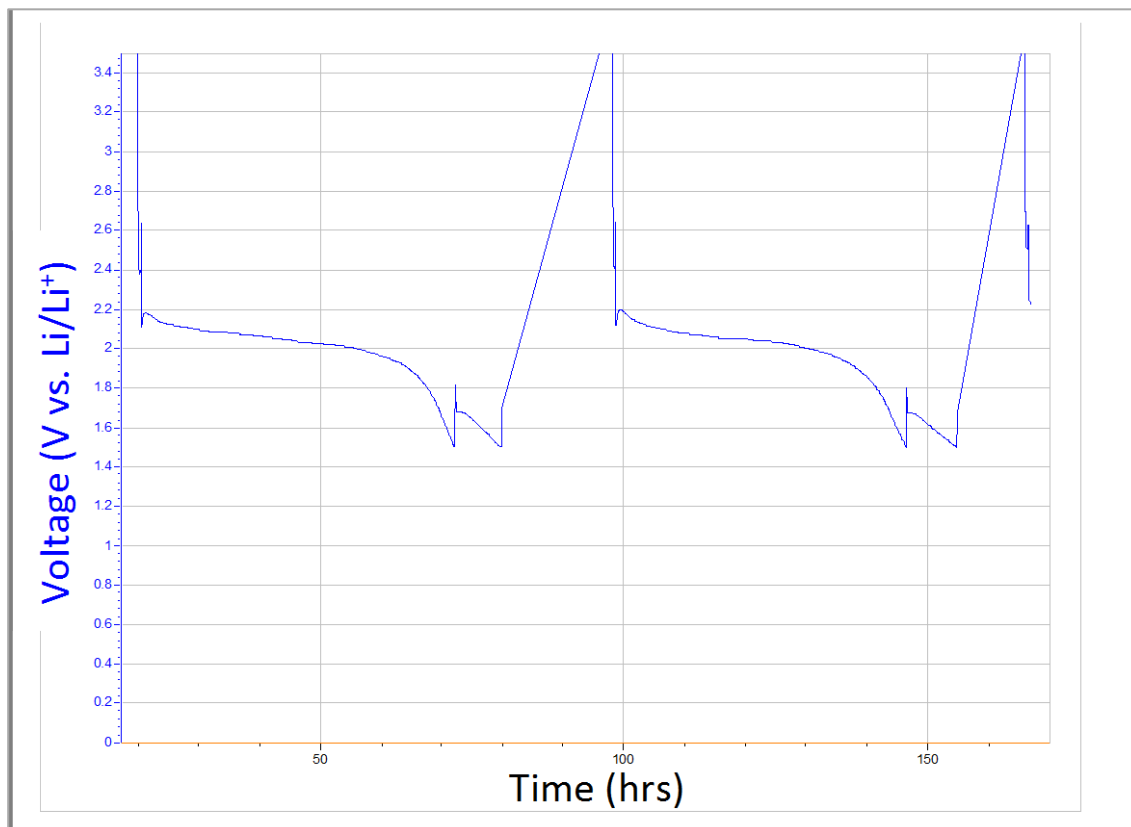

Figure II-597. Voltage profile of an *in-situ* self-formed battery fabricated using newly implemented maskless scalable patterning technique
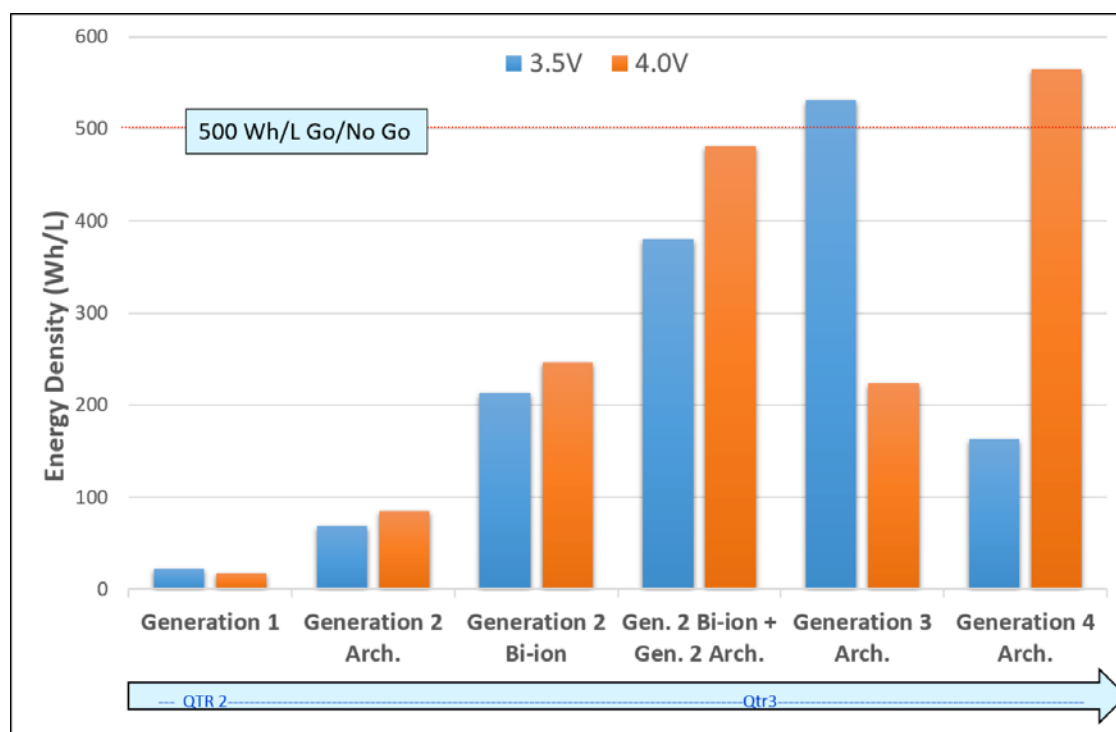
Figure II-598. Energy density in the first discharge at slow rate plotted upon formation at 3.5 and 4.0 V for various architecture combined with new bi-ion conductor chemistry. Labels indicate approach that gained the generation improvement.

Maskless scalable patterning implementation

In order to develop a feasible and economically viable pathway to manufactures using vapor deposition, masks should be eliminated from the process flow. In this spirit, a maskless scalable patterning technique that offers tremendous benefits towards a practical pathway to high throughput, low material loss fabrication of complex architectures was implemented. In addition to the ulterior benefits, this new technique more immediately enables time and cost saving at the program level. This was a significant leap forward as we achieved the implementation of the maskless process one year ahead of time. Moving to the new makless approach helped us to achieve the significant boost in energy density as described as we moved from generation 1 to generation 2. All other fabrications pathways were eliminated to solely pursue the maskless scalable patterning technique throughout the program.

Hybridization

In the fourth quarter, we shifted our focus toward improving rate capability. Consequently, architecture and hybridization of transport pathways were investigated in parallel. Each approach contributed in different ways to the advancement of our full cell performance. While further changes to the architecture did not significantly contribute to a steep change in rate capability, overall higher energy and utilization were realized. In contrast, hybridization resulted in greater than an order of magnitude increase in our discharge current densities and enabled us to achieve the C/10 rate capability of our year-end go-no go goal. Figure II-599 reveals the cell in-situ formation is followed by a full discharge at C/2 rate. In short, we have demonstrated a path to achieve over an order of magnitude improvement in current density leading to initial results achieving > C/10 discharge rates.
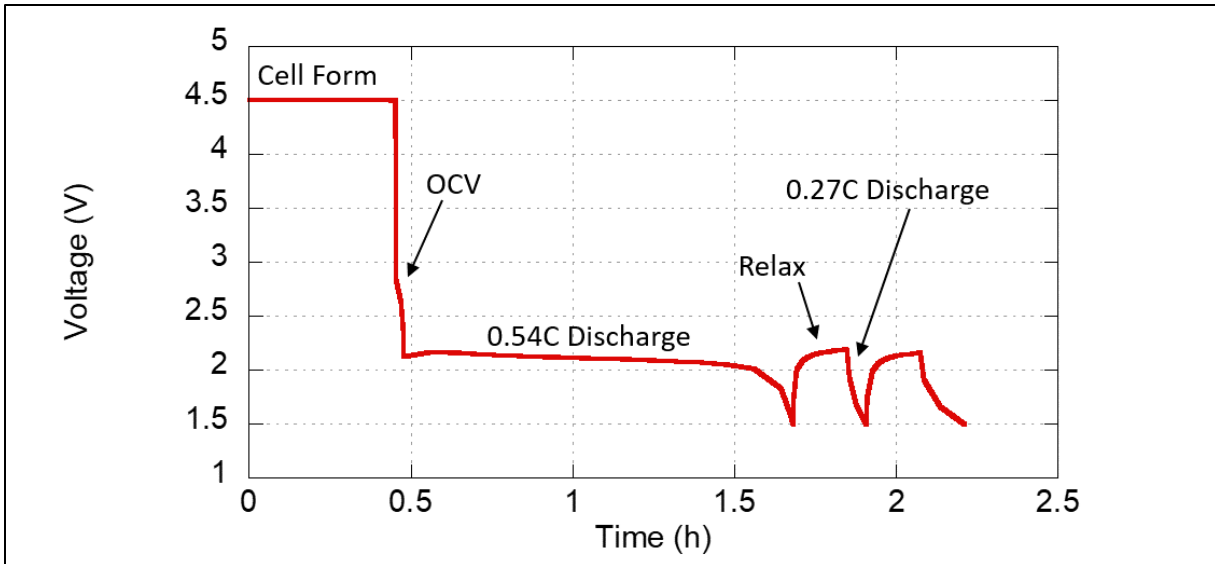
Figure II-599. Voltage profile of *a* cell utilizing hybridization of the transport pathways showing the *in-situ* formation and first discharge

Conclusions

Consistent progress has been realized during FY17 through advancements in chemistry, cell architecture and hybridization of transport pathways. The main key finding to date can be summarized as follow:

- Maskless scalable patterning technique was successfully implemented to fabricate solid-state full-cells.

- Self-formed cells' energy density increased from 5, to 70 to 120% of the year-end go-no goal 500 Wh/L in the 2nd, 3rd, and 4th quarter, respectively to achieve 570 Wh/L.

- Self-formed cells' positive reactive collector utilization increased from approximately 1, to 14, to 24% in the 2nd, 3rd, and 4th quarter, respectively.

- Bi-ion solid-state conducting glass compositions with $> 1 \times 10^{-4}$ S/cm conductivity after formation were fabricated and successfully integrated in full solid-state cells.

- Hybridization of transport pathways enabled improvement of current density by one order of magnitude leading to initial results achieving $> C/10$ discharge rates.

II.J   Beyond Li-ion R&D: Lithium-Air Batteries

II.J.1   Rechargeable Lithium-Air Batteries (PNNL)

Ji-Guang Zhang, Principal Investigator
Pacific Northwest National Laboratory
902 Battelle Boulevard
Richland, WA 99354
Phone: 509-372-6515; Fax: 509-375-2186
E-mail: jiguang.zhang@pnnl.gov

Wu Xu, Co-Principal Investigator
Pacific Northwest National Laboratory
902 Battelle Boulevard
Richland, WA 99354
Phone: 509-375-6934; Fax: 509-375-2186
E-mail: wu.xu@pnnl.gov

Tien Duong, Technology Manager
U.S. Department of Energy
Phone: 202-586-7836
E-mail: Tien.Duong@ee.doe.gov

Start Date: October 1, 2015   End Date: September 30, 2018
Total Project Cost: $600,000   DOE share: $600,000   Non-DOE share: $0

Project Introduction

It is well known that the state of the art lithium (Li)-ion batteries is a mutual technology and may reach their practical limit on specific energy (~ 300-350 Wh kg^{-1}) in the near future. Therefore, a worldwide effort has been made to explore new battery chemistries that may far exceed the specific energy of Li-ion batteries. Among the alternative energy storage systems, Li-air batteries have triggered worldwide research interest since the first nonaqueous Li-air battery was unveiled in 1996 due to their extremely high theoretical specific energy density (~5,200 Wh kg^{-1} when the weights of Li and O_2 are included). However, before the commercialization of Li-air batteries, considerable challenges still face Li-air batteries and need to be overcome. These challenges include instability of electrolyte, high overpotential, and severe corrosion of Li anodes. These problems cause poor round-trip efficiency and short cycle life in the stat of the art Li-air batteries. Thus, efficient strategies for further development of ultrahigh-energy-density Li-air batteries suitable for application in electric vehicles include development of electrolytes that are more stable against superoxide and Li metal anodes, design of alternative catalysts and carbon-based or carbon-free air electrodes, stabilization of Li metal anodes, and exploration of new insights into the mechanisms of oxygen reduction/evolution reactions (ORR/OER) are critical to promote further development of ultrahigh-energy-density Li-air batteries for potential application in electric vehicles.

Objectives

The objective of this project is to develop rechargeable lithium-oxygen (Li-O_2) batteries with long-term cycling stability through in-depth research on more stable electrolytes and highly efficient catalysts for air electrodes, protection of Li metal anodes, and deeper insight into the ORR/OER mechanisms behind the electrochemical performance of Li-O_2 cells.

Approach

The objectives outlined above will be accomplished by developing new concentrated electrolytes, protection for both Li metal anodes and carbon-based air electrodes, highly efficient catalysts produced by in-situ electrochemical pretreatment, and in-depth study of the effect of temperature on discharge behaviors of Li-O_2 batteries. These strategies are greatly expected to significantly improve cycling stability of Li-O_2 batteries and deepen our insight into Li-O_2 battery chemistries.

Results

We have made significant progresses in electrolytes, protection of electrodes (both carbon-based air-electrode and Li anode), efficient catalysts, and underlying mechanisms in Li-O_2 batteries in FY17 as described below.

1. Concentrated electrolytes with optimized salt-solvent coordination for more stable Li-O_2 batteries

Lithium bis(trifluoromethanesulfonyl)imide (LiTFSI)-dimethyl sulfoxide (DMSO) electrolytes were prepared according to the molar ratio of LiTFSI salt to DMSO solvent at 1:3, 1:4, and 1:12; these are denoted as LiTFSI-nTFSI, where n = 3, 4, or 12, respectively. Figure II-600 shows the electrochemical performance of Li-O_2 cells composed of a carbon nanotube (CNT) air electrode and Li metal anode using the three different salt-concentration electrolytes. The LiTFSI-3DMSO electrolyte leads to the most stable cycling for at least 90 cycles and the voltage profiles are very stable. The three electrolytes (LiTFSI-12DMSO, LiTFSI-4DMSO, and LiTFSI-3DMSO) can be considered to contain the free DMSO solvent, Li^+-$(DMSO)_4$ solvate, and the $TFSI^-$-Li^+-$(DMSO)_3$ complex. According to computational calculations of Gibbs activation energy barriers for C–H bond scission in DMSO, Li^+-$(DMSO)_4$, and $TFSI^-$-Li^+-$(DMSO)_3$ by the attack of $O_2^{\bullet-}$, electrolytes with salt-solvent coordination (i.e., LiTFSI-4DMSO and LiTFSI-3DMSO) have higher Gibbs activation energy barriers than the free DMSO solvent molecules, indicating improved stability of the electrolyte against the attack of superoxide radical anions. Moreover, the $TFSI^-$-Li^+-$(DMSO)_3$ complex has an even higher activation energy barrier than the Li^+-$(DMSO)_4$ solvate. Therefore, the stability of such a concentrated LiTFSI-3DMSO electrolyte has been greatly improved.

2. In-situ induced protection films formed on both air electrode and Li metal anode of Li-O2 cells

We have demonstrated a simple one-step in-situ electrochemical pre-charging strategy to simultaneously generate thin protective films on both the CNT air electrode and Li metal anode. These forms can protect both electrodes to significantly suppress the attack of highly reactive reduced oxygen species, as shown in Figure II-601a. The pretreatment of the assembled Li‖CNT cells was conducted by charging the cells under argon (Ar) gas from open-circuit voltage (OCV) to 4.3 V at 0.1 mA cm^{-2} and then holding the cells at 4.3 V for 0, 5, 10, 15, and 20 min. The number of stable cycles of the Li-O_2 cells with the aforementioned pretreatment (4.3 V/0 min, 4.3 V/5 min, 4.3 V/10 min, 4.3 V/15 min, and 4.3 V/20 min) and without pretreatment are 62, 63, 110, 95, 72, and 43, respectively (Figure II-601b). This demonstrated that the simple pretreatment did enhance the cycling stability of the Li-O_2 cells even without mediators in the electrolyte or catalysts on the air electrode. After cycling, the scanning electron microscope (SEM) images of the cycled CNT air electrode without pretreatment show some large breakage at the air-electrode surface (Figure II-601c) and thick side-reaction products from decomposition of CNTs and electrolyte (Figure II-601c, Figure II-601d). These exposed bare CNTs became larger and thicker (Figure II-601d), due to serious side reactions of reactive reduced oxygen species with electrolyte components and the CNT electrode. The thickness and the coverage of some coated layers on the CNT electrode pretreated at 4.3 V/10 min (Figure II-601e, Figure II-601f) are significantly less. The cycled Li metal anode without pre-charging treatment exhibits severe corrosion of the vast majority of bulk Li metal (Figure II-601g) and a large amount of corrosion products are loosely packed on the Li metal surface (Figure II-601h). However, the cycled Li metal anode with pretreatment retains a thick bulk Li metal layer without corrosion (Figure II-601i), and the surface layer is relatively flat and compact with only a few cracks (Figure II-601j). This shows that the optimal pre-charging treatment could significantly protect both the CNT electrode and Li metal anode during long-term cycling, thus leading to greatly enhanced cycling stability of Li-O_2 cells.
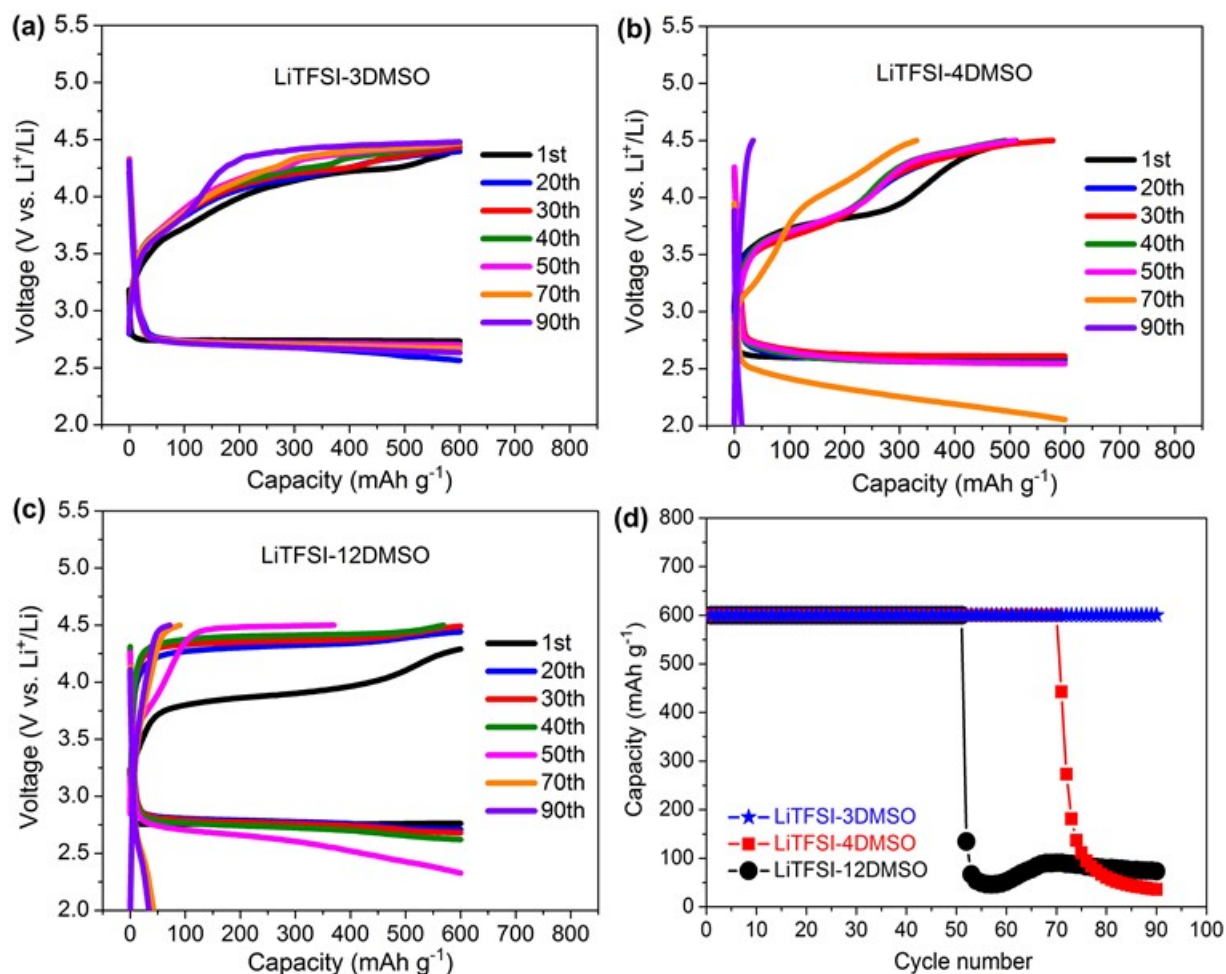
Figure II-600. Electrochemical performance of Li-O₂ batteries with three LiTFSI-DMSO electrolytes cycled under capacity-limited protocol (600 mAh g⁻¹) in the voltage range of 2.0 to 4.5 V at 0.1 mA cm⁻². (a-c) Voltage profiles for LiTFSI-3DMSO electrolyte (a), LiTFSI-4DMSO electrolyte (b), and LiTFSI-12DMSO electrolyte (c). (d) The corresponding cycling stability of the three electrolytes.
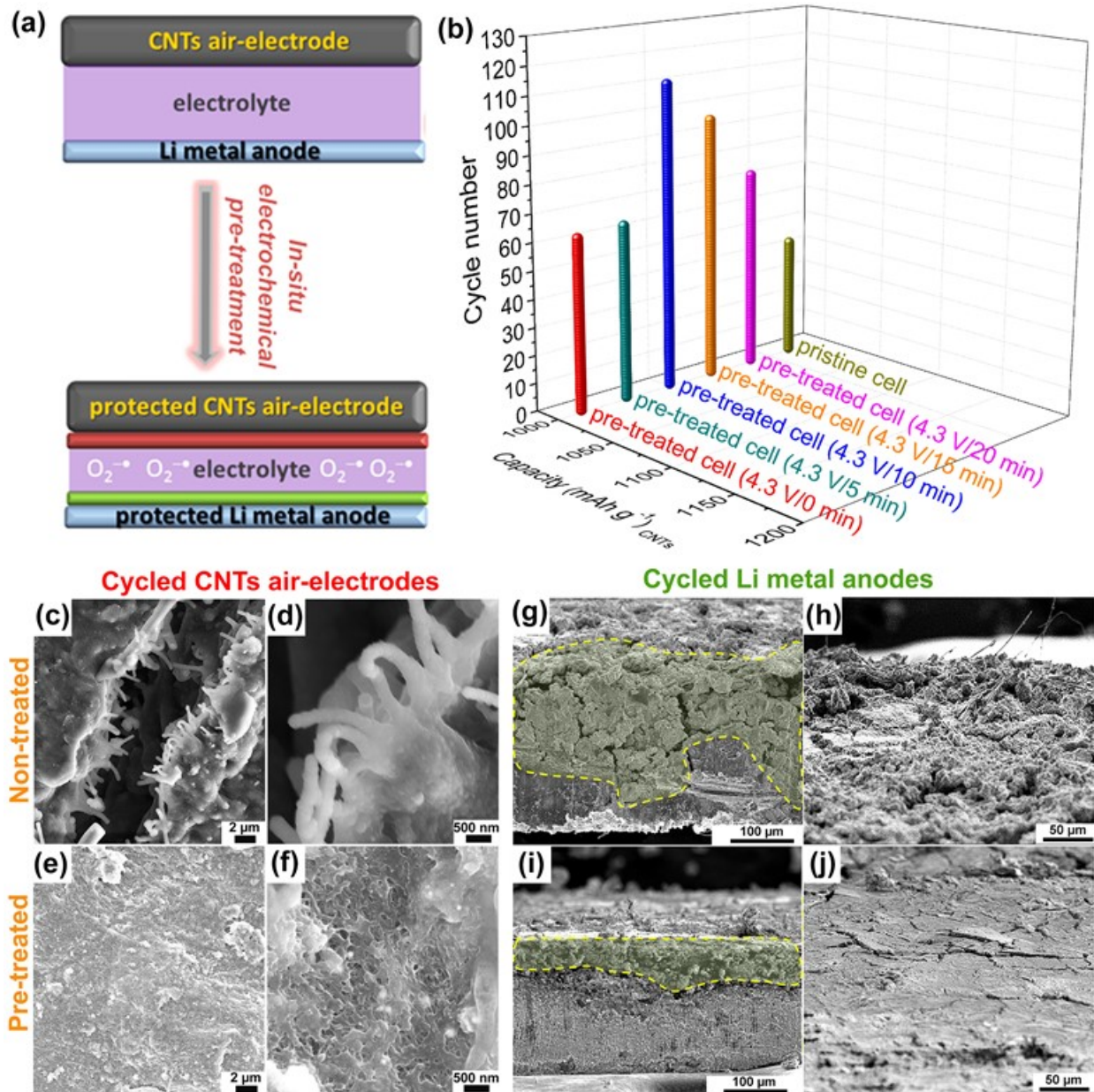
Figure II-601. (a) Schematic of the operation principle of prior protection for CNT air electrode and Li metal anode after in-situ electrochemical process. (b) Stable cycling life of Li-O_2 cells without and with pretreatment cycled at 0.1 mA cm^{-2}. (c-f) SEM surface-view images of the CNT air electrode without pretreatment after 70 cycles (c, d), and the CNT air electrode with 4.3 V/10 min pre-charging treatment after 110 cycles (e, f). (g-j) SEM images of corresponding cycled, untreated Li metal anode (g, h) and pretreated Li metal anode (i, j), where (g, i) are cross-section views and (h, j) top views.

The variations of cell impedances with cycle time were further investigated for pre-treated and pristine Li-O_2 cells, and the corresponding electrochemical impedance spectra plots at the charged states are shown in Figure II-602a and Figure II-602b, respectively. The corresponding fitting results of the electrolyte resistance (R1), the total resistance (R2) containing the surface film resistance (R_{SEI}) and the charge transfer resistance (R_{ct}) as a function of cycle numbers are also provided in Figure II-602c. It is clearly seen from Figure II-602c that the pre-treated Li-O_2 cell at the initial stage has a smaller R1 and R2 than those with the pristine cells. This is because the Li metal anode in the pre-charged cell has already been well protected before O_2 was introduced so the reactions between Li, electrolyte and O_2 are limited. The cell impedances of R2 decrease from the 1st

cycle to the 20th cycle, which is probably because both CNTs electrode and Li metal anode, either pre-treated or untreated, gradually reach their own well protected condition with the coverage of the electrolyte decomposition products thus give lower cell impedances. After that, the Li-O$_2$ cell after the optimal pre-treatment only shows slight increase in cell impedance from 20th cycle to 110th cycle, while the cell without pre-treatment shows a rapid increase in cell impedance from 20th cycle to only 70th cycle. This is because the electrochemical pre-charging process generates protective layers on both CNTs electrode surfaces and Li metal anode, which suppress the side reactions of reduced oxygen species attacking both CNTs electrode and Li metal anode, as show in Figure II-601a.
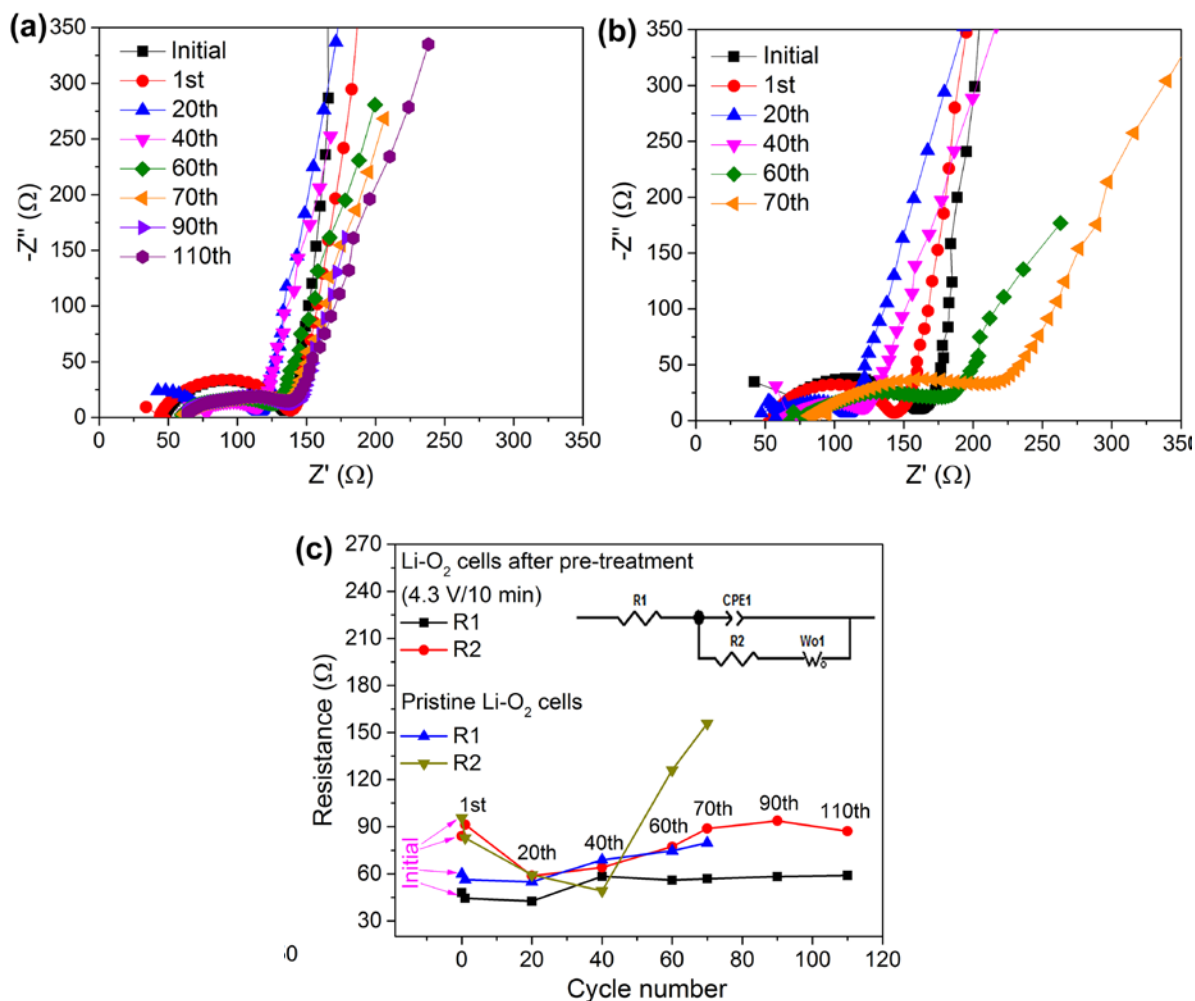
Figure II-602. The a.c.-impedance spectra of the Li-O$_2$ cells after pre-treatment at 4.3 V/10 min during 110 cycles (a), and pristine Li-O$_2$ cells during 70 cycles (b). (c) Evolution of fitted resistance values of the above Li-O$_2$ cells after pre-treatment at 4.3 V/10 min and pristine cells. Inset: The equivalent circuit used to it the impedance spectra.

To further improve cycling efficiency and life of Li-O$_2$ cells, a one-step in-situ electrochemical pretreatment strategy on the optimization of RuO$_2$/CNTs catalysts for Li-O$_2$ batteries. Figure II-603 shows that the cycle life of Li-O$_2$ cells with the optimized RuO$_2$/CNT air electrode and Li metal can reach 190 cycles at 0.1 mA cm^{-2} under a capacity protocol of 1000 mAh g^{-1}, while the cycling life of the pristine cells can survive only 51 cycles, which is very limited. Considering the extremely stable pretreated RuO$_2$/CNTs and severe corrosion of the Li metal anode, we paired the above cycled pretreated air electrode with a new Li metal anode to get a new cell, which was cycled at 0.2 mA cm^{-2}. The new Li-O$_2$ cells composed of cycled air electrode and new Li anode can be further cycled for at least 125 more cycles. This indicates that the novel in-situ electrochemical

approach developed in this work greatly enhanced the cycling stability of Li-O$_2$ cells. More work is currently under way.
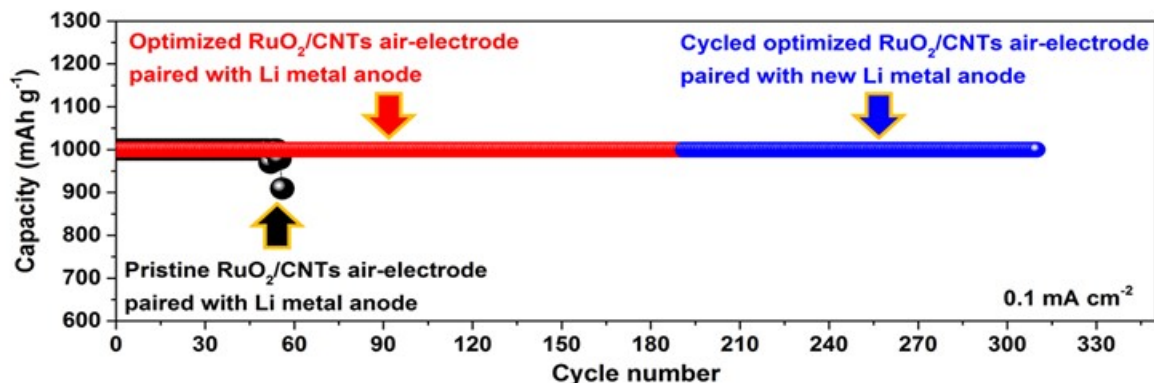
Figure II-603. Cycling performances of Li-O$_2$ cells with optimized in-situ pretreated RuO$_2$/CNT air electrode (red line) and pristine RuO$_2$/CNT air electrode (black line), cycled at 0.1 mA cm^{-2} in 1 M LiTf-Tetraglyme electrolyte. Blue line is the cycle life of the freshly assembled Li-O$_2$ cell with the cycled pretreated air-electrode after 190 cycles and new Li metal anode, under the same conditions.

3. In-depth Understanding on the temperature dependence of oxygen reduction mechanism in nonaqueous Li-O$_2$ batteries

An in-depth investigation on the temperature dependence of the chemistry and electrochemistry that govern the operation of the Li-O$_2$ cells has been made. The cells composed of a Li metal anode, an air electrode (consisting of CNTs deposited on carbon paper), a glass-fiber–based separator, and 1,2-dimethoxyethane-based electrolyte. Figure 5a shows that the discharge capacity of the cells initially decreases slowly from 7,492 mAh g^{-1} at 40°C to 2,930 mAh g^{-1} at 0°C, then increases sharply to an extraordinarily high capacity of 17,716 mAh g^{-1} at −20°C. A clear minimum capacity occurred at a temperature of ~ 0°C. The temperature dependence of the lifetime of superoxide, the electrochemical kinetics, and the discharge capacities of Li-O$_2$ batteries in the temperature range from −20°C to 40°C are summarized in Figure 5b. The lifetime of O$_2^{\bullet-}$ and the discharge capacities are from experimental results, and electrochemical kinetics data are based on formula calculation. As the temperature increased from −20°C to 40°C, the lifetime of the O$_2^{\bullet-}$ obtained from both nuclear magnetic resonance (NMR) and electron paramagnetic resonance (EPR) analysis decreases while the electrochemical kinetics increases, and an obvious temperature turning point at 0°C can be observed in Figure 5a. More interestingly, two sharp changes of lifetime of O$_2^{\bullet-}$ and electrochemical kinetics that occur in the temperature ranges of −20°C~0°C and 0°C~40°C, respectively, are coincident with the change trend of discharge capacities. It is worth noting that the dominant mechanism for the ORR process in the Li-O$_2$ cell changes at ~0°C. Briefly, at low temperatures, the lifetime of O$_2^{\bullet-}$ plays a dominant role, so the discharge capacity is quite high even though the electrochemical kinetics is very slow. At sub-ambient temperatures from 0 to 10°C, both the lifetime of O$_2^{\bullet-}$ and the electrochemical kinetics are slow, so the discharge capacity is low. At elevated temperatures (20~40°C), the electrochemical kinetics plays a dominant role, and thus the discharge capacity increases.
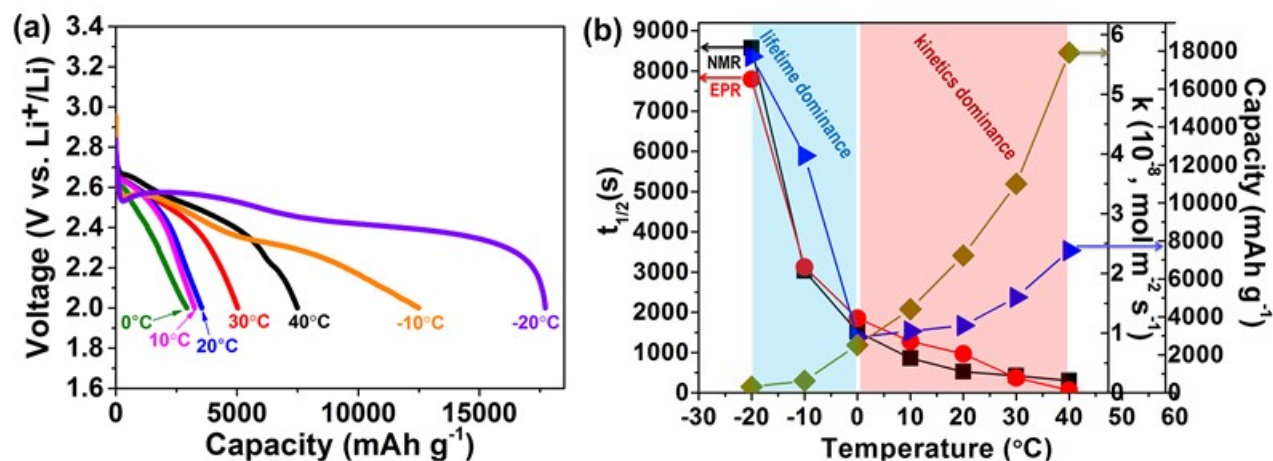
Figure II-604. (a) Discharge curves of Li-O₂ coin cells composed of CNT air electrodes at a current density of 0.1 mA cm⁻² at various temperatures. (b) Temperature dependence of the experimental lifetime of superoxide from NMR and EPR, the calculated electrochemical kinetics, and the discharge capacities at different temperatures.

Conclusions

- The highly concentrated LiTFSI-3DMSO electrolyte, in which only TFSI⁻-Li⁺-(DMSO)₃ exists but no Li⁺-(DMSO)₄ solvates or free DMSO solvent molecules, has been identified as an optimally stable DMSO-based electrolyte against the attack of reduced oxygen species to the Li metal anode.

- A facile in-situ electrochemical pre-charging method has been developed to simultaneously produce ultrathin protective films on both CNT air electrodes and Li metal anodes. Those protective films can significantly suppress and mitigate the well-known oxidation of CNT air electrodes by reduced oxygen species and severe corrosion of Li metal anode upon cycling; thus, the cycling life of pretreated Li-O₂ cells can be extended even to 110 cycles without requiring efficient catalysts or redox mediators.

- Li-O₂ cells based on the pretreated RuO₂/CNTs air electrode demonstrated superior cycling stability due to the extremely high stability and catalytic capability of the ultrafine RuO₂ catalyst-decorated air electrodes. Next, a more appropriate stable anode will be explored to pair with the RuO₂/CNT air electrode and realize high energy, stable Li-O₂ batteries.

- The lifetime of superoxide/LiO₂ and the electrochemical kinetics are two major factors determining the temperature dependence of ORR. The lifetime of superoxide and the solution pathway play a dominant role in the battery capacity in the temperature range of −20°C to 0°C, but the electrochemical kinetics of oxygen reduction and the surface pathway dominate the discharge behavior between 0°C and 40°C. The in-depth understanding of the temperature effect on the discharge mechanisms of Li-O₂ batteries will enable more rational design of high energy Li-O₂ batteries and other metal-air batteries.

Key Publications

1. B. Liu, W. Xu, J.-G. Zhang, Invited book chapter entitled, "Stability of Li metal anode in Li-air batteries", *Wiley Publishing Group*, **2017**, in press.

2. B. Liu, W. Xu, P. Yan, S. T. Kim, M. H. Engelhard, X. Sun, D. Mei, J. Cho, C. Wang, J.-G. Zhang, "Stabilization of Li metal anode in DMSO-based electrolytes via optimization of salt-solvent coordination for Li-O2 batteries", *Advanced Energy Materials*, **2017**, 7, 1602605. (Featured as Frontispiece image)

3. B. Liu, W. Xu, J. Zheng, P. Yan, E. D. Walter, N. Isern, M. E. Bowden, M. Engelhard, S. T. Kim, J. Read, B. D. Adams, X. Li, J. Cho, C.-M. Wang, J.-G. Zhang, "Temperature dependence of oxygen reduction mechanism in non-aqueous Li-O_2 batteries", *ACS Energy Letters* **2017**, 2, 2525-2530. (A "most read" article)

4. B. Liu, W. Xu, J. Tao, P. Yan, J. Zheng, M. H. Engelhard, D. Lv, C. Wang, J.-G. Zhang, "Enhanced cyclability of lithium-oxygen batteries with electrodes protected by surface films induced via in-situ electrochemical process", *Advanced Energy Materials* **2017**, DOI:10.1002/aenm.201702340, in press.

5. L. Luo, B. Liu, S. Song, W. Xu, J.-G. Zhang, C. Wang, "Revealing the reaction mechanisms of Li-O_2 batteries using environmental transmission electron microscopy", *Nature Nanotechnology* **2017**, 12, 535.

6. S. Song, W. Xu, R. Cao, L. Luo, M. H. Engelhard, M. E. Bowden, B. Liu, L. Estevez, C.-M. Wang, J.-G. Zhang, "B_4C as a stable non-carbon-based oxygen electrode material for lithium-oxygen batteries", *Nano Energy* **2017**, 33, 195-204.

7. S. Song, W. Xu, J. Zheng, L. Luo, M. H. Engelhard, M. E. Bowden, B. Liu, C.-M. Wang, J.-G. Zhang, "Complete Decomposition of Li_2CO_3 in Li-O_2 batteries using Ir/B_4C as noncarbon-based oxygen electrode", *Nano Letters* **2017**, 17, 1417-1424.

8. W. Xu, B. Liu, J.-G. Zhang, "Preformation of solid electrolyte interphase on electrodes for rechargeable lithium metal batteries", PCT/US17/56081.

9. B. Liu, P. Yan, W. Xu, J. Zheng, Y. He, L. Luo, M. E. Bowden, C. Wang, J.-G. Zhang, "Electrochemically formed ultrafine metal oxide nano-catalysts for high-performance lithium-oxygen batteries", poster presentation at *2016 MRS Fall Meeting & Exhibit*, November 27-December 2, 2016, Boston, Massachusetts.

10. B. Liu, W. Xu, P. Yan, J. Zheng, M. H. Engelhard, C. Wang, J.-G. Zhang, "Enhanced cycling stability of Li-O_2 batteries through in-situ formed electrode interface layers", oral presentation at *2017 MRS Spring Meeting & Exhibit*, April 17-21, 2017, Phoenix, Arizona.

11. B. Liu, W. Xu, P. Yan, S. T. Kim, M. H. Engelhard, X. Sun, D. Mei, J. Cho, C. Wang, J.-G. Zhang, "Stabilization of Li metal in optimized DMSO-based electrolytes for Li-O_2 batteries", oral presentation at *231st ECS meeting*, May 28-June 1, 2017, New Orleans, Louisiana.

12. W. Xu, B. Liu, S. Song, and J.-G. Zhang, "Development of stable rechargeable lithium-oxygen batteries", invited presentation at *254th ACS National Meeting & Exposition*, August 20-24, 2017, Washington, DC.

II.J.2 Efficient Rechargeable Li/O$_2$ Batteries Utilizing Stable Inorganic Molten Salt Electrolytes (Liox Power)

Vincent Giordani, Principal Investigator

Liox Power, Inc.
129 N Hill Avenue Suite 107
Pasadena, CA 91106
Phone: 626-389-6311
E-mail: vincent@liox.com

Tien Duong, Technology Manager

U.S. Department of Energy
Phone: 202-586-7836
E-mail: Tien.Duong@ee.doe.gov

Start Date: October 1, 2014   End Date: September 30, 2017
Total Project Cost: $1,425,000   DOE share: $1,050,000   Non-DOE share: $375,000

Project Introduction

The rechargeable lithium-oxygen battery has attracted attention due to its large theoretical energy density compared to modern lithium-ion batteries. This large energy density is attributed to the reaction of lithium with molecular oxygen to form lithium peroxide, which grows on the surface of the cathode. While this is a promising chemistry, there are many practical challenges that remain to be solved, such as the decomposition of organic electrolyte in the presence of superoxide anions and large overpotentials on charge. We propose a system which inherently avoids many of the issues associated with organic electrolyte decomposition, while also forming lithium peroxide with a unique morphology. By using a LiNO$_3$/KNO$_3$ eutectic molten salt in place of a conventional solvent/salt electrolyte, solvent decomposition is obviated. In addition, the elevated temperature operation as well as the large concentration of Li$^+$ ions encourage faster diffusion and kinetics. This project aims at solving particularly intractable problems relating to air electrode efficiency, stability and tolerance to the ambient environment. Furthermore, these solutions may translate into reduced complexity in the design of a Li-air stack and system, which in turn may improve prospects for use of Li-air batteries in EVs. Additionally, the project provides materials and technical concepts relevant for the development of other medium temperature molten salt Li battery systems of high specific energy, which may also have attractive features for EVs.

Objectives

The objective of this project is to develop high specific energy, rechargeable Li-air batteries having lower overpotential and improved robustness under ambient air compared to current Li-air batteries. The technical approach involves replacing traditional organic and aqueous electrolytes with a nonvolatile, inorganic molten salt comprising nitrate anions and operating the cell at elevated temperature (>80°C). The research methodology includes powerful in situ spectroscopic techniques coupled to electrochemical measurements (e.g., operando electrochemical mass spectrometry) designed to provide quantitative information about the nature of chemical and electrochemical reactions occurring in the air electrode.

Approach

Replace volatile, unstable and air-intolerant organic electrolytes common to prior research with inert molten nitrate electrolytes and operate cell above liquidus temperature (> 80°C). Improve reversibility and rate capability since discharge products (Li$_2$O$_2$, Li$_2$O, LiOH and Li$_2$CO$_3$) are stable and sparingly soluble in molten nitrate electrolytes. Combine quantitative gas analysis (pressure monitoring, mass spectrometry) with precise coulometry, as well as in situ spectroscopic techniques such as Raman to analyze air electrode processes.

Results

Demonstrate discharge specific energy and energy density ≥ 500 Wh/Kg and ≥ 800 Wh/L, respectively, based on air electrode mass and volume

We evaluated the O_2 cathode discharge specific energy and energy density. Composite cathodes comprising Super P carbon black, PTFE binder, and $LiNO_3$-KNO_3 eutectic weighed ca. 4 mg/cm^2 (all components without the mesh current collector), electrode thickness was ca. 100 microns. Mass ratio between carbon, binder, and electrolyte, was 78/2/20 wt.%, respectively. Li/O_2 cells were discharged to 2.5 V cutoff, at a current density of 0.32 mA/cm^2 ($A_{cathode}$= 0.79 cm^2), and at 150°C. With a discharge capacity of 335 Ah/kg (170 Ah/L) of air electrode (carbon + binder + eutectic, Figure II-605a), the calculated corresponding discharge specific energy and energy density at $E_{disch.}$ ≈2.7 V were 900 Wh/Kg and 460 Wh/L, respectively.
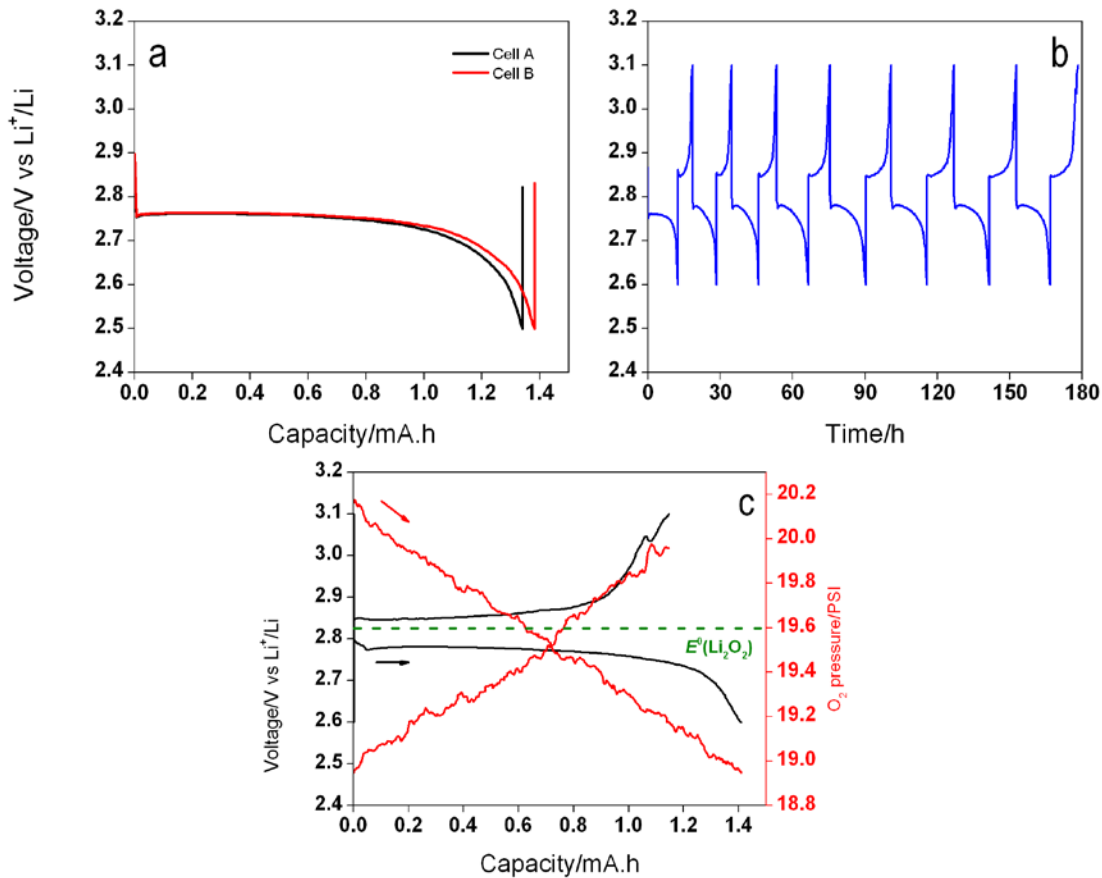
Figure II-605. a. Galvanostatic discharge curves for Li/O_2 cell containing a $LiNO_3$-KNO_3 electrolyte and a carbon-based air electrode (T= 150°C, PO2= 1.4 atm, j= 0.32 mA/cm^2). b. Cycling profile of a molten nitrate Li/O_2 cell using a boron carbide-based air electrode (T= 150°C, j= 0.13 mA/cm^2, B4C loading ~5 mg/cm^2). c. Corresponding in-situ pressure analysis for cell depicted in b.

Amongst other recently tested conducting ceramic electrode materials (FY 2016 Q3), boron carbide nanopowders (B_4C) were shown to exert promising cycling behavior in the molten salt electrolyte (Figure II-605b,c). We measured e$^-$/O_2 molar ratios using mass spectrometry and found 2.0 for both discharge and charge half-cycle, supporting reversible formation of Li_2O_2 as the discharge product, with OER/ORR ratio of 0.85, consistent with solution-phase mechanism of Li_2O_2 growth and/or side reaction with the carbide material to form lithium carbonate. SEM analysis of a discharged electrode showed micron-sized ORR product deposited onto glass fibers (separator material), leading to electrical disconnection and low Coulombic efficiency (≈85%).
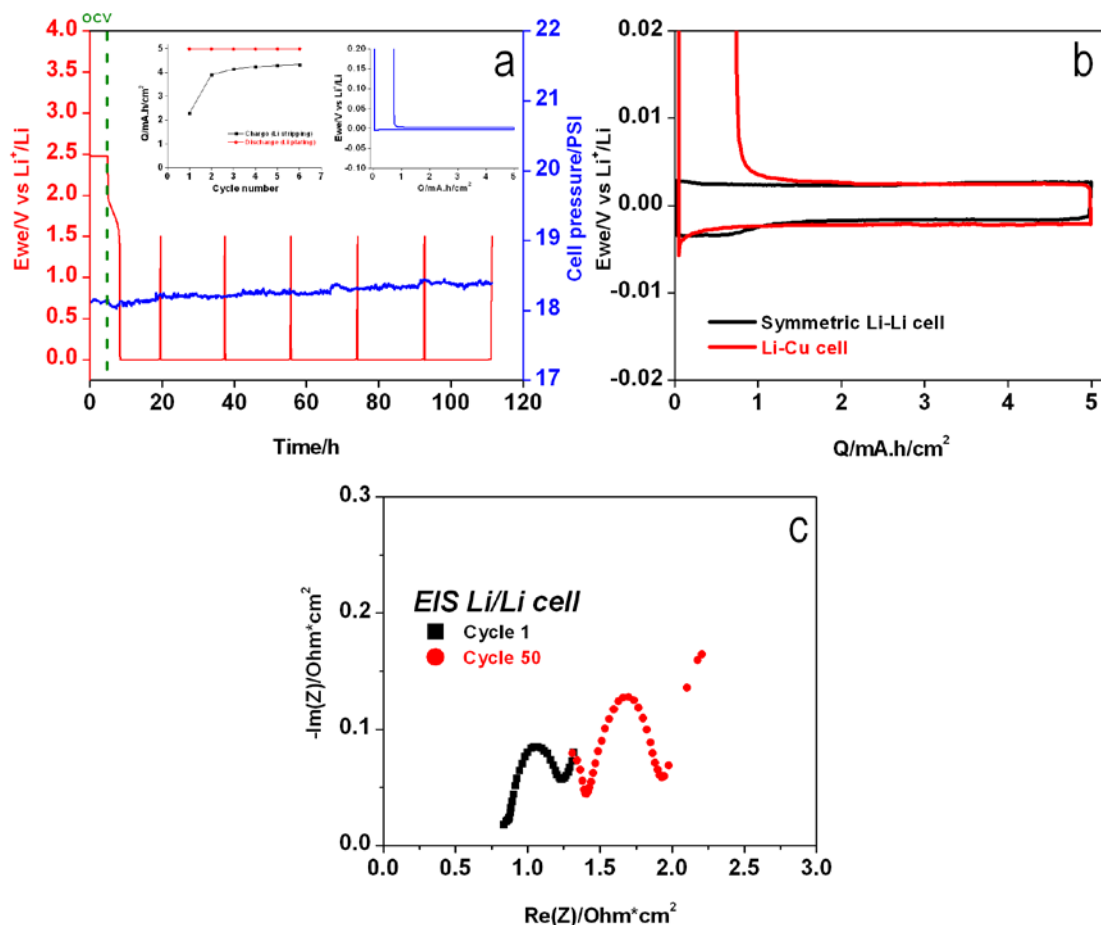
Figure II-606. a. Li plating/stripping onto Cu (ALi=ACu=0.502 cm²) at j= 0.5 mA/cm², at 150°C, under Ar, in LiNO₃-KNO₃ melt (Inset: Q vs Cycle number and Li plating/stripping load curve). b. Cycling curve comparison between Li-Li symmetric cell and Li-Cu cell employing LiNO₃-KNO₃ melt, at 0.5 mA/cm², at 150°C. c. EIS data derived from cycled Li-Li symmetric cell (estimated electrolyte thickness: 0.5 mm, ALi= 0.502 cm²).

Study of the Li metal/molten nitrate interface shows an increase in area specific resistance (ASR) with cycle number (both bulk and interfacial resistances), continuous increase in pressure (Figure II-606a), consistent with SEI reaction: $2Li + NO_3^- = Li_2O + NO_2^-$, with nitrite anion being further reduced by Li to generate nitric oxide and nitrogen (confirmed by mass spectrometry), and low coulombic efficiency for Li stripping/plating (≈87%). Addition of few wt.% CsNO₃ into the melt was shown to stabilize the Li interface. Cs⁺ cations are thought to improve the SEI on lithium metal.

Scale-up downselected cell components for 4 mAh and 10 mAh cells

We investigated the lithium metal anode/solid electrolyte interface. Molten nitrate electrolytes are known to slowly decompose onto Li metal and therefore a solid electrolyte is required to prevent such reaction and improve battery cycle life. LLZO garnet-type pellets (1 cm diameter, 0.3 mm thickness) were hot-pressed and sintered for 36 hours at 1100°C under inert gas. Li/LLZO/Li symmetric cells were constructed in an Ar-filled glove box and operated at lithium melting point (ca. 185°C). Figure II-607 shows Li stripping/plating cycling data at 0.1 mA/cm² and 2 h per each half cycle with electrochemical impedance spectroscopy recorded every 80 hours of cycling.
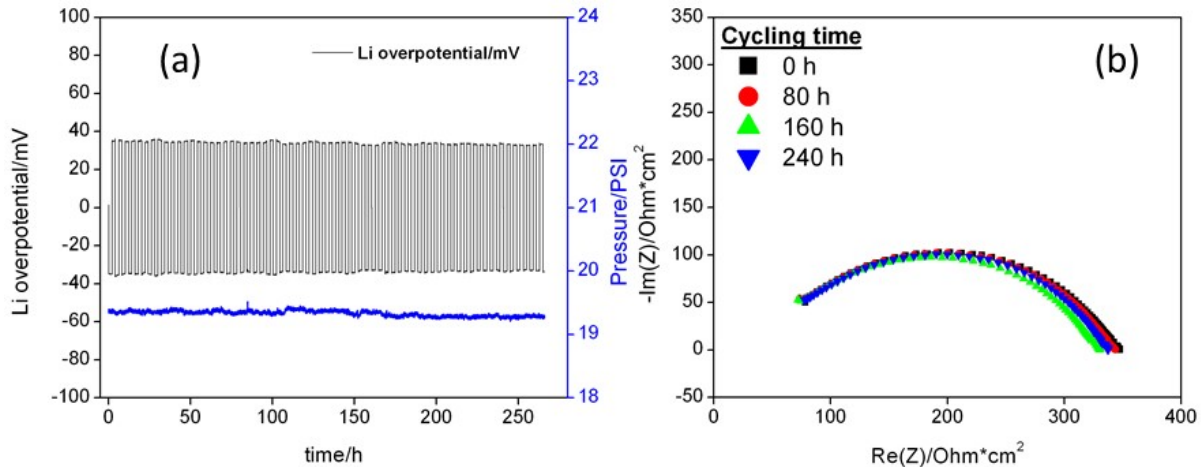
Figure II-607. a. Li/LLZO/Li symmetric cell cycling at 185°C (with in situ cell pressure analysis) at 0.1 mA/cm^2 with b. corresponding EIS analysis recorded at OCV (AC signal: 10 mV, from 1 MHz to 1 Hz).

Typical bulk electrolyte and interfacial resistance were found to be roughly 40 Ω.cm^2 and 300 Ω.cm^2, respectively. Li/O$_2$ cells using LLZO-protected Li anode were also tested. The air cathode/catholyte consisted of a 2-to-1 mixture LiNO$_3$:KNO$_3$ eutectic with Super P Carbon (containing 5% PTFE). Tests were conducted at 185°C to ensure good Li-LLZO-catholyte contact. It is expected that the elevated temperature may cause rapid carbon degradation in presence of ORR products as well as enhanced Li$_2$O$_2$ solubility (leading to poor rechargeability). Separately, we analyzed ORR discharge product morphology using a boron carbide air cathode. Boron carbide O$_2$ cathodes were collected from OCV and discharged molten nitrate Li/O$_2$ cells, rinsed in an organic solvent to remove excess nitrate salt, and analyzed by SEM (Figure II-608c). Li$_2$O$_2$ large crystals (several microns) were observed on boron carbide surfaces and XRD was used to confirm the lithium peroxide discharge product.
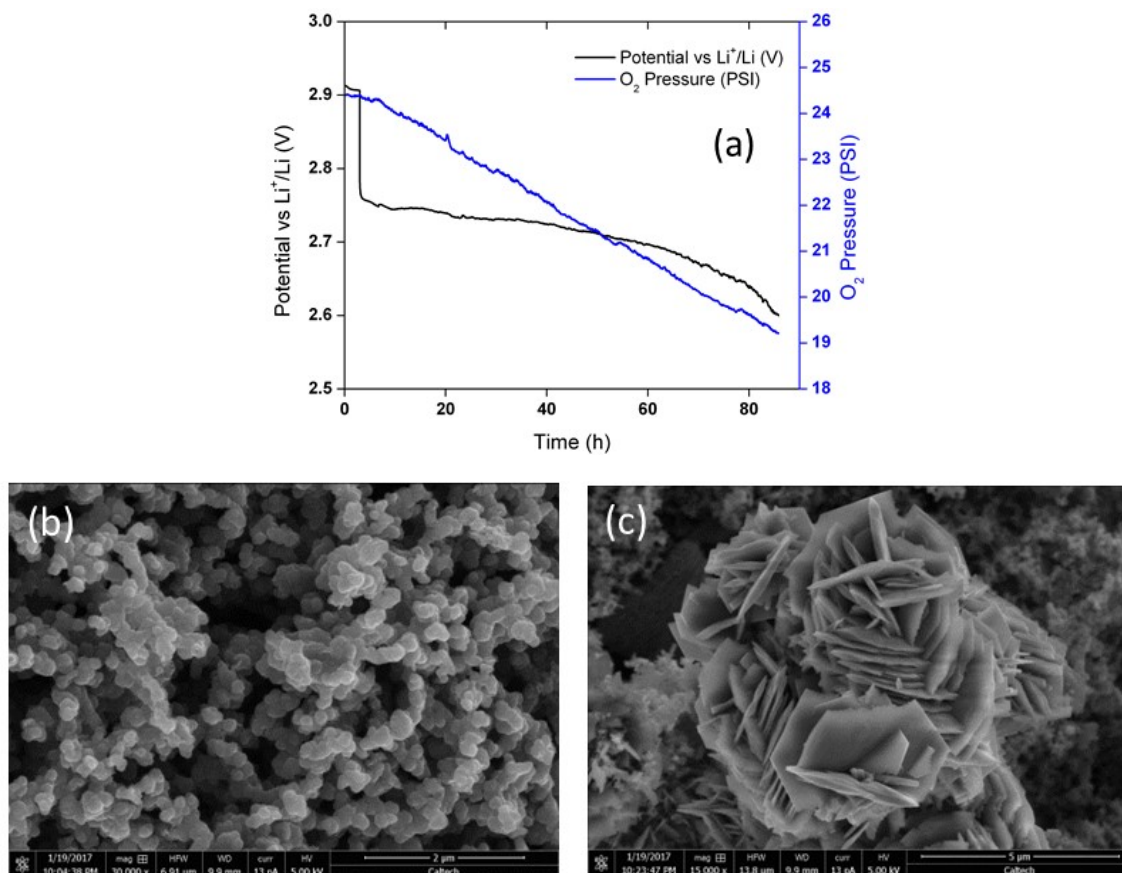
Figure II-608. a. Li/O2 cell discharge curve using a LLZO-protected Li anode and a molten nitrate catholyte (j= 0.05 mA/cm^2, 185°C, mcarbon= 5 mg/cm^2, mnitrate= 10 mg/cm^2). SEM analysis of Boron Carbide air electrode b. before and c. after discharge under O2 in LiNO$_3$-KNO$_3$ eutectic at 150°C.

In both the lithium-oxygen and nitrate reduction systems, the reaction product grows in the form of large crystals on the surface of the electrode catalyst. These large crystals pose an interesting design question with respect to accommodating this kind of discharge product. In order to study the interplay of pore size and surface area, we design structured lattice electrodes for nitrate reduction where we have direct control over both of these properties (Figure II-609a). Using this structured electrode, we can compare the electrochemical performance of a thin film electrode, a lattice electrode, and a nanoparticle electrode. While the surface area (and therefore reaction kinetics) of the nanoparticles far exceeds the thin film and lattice as evidenced by the CV scans (Figure II-609b), the discharge capacity does not (thin film: 1.7 mAh/m$^2_{geometric}$; lattice: 4.1 mAh/m$^2_{geometric}$; nanoparticle 5.1 mAh/m$^2_{geometric}$). In fact, the thin film and lattice electrode's discharge capacities differ by a factor equal to their difference in surface area. This however is not true of the nanoparticle electrode, demonstrating the importance of available pore volume to accommodate growth of the discharge product.
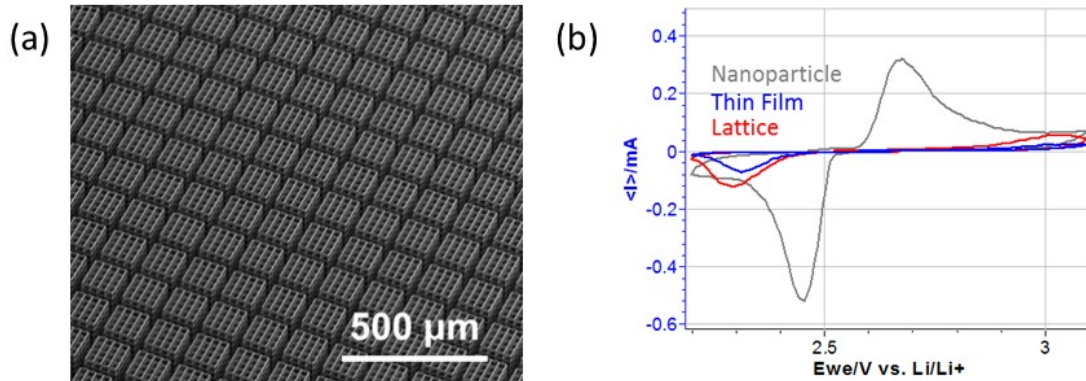
Figure II-609. a. SEM of a nickel coated structured electrode. b. CV at 150 °C and a scan rate of 0.01 mV/s for three nickel electrode morphologies performing nitrate reduction (electrolyte: LiNO$_3$-KNO$_3$ eutectic).

Demonstrate ≥10 cycles at ≥ 90% round-trip energy efficiency in laboratory-scale Li-air cells comprising a molten nitrate electrolyte and protected Li electrode

We investigated the cycling performance of 2-electrode lithium cells comprising a solid electrolyte and a molten salt electrolyte contained within the cathode. The molten salt electrolyte consisted of our binary alkali metal nitrate mixture and the solid electrolyte of a LLZO 1 cm^2 disc of about 300 microns. Cells were operated at 175°C to ensure good solid electrolyte performance and a molten state for our nitrate salts. The cathode chemistry consisted of either the lithium-oxygen chemistry to form Li$_2$O$_2$ as the discharge product, or the electrochemical reduction of nitrate anions to form Li$_2$O and nitrite species. Figure II-610 shows the 3rd discharge/charge cycle of protected lithium anode cells using an alkali metal nitrate molten salt catholyte. On the left, the cell uses a porous carbon cathode and is cycled under O$_2$ gas. A typical ~2.7 V discharge plateau is observed, consistent with oxygen reduction reaction and the formation of solid lithium peroxide within the cathode porous structure (Super P carbon). Relatively high discharge capacity in Li/O$_2$ cell (1360 mAh/g of carbon, ~6.5 mAh/cm^2) was achieved. However the high temperature seemed to accelerate carbon decomposition in O$_2$ cell leading to poor reversibility and cyclability. XRD analysis post mortem revealed large quantities of Li$_2$CO$_3$ deposited on the cathode surface. On the right plot, the cell uses a porous nickel cathode and is cycled under argon gas. The typical 2.5 V discharge plateau corresponds to electrochemical reduction of nitrate anion based on the following cathode reaction: $2Li^+ + 2e^- + NO_3^- \rightarrow Li_2O + NO_2^-$. Lithium oxide fills up the cathode porous structure while nitrite anion dissolves in the melt. We observed a 45% active material utilization (nitrate anion reduction) with high reversibility, however the high discharge capacity was maintained for only a few cycles.
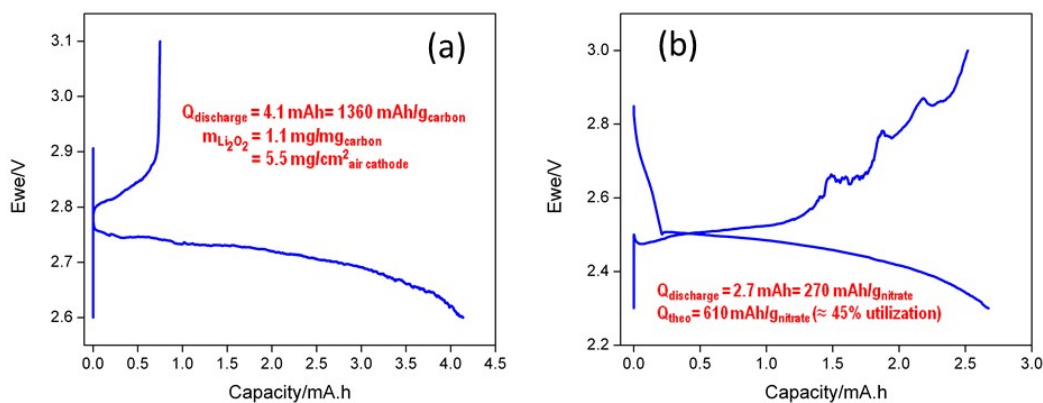

Figure II-610. a. Li/O2 cell voltage profile at 175°C using Super P Carbon:PTFE (95:5 wt.%) cathode at 0.05 mA/cm^2 current density (mcarbon= 3 mg, mnitrate= 6.5 mg). b. Molten nitrate Li cell voltage profile at 175°C using nanoporous nickel cathode (Ni:LiNO$_3$-KNO$_3$ eutectic 50:50 wt.%) at 0.05 mA/cm^2 current density (mNi= mnitrate= 10 mg).

Fabricate and test 4 and 10 mAh cells

We fabricated and tested full Li/nitrate and Li/O$_2$ cells utilizing a solid electrolyte between the negative and the positive electrode, the latter being constituted of either amorphous carbon black (Li/O$_2$) or Ni nanoparticles (Li/nitrate), both cathode active materials intimately mixed with the alkali molten nitrate electrolyte. Cells were being tested at 150°C and at a current density of 0.2 mA/cm^2. The solid electrolyte consisted of a LLZO 1 cm^2 disc of about 200 microns. The discharge capacity was limited to 4 mAh.
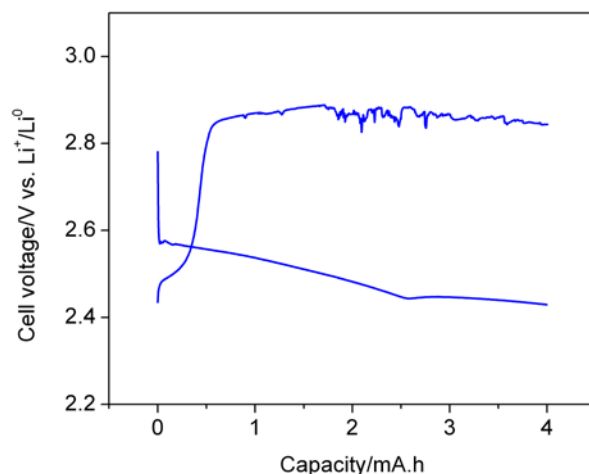

Figure II-611. Molten nitrate Lithium cell voltage profile (3rd cycle) at 150°C using nanoporous nickel/nitrate catholyte and LLZO-protected Li metal anode (Ni to LiNO$_3$-KNO$_3$ eutectic 1:1 wt.%, 0.2 mA/cm^2, mNi= mnitrate= 10 mg/cm^2).

Figure II-611 shows the first three discharge/charge cycles of a protected lithium anode cell using an alkali metal nitrate molten salt catholyte. The cell uses a porous nickel cathode (~10 mg/cm^2 Ni loading) and is cycled under argon gas. The typical ~2.6 V discharge plateau corresponds to electrochemical reduction of nitrate anion, based on the following reaction: $2Li^+ + 2e^- + NO_3^- \rightarrow Li_2O + NO_2^-$. Lithium oxide fills up the cathode porous structure while nitrite anion dissolves in the melt.

Conclusions

As alternative to unstable carbon-based O$_2$ cathode, we screened electrode materials with improved chemical stability in molten nitrate Li-air cells at 150°C. IrO$_2$ and B$_4$C exhibited promising electrochemical performance. However, OER/ORR molar ratios (amount of oxygen formed during charge vs. amount of oxygen consumed during discharge of the electrochemical cell) lower than 1 prevailed. Such behavior is consistent with solution-phase mechanism for lithium peroxide discharge product formation and hence causing electrical loss during cycling. Furthermore, we have shown the positive effect of Cs$^+$ additive (e.g., CsNO$_3$ salt) on both lowering molten salt electrolyte melting point (~100°C) and enhancing Li metal anode cyclability. We studied garnet-type solid electrolytes such as LLZO and demonstrated good cycling behavior in symmetric Li/Li cells. These garnets were tested in Li metal cells using molten nitrate as the catholyte. Chemical tests coupled to XRD showed good stability for LLZO when in contact with molten nitrate salts. More fundamental work went into designing nano-structured electrode to better accommodate lithium oxygen discharge products (e.g., Li$_2$O, Li$_2$O$_2$). We confirmed novel rechargeable oxyanion redox cathode chemistry, based on reversible nitrate anion reduction on high surface area porous nickel electrodes. Future work includes a) improving Li stripping/plating rate capabilities using a solid electrolyte at 100-150°C, b) increasing practical capacity (areal, gravimetric, volumetric) including active and inactive components for both O$_2$ and oxyanion redox cells, c) engineering efficient elevated temperature thermal management and system designs for EV applications.

Key Publications

Publications

1. Burke et al., ACS Energy Letters, 2016, 1(4), 747-75

2. Knudsen et al., J. Electrochem. Soc., 2016, 163(9), A2065-71

3. High Capacity, Rechargeable Lithium Battery Using Oxyanion Conversion Reaction Cathode. D Addison, H Tan, D Tozier, J Uddin, J Greer, G Chase, V Giordani (In preparation)

Patents

1. Intermediate temperature alkali metal/oxygen batteries employing molten nitrate electrolytes. J Uddin, D Addison, V Giordani, US Patent 2016/0049707 (2016)

2. Rechargeable batteries employing catalyzed molten nitrate positive electrode. D Addison, V Bryantsev, G Chase, V Giordani, J Uddin, W Walker, US Patent 2016/0204418 (2016)

II.J.3 Lithium-Air Batteries (ANL)

Khalil Amine, Principal Investigator
Argonne National Laboratory
9700 S. Cass Avenue
Argonne, IL 60516
Phone: 630-252-3838
E-mail: amine@anl.gov

Larry Curtiss, Co-Principal Investigator
Argonne National Laboratory
9700 S. Cass Avenue
Argonne, IL 60516
Phone: 630-252-7380
E-mail: curtiss@anl.gov

Jun Lu, Co-Principal Investigator
Argonne National Laboratory
9700 S. Cass Avenue
Argonne, IL 60516
Phone: 630-252-7380
E-mail: junlu@anl.gov

Tien Duong, Technology Manager
U.S. Department of Energy
Phone: 202-586-7836
E-mail: Tien.Duong@ee.doe.gov

Start Date: October 1, 2014   End Date: September 30, 2019
Total Project Cost: $2,700,000   DOE share: $2,700,000   Non-DOE share: $0

Project Introduction

Lithium-air batteries can be considered the 'holy grail' of lithium batteries because they offer, in principle, at least ten times the energy density of conventional lithium-ion systems. While the inherent energy potential of lithium metal approaches that of gasoline, today's battery manufacturers have not yet been able to unlock this potential. While today's lithium-ion batteries may provide acceptable power for hybrid electric vehicles (HEVs) and all-electric vehicles (EVs), they do not as yet provide sufficient energy for an acceptable driving distance. A breakthrough in Li-air battery technology would significantly increase the possibility of extending the electric range of these vehicles with the added advantages of reducing battery cost and weight.

Li-air battery technology has many challenges and requires significant research efforts to meet these challenges and to unlock its full potential. The successful implementation of non-aqueous Li-air cells has been hampered because of severe materials problems that have limited electrochemical performance. These include (1) the non-aqueous electrolytes can be unstable under both the charge and discharge conditions, thereby seriously limiting cycle life; (2) during discharge, the solid and insoluble Li_2O_2 and/or other Li_2O products are deposited on the surface or within the pores of the carbon cathode, thereby passivating the surface as well as clogging the pores and restricting oxygen flow; (3) degradation of the lithium anode due to oxygen crossover destroys the integrity and functioning of the cell; and (4) commonly used transition metal cathode catalysts, do not access the full capacity of the oxygen electrode or enable sufficiently high rates.

The team led by Dr. Khalil Amine and Dr. Larry Curtiss at Argonne National Laboratory (ANL) is working on problems that limit the electrochemical performance of the Li-air battery, including the stability of the organic electrolytes, cathode catalysts, and stability of the lithium anode under oxygen-crossover conditions. This effort will lead to the development of a reversible lithium air battery that provides much higher energy density than state-of-the-art lithium ion battery for powering electric vehicles. The technology, if successful, can also benefit many military applications that require very high energy density such as satellite, military vehicles for silent watch and operation.

Objectives

The objective is to develop stable electrolytes and new cathode architectures for lithium air batteries to lower the charge overpotential, improve the cell efficiency, and increase cycle life. New electrolytes are needed to prevent gradual electrolyte decomposition that occurs in the presence of the reduced oxygen species, especially superoxide anion (O_2^-) from the discharge process. Discovery of such electroytes can increase cycle life. Commonly used carbons and cathode catalysts do not access the full capacity of the oxygen electrode and can cause significant charge overpotentials, which lowers efficiency and limits cycle life. Therefore, there is a need for improved catalysts and cathode materials. Understanding the oxygen crossover effect at the anode on the electrochemical performance of Li-air battery is important to understanding the lithium electrode degradation due to oxygen crossover and thus reduces the cycle life.

Approach

Issues that limit the performance of the Li-air battery include (1) electrolytes decomposition; (2) inefficient cathode materials; and (3) lithium electrode degradation. This project addresses the cycle life problem of Li-air batteries through experimental and theoretical investigation of (a) the discharge formation mechanism and relationship to electrolytes, (b) investigation of the morphology and composition of the discharge product, and (c) investigation of electrolyte decomposition mechanisms. This understanding is being used to (1) develop new cathode materials to promote formation of discharge morphologies such as those involving superoxides with better conductivity to decrease charge overpotentials, (2) cathode and electrolyte materials that donot degrade with cycling and (c) electrolyte modification to protect the lithium anode. The experimental work to create advanced electrolytes, carbons, catalysts, cathodes, and anodes is guided by theory and modeling. The experimental results will be thoroughly analyzed with very sophisticated analytical techniques and used to fine-tune the computational studies. Fundamental understanding of the underlying principles will be provided to greatly facilitate the next steps in the development cycle

Collaborators include Professor Kah Chun Lau (University of California-Norridge), Professor Amin Salehi (University of Illinois-Chicago), Professor Yang-Kook Sun (Hanyang University), Professor Yiying Wu (Ohio State University), Dr. Dengyun Zhai (China). We utilize several facilities at Argonne National Laboratory including the Advanced Photon Source, the Center for Nanoscale Materials, and the Argonne Leadership Computing Facility.

Results

Hollow graphene nanocages with Pt nanoparticles for Li-O_2 cathodes

Ultra-small Pt coated hollow graphene nanocages have been synthesized as cathodes for Li-O_2 batteries to find a catalyst that can lower charge overpotentials. They give a charge voltage plateau is 3.2 V at the current density of 100 mA/g and below 3.5 V when the current density is increased to 500 mA/g. The unique hollow graphene nanocages (HGN) matrix can not only provide numerous nano-scale tri-phase regions as active sites for efficient oxygen reduction, but also offer sufficient amount of meso-scale pores for rapid oxygen diffusion. Furthermore, with strong atomic-level oxygen absorption into its subsurface, ultra-small Pt particles can serve as the nucleation site for Li_2O_2 growth. The Li_2O_2 has a favorable morphology with small size and amorphous state, which can decompose more easily during recharge. Meanwhile, the conductive hollow graphene substrate can enhance the catalytic activity of noble metal Pt catalysts due to the graphene-metal interfacial interaction.

The synthetic strategy for HGNs involves the combustion of metal Mg with dry ice to produce cubic nanoparticles of MgO covered by few graphite carbon layers. The HGNs are obtained by removing the cubic MgO from inside of the graphene with dilute hydrochloric acid. Finally, the Pt nanoparticles were homogeneously deposited on the surface of the HGNs by PVD. The porous hollow nanocage architecture of HGNs, and the homogeneity of Pt catalysts were confirmed with transmission electron microscopy (TEM) at different magnifications.

The electrochemical performances of pristine and Pt-HGNs as the cathodes in a Li-O_2 cell were investigated under capacity-controlled conditions to minimize side reactions. With a nano-Pt catalyst, the Pt-HGNs electrode exhibited a stable discharge curve at approximately 2.75 V for cycles. It also showed a charge voltage below 3.2 V closing with a value of 2.96 V after initial three cycles, and steadily remained below 3.5 V for at least 10 cycles. Thus, with enhanced conductivity and unique porous structure, the Pt-HGNs exhibit a very low charge overpotential for a Li-O_2 battery using a Pt cathode catalyst.

Moreover, the poor rate performance of the typical aprotic Li-O_2 cell was found to be improved by using the Pt-HGNs cathode. The Pt-HGN cathode showed the discharge plateau staying above 2.6 V, and the charge mid-capacity potential below 3.5 V, even when operated at high current density ~500 mA/g. The excellent electrochemical performance may be attributed to the improved oxygen evolution reaction (OER) kinetics facilitating efficient decomposition of Li_2O_2.

Air cathode based on a novel triple phase structure

In the Li-O_2 battery the oxygen gas and electrolyte often compete for pathways in the conventional cathode based on a porous carbon cathode, which limits the performance of the battery. In this work, we have used a novel air cathode based on a novel triple phase structure by using a common textile. The hierarchical networked structure of the textile leads to decoupled pathways for electrolyte and oxygen gas, which facilitate the transport of both components, significantly improving battery performance. The oxygen flows through the woven mesh constructed by the textile fibers while the electrolyte diffuses along the textile fibers. Due to the facilitated transport, the Li-O_2 battery based on this textile-based cathode shows a high discharge capacity of 8.6 mAh/cm^2, low overpotential of 1.2 V, and stable operation of over 50 cycles. The decoupled transport pathway design has the potential for a flexible Li-O_2 battery design.

The concept of the breathable cathode is based on that of a textile, i.e., the surface is densely coated layer of carbon nanotubes (CNT). The hierarchical structure of the textile forms the channel for the flow of electrolyte while the textile material naturally has a good affinity with liquid electrolyte. Therefore, the electrolyte flows underneath the active sites on the CNT layer where the reaction happens. The mesh holes on the textile provides sufficient space for the oxygen to flow through, since it has been shown that the gas flow channel should have big enough size to facilitate oxygen reduction during discharge. Thus, the liquid electrolyte and the oxygen gas flow on the different sides of the active CNT layer without competing for space. The decoupled pathways for electrolyte and oxygen gas are crucial for the performance of the Li-O_2 battery. All the active sites on the CNT layer always have sufficient electrolyte and oxygen input during the discharge and can be fully utilized. The CNTs are decorated with palladium nanoparticles with size of ~10 nm as the catalyst. Similar to the active CNT layer, the Pd catalysts in this case are fully exposed to the electrolyte and the oxygen gas.

The rechargeability of Li-air battery with the textile-based cathode is very good as seen in Figure II-612. The battery was cycled with a current density of 0.1 mA/cm^2 and a charge/discharge capacity limit of 1 mAh/cm^2. Almost no performance drop was observed even after 50 cycles. The rechargeability of the battery was also studied via the characterization of discharge product. The XRD results indicate the formation of Li_2O_2. Moreover, Raman spectroscopy and XPS were employed to analyze the discharge product. In the Raman spectrum a distinct peak at 800 cm^{-1} was observed, which corresponds to amorphous Li_2O_2. In O 1s XPS spectrum after discharge, a peak at 528 eV was detected, which is the characteristic peak of Li_2O_2. Both results indicate that the discharge product is Li_2O_2.
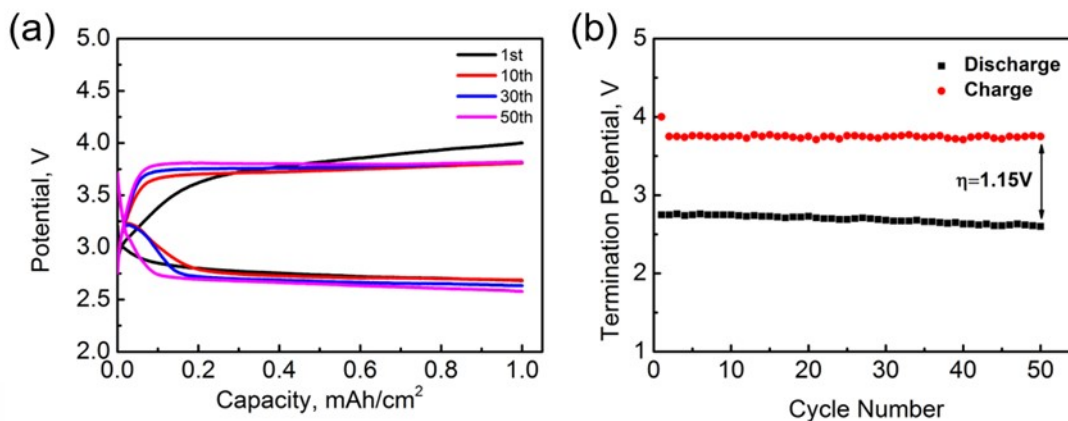
Figure II-612. (a) Discharge/charge profile of a Li-O$_2$ cell using the "textile" concept for 50 cycles. (b) The termination voltage of charge/discharge for 50 cycles.

Titration methods for a Li-O$_2$ battery

Fundamental understanding of reactions of lithium peroxides and superoxides is essential for the development of Li-O$_2$ batteries. We carried out an investigation of the hydrolysis of lithium superoxide as produced in a Li-O$_2$ cell under some conditions. Unlike KO$_2$ and NaO$_2$, the hydrolysis of LiO$_2$ does not produce H$_2$O$_2$. Similarly, the reactivity of Li$_2$O$_2$ toward water differs from LiO$_2$, in that Li$_2$O$_2$ results in H$_2$O$_2$ as a product. Based on this a titration method that depends on the reaction of a Li-O$_2$ discharge product with a Ti(IV)OSO$_4$ solution, has been developed that provides a useful diagnostic technique to provide information on the composition of a discharge product in a Li-O$_2$ battery

Initially, a Li-O$_2$ cell with an Ir-rGO (reduced graphene oxide) cathode was used to produce a LiO$_2$ discharge product. The reaction of the LiO$_2$ discharge product with water was investigated using a spectrophotometric method to assess the amount of hydrogen peroxide produced. In this procedure we first establish a calibration curve by adding incremental amounts of Li$_2$O$_2$ to the test reagent Ti(IV)OSO$_4$. The discharge product LiO$_2$ on the Ir-rGO cathode is then reacted with the acidic solution of Ti(IV)OSO$_4$ after removal of the electrolyte, but with the cathode material still present. Under the experimental conditions, Ti(IV) exists as TiO$_2^+$(aq) complexed with SO$_4^{2-}$ ion in 1.0 M H$_2$SO$_4$. If hydrogen peroxide is present, a color change to yellow/orange occurs due to the formation of a titanium peroxide complex, TiO$_2$SO$_4$. When the acidic solution of Ti(IV)OSO$_4$ was added to the LiO$_2$ discharge product the liquid remained colorless as shown in Figure II-613 and no notable UV-Vis intensity change was observed. From the UV-Vis spectra, the absorbance intensity is essentially negligible based on a calibration curve, which indicates the absence of hydrogen peroxide. The LiO$_2$ results are in contrast to the case for KO$_2$ and NaO$_2$ where an obvious color change is observed for this procedure, consistent with the presence of a hydrogen peroxide product. It is also in contrast to the case of of a known discharge product of Li$_2$O$_2$ where the same titration test tested positive (i.e., color change) for the presence of H$_2$O$_2$.

We have extended this method to assess the amount of LiO$_2$ present to make it a more powerful tool to provide quantitative information on the amounts of both LiO$_2$ and Li$_2$O$_2$ present in the discharge product. The two titration techniques are based on the hydrolysis reactions of LiO$_2$ and Li$_2$O$_2$ given by reactions 1 and 2, respectively.

$$4LiO_2 + 2H_2O \rightarrow 3O_2 + 4LiOH \qquad \text{(Reaction 1)}$$

$$Li_2O_2 + 2H_2O \rightarrow 2LiOH + H_2O_2 \qquad \text{(Reaction 2)}$$
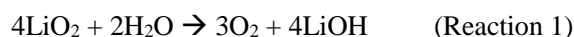
Thus, the hydrolysis of LiO$_2$ derived doesnot result in H$_2$O$_2$ as a product that is detected for hydrolysis of Li$_2$O$_2$ as well as KO$_2$ and NaO$_2$.

Figure II-613. Photograph of cathode discharged to 1000 mAh/g, dried under Ar for 1 hr, and then soaked in 3 mL of TiOSO$_4$(aq). No apparent color change occurred upon titration indicating no Li$_2$O$_2$ is present

In order to develop a titration technique to directly determine the amount of the LiO$_2$ discharge product, we have tested for the expected LiOH product from Reaction 1, which is the reaction of water with LiO$_2$. This was done by pH measurement of a solution after addition of a known quantity of H$_2$O to a cathode after one discharge cycle in a Li-O$_2$ cell with an Ir-rGO cathode under the same conditions as described for the titration based on Ti(IV)OSO$_4$ solution described above. The resulting solution was strongly basic with a pH of 11.84, consistent with the presence of OH- anion from LiOH. In addition, by analysis of the current used and the discharge time it is possible to determine quantitatively the amount of OH- anion produced. In the case of the discharge product from the Ir-rGO electrode this is 95% of that expected based on Reaction 1. Thus, this new titration method confirms that LiO$_2$ is present in the discharge product, consistent with other characterization techniques such as DEMs and Raman. It also provides a new technique for assessing Li-O$_2$ product composition.

Conclusions

During the past year we have shown that platinum-coated hollow graphene nanocages can be used as cathodes in Li-O$_2$ batteries and give low charge overpotentials. A novel air cathode based on a novel triple phase structure by using a common textile was employed in a Li-O$_2$ cell. The hierarchical networked structure of the textile leads to decoupled pathways for electrolyte and oxygen gas, which facilitate the transport of both components, significantly improving battery performance. Finally, two titration methods were developed to test for LiO$_2$ and Li$_2$O$_2$, which will help in characterization of the composition of discharge products in Li-O$_2$ batteries.

Key Publications

1. "Concentrated Electrolyte for the Sodium–Oxygen Battery: Solvation Structure and Improved Cycle Life," M He, K. C. Lau, X Ren, N Xiao, W. D. McCulloch, L. A. Curtiss, Y Wu, Angewandte Chemie **128** (49), 15536-15540 (2016).

2. "Lithium Superoxide Hydrolysis and Relevance to Li-O$_2$ Batteries," H. Wang, Y. Lee, R. S. Assary, C. Zhang, X. Luo, P. C. Redfern, J. Lu, Y. Lee, D. Kim, T. Kang, E. Indacochea, K. Lau, K. Amine, and L. A Curtiss J. Phys. Chem. C, **121**, 9657-9661 (2016) DOI: 10.1021/acs.jpcc.6b12950

3. "Platinum-Coated Hollow Graphene Nanocages as Cathode Used in Lithium-Oxygen Batteries," F. Wu, Y. Xing, X. Zeng, Y. Yuan, X. Zhang, R. Shahbazian-Yassar, J. Wen, D. J. Miller, L. Li, R. Chen, J. Lu, J. and K. Amine, Adv. Funct. Mater., **26**: 7626–7633 (2016) doi:10.1002/adfm.201602246

4. Patent: "Lithium-oxygen batteries incorporating lithium superoxide," Jun Lu, Khalil Amine, Larry A Curtiss, Kah Chun Lau, Yang-Kook Sun, Yun Jung Lee, Xiangyi Luo, 2017/1/24, US Patent Office, Patent number 9553316

II.K   Beyond Li-ion R&D: Sodium-Ion Batteries

II.K.1   Exploratory Studies of Novel Sodium-Ion Battery Systems (BNL)

Xiao-Qing Yang, Principal Investigator
Chemistry Division
Brookhaven National Laboratory
Bldg. 555, Brookhaven National Lab.
Upton, NY 11973
Phone: 631-344-3663
E-mail: xyang@bnl.gov

Seongmin Bak, Co-Principal Investigator
Chemistry Division
Brookhaven National Laboratory
Bldg. 555, Brookhaven National Lab.
Upton, NY 11973
Phone: 631-344-4142
E-mail: xyang@bnl.gov

Tien Duong, Technology Manager
U.S. Department of Energy
Phone: 202-586-7836
E-mail: Tien.Duong@ee.doe.gov

Project Introduction

In order to meet the challenges of powering PHEVs, the next generation of rechargeable battery systems with higher energy and power density, lower cost, better safety characteristics, and longer calendar and cycle life beyond lithium-ion batteries, which is today's state-of-the-art technology, need to be developed. Recently, Na-ion battery systems have attracted more and more attention due to the more abundant and less expensive nature of Na resources. However, building a sodium battery requires redesigning battery technology to accommodate the chemical reactivity and larger size of sodium atoms. Since Na-ion battery research is an emerging technology, new materials to enable Na electrochemistry and the discovery of new redox couples and the related diagnostic studies of these new materials and redox couples are quite important. In sodium electrochemical systems, the greatest technical hurdles to overcome are the lack of high-performance electrode and electrolyte materials which are easy to synthesize, safe, non-toxic, with long calendar and cycling life and low cost. Furthermore, fundamental scientific questions need to be further elucidated, including (1) the difference in transport and kinetic behaviors between Na and Li ions in analogous electrodes; (2) Na insertion/extraction mechanism; (3) solid electrolyte interphase (SEI) layer on the electrodes from different electrolyte systems; and (4) charge transfer in the electrolyte–electrode interface and Na+ ion transport through the SEI layer. This project will use the synchrotron-based in situ x-ray diagnostic tools developed at BNL to evaluate the new materials and redox couples, to explore in fundamental understanding of the mechanisms governing the performance of these materials and provide guidance for new material developments. This project will also focus on developing advanced diagnostic characterization techniques to investigate these issues, providing solutions and guidance to solve the problems. The synchrotron-based in situ X-ray techniques (x-ray diffraction and hard and soft x-ray absorption) will be combined with other imaging and spectroscopic tools such as high resolution transmission electron microscopy (HRTEM), mass spectroscopy (MS), as well transmission x-ray microscopy (TXM). In FY2017, this BNL team has built a good

working relationship with several beamlines at the newly built National Synchrotron Light Source II (NSLSII) with assigned beamtime at hard x-ray nanoprobe (HXN) beamline, x-ray Powder diffraction (XPD). By collaborating with Dr. Dong Su and Dr Huoling Xin, this team also has sufficient time using the HRTEM. The BNL team has been closely working with top scientists on new material synthesis at ANL, LBNL, SLAC, and PNNL, with U.S. industrial collaborators at General Motors and Johnson Controls, and international collaborators in Japan and South Korea. In FY2017, results through these collaborations were published on high impact journals such as JACS and Advanced Energy Materials.

Objectives

The primary objective of this proposed project is to develop new advanced in situ material characterization techniques and apply these techniques to explore the potentials, challenges, and feasibility of new rechargeable battery systems beyond the lithium-ion batteries (LIBs), namely the sodium-ion battery systems for plug-in hybrid electric vehicles (PHEV). In order to meet the challenges of powering PHEVs, new rechargeable battery systems with high energy and power density, low cost, good abuse tolerance, and long calendar and cycle life need to be developed. This project will use the synchrotron-based in situ x-ray diagnostic tools, combined with HRTEM, STEM, and TXM imaging techniques developed at BNL to evaluate the new materials and redox couples to enable a fundamental understanding of the mechanisms governing the performance of these materials and provide guidance for new material and new technology development regarding Na-ion battery systems.

Approach

- A combination of time resolved X-ray diffraction (TR-XRD) and mass spectroscopy (MS), together with in situ soft and hard X-ray absorption (XAS) during heating and transmission electron microscopy (TEM) to study the thermal stability of the Na battery electrode materials.

- Synchrotron-based X-ray diffraction (XRD), X-ray absorption spectroscopy (XAS), to elucidate and differentiate the contribution from each component and element to the capacity and structural changes of various cathode and anode materials for Na-ion batteries.

- Extended collaboration with other US and international academic institutions and US industrial partners.

Results

1. Using synchrotron-based XRD to study a new cathode material for sodium-ion batteries: the V2C material, as a new member of the two-dimensional transition metal carbides, so-called MXenes.

In FY2017, this project carried out the studies of a new cathode material for sodium-ion batteries. A V_2C material, as a new member of the two-dimensional transition metal carbides, so-called MXenes, was synthesized in a way containing surface functional groups (denoted as V_2CT_x, where T_x are surface functional groups) and studied as anode materials for Na-ion batteries. V_2CT_x anode exhibits reversible charge storage with good cycling stability and high rate capability through electrochemical test. The charge storage mechanism of V_2CT_x material during Na^+ intercalation/deintercalation and the redox reaction of vanadium were studied using a combination of synchrotron-based X-ray diffraction (XRD) and hard X-ray absorption near edge spectroscopy (XANES). Figure II-614a presents *ex situ* XRD patterns at the 2θ angle range corresponding the (002) reflection of V_2CT_x at several charge/discharge (i.e., sodiation/desodiation) states during first cycle (the charge-discharge curve is also plotted on the right panel of Figure II-614a). During the first sodiation process, the (002) diffraction peak in the XRD pattern moved from 9.3 ° to 8.1 ° from the OCV state to the 0.1 V state, corresponding an expansion of the interlayer distance from 9.53 Å to 10.93 Å. As illustrated in Figure II-614b, beside the Na^+ absorption at the surface of V_2CT_x, resulted in the capacitor-like capacity, additional energy storage also occurred through Na^+ intercalation between layers of V_2CT_x. This behavior is similar to those of previous reports on Ti_2CT_x and V_2CT_x MXene materials. However, during subsequent desodiation (or deintercalation) process, the contraction of interlayer distance (~ 1.03 Å) is much smaller than the 1.40 Å expansion during first sodiation.
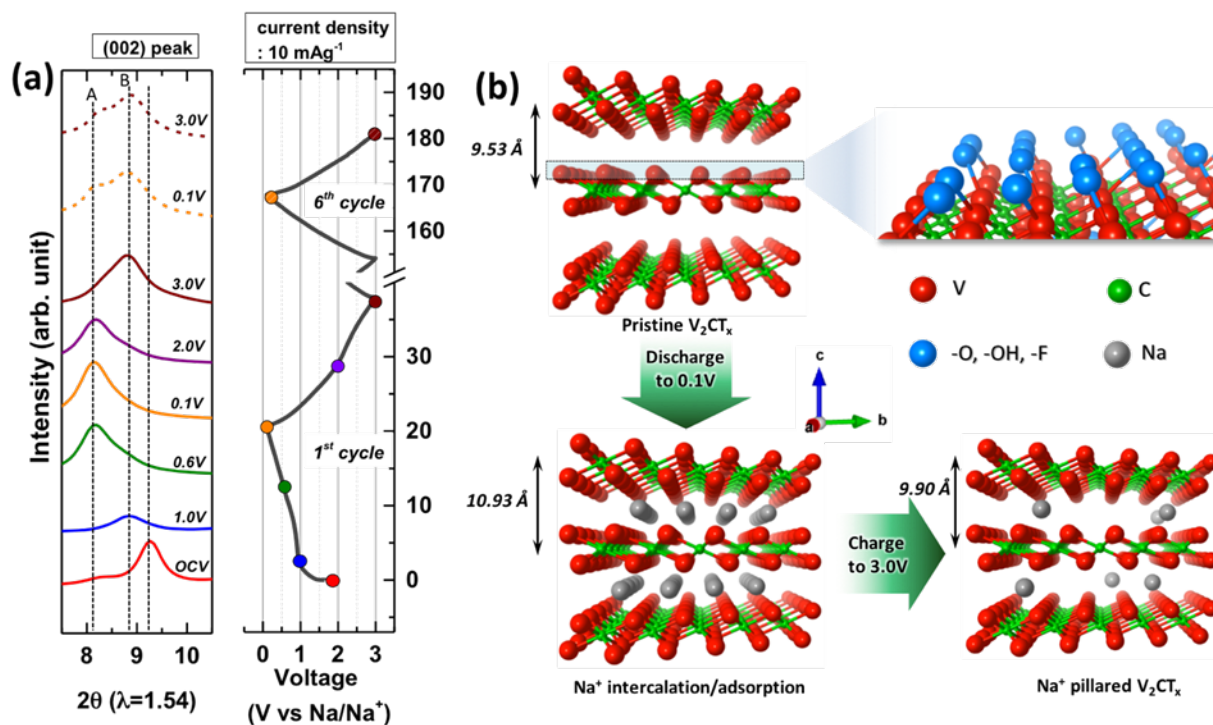
Figure II-614. (a) *Ex situ* XRD patterns (left) for V_2CT_x upon electrochemical sodiation/desodiation cycling (right), and (b) schematic illustration of the expansion/contraction behavior of V_2CT_x during sodiation/desodiation process: the interlayer distance of V_2CT_x is increased upon Na^+ intercalation during sodiation process, then partially reduced upon Na^+ deintercalation due to the trapped Na^+ between V_2CT_x layers behaves as a pillar during desodiation process.

2. Using synchrotron-based ex situ hard x-ray absorption at vanadium K-edge to study the MXene material V₂C as new anode material for sodium ion batteries during charge-discharge cycling

In FY2017 this project also carried out the *ex situ* hard x-ray absorption studies at vanadium K-edge of MXene material V_2C as new anode material for sodium ion batteries during charge-discharge cycling. The *ex situ* V *K*-edge XANES spectra presented in Figure II-615a were measured on samples harvested from cells discharged and charged to different voltages during the first cycle (OCV→0.1V→3V), as shown on the charge/discharge curve in Figure II-615b. The V *K*-edge XANES spectra presented in Figure II-615a show a relatively weak pre-edge peak (marked as A) at 5470 eV and a strong main absorption peak (marked as B) at around 5485 eV. The pre-edge absorption is associated with the transition to hybridized electronic states of the metal $3d$ and carbon $2p$ orbitals. The pre-edge peak of V_2CT_x spectra can be assigned to the transition of a $1s$ electron to the hybridized t_{2g} (V $3d$ + C $2p$) and e_g (V $3d$ + C $2p$) orbitals. And the main absorption peak "B" involves the dipole allowed transition of $1s$ electrons to unoccupied V $4p$ states. The spectra for V_2CT_x at different discharge/charge states do not show significant differences in shapes, but the edge shift is clearly observable during both discharge and charge process (inset in Figure II-615a). A plot of the V *K*-edge energies, at half height of normalized XANES spectra, as a function of sodiation/desodiation state in Figure II-615c clearly show the consistent energy position changes from one voltage step to the next. During first sodiation process from OCV to 0.1 V, the edge shifts to lower energy, which reflects the reduction of vanadium. During desodiation process from 0.1 V to 3 V, the edge shifts back to the higher energy indicating the oxidation of vanadium.
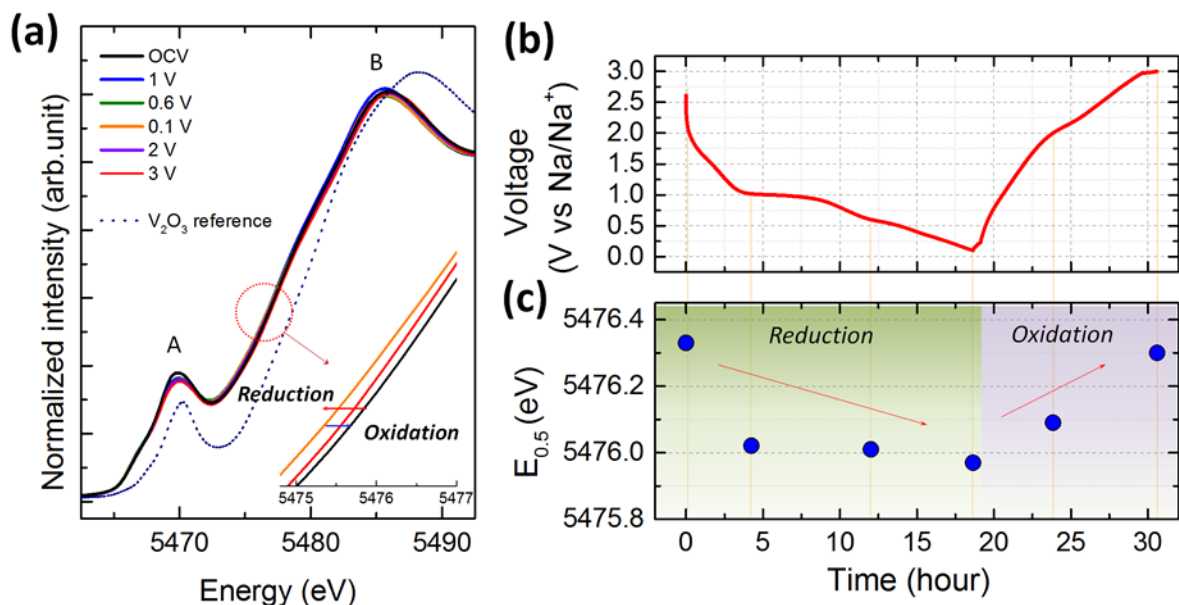
Figure II-615. (a) *Ex situ* V *K*-edge XANES spectra of V$_2$CT$_x$ at selected cell voltages during first sodiation/desodiation process (OCV→0.1V→3V), (b) corresponding voltage profile, and (c) variation of V edge energy (at half height of normalized XANES spectra) at selected cell voltage.

3. Using synchrotron-based ex situ soft x-ray absorption at vanadium L-edges to study the MXene material V$_2$C during charge-discharge cycling

In FY2017, using *ex situ* soft x-ray absorption at vanadium L-edges to study the MXene material V$_2$C during charge-discharge cycling has been carried out. Figure II-616 shows the V $L_{2,3}$-edge sXAS spectra collected from five V$_2$CT$_x$ electrodes cycled to different voltages using both (a) bulk sensitive TFY and (b) surface-sensitive TEY. The overall sXAS spectra can be divided into two regions, the L_3-edge at the energy range of 510-520 eV and the L_2-edge at 520-530 eV. It is apparent that L_3-edge in TFY spectra display dramatic voltage-dependent changes, which are related to the vanadium redox reactions in the bulk V$_2$CT$_x$. The 516.7 eV peak intensity decreases from 1 V to 0.1 V and increases from 0.1 V to 3 V, while the lower energy peak at 513 eV shows just the opposite trend. The two sXAS features are related to the two different oxidation states of V, i.e., the high energy peak at 516.7 eV represents a higher oxidation state and its intensity increases when the average oxidation state of vanadium increases. Therefore, the changes in sXAS intensity and line shape changes clearly demonstrate the reduction of the V ions during the initial discharge from 1.0 V down to 0.1 V. Unlike in the V K-edge spectra, where the reduction of average oxidation of vanadium was indicated by the edge shift to lower energy, for the L_3 edge spectra, such reduction is indicated by the reduction of intensity ratio of 516.7 eV/513 eV peaks, which can be clearly observed by the significant enhancement of the 513 eV peak intensity at 0.1 V (sodiated). Due to the sensitivity of the transition-metal *L*-edge sXAS to the valence 3*d*, the data in Figure II-616 also show clearly that the V *L*-edge line shape does not fully recover when the V$_2$CT$_x$ electrode is charged back to 3 V from its discharged state (0.1 V). This indicates that the V redox is not fully reversible in the initial cycle, which is consistent with the low Coulombic efficiency obtained by electrochemical test. Another observation is that the surface-sensitive TEY spectra (Figure II-616b) show much weaker change, compared with that of the bulk probing TFY (Figure II-616a), indicating less changes in vanadium oxidation states at the surface of V$_2$CT$_x$ electrode during cycling. Combining these results with those of XRD and V *K*-edge XANES, it can be concluded that the redox reaction of vanadium mainly takes place in the bulk of V$_2$CT$_x$ during Na$^+$ intercalation/deintercalation rather than at the surface.
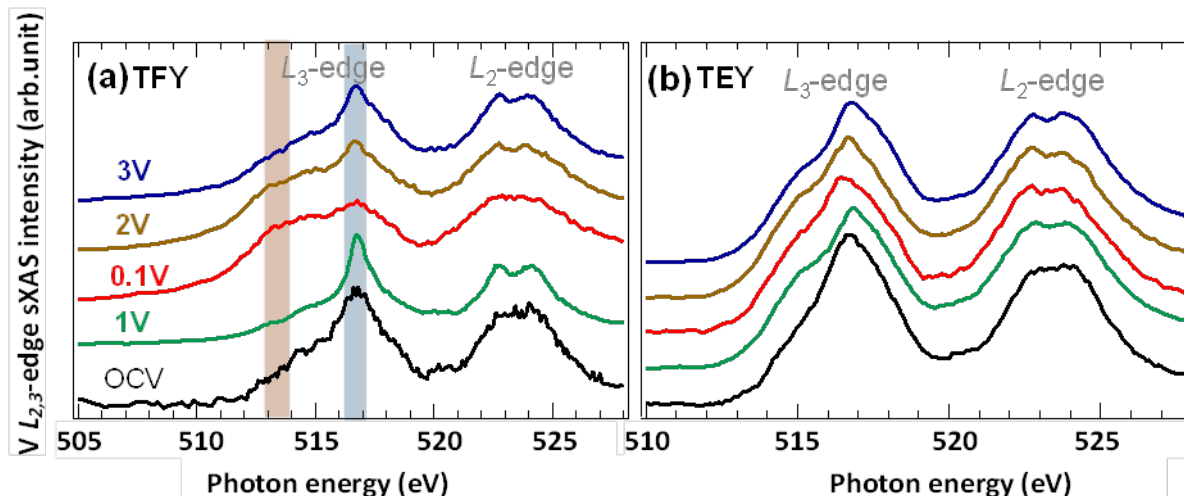
Figure II-616. V $L_{2,3}$-edge sXAS spectra collected on electrodes that are cycled to different voltages. (a) Bulk-sensitive total fluorescence yield (TFY), and (b) surface-sensitive total electron yield (TEY).

4. Using synchrotron-based in-situ X-ray absorption near-edge spectroscopy to study β-NaCu₀.₂Mn₀.₈O₂

In FY2017, the studies of a new cathode material, Cu-doped β-NaMnO$_2$ layered material for sodium-ion batteries have been completed. The *in-situ* X-ray absorption near-edge spectroscopy for β-NaCu$_{0.2}$Mn$_{0.8}$O$_2$ have been performed to explore the charge transfer mechanism. As shown in Figure II-617, the normalized in-situ XAS data indicates that Cu exist as Cu^{+2} and Mn have a oxidization state that is between Mn^{+3} and Mn^{+4}. The Mn K-edge spectra shift to higher energy region upon charged to 4.0 V, which nearly overlap with the K-edge of MnO$_2$ suggesting that Mn^{+3} ions are oxidized to Mn^{+4} state. For Cu, however, the shift is much less significant, which indicate that Cu is not the major contributor for the charge compensation mechanism. Nevertheless, both Mn and Cu XAS spectra feature pronounced shoulder peaks upon charge. This peak is probably due to the ligand-to-metal charge transfer process, which implies a strong covalency between M (Cu or Mn) and O upon the charging process.
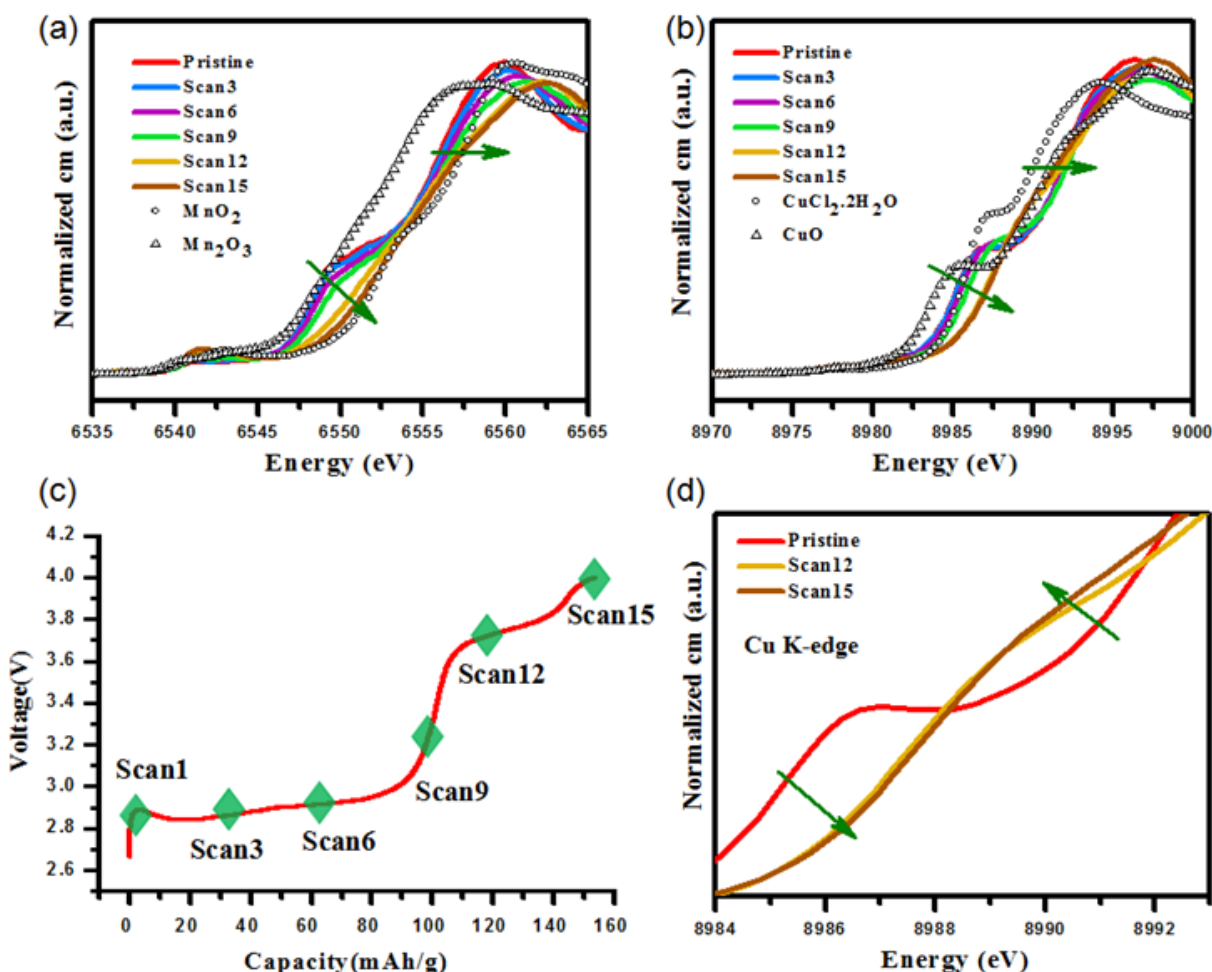
Figure II-617. Charge compensation mechanism upon Na deintercalation/intercalation in β-NaCu$_{0.2}$Mn$_{0.8}$O$_2$. (a) in-situ XAS spectra at Mn K-edge collected at different charge/discharge states; (b) in-situ XAS spectra at Cu K-edge collected at different charge/discharge states (c) The load curve of β-NaCu$_{0.2}$Mn$_{0.8}$O$_2$ during the first charge process for in-situ XAS. (d) The enlarged XAS spectra at Cu K-edge.

Conclusions

V$_2$CT$_x$ MXene shows reversible electrochemical charge storage with good cycling stability and high rate capability which are important characteristics for the high power battery and Na-ion capacitor applications. The charge storage mechanisms were studied using a combination of ex/in situ synchrotron-based XRD, XANES and sXAS. The XRD results confirm that the expansion/contraction of the interlayer space of V$_2$CT$_x$ upon Na$^+$ intercalation/deintercalation during first cycle. V K-edge XANES results clearly show the redox reaction of vanadium during the Na$^+$ intercalation/deintercalation, which implies that the redox reaction at the transition metal (M) site in MXene is responsible for the electrochemical charge storage. The results of V $L_{2,3}$-edge sXAS experiments provided further direct evidence of such a redox reaction of vanadium within the MXene. In addition, C and O K-edge sXAS results shows potentially important features related to the reversible formation/decomposition of CO$_3^{2-}$ species upon sodiation/desodiation. This surface related reaction is still not fully understood, but may provide valuable information for further understanding of V$_2$CT$_x$ electrodes as well as CO$_3^{2-}$ related redox systems. For β-NaCu$_{0.2}$Mn$_{0.8}$O$_2$ XAS results show that Cu exist as Cu^{+2} and Mn have a oxidization state that is between Mn^{+3} and Mn^{+4} and Mn^{+3} ions are oxidized to Mn^{+4} state. while Cu is not the major contributor for the charge compensation mechanism.

Key Publications

1. Zhizhen Zhang, Qinghua Zhang, Jinan Shi, Yong S. Chu, Xiqian Yu, Kaiqi Xu, Mingyuan Ge, Hanfei Yan, Wenjun Li, Lin Gu*, Yong-Sheng Hu*, Hong Li, Xiao-Qing Yang, Liquan Chen, Xuejie Huang, "A self-forming composite electrolyte for solid-state sodium battery with ultra-long cycle life" *Adv. Energy Mater.*, (October, 2016), DOI: 10.1002/aenm.201601196.

2. Ming-Hui Cao, Yong Wang, Zulipiya Shadike, Ji-Li Yue, Enyuan Hu, Seong-Min Bak, Yong-Ning Zhou*, Xiao-Qing Yang* and Zheng-Wen Fu* "Suppressing the chromium disproportionation reaction in O3-type layered cathode materials for high capacity sodium-ion batteries", *J. Mater. Chem. A*, 2017, 5, 5442-5448, DOI: 10.1039/C6TA10818K

3. Hu-Rong Yao, Peng-Fei Wang, Yue Gong, Jienan Zhang, Xiqian Yu, Lin Gu, Chuying OuYang, Ya-Xia Yin, Enyuan Hu, Xiao-Qing Yang, Eli Stavitski, Yu-Guo Guo*, and Li-Jun Wan, "Designing Air-Stable O3-Type Cathode Materials by Combined Structure Modulation for Na-Ion Batteries", *J. Am. Chem. Soc.*, 2017, 139 (25), pp 8440–8443, DOI: 10.1021/jacs.7b05176, Publication Date (Web): June 9, 2017

4. Qin-Chao Wang, Enyuan Hu, Yang Pan, Na Xiao,Fan Hong, Zheng-Wen Fu, Xiao-Jing Wu, Seong-Min Bak, Xiao-Qing Yang, and Yong-Ning Zhou, "Utilizing Co2+/Co3+ Redox Couple in P2-Layered Na0.66Co0.22Mn0.44Ti0.34O2 Cathode for Sodium-Ion Batteries", *Advanced Science*, publication date: July 6, 2017, DOI: 10.1002/advs.201700219

5. Zulipiya Shadike, Yong-Ning Zhou, Lan-Li Chen, Qu Wu, Ji-Li Yue, Nian Zhang, Xiao-Qing Yang, Lin Gu, Xiao-Song Liu, Si-Qi Shi, Zheng-Wen Fu, "Antisite occupation induced single anionic redox chemistry and structural stabilization of layered sodium chromium sulfide", *Nature Communications*, Published online 2017 Sep 18. DOI: 10.1038/s41467-017-00677-3.

II.K.2 Advanced Organic Materials for Batteries (Stanford University)

Yi Cui, Principal Investigator
Stanford University
Department of Materials Science and Engineering
Stanford, CA 94305
Phone: 650-723-4613
E-mail: yicui@stanford.edu

Zhenan Bao, Principal Investigator
Stanford University
Department of Chemical Engineering
Stanford, CA 94305
Phone: 650-723-2419
E-mail: zbao@stanford.edu

Tien Duong, Technology Manager
U.S. Department of Energy
Phone: 202-586-7836
E-mail: Tien.Duong@ee.doe.gov

Start Date: October 1, 2016   End Date: September 30, 2017
Total Project Cost: $300,000   DOE share: $300,000   Non-DOE share: $0

Project Introduction

Recent advances in lithium-ion battery (LIB) technology have improved energy densities of practical cells to values as high as 250 Wh kg^{-1}. However, applications of LIBs in electric vehicles still require increased energy density due to the high cost and poor range capability of current technology. To advance the current battery technology for grid storage applications, organic materials with versatile functionalities can play key roles to improve energy density cycle stability and material sustainability. This study pursues three main directions of using advanced organic materials: 1) designing polymer coating for a dendrite-free Li metal anode, 2) improving reaction kinetics of a Li/S battery, 3) developing a high energy density cathode for sodium storage.

Objectives

1. Identify the critical factors that influence the dendrite-free growth of Li metal in the presence of a polymer coating and develop an understanding of the interface between the polymeric coating and the Li metal.

2. Present a simple and effective strategy to activate Li$_2$S near its equilibrium potential by adding a small aromatic molecule in the electrolyte as a redox mediator (RM).

3. Demonstrate a high-performance sodium host by using a biomass-derived ionic compound, disodium rhodizonate, based on unprecedented four-sodium storage chemistry.

Approach

In developing polymer coating, we systematically chose a small number of polymers to isolate chemical and mechanical factors, including our previously published self-healing polymer (SHP), a self-healing elastomer (SHE) with similar chemistry to the SHP, polyurethane (PU), poly (ethylene oxide) (PEO), poly (vinylidene fluoride) (PVDF), and an elastomeric poly (vinylidene fluoride-co-hexafluoropropylene) (PVDF-HFP). In the first year, the team focused on gaining a more complete fundamental understanding of this newly proposed concept. Standard electrochemical and spectroscopic techniques including EIS, FTIR, SEM, and XPS were

used to examine Li metal that is electrodeposited through a polymer coating and the resulting solid electrolyte interphase (SEI).

For the sulfur electrode design, we prepared monodispersed 800 nm Li_2S particles as a cathode material to have homogeneous and consistent reaction chemistry and to monitor morphology evolution of the particles during battery cycling. We introduced a redox-active small molecule that is highly soluble in the conventional Li-S battery electrolyte of 1 M lithium bistrifluoromethanesulfonimidate (LiTFSI) in dioxolane/dimethoxy-ethane (1:1, DOL/DME). The RM to sulfur ratio was kept at 1:10.

We also conducted a systematic study on the electrochemical performance of disodium rhodizonate ($Na_2C_6O_6$) by controlling active particle sizes and electrolyte conditions. Using *in situ* synchrotron X-ray diffraction (XRD) combined with *ex situ* scanning electron microscopy (SEM), sodium-driven structure and morphology changes can be monitored during the sodiation/desodiation process.

Results

Designing polymer coating for a dendrite-free Li metal anode

On the anode side, Li metal has the highest specific capacity (3860 mAh/g_{Li}), and, when paired with high voltage metal oxide materials or high capacity sulfur cathodes, Li metal full cells can potentially enable energy densities higher than 500 Wh kg^{-1}. Unfortunately, the growth of porous Li during cycling causes low Coulombic efficiency and Li dendrites have the potential to short circuit the cell, leading to safety concerns.

As can be clearly seen in Figure II-618, all of the Li deposited with the various polymers have different morphologies and sizes. In contrast to what is expected from Classical nucleation theory, we found that the overpotential at the Li nucleation event was approximately the same for every polymer coating tested. We noticed that the local morphology of Li deposited in the presence SHP coatings and SHE coatings looked very similar while the global deposition was significantly different. This indicates that the polymer chemistry is important for dictating the morphology of the Li nuclei. We are currently in the process of correlating the Li metal surface inhibition, as measured by exchange current density, with the surface energy and dielectric constant of the different polymers.
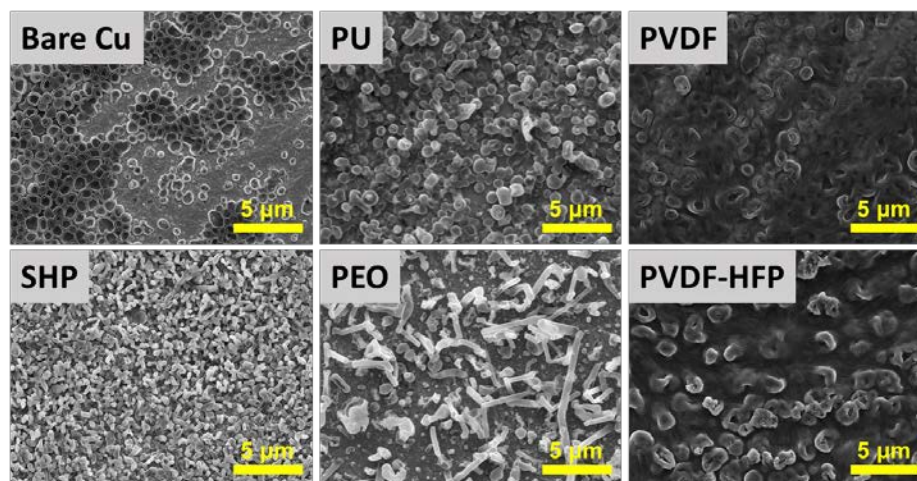
Figure II-618. Ex-situ SEM of the initial nucleation of Li on polymer-coated Cu foil. See top inset for polymer identity. Deposition current density was 1 mA/cm² and a capacity of 0.1 mAh/cm² was deposited in each case.

Improving reaction kinetics of a Li/S battery

Lithium-sulfur (Li-S) batteries have attracted great interest because of their abundance and high theoretical energy density of 2500 Wh kg^{-1}. Utilization of lithium sulfide (Li_2S) as a cathode material in Li-S batteries provides a safe and facile way to build Li-S batteries by directly solving problems from sulfur volume

expansion and lithium metal anode. However, the insulating nature of Li_2S leads to voltage polarization on charging which largely limits their electrochemical activities.

We introduced a small aromatic molecule in the electrolyte as a RM to activate Li_2S near its equilibrium potential (Figure II-619a). Upon charging, a RM with a redox potential that is slightly higher than the oxidation potential of Li_2S can be reduced and will oxidize the Li_2S particles at the surface. Then, the RM can be oxidized back at the current collector. Therefore, the RM molecule shuttles electrons between Li_2S and current collector continuously, facilitating charge transfer kinetics throughout the electrode. Indeed, we confirmed that oxidation of the Li_2S electrode is possible at 2.3 V when using a RM to sulfur ratio of 1:10 at a 0.1C (Figure II-619b).
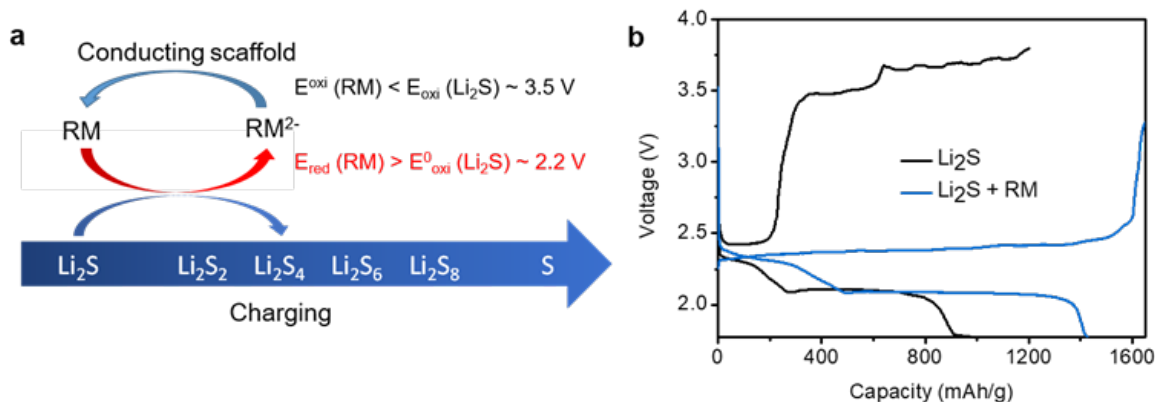

Figure II-619. a) The reaction mechanism of Li_2S oxidation with a redox mediator (RM). b) Voltage profiles of Li_2S electrodes in the first charge/discharge cycle with and without a RM in a DOL/DME electrolyte.

It is important to note that, in the presence of a RM, the morphology of Li_2S particles can be retained after prolonged charge/discharge cycles. As shown in Figure II-620a, spherical 800 nm Li_2S particles are still predominant in the SEM image after 250 charge/discharge cycles, while the particles turn into flat chunks without the RM. This strong contrast in the morphology evolution suggests a clear difference in the reaction chemistry with and without RM molecules in accordance with our hypothesis. Given the homogeneous morphology, introduction of RM molecules indeed facilitates a simultaneous reaction of Li_2S particles throughout the electrode. Furthermore, the continuing particle shape reflects limited diffusion of the reaction intermediates. The homogeneous reaction chemistry and limited diffusion of intermediates by introducing RM resulted in outstanding cycle stability of the Li_2S electrode at 0.5C (Figure II-620b).
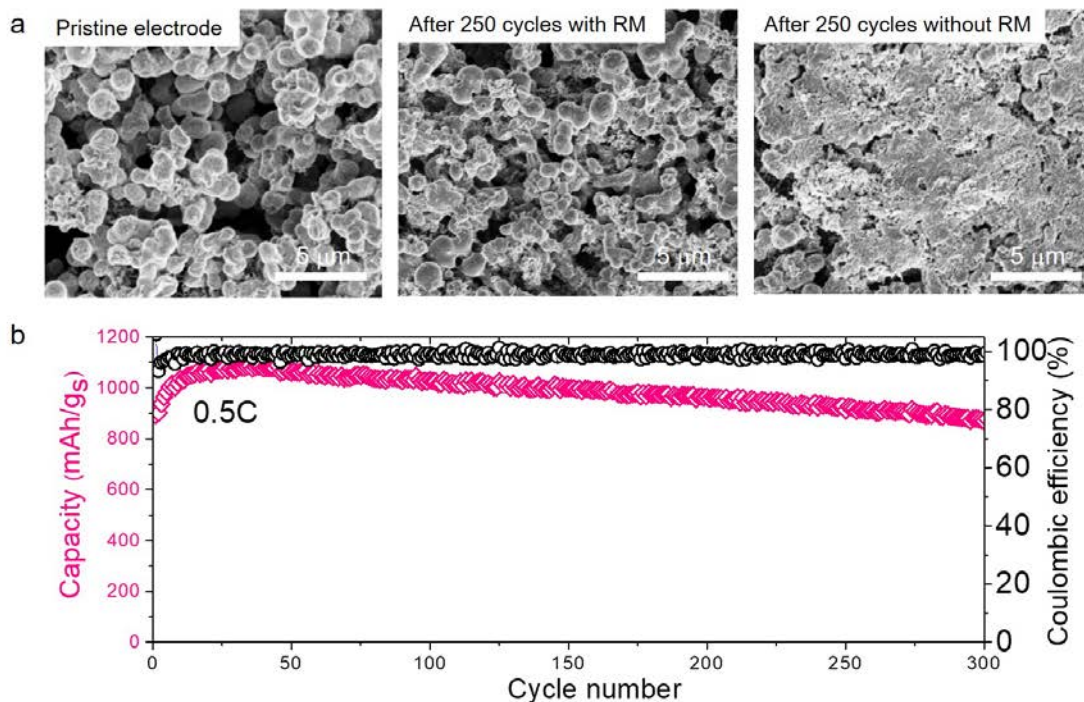
Figure II-620. a) *Ex situ* SEM to monitor morphology evolution of Li₂S particles after 250 cycles with and without RM molecules. b) Capacity retention of a Li₂S electrode in presence of the RM in the electrolyte at 0.5C.

Developing a high energy density cathode for sodium storage

The rise of renewable solar and wind power is demanding sustainable storage technologies using components that are inexpensive, earth abundant and environmental friendly. This has prompted the development of sodium ion batteries (SIB) because of its low cost and the inexhaustible sodium resources. Given the abundance and high theoretical specific capacity of 501 mAh/g, disodium rhodizonate ($Na_2C_6O_6$) is one of the most promising cathode materials for SIB, which can be obtained from biomass through green chemistry. However, substantially lower reversible capacities have been obtained in previous studies compared to the theoretical value, while understanding on this discrepancy has been limited.

To probe the phase transformation disodium rhodizonate during sodium insertion/desertion, *in situ* synchrotron XRD was performed using 300 nm $Na_2C_6O_6$ electrode in a DEGDME electrolyte (Nano/DEGDME). As shown in Figure II-621a, we clearly observed the phase transformation from α to γ during the initial plateau at 2.0 V of discharge, showing the gradual increase and decrease of characteristic peaks from γ phase and α phase, respectively. Then, when charging to 2.9 V, a positive shift in the characteristic peaks of γ phase was observed. Upon charging from 2.9 V to 3.2 V, we finally observe a two phase region, corresponding to phase transformation from γ−$Na_{2.5}C_6O_6$ to α−$Na_2C_6O_6$ (Figure II-621b), demonstrating the reversible phase transition during the discharge/charge process. We attribute the distinctive plateau around 3.0 V in Nano/DEGDME (Figure II-621a, highlighted in a circle) to this two-phase region.

We further monitored sodium-driven morphological changes was during the first cycle by SEM. As shown in Figure II-621c, the pristine electrode consists of 300 nm-sized $Na_2C_6O_6$ particles and conductive carbon particles which are smaller than 50 nm. Upon sodiation, the nanoparticles maintained the initial structure as a whole; when recharging to 2.9 V, they still showed the similar morphology. In contrast, once charged up to 3.2 V, in which case the electrode fully recovered the original α phase, we observed noticeable change in the particle morphology. As shown in Figure II-618e with high magnification, nanosized grains smaller than 50 nm were formed within the particle, while maintaining the integrity of the network structure in the following cycles.
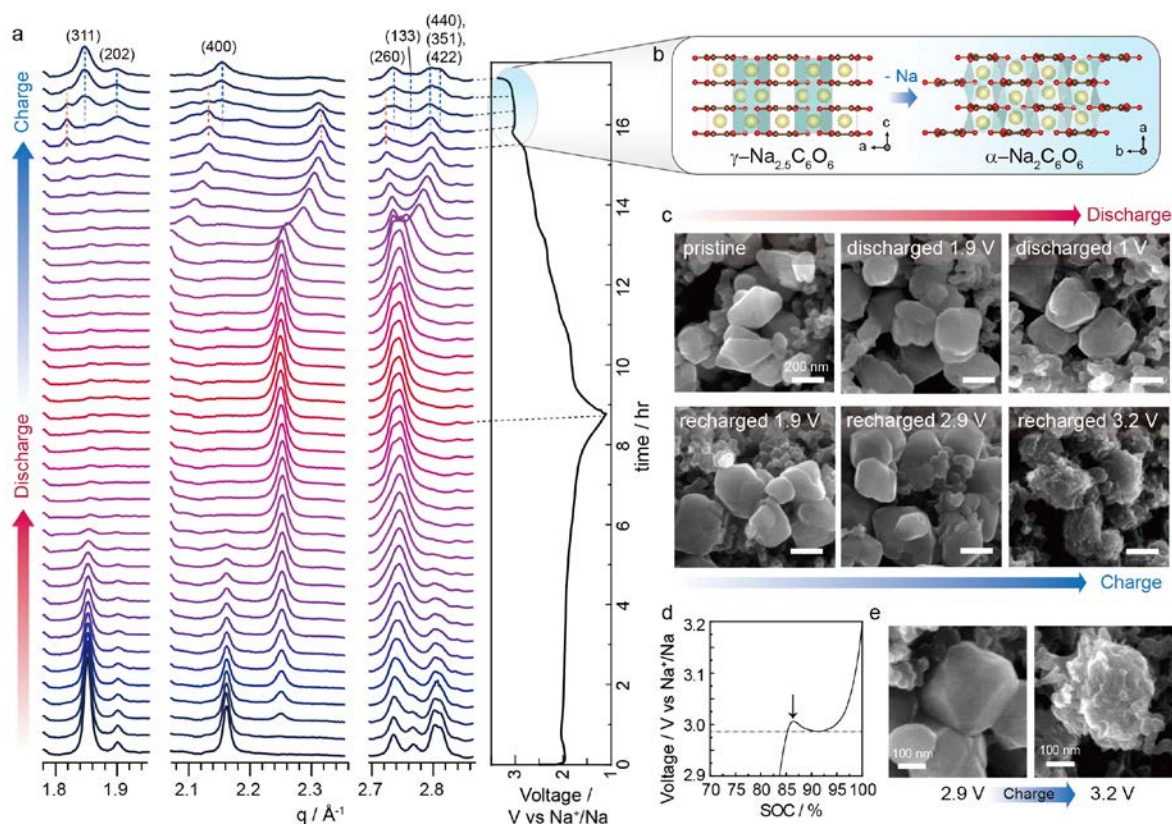
Figure II-621. Structural and morphological changes during reversible phase transformation of $Na_2C_6O_6$. a, *In situ* synchrotron XRD patterns of nanoparticle electrodes collected for the every 0.1 Na-stoichiometry change. b, Crystal structure change of $Na_{2+x}C_6O_6$ when charged above 2.9 V. c, *Ex situ* SEM images of nanoparticle electrodes at different states of charge during the first cycle. d-e, Dramatic morphology change and the corresponding voltage profile during the phase transformation.

Based on the above investigation, we propose redox mechanisms of $Na_2C_6O_6$. During sodiation, the α phase of $Na_2C_6O_6$ is transformed into γ phase, which is energetically more favorable with the additional sodium. When removing the sodium during charging, the reverse structural change is kinetically suppressed, which leads to a premature desodiation in most cases at the voltage limit set to secure structural stability. Thus, the charged electrode remains in the γ phase as partially-sodiated species ($Na_{2+x}C_6O_6$), which significantly limits the redox capability of the electrode in subsequent cycles. Nevertheless, the reversible phase transformation in the stable potential window becomes possible by decreasing the particle size and selecting a proper electrolyte. Among the electrolytes, DEGDME appears to be the most efficient in facilitating the phase transformation.
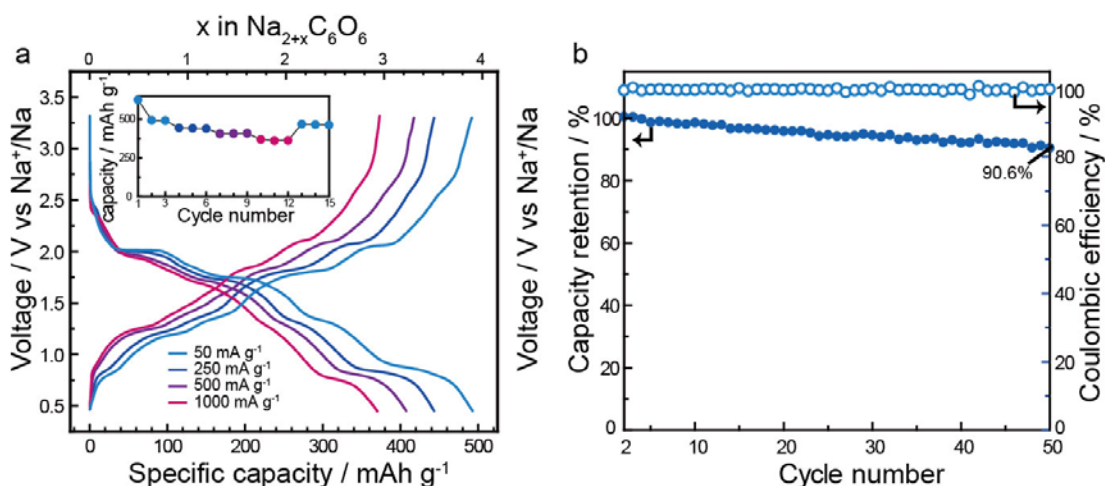
Figure II-622. Electrochemical four-sodium storage of $Na_2C_6O_6$ electrodes in half cells and full cells. a, Rate capability and corresponding cycle performance (inset) of $Na_2C_6O_6$ electrode from 0.5-3.3 V. b, Cycle retention of $Na_2C_6O_6$ electrodes at 500 mA g^{-1} corresponding voltage profile (inset) for 50 cycles.

The understanding of the sodiation mechanism of $Na_2C_6O_6$ indeed allowed us to demonstrate a four-electron process in a Na-ion cell for the first time. This was demonstrated in an enlarged potential window from 0.5 to 3.2 V. As shown in Figure II-619a, a reversible capacity of 498 mA h g^{-1} was obtained at 50 mA g^{-1} in Nano/DEGDME, which is as high as 95% of the theoretical capacity (Figure II-622a). Even at the very high rates of 500 mA g^{-1} and 1000 mA g^{-1}, the electrode retained a specific capacity of 408 mAh g^{-1} and 371 mAh g^{-1}, respectively. The $Na_2C_6O_6$ electrode showed good capacity retention upon cycling (Figure II-622b). After 50 cycles, about 90.8% capacity of the second cycle was still available in the potential window of 0.5 to 3.2 V at 500 mA g^{-1}. We obtained the maximum specific energy density nearly 726 Wh kg^{-1}, where the weight is based on the cathode mass of $Na_2C_6O_6$, with a high energy efficiency above 87% surpassing the performances of any other cathode candidates for SIB.

Conclusions

We identified a group of chemically and mechanically diverse polymers to study the effects of different polymer coatings on the nucleation and growth of Li metal films. Using these polymers, we observed the effect of smaller and more uniform Li nuclei observed originally with our SHP can be generalized to multiple polymer coatings and can be attributed to the increased nucleation overpotential due to the presence of the polymer coating. However, the nucleation overpotential does not sufficiently explain the various shapes of the Li metal nuclei, which are highly dependent on the chemistry of the polymer coating. Work is presently in progress to identify the critical factors that influence Li metal nuclei morphology in the presence of polymer coatings.

We confirmed that the introduction of RM can facilitate Li_2S oxidation near its equilibrium potential as low as 2.3 V. The continuing homogeneous morphology of the electrode in the prolonged cycling suggested a simultaneous reaction of Li_2S particles throughout the electrode and limited diffusion of the reaction intermediates. This in turn allowed excellent capacity retention of the Li_2S electrode over 300 cycles in the presence of RM in the electrolyte.

We achieved full utilization of four Na-ion storage in $Na_2C_6O_6$ based on the understanding of the redox mechanism associated with structural and morphological changes during cycling. We discovered that the deteriorating redox activity of $Na_2C_6O_6$ upon cycling originated from irreversible phase transformation, and identified active particle sizes and electrolyte conditions as key factors to complete the phase transformation during desodiation. The resulting electrochemical performances of $Na_2C_6O_6$ electrode including a specific

energy density of 726 Wh $kg_{cathode}^{-1}$, a high energy efficiency above 87 %, and a good cycle retention surpass any reported performances of cathode candidates for SIB.

Key Publications

1. Lee, M.; Hong, J.; Lopez, J.; Sun, Y.; Feng, D.; Lim, K.; Chueh, W. C.; Toney, M. F.; Cui, Y.; Bao, Z. High-Performance Sodium–Organic Battery by Realizing Four-Sodium Storage in Disodium Rhodizonate. *Nature Energy* **2017**, *2*, 861–868.

2. Tsao, Y.; Chen, Z.; Rondeau-Gagné, S.; Zhang, Q.; Yao, H.; Chen, S.; Zhou, G.; Zu, G.; Zu, C.; Cui, Y.; Bao, Z., Enhanced Cycling Stability of Sulfur Electrodes through Effective Binding of Pyridine-Functionalized Polymer. *ACS Energy Lett.* **2017**, 2, 2454–2462.

3. Zheng, G.; Wang, C.; Pei, A.; Lopez, J.; Shi, F.; Chen, Z.; Sendek, A. D.; Lee, H.-W.; Lu, Z.; Schneider, H.; Safont-Sempere, M. M.; Chu, S.; Bao, Z.; Cui, Y. High-Performance Lithium Metal Negative Electrode with a Soft and Flowable Polymer Coating. *ACS Energy Lett.* **2016**, 1247–1255.

4. Bao, Z.; Cui, Y.; Zheng, G.; Wang, C.; Lopez, J.; Pei, A. U.S. Patent US20170062830 A1

II.L   Beyond Li-ion R&D: Battery500 Innovation Center

II.L.1   Innovation Center for Battery500 (PNNL)

Jun Liu, Principal Investigator
Pacific Northwest National Laboratory
902 Battelle Boulevard
Richland, WA 99354
Phone: 509-375-4443
E-mail: jun.liu@pnnl.gov

Yi Cui, Co-Principal Investigator
Stanford University/SLAC
450 Serra Mall
Stanford, CA 94305
Phone: 650-723-4613
E-mail: yicui@stanford.edu

Tien Duong, Technology Manager
U.S. Department of Energy
Phone: 202-586-7836
E-mail: Tien.Duong@ee.doe.gov

Start Date: September 1, 2016   End Date: September 30, 2021
Total Project Cost: $8,000,000   DOE share: $8,000,000   Non-DOE share: $0

Project Introduction

Lithium (Li)-ion batteries play a critical role in modern day technologies, but their specific energy (Wh kg^{-1}) and energy density (Wh L^{-1}) are approaching the maximum practically achievable values based on existing manufacturing processes with the conventional cathode and anode materials. The large scale deployment of electric vehicles and ever-increasing demand of modern technologies require further increase in cell energy and cost reduction. Li-metal batteries are regarded as the "Holy Grail" of high-energy-density systems because Li metal has an ultrahigh theoretical specific capacity (3860 mAh g^{-1}), the lowest redox potential (-3.040 V vs. standard hydrogen electrode), and low gravimetric density (0.534 g cm^{-1}). However, the practical application of Li metal anode still faces several significant challenges, including safety concern due to Li dendrite growth, limited cycle life because of low Li Coulombic efficiency, and large volume change during Li stripping and redeposition if a two-dimensional (2D) flat Li foil is used. In addition, developing next generation rechargeable Li metal batteries with a specific energy higher than 300 Wh kg^{-1}, up to 500 Wh kg^{-1}, is still a significant challenge. Many groups are focusing on the fundamental breakthroughs in electrode materials and control of the deleterious side reactions in such new battery concepts. Solid-state Li batteries using solid electrolytes have recently received wide attention due to the inherent high safety and decent energy. There have been intense efforts to improve the bulk conductivity, interfacial charge transport and stability for the manufacturing of the solid-state cells. A very desirable strategy is to take advantage of the electrode materials that are commercially or nearly commercially available, and introduce the least perturbation to the cell configuration and manufacturing process of the current technologies. Based on this considerations, two battery chemistries, high nickel content lithium nickel-manganese-cobalt oxide (high-Ni NMC, Ni>60%), coupled with Li metal anode, and Li-S chemistry, have the potential to achieve an energy density of at least 500 Wh kg^{-1}.

Objectives

The Battery500 Consortium aims to develop commercially viable Li battery technologies with a cell level specific energy of 500 Wh kg^{-1} through innovative electrode and cell designs that enable the extraction of the

maximum capacity from advanced electrode materials. In addition, the project aims to be able to achieve 1000 cycles for the developed technologies.

Approach

The Battery500 Consortium will utilize first class expertise and capabilities in battery research in the United States and develop an integrated and multidisciplinary approach to accelerate the development and deployment of advanced electrode materials in commercially viable high energy batteries. The Li anode combined with a compatible electrolyte system and two cathodes—one high-Ni $LiNi_xMn_yCo_zO_2$ (NMC) and another sulfur (S)—will be studied and developed to reach high energy density. The project focus is to design novel electrode and cell architectures in order to meet the 500 Wh kg^{-1} goal. The consortium will work closely with R&D companies, battery/materials manufacturers and end-users/OEMs to ensure that the developed technologies are aligned with industry needs and can be transitioned to production. The out-year goals for FY17 include: (1) completion of first phase full cell fabrication and testing based on the consortium recommended protocols, demonstrating 300 Wh kg^{-1} full cell capacity, (2) provision of analytical results for materials selection, cell design and fabrication, and further refinement for 2018, and (3) completion of the selection and launching of seedling projects for Battery500.

Results

1. Project Leadership and Coordination

The whole consortium team has three keystone projects and has organized various teams, including the research teams, the Leadership Team, the Executive Committee, the Advisory Board and the Industry Committee, and set up their roles and responsibilities. A total of 14 projects are defined. A Working Committee, made of one representative from each institution was formed with the function of keeping the whole consortium updated of the research progresses through biweekly telephone conferences. Several large core groups, including the NMC cathode group, the anode group, the diagnostic group, and the S group, were formed. The coordinator for each large core group is responsible for organizing biweekly phone conferences to exchange research results and discuss important issues within each project throughout the whole first quarter. These teleconferences were also announced through the whole consortium to welcome PIs, research scientists, postdocs, and students from other project to attend and provide their inputs. In addition, several sub-groups were also formed, including the electrolyte group, the characterization group, the diagnostic and electrochemical characterization group, and the cell design and fabrication group. These subgroups are responsible for ensuring regular communications and meeting program goals on the project level. A drop box folder dedicated to Battery500 has also been set for communications and file exchanges within the consortium.

The integrated efforts of the consortium team have been effective. The biweekly telephone conferences for the leader team, the Working Committee, as well as for each Keystone project and special task teams (such as cathode, anode, and diagnostic teams) were held regularly. The summaries of the teleconferences for the Working Committee were emailed to all PIs afterward, while the presentations of the technical conferences were distributed even more widely including staff scientists, postdocs and students who are working on the Battery500 projects. At many tele-conferences, the young scientists (postdocs and students) are the main presenters and their active involvements during and after tele-conferences are the key factors to achieve the milestones of FY2017.

The FY2017 first quarterly review/annual meeting was held at SLAC on January 20, 2017, and the other three quarterly review meetings were held at University of Texas at Austin from April 27 to 28, 2017, University of Washington (UW) in Seattle from July 11th to 12th, 2017, and UCSD in San Diego from October 18th to 19th, 2017, respectively. Averagely about 50 people attended these review meetings, including DOE Program managers, the Executive Committee members, the PIs, staff scientists, and a big group of postdocs and students. At each review meeting, the DOE Program managers gave updates of the DOE programs, the Consortium Director (Jun Liu) gave overviews of the consortium, and invited PIs and postdocs gave the updates of the keystone projects and technical progresses related to quarterly review topics. Starting from the second review meeting, a poster session was included to exchange the progresses of different projects among

the consortium. Two best poster awards were installed starting from the third quarterly review to acknowledge the great contributions of postdocs and their teams. In the third quarterly review meeting, an "Exceptional Team Contribution Award" was presented to Prof. Stan Whittingham.

The first Advisory Board meeting was held in Washington DC with participation from the DOE program managers, representatives from USABC, IBM, FMC, Naatbatt and Tesla.

2. Keystone Project 1: Materials and Interfaces

The preliminary screening and selection of most promising candidates of commercial cathode materials, electrolytes (salts, solvents and additives), and separators were first evaluated and the baseline materials were set up for the first phase full cell assembly and testing.

On high-Ni NMC cathodes, the baseline materials of NMC622 and NMC811 from commercial source (EcoPro) were first characterized and evaluated at different loadings and current densities. EcoPro NMC622 shows high dependence of rate performance on sample loading, and high loading leads to poor electrochemical performance at higher rates. Although the NMC811 does not show significant electrochemical dependence on loading, we observed hints of the formation of a second phase at above 4.2 V in NMC811. Then, high-Ni NMC materials with Ni content of 60~94% have been synthesized in-house and characterized. These show the desired meatball morhology (Figure II-623a) with very uniform particle sizes. The electrochemical performance indicates as expected that the higher Ni contents lead to higher capacities (Figure II-623b), but worse cycling stability (Figure II-623c). Al doping and surface coating with Al-containing materials (*e.g.*, Al_2O_3) have been used to improve the high Ni content NMC materials (NMC622, NMC811, and NMC90505). Al doping in the high-Ni NCO greatly enhances the cycling stability (Figure II-623d). Our results show that such Al doping and Al_2O_3 coating play critical roles in capacity retention.

On high-Ni content cathode materials, further studies were conducted to understand the performance degradation, including both NCA and NMC. The cathode degradation include particle cracks, decreased crystallinity, active mass dissolution, loss of active Li ions and the irreversible surface structural rearrangements upon Li extraction during battery operation. In addition, the enhancement of cycling stability in 2% Al-doped high-Ni NCO was found to be due to the formation of a thinner SEI layer and a more ordered surface structure with no abrupt phase change. Last, the better rate capability of high-Ni NMC was studied by EIS and LPR techniques. The origins for the improved electronic and ionic conductivities are related to the defect levels (Li/Ni mixing or cation vacancies which could introduce holes as charge carriers and the weakened Li-O bonding or more structural defects (vacancies) (which facilitate Li^+ jumping), respectively.

On Li metal anodes, several in-situ and ex situ grown films have also been developed to protect the Li metal anode. A core−shell nanoparticle coating has been prepared as an interfacial layer for dendrite free Li metal anodes. An adaptive "solid-liquid" interfacial layer was also developed to protect Li metal anode. In addition, a robust coating layer of crystalline methyl lithium carbonate was formed in-situ on Li metal surface through a solution chemical process and dendrite free Li metal anode was observed after long-term cycling at 3 mA cm^{-2} in conventional $LiPF_6$/carbonate-based electrolyte. In other approaches, an inorganic/organic hybrid coating based on Cu_3N-SBR has been developed to protect 3D porous Li metal anode; a thin and dense LiF coating was generated on Li metal surface by using gaseous phase Freon method, which leads to enhanced stability of Li metal in electrolytes and even in air. An electrolyte-proof structured Li-ion conductive nanocomposite (Li-$Li_{22}Si_5$-Li_2O) was also developed by embedding Li in Li^+ conductive scaffold and then pressing into pellets, which shows stable dimensions, impedance and voltage polarization during long-term stripping and redeposition processes. A Janus separator with one side coated with an ultrathin Cu film was developed to suppress Li dendrites and to improve the cycling stability of Li anode.
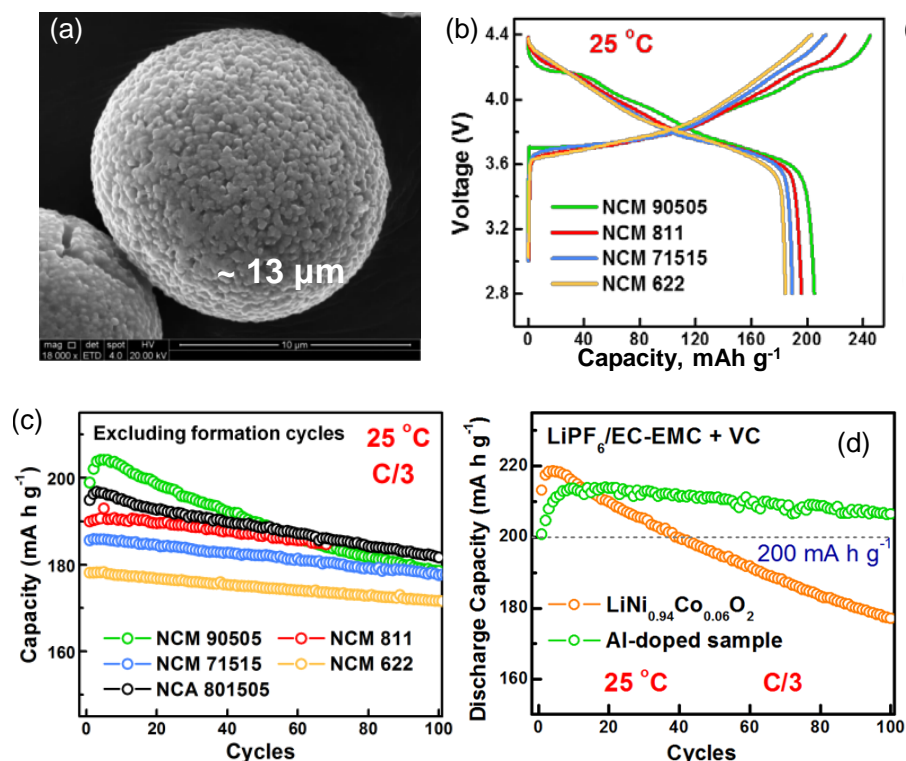
Figure II-623. (a) Morphology of the in-house synthesized high-Ni NMCs showing spheres with the primary and secondary particles. (b) First cycle votage profiles and (c) cycle life of Li||NMC cells between 4.4 and 2.8 V. (d) Comparison of the cycling performance of high-Ni $Li_{0.94}Co_{0.06}O_2$ with and without Al doping in cells with Li-metal anode.

On electrolytes, several new electrolyte formulations have been developed to enable Li deposition/stripping with electrochemical stability window expanded to voltage over 4.3 V and Coulombic efficiency (CE) improved to more than 98%. These new electrolytes are based on LiFSI salt and solvent mixture of sulfones, carbonates, phosphates and other co-solvents. Specifically, an electrolyte using LiFSI salt in a mixture of phosphate solvent and a co-solvent has a Li CE as high as 99.3% and provides stable cycling for at least 200 cycles at C/3 rate in the voltage range of 2.8 to 4.4 V in Li||NMC622 cells (Figure II-624). More importantly, such LiFSI-phosphate electrolytes are non-flammable, which is critical for safe operation of Li metal batteries. One of the electrolytes has been used in the 1 Ah pouch cells delivered for Year 1 project and enabled the high capacity cells to be cycled for 50 cycles under realistic conditions required for the project.
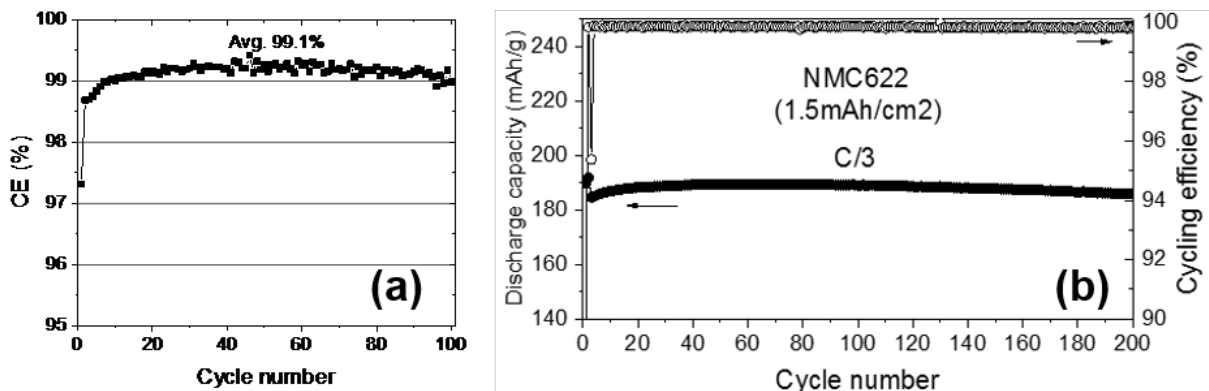

Figure II-624. Cycling stability of LiFSI-phosphate electrolytes (E313) in various cell systems, (a) Li||Cu, and (b) Li||NMC622.

3. Keystone Project 2: Electrode Architectures

The goal of Keystone 2 is to design, model, fabricate and characterize the effect of electrode architecture on electrode and cell performance in order to reach the goal of 500 Wh kg^{-1} cell specific energy. Included in this Keystone are architecture design of thick cathodes (UCSD), Li metal electrode architectures (PNNL and Stanford), inorganic (UT-Austin) and polymer (Stanford) electrolytes, and electrode performance modeling (UW).

In the area of thick cathodes, cycling performance of the baseline NMC622 material was first measured as a function of type and amounts of binder, carbon, and active material loadings. A new electrode architecture with high amount of straight voids in the electrode was fabricated. Electrochemical impedance measurement confirmed a reduction of tortuosity. Modeling of an electrode with graded porosity shows improved power capability as well. These two examples show the potential of designing electrode architectures to achieve higher power density. After establishing baseline performance, efforts have focused on developing innovative electrode architectures to reduce tortuosity by creating vertical, straight channels in electrodes. Scalable methods are developed to create vertical openings, and additional processing steps are used to adjust the density and gap width. The effective electrolyte conductivity of electrodes with the same overall porosity of 30% is shown to increase with the initial gap area. This positive correlation confirms that microstructure control can be effective in reducing resistance of electrolyte transport in electrodes. Further work has included: 1) evaluating thick cathodes provided by Maxwell; 2) performing systematic baseline measurement of NMC 811 to understand performance limiting factors; and 3) assessing the power performance of electrodes with advanced architectures. Two main conclusions are: 1) Li metal cycling stability affects the evaluation of thick cathodes due to its failure; and 2) at the targeted C/3 rate, electrode performance appears to be limited by electronic rather than ionic transport. Two Maxwell NMC 622 electrodes have thicknesses of 100 and 190 µm and active materials loadings of 30 and 60 mg cm^{-2}, respectively (Figure II-625a, b). At a C/3 rate, the electrodes deliver very similar specific capacities: 165.7 vs 162.5 mAh g^{-1} (Figure II-625c). This indicates that under this testing condition, the loading does not limit rate performance. Cycling tests in coin cells show that a higher cathode loading leads to an earlier cell failure due to the increased Li utilization and electrolyte consumption (Figure II-625c). Replacing the Li and electrolyte after 100 cycles and cycling at C/10, the 30 mg cm-2 622 cell has resurrected the capacity, as shown in Figure II-625d, showing the stability of the cathode but the instability of the electrolyte and Li anode. This observation indicates that Li metal failure and electrolyte consumption are responsible for cell performance decay when testing thick electrodes. The limiting factors for thick cathode rate performance is further evaluated by testing electrodes with different loadings at different current densities. Electrodes with areal loadings of 10-60 mg/cm^2 all deliver similar specific capacity as long as the areal current density is similar, which is consistent with the results obtained from the Maxwell electrodes.
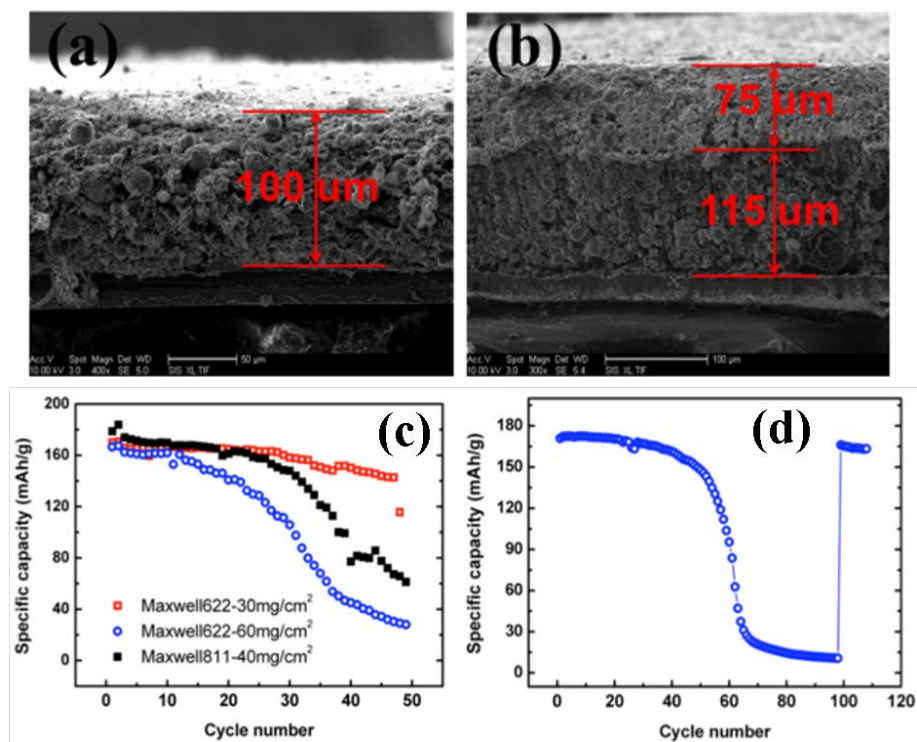
Figure II-625. (a, b) Cross-section SEM images of two Maxwell NMC622 thick electrodes: (a) 30 mg cm-2; (b) 60mg cm-2. (c) Cycling performance at C/3 of three 622/811 cells of different cathode loadings. (d) Specific capacity with cycling for the 30 mg cm-2 NMC 622 electrode at C/3 for the first 100 cycles and subsequent resurrection of the cell by replacement of Li anode and electrolyte.

Electrode design for Li anode has focused on developing 3D hosts for Li deposition and 3D structured Li/carbon composite anodes, which reduce effective current density and maintain macroscopic dimension, both of which promise longer cycle life. 3D structured Li/carbon composite anodes based on carbon cloth (CC), carbon film (CF) and carbon paper (CP) have been developed. All Li‖NMC622 cells using Li/carbon composite anodes demonsrate much better rate capability and long-term cycling stability than those using Li foil anodes when the same conventional $LiPF_6$/carbonate electroltye was used. For example, the Li/CC‖NMC622 cells can retain 92% of capacity after 300 cycles at C/3 rate (0.52 mA cm^{-2}) in the voltage range of 2.8 ~ 4.4 V.

The team has also pursued 3D architectures for Li metal in order to manage volume change, reduce effective current density, suppress dendrite formation and increase cycle life. A porous Ni framework fabricated in house that is less than 50 µm thick, can be filled with Li metal, and more importantly, form a dense layer on its surface after cycling which enables fast ion transport. Figure II-626 shows the cross sectional images of a designed 3D porous Li host made of lithium oxide and lithiated silicon. By using a robust host structure, macroscopic dimensional changes are minimized.

Figure II-626. SEM images of the cross section of a porous 3D host for Li metal plating and stripping, demonstrating its macroscopic dimensional stability.

Another method to control Li deposition is through the use of a flowable, highly viscoelastic polymer coating which promotes more uniform nucleation of Li. A soft/hard adaptable polymer is flowable under low shear rate but becomes stiff under high shear rate. This mechanism is effective in regulating Li growth to prevent the formation of Li filaments. Further, new polymer electrolytes were designed to offer higher ion conductivities and stable interface with Li by manipulating the Li ion coordination environment. Finally, a solid electrolyte $Li_{3/8}Sr_{7/16}Hf_{1/4}Ta_{3/4}O_3$ (LSHT) has shown a room temperature conductivity of 3.8×10^{-4} S cm^{-1} at 25°C and demonstrated good stability with Li metal.

Results obtained so far in Keystone 2 have established that architectural control is essential for both the Li anode and the oxide cathode in order to meet the design goal of the Battery500 program. In the case of both electrodes, 3D design will be coupled with optimization of interfacial chemistry to offer high efficiency and cycling stability. Work continues in further development of electrode architectures guided by modeling and with increased coordination with the Characterization team in the Consortium to understand the mechanisms of performance improvement.

4. Keystone Project 3: Cell Fabrication, Testing and Diagnosis

The Keystone 3 has first jointly established methods for evaluation of high energy cells both electrochemically and through the use of advanced characterization techniques and resources, set up methods for the preparation of 1 Ah or larger cells, and used different models to identify cell design parameters for achieving both 300 and 500 Wh kg^{-1}. Cell designs for both 300 Wh kg^{-1} and 500 Wh kg^{-1} of Li||NMC622 and Li||S chemistries were determined using a combination of computational methods with experimental input by a combined team of researchers at INL, PNNL and UW. Activities also included means to develop a greater understanding of full cell aging dynamics and design implications. With regard to cell design, multiple computational methods were used for verification purposes. These include finite element modeling, partial two dimensional (P2D) and reduced order P2D approaches. As shown in Figure II-627a good agreement was attained between the computational methods and the experimental data for the Li||NMC622 chemistry. Additionally, there was good agreement between the different methods with variance between the three methods on the order of less than 5% across multiple cell designs. Overall the methods were used to determine that, depending on the quantity of electrolyte used, that the thickness of the positive NMC622 electrode ranged from 170 to 270 μm. These cell design determinations served as a starting point to help facilitate the construction of 1 Ah Li||NMC622 cells to meet the milestone of 300 Wh kg^{-1}.
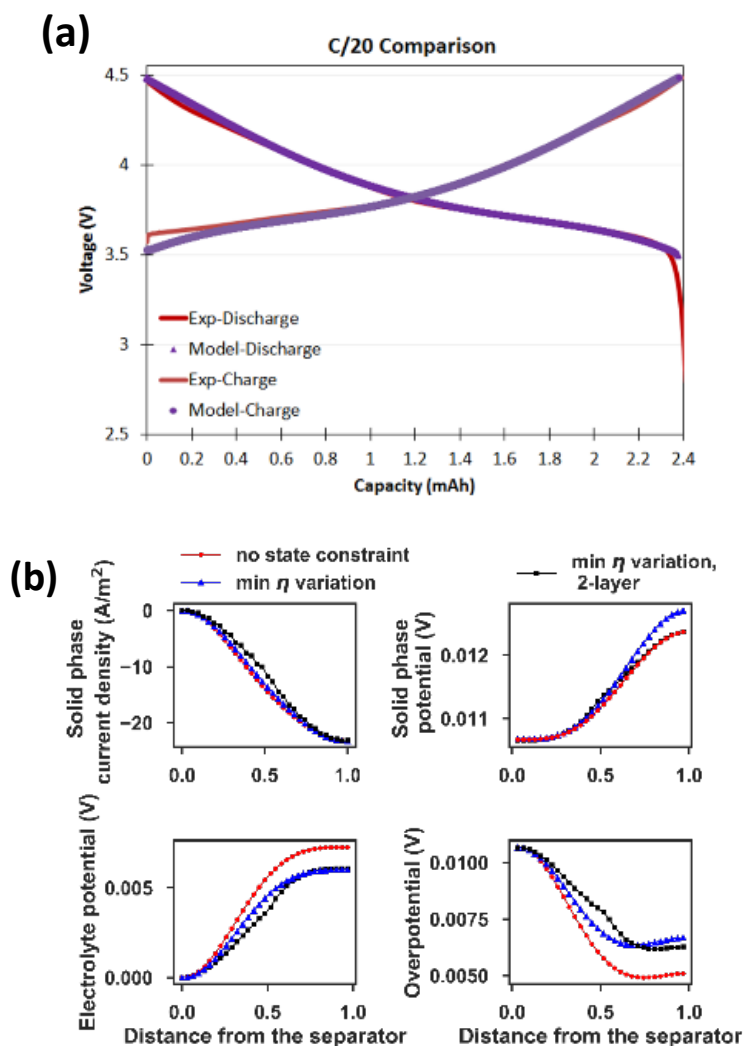
Figure II-627. (a) Comparison of calculated and experimental charge/discharge curves for a Li||NMC622 cell. (b) Internal profiles for solid phase current density, solid phase potential, electrolyte potential and overpotential (clockwise from top left). The dashed red line and blue lines are for different porosity uniform electrodes while the black line is associated with a graded porosity electrode.

In line with the cell design activities various electrode optimization routes were used to look at the impact of graded electrodes to enhance the performance of thick NMC622 electrodes (Figure II-627b). This work at UW was completed both to understand the impact of grading and to implement computational approaches which significantly reduce the amount of time needed to perform calculations. The new approach is much faster (up to 1000 times) compared with the conventional approaches including the common sequential optimization approach.

A key component of Keystone 3 activities for FY2017 involved developing a more robust understanding on how to effectively transition technologies from early demonstration in small coin-type cells to larger format pouch cells. One of the key considerations for achieving high energy cells is a pouch cell using lean electrolyte and a limited source of Li metal. For the present work these values equate to Li foil that is 50 μm thick and electrolyte loading of 3 g Ah^{-1}. This is considerably different from most data reported in the laboratory studies in the literature. To help facilitate the transition from laboratory activities to pouch cell development, a set of standard protocols for evaluating promising materials using similar lean electrolyte and limited Li was developed and distributed to the team.

In cell fabrication, great team efforts have been made to reach the 300 Wh kg^{-1} specific energy and the 50 cycle life goals in a real 1 Ah pouch cell, not just in a ~4 mAh coin cell with large amount of extra electrolyte and Li metal anode. When extra electrolyte and Li metal are used in a coin cell, the cycle life can be extended to several hundred cycles. However, the real specific energy is rather low when all the weights of the cell components are counted. In order to reach the real 300 Wh kg^{-1} goal, the team carefully calculated the required weight limit for each component, such as cathode, anode, separator, electrolyte, Cu and Al current collectors, tabs, and package material. With the limited electrolyte and Li metal in the prepared pouch cells and even in coin cells, a severe limitation in cycle life was observed. All cells failed after less than 15 cycles when the conventional LiPF$_6$/carbonate liquid electrolyte was used. The short cycle life is caused by the interaction between the Li metal and the conventional LiPF$_6$/carbonate liquid electrolyte, which generated significant quantities of "dead" Li and caused electrolyte depletion. Even after refilling the electrolyte, the cells had only half of the original capacity and faded quickly. A new electrolyte was developed to reduce the reaction between the Li metal and the electrolyte, which significantly extended the cycling life of the 300 Wh kg^{-1} pouch cell. The FY2017 milestone of 50 cycling life was used with this new electrolyte developed (see Figure II-628). The importance of this achievement is not only reaching the milestone, but also providing guidance for future research approaches to increase the specific energy and the cycle life. The results on the 300 Wh kg^{-1} showed that the FY18 efforts need to focus on solving the "dead" Li and the electrolyte depletion problems by developing Li metal protection methods, such as surface modification of Li, modified separator, and new electrolyte additives and new electrolyte systems.
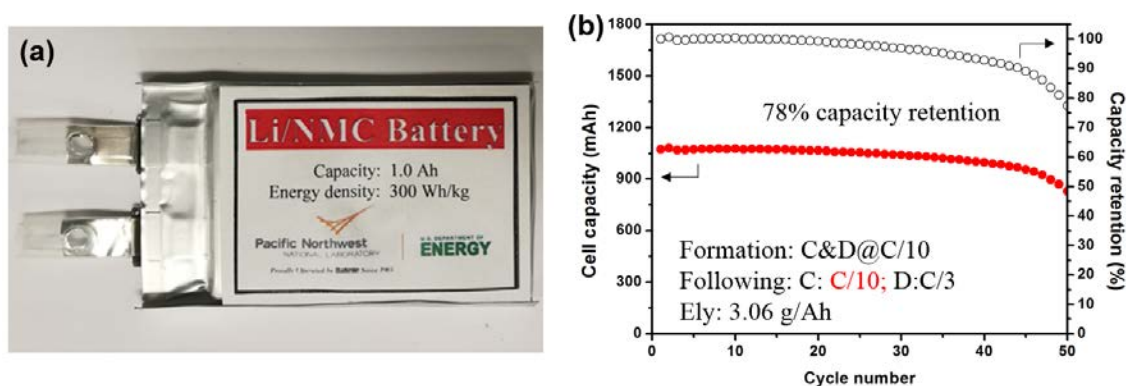

Figure II-628. (a) Picture of the 1 Ah and 300 Wh kg^{-1} pouch cell with Li||NMC622 system. (b) Cell capacity and capacity retention vs cycle number for a 1.1 Ah, 300 Wh kg^{-1} Li||NMC 622 pouch cell with a PNNL developed electrolyte. The capacity retention of 78% is obtained at the 50th cycle.

Performing analysis of fading mechanisms during cycling provides a pathway to identify gaps in cell design. Such analysis enables other keystone areas to refine materials or designs to improve performance. As part of this process, differential capacity (dQ/dV) analysis was performed to understand the performance of both positive and negative electrode materials. The robust diagnostic and prognostic approach also provide information on both kinetic and thermodynamic fade modes. The dQ/dV results and other corresponding data confirm that the capacity fading was not due to the positive electrode (NMC 622) performance, but was instead associated fade of the Li metal negative electrode and overall transport limitations. Initial work looking at cell variability was extended to study the role that reducing electrolyte volume has on cell fading providing support to the 1 Ah cell design. In addition, key parameters which will enable optimization of both cell performance and energy density, have been evaluated including electrode thickness, porosity, tortuosity and overall loading of active high Ni NMC materials or of sulfur. Initial bounds for each parameter have been identified and are being refined to understand the full sensitivity of the parameters on overall cell design. In conjunction with parametric analysis, cell models looking at how to more effectively the architectures in a Li metal battery have been established. Figure II-629a includes the general premise for the initial model which includes a porous positive electrode and a planar Li metal negative electrode. A key component of the Li metal side of the cell is

that a moving boundary due to SEI reactions is included. Figure II-629b includes predicted values using this model and experimental data collected for a cell that had an NMC 622 positive electrode. With the inclusion of the moving boundary good agreement between model and experiment have been identified.
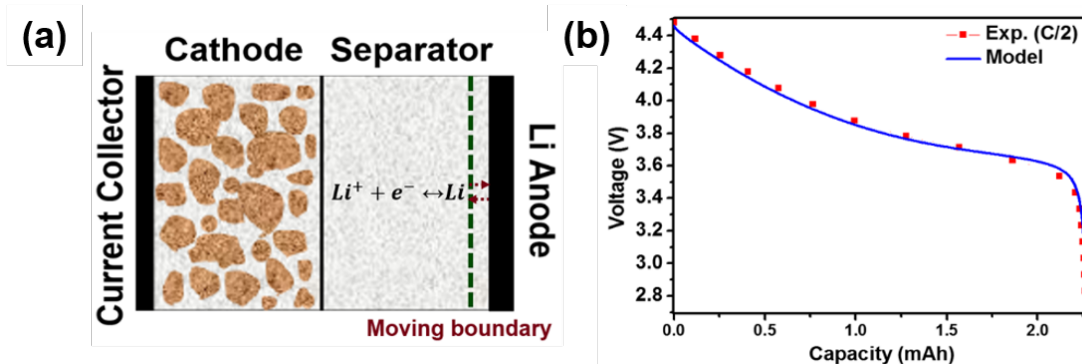

Figure II-629. (a) Schematic of modelled system and (b) comparison between model and experimental data for a NMC622 cell.

The team is developing novel characterization methods to quantify Coulombic efficiency losses in Li metal anodes which allow identification of "dead" Li and other Li loss mechanisms. X-ray diffraction (XRD) has been developed to accurately track metallic Li through plating and stripping cycles. Figure II-630 shows diffraction data that allow quantification of metallic "dead" Li and comparison to Coulombic efficiency. Figure II-631 (a) shows the Li (110) peak intensity through four plating and stripping cycles. We attribute the metallic Li intensity left at the end of a cycle to "dead" Li and create an efficiency ratio of the amount of Li stripped to the amount of Li plated, measured through XRD. These results are shown in Figure II-631 (b) along with the Coulombic efficiency and represent the first quantitative distinction between dead Li and Coulombic inefficiency. Future work will involve a direct comparison to modelling efforts with Keystone 3 and spatially-resolved micro-diffraction measurements.
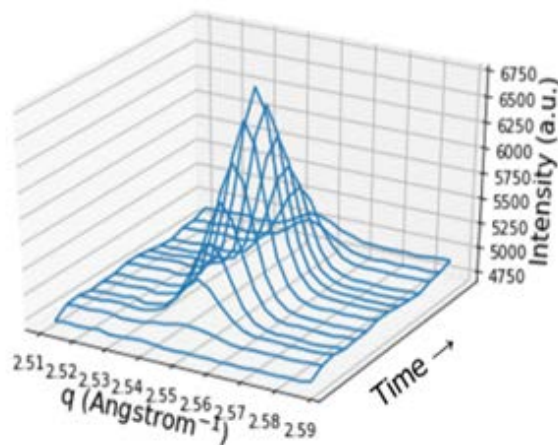

Figure II-630. One-dimensional intensity vs. q (scattering vector) at the Li (110) peak through one plating and stripping cycle at 1.5 mA cm^{-2}.
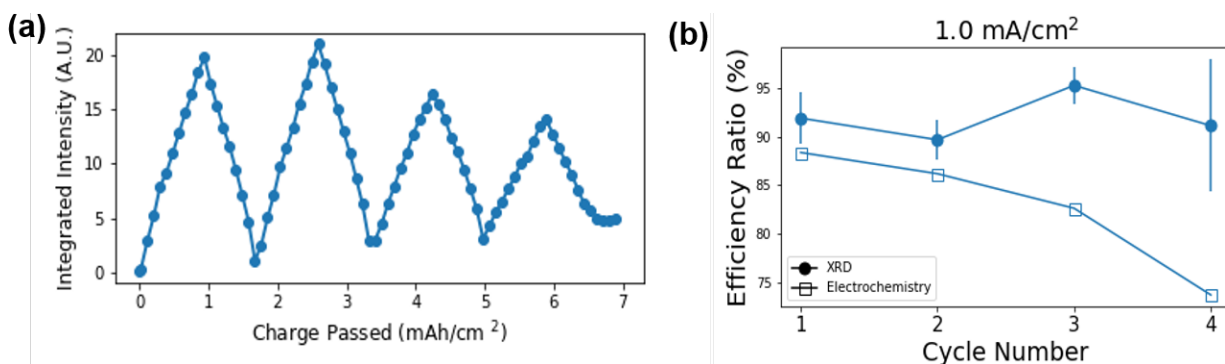
Figure II-631. Representative results from in situ XRD measurements of Li plating onto copper substrate. (a) Integrated intensity of Li (110) XRD peak vs. time passed throughout four Li plating and stripping cycles at 1.0 mA cm^{-2} in 1 M LiPF$_6$ in EC/DMC. (b) Corresponding electrochemical (Coulombic) and XRD efficiencies (ratio of amount stripped to plated).

For determination of Li‖S cell design a liquid-solid composite electrolyte was studied. The average operating voltage at the C/3 rate and C/5 rate discharge was determined by a finite element model using COMSOL, with the discharge capacity limited in the range from 800 to 1100 mAh g^{-1} sulfur. As with the Li‖NMC622 cells the computational results were compared to experimental data to ensure close alignment between the real and computed designs. After reaching agreement a parametric method was used with various electrode thicknesses and porosities to determine routes capable of achieving a 500 Wh kg^{-1} cell design. These calculations indicate that there are multiple challenges for the Li‖S system to achieve 500 Wh kg^{-1}. Key technical hurdles include solid state ionic conductivity (for the solid component of the electrolyte) and total amount of electrolyte. Activities are currently underway to understand how to mitigate these limitations for the cell design.

The other set of key activities for Keystone 3 in FY2017 was on characterization of both high Ni NMC cathodes and Li metal at BNL, UCSD and SLAC. For the cathodes, activities focused on understanding the effect of high Ni in the NMC if the Ni is increased to 90% or higher. Local structure for 11 different NMC phases was performed using multiple methods to understand relationships between the samples. In addition, depth profiling of cathodes with thicknesses up to 200 μm (in coordination with Keystone 2) also occurred showing distinct differences in performance and charging/discharging efficiency as a function of depth. Both cathode activities will play a prominent role in understanding how to effectively use high Ni NMC and to effectively use thick electrodes for high energy density Li‖NMC cells.

With regard to Li metal an emerging focus is on the quantification of Li loss and the identification of inactive Li. Across multiple studies spanning keystone areas this was identified as a significant issue that needs to be addressed. Early evaluation using multiple techniques including cryo-TEM, XRD and electrochemical methods has identified that there are key factors associated with both the initial deposition of Li metal on electrodes as well as significant evolution in performance which is not directly correlated with other measurements such as CE. Future activities will be more directly focused on this area and on improving understanding of the relationship between lean electrolyte and limited Li to support the development of pouch cell designs beyond 300 Wh kg^{-1}.

Based on the calculation, testing and characterization of electrode materials, coin cells and pouch cells, Battery500 established standard testing protocols for both NMC and S cells for FY2018, which specific the amount of cathode, anode and electrolyte materials, as well as the formulation procedure and charge discharge rates. All team members are required to use the standard testing protocols when reporting results related to the cell level specific energy and/or the cycling life of the cells and/or electrode materials.

Conclusions

Established the criteria to achieve the 500 Wh kg^{-1} goal for both high Ni NMC and sulfur systems.

Demonstrated progress on the Keystone Projects:

- Developed synthetic approaches, doping methods and surface coatings to stabilize high Ni NMC cathodes exhibiting ~220 mAh g^{-1} with superior cyclability, rate capability, and power density compared to the control cell.

- Developed several electrolytes with greatly improved stability towards both NMC cathode and Li metal anode with Coulombic efficiency higher than 98%.

- Developed new concepts on self-healing polymers and ordered architectures to control lithium metal deposition.

- Developed new perovskite solid state electrolytes with good Li ion conductivity.

- Demonstrated good progress on electrode architectures and full cell performance.

- Established standard testing protocols and requirements for using the standard testing protocols.

Key Publications

1. A. Pei, G. Zheng, F. Shi, Y. Li, and Y. Cui, "Nanoscale nucleation and growth of electrodeposited lithium metal", *Nano Lett.*, 2017, **17**, 1132-1139.

2. J. Zheng, M. H. Engelhard, D. Mei, S. Jiao, B. J. Polzin, J.-G. Zhang, and W. Xu, "Electrolyte additive enabled fast charging and stable cycling lithium metal batteries", *Nature Energy*, 2017, **2**, 17012.

3. D. Lin, Y. Liu, and Y. Cui, "Reviving the lithium metal anode for high-energy batteries", *Nature Nanotech.*, 2017, **12**, 194-206.

4. W. Liu, W. Li, D. Zhuo, G. Zheng, Z. Lu, K. Liu, and Y. Cui, "Core-shell nanoparticle coating as an interfacial layer for dendrite-free lithium metal anodes", *ACS Central Sci.*, 2017, **3**, 135-140.

5. K. Liu, A. Pei, H. R. Lee, B. Kong, N. Liu, D. Lin, Y. Liu, C. Liu, P.-C. Hsu, Z. Bao, and Y. Cui, "Lithium metal anodes with an adaptive 'solid liquid' interfacial protective layer", *J. Am. Chem. Soc.*, 2017, **139**, 4815–4820.

6. W. Li, A. Dolocan, P. Oh, H. Celio, S. Park, J. Cho, and A. Manthiram, "Dynamic behavior of interphases and its implication on high-energy-density cathode materials in lithium-ion batteries", Nature Commun., 2017, **8**, 14589.

7. S. B. Lee, C. Pathak, V. Ramadesigan, W. Gao, and V. R. Subramanian, "Direct, efficient, and real-time simulation of physics-based battery models for stand-alone PV-battery microgrids", *J. Electrochem. Soc.*, 2017, **164**, E3026-E3034.

8. Y. Xu, E. Hu, K. Zhang, X. Wang, V. Borzenets, Z. Sun, P. Pianetta, X. Yu, Y. Liu, X.-Q. Yang, and H. Li, "In situ visualization of state-of-charge heterogeneity within a licoo$_2$ particle that evolves upon cycling at different rates", *ACS Energy Lett.*, 2017, **2**, 1240-1245.

9. S. Rustomji, Y. Yang, T. K. Kim, J. Mac, Y. J. Kim, E. Caldwell, H. Chung, and Y. S. Meng, "Liquefied gas electrolytes for electrochemical energy storage devices", *Science*, 2017, **356**, 1351.

10. W. Li, B. Song, and A. Manthiram, "High-voltage positive electrode materials for lithium-ion batteries," *Chem. Soc. Rev.*, 2017, **46**, 3006-3059.

11. W. Li, U.-H. Kim, A. Dolocan, Y.-K. Sun, and A. Manthiram, "Formation and inhibition of metallic lithium microstructures in lithium batteries driven by chemical crossover", *ACS Nano*, 2017, **11**, 5853–5863.

12. K. Park and J. B. Goodenough, "Dendrite-suppressed lithium plating from a liquid electrolyte via wetting of Li_3N," *Adv. Energy Mater.*, 2017, **7**, 1700732.

13. D. Lin, J. Zhao, J. Sun, H. Yao, Y. Liu, K. Yan, and Y. Cui, "Three-dimensional stable lithium metal anode with nanoscale lithium islands embedded in ionically conductive solid matrix", *Proc. Natl. Acad. Sci. U.S.A.* 2017, **114**, 4613-4618.

14. H. Wang, D. Lin, Y. Liu, Y. Li, and Y. Cui, "Ultrahigh-current density anodes with interconnected Li metal reservoir through overlithiation of mesoporous AlF_3 framework", *Sci. Adv.* 2017, **3**, e1701301.

15. H. Lee, X. Ren, C. Niu, L. Yu, M. H. Engelhard, I. Cho, M.-H. Ryou, H. S. Jin, H.-T. Kim, J. Liu, W. Xu, and J.-G. Zhang, "Suppressing lithium dendrite growth by metallic coating on separator", *Adv. Funct. Mater.*, 2017, 1704391. DOI: 10.1002/adfm.201704391

16. B. D. Adams, J. Zheng, X. Ren, W. Xu, and J.-G. Zhang, "Accurate determination of coulombic efficiency for lithium metal anodes and lithium metal batteries", *Adv. Energy Mater.*, 2017, 1702097. DOI: 10.1002/aenm.201702097 (Partially supported by Battery500)

17. K. Shah, N. Balsara, S. Banerjee, M. Chintapalli, A. P. Cocco, W. K. S. Chiu, I. Lahiri, S. Martha, A. Mistry, P. P. Mukherjee, V. Ramadesigan, C. S. Sharma, V. R. Subramanian, S. Mitra, and A. Jain, "State of the art and future research needs for multiscale analysis of Li-ion cells", *J. Electrochem. En. Conv. Stor.*, 2017, **14**, 020801.

18. X. Wang, M. Zhang, J. Alvarado, S. Wang, M. Sina, B. Lu, J. Bouwer, W. Xu, J. Xiao, J.-G. Zhang, J. Liu, and Y. S. Meng, "New insights on the structure of electrochemically deposited lithium metal and its solid electrolyte interphases via cryogenic TEM", *Nano Lett.*, 2017, **DOI:** 10.1021/acs.nanolett.7b03606.

III.   Testing and Analysis

III.A   Cost Assessments and Requirements Analysis

III.A.1   BatPaC Model Development (Argonne National Laboratory)

Shabbir Ahmed, Principal Investigator
Argonne National Laboratory
9700 S. Cass Avenue
Argonne, IL 60439
Phone: 630-252-4553
E-mail: ahmeds@anl.gov

Samuel Gillard, Technology Manager
U.S. Department of Energy
Phone: 202-287-5849
E-mail: Samuel.Gillard@ee.doe.gov

Start Date: October 1, 2012   End Date: October 31, 2018
Total Project Cost: $700,000   DOE share: $700,000   Non-DOE share: $0

Project Introduction

A performance and cost model (BatPaC) was developed at Argonne to design automotive Li-ion batteries that can meet the specification of a given vehicle, and then to estimate the cost of manufacturing that battery. It is the product of long-term research and development at Argonne through sponsorship by the U.S. Department of Energy.

Over a decade, Argonne has developed methods to design Li-ion batteries for electric-drive vehicles based on modeling with Microsoft® Office Excel spreadsheets. These design models provided all the data needed to estimate the annual materials requirements for manufacturing the batteries being designed. This facilitated the next step, which was to extend the effort to include modeling of the manufacturing costs of the batteries.

The BatPaC model has been peer reviewed and is available on the web. It captures the interplay between design and cost of Li-ion batteries for transportation applications. Moreover, BatPaC is the basis for the quantification of battery costs in U.S. EPA and NHTSA 2017-2025 Light-Duty Vehicle Technical Assessment. This assessment is then used to determine what mileage (i.e., CAFE) and CO_2 emission standards are optimal from a cost-benefit analysis.

Objectives

To develop and utilize efficient simulation and design tools for lithium ion batteries to predict

- Overall and component mass and dimensions
- Cost and performance characteristics when manufactured in large volume

Approach

The battery pack design and cost calculated in BatPaC represent projections for a specified level of annual battery production (10,000-500,000). As the goal is to predict the future (~5 years) cost of manufacturing batteries, a mature manufacturing process is assumed. The model designs a manufacturing plant with the sole purpose of producing the battery being modeled. The assumed battery design and manufacturing facility are based on common practice today but also assume some problems have been solved to result in a more efficient production process and a more energy dense battery. Our proposed solutions do not have to be the same

methods used in the future by industry. We assume the leading battery manufacturers, those having successful operations in the near future, will reach these ends by some means.

For a selected battery chemistry, BatPaC solves the governing equations to determine the size of each layer, cell, and modules that make up the battery pack that can meet the desired requirements for power and energy. This allows the calculation of the mass of each material, the volume of the components, and the heat removal needed during discharge. The cost of the pack is then estimated based on a predefined manufacturing process.

Current effort is directed at

- Improving the design capability by including correlations derived from continuum modeling and updating the default material properties to reflect recent experimental and industrial performance data

- Reducing the uncertainty of model predictions by setting up independent models of the manufacturing processes

- Validating the results through discussions with manufacturers and component developers.

- Updating the cost of materials used in BatPaC calculations.

Collaboration

- Oak Ridge National Laboratory, Idaho National Laboratory, National Renewable Energy Laboratory, B&W-MEGTEC

Results

Key Accomplishments

- An analysis was conducted to compare the estimated costs of cells and packs for different electrode chemistries

- The model was revised to enable design for fast charge capability and was used to estimate the impact of fast charging lithium ion batteries

- A drying model has been developed to gain insight into the effects of electrode drying conditions

- The default material properties were improved to reflect recent results obtained from cell testing during teardowns by commercial companies

Cell Cost vs. Electrode Combinations

The BatPaC model was used to estimate the future cost of cells for automotive battery packs for a number of electrode combinations. The comparisons were made on the basis of a pack with an energy storage capacity of 100 kWh$_{Total}$ (85 kWh$_{Useable}$), 300 kW, where the pack was designed with 168 cells and 315 V. The price of the materials used in the cells are as shown in Table III-1. The packs are produced in a battery manufacturing plant at a production volume of 100,000 packs per year.

Table III-1: Electrode material costs to estimate the cost of battery packs.

Materials	Price	
NMC333	19.00	$/kg
NMC622	18.50	$/kg
LMRNMC	18.50	$/kg
Sulfur	5.00	$/kg
OxideSpinel	8.00	$/kg
Carbon	6.80	$/kg
Binder PVDF	10.00	$/kg
Binder Solvent (NMP)	3.20	$/kg
Graphite	15.00	$/kg
Graphite-Silicon	25.00	$/kg
Silicon	25.00	$/kg
Lithium	100.00	$/kg
Magnesium	4.00	$/kg
Carbon Black	6.80	$/kg
Binder	10.00	$/kg
Positive Current Collector	0.30	$/m²
Negative Current Collector	1.20	$/m²
Separator	1.20	$/m²
Electrolyte	17.00	$/L

The prices of the cells shown in Figure III-1 represent best case projections where it is assumed that the problems with the electrode chemistries have been resolved, that performance is not limiting, and the manufacturing process has matured. The graphite-NMC333 combination is estimated to cost $146 per kWh$_{Useable}$, where the cost of the cathode and the anode materials contribute $40 and $16, respectively. The cell costs are lowered with lower cobalt content (NMC622, LMRNMC). The introduction of lithium in the anode escalates the price but is offset by the lower cost of sulfur anodes. It is notable that many of the combinations in the right side of the figure have much developmental challenges, which if/when resolved, offer the opportunity for lower cost cells.
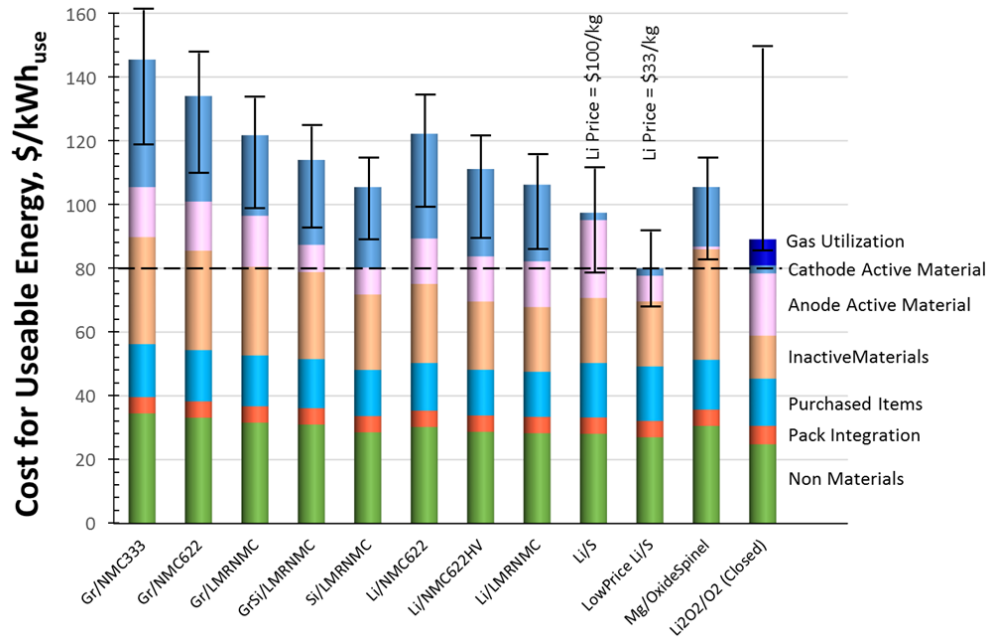
Figure III-1. Estimated costs of cells in automotive battery packs with different combination of electrodes. The packs are rated for 100 kWh$_{Total}$ (85 kWh$_{Useable}$), 300 kW, 315 V, 168 cells, and produced at a plant volume of 100K packs/year

Fast Charging

The BatPaC model algorithm was modified to allow the electrode thickness to be determined by the most limiting constraint among (i) the sustained discharge and (ii) the maximum allowable current density (MACD) for fast charging. Earlier studies have suggested that the cells lose their capacity rapidly when charged at certain current densities, e.g., 4.0 mA/cm^2 [1]. A study of the added constraint of fast charging and its impact on the cost of the cells was conducted. The study was based on a pack rated for 100 kWh$_{Total}$, 85 kWh$_{Useable}$, 300 kW, 315 V, from 168 cells. The cell cost was estimated for a plant production volume of 100,000 packs per year.

Fast charging of a cell is challenged by deactivation caused by lithium deposition in the anode and / or rapid temperature rise to above acceptable limits. BatPaC designs the electrodes to prevent the lithium deposition scenario by limiting the current density to a maximum allowable value. The model's heat balance calculations estimate the heat generated and therefore the temperature rise in the cell under adiabatic conditions. The designed packs have coolant flows and a more rigorous analysis is appropriate to address the heat transfer from the cell center to the coolant channels at the module wall.

The current needed to raise the state of charge (SOC) of a cell increases inversely with the time available. Setting a limit on the current density requires increase in the cell area to process the required current, i.e., the electrode becomes thinner. Figure III-2 shows the relationship between the charging time allowed to raise the SOC by 80% and the anode thickness. At charging times greater than 59 minutes, the curve is flat because in this region the anode thickness is not limited by the MACD but rather by the sustained power requirement. At less than 59 minutes, where the design is MACD-limited, the anode becomes progressively thinner, reaching 20 microns at ~10 minutes. Thin electrodes and larger areas mean that the cells require more inactive materials such as the current collectors, separators, etc., which increase the size of the cells. These additions increase the cost and is reflected in the non-linear trend of the cost curve in Figure III-2. At 10 minutes, the cost of the cell is $181 per kWh$_{Total}$ ($213 per kWh$_{Useable}$). As mentioned earlier, faster charging to achieve a given recharge requires a larger current and therefore a more powerful charging infrastructure. Figure III-3 plots the charger power required to recharge the cells in the pack as a function of the charging time. In order to raise the cell SOC by 80% in 10 minutes will require a charger power of ~550 kW.
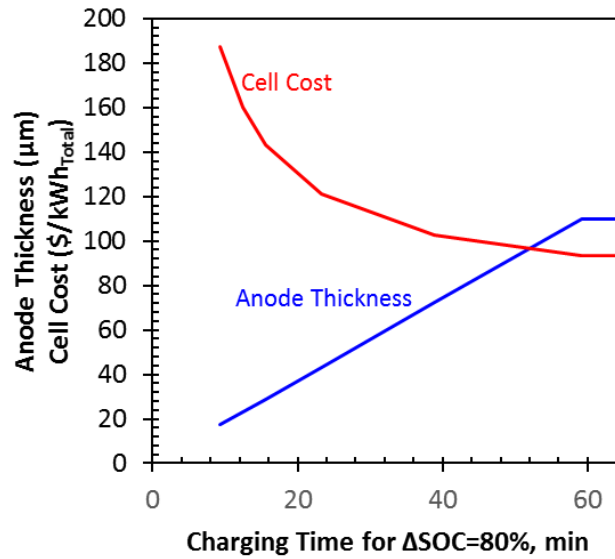
Figure III-2. Effect of charging time on anode thickness and cell cost. ΔSOC=80%
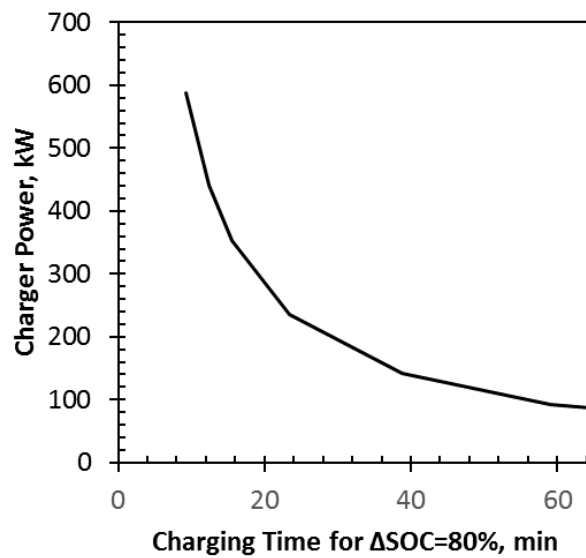

Figure III-3. Effect of charging time on charger power requirement. ΔSOC=80%

For the above simulations the maximum allowable current density was set at 4 mA/cm^2. With continuing development of the anode material it is likely the anode layer will be able to tolerate higher current densities without lithium plating. Figure III-4 shows the effect of the MACD on the anode thickness, the post-charge cell temperature, and the cell cost for charging times of 20, 15, and 10 minutes. In Figure III-4(a) for the 20 minute charging time, the anode layer can be as thick as 110 microns where it is limited by the sustained power requirement (and not by the MACD) at MACD > 11.9 mA/cm^2. For the 15 minute charge, the corresponding MACD is 15.8 mA/cm^2, while for the 10 minute charge that point is at a MACD $\gg$ 16 mA/cm^2. Since the amount of inactive materials increase with thinner electrodes (sloping part of the curves), the cell mass increases at lower MACD.
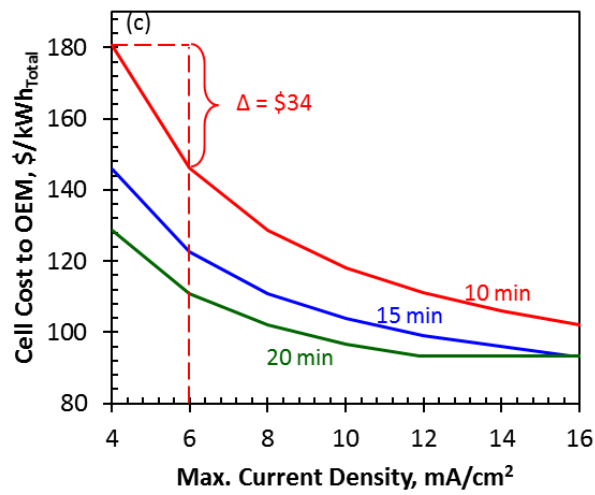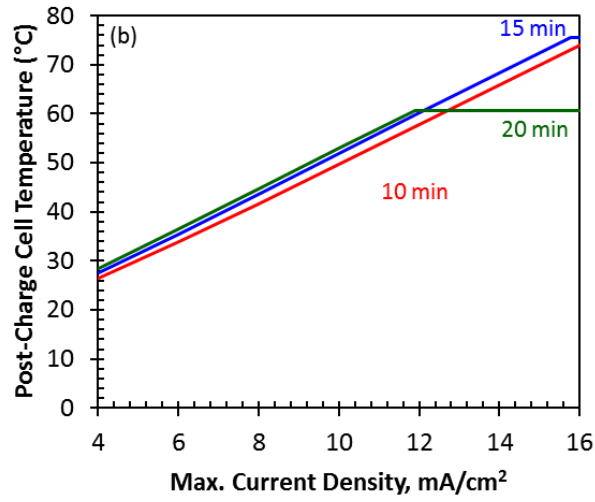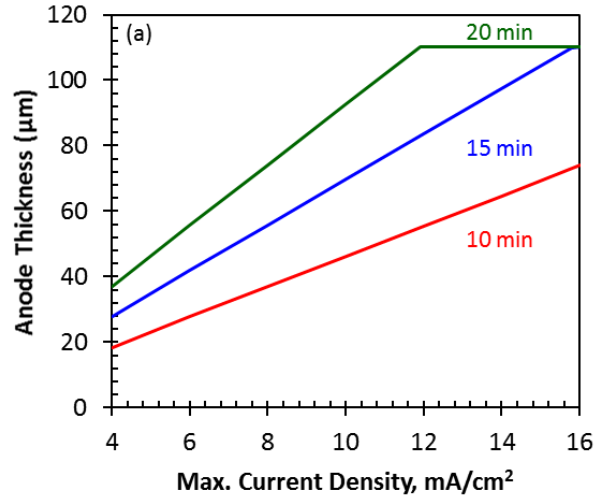
Figure III-4. Effect of the maximum allowable current density (MACD) on anode thickness, cell temperature, and cell cost. ΔSOC=80%

Figure III-4(b) shows the effect of the MACD on the post-charge cell temperature (assuming the cells were at 10°C at the beginning of the charge and there is no heat removal). The current needed for a given combination of charging time and ΔSOC=80% is constant. However, in the region to the left of the knee, the final cell temperature is lower at decreasing MACD, because the cells have thinner electrodes but larger cell mass to absorb the generated heat. The region to the right of the knee is flat because here the anode thickness remain constant (no longer determined by the MACD constraint) and therefore the thermal mass remains constant.

Figure III-4(c) shows that the cells cost more at MACD values to the left of the knee because the thinner cells require additional inactive materials. The shorter charging times require more current flow, which when combined with the MACD constraint, requires still thinner electrodes. The net result is that the costs increase sharply as the MACD and the charging times are reduced. For the case of a 10 minute charge at a MACD of 4 mA/cm^2, the cells cost \$181/kWh$_{Total}$. Relaxing the charging time from 10 minutes to 15 minutes can reduce the cost of the cells by \$34/kWh$_{Total}$.

Solvent Drying

A mathematical model was set up to study the drying of the solvent n-methyl pyrrolidone (NMP) from the cathode coating. The base scenario was the drying of a 150-micron thick electrode layer packed with 10-micron particles, 60 wt.% solvent content, with flowing air at 95°C as the drying medium. Solution of the model equations reveal that the electrode layer reaches the air temperature within a fraction of a second but the time required for drying is 54 seconds, where drying is assessed to be complete when the solvent content drops to 0.01 wt.%. Figure III-5 shows the solvent content (liquid + vapor) to drop sharply initially and then more slowly because of mass transfer limitations. The drying rate, defined as the rate of solvent leaving the electrode layer, is seen to show a similar trajectory. It is interesting that 50% of the solvent is removed in 10 seconds and 90% in 30 seconds, but to remove the remaining 10% of the solvent it requires 24 seconds or 45% of the total drying time.
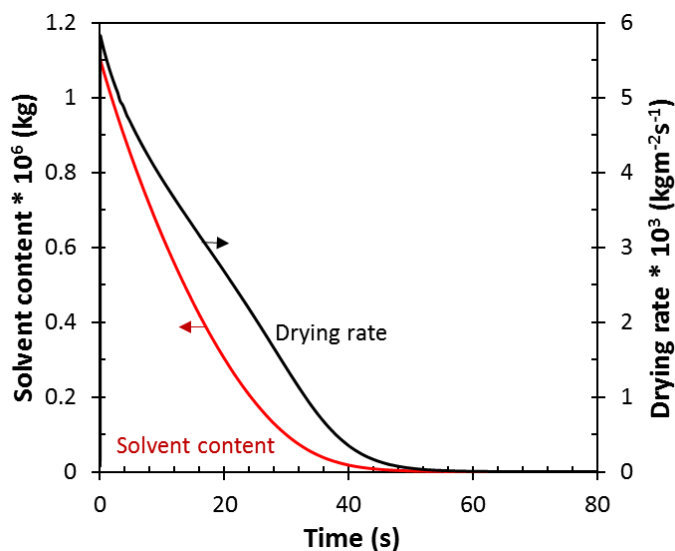
Figure III-5. Solvent content in electrode layer and the drying rate as a function of time.
150 µm layer, 95°C air temperature

A comparison of the drying rates for NMP and water (Figure III-6) shows that even though the latter has a latent heat of vaporization that is 4.5 times that of NMP on a mass (kg) basis, and a higher specific heat, the water dries almost 4 times faster than NMP. This is possibly due to the much higher vapor pressure of water at the simulated temperature of 95°C.
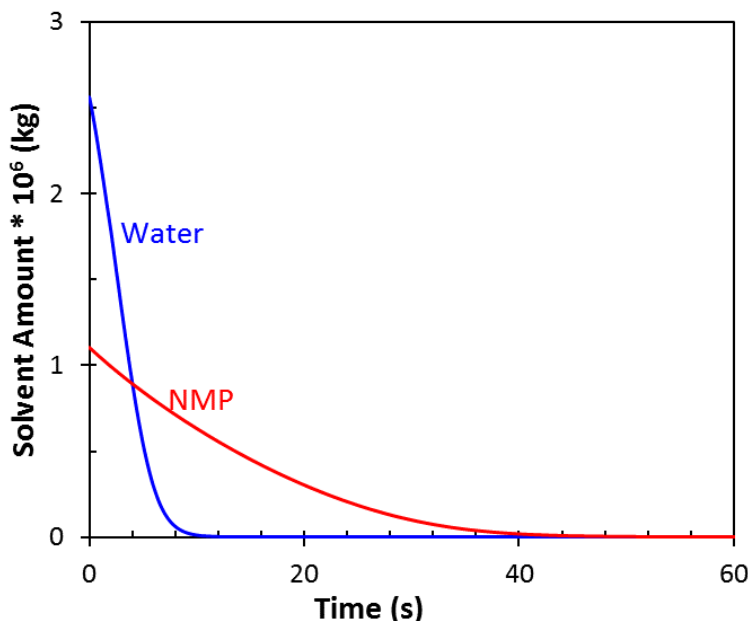
Figure III-6. Comparison of drying of electrode layer with NMP and water solvents. 150 μm layer, 95°C air temperature. The electrode was loaded with the same volume of solvent

Conclusions

The BatPaC model has been improved to expand the capabilities and fidelity of the model. These include

- Updates on the electrode design calculations and default property and material cost data

- Revision of the calculations for the fast charging designs

BatPaC and an independent drying model were exercised to gain a better understanding of key processes in the manufacturing of the lithium ion cells.

- A study was conducted to compare the cell costs using different electrode combinations.

- Low allowable current density (to prevent lithium deposition) and short charging times limit the electrode thickness, increasing the mass of inactive materials which contribute to higher cell costs.

- A mathematical model of the solvent drying process indicates that the last 10% of the solvent removal takes up nearly 50% of the drying time. For one set of conditions, a comparison of NMP and water drying indicates that the drying time can be significantly reduced if water can be used as the solvent.

Key Publications

1. S. Ahmed, P.A. Nelson, C. Michelbacher, "Extreme fast charging and battery cost implications," presented at the 2017 DOE Vehicle Technologies Office Annual Merit Review and Peer Evaluation Meeting, Washington, DC, June 5-9, 2017

2. S. Ahmed, P.A.Nelson, K.G. Gallagher, N. Susarla, D.W. Dees, "Cost and energy demand of producing nickel manganese cobalt cathode material for lithium ion batteries," Journal of Power Sources 342 (2017) 733-740

3. D.L. Wood, J.D. Quass, J. Li, S. Ahmed, D. Ventola, C. Daniel, "Technical and economic analysis of solvent-based lithium-ion electrode drying with water and NMP," Drying Technology, May 2016.

4. S. Ahmed, I. Bloom, A.N. Jansen, Paul A. Nelson, *et. al.*, " Enabling fast charging – A battery technology gap assessment," Journal of Power Sources 367 (2017) 250-262

5. N. Susarla, S. Ahmed, D.W. Dees, "Modeling and analysis of solvent removal during Li-ion battery electrode drying," submitted to the Journal of Power Sources.

References

1. K. Gallagher, S. Trask, C. Bauer, T. Woehrle, S. Lux, M. Tschech, P. Lamp, B. Polzin, S. Ha, B. Long, Q. Wu, W. Lu, D. Dees and A. Jansen, "Optimizing Areal Capacities through Understanding the Limitations of Lithium-Ion Electrodes," *Journal of The Electrochemical Society,* vol. 163(2), pp. A138-A149, 2016.

III.B Battery Testing

III.B.1 Battery Performance and Life Testing (ANL)

Ira Bloom, Principal Investigator
Argonne National Laboratory
9700 South Cass Avenue
Argonne, IL 60439
Phone: 630-252-4516
E-mail: ira.bloom@anl.gov

Samuel Gillard, Technology Manager
U.S. Department of Energy
Phone: 202-287-5849
E-mail: Samuel.Gillard@ee.doe.gov

Start Date: October 1, 2017   End Date: September 30, 2022
Total Project Cost: $1,800,000   DOE share: $1,800,000   Non-DOE share: $0

Project Introduction

Batteries are evaluated using standard tests and protocols that are transparent to technology. These protocols are based on those developed by the USABC [1-4].

Objectives

- Provide DOE, USABC, and battery developers with reliable, independent and unbiased performance and life evaluations of cells, modules and battery packs.

- Benchmark battery technologies that were not developed with DOE/USABC funding to ascertain their level of maturity.

Approach

The batteries are evaluated using standardized and unbiased protocols, allowing a direct comparison of performance within a technology and across technologies. For those tested using the USABC methods, the performance of small cells can be compared to that of larger cells and full-sized pack by means of a battery scaling factor [1, 2]. The results described below arose from work in two different areas, 12-V start/stop testing and US-China battery test protocol comparisons.

Results

Batteries, which were fabricated during programs with developers, were sent to Argonne for evaluation. Here, the purpose of evaluation is two-fold: to provide confirmation of other test information and to provide an independent assessment of the state of the given battery technology, that is, how does it compare to the USABC [1-4] and/or project goals? A list of program deliverables associated with Argonne is given in Table III-2, along with their status. One of these deliverables is discussed further below.

Table III-2: Status of Deliverables for Testing

Developer	Sponsor	Quantity x System Level	Application	Status
JCI	USABC	9 x Cell	PHEV-20	complete
JCI	DOE FOA	45 x Cell	PHEV-20	complete
Leyden	USABC	30 x Cell	12-V S/S	complete
Maxwell	USABC	26 x Cell	12-V S/S	complete
Maxwell	USABC	1 x Module	12-V S/S	on-going
24-M	USABC	6 x Cell	EV	complete
24-M	USABC	18 x Cell	EV	on-going
24-M	DOE FOA	14 x Cell	EV	on-going
Xerion	USABC	21 x Cell	PHEV-20	expected
3M	2013 ABR	12 x Cell	EV	complete
Navitas	DOE FOA	24 x Cell	EV	on-going
Navitas	DOE FOA	13 x Cell	EV	complete
Tiax	2013 ABR	26 x Cell	EV	complete
ANL (J. Zhang)	DOE FOA	15 x Cell	EV/PHEV	complete
Seeo	DOE	6 x Cell	EV	complete
LGChem	DOE	10 x Cell	PHEV-40	on-going
XALT	DOE FOA	24 x Cell	EV	on-going
Wildcat	DOE	20 x Cell	EV	complete
WPI	USABC	80 x Cell	Recycling/PHEV-20	expected
SiNode	USABC	9 x Half cell	EV	on-going
SiNode	USABC	8 x Cell	EV	on-going
SiNode	USABC	20 x Cell	EV	expected
Microcure	DOE	6 x Cell	EV	complete
Farasis	USABC	68 x Cell	Recycling/PHEV-20	expected
Daikin	DOE	9 x Cell	EV/PHEV	on-going
Celgard	USABC	6 x Cell	EV	expected
ANL-CAMP	DOE	15 x half cell	XFC-GITT	expected
ANL-CAMP	DOE	15 x Cell	XFC-GITT	expected

12-V Start/Stop

Lithium-ion batteries are being proposed for many automotive applications, such as use in 12-V start/stop vehicles. Here, the engine is turned off instead of idling while the vehicle is stopped, reducing fuel costs and pollution. It's ideal use would be where the vehicle spends a lot time in city traffic.

Cells containing $LiMn_2O_4/Li_4Ti_5O_{12}$ (LMO/LTO) chemistry were tested using the procedures and methods outlined in the USABC 12-V Start/Stop manual [4]. Here, the cells were tested for calendar life at 30, 40, 50 and 60°C and for cycle life at 30°C. Reference performance tests (RPTs) were used to gauge changes in cell performance at 30°C. RPTs were conducted at the beginning of testing and then every 32 days or 23,040 cycles for the calendar and cycle life cells, respectively. The RPT consisted of a C/1 capacity measurement and the hybrid pulse-power capability test at the low-current values. The results of the RPTs were used to determine trends in cell performance decline.

In the calendar aging experiment at 30 and 40°C, the relative capacity initially declined slightly, but, with continued testing, seemed to reach a steady state, as shown in Figure III-7. However, the cells tested at 50 and 60°C exhibited large changes in relative capacity as the test continued. Most likely, the rapid decrease in relative capacity was caused by gas formation in the cells.

Figure III-8 shows the trend in relative capacity with cycle count for the cycling experiment. Here, the relative capacity seemed to reach a steady value of ~0.97 after ~92,160 cycles.
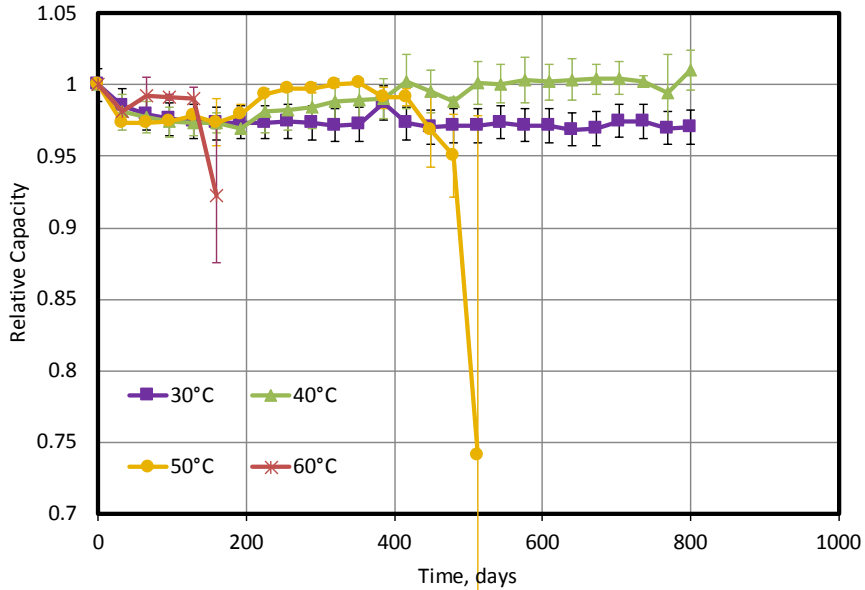

Figure III-7. Average relative capacity vs. time for the calendar life cells. The error bars represent ±1σ
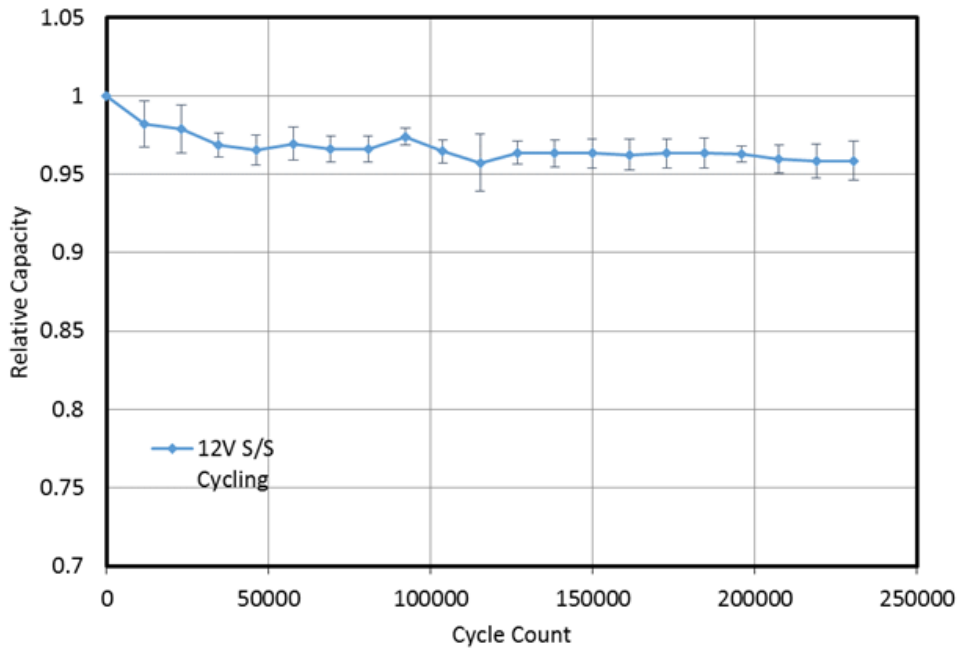
Figure III-8. Average relative capacity vs. time for the cycle life cells. The error bars represent ±1σ

Plots of the change in average relative resistance at 50% SOC (2.496 V) are shown in Figure III-9 and Figure III-10. The resistance growth in the calendar life cells at 30 and 40°C displayed what appeared to be linear-with-time kinetics. With this assumption, the slopes of these best-fit lines were 5.97×10^{-4}/day (r^2=0.97) and 9.84×10^{-4}/day (0.84), respectively. However, at 50 and 60°C, the rates of resistance increase were nonlinear. At these temperatures, the data seem to follow a linear-with-time trend followed by a period of rapid increase. In the 50°C case, the linear portion was from 0 to 352 days and that for the 60°C data, 0 to 128 days. The slopes of the lines in the regions are 2.62×10^{-3}/day (r^2=0.98) and 7.68×10^{-3}/day (r^2=0.99). Indeed, using these values shows that resistance increase process seems to follow Arrhenius-like kinetics with an activation energy of 72.2 kJ/mol.
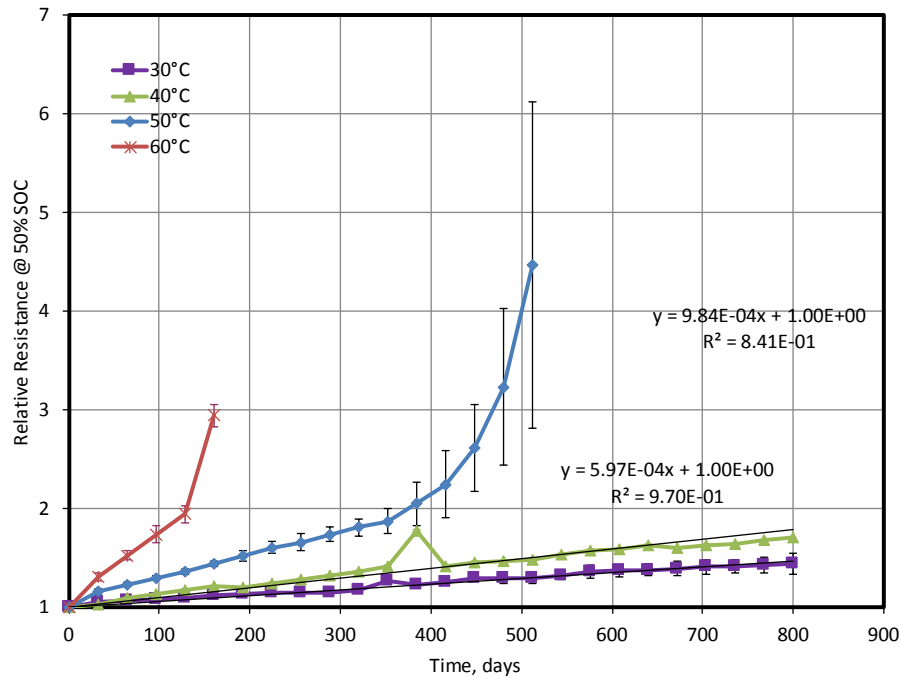

Figure III-9. Average relative resistance vs. time for the calendar life cells. The error bars represent ±1σ
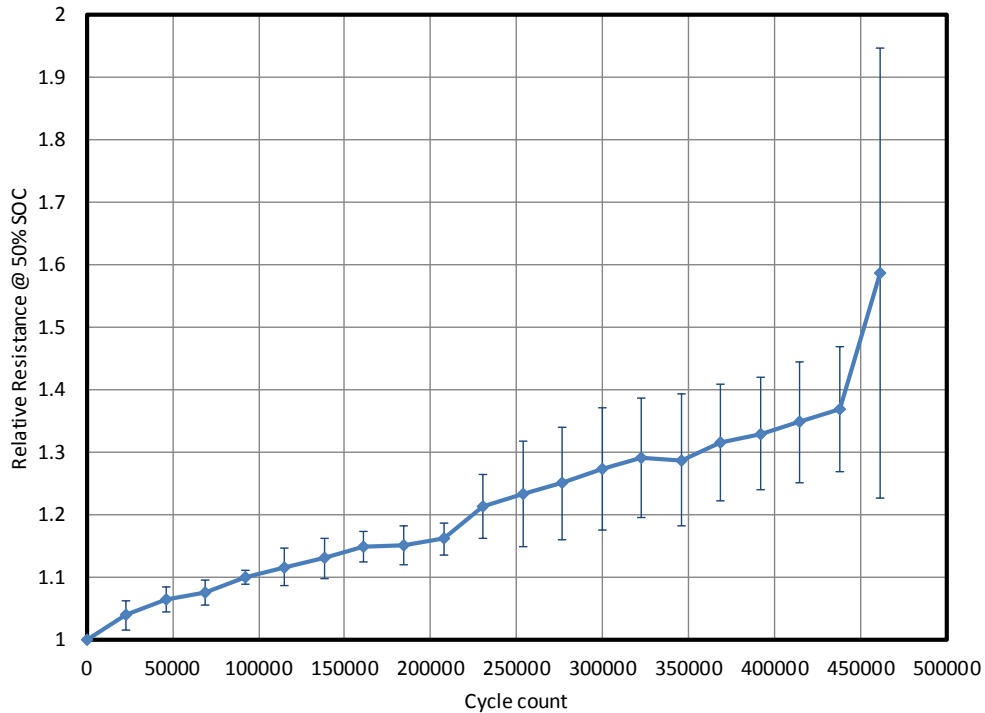
Figure III-10. Average relative resistance vs. count for the cycle life cells. The error bars represent ±1σ

Examining the data in Figure III-10 shows that the points before 437,760 cycles seem to follow a linear trend. Indeed, applying least-squares fitting to these points shows that the slope of the best-fit line is 8.72×10^{-7}/cycle (r^2=0.98).

Figure III-11a and Figure III-11b show the plots of relative power (1 s) vs. time for the calendar and cycle life cells, respectively. The data in Figure III-11a shows that the relative power of the 50 and 60°C cells falls sharply, possibly indicative of a cell near failure, at 448 and 128 days, respectively. Using the lower temperature data and the rest of the higher temperature data shows that power fade followed $at^{1/2}$ kinetics in this temperature range. The values of a were -8.70×10^{-3}/day (r^2=0.89), -1.36×10^{-2}/day (0.93), -2.36×10^{-2}/day (0.97), and -3.84×10^{-2}/day (0.99), respectively. Based on these values of the rate of power decrease, the degradation process seems to follow Arrhenius-like kinetics. The activation energy for the process was 41.9 kJ/mol. Similarly, the 1-s relative power data in Figure III-11b displays a sharp decline after about 420,000 cycles. Excluding the data after point shows that the remaining points can be fit to a line with a slope of -6.26×10^{-7}/cycle (0.97).
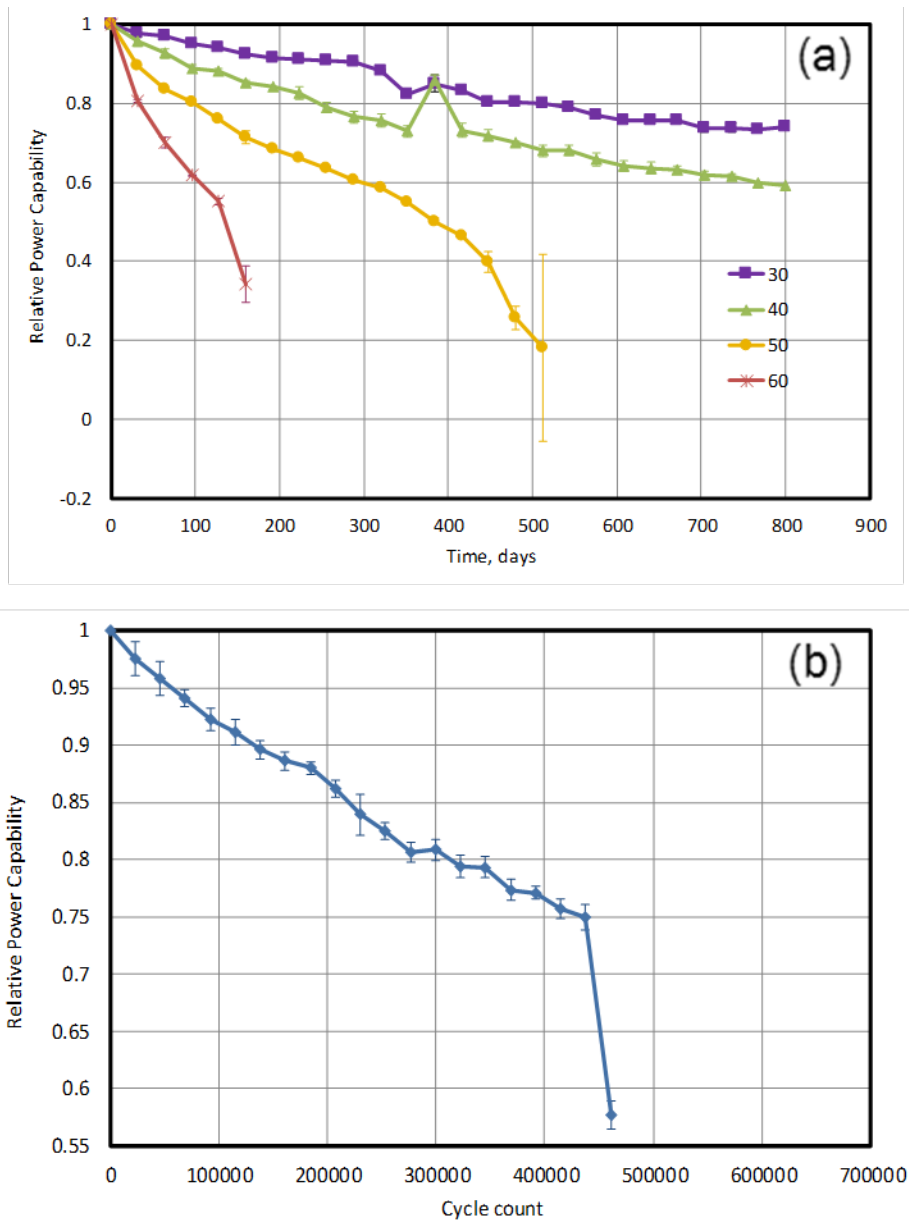
Figure III-11. (a) Relative power vs. time for the calendar life cells. The error bars represent ±1σ (b) Relative power vs. cycle count for the cycle life cells. The error bars represent ±1σ. σ

US-China Protocol Comparison: Fast Charge

The US and China have independently developed battery test protocols to track performance change with aging. On the surface, the test protocols appear to be different. The purpose of these experiments is to determine if the protocols produce different results, and, if they do, how different the results are. We previously reported that the battery aging protocols produce very similar data once certain parts of test are considered. For example, in testing for hybrid electric vehicle applications, the China cycling [5] and calendar tests use a single pulse at 50% DOD, while those used by the USABC use many pulses [1-4]. Once the differences were taken into account, the results were very similar [6]. We extended this study to evaluate fast-charge protocols using commercial LiFePO$_4$ cells.

As a starting point, we compared the aging characteristics of performing fast charging 100% of the time using a constant-current, constant-voltage charge (CC-CV) at 30°C to that used in China, which was the same protocol, but at 25°C. The charge rates in this study range from 1- to 6-C.

Figure III-12 and Figure III-13 show the trend in average relative capacity change with Ah throughput for the CC-CV and Chinese protocols, respectively. As expected, there was not much difference between the two figures since the test temperatures differed by only 5°C, at the low charge rates. There are differences in the performance degradation rates at the 4- and 6-C rates.
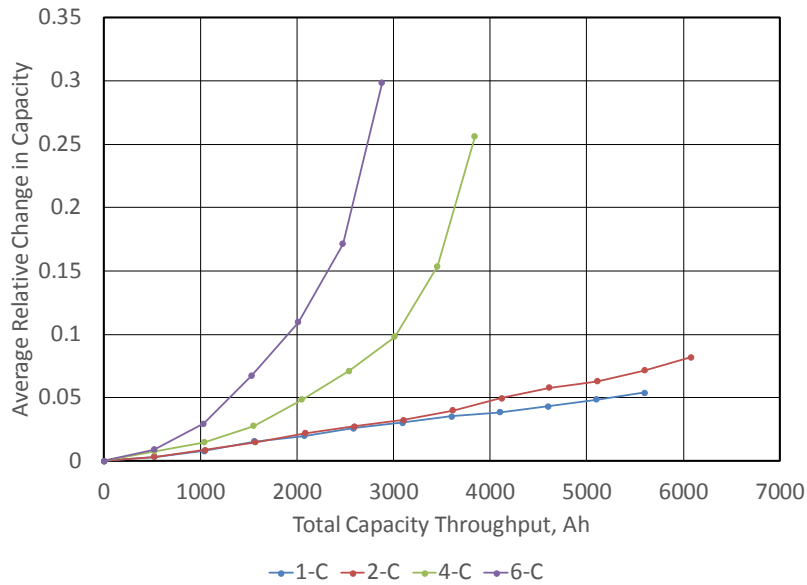

Figure III-12. Average change in relative capacity vs. total capacity throughput for cells tested using the CC-CV protocol
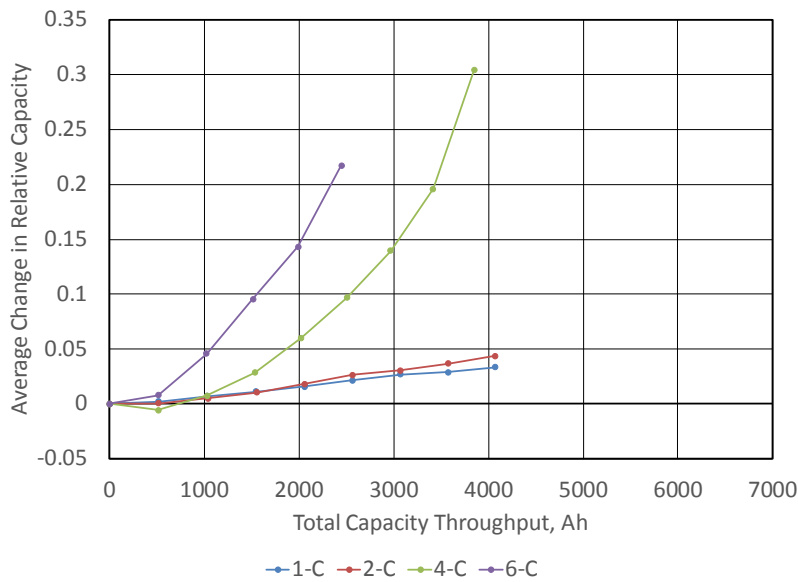

Figure III-13. Average relative capacity vs. total capacity throughput for cells tested using the China protocol

Significant differences between the test protocols was found during post-test examination of the cells. This is shown in Figure III-14.
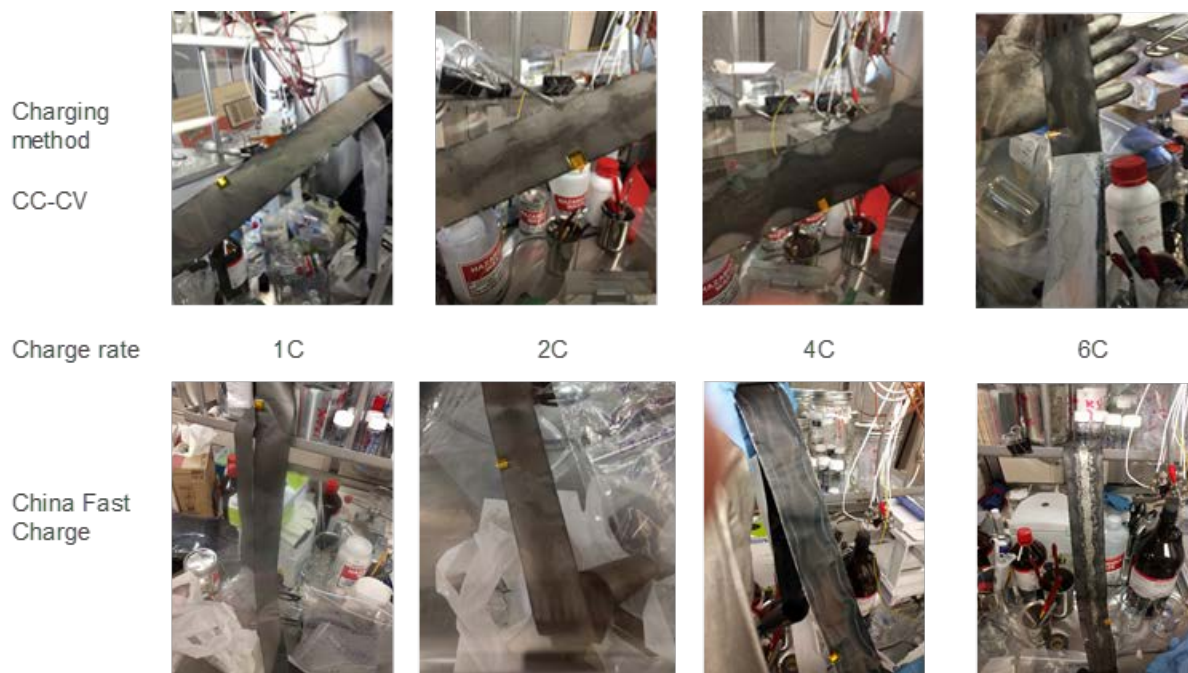

Figure III-14. Optical images of the negative electrodes taken during the post-test analysis of the fast-charge cells from the CC-CV and China test protocols

All images in Figure III-13 show signs of change in the negative electrode, which is based on graphite. The degree of change increases with increasing charge rate, as expected. At 6-C, the CC-CV anode appears to be just graphite, but that from the China protocol has a distinct greyish band running along the center line, which, most likely, is lithium metal. The post-test examination continues.

Conclusions

12-V Start/Stop

The power capability of cells containing LMO/LTO chemistry degraded ~26% over the course of 800 days at 30°C. In the cycle life test, the cells accrued 437,760 cycles before a sharp decline in performance was observed.

US-China Protocol Comparison: Fast Charge

The fast charge protocols used produced very similar changes in the electrochemical performance of the LiFePO$_4$ cells. The 5°C difference between them is enough to produce what appears to be lithium deposition on the anode in the China protocol case.

Key Publications

1. Fast charging of lithium-ion batteries: Effect of charge protocol. David C. Robertson, Nancy Dietz Rago and Ira Bloom, ABAA-10 meeting, Oct. 23-25, 2017, Oakbrook, IL

2. Enabling Fast Charging – A Technology Gap Assessment. Christopher Michelbacher, Shabbir Ahmed, Ira Bloom, Andrew Burnham, Barney Carlson, Fernando Dias, Eric J. Dufek, Andrew N. Jansen, Matthew Keyser, Anthony Markel, Andrew Meintz, Manish Mohanpurkar, Ahmad Pesaran, Don Scoffield, Matthew Shirk, Thomas Stephens, Tanvir Tanim, Ram Vijayagopal, and Jiucai Zhang, US DOE report, INL/EXT-17-41638, October 2017

3. Enabling Fast Charging – Introduction and Overview. Christopher Michelbacher, Shabbir Ahmed, Ira Bloom, Andrew N. Jansen, Tanvir Tanim, Eric J. Dufek, Ahmad Pesaran, Andrew Burnham, Richard B. Carlson, Fernando Dias, Keith Hardy, Matthew Keyser, Cory Kreuzer, Anthony Markel, Andrew Meintz, Manish Mohanpurkar, Don Scoffield, Matthew Shirk, Thomas Stephens, Ram Vijayagopal, and Jiucai Zhang, J. Power Sources, <u>367</u> (2017) 214-215.

4. Enabling Fast Charging – A Battery Technology Gap Assessment. Shabbir Ahmed, Ira Bloom, Andrew N. Jansen, Tanvir Tanim, Eric J. Dufek,Ahmad Pesaran, Andrew Burnham, Richard B. Carlson, Fernando Dias, Keith Hardy, Matthew Keyser, Cory Kreuzer, Anthony Markel, Andrew Meintz, Christopher Michelbacher, Manish Mohanpurkar, Paul A. Nelson, David C. Robertson, Don Scoffield, Matthew Shirk, Thomas Stephens, Ram Vijayagopal, and Jiucai Zhang, J. Power Sources, <u>367</u> (2017) 250-262

5. Enabling Fast Charging – A Vehicle Technology Gap Assessment. Andrew Meintz, Jiucai Zhang, Ram Vijayagopal, Cory Kreuzer, Shabbir Ahmed, Ira Bloom, Andrew Burnham, Barney Carlson, Fernando Dias, Eric J. Dufek, James Francfort, Andrew N. Jansen, Matthew Keyser, Anthony Markel, Christopher Michelbacher, Manish Mohanpurkar, Ahmad Pesaran, Don Scoffield, Matthew Shirk, Thomas Stephens, and Tanvir Tanim, J. Power Sources, <u>367</u> (2017) 216-227

6. Enabling Fast Charging – A Infrastructure Technology & Economics Gap Assessment. Andrew Burnham, Eric J. Dufek, Thomas Stephens, James Francfort, Christopher Michelbacher, Barney Carlson, Jiucai Zhang, Ram Vijayagopal, Fernando Dias, Manish Mohanpurkar, Don Scoffield, Matthew Shirk, Shabbir Ahmed, Ira Bloom, Andrew N. Jansen, Matthew Keyser, Cory Kreuzer, Anthony Markel, Andrew Meintz, Ahmad Pesaran, and Tanvir Tanim, J. Power Sources, <u>367</u> (2017) 237-249

7. Enabling Fast Charging – Battery Thermal Considerations. Matthew Keyser, Ahmad Pesaran, Qibo Li, Shriram Santhanagopalan, Kandler Smith, Eric Wood, Shabbir Ahmed, Ira Bloom, Eric Dufek, Matthew Shirk, Andrew Meintz, Cory Kreuzer, Christopher Michelbacher, Andrew Burnham, Thomas Stephens, James Francfort, Barney Carlson, Jiucai Zhang, Ram Vijayagopal, Keith Hardy, Fernando Dias, Manish Mohanpurkar, Don Scoffield, Andrew Jansen, Tanvir Tanim, Anthony Markel, J. Power Sources, <u>367</u> (2017) 228-236

References

1. FreedomCAR Battery Test Manual for Power-Assist Hybrid Electric Vehicles, DOE/ID-11069, October 2003.

2. FreedomCAR Battery Test Manual for Plug-In Hybrid Electric Vehicles, June 2010.

3. Electric Vehicle Battery Test Procedures Manual, Revision 2, January 1996.

4. Battery Test Manual for 12 Volt Start/Stop Vehicles, Rev. 1, May 2015, INL/EXT-12026503.

5. National Development and Reform Committee of the People's Republic of China, 2006, Lithium-Ion Batteries for Electric Vehicles, Auto Industry Standard QC/T 743-2006, China Plan Publishing Company, March, <u>http://www.d1ev.com/uploadfile/newsfile/20130819022042_547.pdf</u> (in Chinese).

6. David C. Robertson, Jon P. Christopherson, Taylor Bennett, Lee Walker, Fang Wang, Shiqiang Liu, Bin Fan, and Ira Bloom, J. Power Sources, 306 (2016) 268-273. DOI: 10.1016/j.jpowsour.2015.12.004

III.B.2 Electrochemical Performance Testing (INL)

Matthew Shirk, Principal Investigator
Idaho National Laboratory
2525 Fremont Avenue
Idaho Falls, ID 83402
Phone: 208-526-7216
E-mail: matthew.shirk@inl.gov

Samuel Gillard, Technology Manager
U.S. Department of Energy
Phone: 202-287-5849
E-mail: Samuel.Gillard@ee.doe.gov

Start Date: October 1, 2016   End Date:September 30, 2017
Total FY17 Project Cost: $4,609,421   DOE FY17 share: $4,609,421   Non-DOE share: $0

Project Introduction

The Battery Test Center at Idaho National Laboratory has been supporting the evolution of electrified transportation through high-quality, independent testing of electrical energy storage systems for more than 30 years. Independent testing provides data for quantitative assessment of technology gaps. Test methods and techniques are continuously improved to offer data on relevant metrics as vehicle applications evolve. Advancing electrified powertrain transportation, such as EV, PHEV, and HEV technologies, is a top priority within the Department of Energy (DOE) given the potential to increase energy security through reduction of US dependence on foreign oil. The INL Battery Test Center (BTC) is a world leader in science-based performance testing and assessment of advanced electrochemical energy storage technologies, primarily for automotive applications. The BTC at INL has been designated by DOE as a core capability and the lead test facility for supporting USABC through testing activities. The development of batteries and other energy storage devices requires validation testing from an independent source to accurately characterize the performance and life capability against the established USABC technical targets for EVs, PHEVs, 12 V Start/Stop, HEV, and other emerging electric drive system applications. Gaps in performance relative to targets are used as a metric to guide R&D priorities.

Objectives

The primary objective of the program is to provide high fidelity, science-based performance and life testing, analysis, modeling, and reporting. To ensure the data produced are relevant to industry and government, it is also a key objective to update test and analysis procedures to maintain alignment with industry needs and to develop new procedures for promising future applications.

Approach

The INL Battery Test Center (BTC) utilizes over 20,000 square feet of laboratory space and is equipped with over 700 test channels for advanced energy storage testing at the cell-level (e.g., up to 7V, 300A), module-level (e.g., up to 65 V, 250A), and pack-level (e.g., 500-1000 V, 500A). Test equipment is programmed to perform test profiles while simultaneously monitoring for compliance with operating limits such as voltage, current and temperature. Batteries and other energy storage devices are typically subjected to an electrical test sequence while housed inside precision thermal chambers to ensure consistent and repeatable results by maintaining consistent ambient temperature conditions. To enhance performance testing across a wide range of thermal conditions, driven by automotive usage scenarios, the thermal chambers can be operated across a broad temperature range (e.g., -70 to 200°C).

Successful performance testing and accurate life modeling are highly dependent on the fidelity of the acquired test data. The INL BTC has developed advanced calibration verification and uncertainty analysis methodologies to ensure that voltage, current, and temperature measurements are within the tolerance specified by the test equipment manufacturer (e.g., 0.02% of the full scale). These measured test parameters are subsequently used in various mathematical combinations to determine performance capability (e.g., resistance, energy, power, etc.). INL has also quantified the error associated with these derived parameters using the accuracy and precision of the relevant measured parameter (e.g., voltage) to ensure high-quality and repeatable results and meaningful presentation.

The INL BTC utilized a high capacity shaker table perform non-destructive tests to characterize reliability and safety of new cell topologies to mechanical vibration and shock Unconventional and unproven cell designs are the main focus of mechanical vibration and shock testing at INL. The shaker table laboratory is equipped with both safety shielding and thermal control chambers and is co-located with battery test equipment to allow performance testing immediately before and after vibration testing has occurred.

Adjacent to the shaker table are two fire-rated isolation rooms that can be used for tests that push the known limits of operation, but have yet to be proven to be safe, though expected to be non-destructive. Examples of testing near the limit could include extreme fast charging, subtle over- or under-charging, high-temperature thermal characterization for under-hood systems, among many others. These isolation rooms allow for safe testing of unproven cell technologies at or near the design limit. These complimentary non-destructive evaluation capabilities comprise INL's Non-Destructive Battery Evaluation Laboratory.

Results

The INL BTC continues to test articles of various sizes and configurations using the standardized test protocols developed with industry partnerships for each electric drive vehicle application. Table III-3 and Table III-4 summarize the testing activities under the USABC and Benchmarking Programs, respectively, for FY17. Technologies developed through USABC contracts are aged and tested against the appropriate application target (EV, HEV, PHEV, 12 V S/S, 48 V HEV) and, where applicable, they are compared to previous generations of test articles from the same developer. 252 articles were tested for USABC in FY17, including 6 modules and 246 cells. The purpose of the Benchmark program is to evaluate device technologies that are of interest to the Vehicle Technologies Office within DOE, but are not deliverables developed under a contract. In some cases, Benchmark devices are used to validate newly developed test procedures and analysis methodologies. 117 cells were tested for the Benchmark program in FY17. Advanced cells from the Applied Battery Research (ABR) program were life and performance tested at INL, using modified testing procedures based on the program goals. INL BTC tested and reported on 87 cells for ABR, with 63 cells continuing, but nearing completion of testing at the end of FY17. (See Table III-5.) The final two sets of cells delivered through the FOA released in FY 2011, titled 'Develop Advanced Cells and Design Technology for Electric Drive Vehicle Batteries', completed testing as well. (See Table III-6.)

Analysis was performed for all articles tested, and results were presented regularly at quarterly review meetings and USABC Technical Advisory Committee (TAC) meetings to USABC OEM, DOE VTO representatives, developers, and national laboratory staff. INL worked with the USABC test methods committee to develop the methodology and publish the manual for testing 48V mild hybrid battery systems as well.

Table III-3: Articles Tested for USABC

Developer	Application	System	Number of Articles Tested	Status at Year End
Leyden	EV	Cell	9	Complete
LG/CPI	PHEV	Cell	23	Complete
LG/CPI	12 V Stop/Start	Cell	12	Complete
LG/CPI	EV	Cell	12	Complete
LG/CPI	12 V Stop/Start	Module	1	Complete
NOHMS	PHEV	Cell	15	Complete
LG/CPI	EV	Cell	12	Complete
NOHMS	PHEV	Cell	18	Complete
SAFT	12 V Stop/Start	Cell	3	Complete
NOHMS	PHEV	Cell	18	Ongoing
Saft	12 V Stop/Start	Cell	15	Ongoing
Amprius	EV	Cell	24	Ongoing
Envia	EV	Cell	17	Ongoing
LG/CPI	12 V Stop/Start	Cell	15	Ongoing
FARASIS	EV	Cell	8	Ongoing
24M	EV	Cell	3	Ongoing
SAFT	HEV	Cell	14	Ongoing
SAFT	12 V Stop/Start	Cell	15	Ongoing
LG/CPI	12 V Stop/Start	Cell	15	Ongoing
LG/CPI	12 V Stop/Start	Module	3	Ongoing

Table III-4: Articles Tested for Benchmark

Developer	Application	System	Number of Articles Tested	Status at Year End
Hydroquebec	PHEV	Cell	13	Complete
Toshiba	12 V Stop/Start	Cell	1	Complete
AESC/Nissan	EV	Cell	24	Complete
LG Chem	EV	Cell	4	Complete
ORNL	EV	Cell	6	Complete
ORNL	EV	Cell	6	Complete
Toshiba	EV	Cell	18	Ongoing
Toshiba	12 V Stop/Start	Cell	12	Ongoing
EIG LTD	12 V Stop/Start	Cell	20	Ongoing
LG/CPI	PHEV	Cell	13	Ongoing

Table III-5: Articles Tested for Applied Battery Research (ABR)

Developer	Application	System	Number of Articles Tested	Status at Year End
Penn State	EV	Cell	12	Complete
ANL	EV	Cell	12	Complete
Penn State	PHEV	Cell	15	Ongoing
Farasis	EV	Cell	12	Ongoing
Farasis	PHEV	Cell	12	Ongoing
ANL	PHEV	Cell	12	Ongoing
Envia	EV	Cell	12	Ongoing

Table III-6: Articles Tested for the 2011 FOA: 'Develop Advanced Cells and Design Technology for Electric Drive Vehicle Batteries'

Developer	Application	System	Number of Articles Tested	Status at Year End
ANL/Miltec	EV	Cell	9	Complete
Applied Materials	EV	Cell	15	Complete

Conclusions

Reliable battery performance and life testing is critical for the successful evolution and commercialization of efficient vehicles. The INL BTC is a DOE core capability that is well equipped to conduct accelerated aging protocols and aggressive test protocols on battery technologies of various sizes and shapes while ensuring high quality, repeatable results as an independent source of science-based performance assessment for DOE, the automotive industry, and battery developers. As such, testing for key programs funded through the Vehicle Technologies Office of DOE was conducted. A total of 480 devices were tested in FY17. In FY18, INL plans to continue this level of support for multiple programs with broad support for the USABC and Benchmark programs in particular, having completed support of the 2011 FOA program and nearing completion of ABR testing. In addition to testing and life modeling, INL will also continue developing and refining standard test protocols and analysis procedures in collaboration with USABC.

Key Publications

1. Tanvir Tanim, Matt Shirk, Randy Bewley, Eric Dufek, Boryann Liaw. Fast Charge Implications: Pack and Cell Analysis and Comparison, Submitted to Journal of Power Sources

2. Battery Test Manual for 48 Volt Mild Hybrid Electric Vehicles, Idaho National Laboratory, March 2017, INL/EXT-15-36567

III.B.3 Battery Safety Testing (SNL)

Leigh Anna M Steele, Principal Investigator
P.O. Box 5800, Mail Stop 0614
Albuquerque, NM 87185
Phone: 505-844-9290
E-mail: LSteele@sandia.gov

Samuel Gillard, Technology Manager
U.S. Department of Energy
Phone: 202-287-5849
E-mail: Samuel.Gillard@ee.doe.gov

Start Date: October 1, 2016   End Date: September 30, 2017
Total Project Cost: $1,000,000   DOE share: $1,000,000   Non-DOE share: $0

Project Introduction

Abuse tests are designed to determine the safe operating limits of HEV\PHEV energy storage devices. Testing is intended to achieve certain worst-case scenarios to yield quantitative data on cell\module\pack response, allowing for failure mode determination and guiding developers toward improved materials and designs. Standard abuse tests with defined start and end conditions are performed on all devices to provide comparison between technologies. New tests and protocols are developed and evaluated to more closely simulate real-world failure conditions.

When scaling from cell to the battery level, a detailed understanding of cell interactions provides insight on safety performance. Single point failures from a cell or group of cells can be initiated by a number of triggers including internal short circuit, misuse or abuse, or component failure at the battery or system level. Propagation of a single failure event (regardless of the initiation trigger) through an entire battery, system, or vehicle is an unacceptable outcome with regards to EV battery safety. In this FY, our work has focused on evaluating the propagation of a single cell thermal runaway event through a battery using a variety of design considerations with an emphasis on passive thermal management impacts. This has been coupled with thermal modeling by NREL for these testing conditions. In addition, alternative failure initiation methods have been evaluated to provide direct comparisons of possible energy injection between modes. This data was compiled to better identify what propagation test method is appropriate given certain battery designs. Expanding the analysis of short circuit current during failure propagation has been done for EV relevant chemistries. Ongoing test development and validation to obtain these values has been achieved.

While robust mechanical models for vehicles and vehicle components exist, there is a gap for mechanical modeling of EV batteries. The challenge with developing a mechanical model for a battery is the heterogeneous nature of the materials and components (polymers, metals, metal oxides, liquids). Our work will provide empirical data on the mechanical behavior of batteries under compressive load to understand how a battery may behave in a vehicle crash scenario. This work is performed in collaboration with the U.S. Council for Automotive Research (USCAR) and Computer Aided Engineering of Batteries (CAEBAT). These programs have supported the design and development of a drop tower testing apparatus to close the gap between cell/string level testing and full scale crash testing with true dynamic rate effects. This work is discussed in further detail in the annual report submitted by NREL. Additional modeling efforts lie in being able to better predict failure propagation within larger battery systems. Sandia's battery safety testing provides testing support to better aid in thermoelectrical model development at NREL and SNL.

Materials characterization to better understand batteries that have undergone abusive conditions is of interest. Our partnerships with Argonne National Lab (ANL) and Oak Ridge National Lab (ORNL) through the Post

Test Analysis Program for ABR, spans the building of cells with known materials (ORNL), overcharge testing to various states (SNL), and the posttest analysis of the cells (ANL). In addition, testing to support the Si-Deep Dive Program has been leveraged to gain a better understanding of the safety implications for these materials.

Objectives

- Serve as an independent abuse test laboratory for DOE and USABC

- Abuse testing in accordance with the USABC abuse testing manual

- Successful testing of all deliverables from developers under USABC contracts

- Evaluate failure propagation through addition of thermal management and alternative initiation methods

- Short circuit current evaluation during failure propagation in battery strings of EV relevant chemistries

- Laser initiated failure within batteries of various formats

- Provide testing data to support modeling efforts developed by NREL

- Provide mechanical testing support to develop and validate mechanical models for EV batteries through CAEBAT program

- Design and develop a dynamic drop testing capability to support CAEBAT

- Provide abuse testing support for ABR Post Test program and Si Deep Dive

- Publish Sandia Abuse Testing Procedures: Unlimited release

Accomplishments

- Successful testing of cell and module deliverables through USABC contracts including:

    o Maxwell (12 V SS)

    o LG Chem (12 V SS)

    o Envia (EV)

    o Amprius (EV)

    o NOHMS (Electrolyte)

    o 24M Technologies (EV)

- Exercised testing method to analyze short circuit current between cells during failure propagation on various cell chemistries (EV relevant) for direct comparisons

- Completed multi-cell propagation testing with the inclusion of passive thermal management (spacers); preliminary simulated results using NREL thermal models show good agreement with test data

- Developed method for 3-point bend testing, single cell constrained testing in different orientations, and design/fabrication of dynamic drop testing apparatus in support of CSWG/CAEBAT

- Successful demonstration of laser induced battery failures on various cell formats

- Supported posttest analysis program with batteries (3 chemistry types) overcharged at various states

- Hosted 2nd Annual IBSW in Albuquerque sponsored by DOE through T2M funds

- Stood up large scale testing capability at Sandia's Burn Site and successfully completed testing of USABC modules

Approach

Abuse tolerance tests evaluate the response to expected abuse conditions. The goals of abuse and safety testing include a) testing to failure of energy storage devices and documentation of conditions that caused failure, b) systematic evaluation of failure modes and abuse conditions using destructive physical analysis (DPA), c) provide quantitative measurements of cell/module response, d) document improvements in abuse response, and e) develop new abuse test procedures that more accurately determine cell performance under most probable abuse conditions. Electrical (overcharge/overvoltage, short circuit, over discharge/voltage reversal, and partial short circuit), mechanical (controlled crush, penetration, blunt rod, drop, water immersion, laser induced short circuit, mechanical shock and vibration) and thermal abuse (thermal stability, simulated fuel fire, elevated temperature storage, rapid charge/discharge, and thermal shock cycling) cover the main categories of possible conditions evaluated. These techniques are applied to USABC deliverables and the results reported to DOE and USABC.

Research and development batteries used for simulating internal short circuits, propagation testing (alternative initiators and passive thermal management), and short circuit current evaluation are based on commercial-off-the-shelf (COTS) $LiCoO_2$ 18650 and pouch cells, NMC and NCA 18650, and LFP 18650 (designed for energy) and 26650 (designed for power) cells. Cell failure and thermal runaway initiated by various methods were investigated this FY, including overcharge, laser initiation, and mechanical nail penetration into a single cell within a pack.

Results

Battery Abuse Testing

This FY, Sandia's standard abuse testing practices were published in an unlimited release report. The notable highlights include enhanced safety basis, updates to testing protocols according to current testing methods/capabilities, use of empirical data to support test conditions, addition of failure propagation and flammability tests, and providing clarity in the definitions for a hazard severity rating system. SNL provided independent testing on all USABC deliverables in FY17 with testing results reported at TAC. The actual USABC testing results are Protected Information and are prohibited from public release. However, representative data is shown in Figure III-15 for COTS cells purchased on the open market and assembled into a multi cell pack that underwent thermal abuse. This validation test was performed to stand up permanent operations at SNL's large-scale testing facility to support USABC module tests and was completed in FY17.

Thermal ramp testing on a 12-cell pack (~1kWh) according to the USABC Abuse Testing Manual was performed. Cells were heated at a rate of 5°C/min to 250°C or failure (whichever occurs first). Complete propagation through the pack was achieved with a 5-min total burn time and peak temperatures of 800°C. The addition of this remote site has helped to increase throughput of test deliverables and also serves as a safer means to handle multi-cell packs posttest by removing residual energy through remotely operated propane torches. This significantly reduces risk to personnel and improves our safety basis.
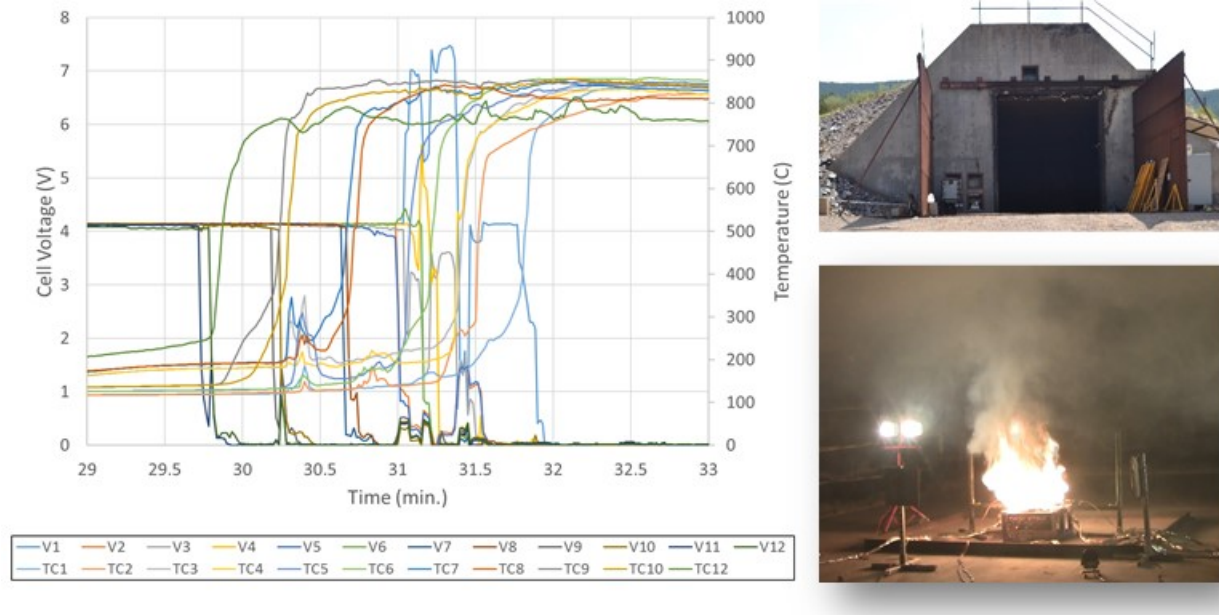
Figure III-15. Representative cell temperatures and voltages during a thermal ramp test of a multicell 1kWh Li-CoO$_2$ pack

The failure propagates through the entire pack, starting with cell 12 undergoing runaway once the battery skin temperature reaches 200°C. The failure cascades through the remaining cells, over 2 minutes, with onset temperatures of thermal runaway ranging between 125 and 200°C (skin temperatures).

Propagation Testing with Passive Thermal Management

A number of studies evaluating the response of single cells to field and abusive failures have been conducted at Sandia, however, less attention has been paid to how a battery system responds to the energetic failure of a constituent cell. A single cell failure may be a relatively rare occurrence, but the consequence of that failure can be significantly greater if these failures propagate through the entire battery. To build on SNL's past research in propagation testing, passive thermal management between pouch cells was targeted this FY. To study this further, we tested a series of small batteries constructed with COTS pouch cells to investigate the effectiveness of simple thermal management systems (spacers of various materials and thicknesses) on the extent of propagation.

In our experimental work, batteries consisting of 3 Ah LiCoO$_2$ COTS pouch cells were constructed in a 5-cell close packed system allowing for maximum surface area contact with one another to aid in thermal transfer; shown in Figure III-16. We previously investigated failures of a single cell located within the pack in both series and parallel configurations (unmitigated). Regardless of electrical connectivity, the surface area contacts between cells allowed for enough thermal transfer to aid in propagation to neighboring cells suggesting a greater contribution to the extent of propagation. To reduce variables for this test series, the cells were not electrically connected and the passive thermal management device of choice was placed between each cell as seen in Figure III-16.
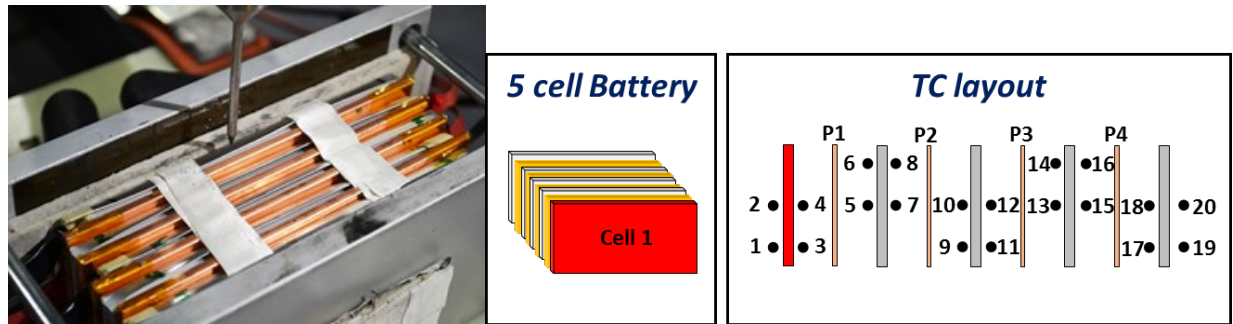
Figure III-16. Testing setup for COTS 3Ah 5-cells pack with passive thermal management (copper spacer of 1/8" thickness shown in picture). Failure initiation by nail penetration into cell 1 with the following thermocouple (TC) and copper (C)/or aluminum mapping consistent between tests

Both aluminum and copper plates, at 1/8, 1/16, and 1/32" thickness, were cut to the battery dimensions to act as a passive thermal management barrier and the testing matrix shown in Table III-7 was achieved; where A stands for aluminum and C stands for copper.

Table III-7: Passive Thermal Management Testing Matrix and Results

Test Pack ID	Test Description	Extent of Propagation
Baseline	No thermal management	Complete propagation
A-1	1/8 inch Al plates between cells	No propagation
A-2	1/16 inch Al plates between cells	Limited propagation (to cell 2)
A-3	1/32 inch Al plates between cells	Complete propagation
C-1	1/8 inch Cu plates between cells	No propagation
C-2	1/16 inch Cu plates between cells	Limited propagation (to cell 2)
C-3	1/32 inch Cu plates between cells	Complete propagation

The packs were fully instrumented with thermocouples (4 TC's per cell) and individual cell voltages monitored to observe the extent of propagation. Figure III-17 shows representative data sets with aluminum passive management showing reduced extent of propagation achieved when a slight increase in material thickness from 1/16" to 1/8" was implemented. When plate thickness is decreased to 1/32", full propagation is observed.
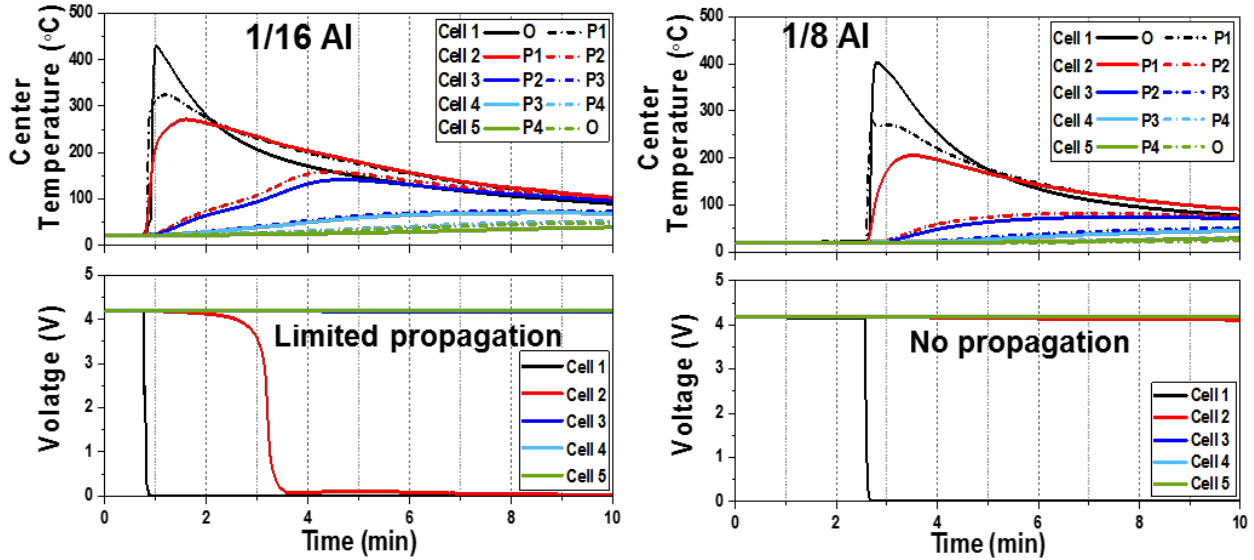
Figure III-17. Temperature and voltage data collected during propagation testing with the additional of thermal management (aluminum spacers). Left plots show limited propagation to the neighboring cell with 1/16" aluminum (cell 2 voltage drop at 3.5 min into test) and right plots show no propagation with 1/8" aluminum between cells

As mentioned, this series of tests were also performed using copper as the barrier. Overall, copper and aluminum behaved similarly in the ability to reduce propagation using the 1/16" plates and completely eliminated propagation with the 1/8" thick material. However, a faster voltage drop is observed for cell 2 in the 1/16" case with aluminum, which supports the higher thermal conductivity of copper over aluminum. Temperature data from each experiment was gathered to not only observe the extent of propagation but also the rate at which heat transfer between the cells occurs. This data has been provided to modeling partners at NREL for validation of preliminary thermal models with the inclusion of passive thermal management. Thermal data from the A-1 testing case (1/18" Al) was evaluated and results shown in Figure III-18.
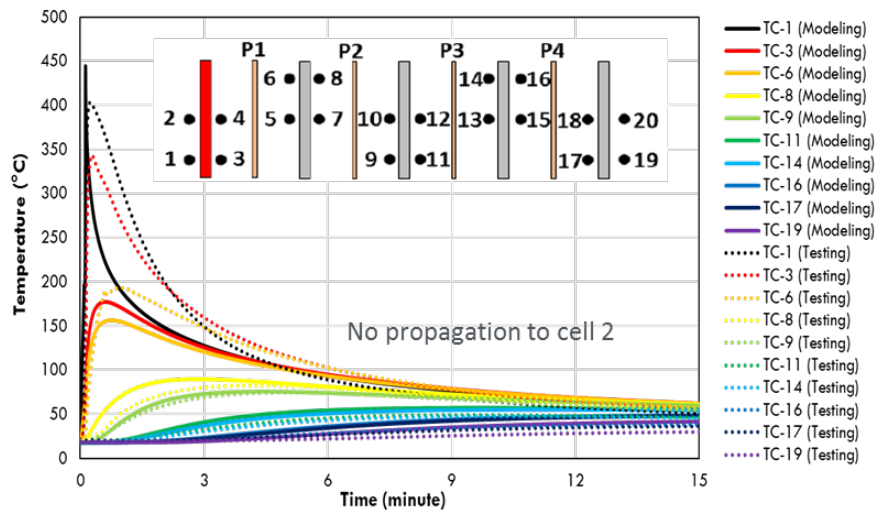

Figure III-18. Cell temperature data collected both experimentally and simulated by NREL's model during failure propagation testing for Al-1 case showing good agreement

Initial simulations show good agreement with testing results regarding peak temperature and timing to reach peak temperatures. The temperature does drop much faster in the simulated results which would be due to the following assumptions made in the simulation: 1) model assumes constant heat source that triggers cell uniformly within 5.5secs but test cell was shorted out gradually 2) deformation and displacement of cells will affect the contact between cells and passive management as well as readings from thermocouples and 3) the effluents from vented cells and their effect on temperature were not accounted for in the model. Future work in this area includes calibrating the model to include artifacts of a short circuit then applying the optimized model to the remainder of experiments for comparisons.

Quantify Short Circuit Current During Failure Propagation: Cell Chemistry Effects

As realized during previous failure propagation testing, high short circuit currents from non-abused cells discharging into the failure point exist. Sandia has developed a method to quantify these currents and validated the test setup for a variety of cells. In order to better compare relevant chemistries for EV applications, follow on work was completed to expand testing beyond $LiCoO_2$ and LFP using COTS 3Ah NMC and 3.1Ah NCA 18650 cells. In addition, improvements in fixturing to ensure connectivity between cell 1 (failure point) and cell 2 (un-abused cell) were achieved; obtaining a constant path for current flow where peak currents could be measured. Two cell strings were assembled in a 1S2P configuration in the apparatus shown in Figure III-19. To maintain contact with the failed cell upon thermal runaway a spring was added at the nail to apply counter pressure to the cell. Comparison data of testing with and without the improved mechanical contact have been provided below.
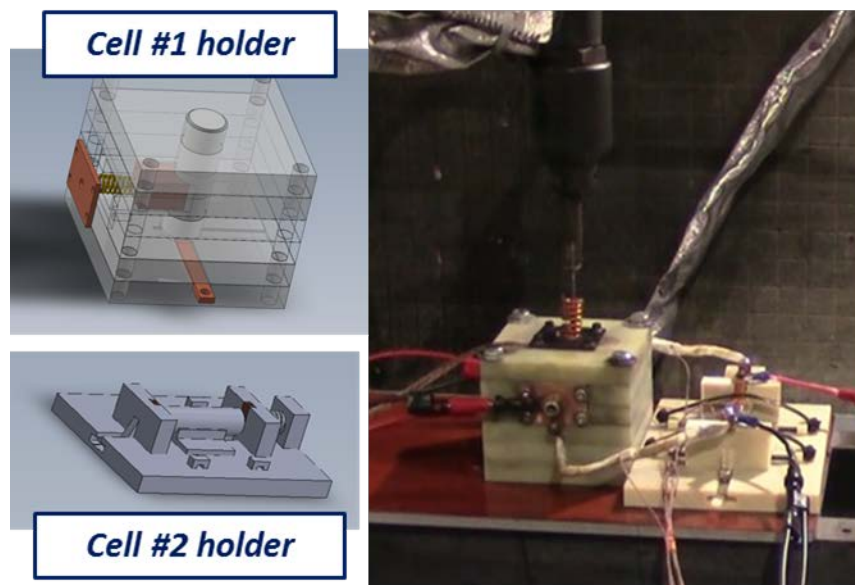

Figure III-19. Schematic for 1S2P setup bridged by constantan wire to measure short circuit current during failure propagation. Improved mechanical robustness achieved through cell holders and additional pressure applied at the failure point to maintain contact during runaway event.

The cells were joined using constantan wire of a known resistance to allow for current measurements between cells to be obtained. Mechanical insult of cell 1 (top) was performed while cell 2 (bottom) remained untouched allowing for the cell to discharge through the electrical connections of the string. Representative data for a 1S2P NMC 18650 cell string is shown in Figure III-20 with no extra mechanical contact during testing (top) and improved mechanical contact during test (bottom).
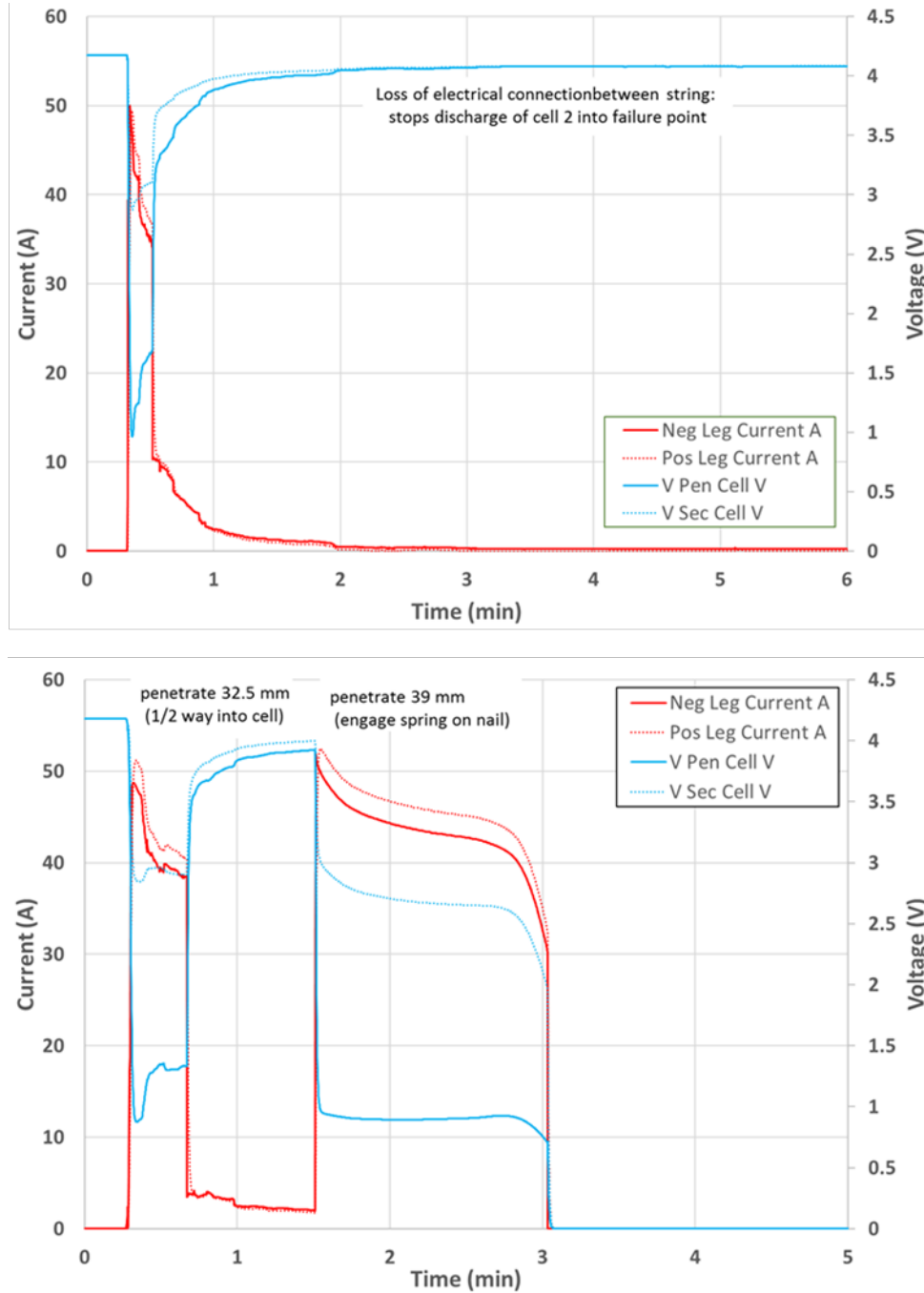

Figure III-20. String current across bridge and voltage measured during the failure propagation test for NMC 18650 in no extra mechanical contact during test (top) and with improved mechanical contact (bottom) in 1S2P configuration

Although the peak currents are similar in both cases (~50A), the improvement in mechanical connectivity allowed for cell 2 to discharge for a longer period of time (3 min) resulting in a higher total energy discharged into cell 1 (results summary shown in Table III-8). This reinforces the idea that battery connectivity within packs can play a critical role during failure propagation. Especially in the case where thermal contact between cells doesn't dominate the failure mechanism. Table III-8 shows short circuit current comparison data for various cell chemistries collected over the last two years. It is of note that, while LFP is a more benign chemistry, it is able to sustain a discharge for much longer resulting in larger total energy output into failure point. This allows for energetic failures to occur when seemingly benign cells are electrically connected as has been supported in past testing data with these LFP strings. The robustness of the cell connections impacts the extent of energy being discharged into the failure point as shown in Figure III-20 above. Lastly, cell design can also impact short circuit current through discharge rate capacity and/or the use of internal safety devices. This is relevant for the NCA cells, which have a max discharge rate of 2C, resulting in lower total energy discharged during propagation, while all other chemistries tested were rated for >3C discharge rates. In addition, a sharp loss of string voltage was observed when NCA cell 1 was penetrated suggesting there could be an internal safety device included by the COTs manufacture to prevent the extent of short circuiting.

Table III-8: Summary of Results for Short Circuit Current during Failure Propagation

Chemistry	Nominal Capacity (Ah)	Max rated discharge current for cell	Peak current during short circuit (A)	Total Energy discharged into Cell 1 (KJ)
LFP (18650)	1.5	5.6A (3.7C)	37	14.9
LFP (26650)	2.6	42A (16C)	30	15.0 (av)
LiCoO₂ (18650)	2.2	6.2A (2.8C)	90	2.94 (av)
NMC (18650)	3	20A (6.7C)	80	5.3 (std setup), 0.027 (robust mechanical contact)- lost battery connection
NCA (18650)*	3.1	6.2A (2C)	35	0.29 (std setup), 0.75 (robust mechanical contact)

*Internal safety device might be preventing an external short current

We plan to continue to improve this testing method and apply it to more complex cell strings and electrical configurations in hopes to better quantify the impact of short circuit current during failure propagation in the next level of assemblies.

Alternative Method Development to Simulate Internal Short Circuits: Laser Initiation

Development of a test that better simulates an internal short circuit (ISC) within a cell is of interest. Traditionally, methods like nail penetration or implantable defects/devices have been used to simulate ISC. Both of these methods are invasive and require altering the cell during development or testing. Alternative means have been investigated at SNL including the use of a 40W IR pulse laser in hopes to reduce external damage; initiating a short within the first few electrode layers. Demonstration of this method has been achieved in various cell formats (pouch and cylindrical) as part of the USABC working group with SNL leading testing efforts. Representative data for a COTS 3 Ah LiCoO₂ pouch cell that has undergone thermal runaway initiated by 20 x 1.9 J pluses (~38 J total energy) laser is shown in Figure III-21. The cell exhibits a hard short represented by the quick heating rate and drop in cell voltage. The overall laser power was optimized to initiate a runaway event but there were several examples of this method resulting in a soft short (high impedance short) using 4 pulses (7.6 J total energy) where the cell self-discharged over a period of 24 hours without undergoing a thermal runaway.
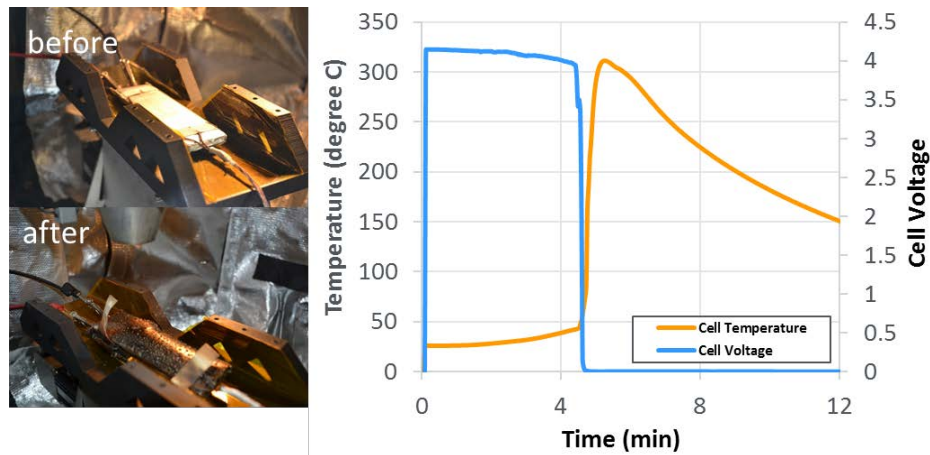
Figure III-21. Left: Still images (pre and posttest) and right: temperature and voltage data as a result of successful thermal runaway initiated by a 20 pulse laser

The failure conditions were applied to a discharged cell (0% SOC) so posttest analysis could be performed. These results were compared to a nail penetration test on the same cell type shown in Figure III-22. The external view shows a ~1 mm hole from the laser compared to a >3 mm hole generated from nail penetration, which supports that the laser (overall) is less destructive on the cell. Comparing internal damage through CT images, the laser initiation only impacts the first few electrode layers compared to nail penetration which damages the entire cell, proving laser testing to be a better representation of an ISC test.
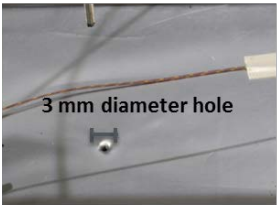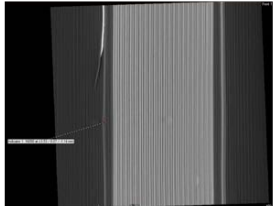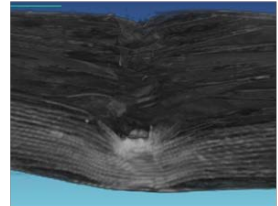

Figure III-22. External and CT images comparing electrode damage on discharged cells using 20 pulse laser or blunt rod

Follow on testing included attempts to seal the hole resulting from the laser striking the cell (Figure III-22) to remove the possible reaction with oxygen. To accomplish this, a fused silica slide (IR transparent) was placed on the surface of the cell and sealed with kapton tape. Successful initiation of failure was achieved through the slide and the seal maintained intact until full runway occurred. Once the system was optimized for pouch cells, testing shifted toward cylindrical cans. COTS cells of $LiCoO_2$ and NCA were utilized. The cell surface was painted black to reduce laser reflectivity and allow for better absorption. For the $LiCoO_2$ case, slight cell heating and voltage drop occurred but no thermal runaway was initiated. There was visual damage beyond the cell's outer surface, which was further evaluated through CT (shown in Figure III-23).
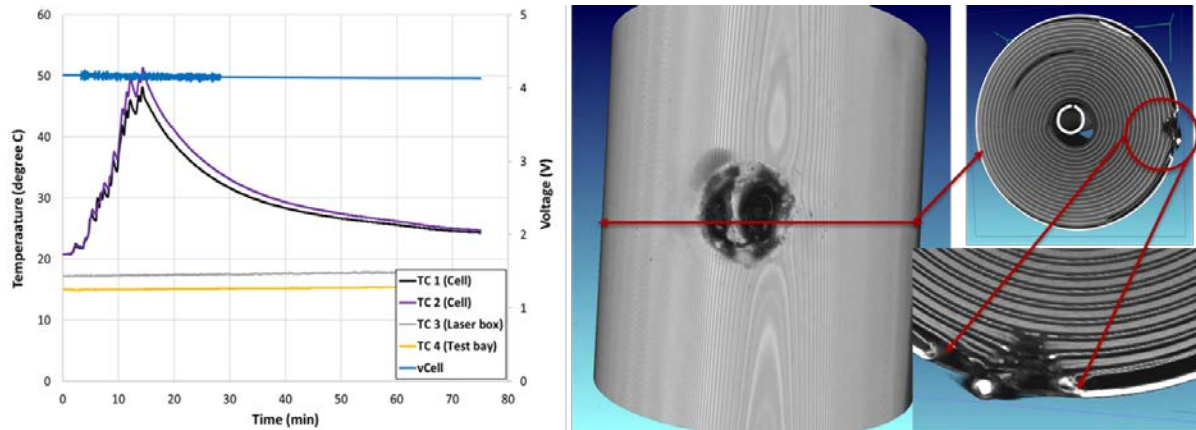
Figure III-23. Temperature and voltage data from laser testing in a COTS 3 Ah LiCoO$_2$ cylindrical cell and CT analysis of internal damage

Since initiation of a thermal runaway within the first cell chemistry proved challenging, focus switched to a higher capacity NCA cell (3.1A) in hopes that the reduced can thickness would allow for a failure to be initiated. Rapid runaway was achieved using 5 x 5.4J (27 J) as shown in Figure III-24. Peak battery skin temperatures reached 700°C and thermal runway with self-ignition was observed. Further optimization of the testing method needs to be developed to demonstrate repeatability and consistency, but preliminary results show promise as an alternative initiation method that could better represent an internal short circuit test. In addition, the laser power can be tuned to better initiate failure based on battery architecture.
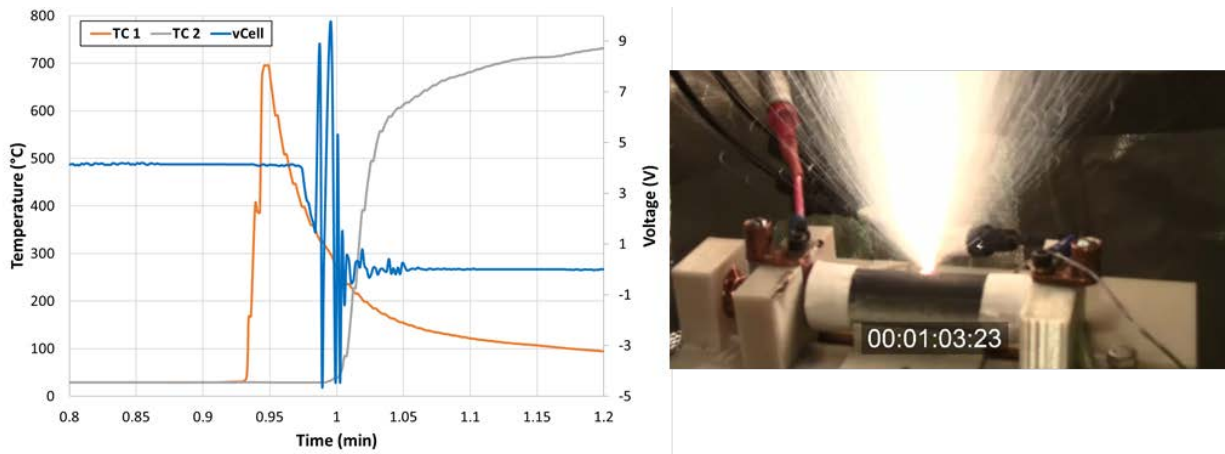
Figure III-24. Temperature and voltage data collected during runaway initiated by laser in a COTS 3.1 Ah NCA cylindrical cell

Energy Injection Comparison Between Failure modes for Propagation Testing
It is of interest to better understand the impacts specific abuse conditions have on failure propagation. One way to make this comparison is by calculating energy injection needed to initiate a failure during each mode. SNL has investigated several standard abuse conditions including nail penetration, thermal ramp and overcharge as well as some less traditional failure initiators like pulse laser and undirected light. A summary of the conditions and associated estimated energies are listed in Table III-9.

Table III-9: Energy Injection Comparisons between Failure Modes

Test	Energy Source	Conditions	Estimated Energy
Nail Penetration	Mechanical	20 mm penetration ~200 lb peak load	1.8 J
20 Pulse laser	IR Laser	20 1.9 J pulses	38 J
Undirected light	Quartz lamp	Exposure to light source through aperture	6000 J*
Thermal Ramp	Thermal	Heat to 200°C	6300 J**
Overcharge	Electrical	1C to 200% SOC	43200 J***

* Based on radiometer measured flux through aperture

** Calculated for hypothetical 40g cell – larger cells will require more energy

*** Calculated for a hypothetical overcharge at 3 A and 4 V at a 1C rate

Significantly less energy is required for laser induced failures compared to overcharge/thermal ramp, however more energy is required for laser induced failure when compared to nail penetration. When trying to keep variables at a minimum during testing, it is important to note that the additional energy required to push a single cell into runaway by overcharge and thermal ramp could have an impact on the neighboring cells through heat transfer changing the overall propagation results. Although nail penetration is a highly effective way to initiate a single cell failure, it is very intrusive and is not always ideal at the system level where cells might not be as accessible. As previously shown, laser initiation is much less destructive to the cell but, again, might not be ideal when packaging limits cell accessibility. In addition, this method needs to be matured to ensure repeatability in the hope that the resulting data can be used for design of experiments to study propagation.

Preliminary testing was done to compare propagation results from a single cell failure initiated by nail penetration or overcharge at a 1C rate. Cell 1 in a 5 cell string underwent failure via one of the two methods and full propagation through the string was achieved. The representative data for both are shown in Figure III-25.
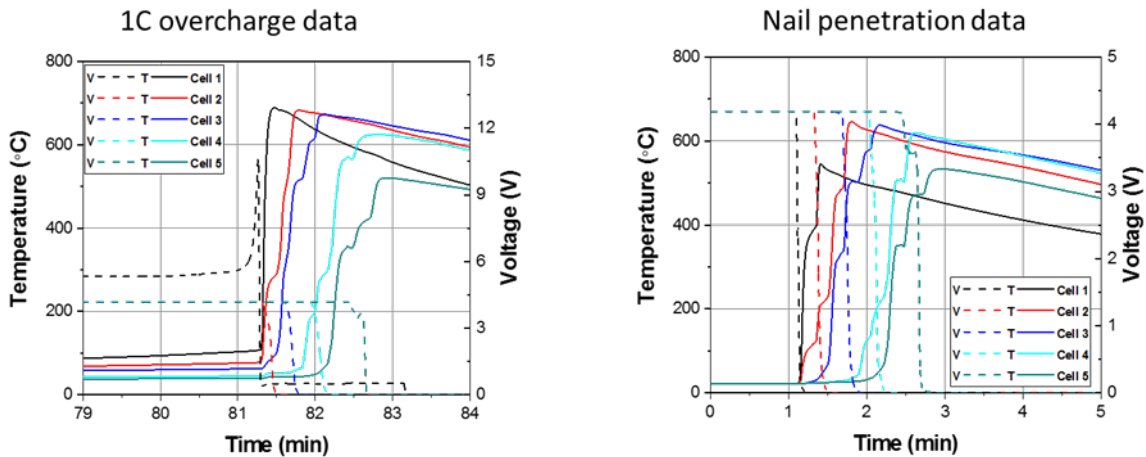
Figure III-25. Voltage and temperature data collected during failure propagation testing initiated by overcharge of cell 1 (left) or nail penetration of cell 1 (right)

The overcharged cell failure was more energetic (faster heating rate during runaway) than the nail penetrated cell; however, the overall rate of propagation was similar between the two tests. Full propagation was achieved in ~ 1 min by both methods with peak battery temperatures also in agreement between tests. Follow on testing

to compare failure modes during propagation within strings is needed to better couple energy injection results to aid in test development.

Mechanical Testing

Sandia is providing mechanical testing support to the VTO CAEBAT program to set boundary parameters for mechanical models and to validate predictions made by the numerical models. Further details are available in the annual report submitted by NREL. Leveraging the need for true dynamic rate experiments to be performed through this consortium, a drop tower was designed and is currently being assembled at SNL. Future efforts will include designing testing protocol for the unit and validation experiments leading to data for CAEBAT missions.

Conclusions

Development and testing of higher energy, larger format cells and modules continues for USABC developers in hopes to meet the EV Everywhere 2022 goals. We provide a means to field the most inherently safe chemistries and designs to help address the challenges in scaling up lithium ion technologies of interest. This has required careful control and monitoring of tests with the potential of high energy release as well as standing up a larger facility at SNL to support module level testing this FY. This has provided critical information to cell developers to aid in the development of increasingly abuse tolerant cell chemistries and module designs. This independent testing is also necessary to perform objective evaluations of these various designs and chemistries by the DOE and US automobile manufacturers. SNL has completed abuse testing support for all USABC deliverables to date.

Understanding battery design effects on failure propagation was investigated this FY with a focus on passive thermal management within pouch cell formats. The use of a simple management system (spacer) proves to reduce or even eliminate propagation between cells depending on the material thickness. This effort has been coupled with NREL models showing good agreement between testing data and primarily thermal simulations. Further optimization is needed in order to provide predictive models for battery failures which continues to be of interest to the community. Expansion of short circuit current observed during failure propagation between cells was achieved this year with a focus on relevant EV battery chemistries. COTS cells of different sizes and chemistries were assembled in 2 cell strings in a 1S2P configuration using constantan bridge wires of known resistance to obtain current. Testing results allow for comparison between chemistries to be made.

Alternative testing methods to simulate an internal short circuit were evaluated with SNL's focus on laser initiation. Successful initiation of thermal runaway within pouch and cylindrical cells was achieved. Comparing with nail penetration, this mode of failure proves to be less destructive and invasive into the cell, only effecting the first few electrode layers. Follow on testing is needed to optimize testing conditions and improve consistency.

There has been an increasing need within the community to better understand the effects of the failure modes on a single cell when designing test methods for propagation. One method for comparing this effect between modes is through the calculated energy injected needed to cause a cell failure. A summary of traditional modes' (thermal ramp, overcharge, and nail penetration) and non-traditional modes' (laser and undirected light) calculated injected energy was completed. These values can be used to help aid in experimental design depending on battery architecture and needs during test development.

SNL continues to provide testing support and data to help build and validate models with other national lab partners through the CAEBAT VTO program. Additional abuse testing support for the VTO post mortem program and Si-Deep Dive expanded this year which included overcharging cells of various chemistries manufactured by ORNL to different states followed by posttest analysis done by ANL. Also, initial abuse testing of Si-based cells has been achieved to better understand the safety impacts of this emerging chemistry.

Key Publications

1. L Steele et al. "Abuse Testing Update" USABC TAC, Washington, DC October 2016

2. J Lamb et al. "Impact of battery size and charge on the thermal runaway of lithium ion batteries" PRIME 2016, Honolulu, HI, October 2016

3. J Lamb et al. "Internal cell failure initiation" Battery Safety Council, Washington, DC, January 2017

4. L. Steele and J. Lamb "Search for the Super Battery" Nova Season 44 Episode 3.

5. L Steele et al. "Abuse Testing Update" USABC TAC, Southfield, MI, February 2017

6. L Steele et al. "Battery Safety and Reliability" PBS Science Café, ABQ, NM, March 2017

7. J Lamb et al. "Advanced techniques for understanding battery failure and its consequences" 2nd International Battery Safety Workshop, Albuquerque, NM, May 2017

8. J Lamb et al. "Alternative battery failure initiation methods" ECS Meeting, New Orleans, LA, May 2017

9. L Steele et al. "Abuse Testing Update" USABC TAC, Southfield, MI, May 2017

10. 2017 DOE Annual Peer Review Meeting Presentation

11. J. Lamb et al. "Laser Induced Short Circuit Progress" USABC TAC, July 2017

12. C. Orendorff, J. Lamb, L. Steele "Recommended Practices for Abuse Testing Rechargeable Energy Storage System (RESSs)" Sandia National Laboratories SAND Report SAND2017-6925 (July 2017)

13. J. Lamb, et al. "Development of Propagation Battery Failure Tests" The Battery Show, Novi, MI September 2017

14. I. Bloom et al, "Effect of overcharge on $Li(Ni_{0.5}Mn_{0.3}Co_{0.2})O_2$ / Graphite lithium ion cells with poly(vinylidene fluoride) binder. III — Chemical changes in the cathode" submitted to J Power Sources (Sept. 2017).I

15. I. Bloom et al. "Effect of overcharge on lithium-ion cells containing $Li(Ni_{0.5}Mn_{0.3}Co_{0.2})O_2$ cathodes: NMP-soluble binder. II — Chemical changes in the anode" submitted to J Power Sources (Sept. 2017).

16. I. Bloom, "Effect of overcharge on $Li(Ni_{0.5}Mn_{0.3}Co_{0.2})O_2$/Graphite lithium ion cells with poly(vinbylidene fluoride) binder. I. Microstructural changes in the anode" submitted to J Power Sources (Sept. 2017).

III.B.4 Battery Thermal Analysis and Characterization Activities (NREL)

Matthew Keyser, Principal Investigator

National Renewable Energy Laboratory
15013 Denver West Parkway
Golden, CO 80401
Phone: 303-275-3876
E-mail: Matthew.Keyser@nrel.gov

Samuel Gillard, Technology Manager

U.S. Department of Energy
Phone: 202-287-5849
E-mail: Samuel.Gillard@ee.doe.gov

Project Introduction

While EVs promise to curb America's need for imported oil, designing high-performance, cost-effective, safe, and affordable energy-storage systems for these cars can present challenges, especially in the critical area of battery thermal control. As manufacturers strive to make batteries more compact and powerful, knowing how and where heat is generated becomes even more essential to the design of effective thermal-management systems. NREL's thermal characterization activities provide developers, manufacturers and OEMs with the knowledge necessary to assure that batteries are designed to perform strongly, last a long time, and operate at maximum efficiency.

The Vehicle Technologies Office has a goal of producing batteries for $100 kWh that will be capable of 1000 cycles and have a 10+ calendar year life [1]. In order to meet these metrics, the battery packs will need to have higher energy densities resulting in a very compact system. Even if the energy efficiency of the next generation of batteries increases, because of the compactness of these batteries more heat is being generated per unit volume with less heat transfer area. Thus, more advanced heat rejection systems are needed to keep the battery temperatures in the "goldilocks" zone that prevents acceleration of the aging mechanisms within the battery.

The chemistries of advanced energy-storage devices—such as lithium-based batteries—are very sensitive to operating temperature. High temperatures degrade batteries faster while low temperatures decrease their power and capacity, affecting vehicle range, performance, and cost. Understanding heat generation in battery systems—from the individual cells within a module, to the inter-connects between the cells, and across the entire battery system—is imperative for designing effective thermal-management systems and battery packs.

Inadequate or inaccurate knowledge of the thermal characteristics of batteries makes it difficult to design effective thermal-control systems. This can negatively affect lifespan, safety, and cost, ultimately resulting in negative consumer perception and reduced marketability. In 2012, Nissan had to address problems with the battery for its Leaf fully-electric vehicle (EV) losing capacity in the hot Arizona climate. Many attributed this issue to inadequate battery-thermal management.

Accurately measuring battery thermal performance under various electrical loads and boundary conditions makes it possible for battery-system engineers to design effective thermal-management systems. NREL, with the funding from DOE VTO, has developed unique capabilities to measure the thermal properties of cells and evaluate thermal performance of active, air, and liquid cooled battery packs. Researchers also use electro-thermal finite element models to analyze the thermal performance of battery systems in order to aid battery developers with improved thermal designs. In addition, our lumped capacitance multi-node battery-vehicle-ambient model can predict the temporal temperature of batteries as a function drive cycle, ambient

temperature, and solar radiation. These one-of-a-kind tools allow NREL to work with the battery manufacturers and OEMs to meet stringent EV life, performance, cost, and safety goals.

Objectives

- Thermally characterize battery cells and evaluate thermal performance of battery packs provided by USABC developers.

- Provide technical assistance and modeling support to USDRIVE/USABC and developers to improve thermal design and performance of energy storage systems.

- Quantify the impact of temperature and duty-cycle on energy storage system life and cost.

- Address high energy storage cost due to battery packaging and integration costs

- Reduce the cost, size, complexity, and energy consumption of thermal management systems

- Optimize the design of passive/active thermal management systems—explore new cooling strategies to extend the life of the battery pack.

Approach

NREL has measured the thermal properties of the cells and batteries with many different chemistries (lead acid, NiMH, and many versions of lithium cells) through heat generation, heat capacity, and infrared thermal imaging; conducted performance thermal testing of battery and ultracapacitor modules and packs; analyzed the thermal performance of cells and modules; and developed thermal models. Researchers perform thermal testing, analysis, and modeling (1) to assist DOE/USABC battery developers in designing cells/modules/packs for improved thermal performance, and (2) to evaluate and validate the thermal performance of cell/module/pack deliverables from DOE/USABC battery developers and suppliers.

NREL's equipment can benchmark how changing the design of the cell using a different cathode, anode, current collector, electrolyte, additive, or separator affects the overall performance of the cell. The information garnered from these tests helps battery and advanced vehicle manufacturers improve their designs, while providing critical data for the development of thermal management systems that will reduce the life-cycle cost of battery systems. Using NREL's unique R&D 100 Award-winning calorimeters and infrared thermal imaging equipment, we obtain thermal characteristics of batteries and ultracapacitors developed by USABC battery developers and other industry partners. NREL supports the Energy Storage Technical Team by participating in various work groups such as the Amprius, LG CPI, Envia, Maxwell, Saft, Farasis, 24M and USABC Working Groups.

Results

The following narrative outlines some of the more interesting insights garnered from NREL's testing over the past year. The outline below is not meant to an exhaustive study of NREL's work but rather to help the reader understand how NREL's unique thermal characterization technologies are used to improve the energy storage technologies in conjunction with industry and USABC.

Figure III-26 shows the efficiency of cells tested in FY15/FY16/FY17 at NREL at a calorimeter temperature of 30°C. The lithium ion cells were fully discharged from 100% SOC to 0% SOC under a C/2, C/1, and 2C currents. It should be noted that the cells in the figure are for both power and energy cells and have been developed for the HEV, PHEV, EDV, and/or the 12 Volt Start/Stop programs within USABC. The figure shows a general trend with regards to the choice of anode on discharge efficiency. The graph indicates that the lithium titanate oxide (LTO) systems are the most efficient, followed by the graphite cells, and then the silicon blended cells. One confounding factor in the data is that the LTO cells are typically formulated to be power cells. Therefore, the thickness of the electrode and current collectors will have a positive effect on the efficiency of the system. In contrast, the silicon blend cells were designed with energy density as a primary

consideration resulting in these systems having slightly lower efficiencies. Adjusting for the electrode thickness confounding factor, the general trend still shows that the stable structure of LTO systems allows for higher energy efficiencies and confirms that the silicon systems may require improvements with regards to their electrical conductivity when used under conditions such as fast charge. DOE and USABC are investigating each of these chemistries to improve energy density, power density, cycle life and/or cost benefits. NREL's calorimeters provide the fundamental understanding of whether the inefficiencies shown below are due to chemistry or cell design.
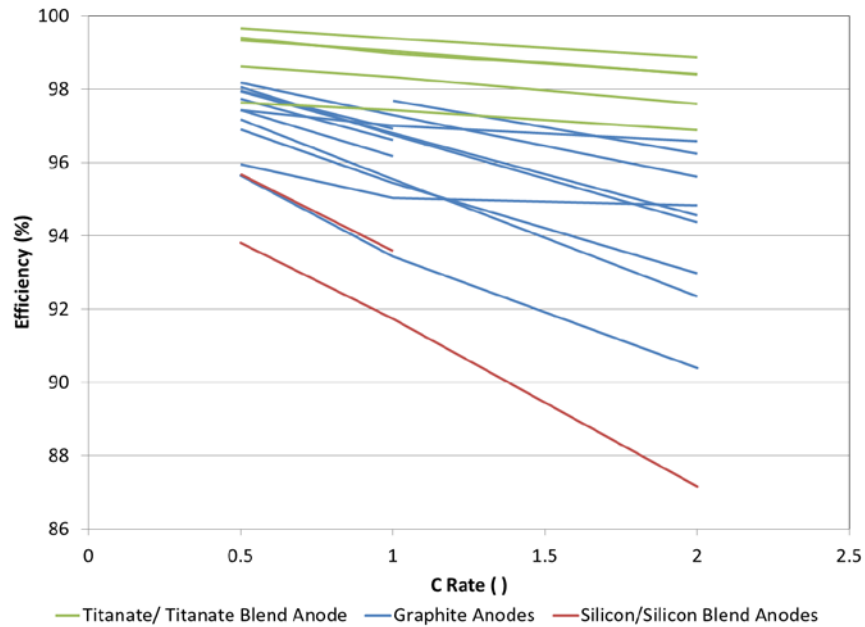

Figure III-26. Efficiency of cells tested at 30ºC in NREL's calorimeters during FY15/FY16/FY17
Credits/Source: NREL- Aron Saxon

Figure III-27 shows the partial charge and discharge efficiencies of a blended silicon system tested at NREL. The data trends indicate that the charge efficiency is higher than the discharge efficiency for c-rates less than C/1 and for the same amp-hour capacity returned/supplied–atypical of graphite systems and similar to titanate cells. The higher charge efficiency may be due to the voltage hysteresis associated with silicon systems–very similar to the hysteresis of NiMH batteries. To better understand this theory, it is necessary to understand how the heat efficiency is calculated. The heat efficiency of a cell is calculated with the following equation where the CalorimeterHeatMeasured is a direct calorimeter measurement of the heat from the cell after a cycle is completed and the ElectricalEnergyInOut is the amount of energy supplied or removed from the cell.

$$Heat\ Efficiency = \left(1 - \frac{CalorimeterHeatMeasured}{ElectricalEnergyInOut}\right) * 100$$

If the heat measured by the calorimeter is equal for both charge and discharge (it's not) and the same number of amp-hours are supplied/removed to/from the cell, then the charge efficiency will always be greater due to the voltage hysteresis. However, we can limit the voltage hysteresis by cycling the cell at a very low rate current. The data in Figure III-27 shows that even when the cell is cycled at C/10 discharge/charge rate, the charge heat efficiency is greater than the discharge heat efficiency but the two efficiencies are more equivalent at this lower rate. Finally, it should also be noted that the charge efficiency appears to trend lower once higher c-rates (C/1) are used – the joule heating effect is beginning to dominate and it is surmised that the trend will reverse at the higher rates.
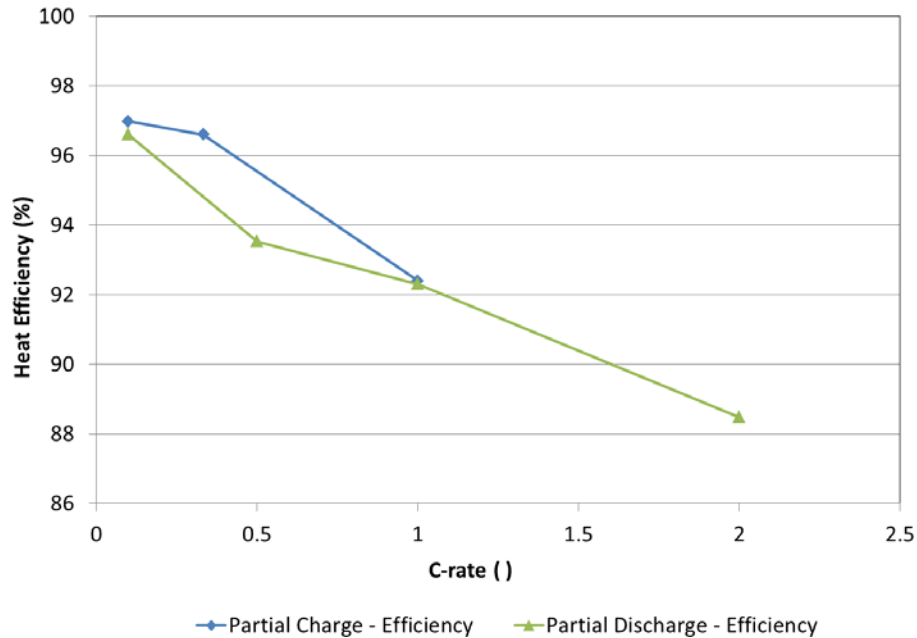
Figure III-27. Efficiency of silicon blended cells tested at 30°C in NREL's calorimeters under charge/discharge currents

Credits/Source: NREL- Aron Saxon

NREL's calorimeters were designed to be accurate enough to measure the electrochemical response from batteries under test – this capability allows NREL to understand benefits associated with design and chemistry changes to the cell. Figure III-28 shows the entropic heat generation rates normalized to the Ah capacity of the cell for the three different anodes – graphite, LTO, and silicon - at 30°C and under a constant current discharge. The cells in this figure were cycled over their entire depth of discharge range at a very low current – minimizing the current decreases the joule heating of the cell and allows for the entropic heat signature to be assessed. As shown in the figure, the cells can undergo endothermic and exothermic heat generation over the cycling range. The primary differences in the heat signatures from the three versions of the cell are due to the electrochemical changes in the anode since the cathode for each cell is a variation on the NMC chemistry. The graphite system is a fairly dynamic system undergoing several phase changes as the cell is cycled. The LTO system is slightly endothermic at the beginning of discharge; however, this endothermic response was due to a conductive additive incorporated into the anode and cannot be attributed to the titanate chemistry. LTO anodes are very stable structures and will show very little endothermic/exothermic heating within the cell. The final chemistry shown in the graph is for silicon blended cell which even though blended with graphite does not show the characteristic phase changes associated with the graphite only anodes. Furthermore, the silicon systems show a higher normalized heat generation rate as compared to the titanate and graphite anodes backing up the efficiency data shown previously in Figure III-26.
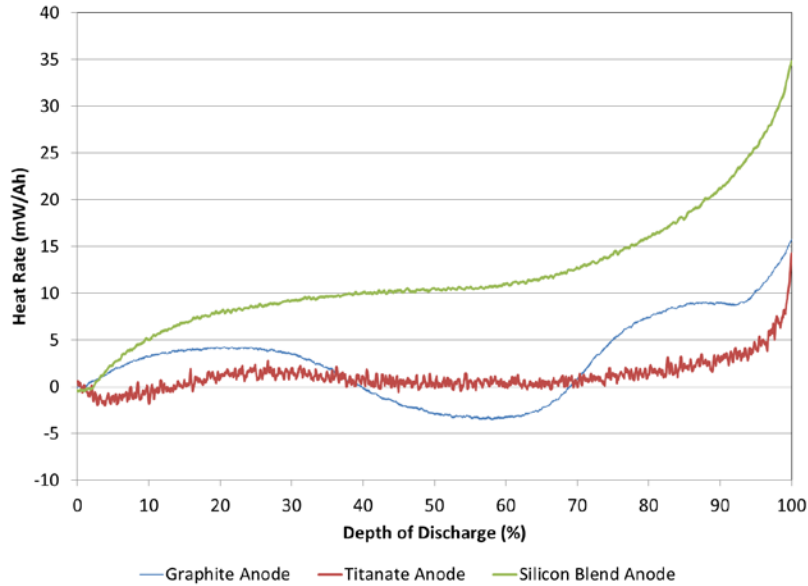
Figure III-28. Entropic response to graphite, titanate and silicon blended cells test at 30ºC

Credits/Source: NREL- Aron Saxon

Figure III-29 shows another unique finding from NREL's FY17 testing. The Figure shows the heat efficiency of an ultracapacitor tested in NREL's calorimeter at a temperature of 30ºC and under a constant current discharge/charge. Of note, the discharge efficiency increases as the current increases – atypical of battery systems tested at NREL. The increase in efficiency relates to where the charge is being stored within the cell – the Helmholtz layer near the electrode surface or in the volume of the electrolyte [2]. In essence, the calorimeter can distinguish between the heat contributed from the electrostatic resistance of the supercapacitor and the reversible entropic heating effects. Even though the endothermic heating response is minimal for this cell, the "cooling" effect could be used to minimize or limit the maximum temperature of the cell while in use.
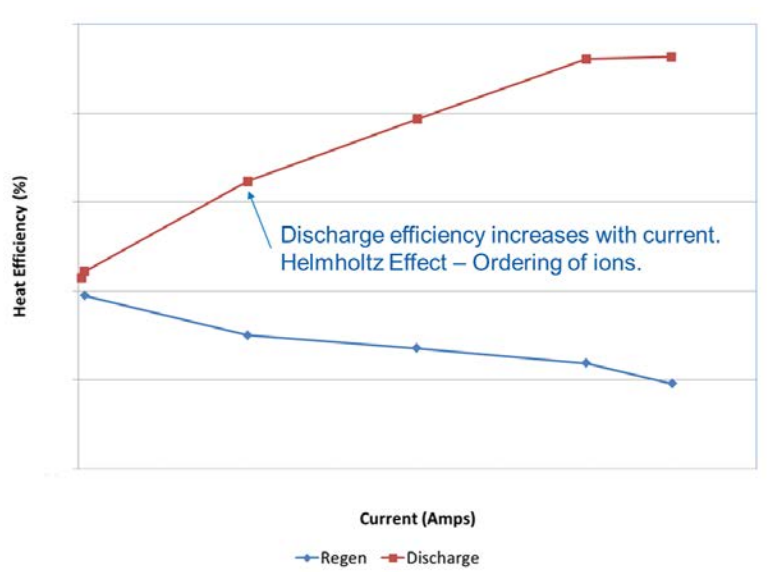

Figure III-29. Heat efficiency of an ultracapacitor under test in the calorimeter at 30ºC

Caption Credits/Source: NREL- Matt Keyser

Conclusions

NREL has thermally tested cells, modules, and/or packs from LG CPI, Envia, Farasis, Maxwell, and Saft during FY17. We've provided critical data to the battery manufacturers and OEMs that can be used to improve the thermal design of the cell, module, pack and their respective thermal management systems. The data included heat generation of cells under typical profiles for PHEV, EV, and 12 Volt Start/Stop applications, which is essential for designing the appropriate sized battery thermal management system. In FY18, NREL will continue to thermally characterize cells, modules, packs for USABC, DOE, and USDRIVE but the focus will shift to fast charging applications.

Key Publications

1. M. Keyser, A. Pesaran, et al., Enabling Fast Charging – Battery Thermal Considerations, Journal of Power Sources, 2017, 367 (228-236)

2. S. Ahmed, I. Bloom, et al., Enabling Fast Charging – A Battery Technology Gap Assessment, Journal of Power Sources, 2017, 367, (250-262)

3. 2017 DOE Annual Peer Review Meeting Poster on Battery Thermal Analysis and Characterization Activities

References

1. David Howell, Electrochemical Energy Storage R&D Overview, Annual Merit Review, Washington, DC, 2017

2. H. Gualous, H. Louahlia, et al., Supercapacitor Characterization and Thermal Modelling with Reversible and Irreversible Heat Effect, IEEE Transactions on Power Electronics, Vol. 26, NO. 11, November 2011

III.C Recycling and Sustainability

III.C.1 Life Cycle Assessment of Li-ion Batteries (ANL)

Jarod Kelly, Principal Investigator

Argonne National Laboratory
9700 S. Cass Avenue
Lemont, IL 60439
Phone: 630-252-6579
E-mail: jckelly@anl.gov

Samuel Gillard, Technology Manager
U.S. Department of Energy
Phone: 202-287-5849
E-mail: Samuel.Gillard@ee.doe.gov

Start Date:October 1, 2016   End Date: Ongoing
Total Project Cost: $125,000   DOE share: $125,000   Non-DOE share: $0

Project Introduction

Quantifying the embodied energy and environmental impact of lithium-ion batteries (LIB) is key to understanding the potential for reducing energy use and pollutant emissions from the transportation sector via the use of electric vehicles. This project investigates the material and energy flows pertaining to battery material production, battery manufacturing and assembly, and battery recycling, to characterize the life-cycle energy and environmental burdens of LIB. By interacting with battery manufacturers and recyclers, we obtain primary data on the energy and water use for commercialized LIB production and recycling, and identify environmental impact drivers, production bottlenecks, and other barriers, for LIB production and recycling. A framework of an environmental ranking tool for LIB is also developed and presented to the global sustainability research community for feedback.

Objectives

- Quantify progress toward reducing transportation-sector life-cycle petroleum use and GHG emission via electric vehicle use

- Identify bottleneck, both energy- and emission-intensive, stages in LIB production to inform and guide research and development of the Vehicle Technologies Office (VTO) and other stakeholders

- Acquire and integrate LIB assembly data through communication with Chinese collaborators and battery industry

- Assess different criteria and frameworks for an environmental ranking system of automotive LIB using the Greenhouse gas Regulated Energy and Emissions and Transpiration (GREET®) model

Approach

In our initial work, we developed cradle-to-gate energy consumption and air emissions for electric vehicle batteries with an $LiMn_2O_4$ cathode. These data were incorporated into Argonne's GREET model and released in GREET1_2014. Life cycle analysis (LCA) of batteries with other cathode materials based on detailed process data has been used to identify potential environmental roadblocks to battery production, and to compare energy savings and emissions reductions enabled by different types of recycling processes. Analysis of recycling processes revealed cathode recovery as a key to process economic viability for low-Co cathodes. The cathode materials that were the focus of that work were lithium cobalt oxide ($LiCoO_2$), lithium iron

phosphate ($LiFePO_4$), nickel manganese cobalt ($LiNi_{0.4}Co_{0.2}Mn_{0.4}O_2$), and an advanced cathode that has been the subject of research at Argonne, $0.5Li_2MnO \cdot 0.5LiNi_{0.44}Co_{0.25}Mn_{0.31}O_2$ (LMR-NMC). The anode paired with each of these cathode materials is typically graphite, although we have also developed an analysis for silicon and pure lithium anodes. In FY16, we added material and energy flows for the production of nickel cobalt aluminum ($LiNi_{0.8}Co_{0.15}Al_{0.05}O_2$), an important cathode material, in GREET.

In FY17, energy and water consumption for LIB production was compiled via two routes. The first was through literature review, and the second was via site visits to two leading Chinese LIB manufacturers conducted in March 2017. In addition to LIB manufacturers, site visits were also made to a leading Chinese LIB recycler where process design, together with material and energy flows of a commercialized hydrometallurgical LIB recycling process were obtained. Collected data were analyzed, compared to literature, and incorporated into the GREET model as appropriate, which produced new estimates of life-cycle energy use and environmental impacts of both LIB manufacturing and recycling.

Mimicking the Electronic Product Environmental Assessment Tool (EPEAT) program, the framework for a Battery Environmental Assessment Tool (BEAT), was developed, and later presented at the 2017 Joint Conference - 9th biennial conference of the International Society for Industrial Ecology for feedback.

Results

Battery Production Life Cycle Modeling

Data that we collected from our site visits to Chinese LIB manufacturers showed that these industrial-scale (2GWh per year), at-capacity plants (40,000 cells per day rated capacity, 30,000 cells per day throughput), consume about 170 MJ of energy in order to produce 1 kWh LIB. Of this 170 MJ of energy, 30 MJ is comprised of electricity demand, and the remaining 140 MJ is heat demand. Dry room operation and electrode drying are the most energy-intensive LIB production processes, accounting for 56% and 42% of the total energy consumption, respectively. The 170 MJ/kWh energy intensity is significantly lower than what has been reported in the literature, which ranges from 590 to 2300 MJ/kWh. By examining previously reported energy intensities together with their associated plant capacities we determined that as the production capacity of a LIB plant increases, the energy intensity for LIB production decreases, this is likely due to economies of scale, particularly the ability to increase throughput in the energy intensive dry room stage, and more efficient process design.

The contribution of process energy to the total cradle-to-gate energy for LIB production is shown in Figure III-30. In addition to energy, the process water requirement for LIB manufacture and assembly is estimated to be 8.6 gallon per kWh battery produced based on our site visits, and this accounts for 7% of the cradle-to-gate water consumption in LIB production.

While lead acid batteries and LIBs serve very different functions within the automotive sector, we are often asked to compare the two in order to understand the different environmental impacts they have. Figure III-31 shows a collection of comparisons between lead acid batteries (from virgin production and using current practices having 73% recycled lead) and LIB. It presents the energy use, GHG, and SO_x results for lead acid and LIBs (LCO as solid bar, and LMO as dashed line) considering a per-kg, per-Wh, and per-lifetime basis. Results indicate that lead acid batteries generally have an advantage in energy and environmental metrics on both a per-kg and per-Wh basis over LCO and LMO, though LMO's SO_x emissions are comparable to lead acid's current practice on a Wh basis. When considering the lifetime of the batteries within vehicles we observe that LMO batteries outperform lead acid batteries in each of those metrics considering regardless of lead acid battery production assumption. But, we observe that LCO outperform virgin lead acid batteries in all categories, but not LCO lags lead acid batteries produced from recycled lead in the GHG and SO_x metrics.
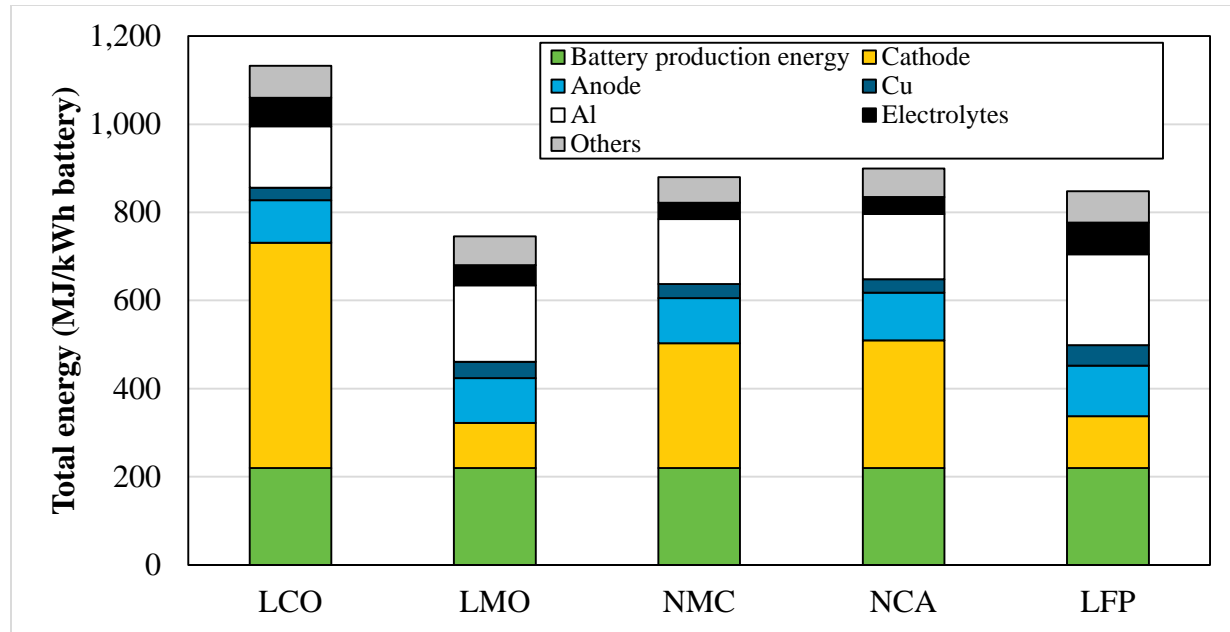
Figure III-30. Total energy breakdown for LIB production. LCO stands for LIB based on $LiCoO_2$ cathode material, LMO $LiMn_2O_4$, NMC $LiNi_{1/3}Mn_{1/3}Co_{1/3}O_2$, NCA $LiNi_{0.8}Co_{0.15}Al_{0.05}O_2$, LFP $LiFePO_4$

In Figure III-32, we compare ICEV and BEV, charged using the US grid on both GHG and SO_x emissions. The results, presented on a per-kilometer basis, consider midsize sedans for BEVs with LCO and LMO batteries, along with a standard midsize ICEV. GHG emissions for the LCO and LMO are nearly equal and significantly lower than the ICEV GHG emissions, while ICEV has lower SO_x emissions than either BEV, with LCO having significantly higher SO_x than the LMO, owing to differences in ore mining and processing emissions.
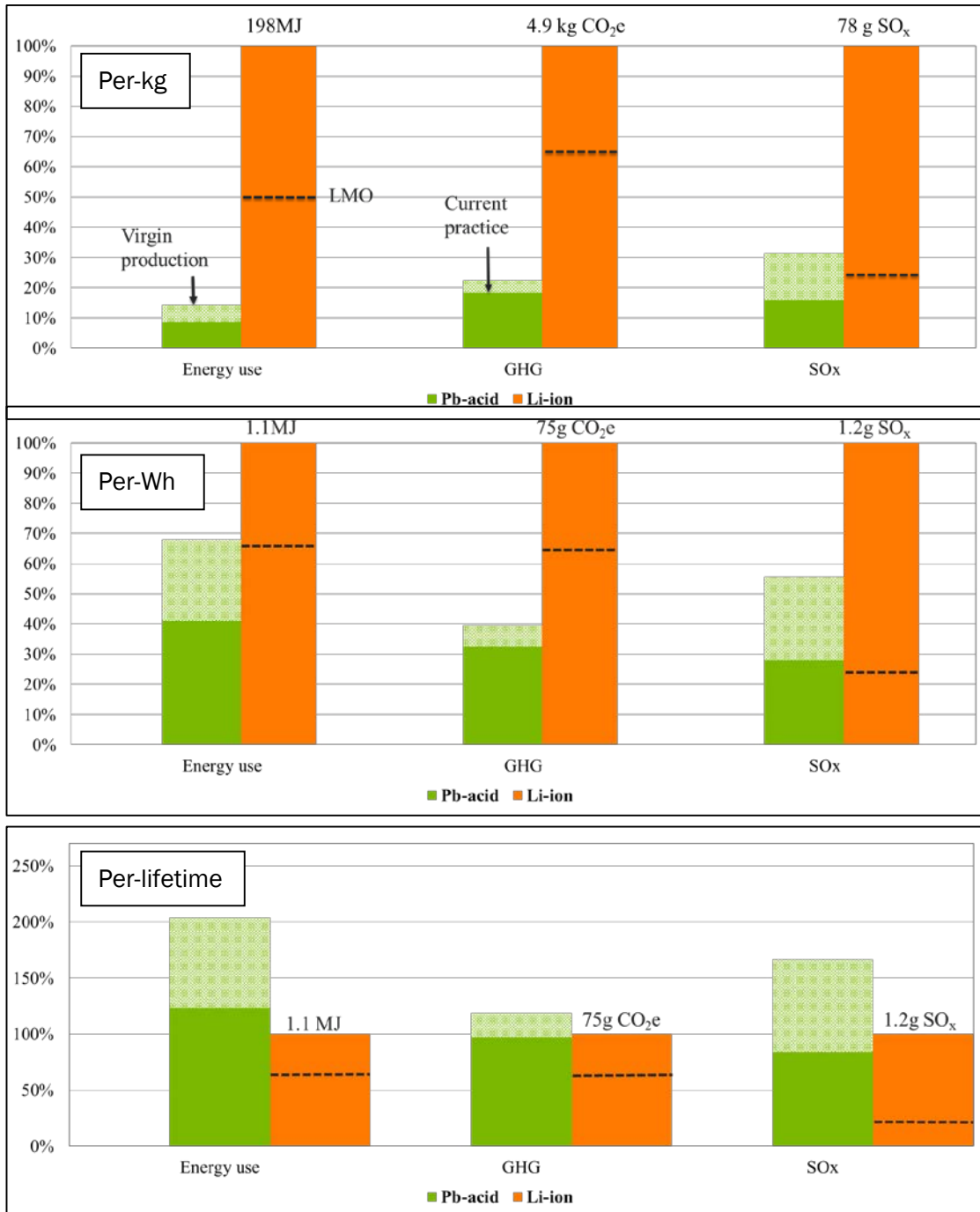
Figure III-31. Comparison of lead acid and LIB energy use and emissions on a per-kg, per-Wh, and per-vehicle lifetime basis, dashed line represents LMO results within LIBs. Lifetime basis assumes three lead acid batteries and one LIB per vehicle lifetime. Solid orange LIB is LCO while black dashed line is LMO
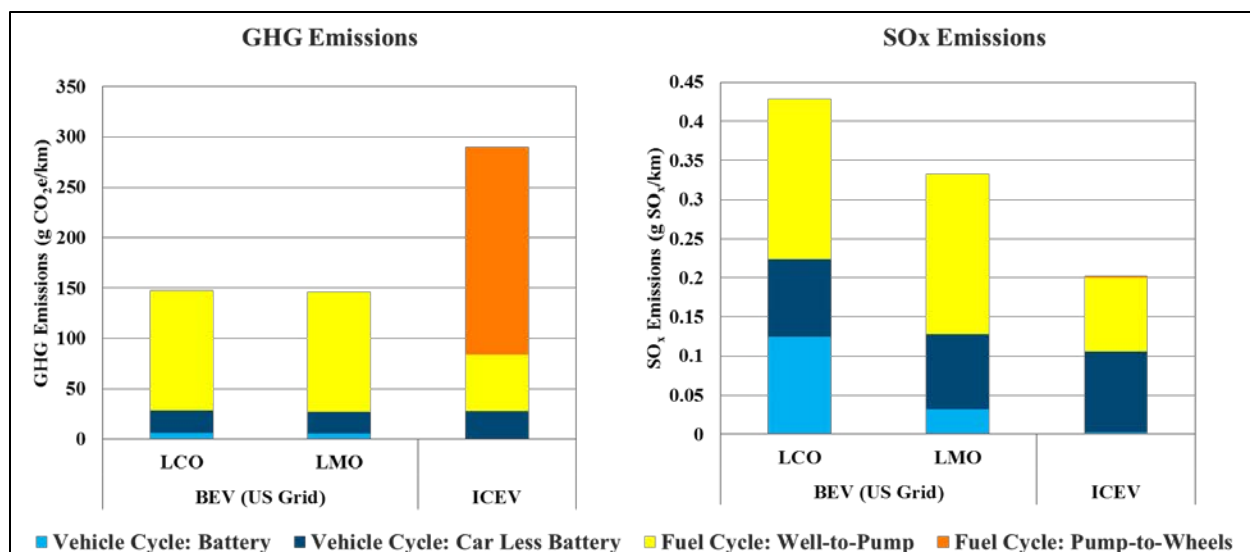
Figure III-32. BEVs and ICEV considering GHG and SO$_x$ emissions on a per kilometer basis. BEVs utilized LMO and LCO cathode chemistries for the two LIB comparisons.

Battery Recycling Life Cycle Modeling

While battery recycling is the primary focus of a complementary battery analysis task, we have worked closely with those researchers in order to ensure data and knowledge sharing. That task, through communications with collaborators at the Beijing Institute of Technology, and China Automotive Technology and Research Center, identified that LIB recycling has been commercialized in China, and all leading LIB recyclers in China adopt the hydrometallurgical recycling technology. A detailed recycling process has been formulated and included in the GREET model. From a life cycle perspective, we observe that direct physical recycling technology has the biggest potential to reduce the energy use and environmental impacts of LIBs, by recovering more components of the spent battery.

BEAT: Battery Environmental Assessment Tool

We examined different criteria and frameworks for applying the lithium-ion battery module within GREET, or a derivative of it, towards an environmental certification, or ranking system, for automotive lithium-ion batteries in a manner similar to that of the Electronic Product Environmental Assessment Tool (EPEAT), supported by the U.S. EPA. EPEAT is a program that provides environmental product ratings of PCs and displays, imaging equipment, and televisions. After thorough review of EPEAT, and a comprehensive life-cycle evaluation of LIB using GREET, with a focus on energy and environmental metrics, as well as recyclability, we proposed the Battery Environmental Assessment Tool (BEAT) framework, depicted in Figure III-33. This framework was presented at the 2017 Joint Conference - 9th Biennial Conference of the International Society for Industrial Ecology, 25th Annual Conference of the International Symposium on Sustainable Systems and Technology in Chicago, which allowed critical feedback from a variety of academic and industrial colleagues.

IEA Interaction

In support of the International Energy Agency (IEA) activities related to the assessment of environmental aspects and life cycle analysis of electric vehicles, we provided analysis of the US battery electric vehicle (BEV) and plug-in hybrid electric vehicle (PHEV) fleets. These data were incorporated into a harmonization study that compared BEV and PHEV in various countries throughout the world. Due to the unique U.S. circumstances of vehicle characteristics, driving and ownership patterns, as well as vast differences in regional U.S. electrical grids, we developed sales-weighted average vehicle profiles in the U.S. and simulated them within a sales-weighted electrical grid.
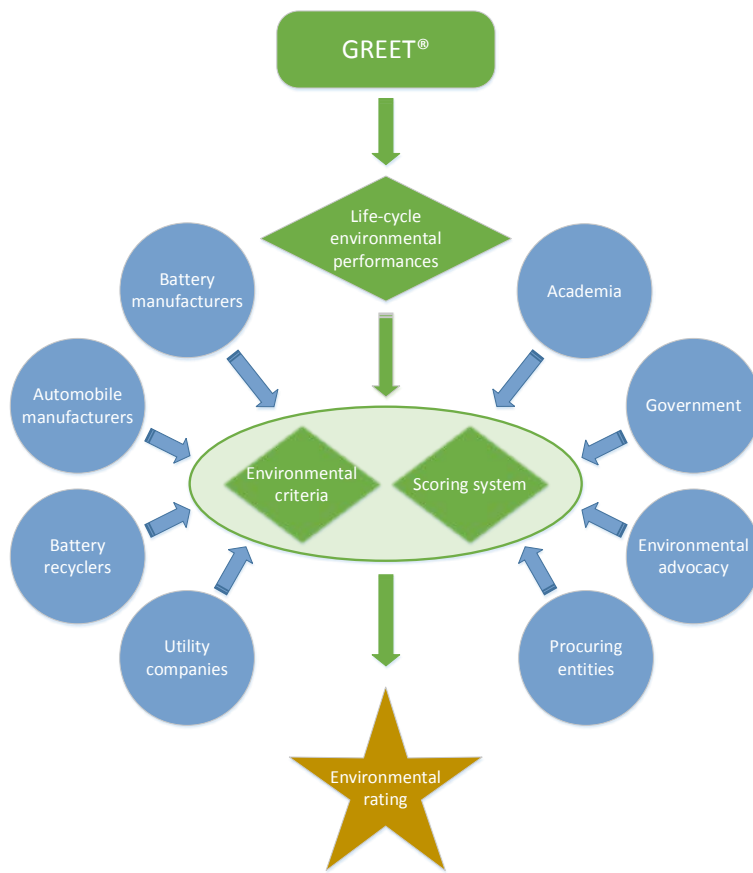
Figure III-33. Framework for BEAT

Conclusions

During the course of FY17 battery LCA research, we determined that dry room operation and electrode drying accounts for over 90% of process energy consumption for LIB production. We were able to ascertain this through collaboration and on-site visits with Chinese LIB battery manufacturers. We have further identified that upstream production of active cathode material, and process energy use are the major contributors to environmental burdens of LIB. In agreement with our previous findings, we show that recycling of spent batteries offers a large opportunity for battery life-cycle environmental impacts reduction. We have proposed a LIB environmental product rating framework called BEAT, which encourages sustainable design, production, use, and recycling of LIBs. We have also provided support to the analysis of BEV and PHEV in the IEA's effort to provide a globally harmonized analysis of such vehicles. While significant progress has been made in FY17, continuous interaction with stakeholders is crucial to conduct the most representative and accurate LCA of LIBs.

Key Publications

1. Dai, Qiang, Jennifer Dunn, Linda Gaines and Jarod Kelly. "Battery Environmental Assessment Tool (BEAT): Documenting the Sustainability of Li-ion Batteries." Abstract of presentation at the 2017 Joint Conference - 9th biennial conference of the International Society for Industrial Ecology, 25th annual conference of the International Symposium on Sustainable Systems and Technology, Chicago, IL US, June 25, 2017 - June 29, 2017.

2. Dai, Qiang, Jennifer Dunn, Jarod Kelly, and Amgad Elgowainy. "Update of Life Cycle Analysis of Lithium-ion Batteries in the GREET Model". 2017. Argonne White Paper. https://greet.es.anl.gov/publication-Li_battery_update_2017.

III.C.2   Battery Production and Recycling Materials Issues (ANL)

Linda Gaines, Principal Investigator
Argonne National Laboratory
9700 S. Cass Avenue
Argonne, IL 60439
Phone: 630-252-4919
E-mail: lgaines@anl.gov

Samuel Gillard, Technology Manager
U.S. Department of Energy
Phone: 202-287-5849
E-mail: Samuel.Gillard@ee.doe.gov

Start Date: January 1, 2008   End Date: September 30, 2019
Total Project Cost: $125,000   DOE share: $125,000   Non-DOE share: $0

Project Introduction

Examination of the production of batteries from raw material acquisition to assembly illuminates the stages of this supply chain that incur the greatest energy and environmental burdens. Recycling of material from spent batteries will be a key factor in alleviating potential environmental and material supply problems. We examine battery material production, battery assembly, and battery recycling processes that are available commercially now or have been proposed. Battery materials, assembly, and recycling processes are compared on the basis of energy consumed and emissions, suitability for different types of feedstock, and potential advantages relating to economics and scale. We compare the potential of recycling processes to displace virgin materials at different process stages, thereby reducing energy and scarce resource use, as well as potentially harmful emissions from battery production. Although relatively few automotive batteries have been produced to date, viable processes will be required to recycle them when they are no longer usable. Secondary use of the batteries could delay return of material for recycling.

Objectives

- Examine material scarcity issues that may influence viability of automotive lithium-ion batteries

- Characterize lithium-ion battery recycling in the United States and abroad to identify the most promising recycling technologies as they evolve, barriers to recycling, and influence of recycling on material scarcity

- Engage with the international battery recycling community to exchange information and identify paths to advancing battery recycling technology and enabling adoption

- Postulate improved recycling processes to maximize material recovery

- Determine impact of battery reuse on recycling processes and economics

- Formulate actions to address developing technical and institutional issues concerning used batteries

Approach

We estimated the maximum reasonable demand for battery materials, based on extremely aggressive scenarios for penetration of electric-drive vehicles. We combined vehicle demand growth with detailed battery designs and looked at how lithium demand might grow world-wide. We also estimated how much material could be recovered by recycling, thus reducing demand for virgin materials. We determined that cumulative world demand for lithium to 2050 would not strain known reserves. More recent estimates of material demand for all

uses also identifies cobalt as a key material (see Table III-10). Although cobalt supplies could be a significant constraint, the envisioned move away from chemistries containing large quantities of cobalt may obviate the worst potential problems.

Table III-10: Material Demand to 2025 vs. USGS Reserve Estimates

Material	Demand (1000 tons)	Reserves (1000 tons)
Lithium	223	14,000
Cobalt	714	7,000
Nickel	712	78,000

Life cycle analysis (LCA) is being used to further identify potential environmental and economic roadblocks to battery production, and to compare energy savings and emissions reductions enabled by different types of recycling processes. Economic analysis of recycling processes revealed cathode recovery as a way to achieve economic viability for recycling of low-Co cathodes. Examination of environmental impacts determined that emissions of sulfur oxides could be minimized by recycling any of the transition metals generally smelted from sulfide ores.

Close interactions with stakeholders are sustained to remain on top of technological and legislative developments associated with LIB production and recycling, and to maintain Argonne's position as the world's leader in battery recycling research and analysis. During FY17, Argonne staff 1) gave invited talks and presentations to government, industry, AABC, ILA, ABA, Battery Industry Day, ACT Expo, NAATBATT Workshop, and numerous visitors; 2) ran a breakout session at Argonne's Battery Industry Day; 3) served on SAE, NAATBATT recycling committees and the Scientific Advisory Committee of Responsible Battery Coalition; 4) negotiated potential battery recycling and modeling work with ILA, ALABC, RBC, and INEMI; and 5) responded to countless requests for information. Argonne has examined recycling processes and businesses for other battery types, in particular lead-acid, to determine what lessons can be learned from successfully established systems.

Results

Based on our analysis, recycling provides energy conservation benefits and reduces the local impacts of metal recovery and purification. Benefits differ by recycling process and increase as more materials are recovered. Figure III-34 shows how energy to produce a cell can be reduced by use of more types of recovered materials. Recycling is especially beneficial when cathode materials contain nickel or cobalt. In the case of LiCoO2, the recovery and purification of the metal dominates the overall energy consumption of producing this cathode material, so recycling results in significant energy savings (and sulfur emission reductions).

Stakeholders at the Argonne battery recycling workshop (held at the very end of FY16) agreed on several points that require additional work. Although recycling technologies have been demonstrated, basic process R&D is needed to determine the optimal recycling method for each Li-ion chemistry, especially lower cobalt cathode materials. For such materials, it appears that direct recycling, still only demonstrated at bench scale, offers the only real prospect of being economically feasible, but a segregated feed stream would be required. For any process, the goal is to maximize the yield of valuable materials at lower recycling cost. Optimized processes would then require demonstration on a larger scale, but this might not be sufficient because manufacturers are skeptical about putting recycled material back into batteries. Therefore, we need to develop product specifications that recycled materials must meet. Furthermore, there is not yet enough material available to support full-scale infrastructure for collection and processing. There should be enough material from consumer electronics, but those batteries are generally not getting collected, let alone recycled. The potential for restrictive government regulations also hinders recycling business development, so the industry could consider pre-emptive self-regulation. Challenges to be faced for Li-ion battery recycling are shown in Table III-11, with suggestions for how they can be addressed.

Table III-11: Challenges for Li-Ion Battery Recycling

Challenge	R&D Needed to Address
Long-term performance of some recycled materials is not proven	Long-term testing
There is no standard chemistry or design	Convergence of chemistries and designs Flexible processes Design for recycling Automation
There are no regulations, so restrictive ones could be imposed	Fashioning regulations that will protect health and safety without hindering recycling
Many of the constituents have low market value	Process development to recover multiple high-value materials
Low value of mixed streams, prevention of fires and explosions	Effective labeling and sorting

Detailed understanding of recycling processes will be necessary to maximize material recovery. A simple experiment was conducted to demonstrate how pH and temperature affect the loss of Li in cathode material. High pH has no impact, but low pH (acid conditions) remove much of the lithium (see Figure III-34); this information will help enable efficient recycling process design. Additional experiments will be proposed to fully characterize properties of potentially recoverable materials. In particular, low-temperature processes that can recover usable cathode material will be characterized in detail. We hope to determine such things as whether mild treatment could remove surface layers without disturbing the crystal morphology.
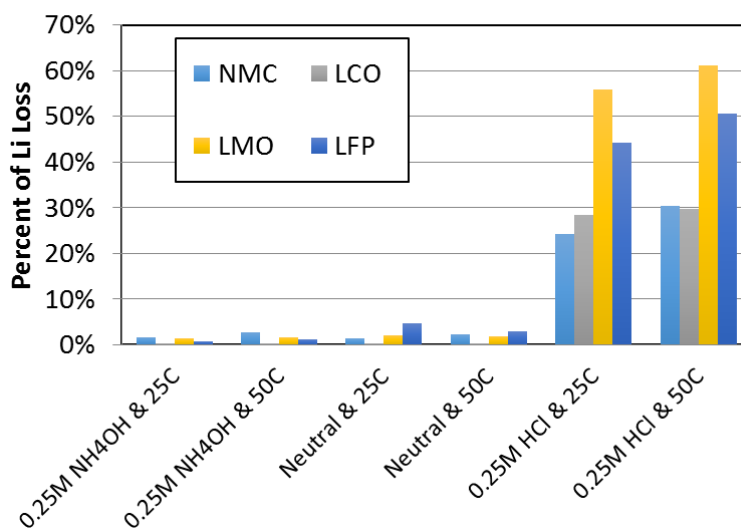

Figure III-34. Dependence of lithium loss on severity of treatment

Through communications with our collaborators at Beijing Institute of Technology, and China Automotive Technology and Research Center, we learned that LIB recycling has been commercialized in China, and all leading LIB recyclers in China adopt the hydrometallurgical recycling technology. Detailed recycling process design, obtained from our site visit, is depicted in Figure III-35. Securing reliable supplies of spent LIBs at reasonable costs is the major challenge facing Chinese LIB recyclers.
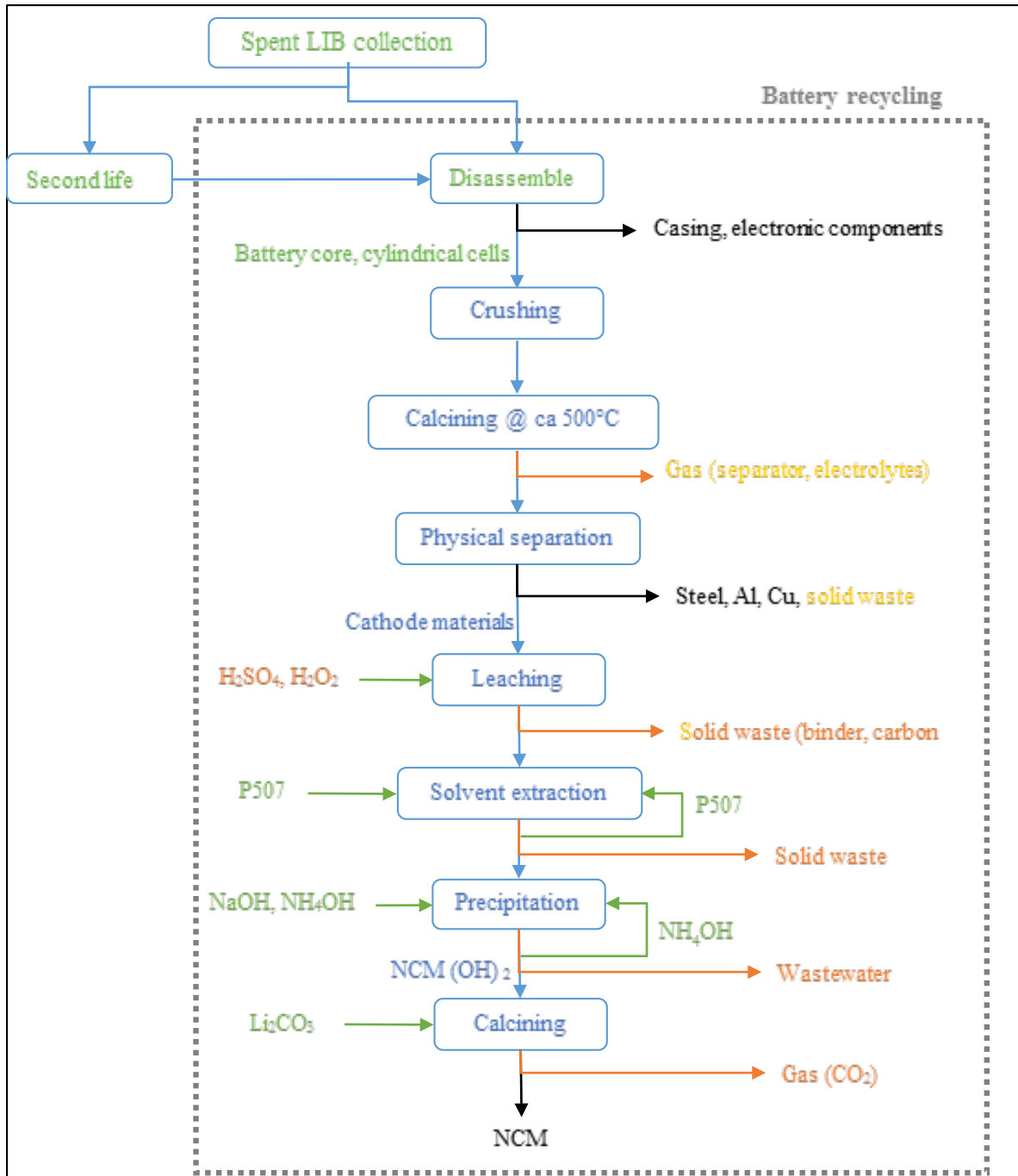
Figure III-35. Process Flow Diagram for Commercialized Hydrometallurgical Recycling Process for LIB

In contrast, LIB recycling has yet to be fully commercialized in the U.S. Retriev operates a plant featuring intermediate recycling technology, but it is not running at capacity. Direct recycling technology is under development at laboratory-scale. The direct physical recycling technology, however, has the biggest potential to reduce energy use and environmental impacts of LIB, by recovering more components of the spent battery, as can be observed in Figure III-36. Barriers to growth of LIB recycling in the U.S. include low collection rate of spent LIB, unstandardized LIB designs, confusion over liability for LIB recycling, and uncertainty in the market for recovered materials. Several companies are moving forward with plans for hydrometallurgical recycling in the US, and each employs a different set of process steps. We continue to gather detailed recycling process information to include in our ReCell closed-loop lifecycle, which will serve as a useful tool in comparing process costs and environmental impacts.
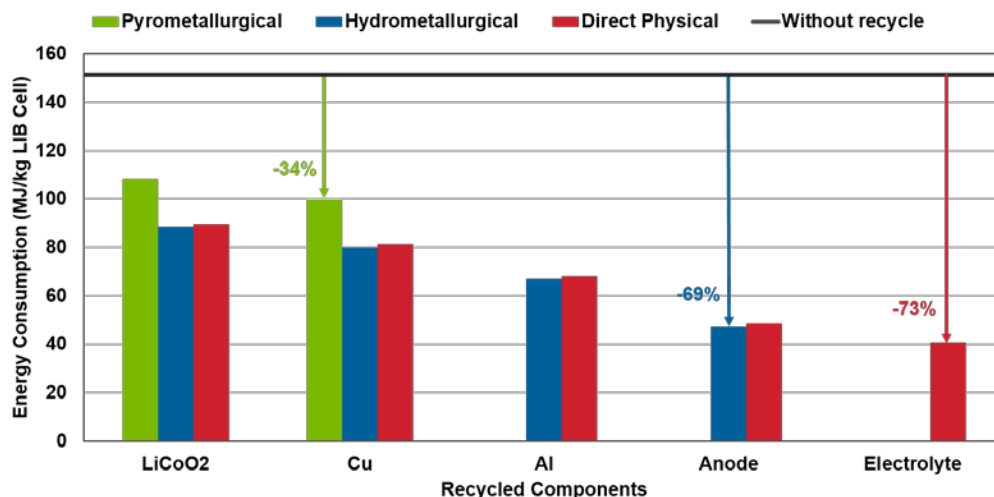

Figure III-36. Increase in energy savings as more materials are recycled to useful products

Conclusions

Recycling has the potential to significantly reduce both demand for raw materials and energy and environmental impacts of battery production. However, technical and economic barriers must be overcome before recycling will be available on a large scale. Through engagement with stakeholders, publications and presentations, Argonne has disseminated its research results in this area and fostered open discussion of technical, institutional, and economic issues involved in recycling of lithium-ion batteries.

Key Presentations/Publications

1. Gaines, Linda. "Li-ion Battery Recycling: Using Lifecycle Analysis to Avoid Roadblocks." Slide presentation at the 2016 NAATBatt Workshop on Advanced Battery Recycling, Ann Arbor, MI, November 30, 2016.

2. Gaines, Linda and Jeff Spangenberger. "Recycling of automotive li-ion batteries: Government perspective." Slide presentation at the 2017 SAE Government/Industry Meeting, Washington, DC, January 25–27, 2017.

3. Gaines, Linda. "Recycling of Automotive Li-Ion Batteries." Institutional Talk at Argonne National Laboratory, February 23, 2017. (American Bar Association webinar)

4. Gaines, Linda. "Recycling of Automotive Lithium-Ion Batteries." Slide presentation at the 2017 Advanced Clean Transportation Expo, Long Beach, CA, May 1, 2017.

5. Gaines, Linda and Qiang Dai. "Compare and Contrast: Pb-acid and Li-ion Batteries." Slide presentation at the 17th Advanced Automotive Battery Conference, San Francisco, CA, June 19–22, 2017, and International Lead Association Meeting, Berlin, Germany, June 28–29, 2017.

III.C.3   Closed-loop Battery Recycling Model (ANL)

Jeffrey Spangenberger, Principal Investigator
Argonne National Laboratory
9700 S. Cass Avenue
Argonne, IL 60439
Phone: 630-252-5543
E-mail: jspangenberger@anl.gov

Samuel Gillard, Technology Manager
U.S. Department of Energy
Phone: 202-287-5849
E-mail: Samuel.Gillard@ee.doe.gov

Start Date: July 1, 2017   End Date: September 30, 2018
Total Project Cost: $275,000   DOE share: $275,000   Non-DOE share: $0

Project Introduction

The number of battery powered vehicles sold in the US has grown from 52,500 units in 2012 to over 160,000 vehicles sold in 2016; that is a 300% increase in just 4 years. These vehicles will start reaching their end of life over the next several years and processing of these batteries will need to be addressed. There are currently a few companies that accept lithium ion batteries from vehicles for recycle, but in most cases it costs vehicle owners money to have them properly treated. The value from recycled batteries comes predominately from its cobalt content, but it is this very reason that battery manufacturers are working to reduce the cobalt content making the value of the obsolete batteries even less. It is critical that a cost-effective system be developed for handling these products. Without this element, batteries will be mishandled resulting in health, safety and even cost implications. A properly designed recycling infrastructure is also key to addressing public health, environment and material scarcity issues, and national security.

To expedite the development of a sustainable, revenue positive, advanced battery recycling infrastructure, Argonne has developed a high-level, closed-loop battery recycling model using internal Argonne funding. The baseline model was designed with industry-wide generic recycling technology paths (pyrometallurgical, hydrometallurgical, and direct) and unit processes, and with the flexibility for individual companies to modify the model to add company-specific technologies and processes. It is modularized to enable changes and expansions. The model, which leverages Argonne's BatPaC and GREET models, is capable of providing cost and environmental impacts through the many stages and processing steps of a lithium-ion battery's lifecycle. The tool provides insight into the impacts of battery recycling and other process steps to allow all stakeholders to simulate and visualize the broader cost and environmental impacts. The model gives the stakeholder a high-level preview of the implications that process and chemistry selection changes could have on their interests, as well as other stakeholders' interests. The tool is intended to help develop improved battery recycling processes and verify critical materials recovery. This model will accelerate battery research, guiding its direction towards the optimization of both process specific, and overall, economic, energy, and environmental impacts.

Objectives

The overall objective for this project includes further advancement of the model with a focus of increasing the accuracy of the output generated. To do this the following objectives have been identified:

- Add nickel-rich cathode chemistries to the model to increase the number of chemistries available for evaluation

- Complete an updated model that is more accurate than the baseline model and incorporates a more intuitive user interface so it is more inviting to potential users

- Report out modeling results to identify opportunities for improvement amongst the various stages of a battery's life

- Integrate battery cathode and cell manufacturing into the model and identify technical gaps

- Perform a preliminary investigation of Li-S battery chemistry recycling and report on the findings

Approach

This project was started in Q4 of 2017. As a result, only selected objectives were addressed during FY17. These include the addition of nickel-rich cathode chemistries and the start of building a newly structured model that is easier to use and incorporates new information obtained through literature review and interaction with stakeholders.

In order to address the newer cobalt-poor cathodes, NMC 622 and NMC 811 were added (NCA was already available for use) to the list of cathodes available. This required the use of Argonne's BatPaC model for the generation of a bill of materials. For the case of NMC 811, not available in BatPaC, a cathode model needed to be developed in order to identify the bill of materials from BatPaC. In addition, all of the equations in the existing closed-loop model were updated to include the selection of these cathode chemistries.

In order to design an improved model, literature reviews and interaction with stakeholders was undertaken. This will be an ongoing activity throughout this project to make sure the information is as accurate and relevant as possible. Battery manufacturers, OEMs, battery recyclers and material providers were contacted.

Future work involves the incorporation of new information from stakeholders throughout FY18 into the updated model. Additionally, the focus of this initial work was not to obtain specific results from the model, but rather address previously identified gaps to create a more robust model. (See Figure III-37.)
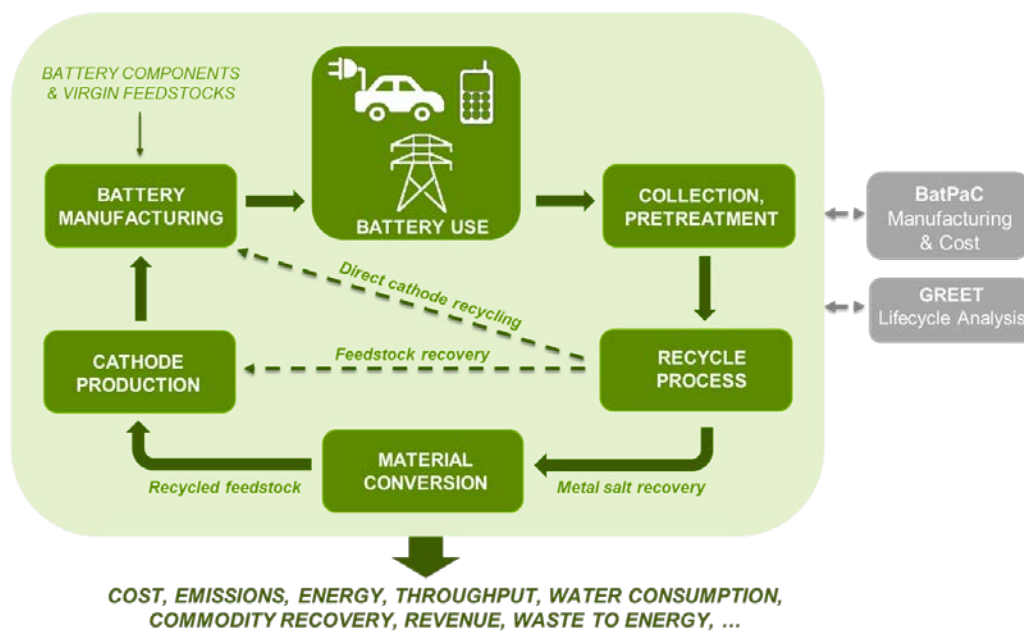

Figure III-37. Closed-loop flow of the battery recycling model

Results

The addition of NMC 622 and NMC 811 to the model allows these cathodes to be included in evaluations using the baseline model configuration. Using these and the other cathodes, the baseline model demonstrated appropriate outputs. Examples of these indicate the pyrometallurgical route was the least cost effective method of recycling end of life batteries while the hydrometallurgical route demonstrated an improved cost scenario.

Direct recycling, which is only at lab scale currently, has the most potential for cost recovery and reduction of environmental impact but there are many challenges that direct recycling still face before becoming a reality. Concerning energy savings, preliminary output from the model indicates that there is potential for all three recycling methods to reduce the energy required to make new cells with recycled cathode material. As compared to manufacturing cells with virgin cathode pyrometallurgical, hydrometallurgical and direct show potential to use about 90%, 75% and 60% of the required energy to that of virgin.

The biggest result of this work thus far involves the identification of gaps that exist in the model and working to address them. The largest gaps are obtaining detailed process flow sheets and unit operations for the various recycling processes. Comprehensive pyrometallurgical process flows for industrial scale installations are closely guarded in order to maintain a competitive advantage. There are currently no hydrometallurgical processes designed specifically for battery recycling in the U.S. so information is more difficult to obtain. Direct recycling has not yet reached pilot scale so information on a full scale facility is not available and future processes are still being developed. Without this critical information there are many assumptions made regarding equipment costs, material costs and operating expenses. This lack of information also results in less clarity of the environmental impacts that these systems have. Literature reviews and costing models are used to obtain much of the information.

Conclusions

There are currently very few lithium ion, plug-in vehicle batteries reaching recycling facilities. The number of these batteries that are going to be reaching their end of life and needing to be treated in a cost effective and in an environmentally friendly manner is going to dramatically increase in the next several years. There remains a significant challenge to get a cost effective infrastructure in place quickly enough to handle these batteries. Argonne has developed a high-level, closed-loop battery recycling model using internal Argonne funding during FY17. This project's goal is to improve the accuracy and ease of use of the baseline model by using interaction with stakeholders to help identify and fill gaps in the model and to help steer model development so that it can be used in the most productive manner. The successful outcome of this work will be a tool that everyone can use to help accelerate the development of the most cost effective battery recycling systems and with a reduction of environmental impacts over entire lifecycle of the battery.

IV. U.S. China Clean Energy Research Center (CERC)

IV.A Development of High Energy Battery System with 300Wh/kg (ANL)

Khalil Amine, Principal Investigator

Argonne National Laboratory
9700 S Cass Avenue
Lemont, IL 60439
Phone: 630-252-3828
E-mail: amine@anl.gov

David Howell, Technology Manager

U.S. Department of Energy
Phone: 202-586-3148
E-mail: David.Howell@ee.doe.gov

Start Date: October 1, 2016   End Date: September 30, 2019
Total Project Cost: $2,760,000   DOE share: $1,730,000   Non-DOE share: $1,030,000

Project Introduction

Transformational changes in battery technologies are critically needed to enable the effective use of renewable energy sources, such as solar and wind, and to allow for the expansion of the electrification of vehicles. For these applications, batteries must store more energy per unit volume and weight, and they must be capable of undergoing many thousands of charge-discharge cycles. Therefore, developing high-performance batteries is critical to meet these requirements, which certainly relies on material breakthroughs. In the meantime, to enhance the performance and lifetime of batteries (specifically lithium-ion batteries), it is very critical to understand, for example, the formation of the solid-electrolyte interphase (SEI) layer, and the degradation mechanisms in battery electrodes, oftentimes, at the nanometer scale. Under this circumstance, various state-of-the-art in-situ and operando characterization tools are very critical to understanding battery behavior and could help address all the major issues of lithium batteries and beyond. The collaborative work with our colleagues from china will consist of the following:

- Development of advanced in situ characterization tolls to understand failure mechanism in different battery systems with focus on high voltage high energy cathode (230mAh/g)

- Characterization of Silicon-Based Anode Materials and their Solid-Electrolyte Interphase (SEI)

- Characterization of Lithium Sulfur Batteries

- Investigation of the safety of batteries at the component and pack level

- Characterization and development of new catalysts to improve the efficiency of Li-O2 batteries and/or Zinc ion Battery

Objectives

This project will conduct research on rechargeable Li-ion battery and beyond lithium ion to help develop the next generation of advanced batteries that can help expend electrification of vehicles and enable smart grids.

The main objective is to understand and develop advanced battery chemistries based on lithium ion and beyond lithium ion that meet 300wh/kg energy density.

Approach

Task 1 Development of advanced in situ characterization toll to understand failure mechanism in different battery systems with focus on high voltage high-energy cathode (230mAh/g).

For most of battery systems, there is a significant reactivity both at the bulk and the interface of electrodes that are not well understood and are the major cause of both poor cycle life, poor safety and poor efficiency. The first year of this project focus on developing advanced in-situ techniques at ANL, BNL and PNNL in collaboration with our Chinese partners at Tsinghua University, Xiamen University, Peking University and BIT by making use of the advanced user facilities at the above organizations. The techniques developed includes synchrotron-based in situ X-ray techniques (x-ray diffraction, hard and soft x-ray absorption) with other imaging and spectroscopic tools such as high resolution transmission electron microscopy (HRTEM), Scanning transmission electron microscopy (STEM), mass spectroscopy (MS), X-Ray fluorescence microscopy (XRF) and transmission x-ray microscopy (TXM). We uses the time-resolved x-ray diffraction TR-XRD and absorption (TR-XAS) developed at ANL and BNL to study the kinetic properties of electrode materials with structural sensitivity (TR-XRD) and elemental selectivity (TR-XAS). In-situ XANES is used to monitor oxidation state of active metal ions in cathode. This techniques can be used to understand failure mechanism of high voltage, and high energy cathode which will help us develop high capacity high voltage and stable cathode. Another important issue is the thermal stability of new cathode materials which is closely related to the safety of the batteries. This problem is studied using the combined TR-XRD, TR-XAS with mass spectroscopy (MS). This project also proposes to develop a novel in situ X-ray fluorescence (XRF) microscopy combined with X-ray absorption spectroscopy (XAS) technique, which will enable us to track the morphology and chemical state changes of the electrodes and the SEI layer formation and decomposition during cycling.

Task 2 Characterization of Silicon-Based Anode Materials and their Solid-Electrolyte Interphase (SEI)

This work is to investigate Si-based material as the anode including development of in-depth understanding of the SEI protective layer that can be formed on these materials and characterization of the lithium alloying properties of the bulk that will influence the formation of the SEI layers. Finding electrolytes additives that can provide a good protective SEI for silicon-based anodes, as well as operate at higher voltages, would provide for stable cycling performance needed for high energy and high power lithium ion batteries for PHEV and EV applications. The team combine characterization of silicon anode material, electrolytes and electrolyte additives to meet the desired criteria for high energy density Li ion batteries. For the characterization of SEI properties and formation mechanisms on the Si anode materials, we have access to and expertise in the following techniques: SEM, TEM, AFM and STEM Scanning electron microscopy (SEM), transmission electron microscopy (TEM), and scanning tunneling electron microscopy (STEM) are available through the electron microscopy center (EMC) and CNM. Atomic force microscopy (AFM) with electrochemical capability is available in our group. AFM study inside of a dry box is possible. The AFM can be used to study the formation of SEI layer, its thickness, morphology, and mechanical strength, etc.

XPS and SIMS Analysis X-ray photoelectron spectroscopy (XPS) is an ideal tool for surface characterization. Survey scans and high-resolution scans of the Si 2p, C 1s, O 1s, F 1s, Li 1s, and P 2p energy spectra are very informative for the identification of the compounds present on the surface, especially the solid electrolyte interface (SEI). Secondary ion mass spectrometry (SIMS) is a technique to analyze the composition of solid surfaces and thin films by sputtering the surface of the specimen with a focused primary ion beam and collecting and analyzing ejected secondary ions. These secondary ions are measured with a mass spectrometer to determine the elemental, isotopic, or molecular composition of the surface and films. SIMS is the most sensitive surface and thin film analysis technique, being able to detect elements present in the parts per billion range.

XANES X-ray absorption at near edge spectroscopy (XANES) of Si K-edge on a serial of discharge and charge Si-based samples can be carried out at Canadian Light Source (CLS). Our preliminary results using the

XANES technique showed that the Si-containing species are involved in the SEI formation over Si anode, but it seems that the Si-containing SEI is dependent of the discharge and charge process, i.e., the potential applied.

Results

Sodium-ion batteries (SIBs) have been considered as one of the promising power source candidates for the stationary storage industries owing to the much lower cost of sodium than lithium. It is well-known that the electrode materials largely determine the energy density of the battery systems. The team performed a comparative understanding on the structural changes of porous cobalt oxide during its electrochemical lithiation and sodiation process by in operando synchrotron small angel X-ray scattering, X-ray diffraction, and X-ray absorption spectroscopy. It was found that compared to the lithiation process, the porous cobalt oxide undergoes less pore structure changes, oxidation state, and local structure changes as well as crystal structure evolution during its sodiation process, which is attributed to the intrinsic low sodiation activity of cobalt oxide as evidenced by ab initio molecular dynamics simulations. Moreover, it was indicated that the sodiation activity of metal sulfides is higher than that of metal oxides, indicating a better candidate for SIBs. Such understanding is crucial for future design and improvement of high-performance electrode materials for SIBs. This paper has been published by Nano Letters.

Cathode materials are critical to the energy density, power density and safety of sodium-ion batteries (SIBs). Argonne team performed a comprehensive study in collaboration with Microvast, Xiamen University to elucidate and exemplify the interplay mechanism between phase structures, interfacial microstrain and electrochemical properties of layered-structured $Na_xNi_{1/3}Co_{1/3}Mn_{1/3}O_2$ cathode materials for high voltage SIBs. The electrochemical test results showed that $Na_xNi_{1/3}Co_{1/3}Mn_{1/3}O_2$ with an intergrowth P2/O3/O1 structure demonstrates better electrochemical performance and better thermal stability than $Na_xNi_{1/3}Co_{1/3}Mn_{1/3}O_2$ with P2/O3 binary-phase integration and $Na_xNi_{1/3}Co_{1/3}Mn_{1/3}O_2$ where only the P phase is dominant. This result is caused by the distinct interfacial microstrain development during the synthesis and cycling of the P2/O3/O1 phase. In operando high energy X-ray diffraction further revealed that the intergrowth P2/O1/O3 cathode can inhibit the irreversible P2–O2 phase transformation and simultaneously improve the structure stability of the O3 and O1 phases during cycling. The team believe that interfacial microstrain can serve as an indispensable bridge to guide future design and synthesis of high performance SIB cathode materials and other high energy battery materials.

$Li_2Ru_{0.5}Mn_{0.5}O_3$, a high capacity lithium rich layered cathode material for lithium-ion batteries, was subject to comprehensive diagnostic studies including in situ/ex situ X-ray diffraction (XRD), X-ray absorption spectroscopy (XAS), pair distribution function (PDF) and high resolution scanning transmission electron microscopy (STEM) analysis, to understand the correlations between transition metal chemistry, structure and lithium storage electrochemical behavior. Ru-Ru dimers have been identified in the as-prepared sample and found to be preserved upon prolonged cycling. Presence of these dimers, which are likely caused by the delocalized nature of 4d electrons, is found to favor the stabilization of the structure in a layered phase. The in situ XAS results confirm the participation of oxygen redox into the charge compensation at high charge voltage, and the great flexibility of the covalent bond between Ru and O may provide great reversibility of the global structure despite of the significant local distortion around Ru. In contrast, the local distortion around Mn occurs at low discharge voltage and is accompanied by a "layered to 1T" phase transformation, which is found to be detrimental to the cycle performances. It is clear that the changes of local structure around individual transition metal cations respond separately and differently to lithium intercalation/de-intercalation. Cations with the capability to tolerate the lattice distortion will benefit for maintaining the integrality of the crystal structure and therefore is able to enhance the long-term cycling performance of the electrode materials.

Conclusions

1. It was found that compared to the lithiation process, the porous cobalt oxide undergoes less pore structure changes, oxidation state, and local structure changes as well as crystal structure evolution during its sodiation process, which is attributed to the intrinsic low sodiation activity of cobalt oxide as evidenced by ab initio molecular dynamics simulations.

2. The electrochemical test results showed that $Na_xNi_{1/3}Co_{1/3}Mn_{1/3}O_2$ with an intergrowth P2/O3/O1 structure demonstrates better electrochemical performance and better thermal stability than $Na_xNi_{1/3}Co_{1/3}Mn_{1/3}O_2$ with P2/O3 binary-phase integration and $Na_xNi_{1/3}Co_{1/3}Mn_{1/3}O_2$ where only the P phase is dominant. This result is caused by the distinct interfacial microstrain development during the synthesis and cycling of the P2/O3/O1 phase.

3. In situ XAS results confirm the participation of oxygen redox into the charge compensation at high charge voltage, and the great flexibility of the covalent bond between Ru and O may provide great reversibility of the global structure despite of the significant local distortion around Ru.

Key Publications

1. Zheng, J.X., et al., Tuning of Thermal Stability in Layered Li(NixMnyCoz)O2. Journal of the American Chemical Society, 2016. 138 (40): p. 13326-13334.

2. Zhang, Y., et al., Mg-Enriched Engineered Carbon from Lithium-Ion Battery Anode for Phosphate Removal. ACS Applied Materials & Interfaces, 2016. 8(5): p. 2905-2909.

3. Zhang, Y., et al., Mesocarbon Microbead Carbon-Supported Magnesium Hydroxide Nanoparticles: Turning Spent Li-ion Battery Anode into a Highly Efficient Phosphate Adsorbent for Wastewater Treatment. Acs Applied Materials & Interfaces, 2016. 8(33): p. 21315-21325.

4. Zhan, C., et al., Tuning the Mn Deposition on the Anode to Improve the Cycle Performance of the Mn-Based Lithium Ion Battery. Advanced Materials Interfaces, 2016. 3(11).

5. Xu, Y.F., et al., RuO2 nanoparticles supported on MnO2 nanorods as high efficient bifunctional electrocatalyst of lithium-oxygen battery. Nano Energy, 2016. 28: p. 63-70.

6. Jun Lu, Tianpin Wu, Khalil Amine, "State-of-the-art Characterization Techniques for Understanding and Developing Advanced Lithium-ion Batteries", Nature Energy, 2, 17011, 2017.

7. Soroosh Sharifi-Asl, Fernando A Soto, Anmin Nie, Yifei Yuan, Hasti Asayesh-Ardakani, Tara Foroozan, Vitaliy Yurkiv, Boao Song, Farzad Mashayek, Robert F Klie, Khalil Amine, Jun Lu, Perla B Balbuena, Reza Shahbazian-Yassar, "Facet-Dependent Thermal Instability in LiCoO2", Nano Lett., 17(4), 12165-2171, 2017.

8. Ying Bai, Xingzhen Zhou, Chun Zhan, Lu Ma, Yifei Yuan, Chuan Wu, Mizi Chen, Guanghai Chen, Qiao Ni, Feng Wu, Reza Shahbazian-Yassar, Tianpin Wu, Jun Lu, Khalil Amine, "3D Hierarchical nano-flake/micro-flower iron fluoride with hydration water induced tunnels for secondary lithium battery cathodes", Nano Energy, 32, 10-18, 2017

9. Ran Tao, Xuanxuan Bi, Shu Li, Ying Yao, Feng Wu, Qian Wang, Cunzhong Zhang, Jun Lu, "Kinetics Tuning the Electrochemistry of Lithium Dendrites Formation in Lithium Batteries through Electrolytes", ACS Applied Materials & Interfaces, 9(8), 7003-7008, 2017

10. Jiaxin Zheng, Jun Lu, Khalil Amine, Feng Pan, "Depolarization effect to enhance the performance of lithium ions batteries", Nano Energy, 33, 497-507, 2017.

11. Guoqiang Tan, Wurigumula Bao, Yifei Yuan, Zhun Liu, Reza Shahbazian-Yassar, Feng Wu, Khalil Amine, Jing Wang, Jun Lu, "Freestanding highly defect nitrogen-enriched carbon nanofibers for lithium ion battery thin-film anodes", Journal of Materials Chemistry A, 5, 5532-5540, 2017.

12. Ogechi Ogoke, Gang Wu, Xianliang Wang, Anix Casimir, Lu Ma, Tianpin Wu, Jun Lu, "Effective strategies for stabilizing sulfur for advanced lithium–sulfur batteries", Journal of Materials Chemistry A, 5, 448-469, 2017.

13. Xu, G. L.; Sheng, T.; Chong, L. N.; Ma, T. Y.; Sun, C. J.; Zuo, X. B.; Liu, D. J.; Ren, Y.; Zhang, X. Y.; Liu, Y. Z.; Heald, S. M.; Sun, S. G.; Chen, Z. H.; Amine, K. Insights into the Distinct Lithiation/Sodiation of Porous Cobalt Oxide by in Operando Synchrotron X-ray Techniques and Ab Initio Molecular Dynamics Simulations. Nano Letters 2017, 17, 953-962.

14. Xu, G. L.; Amine, R.; Xu, Y. F.; Liu, J. Z.; Gim, J.; Ma, T. Y.; Ren, Y.; Sun, C. J.; Liu, Y. Z.; Zhang, X. Y.; Heald, S. M.; Solhy, A.; Saadoune, I.; Mattis, W. L.; Sun, S. G.; Chen, Z. H.; Amine, K. Insights into the structural effects of layered cathode materials for high voltage sodium-ion batteries. Energy & Environmental Science 2017, 10, 1677-1693.

15. Lyu, Y. C.; Hu, E. Y.; Xiao, D. D.; Wang, Y.; Yu, X. Q.; Xu, G. L.; Enrlich, S. N.; Amine, K.; Gu, L.; Yang, X. Q.; Li, H. Correlations between Transition Metal Chemistry, Local Structure and Global Structure in Li2Ru0.5Mn0.5O3 Investigated in a Wide Voltage Window. Chemistry of Materials 2017, DOI: 10.1021/acs.chemmater.7b02299.

16. Yandong Duan, Bingkai Zhang, Jiaxin Zheng, Jiangtao Hu, Jianguo Wen, Dean J Miller, Pengfei Yan, Tongchao Liu, Hua Guo, Wen Li, Xiaohe Song, Zengqing Zhuo, Chaokun Liu, Hanting Tang, Rui Tan, Zonghai Chen, Yang Ren, Yuan Lin, Wanli Yang, Chongmin Wang, Lin-Wang Wang, Jun Lu, Khalil Amine, Feng Pan, "Excess Li-ion storage on reconstructed surfaces of nanocrystals to boost battery performance", Nano Letters, ASAP, 2017.

(This page intentionally left blank)

(This page intentionally left blank)